A Continuum Robotic Platform for Endoscopic Non-Contact Laser Surgery: Design, Control, and Preclinical Evaluation

Von der Fakultät für Maschinenbau
der Gottfried Wilhelm Leibniz Universität Hannover
zur Erlangung des akademischen Grades
Doktor-Ingenieur
genehmigte

Dissertation

von
Dipl.-Ing. Dennis Kundrat

2022

Acknowledgement

Foremost, I would like to thank my supervisor Prof. Dr.-Ing. Tobias Ortmaier for the great opportunity to join the outstanding team of the European research project μRALP, for his scientific and personal advices, and the possibility to let this thesis be an integral part of my time as a research assistant at the Institute of Mechatronic Systems (imes) at Leibniz Universität Hannover.

Furthermore, I particularly thank my outstanding research colleague Andreas Schoob for many discussions, whiteboard brainstorming, paper sessions, and a lot of travelling around Europe. This was real teamwork and fun! Your work was essential and I owe you much.

The medical technology group members Jakob F. Fast, Samuel Müller, Jan Bergmeier, Sontje Ihler, and Max H. Laves have affected and improved my work with weekly discussions as well as their participation in user studies. This also applies to my outstanding Master student Thomas Piskon. You did a great job! I also wish to thank Lüder A. Kahrs for his advice.

The European project has significantly broadened my horizon. This was mainly due to the outstanding collaboration with my Italian and French colleagues at the Italian Institute of Technology (IIT) in Genova and the FEMTO-ST in Besançon. Many thanks to Leonardo De Mattos and Nicolas Andreff and their team members for many collaborative hours of professional work and enjoyable social events in Italy, France, and the UK.

I further thank my medical colleagues Patrick Schuler, Daniel T. Friedrich, and René Grässlin from Ulm University Medical Centre for their support, great input, and social activities. You helped me a lot and I hope we can continue our collaboration!

I thank everyone at imes for establishing a friendly and productive working environment. In particular, Daniel Kaczor, Kai Eggers, Zygimantas Ziaukas, Steffen Bosselmann, and Tobias Frank have enriched my life with many table football hours. Mauro H. Riva and Svenja Spindeldreier were always available for fruitful discussions.

Thanks to Maria and Jack for the quick proofreading session!

Braunschweig   *Dennis Kundrat*

Kurzfassung

Die Anwendung von Lasertechnologien in chirurgischen Interventionen hat sich aufgrund der atraumatischen Eigenschaften in der Klinik etabliert. Neben manueller Applikation von fasergeführten Lasern mit Gewebekontakt hat sich die kontaktfreie transorale Lasermikrochirurgie (TLM) von Tumoren des Larynx in der HNO-Chirurgie durchgesetzt. Die TLM erfordert zur Tumorresektion jedoch ein langjähriges chirurgisches Training, um die Funktion der angrenzenden Organe zu sichern und damit die Lebensqualität der Patienten zu erhalten. Die Positionierung des mikroskopischen Laserapplikators außerhalb des Patienten kann zudem die direkte Sicht auf das Zielgebiet durch anatomische Variabilität erschweren und den Arbeitsraum einschränken. Weitere klinische Herausforderungen betreffen die Positionierung des Laserfokus auf der Gewebeoberfläche, die Bildgebung, die Planung und Ausführung der Laserablation sowie intraoperative Bewegungen des Zielgebietes. Die vorliegende Dissertation zielt darauf ab, die Limitierungen der TLM durch robotische Ansätze und intraoperative Assistenz zu adressieren. Obwohl ein Trend zur minimal invasiven Chirurgie besteht, sind bislang keine hochintegrierten Plattformen für die endoskopische Applikation fokussierter Laserstrahlung verfügbar. Ebenfalls sind keine Systeme bekannt, die Szeneninformationen aus der endoskopischen Bildgebung in die Ablationsplanung und -ausführung einbeziehen. Für eine situsnahe Fokussierung des Laserstrahls wird in dieser Arbeit zunächst eine miniaturisierte Fokussieroptik zur Integration in endoskopische Systeme vorgestellt. Experimentelle Versuche charakterisieren die optischen Eigenschaften und das Ablationsverhalten. Zur Manipulation der Fokussieroptik wird eine robotische Plattform realisiert. Diese basiert auf einem längenveränderlichen Kontinuumsmanipulator. Letzterer ermöglicht in Kombination mit einer mechatronischen Aktuierungseinheit Bewegungen des Endoskopkopfes in fünf Freiheitsgraden. Die kinematische Modellierung und Regelung des Systems werden in ein modulares Framework eingebunden und evaluiert. Die Manipulation fokussierter Laserstrahlung erfordert zudem eine präzise Anpassung der Fokuslage auf das Gewebe. Dafür werden visuelle, haptische und visuell-haptische Assistenzfunktionen eingeführt. Diese unterstützen den Anwender bei Teleoperation zur Einstellung eines optimalen Arbeitsabstandes. In einer Anwenderstudie werden Vorteile der visuell-haptischen Assistenz nachgewiesen. Die Systemperformanz und Gebrauchstauglichkeit des robotischen Gesamtsystems werden in einer weiteren Anwenderstudie untersucht. Analog zu einem klinischen Einsatz verfolgen die Probanden mit einem Laserspot vorgegebene Sollpfade. Die mittlere Positioniergenauigkeit des Spots beträgt dabei 0,5 mm. Zur Automatisierung der Ablation werden abschließend Methoden der bildgestützten Regelung vorgestellt. Experimente bestätigen einen positiven Effekt der Automationskonzepte für die kontaktfreie Laserchirurgie.

Schlagwörter: Kontinuumsrobotik, Laserchirurgie, Stereobildgebung, Deformationstracking, Laserablation, Bildbasierte Regelung, Anwenderstudie, Intraoperative Assistenz.

Abstract

The application of laser technologies in surgical interventions has been accepted in the clinical domain due to their atraumatic properties. In addition to manual application of fibre-guided lasers with tissue contact, non-contact transoral laser microsurgery (TLM) of laryngeal tumours has been prevailed in ENT surgery. However, TLM requires many years of surgical training for tumour resection in order to preserve the function of adjacent organs and thus preserve the patient's quality of life. The positioning of the microscopic laser applicator outside the patient can also impede a direct line-of-sight to the target area due to anatomical variability and limit the working space. Further clinical challenges include positioning the laser focus on the tissue surface, imaging, planning and performing laser ablation, and motion of the target area during surgery. This dissertation aims to address the limitations of TLM through robotic approaches and intraoperative assistance. Although a trend towards minimally invasive surgery is apparent, no highly integrated platform for endoscopic delivery of focused laser radiation is available to date. Likewise, there are no known devices that incorporate scene information from endoscopic imaging into ablation planning and execution. For focusing of the laser beam close to the target tissue, this work first presents miniaturised focusing optics that can be integrated into endoscopic systems. Experimental trials characterise the optical properties and the ablation performance. A robotic platform is realised for manipulation of the focusing optics. This is based on a variable-length continuum manipulator. The latter enables movements of the endoscopic end effector in five degrees of freedom with a mechatronic actuation unit. The kinematic modelling and control of the robot are integrated into a modular framework that is evaluated experimentally. The manipulation of focused laser radiation also requires precise adjustment of the focal position on the tissue. For this purpose, visual, haptic and visual-haptic assistance functions are presented. These support the operator during teleoperation to set an optimal working distance. Advantages of visual-haptic assistance are demonstrated in a user study. The system performance and usability of the overall robotic system are assessed in an additional user study. Analogous to a clinical scenario, the subjects follow predefined target patterns with a laser spot. The mean positioning accuracy of the spot is 0.5 mm. Finally, methods of image-guided robot control are introduced to automate laser ablation. Experiments confirm a positive effect of proposed automation concepts on non-contact laser surgery.

Keywords: continuum robotics, laser surgery, stereo vision, deformation tracking, laser ablation, image-based control, user studies, intraoperative assistance, extensible manipulator.

Contents

Nomenclature

Notation Standards

Scalar	Lower or upper case (italics): a, A
Matrix	Lower or upper case (bold and italics): $\boldsymbol{a}$, $\boldsymbol{A}$

Coordinate Frames

$(\mathrm{CF})_\mathrm{B}$	Frame of the robotic base
$(\mathrm{CF})_\mathrm{CM}$	Frame of the coordinate measurement machine
$(\mathrm{CF})_\mathrm{E}$	Frame of the robotic end effector
$(\mathrm{CF})_\mathrm{FS}$	Frame of the force sensor
$(\mathrm{CF})_i$	Intermediate segmental frame i of the continuum kinematics
$(\mathrm{CF})_\mathrm{L}$	Frame of the left stereoscopic camera
$(\mathrm{CF})_\mathrm{LI}$	Frame of the left stereoscopic image
$(\mathrm{CF})_\mathrm{LS}$	Frame of the laser focus
$(\mathrm{CF})_\mathrm{M}$	Frame of the master base
$(\mathrm{CF})_\mathrm{O}$	Frame of the optical axis centre
$(\mathrm{CF})_\mathrm{OB}$	Frame of the optical base marker
$(\mathrm{CF})_\mathrm{OE}$	Frame of the optical end effector marker
$(\mathrm{CF})_\mathrm{R}$	Frame of the right stereoscopic camera
$(\mathrm{CF})_\mathrm{RI}$	Frame of the right stereoscopic image
$(\mathrm{CF})_\mathrm{S}$	Frame of the master stylus
$(\mathrm{CF})_\mathrm{T}$	Frame of the surgical target
$(\mathrm{CF})_\mathrm{TB}$	Frame of the tracking base marker
$(\mathrm{CF})_\mathrm{TC}$	Frame of the tracking camera
$(\mathrm{CF})_\mathrm{TE}$	Frame of the tracking end effector marker
$(\mathrm{CF})_\mathrm{W}$	Frame of the world environment

Roman Symbols

$\boldsymbol{a}$	Skew vector
A	Area
A_px	Area per pixel

A_w	Spot area of an incident laser beam
AP_p	Accuracy according to ISO 9283
b	Camera baseline
$\boldsymbol{b}$	Skew vector
b_min	Minimum camera baseline
$b_{\mathrm{TF},i}$	Diameter of tube feeding component i
$\boldsymbol{c}_\mathrm{L}$	Principle point of the left camera
c_tis	Specific heat capacity of a tissue sample
C_{10}	Primary material parameter of Mooney-Rivlin law
C_{11}	Secondary material parameter of Mooney-Rivlin law
$\boldsymbol{C}_\mathrm{L}$	Intrinsic camera matrix of the left camera
d	Disparity
d_co	Diameter of the fibre core material
d_lo	Laser optics diameter
d_m	Inner manipulator diameter
d_s	Diameter of imaging sensor
d_SD	Spindle diameter
d_t	Diameter of endoscopic tip
$\boldsymbol{D}$	Depth map
D_m	Outer manipulator diameter
e_FP	Focal position error
e_PT	Path tracing error
$\boldsymbol{e}_\mathrm{PT}$	Vector of path tracing errors
e_T	Tracking error
e_TP	Total path error
$\boldsymbol{e}_\mathrm{TP}$	Vector of total path errors
E	Irradiance of an incident laser beam
$\boldsymbol{E}$	Essential matrix
E_i	Energy state of gain medium level i
f	Focal length of an optical system
f_0	Frequency of an incoming electromagnetic wave
$\boldsymbol{f}_\mathrm{AC}$	Active constraints forces
$\boldsymbol{f}_\mathrm{H}$	Haptic forces
$\boldsymbol{f}_\mathrm{L}$	Focal lengths of the left camera
f_P	Laser pulse frequency
$\boldsymbol{f}(\Delta\boldsymbol{x}_\mathrm{S})$	Virtual friction forces evaluated at the current residual master position
$\boldsymbol{F}$	Fundamental matrix
F_P	Radiant exposure of a pulsed laser beam
F_SD	Axial force of a spindle drive

F_{T}	Normal force transmitted to actuation tube
FPE	Focal position error
FRE	Fiducial registration error
$\hbar$	Reduced Planck's constant
$\boldsymbol{h}$	Unit quaternion
$\boldsymbol{h}_{\mathrm{AF}}$	Activation function of the secondary task
h_{S}	Projected distance of the segmental end effector
$\boldsymbol{H}_{\mathrm{T}}$	Transformation matrix
i_{rg}	Reduction gear ratio
$\boldsymbol{I}$	Identity matrix
$\boldsymbol{I}_{\mathrm{BP}}$	Binary map of the left camera
I_{D}	Diode current
$\boldsymbol{I}_{\mathrm{L}}$	Image of the left camera
$\boldsymbol{I}_{\mathrm{LC}}$	Binary map of the left camera with laser centroid
$\boldsymbol{I}_{\mathrm{LS}}$	Motion-compensated image of the left camera
$I(z)$	Optical intensity evaluated at position z
$\boldsymbol{J}$	Jacobian matrix
$\boldsymbol{J}_{q\psi}(\boldsymbol{\psi})$	Segmental Jacobian for configuration to joint space mapping
$\boldsymbol{J}_{x\psi}(\boldsymbol{\psi})$	Segmental Jacobian for configuration to task space mapping
$\hat{\boldsymbol{J}}^{*}_{x\psi}(\boldsymbol{\psi}^{*})$	Composed Jacobian for configuration to task space mapping
$\hat{\boldsymbol{J}}_{x\psi}(\boldsymbol{\psi}^{*})$	Composed and reduced Jacobian for configuration to task space mapping
$\hat{\boldsymbol{J}}^{*}_{q\psi}(\boldsymbol{\psi}^{*})$	Composed Jacobian for configuration to joint space mapping
J_{P}	Intensity of a laser pulse
k_{x}, k_{y}, k_{z}	Haptic Cartesian degrees of stiffness
$\boldsymbol{K}_{\mathrm{C}}$	Gain matrix of the kinematics controller
ℓ_{c}	Length of sensor coverage
ℓ_{F}	Length of fibre segment
ℓ_{mc}	Origin of stereo camera overlap
ℓ_{TF}	Length of actuation tube guidance
L	Segmental length
L_{0}	Initial segmental length
$\boldsymbol{L}_{\mathrm{lim}}$	Limits of segmental length
L_{min}	Minimum of segmental length
L_{max}	Maximum of segmental length
m_{tis}	Mass of a tissue sample
M^{2}	Quality index for laser beams
$\boldsymbol{M}_{\mathrm{L}}$	Projection matrix of the left camera
$\boldsymbol{M}_{\mathrm{LS}}$	Measurement matrix of laser positions
$\boldsymbol{M}_{\mathrm{N}}$	Nominal motor torque

n_0	Refractive index of the ambient medium
n_{air}	Refractive index of air
n_{co}	Refractive index of the fibre core material
n_{cl}	Refractive index of the fibre cladding material
n_{N}	Nominal motor revolutions
n_{tis}	Refractive index of tissue
N_{AVG}	Windows size of moving average filter
N_{E}	Number of exited states in a gain medium
N_{G}	Population of equidistant grid points
N_{ψ}	Dimension of the configuration space
N_q	Dimension of the joint space
N_{S}	Number of laser scanning passes
NA	Numerical aperture
O_{p}	Pulse overlap
p_{SD}	Lead of a spindle drive
P_{avg}	Average power of laser source
$P_{\mathrm{F,in}}$	Laser power input to fibre segment
$P_{\mathrm{F,out}}$	Laser power output from fibre segment
$\boldsymbol{P}_{\mathrm{K}}$	Kernel projection matrix
$P_{\max}$	Peak power of laser source
$_{(\mathrm{LI})}\boldsymbol{p}$	2D position of the visible laser spot with respect to $(\mathrm{CF})_{\mathrm{LI}}$
$_{(\mathrm{LI})}\boldsymbol{p}$	2D position with respect to $(\mathrm{CF})_{\mathrm{LI}}$
$_{(\mathrm{LI})}\hat{\boldsymbol{p}}$	Homogeneous 2D position with respect to $(\mathrm{CF})_{\mathrm{LI}}$
P_{T}	Laser power threshold
$_{(\mathrm{RI})}\boldsymbol{p}$	2D position with respect to $(\mathrm{CF})_{\mathrm{RI}}$
$_{(\mathrm{RI})}\hat{\boldsymbol{p}}$	Homogeneous 2D position with respect to $(\mathrm{CF})_{\mathrm{RI}}$
$_{(\mathrm{LI})}\boldsymbol{p}_{\mathrm{LS}}$	2D laser spot position with respect to $(\mathrm{CF})_{\mathrm{LI}}$
$_{(\mathrm{LI})}\boldsymbol{p}_{\mathrm{T}}$	2D position of target grip point with respect to $(\mathrm{CF})_{\mathrm{LI}}$
$_{(\mathrm{B})}\boldsymbol{P}$	3D position with respect to $(\mathrm{CF})_{\mathrm{B}}$
$_{(\mathrm{L})}\boldsymbol{P}$	3D position with respect to $(\mathrm{CF})_{\mathrm{L}}$
$_{(\mathrm{L})}\hat{\boldsymbol{P}}$	Homogeneous 3D position with respect to $(\mathrm{CF})_{\mathrm{L}}$
$_{(\mathrm{L})}\boldsymbol{P}_{\mathrm{LC}}$	3D position of the detected laser centroid with respect to $(\mathrm{CF})_{\mathrm{L}}$
$_{(\mathrm{L})}\boldsymbol{P}_{\mathrm{LS}}$	3D position of the laser spot with respect to $(\mathrm{CF})_{\mathrm{L}}$
$_{(\mathrm{L})}\boldsymbol{P}_{\mathrm{NP}}$	3D nominal laser spot positions with respect to $(\mathrm{CF})_{\mathrm{L}}$
P_{T}	Laser power threshold
$_{(\mathrm{L})}\boldsymbol{P}_{\mathrm{T}}$	3D position of target grid point with respect to $(\mathrm{CF})_{\mathrm{L}}$
PTE	Consolidated path tracing error
$\boldsymbol{q}$	Joint space
q_j	State of joint j

$\dot{q}_j$	Velocity of joint j
$q_{\mathrm{mot},j}$	State of drive j
$\dot{q}_{\mathrm{mot},j}$	Velocity of drive j
$\dot{\boldsymbol{q}}_{\mathrm{P}}$	Joint velocities of the primary task
$\dot{\boldsymbol{q}}_{\mathrm{S}}$	Joint velocities of the secondary task
Q_{P}	Energy of a laser pulse
r_{TF}	Radial distance of actuation tubes
r_{S}	Radial distance between manipulator centre and actuation tube
r_{ST}	Smoothstep radius
R_{M}	Laser mirror reflectivity
R_{S}	Segmental bending radius
RP	Precision according to ISO 9283
$^{\mathrm{B}}\boldsymbol{R}_{\mathrm{E}}$	Rotation matrix from $(\mathrm{CF})_{\mathrm{E}}$ to $(\mathrm{CF})_{\mathrm{B}}$
$^{\mathrm{L}}\boldsymbol{R}_{\mathrm{R}}$	Rotation matrix from $(\mathrm{CF})_{\mathrm{R}}$ to $(\mathrm{CF})_{\mathrm{L}}$
$^{\mathrm{M}}\boldsymbol{R}_{\mathrm{S}}$	Rotation matrix from $(\mathrm{CF})_{\mathrm{S}}$ to $(\mathrm{CF})_{\mathrm{M}}$
$^{\mathrm{L}}\boldsymbol{R}_{\mathrm{T}}$	Rotation matrix from $(\mathrm{CF})_{\mathrm{T}}$ to $(\mathrm{CF})_{\mathrm{L}}$
$\boldsymbol{R}_y$	Elementary rotation matrix about y-axis
$\boldsymbol{R}_z$	Elementary rotation matrix about z-axis
s	Optical scaling factor
s_{SD}	Safety factor for spindle drive design
$\boldsymbol{S}_{\mathrm{E}}$	Jacobian selection matrix
$\boldsymbol{S}_{\mathrm{M}}$	Scaling matrix of master workspace
t	Time
t_{c}	Control loop cycle time
t_{e}	Exposure time
$_{(\mathrm{B})}\boldsymbol{t}_{\mathrm{E}}$	Translation vector of $(\mathrm{CF})_{\mathrm{E}}$ associated to $(\mathrm{CF})_{\mathrm{B}}$
$_{(\mathrm{L})}\boldsymbol{t}_{\mathrm{LB}}$	Parametric representation of the laser beam with respect to $(\mathrm{CF})_{\mathrm{L}}$
$_{(\mathrm{L})}\boldsymbol{t}_{\mathrm{R}}$	Translation vector of $(\mathrm{CF})_{\mathrm{R}}$ associated to $(\mathrm{CF})_{\mathrm{L}}$
$_{(\mathrm{LI})}\boldsymbol{t}_{\mathrm{NP}}$	2D nominal path with respect to $(\mathrm{CF})_{\mathrm{LI}}$
$_{(\mathrm{L})}\boldsymbol{t}_{\mathrm{LC}}$	3D laser centroid tracing trajectory with respect to $(\mathrm{CF})_{\mathrm{L}}$
$^{\mathrm{B}}\boldsymbol{T}_{\mathrm{E}}$	Homogeneous transformation from $(\mathrm{CF})_{\mathrm{E}}$ to $(\mathrm{CF})_{\mathrm{B}}$
$^{\mathrm{TC}}\boldsymbol{T}_{\mathrm{TB}}$	Homogeneous transformation from $(\mathrm{CF})_{\mathrm{TB}}$ to $(\mathrm{CF})_{\mathrm{TC}}$
$^{\mathrm{TC}}\boldsymbol{T}_{\mathrm{TE}}$	Homogeneous transformation from $(\mathrm{CF})_{\mathrm{TE}}$ to $(\mathrm{CF})_{\mathrm{TC}}$
$^{\mathrm{E}}\boldsymbol{T}_{\mathrm{L}}$	Homogeneous transformation from $(\mathrm{CF})_{\mathrm{L}}$ to $(\mathrm{CF})_{\mathrm{E}}$
$^{\mathrm{CM}}\boldsymbol{T}_{\mathrm{TE}}$	Homogeneous transformation from $(\mathrm{CF})_{\mathrm{TE}}$ to $(\mathrm{CF})_{\mathrm{CM}}$
$^{\mathrm{B}}\boldsymbol{T}_{\mathrm{TB}}$	Homogeneous transformation from $(\mathrm{CF})_{\mathrm{TB}}$ to $(\mathrm{CF})_{\mathrm{B}}$
$^{\mathrm{B}}\boldsymbol{T}_1$	Homogeneous transformation from $(\mathrm{CF})_1$ to $(\mathrm{CF})_{\mathrm{B}}$
$^{0}\boldsymbol{T}_1$	Homogeneous transformation from $(\mathrm{CF})_1$ to $(\mathrm{CF})_0$
$^{0}\boldsymbol{T}_2$	Homogeneous transformation from $(\mathrm{CF})_2$ to $(\mathrm{CF})_0$

${}^{1}\boldsymbol{T}_{2}$	Homogeneous transformation from $(CF)_2$ to $(CF)_1$
${}^{2}\boldsymbol{T}_{E}$	Homogeneous transformation from $(CF)_E$ to $(CF)_2$
T_{P}	Laser pulse duty cycle
TCT	Task completion time
TPE	Consolidated total path error
u	Horizontal pixel coordinate
v	Vertical pixel coordinate
$v_{E,max}$	Maximum Cartesian velocity of the robotic end effector
v_{max}	Maximum axial spindle velocity
v_{scan}	Laser scanning speed
$v_{S,max}$	Maximum Cartesian velocity of the master input
$w(z)$	Beam radius evaluated at optical axis position z
w_0	Beam waist radius
$w_{max}(\psi_i)$	Sigmoid function of configuration space parameter i
w_{S}	Sensor width
x	Coordinate along Cartesian x-axis
$\boldsymbol{x}$	Task space pose
$\dot{\boldsymbol{x}}$	Task space velocities
$\boldsymbol{x}_{E}^{*}$	Nominal end effector pose
$\dot{\boldsymbol{x}}_{E}^{*}$	Nominal end effector velocities
$_{(M)}\boldsymbol{x}_{S}$	Pose of the master stylus with respect to $(CF)_M$
$_{(M)}\boldsymbol{x}_{SO}$	Stylus offset with respect to $(CF)_M$
y	Coordinate along Cartesian y-axis
z	Coordinate along Cartesian z-axis
z_{R}	Rayleigh length along optical axis z
z_0	Beam waist location
z_{T}	Triangulated depth

Greek Symbols

α_{h}	Horizontal camera sensor tilt
α_{L}	Camera sensor shear factor
α_{t}	Fibre attenuation coefficient
α_{v}	Vertical camera sensor tilt
β_{S}	Angular spacing of actuation tubes
δ	Angle of segmental bending plane
Δx_{f}	Focal increments of scanner unit
Δx_{t}	Position increments of scanner unit

ΔQ_{las}	Heat flux increment of incident laser beam
Δr	Segmental increment along radial direction
Δt	Temporal increment
ΔT	Temperature increment
Δx_{a}	Axial laser scanner increment
$\Delta \boldsymbol{x}_{\mathrm{E}}$	Residual end effector pose
Δx_{l}	Lateral laser scanner increment
ε	Singularity threshold
ε_{B}	Bending threshold
ε_{C}	Camera optimisation threshold
ε_{H}	Haptics activation threshold
η_{F}	Reflectance half-angle of fibre optic beam propagation
$\boldsymbol{\eta}_{\mathrm{IS}}$	Intersection of laser axis and surface
η_{LS}	Position of laser-surface intersection
η_{SD}	Spindle drive efficiency
γ_{F}	Incident angle of a ray to fibre optics
γ_{max}	Fibre optic acceptance angle
κ_{tis}	Tissue-specific heat conductivity
λ	Wavelength of the laser source
$\boldsymbol{\lambda}_{\mathrm{AG}}$	Adaptive gain matrix of secondary task
$\boldsymbol{\lambda}_{\mathrm{TF}}$	Tuning function matrix of secondary task
μ_0	Friction coefficient
$\mu_{\mathrm{a}}(\lambda)$	Optical absorption evaluated at wavelength λ
μ_{s}	Optical scattering coefficient
μ_{t}	Composed optical attenuation coefficient
Ω_{G}	Set of populated grid points
ρ_{tis}	Density of a tissue sample
σ_{xy}	Lateral offset in fibre optics alignment
ϕ_{h}	Horizontal sensor FoV
ϕ_{v}	Vertical sensor FoV
$\boldsymbol{\psi}$	Segmental configuration space
$\boldsymbol{\psi}^{*}$	Configuration space state of the complete manipulator
$\dot{\boldsymbol{\psi}}^{*}$	Configuration space velocities of the complete manipulator
$\boldsymbol{\psi}_{\mathrm{lim}}$	Configuration space limits
$\dot{\boldsymbol{\psi}}_{\mathrm{S}}$	Configuration space velocities of the secondary task
π	Segmental bending plane
τ_{P}	Pulse duration
τ_{SD}	Torque of the spindle drive
τ_{therm}	Thermal relaxation

θ Segmental bending angle
Θ Linear divergence angle of a laser beam
$\boldsymbol{\theta}_{\mathrm{lim}}$ Segmental bending angle limits
θ_{max} Maximum of segmental bending angle
θ_{min} Minimum of segmental bending angle

Acronyms

AC   Actuation Unit
ADI   Analysis, Design, and Interfaces
ANOVA   Analysis of Variances
AS   Active Scene Stabilisation
AU   Actuation Unit
BLDC   Brushless Direct Current
CAD   Computer Aided Design
CAM   Camera Module
CAN   Controlled Area Network
CE   Coupling Efficiency
CI   Confidence Interval
CLIK   Closed Loop Inverse Kinematics
CMM   Coordinate Measurement Machine
CNN   Convolutional Neural Network
CT   Computed Tomography
CW   Continuous Wave
DF   Depth of Field
DI   Digital Input
DK   Direct Kinematics
DLD   Direct Linear Drive
DO   Digital Output
DoF   Degree of Freedom
DZ   Damage Zone
EAP   Electroactive Polymer
EMC   Electromagnetic Compatibility
ERC   External Robotic Controller
FD   Fast Decay
FEA   Finite Element Analysis
FoV   Field of View
FPE   Focal Position Error
FWHM   Full Width at Half Maximum

GR	Graded Index
GPGPU	General Purpose Graphics Processing Unit
HMD	Head-Mounted Display
HMI	Human-Machine Interface
HSV	Hue Saturation Value
IBVS	Image-based Visual Controller
IC	Integrated Circuit
IDK	Inverse Differential Kinematics
IMC	Integrated Motion Controller
IR	Infrared
IRC	Internal Robotic Controller
IVV	Integration, Validation, and Verification
LASER	Light Amplification by Stimulated Emission of Radiation
LED	Light Emitting Diode
LMU	Linear Motion Unit
LT	Laser Transition
LVDT	Linear Variable Displacement Transducer
MDF	Medium Density Fibreboard
MEMS	Micro-Electro-Mechanical Systems
MIS	Minimally Invasive Surgery
MM	Multi Mode
MR	Mesh Refinement
MRI	Magnetic Resonance Imaging
MSM	Mechatronic System Models
NA	Numerical Aperture
NBI	Narrow Band Imaging
NOTES	Natural Orifice Transluminal Endoscopic Surgery
NS	Non-Stabilised
OEM	Original Equipment Manufacturer
OCT	Optical Coherence Tomography
OP	Optical Pumping
OR	Operating Room
PBVS	Position-based Visual Controller
PCB	Printed Circuit Board
PFC	Path Following Controller
PoC	Proof of Concept
PTC	Positive Temperature Coefficient
PTFE	Polytetrafluoroethylen
PWM	Pulse Width Modulation

RCM	Remote Center of Motion
RMS	Root Mean Square
RMSE	Root Mean Square Error
RoI	Region of Interest
SD	Standard Deviation
SM	Single Mode
SMA	Shape Memory Alloy
SNR	Signal-to-Noise Ratio
SPI	Serial Peripheral Interface
TEM	Transversal Eigenmodes
TLM	Transoral Laser Microsurgery
TLX	Task Load Index
TM	Template Matching
TRL	Technology Readiness Level
UART	Universal Asynchronous Receiver/Transmitter
UI	User Interface
VHA	Visuo Haptic Assistance
WLC	Wafer Level Camera
μRALP	Micro-Technologies & Systems for Robot-Assisted Laser Phonomicrosurgery

1 Introduction

Successful diagnosis and treatment of cancer are regarded as major societal challenges for improvement of health, decrease of mortality, demographic changes, and general wellbeing in the Western hemisphere. The prevalence of benign and malign cellular disorders is manifold and may affect various organs of the human body as highlighted in Figure 1.1a [TSWJ16]. In particular, incident rates in lung, breast, and colorectum are high (> 10%) and likewise cause high mortality (see Figure 1.1b) [BFS$^+$18]. Unfortunately, first diagnoses are frequently obtained in advanced stages due to non-specific symptoms. By contrast, disorders in the head and neck region directly impact the quality of daily life. If located in the voice box, cancerous disorders may impede breathing, voice generation, and disturb swallowing sequences [RdLvdB$^+$14]. Pathologies are macroscopically classified into three types of lesions: 1) benign cysts, polyps, or nodules that do not infiltrate the epithelium, 2) malign carcinoma that have already infiltrated the epithelium at cellular level, and 3) intermediate types that describe transition phenomena.

The laryngeal framework presented in Figure 1.2a particularly represents a challenging tortuous morphology with constrained access for surgical treatment. The larynx connects the oral cavity and pharynx with the trachea [BM11]. The anatomy is further composed of three compartments
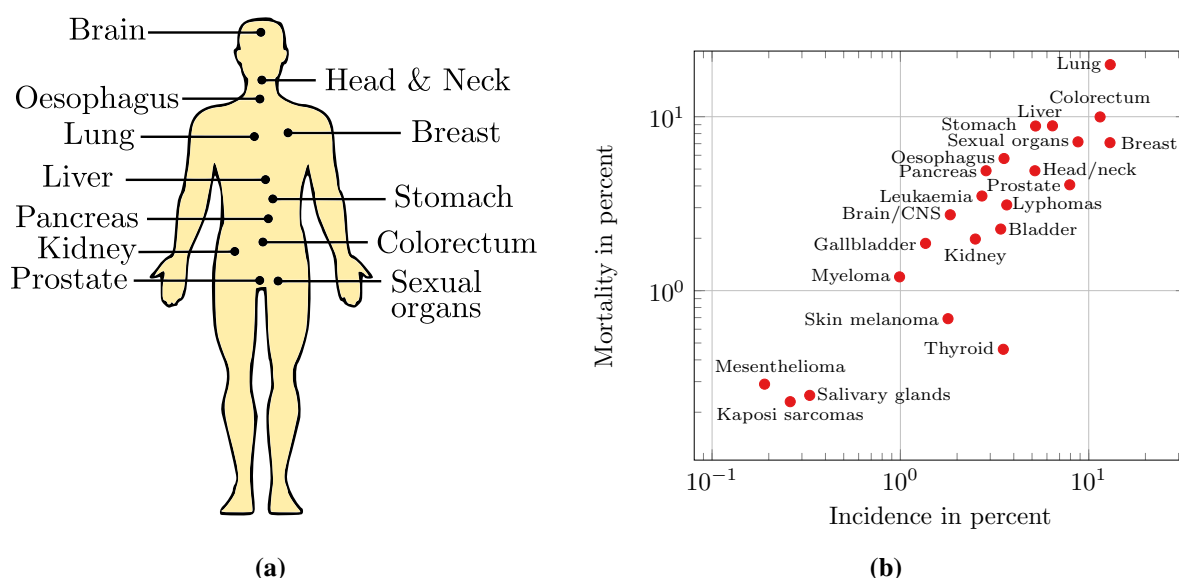
Fig. 1.1: (a) Frequent cancers in humans. (b) Cancer incidences and mortalities estimated by the International Agency for Research on Cancer in year 2018 of worldwide population (both sexes and all ages) related to the total number of records [BFS$^+$18].

with complex connections of cartilages and muscles. The vocal folds are located in the glottic compartment and show a layered anatomy of ligaments and muscle fibres. Adduction/contraction of the structure enables airway protection from foreign bodies. Beyond that, voice generation is governed by oscillation of the ligaments located in the air flow and its frequency modulation by muscular contractions. Within the domain of laryngeal cancers, glottic carcinoma are the most frequent pathology [PKW+16]. Relevant causes of head and neck cell disorders are often due to excessive smoking and regular alcohol consumption [AML+11]. Recent work has identified effects of human papillomavirus from sexual activities [Aup20]. Even though incident rates of laryngeal cancer are low compared to other cancers, the impact on life is significant. This constantly demands for novel diagnostic and therapeutic strategies to accommodate prospective challenges arising from demographic changes, especially in the Western hemisphere and high-income countries [HFS+11].

Therefore, transoral microsurgery of laryngeal cancer has been introduced to establish minimally invasive surgery (MIS) for optimised postoperative outcomes in comparison to traditional open surgery [KTD03]. This procedure has been further advanced to transoral laser microsurgery (TLM) facilitating tissue dissection under challenging conditions without physical contact and reduced surgical trauma [RA11]. Although this intervention constitutes one of the most common laser surgeries, lasers also represent a versatile instrumentation for other therapies with MIS access not only limited to cancer [AB16]. The physics behind lasers allow the same principles to be applied to a multitude of tissues using minor modifications of the system. Multiple laser systems have been studied within specific fields of medicine. In the abdomen, laser-assisted MIS procedures have been deployed to laparoscopic and natural orifice transluminal endoscopic surgery (NOTES) for resection of the pancreas [SLL+18], kidney [KKM+14, DMH+18], liver [CWT+09], prostate [BFFD+16], or stomach [SKH94]. Another example in the aerodigestive tract are oesophageal interventions [PCD87].
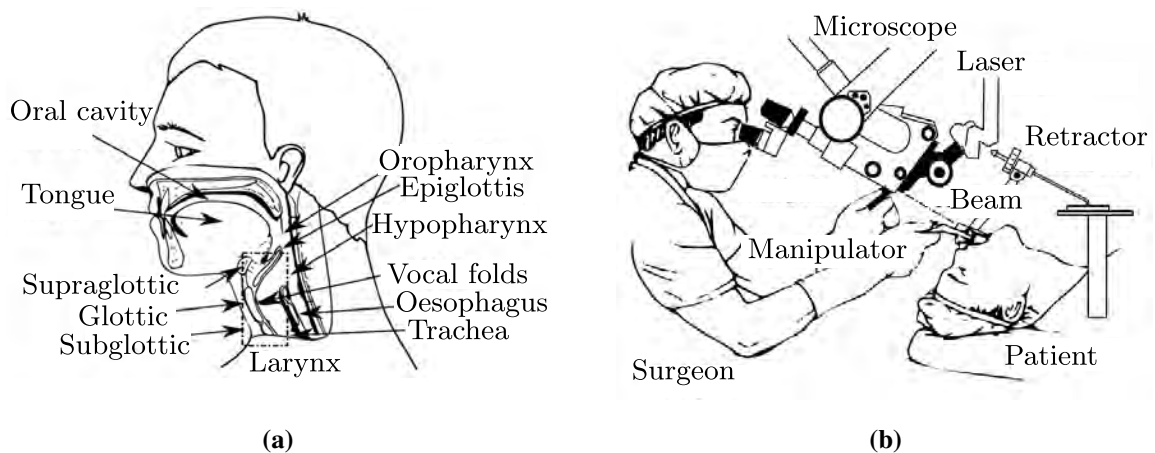
Fig. 1.2: (a) Sagittal anatomy of the human aerodigestive tract. (b) Clinical setup for transoral laser micro-surgery.

1.1 A Success Story: Transoral Laser Microsurgery

If the diagnostic workflow has indicated surgical treatment of the cancerous tissue in affected anatomy (see Figure 1.2a) from preoperative imaging with computed tomography (CT) or more recently magnetic resonance imaging (MRI), TLM is considered the clinical gold standard for atraumatic contact-free resection of carcinomas in the oral cavity, pharynx, and larynx [KRSH11, RA11]. In the general TLM setup depicted in Figure 1.2b [RA11], patients are positioned on their back (supine) under general anaesthesia with intubation for ventilation while their neck is hyperextended. Subsequently, the larynx is exposed using direct laryngoscopy. This enables microscope-based localisation and visualisation of the specific lesion. If required, inspection of the pathology may be complemented by additional endoscopic equipment or narrow-band-imaging (NBI) to detect characteristic differences in the mucosal vascularisation [PDBPN12].

The laryngoscope is attached to a suspension arm to maintain the exposure and realise a direct line-of-sight to the surgical area. The optical path of a surgical microscope with integrated mirror-based laser manipulator is aligned with the laryngoscope for view magnification and deflection of the laser beam onto the tissue surface. The beam is preferably generated by carbon dioxide (CO_2) laser sources at wavelengths of $\lambda_{CO2} = 10.6\,\mu m$ and delivered to the pathology through the laryngoscope with an unimpaired view in a distance of up to $50\,cm$.

Primarily, the lesion is delineated with low laser power settings according to the surgical planning in order to define and assess the safety margin. Those margins are commonly below $1\,mm$ in the larynx to preserve the functionality of adjacent structures [FKS18]. Hence, the clinician activates the laser with a foot pedal and executes the manual beam deflection with the manipulator attached to the microscope. Generally, the tissue is pulled laterally using customised surgical forceps to protect the surrounding tissue. Tumour sizes determine the resection strategy, i.e. en bloc or sequential. This decision is also supported by histopathological assessments to exclude recurrence of cell disorders based on the excision radicality. Following this strategy, highly trained clinicians with excellent hand-eye coordination are required to reduce the risk of collateral damage [BPZ$^+$13]. Nowadays, advanced laser scanning manipulators, e.g. the Digital Acublade Scanning Micromanipulator (Lumenis Ltd., Yokneam, Israel) or SoftScan plus R (KLS Martin Group Tuttlingen, Germany), have been introduced to minimise the thermal input based on automated pattern generation (line, circle) or multiple passes within a workspace of a few millimetres. Additional equipment has addressed the focal quality, e.g. Micro Point 2 (KLS Martin Group, Tuttlingen, Germany), to reach specific ablation thresholds. Those systems have decreased operative times and optimised laser-tissue interactions [RLND08]. However, the surgical outcome of TLM is mainly determined by individual clinical experiences. This also comprises the selection of the laser source and the adjustment of specific parameters for the surgical task.

TLM has demonstrated several advantages over conventional cold instrumentation. The introduction of CO_2 lasers has significantly improved the workflow due to haemostatic control; thus, intra- and

postoperative complication rates have been drastically minimised and survival rates are comparable to open laryngectomy [MLY$^+$17]. Moreover, the atraumatic access reduces hospitalisation times, voice formation is commonly preserved due to minimal scarring, and the improved workflow efficiency results in economic benefits [PPVP18].

1.2 Emerging Technologies in Laser Surgery and Robotic Manipulation

In the sections below, state-of-the-art technologies for soft tissue laser surgery, robot-assisted (laser) manipulation, and user assistance in MIS are discussed. Related work has addressed various technical and clinical aspects in the domain of (robotic) laser surgery, however, major challenges regarding safe and reliable endoscopic laser delivery still remain.

1.2.1 Soft Tissue Laser Surgery

Clinical routines have established the use of continuous wave (CW) CO_2 lasers for ablation of soft tissue lesions as discussed earlier for TLM. However, induced thermal damage and trauma to adjacent areas may affect the postoperative tissue recovery due to scarring from collagen deposition [MCF$^+$13].

Those shortcomings have been addressed in recent years with novel laser sources, e.g. solid state, that enable pulsed laser delivery. As an example, sources that aim at optimisation of thermal interactions are erbium-doped yttrium-aluminium-garnet (Er:YAG), picosecond infrared (PIRL), holmium-doped yttrium-aluminium-garnet (Ho:YAG), neodymium-doped yttrium-aluminium-garnet (Ho:YAG), or thulium-doped yttrium-aluminium-garnet (Th:YAG) lasers. Fundamental differences between sources are dedicated to emission wavelengths in near and far-infrared spectra at $\lambda_{\text{Nd:YAG}} = 1.064\,\mu\text{m}$, $\lambda_{\text{Th:YAG}} = 2.01\,\mu\text{m}$, $\lambda_{\text{Ho:YAG}} = 2.1\,\mu\text{m}$, $\lambda_{\text{Er:YAG}} = \lambda_{\text{PIRL}} = 2.94\,\mu\text{m}$, and $\lambda_{\text{CO}_2} = 10.6\,\mu\text{m}$. As detailed in Section 2.3, emission wavelengths determine absorption characteristics of non-ionising radiation specifically for water molecules, which moderates the resulting laser-tissue interaction. Moreover, other effects of laser parameters are described in Section 2.1 and in Section 2.2 interaction mechanisms are further summarised.

Laser interactions and ablation characteristics are commonly assessed experimentally on *ex vivo* tissue samples with subsequent morphological measurements, e.g. microscopic imaging, and complementary histopathological evaluation to detect damages at cellular level. An overview of related work on tissue interactions with different infrared laser sources is provided in Table 1.1. Research on soft tissue applications has predominantly addressed CO_2 and Er:YAG sources that have shown positive results for bone and cartilage ablation [SGS$^+$09]. As listed in Table 1.1, damage zones from single and multi pulse Er:YAG irradiation yielded between $10\,\mu\text{m}$ to $500\,\mu\text{m}$ on *ex vivo* specimens harvested from animal or human tissues. By contrast, experiments with CO_2 sources have proven increased damage zones with maximal cellular damage of $810\,\mu\text{m}$ caused by

Tab. 1.1: Overview of soft tissue ablation with infrared laser sources and postexperimental results.

	Experimental parameters							Tissue condition		
	λ (µm)	τ_p (µs)	f_p (Hz)	Q_p (mJ)	$2w_0$ (µm)	P_{avg} (W)	v_{scan} ($\frac{mm}{s}$)	Type	Depth[†] (µm)	DZ[†] (µm)
[ZVM+04]	2.94	-	15	140-250	600	2.1-3.75*	-	H	-	-
[HIMH96]	2.94	200	1-10	30-350	-	3.4[†]*	-	H	-	-
[ZXYZ07]	2.94	-	5	78-628	2000	0.39-3.1*	-	H	360	-
[WD89]	2.94	90	1	7-14*	420*	$7\text{-}14 \cdot 10^{-3}$	-	A	-	10
[SAK+15]	2.94	200	30	10*	400	0.3*	-	A	-	20
[BKK+15]	2.94	$300 \cdot 10^{-6}$	1000	$400 \cdot 10^{-3}$	210	0.4	-	H	-	22
[DCK+91]	2.94	200	2-30	100	150-600	0.2-3	0.18-0.35	H	3500	30
[WD89]	2.94	200	2	38-77*	1000*	-	-	A	-	50
[MCF+13]	2.94	100	20	250	900	5*	-	A	-	130
[BKK+15]	2.94	300	25	80	400	2	-	H	-	171
[BJK+14]	2.94	300	10	80	400	0.8	-	A	-	236
[THE+14]	2.94	50-225	100-500	2.3-12.8	225	1.15-2.22	-	A	1348	305
[RLP+12]	2.94	-	30	60-150	600	1.8-4.5	-	A	-	500
[ZVM+04]	10.6	-	-	-	300	5	-	H	-	-
[MCF+13]	10.6	-	-	-	400	3-5	-	A	-	200
[BKK+15]	10.6	$20 \cdot 10^3$	10	240	400	2.4	-	H	-	365
[BJK+14]	10.6[‡]	$20 \cdot 10^3$	10	240	400	2.4	-	A	-	810
[VCM+10]	1.064	100	60	-	320	3.5	-	H	-	305
[MCF+13]	1.064	100	80	-	320	4	-	A	-	750
[TNR+17]	1.94	$100 \cdot 10^3$	5	20	400	5	-	A	-	500

Notes: Symbols denote laser wavelength λ, pulse duration τ_p, pulse energy Q_p, beam waist diameter $2w_0$, average power P_{avg}, and scanning velocity v_{scan}. Acronyms describe human (H) and animal (A) tissues as well as thermal damage zones (DZ).

[†] Minimum of provided data.* Values are restored from measurement data. [‡] CO_2 laser in superpulse mode.

thermal effects. Similar responses were obtained on different cadaveric soft tissues, e.g. brain, liver, and intestines [DCK+91]. Further work has been dedicated to characterisation of tissue-specific ablation thresholds as well as correlation of ablation depth and pulse delivery [ZXYZ07]. There were no significant differences in postoperative healing (morphology, histochemistry, immunocyto-chemistry) of mucosal tissue identified in 20 patients after *in vivo* CO_2 and Er:YAG irradiation, but damage zones were smaller in Er:YAG trials [ZVM+04]. This assessment comprises epithelial damage, low inflammation, fast healing, and absence of scarring. However, CO_2 sources show advantageous haemostatics. Those observations have been confirmed in independent studies [HIMH96, RLP+12, MCF+13, BJK+14]. Further effects are associated with bactericidal effects from irradiation induced hydroxyl (OH) radicals [LKLF05].

Laser radiation must be transmitted in clinical routines from the source to the surgical area with ergonomic handling and usability to gain the surgeons' acceptance. Established laser delivery systems for soft and hard tissue ablation consist of articulated mirror arms with manually-guided hand pieces. Nonetheless, the latter restricts certain applications such as deployment to anatomical

cavities due to dimensional constraints and flexibility of transmission units. Those challenges can be addressed with flexible fibre-based approaches including solid multimode or hollow core fibres. The latter show increase damage thresholds and flexibility due to smaller bending radii [UMF+13]. By contrast, hollow core fibres are prone to structural damages from insufficient cap sealing, i.e. dust particles may cause intensity accumulation. Solid core fibres are fabricated from sapphire, chalcogenides, and GeO_2 and were introduced to clinical applications due to reliable delivery of high power laser radiation [PNT+06].

1.2.2 Robot-Assisted Laser Surgery

Manual laser delivery with contact or non-contact application is considered the gold standard in clinical routines. In general, the latter focus on delineation and resection of tissue pathologies is based on ablation induced by laser-tissue interaction as described in the previous Section 1.2.1. Normally, hand-held applicators with fibre or mirror-based coupling to the laser source or bare fibres are taken into consideration in open or endoscopic deployment for hard and soft tissue ablation in orthopaedics, orthodontics [DH07], neurology [MCS+16], or urology [ANB+95].

Despite the benefits of laser technology over conventional instrumentation, major challenges associated with manually guided delivery still have to be overcome for optimal surgical outcomes. As an example, limitations are: 1) limited precision of the delineation, 2) restricted delivery and handling (hand-eye coordination) in confined spaces due to remote camera observation and friction in endoscopic working channels, 3) thermal tissue trauma due to an unknown setting of the focal length, 4) intraprocedural adjustment of the focal distance, or 5) heuristic laser parameter settings (e.g. pulse duration and frequency) in combination with target tissue properties and scanning velocities.

In this regard, the following section reviews state-of-the-art methods to particularly improve the first and second limitation with robotic-assistance and navigation, i.e. device designs and miniaturisation for use in endoscopic scenarios. This work introduces a taxonomy for related studies in robot-assisted laser surgery based on the implementation of opto-mechanical beam deflection. The spatial propagation of a laser beam is basically described in Euclidean space with a three-dimensional direction vector and the focal position. Two dominant opto-mechanical designs were identified in literature to modify the beam propagation:

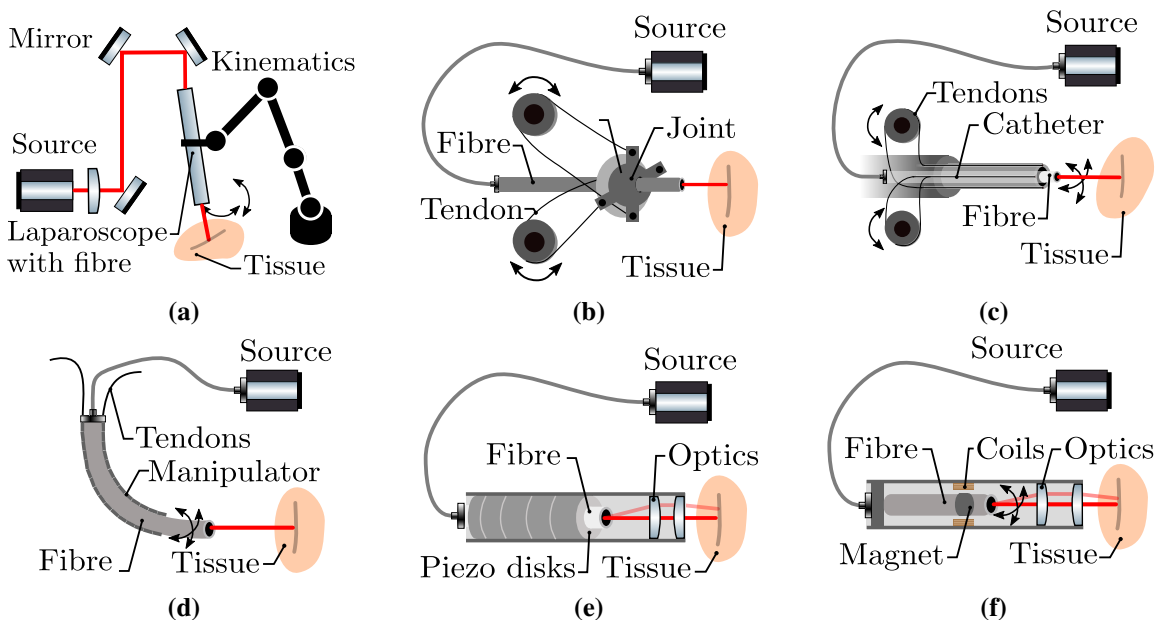1. *Indirect beam deflection*: Beam manipulation through mechanical displacement of beam transmission media, e.g. optical fibres.

2. *Direct beam deflection*: Manipulation of the beam within media or free space based on reflective or refractive optics, e.g. mirrors or lenses.

The remainder of this section discusses related work on both methodologies and amends details for device examples listed in Figures 1.3 and 1.4.

Indirect Beam Deflection

Pioneering work in robotic laser surgery originates from *indirect beam deflection* with conversion of a commercial laparoscope to a laser applicator and its integration to an automation framework as shown in Figure 1.3a, i.e. kinematics with a remote centre of motion (RCM) constraint. The external kinematics enables the displacement of the laparoscope that guides the beam of a CO_2 laser using an optical fibre. Additionally, tablet-based user input for interactive definition of laser trajectories on the target is proposed and feasibility of the robotic concept has been evaluated in preliminary studies [TBR+03, TBS+05, TBS+06].

Subsequent contributions transfer the concept of transmission media displacement to miniaturised mechanisms that facilitate luminal deployment. Fundamentally, all approaches have in common that a (flexible) fibre is rigidly clamped in a certain distance to the fibre tip. Thus, the fibre tip can be displaced and modelled equivalently to beam bending, where forces/torques are loaded orthogonally to the beam axis. As an example, tendon-driven concepts are proposed for luminal applications. Firstly, the module ($\varnothing$ 6 mm) in Figure 1.3b makes use of a spherical joint that guides the fibre [SSL14b, STL15]. The displacement of the tendons causes joint tilting in 2 degrees of freedom (DoF) and corresponding fibre motion. Secondly, a multi-lumen catheter is proposed for guidance of the laser fibre [RDM15]. Tendon displacement introduces bending of the catheter in 2 DoF which is likewise transmitted to the fibre as shown in Figure 1.3c. Equivalently, a fibre is embedded to a 2 DoF tendon-driven bending manipulator ($\varnothing$ 2.4 mm) and enables simple scanning patterns (see Figure 1.3d) [HBE+07]. This concept is further advanced with fibre integration to

Fig. 1.3: Examples of robotic devices with indirect laser beam deflection: (a) laparoscope with external kinematics, (b) tendon-driven spherical joint, (c) tendon-driven multi-lumen catheter, (d) tendon-driven bending manipulator, (e) stacked piezo disks, and (f) electromagnetic forces.

concentric tube robots for transurethal interventions [HHW14] or intracorporeal fibre bending with electro active polymers (EAP) [CBR$^+$18].

Lastly, several studies investigated the surgical outcome of flexible CO_2 fibres (Omniguide, Cambridge, MA, USA) attached to the instrument arms of the da Vinci robotic platform (Intuitive Surgical, Sunnyvale, CA, USA) in different fields of intervention and demonstrated superior results in comparison to conventional approaches, e.g. in laparoscopy or transoral scenarios [BHCS11].

Alternative methods are proposed to overcome limitations of tendon actuation, such as backlash, friction, and dynamics. Optimised response times and miniaturisation are achieved with fibre deflection based on stacked piezo elements that enclose the fibre as depicted in Figure 1.3e [FYSBY14]. The module ($\varnothing\,5\,mm$) enables high scanning rates ($> 900\,Hz$) within small planar workspaces $(150 \times 150)\,\mu m^2$. More recently, a module ($\varnothing\,13\,mm$) with fibre deflection based on magnetic forces was proposed [AM17, APM19]. The optical fibre is equipped with a permanent magnet (see Figure 1.3f) and two miniaturised orthogonal pairs of electromagnetic coils are aligned. Furthermore, feed forward control of the induced magnetic fields enable accurate deflection of the fibre with accuracies in path tracing tasks of $35\,\mu m$.

Direct Beam Deflection

Early work in robot-assisted laser surgery with *direct beam deflection* has focused on ablation of hard tissues, such as bone or cartilage, to overcome limitations of conventional instrumentation, e.g. scalpels or saws. This work comprised of a setup with an Argon laser, an optical beam scanner, and an imaging sensor as conceptually shown in Figure 1.4a [BHP$^+$99]. Results demonstrate that accurate and repeatable 2D control of the laser is feasible. This is mainly governed by use of beam scanners with galvanometer-driven mirrors [Trä12] for fast and precise beam steering based on direct voltage mapping and closed-loop control [SPB$^+$15]. Subsequent work has adapted the concept for cochleostomy and focuses on integration of a CO_2 laser, a scanner unit, and white light imaging for implementation of a visual feedback and control framework [KRW$^+$08]. More recently, a similar opto-mechanical setup is automated, coupled to a surgical microscope for transoral vocal fold surgery [MCDG10, DMC15a, DMC15b]. This approach has demonstrated improved clinical outcome [BDM$^+$13, BWD15]. For the sake of completeness, scanner-based rigid laser endoscopes are taken into account for fetal surgery [YYM$^+$10] and for neurosurgery [LNM$^+$10].

The system in [KRW$^+$08] is improved by increasing the restricted beam scanning workspace with micro-macro manipulation. Hence, the beam scanner is mounted to the end-effector (see Figure 1.4b) of a serial kinematics to enable global repositioning with respect to the surgical target [Bur10]. In this regard, a 3D planning framework based on prior target imaging and registration is described for interactive definition of ablation paths. More recently, the concept is further improved with dynamic focus units for 3D laser spot control, alternative radiation sources (e.g. Er:YAG lasers), intraprocedural ablation depth monitoring, and control with optical coherence tomography
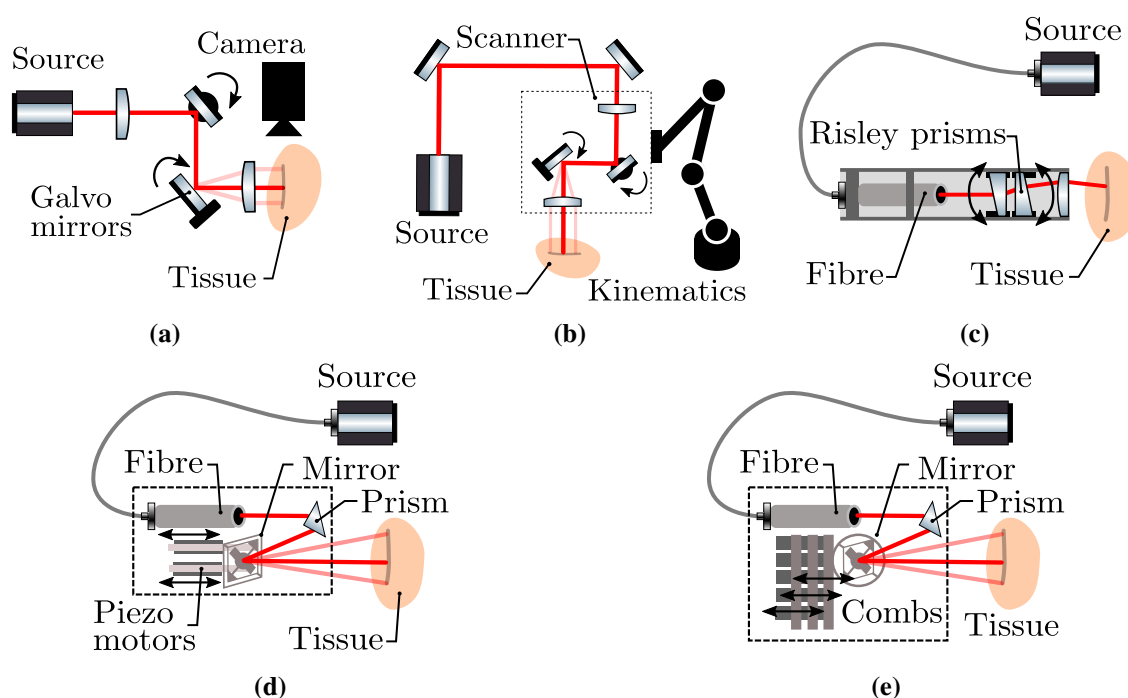
Fig. 1.4: Examples of robotic devices with direct laser beam deflection: (a) galvanometer scanner, (b) galvanometer scanner mounted to serial kinematics, (c) Risley prisms, (e) wafer-based tilting platform with piezo motors, and f) wafer-based tilting platform driven by electrostatic forces.

(OCT) [ZPW$^+$14, FPB$^+$15, FZC$^+$18]. Those concepts are commercialised to the robotic osteotomy platform CARLO® (AOT AG, Basel, Switzerland) which is composed of a scanning-head, Er:YAG laser source, and serial kinematics [DSA$^+$15].

An unique optical design based on Risley prisms targets miniaturisation and integration to an endoscopic device [PRK$^+$12]. The mechanism depicted in Figure 1.4c is based on two consecutively aligned wedged prisms that rotate about the optical axis. Each angular configuration yields a different beam path based on Snell's law of refractive optics. Hence, coordinated rotation of both prisms enables 2D manipulation of the beam with respect to the target surface.

Alternatively, microelectromechanical systems (MEMS) are proposed for miniaturised laser manipulation. In the context of high-power laser surgery and endoscopic integration, a 2 DoF tilting mirror is designed and fabricated at wafer level with actuation by two miniature commercial piezo motors [RTR$^+$17]. The device dimensions yield to $(11 \times 9 \times 42)\,\mathrm{mm}^3$. Figure 1.4d depicts the opto-mechanical integration of the flexible fibre and the prism for redirecting the beam to the centre of the tilting platform. A different MEMS for beam deflection is presented in [PRRA14]. This work uses electrostatic forces generated through applied voltages within three linear comb drives to deflect a micro-mirror platform attached to mobile cantilevers in 3 DoF $(6 \times 4 \times 4)\,\mathrm{mm}^3$. The reader is kindly referred to MEMS scanner reviews with focus on endoscopic imaging, fluorescence, and optical coherence tomography (OCT) [SKD$^+$11, HSJ17].

1.2.3 Robotic Platforms for Minimally Invasive Surgery

This section is dedicated to an overview on robotic systems which have been deployed and evaluated for general use in MIS. Firstly, fundamentals of MIS are presented in the context of robotic assistance. Afterwards, a taxonomy for the design and implementation of robotic devices in related work is presented and complemented by a set of examples for each category. Lastly, a brief overview on spatial manipulator description for use in automation, control, and simulation is provided.

Fundamentals of Instrumentation in Minimally Invasive Surgery

Devices for MIS have been introduced to clinical routines with great success and improved outcome for patients with less trauma and short hospitalisation within the last decade for intraluminal, transluminal, and extraluminal interventions [VLCY13]. For example, interventions comprise insertion of instrumentation through small abdominal incisions in laparoscopy [BSMJ99], the use of long rigid instruments in TLM of the larynx as presented in this work [FSG+16] combined with microscopic vision, or deployment of devices through natural orifices, such as promoted in natural orifice transluminal endoscopic surgery (NOTES) [MRM+06].

The success of MIS is generally based on two groups of devices that are crucial for luminal access and the corresponding imaging and manipulation workflow: 1) *flexible endoscopy* and 2) *steerable instruments*. The design of *flexible endoscopes* typically comprises a bendable shaft that is manually actuated from outside the patient, imaging components located in the tip, an instrument channel for tool deployment, and surgical illumination. The main clinical application is diagnosis due to lack of mechanical stability, i.e. the endoscopic structure impedes force transmission for tissue manipulation. By contrast, dimensions of *steerable instruments* are significantly smaller ($\leq \varnothing 8\,\mathrm{mm}$) in comparison to multifunctional endoscopes (range of $\varnothing 10\,\mathrm{mm}$ to $\varnothing 14\,\mathrm{mm}$) due to absence of imaging, manipulation, and illumination [JAH+15]. Those instruments are fed through abdominal incisions, are introduced to natural orifices, or are advanced into endoscopic instrument channels to provide dedicated functions, e.g. grasping or cutting, in combination with bendable shafts and/or joints located at the instrument tip. Manipulation may use a minimum of three kinematic DoF, i.e. 1 DoF rotation, 1 Dof translation, and 1 DoF bending, and grasping/cutting as an additional functional DoF. However, surgical workflows can demand for additional devices to enable simultaneous imaging and illumination of the surgical scene [VLCY13].

In summary, advanced surgical techniques were introduced to MIS and demonstrated a significant patient benefit. However, there are limitations associated with restricted instrument workspaces, poor dexterity with respect to the surgical task, stability of the platform, and the clinical usability of devices. In the latter instance, highly skilled surgeons and continuous surgical training are essential for the clinical outcome. Thus, several robotic systems were proposed within the last decade to accelerate the success of MIS procedures [GBLF10, YG12].

Taxonomy of Endoscopic and Steerable Robotic Manipulators

Once clinical demands and challenges of MIS were identified, new robotic technologies in research or commercial applications have been reported within the last decades. Hence, the systematic review in this section focuses on the assessment of major design strategies and the identification of design limitations. This knowledge is crucial for proposal and composition of novel manipulator designs which satisfy demands of minimally invasive laser surgery in confined spaces. A systematic literature search was conducted under the following search terms:

- Application in MIS

- Intra-, trans-, or extraluminal deployment

- Manipulator with ≥ 3 Cartesian DoF

- Automation

- Instrument diameter $\leq 18\,\mathrm{mm}$ (largest trocar sizes)

Based on the results of the systematic review, which are presented in detail in later sections, four high-level design strategies have been identified in state-of-the-art and summarised by illustrations in Figure 1.5. In accordance with earlier taxonomies [JAH+15, BRC15], major design categories constitute:

1. *Discrete robots*: Serial/parallel composition of revolute, prismatic, or universal joints with intrinsic or extrinsic actuation principles (see Figure 1.5a).

2. *Hyper-redundant robots*: Serial composition of a large number of discrete revolute or universal joints (passive/active) with intrinsic or extrinsic actuation (see Figure 1.5b).

3. *Continuum robots*: Composition of elastic and flexible structures with absence of discrete joints and intrinsic or extrinsic actuation principles (see Figure 1.5c).

4. *Hybrid robots*: Combination of discrete and continuum mechanisms (see Figure 1.5d).

Related work has established the definition of two generic actuation principles based on the location of the final energy conversion to the mechanical domain: (1) *intrinsic* or (2) *extrinsic* actuation [RD99, BRC15]. For example, *extrinsic* actuation comprises tendon-driven or rod-driven manipulators, where the length of the tendon/rod is adjusted externally with electric/hydraulic/pneumatic motors. If the final conversion is located within the manipulator, such as present in pneumatic soft robots, shape memory alloys (SMA), or integrated miniaturized electric motors, the actuation is classified as *intrinsic*.

The remainder of this section discusses different robotic designs associated to identified categories. This comprises discrete and hyper-redundant devices, continuum robots with constant segmental lengths, continuum robots with variable segmental lengths, and finally concentric tube robots. For a hybrid design the reader is kindly referred to the pioneering work in [CZ17].
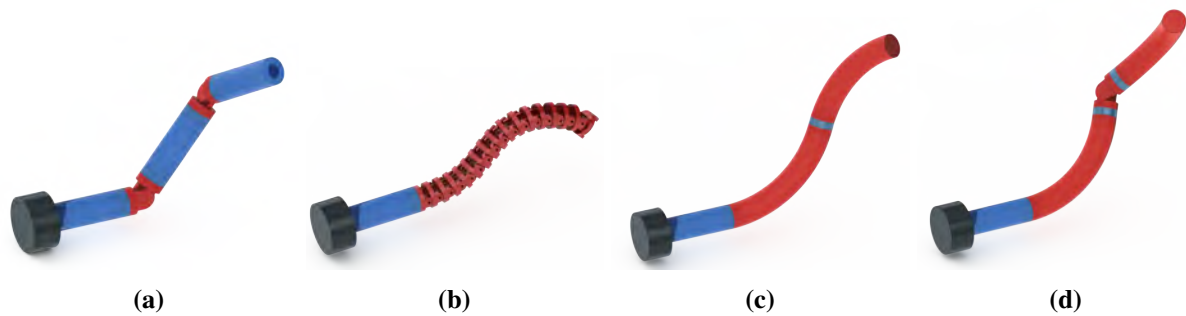
Fig. 1.5: Manipulator designs for MIS: (a) serial, (b), hyper-redundant, (c) continuum, and (d) hybrid
mechanisms. The black part represents the manipulator base, blue components define rigid links,
and red components describe joints or continuum segments.

Discrete and Hyper-Redundant Robots

The majority of endoscopic devices with versatile surgical functionalities and working channels
for instrument deployment use extrinsically actuated (hyper-redundant) serial chains with rigid
links connected by planar or spatial joint designs, e.g. revolute, rolling, or universal joints. The
remainder of this paragraph highlights and summarises discrete endoscopic examples with both
extrinsic and intrinsic actuation reported in related work.

A dexterous 7 DoF endoscopic manipulator (i-Snake®) with intrinsic actuation based on embedded
micro DC motors and a novel wire-driven transmission mechanism ($\varnothing 12$ mm) is proposed for
general MIS applications. The manipulator shown in Figure 1.6a comprises a chain of two
universal and three revolute joints and has been evaluated in *in vivo* animal trials [SNP+11]. The
technology is further advanced to a 7 DoF hyper-redundant device (i²Snake) (see Figure 1.6b) with
extrinsic tendon actuation composed of rolling and revolute joints for luminal surgery ($\varnothing 16$ mm)
in combination with an external serial kinematics for coarse positioning and luminal insertion
[BRGL+18]. In [SSL+14a], universal, revolute joints, and a hyper-redundant section are joined as
depicted in Figure 1.6c to facilitate an extrinsically actuated 5 DoF manipulator ($\varnothing 14$ mm).

In contrast, a hyper-redundant endoscopic robot ($\varnothing 12$ mm) with follow-the-leader capabilities
is composed of a large number of spherical joints with hollow core [DCWZ06]. The latter
accommodates a second manipulator that can be retracted and advanced concentrically within
the core. Principally, the last segment of the outer manipulator is articulated extrinsically with
three tendons and then the inner structure is subsequently advanced to lock the shape. This
design has been successfully transferred to the commercial Flex® robotic system (Medrobotics,
Raynham, MA) that has been clinically approved for transoral and transanal surgery [RMNPL+15,
MHH+17, PPO18]. A similar mechanical design (see Figure 1.6e) replaces the inner manipulator
with an elastic tube to implement the local shape locking [LYR+15]. Alternatively, a tendon-driven
variable-neutral line manipulator ($\varnothing 15$ mm) shown in Figure 1.6f with 6 DoF and rolling joints is
proposed for single port surgery [LKL+14]. In comparison to previously described mechanisms,
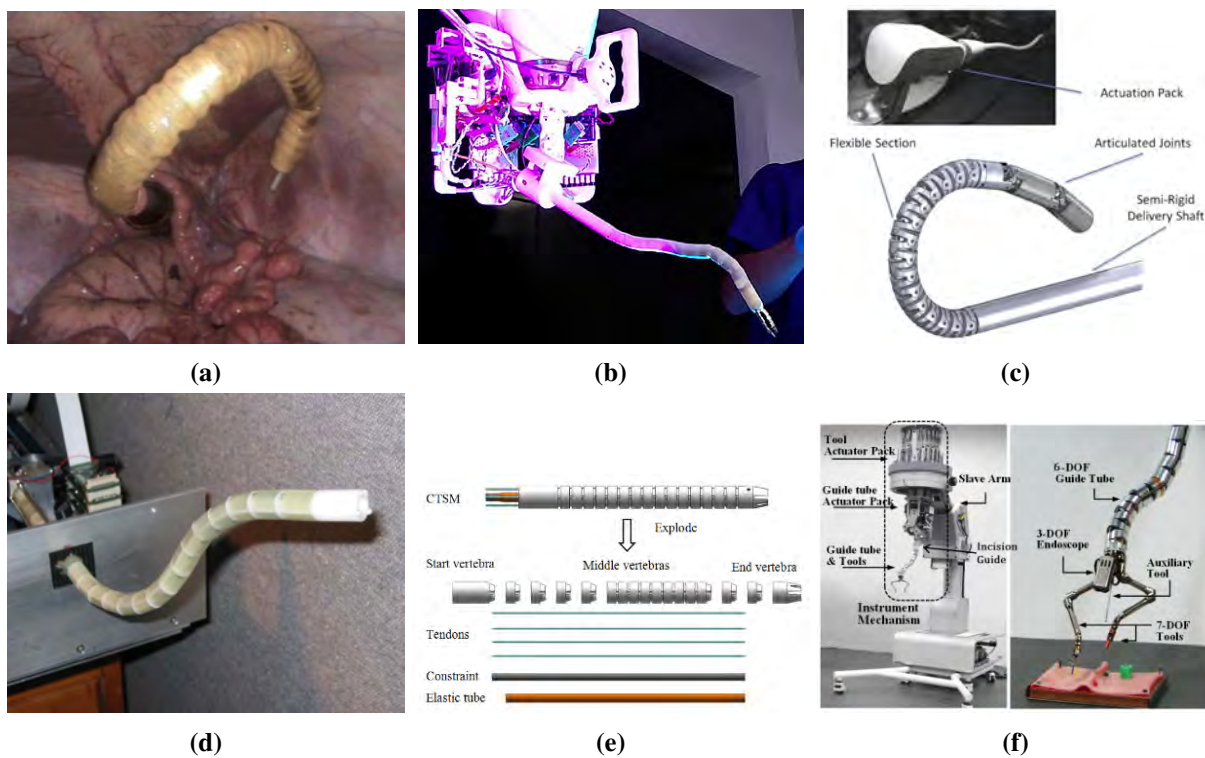
Fig. 1.6: Examples of discrete and hyper-redundant endoscopic manipulators for MIS: (a) Rigid links connected by universal and revolute joints (reprinted from [SNP$^+$11], © 2011 IEEE) , (b) hyper-redundant robot with rolling and revolute joints (reprinted from [BRGL$^+$18], Creative Commons Attribution 4.0 International License (http://creativecommons.org/licenses/by/4.0/)) (c) hybrid manipulator (reprinted from [SSL$^+$14a] , © 2014 IEEE), (d) highly articulated probe (reprinted from [DCWZ06], © 2006 IEEE) (e) constrained hyper-redundant manipulator (reprinted from [LYR$^+$15], © 2015 IEEE), and (f) hyper-redundant manipulator for single port surgery (reprinted from [LKL$^+$14], © 2014 IEEE).

tendon pretensioning enables a displacement of the neutral line and, therefore, improved dexterity [KCKI14]. More recently, a tendon-driven design based on concatenation of multiple universal joints ($\varnothing\,12\,\text{mm}$) is described for flexible instrument delivery and imaging in transnasal access [RSG$^+$17]. However, there exist many other robotic endoscopes for MIS in related works. For the sake of thoroughness, the reader is kindly referred to the comprehensive review in [VLCY13].

Discrete designs were considered for various *steerable instruments*. An overview is provided in [JAH$^+$15], where systems have been systematically classified with respect to different joint types in literature and patents. For example, a highly dexterous 7 DoF manipulator is introduced for transanal micro surgery ($\varnothing\,5\,\text{mm}$) [LWG$^+$17]. The mechanism (see Figure 1.7a) comprises prismatic, revolute, and rolling joints. A similar 9 DoF mechanism ($\varnothing\,5\,\text{mm}$), as presented in Figure 1.7b, is discussed for transluminal surgery and integrates rolling joints and a pan/tilt mechanism of the distal instrument [ABRP07]. Finally, a single port system was equipped with

a 6 DoF manipulator (see Figure 1.7c) for high force/torque transmission ($\varnothing\, 8\,\mathrm{mm}$) taking novel geared revolute joints and an integrated tendon reduction mechanism into account [LKR$^+$13].

Continuum Robots with Constant-Length Segments

The general mechanical design of *continuum robots* is associated with one of the following two subgroups: (1) *backbone-based mechanisms* and (2) *concentric tubes*. Backbone-based devices are composed of elastic continuum bodies that act as the main supporting structure of the mechanism and enable multi DoF deflection with constant segmental lengths or segmental elongation/contraction. Continuum bodies can be manufactured from different materials (e.g. polymers or superelastic NiTi alloy) and structural shapes, such as elastic slotted or non-slotted tubes, rods, springs [BA05], combinations of previous approaches [AGB17a], or other compliant structures. As an example, the latter can comprise flexible silicone components that are manufactured in a moulding and casting procedure [CRG$^+$13] or additively generated structures [MO16]. Beyond that, the reader is kindly referred to [RDM18, GNSA19] for a comprehensive review on design and manufacturing of soft robotic endoscopes. The following paragraph presents design examples of constant-length continuum robots that are summarised in Figure 1.8. Noteworthy, concentric tube robots are discussed in a later section due to fundamental differences in design and working principles.

A multi-backbone continuum manipulator has been introduced for transoral [ST04, SXK$^+$09] and transnasal laryngeal surgery [BDN$^+$13]. The robot comprises multiple segments with flexible primary passive and secondary actuation backbones fabricated of NiTi alloy ($\varnothing < 5\,\mathrm{mm}$). As shown in Figure 1.8a, the primary backbone of each segment is equipped with equidistantly spaced disks that guide the secondary backbones. The latter are attached to the last rigid disk of each

(a)   (b)   (c)
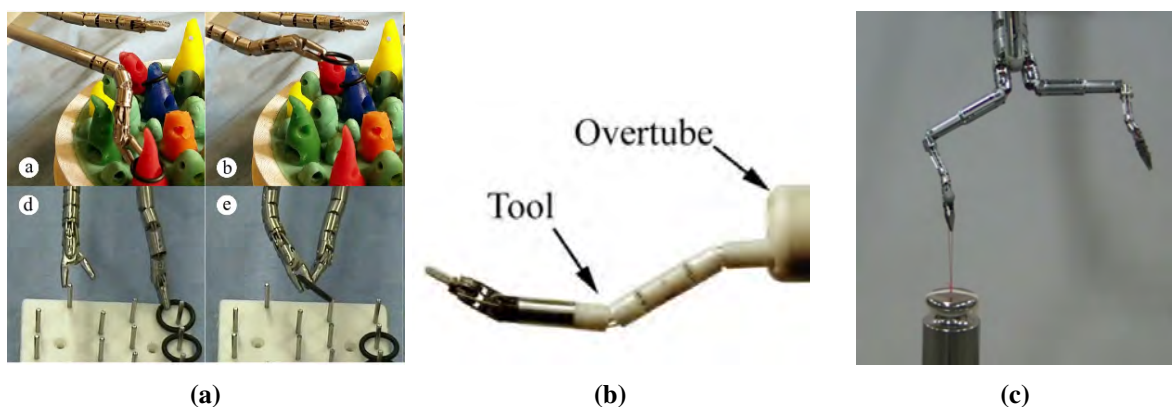
Fig. 1.7: Examples of discrete steerable instruments for MIS: (a) Rigid links connected by rolling and revolute joints (reprinted from [LWG$^+$17], © 2017 IEEE) , (b) rigid links with revolute joints and tilt/ pan mechanism for distal gripper (reprinted from [ABRP07], © 2007 IEEE), and (c)rigid links and geared revolute joints with tendon reduction mechanism (reprinted from [LKR$^+$13], © 2013 IEEE).
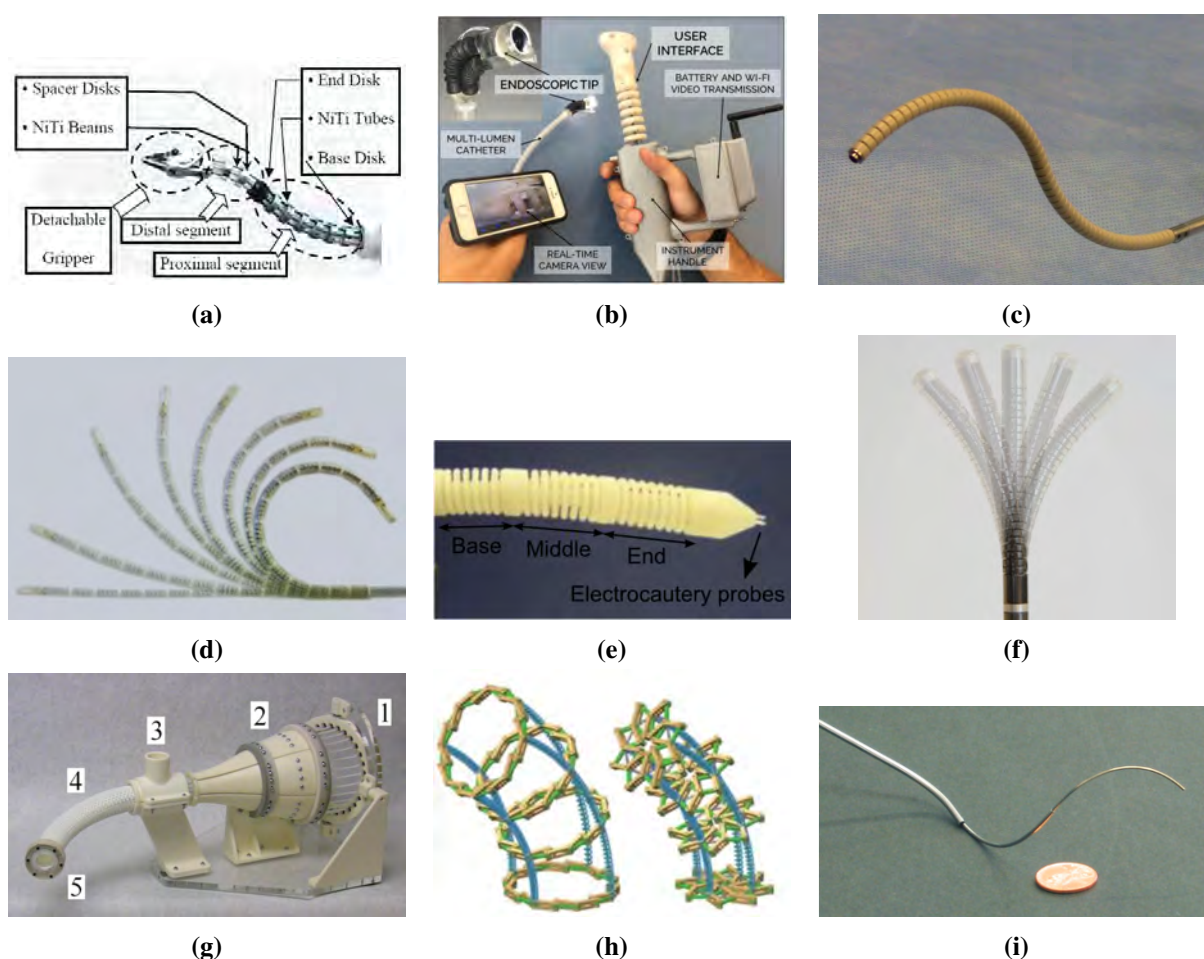
Fig. 1.8: Examples of continuum robots with constant segmental lengths and different scale levels: (a) multi-backbone design (reprinted from [SXK+09], © 2006 IEEE), (b) master-slave configuration (reprinted from [GWC+19], © 2019 IEEE), (c) unidirectional slotted tube (reprinted from [KOK+16], © 2016, with kind permission from Springer Nature), (d) bidirectional slotted tube (reprinted from [AKF+16], © 2016 IEEE), (e) MR-compatible robot with SMA actuation and spring backbone (reprinted from [KCD18], © 2018 IEEE), (f) fluidic muscle actuation of a slotted NiTi tube (reprinted from [SBD+16], © 2016, with kind permission from Springer International Publishing), (g) interlocking fibres (reprinted from [MKHA13], © 2018 IEEE), (h) variable geometry backbone (reprinted from [AOS18], © 2018 IEEE), and (i) concentric tube robot (reprinted from [WOC06], © 2006 IEEE).

segment. Hence, external push/pull displacement of each secondary backbone introduces segmental deflection. Thus, coordinated joint space motion of the secondary backbones based on a kinematic model facilitates 2 DoF, i.e. bending in the bending plane and its rotation about the segmental axis. The design further enables kinematics-based contact detection [BS12] and compliant motion/force control for atraumatic insertion to luminal cavities, contact force estimation [GBS14, BS16], and dynamics analysis [RBT14]. More recently, the design has been advanced and preclinically evaluated for transurethal bladder surgery [GBM+13, PBSH15, SDGD+18]. The same principle is transferred to a device for gastrointestinal endoscopy and integrated to a dual-continuum robot

system design (see Figure 1.8b) composed of a hydraulically-actuated parallel-bellow endoscope ($\varnothing\,13.5\,\text{mm}$), and a multi-backbone master interface [GWC+19].

The miniaturised tendon-driven two-segmental continuum manipulator in Figure 1.8c, also denoted as steerable catheter, is implemented with a slotted monolithic NiTi backbone ($\varnothing\,3.4\,\text{mm}$) for deployment in neurosurgery [KOK+16]. The unidirectional slot layout impedes 2 DoF bending of each segment and demands for external shaft rotation. An advanced multisegmental manipulator at catheter scale ($\varnothing < 3.4\,\text{mm}$) overcomes aforementioned limitations and comprises a flexible MR-safe backbone composed of segments with helical cutouts [AKF+16]. Combined tendon actuation and shaft rotation enable manipulation in 3 DoF. Similarly, a slotted NiTi tube ($\varnothing\,7\,\text{mm}$) with bidirectional slot layout (see Figure 1.8f) is equipped with intrinsic actuation based on four symmetrically arranged artificial muscles (McKibben) with fluidic actuation [SBD+16]. This setup enables bending and rotation about the manipulator axis exclusively based on the embedded actuators. At a larger scale and as depicted in Figure 1.8e, a spring-shaped MR-compatible continuum manipulator ($\varnothing\,12.5\,\text{mm}$) is fabricated additively and actuated intrinsically with shape memory alloy (SMA) springs [KCD18].

Besides reported design embodiments and applications in head and neck or abdominal surgery, a unique mechanism for flexible access to the narrow medullary cavity, i.e. a luminal space in long bones, is shown in Figure 1.8g. It makes use of interlocking fibres that constitute two functions [MKHA13]. Firstly, the circular arrangement of fibres establishes the segmental continuum structure. Secondly, coordinated linear displacement of fibre bundles causes body deflection. The principle has demonstrated high structural stiffness due to internal force distribution under external loads.

Further related work in the field of constant-length manipulators addresses for example helical routing of tendons in a backbone-based manipulator and demonstrated a workspace enlargement of four times in comparison to conventional straight routing [SACB17]. Recently, merits of multi-backbone continuum manipulators with variable backbone geometry, as conceptually shown in Figure 1.8h, are discussed [AOS18]. This mechanism takes the variation of the cross section diameter with angulated scissor linkages into account. An improved dexterity in MIS of discussed manipulators is also expected from collaborative task completion, i.e. two devices perform joint object manipulation [LHJ18]. In addition, articles report on kinematic modelling for constant-length manipulators with different actuation principles under the assumption of constant curvature. In this regard, the reader is kindly referred to comprehensive modelling reviews [CMC+08, RJWJ10, LWRY17]. Real-time shape sensing and estimation for closed-loop control of continuum manipulators are regarded complementary [SLQ+17].

Continuum Robots with Variable-Length Segments

The second category of continuum robots focuses on variable-length manipulators. The design principles enable modification of the segmental curvature based on elongation or compression of the robotic structure independently of the current bending angle [WCMG06]. This results in increased spatial DoF in comparison to constant-length designs. Moreover, this feature is highly beneficial to satisfy demands of dexterous manoeuvres and trajectory following in luminal MIS. On the contrary, variable-length segments demand for complex actuation principles and strategies for decoupling the individual segments. The remainder of the section discusses design examples summarised in Figure 1.9.

Pioneering work targeting object grasping in the field of extensible manipulators is dedicated to the Air-Octor [MJW05] and OctArm [MCC$^+$06]. The conceptual OctArm manipulator (2nd generation of Air-Octor) is shown in Figure 1.9a and is mainly composed of artificial muscles with pneumatic actuation. The latter are assembled of rubber tubes with enclosing braided mesh to moderate the radial expansion into elongation. Design embodiments comprise a single chamber actuated by tendons [NJ07] or multiple chambers with pneumatic actuation only [MCC$^+$06]. The ratio of elongation is set by adjusting the supply pressure.

More recent work transfers this approach to MIS. A soft robot, also denoted as Stiff-Flop (see Figure 1.9b), is implemented with miniaturised polydimethylsiloxan (PDMS) bodies ($\varnothing\,12\,\text{mm} - \varnothing\,25\,\text{mm}$) featuring embedded pneumatic actuation chambers and fluidic connectors.

The bodies are fabricated in a multi-step casting procedure [CRG$^+$13, CRG$^+$14]. Each segment facilitates 3 DoF and it is highly compliant due to the inherent flexibility. Related work further discusses design improvements [FCM$^+$15], integrated stiffening [SSN$^+$16], and force sensing [NSB$^+$14]. A design variation targets an inflatable soft robot with tendon actuation of a single pneumatic chamber that enables deployment with variable elongations dependent of the current length of the tendons [SWA14].

Early work in backbone-based designs ($\varnothing\,13\,\text{mm}$) demonstrated the feasibility of segmental length variation with a mechanism composed of a primary backbone, tendon actuation, and elastic springs for distribution of spacer disks as shown in Figure 1.9d. The length of each segment is controlled through adjustment of tendon lengths and passive motion of the backbone [BW04]. More recently, the authors transferred the design to a long and thin robotic cable ($\varnothing\,10\,\text{mm}$) [TGW14, WNV$^+$16].

A similar extensible manipulator (see Figure 1.9c) with flexible primary backbone and extrinsic tendon/backbone actuation is proposed for exploration of tortuous anatomies [NBK15]. The device ($\varnothing < 3\,\text{mm}$) comprises three segments and is inspired by the designs in [ST04, BW04]. Unlike reported work, segmental deflection is implemented with tendon routing along spacers in a straight path across the structure and primary backbones are of telescopic nature. This facilitates active adjustment of the length of the primary backbone. The equal distribution of spacer disks along the segmental backbone is realised with permanent cylindrical magnets attached to the
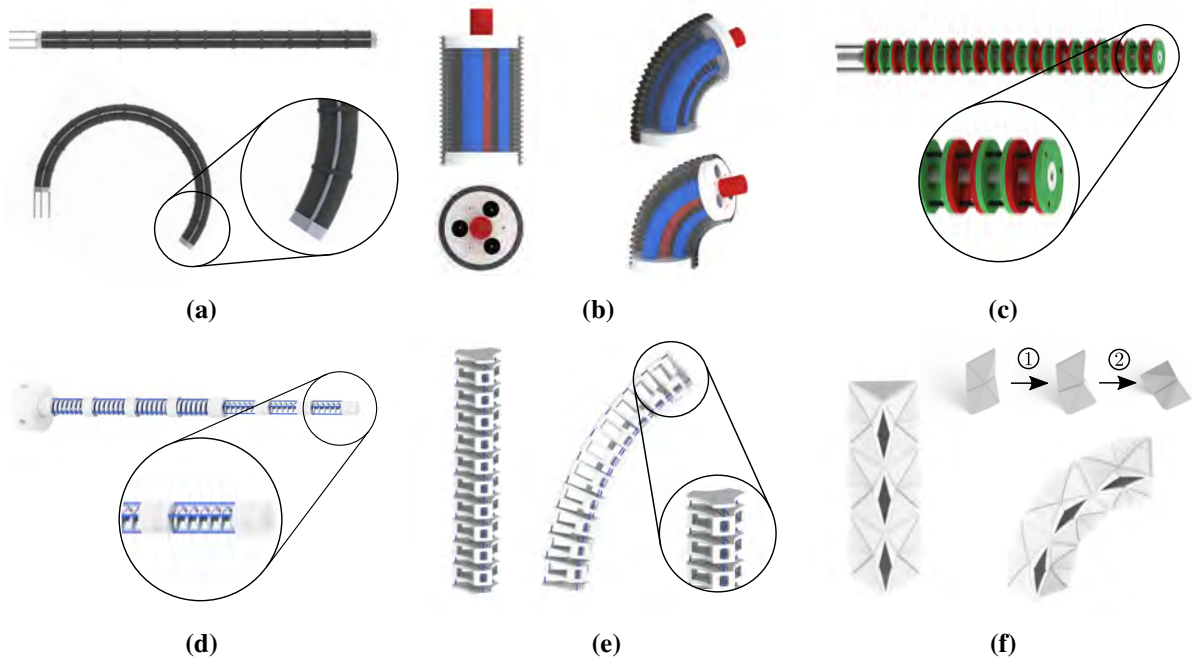
Fig. 1.9: Examples of variable-length continuum manipulators: (a) OctArm robot, (b) single segment of flexible Stiff-Flop manipulator, (c) tendon-driven telescopic robot with magnetic spacer disks, (d) tendon-driven multi-segmental manipulator with spring backbone, (e) stacked compliant modules, (f) origami inspired folding structure.

centre of each spacer. Repulsive magnetic forces cause self-organisation of the disks along the backbone. Beyond that, the design was taken into account for follow-the leader-deployment [NBK16]. A comparable mechanism ($\varnothing\,15\,\text{mm}$) substituted the NiTi tubes of previous work with flexible polymeric tubes [ZSJ$^+$18]. The principle of extension and contraction is implemented with different tendon configurations which drive the relative tubular displacement. Using [NBK15] as an example, spacer disks help to guide tendons, however, the report lacks important details on mechanisms for an equal spacer distribution along the segment to justify the assumption of constant curvature.

Further extensible continuum designs are proposed for generic applications based on stacked compliant [QQL$^+$14] or origami modules [ZQD16] as depicted in Figure 1.9e and Figure 1.9f, respectively. Both, the compliant ($\varnothing\,29\,\text{mm}$) and folding mechanism ($\varnothing\,20\,\text{mm}$), enable variation of manipulator lengths independently of the current bending configuration. In comparison to previous designs, variations in segmental lengths are significantly lower.

Beyond mechanism design, related work in variable-length continuum/soft robotics considers analysis of planar motion envelopes [KW13], comparison of kinematic models under external loads [CLKB19, SSN$^+$19], dynamic models [TWD07a, TWD07b, GG19], and advanced control strategies [BDWN07, KW11, KFW14, FKW18].

Concentric Tube Robots

Concentric tube robotics, also denoted as *active cannulas*, represent a subgroup of continuum robots with small diameter of below $5\,\mathrm{mm}$ [WOC06, SD06]. In general, the instrument shown in Figure 1.8i is composed of multiple concentrically guided flexible NiTi tubes. The latter are extrinsically manipulated in 2 DoF each, i.e. translation and rotation. Conventionally, tubes are precurved with a shape setting heat treatment [GW16]. Alternatively, direct additive fabrication of the curved tubular structure is investigated [EA15, MO16]. The composition of multiple precurved tubes yields manipulator configurations with piecewise constant curvature sections, where design principles and fundamentals of applicable solid mechanics are discussed [DLIB10, MGI18] and optimisation of snapping effects through elastic stability is presented [HPD17, PRAR19]. The shape and dimensions of each tube, e.g. length and curvature, are numerically optimised for MIS applications based on task space metrics and anatomical constraints [BGV+15, GNBK19]. More recently, a hybrid approach in between concentric tube robot and tendon-driven continuum robot [AGB17b] is described for an improved path following performance and concentric tube robots with intrinsic actuation based on electro-active polymers (EAP) are discussed for deployment at small scale [CRA16]. Dual arm manipulation with concentric tube robots is considered for enhanced dexterity as discussed for tendon-driven manipulators in the previous paragraph [CGSB18].

1.2.4 Assistive Feedback in Teleoperated Robotic Surgery

The introduction of teleoperated robotic surgery to the operating theatre and its concomitant progress within the last decade have significantly advanced surgery [PAK+18]. Besides task-specific system design, fundamental robotic configurations for teleoperation are composed of a *slave* that enables surgical manipulation and is commanded remotely from a *master* console. Data exchange between master and slave is handled by a *controller* that determines gains, motion scaling, and virtual coupling [MP12]. In accordance with recent terminology of six autonomy levels in medical robotics [YCC+17], the vast majority of teleoperated systems shows *no autonomy* (e.g. master-slave configuration with motion scaling), *robot assistance* (e.g. virtual fixtures), or *task autonomy* (e.g. autonomous for specific tasks under supervision).

Emerging technologies have demanded for an enhanced immersion corresponding to the level of instrument and task automation. Despite improved dexterity and precision due to motion scaling or tremor filtering of master input, the indirect coupling between instrumentation and surgeon, e.g. electro-mechanical wire-driven mechanisms as used in the commercial DaVinci system, has introduced novel challenges such as loss of haptic feedback or environmental collisions [ODK+07, FDM+18].

Haptic feedback constitutes a desired feature of various applications in robot-assisted surgery. Several strategies have been reported accompanying the progress of robotic surgery. Recent terminology categorises haptics into *cutaneous/tactile* and *kinaesthetic* sensations. *Cutaneous/tactile*

sensation considers temperature, texture, and vibration whereas *kinaesthetic* sensation regards motion, force, compliance, and proprioception [Gru08]. Both senses are closely related to human motor control in order to enable perception and coordination [KAK15]. Most of the master devices proposed for control and haptic feedback in medical robotics target kinaesthetics such as guidance or restriction of limb or body motions due to applied forces/torques [vdPGJD08].

Robotic slave instrumentation generally uses commercial or bespoke force sensing components (e.g. strain gauges, fibre optics, etc.) for direct or indirect measurement of tool-tissue interaction forces at the tip or shaft [vdMS09]. Hence, single or multi DoF haptic master devices are employed to generate and render kinaesthetic feedback based on measured forces or torques through a control scheme to the user. An overview of devices, their mechanical design and control, as well as particular characteristics is provided in review literature [Ker14]. Beyond tailored interfaces for specific research, commercial low end devices such as the Geomagic Touch (3D Systems, Inc., Rock Hill, SC, USA) with 6 DoF kinematics for pose sensing with 3 DoF linear force feedback or advanced devices with 6 active DoF such as Delta or Omega series (Force Dimension, Nyon, Switzerland) are widely used.

Immersive generation and rendering of haptic feedback is significantly affected by the corresponding controller design, i.e. stability of the closed-loop controller is a core criterion. Otherwise, the coupling between operator and master device may result in high magnitude oscillations of the operator's forearm that must be actively damped and compensated. Those phenomena may cause master or slave damages. Common sources of instabilities are time discretization, large force gains computed from virtual springs, conservative damping, and temporal latencies from data transmission. In this regard, studies assessed the impact of damping parameters, physical properties of the operator, masses, and time delays in experimental or simulative trials and composed findings to parameter selection guidelines and provided device specific stability boundaries [DNBS06, DDVD14, HASH14, CO16]. Further work conducted high level analysis dedicated to asynchronous latencies of force feedback and vision [OOS+10].

Advantages of haptic feedback have been demonstrated in various surgical applications dedicated to environmental interaction, e.g. tissue handling and grasping. For example, *ex vivo* and phantom studies demonstrated that active force feedback has significantly lowered force transmission to the tissue for suturing and palpation with reduced prevalence of tissue trauma [BOK+04, WSJH07, ODK+07]. A meta-analysis of 58 publications has revealed significant effects of kinaesthetic assistance on tasks performances [WE15]. This is also addressed by complementing review literature [Oka09, OVRM11]. More recent work focused on future directions of haptic technologies, end user acceptance and innovation [EMF16, MPP17]. However, reports mitigate positive effects of haptic feedback on operators at expert level [MFA+16].

Alternative feedback strategies apply *sensory substitution* with force mapping measured from embedded sensors to a visual representation and superimposition to endoscopic visualisation, e.g. bar plots, force ranges, or warnings if force thresholds are exceeded [RAB+08]. Other studies

considered a visual representation of force directions and magnitudes [HRvdD+12] or intuitive overlays with preservation of salient anatomical features [GMP+15].

Haptic feedback does not exclusively target direct rendering of contact forces. Active or passive anisotropic kinaesthetic guidance can be additionally augmented to the master console and assist the operator to reach a specific target or accomplish a task. Active constraints, also denoted as *virtual fixtures*, combine advantages of human and robots with collaborative control. This addresses human task knowledge with robotic accuracy or human senses with robotic benefits. Local active constraints (e.g. forbidden areas) in task or joint space prevent intrusion or penetration of predefined ranges or areas. For example, this may avoid damage of delicate structures from end effectors or the whole instrumentation [KMS+09]. A second example has demonstrated path error reductions with active constraints between 50% to 90% compared to manual execution of arthroscopy [LKP+13]. An overview of virtual fixtures and constraints with specific application to robotic surgery is given in [ByB13]. More recent approaches augmented directional constraints with viscoelastic friction models to improve the control stability for dynamic path guidance [BDyB14].

Research on feedback in the field of laser surgery is limited due to challenging conditions from optical properties, flexible transmission, and energy delivery. A conceptual work presented a master-slave configuration for extracorporeal laser scanning and potential feedback schemes, but prototypes and evaluation were absent [RS05]. Early assistive concepts targeted navigated bone ablation [SSDL07] or handheld devices with fibre deflection [BVB+09]. Beyond that, concepts for delicate fibre-based tasks in intraocular retinal ablation with micro manipulators or cooperative control frameworks were proposed [CHC15, YMM+16]. More recently, feedback has been transferred to TLM. Firstly, vibrotactile and kinaesthetic feedback guide operators to a nominal ablation depth and prevent tissue damages based on predictive laser-tissue interaction models [FPO+16]. Secondly, challenges of non-contact laser surgery with regard to absence of tactile measurements are addressed. Haptic feedback generated from dense stereoscopic scene reconstruction [SKKO15] of microscopic imaging has been used to guide the user with a commercial master along a surface relief. This enabled perception of the surface topology in the irradiated area and provided additional feature guidance with dynamic active constraints [OBCM17]. Preliminary path delineation experiments have proven advantages on task accuracies.

Further contributions propose vision-based force feedback estimation to provide contact-free sensing of scene deformation and material responses [HKCY18]. For the sake of completeness, mapping of distance metrics to force or vibrotactile representations has considered feedback from laser range finders [YMI09], camera-projector setups, or camera-laser triangulation [ITAP11].

1.3 Limitations and Deficiencies

Research in the field of robotics which applies to endoscopic laser surgery is limited to current day technologies due to challenging conditions and requirements. This specifically addresses

miniaturised laser optics for flexible delivery but likewise dexterous beam manipulation and intuitive assistance for incorporation of spatial beam properties to the procedural workflow. Limitations of related work are summarised as follows:

Non-Contact Laser Delivery to Confined Anatomy

Related work presented in Section 1.2.1 has shown feasibility of gentle ablation with minimised collateral damage to adjacent tissue from Er:YAG laser sources due to pulsed irradiation and specific wavelengths. However, haemostatic control of vascularised tissue is inferior compared to CO_2 sources. Nonetheless, alternative strategies implemented with specific defocusing of the laser beam, absence of water spray, or setting of laser parameters enable a substitution [OPCK13, SMH$^+$19]. Hence, active mechanical or optical mechanisms for endoscopic focal adjustment are essential to meet clinical demands. Experimental results provided in Section 1.2.1 have exclusively considered rigid optical setups that disregard flexible endoscopic access through tortuous paths. In this regard, delivery of radiation at IR spectra and endoscopic scale is challenging due to the restricted availability of fibre technologies for lossless transmission. Recent approaches targeted commercial solid core fibres [FYCF04, CYF04] or bespoke hollow-core designs [UMF$^+$13]. Those shortcomings have affected further miniaturisation of opto-mechanical units for Er:YAG delivery as of currently. Reported clinical applications are limited to, e.g. contact-based endoscopic salivary stone removal [RVNG06]. By contrast, CO_2 lasers in flexible endoscopy have already been applied to gastric or transoral interventions [OMK$^+$13, LIR17]. However, reported cases conduct intracorporeal contact-based ablation with optical fibres or non-contact with extracorporeal microscopic attachments. This motivates research on further technologies towards endoscopic non-contact laser delivery.

Dexterous Endoscopic Manipulation of Focused Laser Radiation

Several mechanisms for manipulation within constrained endoluminal anatomy or body cavities have been presented in Section 1.2.3. Those devices may be deployed via trocar ports or natural orifices. The kinematics design is derived from surgical tasks and features, restricted workspaces or functionality, i.e. suturing envelopes. Those approaches generally disregard specific requirements of laser beams. By contrast, miniaturised scanning units (see Section 1.3) enable direct lateral deflection of the propagating beam but also show restricted workspaces (few millimetres edge lengths). Furthermore, system identification or feedback, e.g. visual sensors, are essential for compensation of positioning errors. However, beam caustics and in particular the focal distance are neglected. This shortcoming further applies to advanced robotic scanners in combination with direct-line-of-sight that have been introduced to TLM. Miniaturisation has also explored laser integration to catheters, but at the expense of dexterity. Alternatively, concentric tube robots have demonstrated superior manipulation performance in confined space, e.g. skull base surgery, but

cannot accommodate multiple sensors/instruments due to the design principle of flexible NiTi tubes. This features multiport deployment of concentric devices to accomplish complex soft tissue interventions with visual monitoring. Hence, an endoscopic device for laser manipulation must implement a highly integrated system design for radiation delivery and concurrent ablation monitoring. This comprises a dexterous endoscopic unit that features a kinematic configuration to execute at least three linear DoF in confined environments and additionally integrates camera and illumination components. A promising kinematic approach is represented by variable-length continuum robots. However, proposed backbone-based designs have yet prevented advanced levels of sensor integration.

User Assistance for Focal Adjustment in Non-Contact Laser Surgery

The accurate adjustment of the focal distance to the tissue surface is a core requirement for non-contact laser delivery. Prior work has demonstrated in Sections 1.2.1 and 1.3 that the extend of resulting tissue damage is determined by the energy input and wavelength of the laser, but also that recent devices have disregarded mechanisms or augmented assistance for non-contact delivery. This also regards the gold standard procedure of TLM, where focal and laser settings are set based on clinical experience. For example, the quadratic relation of beam waist diameter and depth of focus causes a significant reduction ($25\times$) of the usable depth of focus for a spot diameter reduction of factor five [GS13]. On the one hand, this increases the local intensity in the focal distance, on the other hand this demands for accurate spatial adjustments to maintain ablation. Current work is limited to navigated and assisted laser application with external navigation [SSDL07] and an early study on visual guidance for focal adjustment [SKL$^+$16]. Due to the current absence of procedural online assistance, clinicians tolerate spot sizes of $0.3\,\mathrm{mm}$ to $0.5\,\mathrm{mm}$ to maintain ablation. This includes multiple readjustments during the procedure to excise larger tissue volumes [GS13].

User-Centred Performance and Usability Assessment of Robotic Devices for Laser Manipulation

The clinical acceptance and success of novel medical devices is strongly supported by positive outcomes of preclinical performance and usability assessments involving potential end users, i.e. clinical experts. To date, teleoperation of devices and deployment scenarios with low levels of task autonomy are common use cases in medical robotics. In robotic laser surgery, only scanner-based scenarios for TLM including 2D beam displacement were investigated in end user studies [DOCM14]. By contrast, technical characterisation of robotic devices discussed in related work (see Section) was limited to laboratory settings only and disregarded user studies. In this regard, specific approaches for evaluation scenarios and corresponding metrics for robotic 3D laser beam manipulation are absent and have not been discussed in prior work.

Task Automation for Robotic Laser Delivery

Teleoperation of robotic devices is considered state-of-the-art due to clinical regulations [YCC+17]. However, teleoperated control of focused laser radiation employing a robotic master-slave configuration may overcome prior challenges of displacing the laser over a large distance of $500\,\mathrm{mm}$ such as required in TLM. However, this may show spot delineation inaccuracies from concurrent scene motion. Mitigation may be achieved with extensive user training. Therefore, intuitive online planning on microscopic live image has been introduced to scanner-based 2D TLM [MCDG10]. This has been complemented by vision-based control of the scanner unit to improve spot positioning accuracies [DMC15a, AT15] and motion compensation for scanner-based ablation [SKKO17]. Neither those approaches are solely dedicated to direct beam deflection with scanner units nor take focal distances into account.

1.4 Research Contributions

Fundamental directions of this thesis are partly results of the European Research Council project μRALP (FP7-ICT grant agreement no 288663). However, this work overcomes limitations identified in the μRALP project and proposes a novel robotic approach for endoscopic non-contact laser surgery. The work is not only restricted to transoral or laryngeal applications but may also be deployed to other luminal interventions.

As related work has shown, ablation of soft tissue based on pulsed radiation from Er:YAG laser sources at $2.94\,\mu\mathrm{m}$ is considered a promising tool for surgery with less trauma, smaller resection margins, and accurate delineation. For the first time, miniaturisation of suitable optical components and their integration to endoscopic devices has been addressed in this work associated with the μRALP project and beyond. This contribution aims at a novel opto-mechanical system for high power Er:YAG delivery at small scale. Optical properties are characterised and ablation performance is evaluated experimentally. This contribution is mainly published in [KFS+16].

Various robotic devices have been described in literature for luminal applications in MIS. Likewise, several mechanisms for laser displacement in contact or non-contact mode are discussed. Nevertheless, focal adaptation is neglected in most of the reports. To enhance the dexterity and efficiency of laser manipulation in MIS, a novel endoscopic robot design with extensible continuum segments is proposed. The device additionally accommodates a multi-functional tip with stereo imaging, illumination, and laser optics from previous contributions. The kinematics design in combination with online sensor feedback from the tip constitutes a robust mechanism for adjustment of the focal length to the tissue surface. The bottom-up system design including numerical optimisation of the continuum manipulator and camera layout are outlined and the implementation of the prototype is presented. The contribution is complemented by a preliminary experimental study on structural

responses of the flexible segments. Early concepts, designs, methodologies, and prototypes are published in [KSKO14a, KSKO14b, KSKO15, KSKO17, KSP$^+$19, KGS$^+$20].

To enable teleoperation and automation of the proposed robotic platform, a robotic framework within the ecosystems of the robot operating system (ROS) is proposed for device simulation and control. A customised kinematic model for extensible continuum segments is derived and extended from related work to describe forward, inverse, and instantaneous kinematics. In more detail, the framework implements kinematics, haptic, and visual controllers. User interaction is complemented by bespoke user interfaces for endoscopic laser surgery. Accuracy[1] of the kinematic model is validated in experimental studies. Likewise, performance of scene tracking algorithms is evaluated on the selected stereo camera. The highly integrated framework enables refactoring and dissemination to the scientific community in the field of continuum robotics.

Even though the proposed robotic endoscope targets non-contact laser delivery and enables inherent adaptation of the laser focus to the tissue surface through the kinematics design, teleoperation is considered the state-of-the-art. In absence of assistance and tactile perception, the operator must command the distance to the tissue surface based on his experience in endoscopy while being subject to a significant cognitive load to maintain the optimal distance for the pathology delineation, i.e. executing a coordinated motion in multiple DoF. This contribution aims at concepts and implementation of visual, haptic, and visuo-haptic assistance to improve the intraoperative focal adjustment in a master-slave configuration. Assistive features are assessed in an experimental user study with novice and expert users. Methodologies and results are presented in [KSP$^+$19, SKG$^+$19].

Since the application of the robotic endoscope aims at spatial laser delineation and ablation of soft tissue pathologies, the performance in relevant tasks has to be assessed and compared to accuracy metrics derived from clinical requirements. This includes subjective user acceptance. The corresponding contribution targets a user study with novice and expert subjects that mimics a clinical scenario of pathology delineation with a path tracing task on random patterns. By reason of an eye-in-hand imaging configuration, non-stabilised and stabilised endoscopic images are rendered to the user during task completion to analyse the effect of visualisation. Lastly, a preliminary 3D path tracing study is conducted taking assistive features of the previous contribution into account. This work is summarised and published in great part in [KGS$^+$20].

The last contribution targets supervised autonomy of the robotic system for 1) intraoperative camera view assistance and 2) automated execution of ablation paths. Related work has shown that vision-based robotic control may support the surgeon with camera assistance to maintain the surgical target in the field of view (FoV). This also applies to luminal applications as reconfiguration of endoscopes may cause loss of visibility, e.g. in laparoscopic interventions. Automated view adaptation in surgery has been demonstrated with custom kinematics and concentric tube robots [MIT$^+$18], but has never been considered for extensible continuum robots nor has been combined with advanced tracking algorithms. Beyond that, automated execution of laser ablations may reduce the cognitive

---

[1]This work uses the terminology published in [ISO94], i.e. accuracy consists of trueness and precision.

load to the operator, enables fusion with preoperative imaging, and allows for constant velocities along the path. Visual controllers are derived for both approaches and integrated into the robotic framework. Preliminary performance studies demonstrate feasibility of the methodology and the results of the automated path execution are further compared to manual execution.

1.5 Thesis Overview

The outline of this thesis is given in the following. Contents have been published in conference proceedings and scientific journals as referenced in the previous Section 1.4. Early work was supported by five supervised student theses [His14, Mic16, Joh16, Dic17, Pis17]. A visual abstract of chapter directions is provided in Figure 1.10.

Chapter 2 introduces the background of the thesis, which includes laser physics, fibre delivery, and laser-tissue interaction. Furthermore, notation standards of spatial transformations in robotics and vision are described. The chapter concludes with fundamentals on algorithms for stereoscopic depth recovery and motion/deformation tracking, which is frequently used throughout the thesis.

Chapter 3 addresses the opto-mechanical challenge of laser delivery to confined anatomy. A novel focus unit for endoscopic integration is proposed and implemented. Specifications and requirements are derived under the constraint of miniaturisation for robotic integration and further transferred to a design concept. Lastly, optical parameters of the unit are characterised experimentally and the ablation performance is demonstrated on tissue samples.

Chapter 4 is dedicated to the mechatronic design of a robotic platform with extensible continuum segments for non-contact laser surgery in confined spaces. System requirements are derived from prospective surgical applications and are transferred to electro-mechanical concepts. This further comprises additively manufactured extensible continuum segments as well as customised sensor designs. Finally, the integrated robotic prototype is presented.

Chapter 5 deals with the design and evaluation of a holistic framework based on the ROS middleware for kinematics, planning, and control of the novel robotic manipulator described in Chapter 4. Besides derivation of a kinematic model for extensible continuum bodies, the remainder discusses integration of closed-loop strategies, teleoperation concepts with master-slave operation, and scene tracking. The chapter concludes with an experimental evaluation of the kinematic accuracy and precision.

Chapter 6 targets concepts, design, and evaluation of visual and haptic assistance features for focal adjustment in robotic non-contact laser surgery. User studies with novice and expert subjects are conducted to assess the performance of assistive concepts integrated to the robotic framework (see Chapter 5). Objectives aim at improved usability, decreased focal position errors, and optimised task completion times.

Chapter 7 assesses the teleoperation performance of the robotic platform while performing path tracing tasks that mimic ablation patterns. User studies are carried out on certain target patterns and subjects are selected from medical and technical backgrounds with endoscopic knowledge from novices to experts. Main objectives are the identification of path tracing errors and the assessment of task completion times. Postexperimental questionnaires provide subjective user scores. Lastly, a preliminary study on 3D path tracing is presented incorporating assistance proposed in Chapter 6.

Chapter 8 introduces supervised autonomy for task execution and assistance in robotic laser surgery. Firstly, an approach for automatised view assistance is presented and evaluated. Subsequently, processing of online scene information in combination with tracking and visual control algorithms enables automatised execution of ablations path. Likewise, usability is improved by intuitive path planning in the endoscopic live view. The methodology is evaluated in a preliminary study and validated against results of Chapter 7.

Chapter 9 summarises major contributions of this thesis and highlights future work.
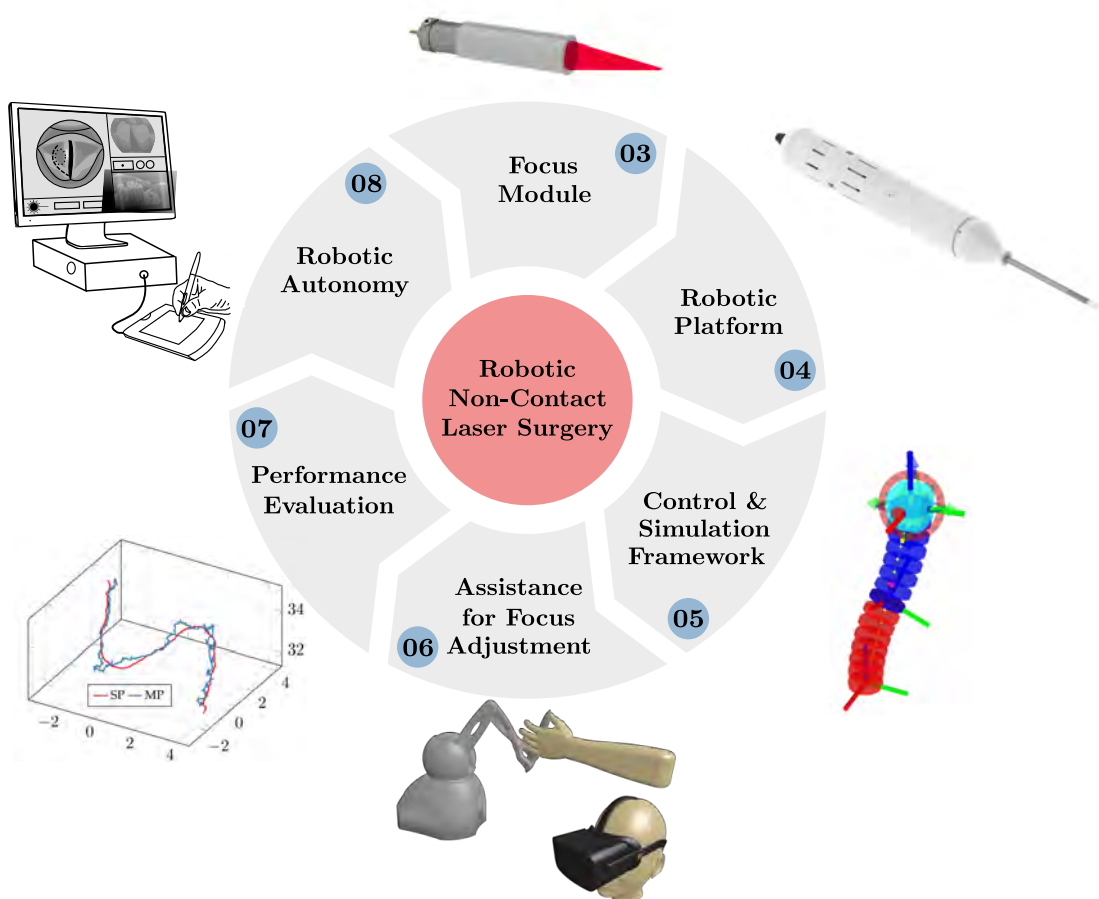
Fig. 1.10: The visual abstract highlights research contributions related to each chapter of this thesis.

2 Background

Relevant background of this thesis is summarised in this chapter. Section 2.1 provides fundamentals on laser physics and corresponding quantum mechanisms. Fibre delivery is introduced in Section 2.2. Laser-tissue interactions are detailed in Section 2.3. Subsequently, spatial notation is described in Section 2.4 for robotic and computer vision. The chapter closes in Sections 2.5 and 2.6 with frequently used algorithms for stereoscopic scene reconstruction and tracking.

2.1 Laser Physics and Caustics

The discovery of generating and amplifying highly directional and coherent monochromatic light in the late 1950s by Mainman et al. has strongly influenced preceding technologies. The innovation was introduced with the acronym *LASER* (light amplification by stimulated emission of radiation) and has become an essential component of daily life for consumer electronics, material processing, metrology, research, or biomedicine.

Subsequent paragraphs provide an overview of laser physics, design of laser devices, and associated unique optical properties. The reader is kindly referred to standard literature for further details [Trä12, Sve16]. The generation of artificial optical radiation induced by electromagnetical waves with spectra from ultra-violet over visible to far-infrared ($\lambda = 0.152\,\mu m$ to $100.0\,\mu m$) is determined by components of the optical system and corresponding physical mechanisms. A generic setup and layout of optical elements for realising a laser is depicted in Figure 2.1a. The gain medium is the core component and consists of solid-state, gas, or liquid media. The latter is located between two reflective mirrors or shows a reflective coating directly applied to the surfaces of employed crystals. The resulting layout forms an optical resonator enabling light emitted from the medium to travel repeatedly within this cavity. The resulting interference determines and maintains distinct stable frequencies and intensity patterns (eigenmodes), while destructive interference suppresses side-effects. Eigenmodes further have longitudinal and transversal representations that can be approximated by HERMITE- or LAGUERRE-GAUSSIAN functions (see Figure 2.1b).

Each component is linked to a specific physical effect and contributes to the generation of laser radiation. In the following section, energy states of an atom of an arbitrary gain medium and interaction with radiation are described with a multilevel state system composed of a ground state (thermal equilibrium) and N_{E} excited states. Transitions between states and resulting effects are described with photon-based quantum mechanics as shown in Figure 2.2.
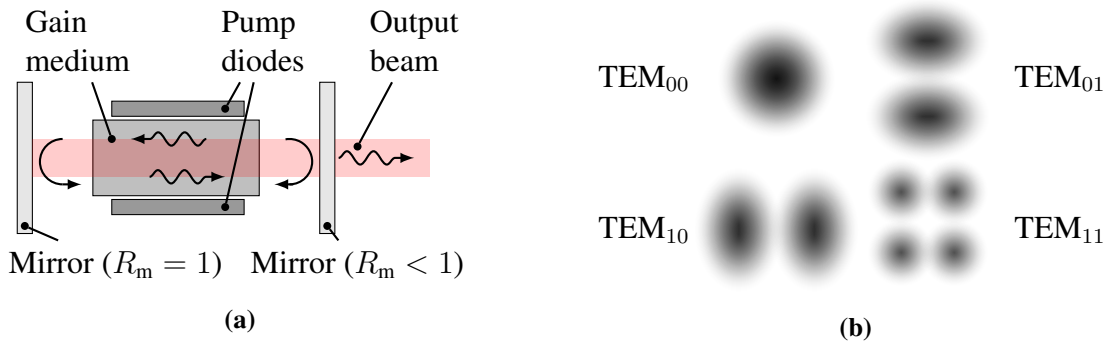
Fig. 2.1: (a) Basic components of a laser resonator with unequal mirror reflectivity R_{m} for output beam generation. (b) Example of transversal eigenmodes (TEM) of a resonance cavity. TEM$_{00}$ represents the transversal base mode also denoted as Gaussian mode.

Spontaneous emission is the principle of instantaneous transition and decay from excited E_2 to ground E_1 energy while simultaneously releasing the energy difference between both states as electromagnetic wave of a photon with frequency f_0 (see Figure 2.2a). The number of atoms in excited state is denoted as population. Exceptionally, non-radiative decay can only occur for releases from kinetic or vibrational energy between interacting atomic groups.

The principle of *stimulated emission* extends the idea of spontaneous emission (see Figure 2.2b). If an electromagnetic wave with frequency f_0 is incident to an atom in excited state, quantum mechanical interaction triggers a decay to ground state, while simultaneously releasing electromagnetical radiation in a photon with similar properties of direction, phase, and polarisation.

Finally, an atom in ground state can be elevated to excited state if electromagnetic waves with frequency f_0 are incident by sourcing energy $\hbar f_0$ from dissolving an incoming photon, where $\hbar$ is PLANCK's constant (see Figure 2.2c). This effect is denoted as *absorption*.

Amplification of coherent light is related to the population, i.e. the amount of atoms in excited states. Hence, optical amplification in a medium is only feasible if the number of atoms in excited state exceeds the number of ground states (population inversion) shifting the distribution into a disequilibrium; otherwise the medium responds with absorption in thermal equilibrium. The
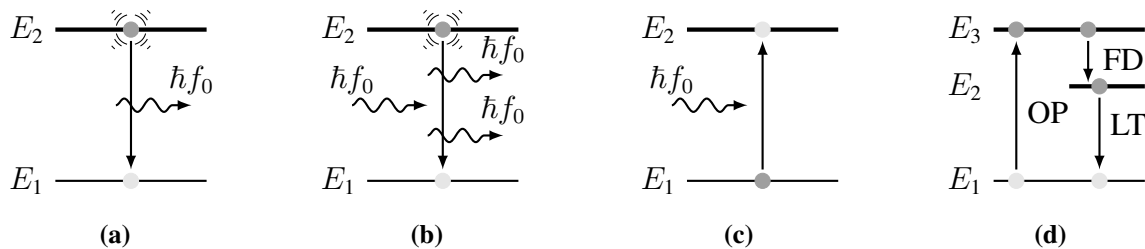
Fig. 2.2: Fundamental quantum mechanical effects: (a) spontaneous emission, (b) stimulated emission, and (c) absorption. The principle of generating a laser transition from population inversion is shown in (d) comprising optical pumping (OP), a fast decay (FD), and laser transition (LT) to ground state.

preservation of population inversion demands a *pumping mechanism* and an extension to a three- or four level state system due to saturation effects (see Figure 2.2d). After elevating the atom to the highest pump state, immediate decay creates a population inversion in the subordinate state causing laser transition to ground or intermediate state. Pumping of gain media is achieved optically or electrically. Solid-state gain media such as Nd:YAG or Er:YAG are pumped optically with high efficiency using diode lasers. The adverse effect of heat input is compensated with fluidic cooling. The pumped gain medium is located within the optical cavity enabling back reflection. In each passage, emitted and reflected photons are amplified in the medium by stimulated emission until stable oscillation is achieved. Above a certain threshold, photon amplification can exceed magnitudes but solely propagation of photons with paraxial direction contributes to oscillation. Both mirrors or coatings contribute to the process, while one mirror enables total reflection and the other partially transmits radiation forming the beam output.

The aforementioned mechanisms determine the unique properties of laser radiation. In comparison to incoherent light sources (e.g. sun or light bulb), lasers are *monochromatic* due to the distinct resonance frequency of light oscillation in the optical cavity. Monochromaticity is further associated to *spatial* and *temporal coherence*. Thus, the local phase lag of two arbitrary emitted electromagnetic waves shows no difference and the temporal phase lag is related to the narrow line-width of the laser. The design as open resonator with a pumped gain medium located between reflective components determines the dominant direction of stimulated emission. In consideration of an ideal setup, *directionality* is solely limited by diffraction. This property is further related to high optical *intensity* from oscillator power output with low divergence.

The spatial expansion of the laser beam radius $w(z)$ perpendicular to the optical axis z of a Gaussian beam after passing through a focusing lens is denoted as laser caustics (see Figure 2.3) and given by

$$w(z) = w_0 \sqrt{1 + \frac{z^2}{z_R^2}}, \tag{2.1}$$

where $w_0 = w(z = 0)$ determines the beam radius at the focal position and $z_R = \pi w_0^2 / \lambda$ the wavelength-dependent RAYLEIGH length. Under the assumption of $z = z_R$, the beam radius is determined to $w(z_R) = \sqrt{2} w_0$. This distance corresponds to a beam expansion of factor $\sqrt{2}$ and can be measured as $1/e^2$ point (fraction of 0.135 of maximum intensity) in experimental beam characterisation [dASdL$^+$09].

The far-field expansion ($z > z_R$) is described by linear divergence angle $\Theta = \lambda / \pi w_0$. Furthermore, optical output power P_{avg} for Gaussian beams remains constant in arbitrary planes along the z-axis. More recently, beam propagation quality is characterised by $M^2 = w_{0,M} \Theta_M / w_0 \Theta$. The ratio of measured and ideal focal radius and divergence ranges from one to several hundreds for ideal Gaussian to diffraction affected beams [HPT08].

Laser systems are commonly operated in CW or pulsed mode. CW lasers (e.g. CO_2 or HeNe) emit power continuously over time and the optical output is limited to available pumping resources. In
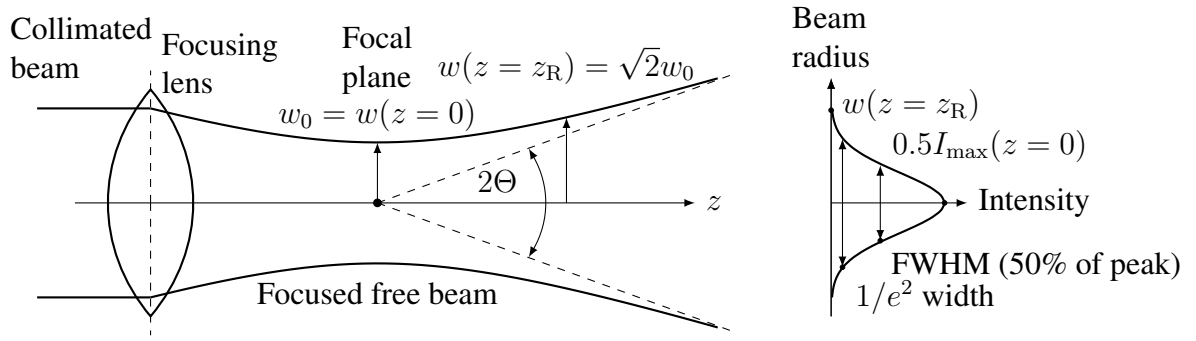
Fig. 2.3: Schematics of focusing a collimated Gaussian beam with a lens: (left) beam propagation and associated parameters. (right) Gaussian intensity distribution in $z = z_\mathrm{R}$ plane. Spot diameter at full width at half maximum (FWHM) and $1/e^2$ point are indicated for experimental determination of beam characteristics.

contrast, pulsed lasers (e.g. Nd:YAG or Er:YAG) emit pulses repetitively at frequency f_P with pulse duration τ_P related to a duty cycle of T_P enabling high peak power. The pulses are generated by optical modulation from Q-switching, gain switching, or mode locking. General performance parameters of pulsed lasers are listed in Table 2.1.

2.2 Fibre-Optic Laser Delivery

Several industrial and medical applications demand for flexible delivery and manipulation of optical radiation in confined spaces such as surgery or integration to robotic components in motion, e.g. laser welding. Optical designs integrate laser sources stationary and provide delivery units based on mirror arms [Dal16]. Alternatively, fibre-based solutions are proposed for guidance of optical radiation to remote locations or dexterous manipulation. Fibre technology has also evolved in the last decades to transmit low power signals for optical communication. Advanced components are dedicated to transmission at different wavelength ranges as well as high-energy laser pulses. The subsequent paragraphs summarise fibre-optic principles due to their relevance for medical technology.

Tab. 2.1: Performance parameters of pulsed laser radiation.

Description	Symbol	Relation	Unit
Spot area	A_w	$\pi w(z)^2$	mm^2
Energy per pulse	Q_P	-	J
Radiant exposure	F_P	Q_P/A_w	$\mathrm{J\,cm}^{-2}$
Irradiance	E	-	$\mathrm{W\,m}^{-2}$
Peak power	P_max	$Q_\mathrm{P}/\tau_\mathrm{P}$	$\mathrm{J\,s}^{-1}$
Average power	P_avg	$Q_\mathrm{P}f_\mathrm{P}$	$\mathrm{J\,s}^{-1}$
Intensity	J_P	P_max/A_w	$\mathrm{J\,mm}^{-2}$
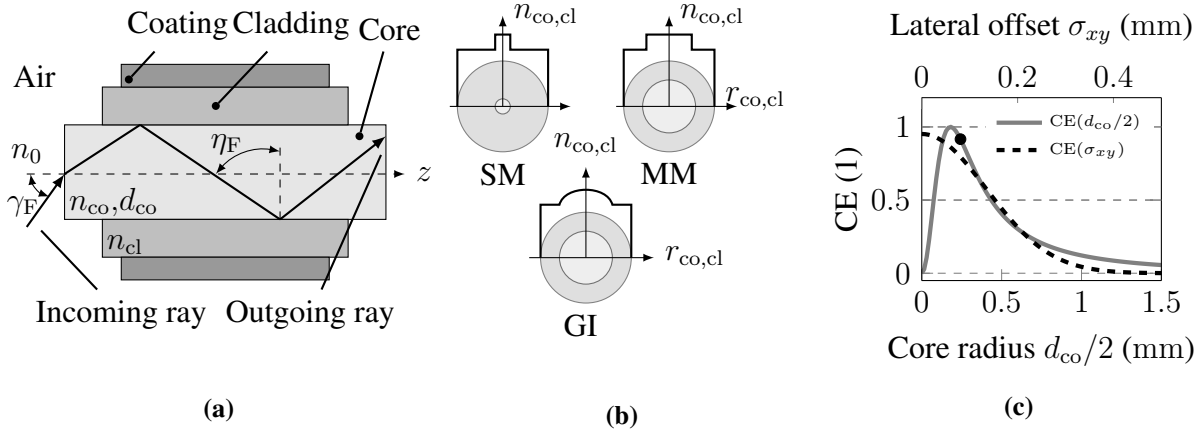
Fig. 2.4: (a) Cross-sectional fibre representation with internal reflection along axis z. (b) Fibre types given by refractive index transition: stepped index single mode (SM), stepped index multi-mode (MM), and graded index (GI) designs. (c) Simulated data of coupling efficiency (CE) for a Gaussian beam with $\lambda = 2.94\,\mu\text{m}$ and focal radius $w_0 = 180\,\mu\text{m}$ as a function of core radius $d_{\text{co}}/2$ and lateral offset σ_{xy} of optical axes. The marker • indicates the CE of a fibre with $d_{\text{co}} = 450\,\mu\text{m}$.

The composition of a fibre is schematically shown in Figure 2.4a. It comprises three components: 1) core, 2) cladding, and 3) coating. The core with diameter d_{co} (between $5\,\mu\text{m}$ to $500\,\mu\text{m}$) and refractive index n_{co} represents the medium for optical propagation. The cladding with refractive index $n_{\text{cl}} < n_{\text{co}}$ encloses the core and enables light transmission within the core due to total internal reflections at the core-cladding interface. Both components are embedded into a protective coating for structural stability and handling. Two types of fibres are established with respect to the transition between n_{co} and n_{cl}. As depicted in Figure 2.4b, stepped index fibres with single or multimode characteristics exhibit a discrete, while graded index fibres provide a gradual transition, respectively.

Single mode fibres show very low core diameter and only allow a single ray to travel [YSLL19]. In contrast, multimode fibres enable propagation with multiple paths but also undergo path length-related dispersion effects. By contrast, graded index designs show superior characteristics owing to ray propagation. As shown in Figure 2.4a, an incoming ray at incident angle γ_{F} undergoes refraction at the core-air interface and is reflected along axis z at the cladding-core interface with half-angle η_{F}. The maximum amount of light to be collected by an optical system, e.g. fibre, is defined by the numerical aperture $\text{NA} = n_0 \sin(\gamma_{\text{max}}) = n_0 \sqrt{n_{\text{co}}^2 - n_{\text{cl}}^2}$, where γ_{max} determines the maximum acceptance angle for internal reflection of the incident ray and n_0 the refractive index of ambient medium, i.e. air or fluid.

The coupling of laser radiation to a fibre optical system relies on optical properties of radiation source and fibre as well as the component's spatial alignment. Firstly, an optimally aligned setup of source, focusing elements, and fibre is considered. This assumes localisation of the fibre tip in the focal plane (see Figure 2.3). Hence, radiation undergoes attenuation [DFW+19] within the

fibre due to manufacturing impurities, scattering, or effects from bending given by attenuation coefficient

$$\alpha_{\text{t}} = -\frac{10}{\ell_{\text{F}}} \log \left(\frac{P_{\text{F,out}}}{P_{\text{F,in}}} \right),$$

(2.2)

where $P_{\text{F,in}}$ and $P_{\text{F,out}}$ describe the measured input and output power, respectively. Parameter ℓ_{F} is the length of the fibre segment. Optical attenuation is further related to the wavelength, i.e. components are optimised to specific ranges such as visible or IR spectra. Further transmission losses are determined by coupling efficiency (CE) of source and fibre. With assumption of an ideal setup, the metrics yields to $\text{CE} = 1$, whereas any presence of losses causes $\text{CE} < 1$. Three types of misalignments of two facing fibre tips are identified experimentally in related work and denoted as *tilt*, *lateral offset*, and *mode-matching* [WT82]. The effect of mode-matching and lateral misalignment on CE is demonstrated in the example shown in Figure 2.4c. The latter takes optical properties of standard components into account. The results underline the significance of an optimal component selection, i.e. fibre diameters, and a precise alignment of optical axes to achieve minimal losses.

2.3 Laser-Tissue Interaction

The interaction of laser radiation and matter (e.g. tissue) is governed by three mechanisms: 1) the wavelength-dependent opto-thermal transmission, 2) the optical response, and 3) laser parameters. This paragraph provides an overview on interaction mechanisms and its relevance for medical applications. The reader is kindly referred to standard literature for detailed information [Nie07, WvG11, RK11].

As shown in Figure 2.5a, incident light to a transparent or opaque specimen causes three physical effects denoted as reflection/refraction, scattering, and absorption. *Absorption* describes the effect of attenuation while the beam propagates through a medium. Energy is converted into local heating or higher vibrational modes of atom/molecular compounds. The term absorbance defines the ratio of incident and absorbed energy as a function of incident wavelength λ. LAMBERT's law[1] provides the analytical representation of attenuation effects within media of absorption coefficient μ_{a}. Absorption spectra of chromophores or molecules exhibit a significant dependency on the incident wavelength due to excitation of molecular modes. With respect to tissue contents of dominant concentration, absorption of water molecules ranges from a minimum of $\mu_{\text{a,H2O}}(\lambda = 500\,\text{nm}) = 1 \times 10^{-4}\,\text{cm}^{-1}$ to a maximum of $\mu_{\text{a,H2O}}(\lambda = 2.94\,\mu\text{m}) = 12\,500\,\text{cm}^{-1}$ and for haemoglobin from a minimum of $\mu_{\text{a,Hb}}(\lambda = 1\,\mu\text{m}) = 1 \times 10^{-1}\,\text{cm}^{-1}$ to a maximum of $\mu_{\text{a,Hb}}(\lambda = 400\,\text{nm}) = 1 \times 10^{2}\,\text{cm}^{-1}$ in the spectral domain of UV to far-infrared [PW74]. Furthermore, peaks are shifted towards shorter wavelengths with increasing temperature.

---

[1]also denoted as Lambert-Beer-law

By analogy to Section 2.2, incident radiation is *reflected* at angle γ_F from the interface of two media, e.g. air and tissue, in presence of smooth surfaces. Otherwise, diffuse phenomena dominate the interaction. The speed of light varies, while passing the interface and causes refraction if constraints of SNELL's law are met; otherwise, total reflection occurs. If radiation propagates through tissue, *scattering* arises as interaction of particles and incident radiation at frequency ranges not matching the natural frequencies of bound particles. Hence, particle oscillation is stimulated in frequency and direction by the incoming electromagnetic wave but differs in amplitude and phase. This is closely related to *dispersion* (kinetic energy losses through absorption) and associated mechanisms are classified into elastic and inelastic processes (e.g. RAYLEIGH and BRILLOUIN scattering). Specific mechanisms are triggered by the fraction of energy transmitted between incident and scattered particles. Tissue specific properties are described by experimental scattering coefficient μ_s.

Previously discussed effects do not arise isolated while irradiating tissue. Mechanisms take place and appear with specific contributions related to the tissue type and incident wavelength. Those samples are defined as *turbid media* and optical properties are characterised by composed attenuation coefficient $\mu_\mathrm{t} = \mu_\mathrm{a} + \mu_\mathrm{s}$. Various direct and indirect *ex* and *in vivo* methodologies for experimental coefficient determination were investigated [SZ11].

Resulting interaction is concurrently determined by optical laser and tissue properties as well as thermal responses. In the last decade, five interaction models were classified for laser systems and tissue specimens from analysis of experimental data relating exposure time t_e and irradiance E_P. This classification yields: 1) *photo chemical interaction*, 2) *thermal interaction*, 3) *plasma-induced interaction*, 4) *photo ablation*, and 5) *photo disruption*. The listing is in the order of decreasing exposure times $t_\mathrm{e} > 1\,\mathrm{s}$ to $t_\mathrm{e} < 1\,\mathrm{ns}$ and increasing irradiance E_P. It is assumed that all interactions demand for similar energy densities. Nevertheless, ultra-short pulses may cause increased temperatures due to local accumulation. In this regard, the *thermal interaction* is discussed in the following.

The chart in Figure 2.5b depicts relations and parameters of thermal interaction. Tissue irradiation, i.e. ablation, is driven by local absorption of energy from laser irradiance E at wavelength λ. This absorption mechanism can be regarded thermodynamically as heat source and stored energy within the tissue is modelled as $Q_\mathrm{las} = m_\mathrm{tis}c_\mathrm{tis}\Delta T$ with mass m_tis of the sample volume, specific heat capacity c_tis, and temperature gradient ΔT. Heat alteration within the tissue volume is dominated by conduction. Radiation and convection are neglected. Temporal unidimensional conduction is given by diffusion

$$\frac{\Delta Q}{\Delta t} = -\kappa_\mathrm{tis}A\frac{\Delta T}{\Delta r}, \tag{2.3}$$
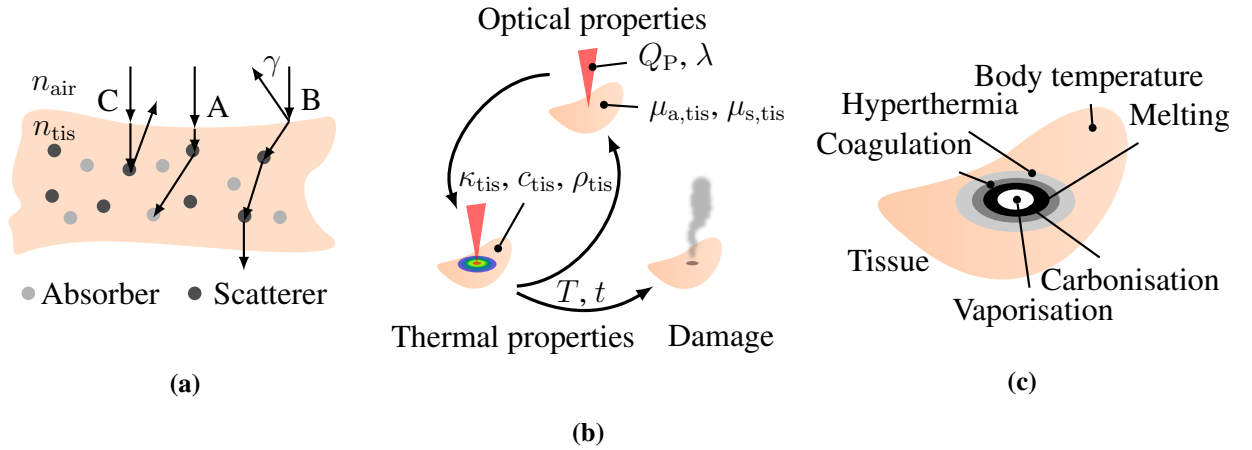
Fig. 2.5: (a) Schematic interaction model of laser radiation and tissue: Path A describes partial scattering and subsequent absorption. Path B demonstrates partial reflection and refraction of an incident ray at the transition from refractive index n_{air} to n_{tis} and scattering of transmitted radiation. Path C shows single scattering with remission. (b) The resulting tissue damage is determined in the first step by optical properties of incident radiation and exposed tissue sample. In the second step, thermal properties of the tissue sample govern the heat distribution. Lastly, the resulting temperature rise and total exposure time cause the resulting damage level. (c) Biological effects of tissue ablation and degeneration after laser irradiation.

where $\Delta T/\Delta r$ defines the local temperature gradient with spatial segment Δr, affected area A, and tissue-specific conductivity κ_{tis}. The latter is related to variations in water and cell content concentrations. Besides, thermal relaxation

$$\tau_{\mathrm{therm}} = \frac{(1/\mu_{\mathrm{a}})^2}{4\kappa_{\mathrm{tis}}} \tag{2.4}$$

enables assessment of heat diffusion after exposure to incident laser pulses of length τ_{p} and conditions $\tau_{\mathrm{p}} > \tau_{\mathrm{therm}}$ or $\tau_{\mathrm{p}} < \tau_{\mathrm{therm}}$. The exposure of cell compounds to heat and corresponding temperature increase may result in reversible and irreversible damages (see Figure 2.5c). The latter cause immediate or short-term necrosis or apoptosis, whereas reversible damages can be repaired by the affected organism. Tissue heating above body temperatures of $40\,^{\circ}\mathrm{C}$ to $50\,^{\circ}\mathrm{C}$ result in local *hyperthermia*. Beyond $50\,^{\circ}\mathrm{C}$ to $100\,^{\circ}\mathrm{C}$, denaturation of cell contents, e.g. collagen or protein, induces *coagulation* and cell necrosis. At $100\,^{\circ}\mathrm{C}$, tissue compounds are ruptured and ejected due to water vaporisation, i.e. ablation is triggered. Beyond $100\,^{\circ}\mathrm{C}$ cell compounds express carbon. This is indicated by darkened surfaces and plume. Further progress of heating results in local melting.

2.4 Spatial Notation in Robotics and Computer Vision

Algorithmic processing and spatial description in robotics and vision require transformation of specific coordinates between different frames, e.g. links of robotic arms or camera projection planes. A Cartesian position $\boldsymbol{P} = (x,y,z)^{\mathrm{T}} \in \mathbb{R}^3$ can be expressed in a specific coordinate frame. For instance, it can be referenced to frame (CF)$_{\mathrm{E}}$, where the subscript denotes the robotic end effector (see Figure 2.6a). This consideration yields $_{(\mathrm{E})}\boldsymbol{P} = (_{(\mathrm{E})}x,_{(\mathrm{E})}y,_{(\mathrm{E})}z)^{\mathrm{T}}$.

The transformation of position $_{(\mathrm{E})}\boldsymbol{P}$ to a different frame, e.g. base frame (CF)$_{\mathrm{B}}$, demands for a mapping that takes orientation and translation between both frames into account. This is achieved by homogeneous transformation $^{\mathrm{B}}\boldsymbol{T}_{\mathrm{E}} \in \mathrm{SE}(3)$ with rotation matrix $^{\mathrm{B}}\boldsymbol{R}_{\mathrm{E}} \in \mathrm{SO}(3)$ and translation vector $_{(\mathrm{B})}\boldsymbol{t}_{\mathrm{E}} \in \mathbb{R}^3$. Its composition yields

$$^{\mathrm{B}}\boldsymbol{T}_{\mathrm{E}} = \left(\begin{array}{c|c} ^{\mathrm{B}}\boldsymbol{R}_{\mathrm{E}} & _{(\mathrm{B})}\boldsymbol{t}_{\mathrm{E}} \\ \hline \mathbf{0} & 1 \end{array} \right) \in \mathrm{SE}(3), \tag{2.5}$$

where $\mathbf{0} \in \mathbb{R}^{1\times3}$. Homogeneous extension of position $_{(\mathrm{E})}\hat{\boldsymbol{P}} = (_{(\mathrm{E})}\boldsymbol{P},1)^{\mathrm{T}}$ enables the direct transformation to the base frame according to

$$_{(\mathrm{B})}\hat{\boldsymbol{P}} = {}^{\mathrm{B}}\boldsymbol{T}_{\mathrm{E}(\mathrm{E})}\hat{\boldsymbol{P}} \in \mathbb{R}^4. \tag{2.6}$$

However, transformation $^{\mathrm{B}}\boldsymbol{T}_{\mathrm{E}}$ is generally unknown and has to be recovered from subtransformations. As an example, transform $^{\mathrm{B}}\boldsymbol{T}_{\mathrm{E}}$ of a serial kinematic chain (see Figure 2.6a) between frames (CF)$_{\mathrm{E}}$ and (CF)$_{\mathrm{B}}$ can be determined by concatenation to

$$^{\mathrm{B}}\boldsymbol{T}_{\mathrm{E}} = {}^{\mathrm{B}}\boldsymbol{T}_{1}{}^{1}\boldsymbol{T}_{2}{}^{2}\boldsymbol{T}_{\mathrm{E}}, \tag{2.7}$$

where $^{\mathrm{B}}\boldsymbol{T}_1$, $^{1}\boldsymbol{T}_2$, and $^{2}\boldsymbol{T}_{\mathrm{E}}$ are unknown transformations that can be obtained from robotic design parameters (e.g. link lengths, joint locations, or joint states). Established methods for *discrete* or *hyper-redundant* manipulators (see Figure 2.6a) consider analytical models based on rigid-link homogenous transformations, e.g. derived from DENAVIT-HARTENBERG tables. The reader is kindly referred to standard literature [SK16]. In contrast, gold standards for kinematic transformations of continuum manipulators (see Figure 2.6b) assume segmental constant curvature due to the absence of discrete joints. Various kinematic models for continuum kinematics are discussed in a comprehensive review [RJWJ10].

Besides spatial transformation in Cartesian space, robotics take further space representations into account [SK16]. Firstly, *joint space $\boldsymbol{q} \in \mathbb{R}^{N_q}$* describes the joint state, e.g. angle, position, pressure level, where N_q defines the total number of actuated or passive joints. Secondly, *task space $\boldsymbol{x} \in \mathbb{R}^6$* is related to the Cartesian space with 3 DoF translation and 3 DoF orientation at a certain location of the manipulator, e.g. pose of the end effector. Both spaces are linked as follows: *Forward kinematics* provide mapping $\boldsymbol{x} = f(\boldsymbol{q})$, while *inverse kinematics* are given by $\boldsymbol{q} = f(\boldsymbol{x})^{-1}$.

Intermediate mappings are introduced in continuum robotics to facilitate transformations between joint and task space. The *configuration space* $\psi \in \mathbb{R}^{N_\psi}$ is introduced, where N_ψ is the specific space dimension. For example, forward kinematics of a continuum manipulator are obtained from composition of $\psi = g(\boldsymbol{q})$ and $\boldsymbol{x} = f(\psi)$ to $\boldsymbol{x} = f(g(\boldsymbol{q}))$.
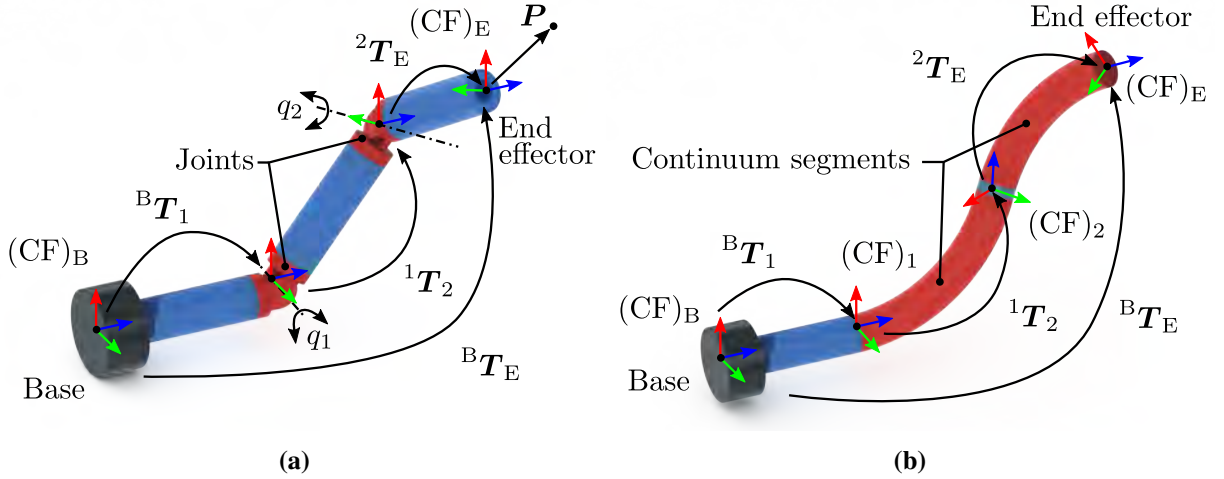
Fig. 2.6: Examples of kinematic transformations for (a) discrete and (b) continuum manipulators. Blue parts define rigid links, red parts describe actuated joints or continuum segments, and black parts represent the manipulator base.

2.5 Stereoscopic Scene Reconstruction

Stereoscopic reconstruction uses two camera sensors to mimic binocular vision for recovery of scene depth. This is specifically required for robotic control tasks and instrument guidance. The setup is conventionally described by baseline b which determines the distance between both sensors and the convergence angle, i.e. the parameter for adjustment of the overlapping FoV. Inspired by the human vision and the anatomy of eyes, sensors are frequently installed in a convergent layout of camera axes with convergence angle α_h (see Figure 2.7a). This increases the spatial overlap of both sensors FoV but likewise reduces the working distance. Additionally, the convergent setup of the camera axes may involve a perspective effect which creates a vertical parallax.

Computational methods demand for mathematical models of the optical system that transforms position $_{(\mathrm{L})}\boldsymbol{P} = \left(_{(\mathrm{L})}x, _{(\mathrm{L})}y, _{(\mathrm{L})}z\right)^\mathrm{T}$ in object space to position $_{(\mathrm{LI})}\boldsymbol{p} = \left(_{(\mathrm{LI})}u, _{(\mathrm{LI})}v\right)^\mathrm{T}$ in image space and vice versa. A recognised representation is the pinhole model illustrated in Figure 2.7b for the left camera with optical centre $(\mathrm{CF})_\mathrm{L}$. The model takes intrinsic camera parameters into account that are composed to camera matrix $\boldsymbol{C}_\mathrm{L} \in \mathbb{R}^{3 \times 3}$. Matrix elements are the principal point $\boldsymbol{c}_\mathrm{L} = (c_u, c_v)^\mathrm{T}$ of the camera and focal lengths $\boldsymbol{f}_\mathrm{L} = (f_u, f_v)^\mathrm{T}$. The latter is given by products of the physical focal length f of the lens and the individual (rectangular) pixel sizes s_u and s_v of the imaging sensor.

Shear factor α_{L} is neglected for the latest sensor designs. Unknown parameters of the intrinsic camera matrix $\boldsymbol{C}_{\mathrm{L}}$ are estimated from pattern-based camera calibration with non-linear optimisation [Zha00]. Hence, projective correspondence of points is given by

$$
s \begin{pmatrix} {}_{(\mathrm{LI})}u \\ {}_{(\mathrm{LI})}v \\ 1 \end{pmatrix} = s_{(\mathrm{LI})}\hat{\boldsymbol{p}} = \underbrace{\boldsymbol{C}_{\mathrm{L}}(\boldsymbol{I}|\boldsymbol{0})}_{M_{\mathrm{L}}} \begin{pmatrix} {}_{(\mathrm{L})}x \\ {}_{(\mathrm{L})}y \\ {}_{(\mathrm{L})}z \\ 1 \end{pmatrix} = \boldsymbol{M}_{\mathrm{L}(\mathrm{L})}\hat{\boldsymbol{P}}, \tag{2.8}
$$

where $s \in \mathbb{R}$ describes an arbitrary scalar and ${}_{(\mathrm{L})}\hat{\boldsymbol{P}}$ and ${}_{(\mathrm{LI})}\hat{\boldsymbol{p}}$ denote the homogeneous representations of position ${}_{(\mathrm{L})}\boldsymbol{P}$. Projection matrix $\boldsymbol{M}_{\mathrm{L}} \in \mathbb{R}^{3 \times 4}$ complements camera matrix $\boldsymbol{C}_{\mathrm{L}}$ by multiplication with $(\boldsymbol{I}|\boldsymbol{0}) \in \mathbb{R}^{3 \times 4}$, where $\boldsymbol{I} \in \mathbb{R}^{3 \times 3}$ is an identity matrix and $\boldsymbol{0} \in \mathbb{R}^3$.

The projection of object point $\boldsymbol{P}$ to both image planes of the stereoscopic setup yields projected points ${}_{(\mathrm{LI})}\boldsymbol{p}$ and ${}_{(\mathrm{RI})}\boldsymbol{p}$, respectively. Both projected points are linked by epipolar geometry. The latter builds upon intersection of left and right camera image planes from a convergent setup (see Figure 2.7a), an epipolar plane constituted by optical centres $(\mathrm{CF})_{\mathrm{L}}$ and $(\mathrm{CF})_{\mathrm{R}}$, and point $\boldsymbol{P}$. This defines epipolar lines in each image plane. Projected points are connected by epipolar constraints with fundamental matrix $\boldsymbol{F} \in \mathbb{R}^{3 \times 3}$:

$$
{}_{(\mathrm{RI})}\hat{\boldsymbol{p}}\boldsymbol{F}_{(\mathrm{LI})}\hat{\boldsymbol{p}} = 0. \tag{2.9}
$$

The correspondence search space can be reduced with Equation (2.9) to only one dimension. Taking additional image rectification into account, images planes are transferred to a parallel layout and the epipolar lines can be aligned horizontally to simplify algorithmic processing and to optimise computational efforts [FTV00]. The consideration of extrinsic stereo camera parameters enables the reformulation of the projective Equation (2.8) to

$$
s \begin{pmatrix} {}_{(\mathrm{LI})}u \\ {}_{(\mathrm{LI})}v \end{pmatrix} = s_{(\mathrm{LI})}\hat{\boldsymbol{p}} = \underbrace{\boldsymbol{C}_{\mathrm{L}}({}^{\mathrm{L}}\boldsymbol{R}_{\mathrm{R}}|_{(\mathrm{L})}\boldsymbol{t}_{\mathrm{R}})}_{{}^{\mathrm{L}}\boldsymbol{M}_{\mathrm{R}}} \begin{pmatrix} {}_{(\mathrm{R})}x \\ {}_{(\mathrm{R})}y \\ {}_{(\mathrm{R})}z \\ 1 \end{pmatrix} = {}^{\mathrm{L}}\boldsymbol{M}_{\mathrm{R}(\mathrm{R})}\hat{\boldsymbol{P}}, \tag{2.10}
$$

where extrinsic rotation ${}^{\mathrm{L}}\boldsymbol{R}_{\mathrm{R}} \in \mathrm{SO}(3)$ and translation ${}_{(\mathrm{L})}\boldsymbol{t}_{\mathrm{R}} = (-b,0,0)^{\mathrm{T}}$ are estimated from stereo camera calibration [SDY05]. After determination of pixel correspondence with epipolar constraints in both image planes and computation of disparity $d = {}_{(\mathrm{LI})}u - {}_{(\mathrm{RI})}u$, triangulation (depth recovery) with $z_{\mathrm{T}} = \frac{bf}{d}$ is feasible, where b denotes the camera baseline and f is the focal length.

This thesis considers in the following technical chapters an advanced algorithm for soft tissue reconstruction [SPK+13, SKKO15, Sch18]. The algorithm takes stereo vision fundamentals into account and uses an optimised correspondence search, i.e. stereo matching, based on a computational workflow (see Figure 2.7c). Rectified images are processed with a census transformation to mitigate
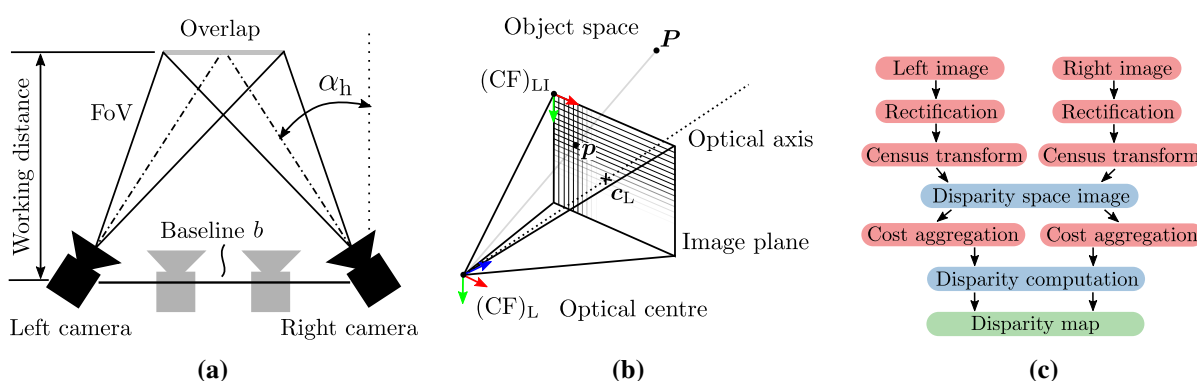
Fig. 2.7: Fundamentals of stereo reconstruction: (a) convergent and parallel sensor layouts, (b) camera pinhole model , and (c) algorithmic flow chart for disparity computation (adapted from [SKKO15]).

impacts of illumination variation. Subsequently, pixelwise correspondence search along epipolar lines is implemented with HAMMING distances accumulated to pixelwise costs. Robust matching in areas of challenging texture is targeted by cost aggregation. The optimal disparity is estimated from minima of aggregated costs. The resulting disparity map is denoised using bilateral filtering to preserve edge features. Consistency checks eliminate invalid disparities. Disparity propagation to adjacent neighbourhoods enables gap filling. The algorithmic implementation benefits from a customised parallelisation deployed to GPGPU with shared memory architectures.

The algorithmic performance has been evaluated on different data sets and stereoscopic hardware. Assessment on *in vitro* data of the public Open-CAS framework (see Figure 2.8a) outperformed existing methods and revealed a reconstruction root mean square error (RMSE) of (1.27 ± 0.68)mm. Deployment to different stereo imaging devices, e.g. customised stereoscopic cameras, a commercial endoscope, and microscope, were assessed with results shown in Figure 2.8b. Reconstruction RMSE from (0.094 ± 0.074)mm for the customised stereocamera embedded to the robotic device in this thesis to (0.176 ± 0.139)mm for a commercial stereo endoscope were measured.

2.6 Stereoscopic Motion and Deformation Tracking

Vision-based motion tracking has been introduced to MIS within the last decades for medical imaging, augmented reality, and robotics. Pioneering work in the field of surgery targeted in particular camera-based detection of heart motion patterns for compensation with robotic assistance and detection of local surface deformation [MY08].

Recovery of scene motion and deformation in the presented work of this thesis adapts a stereoscopic tracking algorithm that has been extended from a monoscopic approach [SLKO16, SKL$^+$16, Sch18]. It is based on a piecewise affine deformation model and takes epipolar constraints (see Section 2.5) into account to establish consistency within both camera images. The algorithm advances prior work on stereoscopic motion estimation with projective camera geometry for
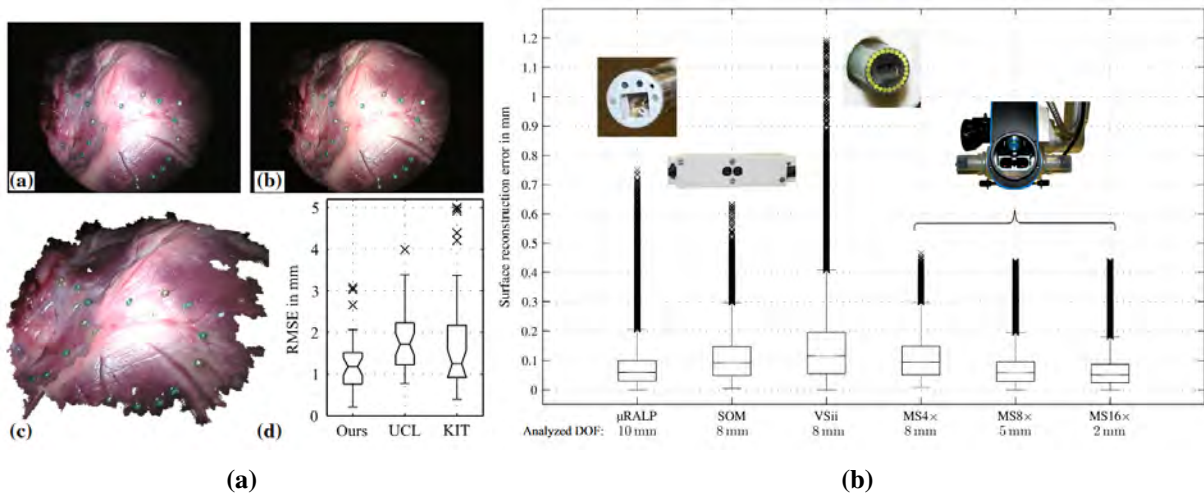
Fig. 2.8: Reconstruction performance: (a) results from Open CAS framework (reprinted from [SKKO15], © with kind permission from Springer Nature), and (b) results for different stereoscopic imaging devices (reprinted from [SKKO15], © with kind permission from Springer Nature).

JACOBIAN matrix computation to a disparity space representation. In contrast to mono view tracking, the stereoscopic approach takes alignment of triangle meshes (local surface approximation) in both images into account (see Figure 2.9b) and minimises corresponding alignment errors. The mesh deformation between consecutive frames is transferred into an energy term and gradient-based optimisation for minimisation of the energy cost function is applied for both images individually.

The performance of the tracking algorithm facilitates online deployment ($> 25\,\text{Hz}$), but results are prone to temporal drift and inaccuracies. Hence, appearance-based mesh refinement (MR) complements the tracking step for drift compensation. Algorithmic details and an example of temporal tracking sequences are shown in Figure 2.9a. Affine-invariant fusion of latest tracking and MR results overcome discarding of intermediate tracking results. By contrast, a sequential approach neglects certain results to satisfy online processing. Computation is complemented by KALMAN filter based upsampling of depths linked to mesh vertices. In absence of tracking measurements, the recent state is predicted from the underlying motion model, while availability of tracking measurements triggers updates of motion estimates.

The algorithmic performance was evaluated in a user study with blood vessel tracing, deployment to *in vivo* data, and motion compensation in scanner-based laser ablation on tissue samples. Results obtained on *in vivo* datasets demonstrate the superior tracking performance of the proposed algorithm over available state-of-the-art trackers. Tracking errors in the direction of depth estimation dominate for all experiments and methodologies. Root mean square (RMS) tracking errors below $1.5\,\text{mm}$ were achieved by concurrent strategies with significantly improved computational efforts ($< 15\,\text{ms}$) even for challenging scene conditions, e.g. partial scene occlusions due to instrument intrusion.

(a)

(b)

(c)

(d)
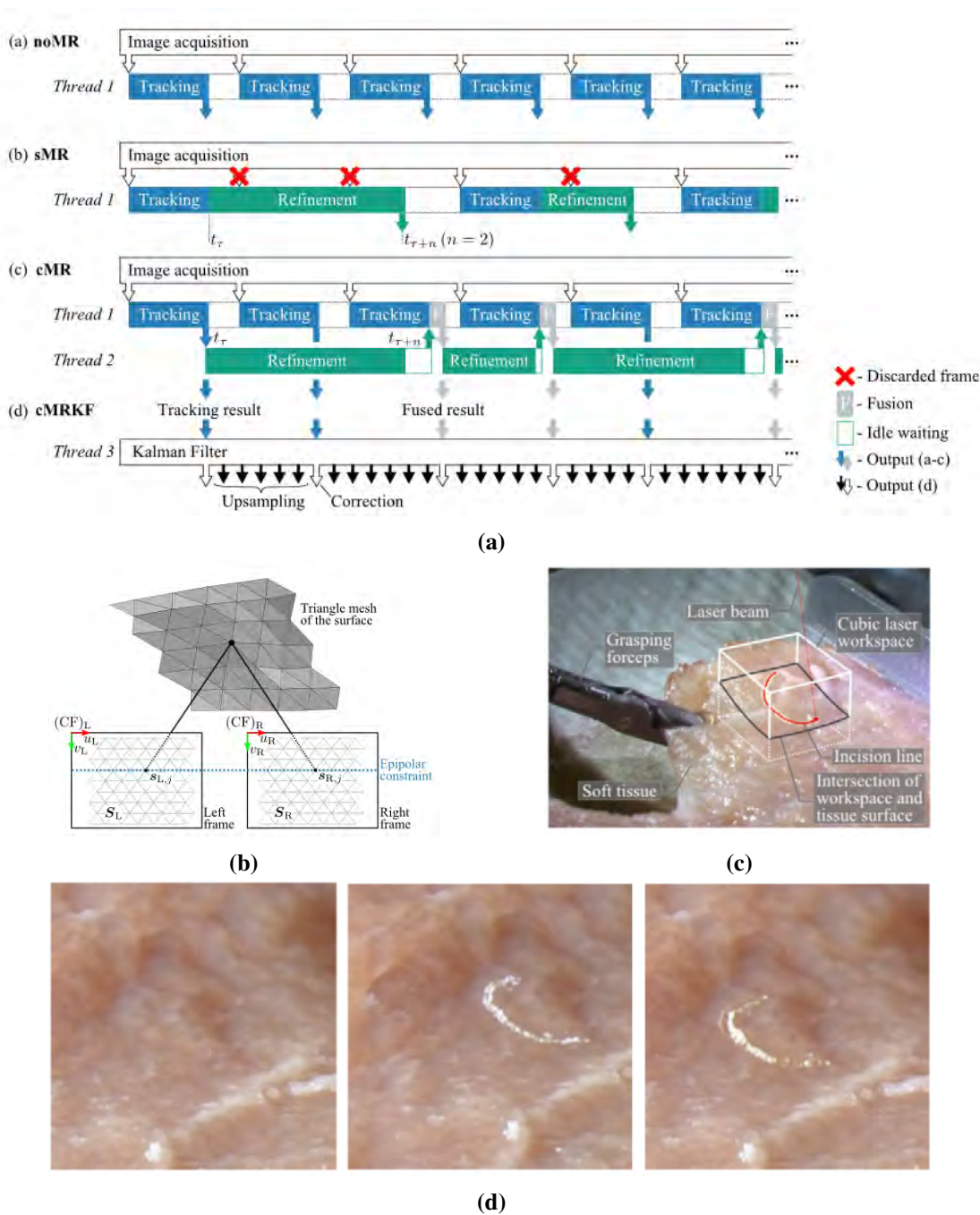
Fig. 2.9: Fundamentals of stereoscopic tracking algorithm and experimental evaluation: (a) sequences of mesh refinement and tracking, (b) stereoscopic representation of surface mesh, (c) experimental setup for compensated laser ablation on porcine tissue samples, and (d) tissue in motion while conducting ablation (all images reprinted from [SKKO17], Creative Commons Attribution 4.0 International License (http://creativecommons.org/licenses/by/4.0/)).

The tracking framework was further integrated to a scanner-based laser ablation system and activated, while ablation patterns were executed on porcine tissue as shown in Figure 2.9c. Simultaneously, specimens executed specific motion patterns using a robotic platform (see Figure 2.9d) and its surface was additionally deformed by instrument manipulation. Results demonstrated that concurrent motion and deformation of the specimen were successfully compensated by tracking feedback and enabled replanning of the scanner motion. Postexperimental assessment of ablation patterns revealed RMSE of less than $0.2\,\mathrm{mm}$ in reference to nominal patterns.

3 A Focus Unit for Endoscopic Non-Contact Laser Ablation

Clinical advantages of IR laser radiation for ablation of soft tissues are extensively discussed in related work (see Section 1.2.1). However, deployment to confined luminal anatomy is conventionally based on manipulation of optical fibres in tissue contact. This may result in gradual intensity losses, contamination, or risk of fibre fractures. Moreover, fibre tip displacement is prone to perturbations from extracorporeal handling. Thus, accurate, preserving, and safe delineation of targeted pathologies requires highly skilled clinicians to obtain moderate results. This also addresses online assessment of laser-tissue interaction to adjust laser source parameters accordingly.

Non-contact fibre manipulation based on an endoscopic robot is proposed in this thesis to overcome limitations of dexterity and laser-tissue interaction. The robot-tissue interface is implemented with a focus module that enables flexible high power radiation delivery to the endoscopic tip and optical reshaping of the beam to gain maximised surface intensities in absence of instrument contact. This can improve laser-tissue interaction due to optimal energy delivery, improved monitoring of ablation phenomena without view obstruction, and enhanced dexterity with endoscopic kinematics. Design and evaluation of a bespoke focus unit for endoscopic integration are presented in the following. More precisely, the opto-mechanical concept and implementation are presented in Section 3.1. Subsequently, optical characteristics of the prototype are determined and experimental protocols for assessment of ablation performance are described in Section 3.2. This is complemented by a feasibility study in a cadaver model. Experimental results of conducted studies are presented in Section 3.3 and discussed in Section 3.4. A conclusion is provided in Section 3.5. The content of this chapter is published to a great extend in [KFS⁺16].

3.1 Opto-Mechanical Design

The design concept of the focus unit shown in Figure 3.1 is primarily governed by dimensional constraints with respect to the enclosing robotic structure. Secondarily, availability of surgical lasers and optical fibres for transmission of high power IR laser radiation is restricted. In this thesis, solid core fibres are considered for laser transmission at $\lambda = 2.94\,\mu m$ with minimal systematic losses (see Section 2.2). In this regard, GeO_2 fibers (Infrared Fibersystems, Silver Springs, MD, USA) with $d_{co} = 450\,\mu m$, NA $= 0.12$, $\alpha_t = 0.5\,dB\,m^{-1}$, and minimal bending radius of $40\,mm$ are used. Prior to opto-mechanical fibre assembly, the cladding is removed manually and fibre tips are cleaved with a LDC-400 fibre cleaver (Vytran LLC, Morganville, NJ, USA). Afterwards, tips are cleaned with isopropanol and visually inspected under magnified light microscopy. An

additional polytetrafluoroethylene (PTFE) tube of $1\,\text{mm}$ diameter encloses and protects the bare fibre. Furthermore, a tailored stainless steel ferrule was manufactured and attached with optical adhesive (OA 81, Norland, NJ, USA) to the fibre tip. This establishes a mechanical interface to the focus unit and enabled fibre displacement for distance adjustment. A two-lens layout (see Figure 3.1a) was selected for the optics prototypic in order to comply with dimensional constraints. Consequently, beam shaping optics are required for successive collimation and focusing of the divergent free beam after fibre transmission with desired optical characteristics. Under consideration of mechanical and optical constraints, specifications were detailed to:

1. Outer module diameter below $8.5\,\text{mm}$ to enable accommodation in the endoscopic tip.

2. Low transmission losses of high power IR radiation at $\lambda = 2.94\,\mu\text{m}$ and beyond $P_{\text{F,in}} = 10\,\text{W}$ fibre input power.

3. Focal length $f = 20\,\text{mm}$ for observation and monitoring within the FoV of embedded chip-on-the-tip stereoscopic cameras.

4. Rayleigh-length $z_{\text{R}} = \pm 2\,\text{mm}$ for compensation of adjustment errors from assembly and robotic kinematics.

The lens selection regarded simulations in the ZEMAX environment (ZEMAX LLC, Kirkland, WA, USA). This comprised raytracing studies to implement the nominal focal length at the specified wavelength. Collimation and subsequent focusing is achieved with a pair of two customised plano-convex CaF_2 lenses (LA5315-D, Thorlabs Inc., Newton, NJ, USA) with anti-reflection coating for incident wavelengths in the range of $1.65\,\mu\text{m}$ to $3\,\mu\text{m}$. Both lenses were processed with optical machining (Laser Zentrum Hannover, Hanover, Germany) to decrease the diameters from $12\,\text{mm}$ to $7.5\,\text{mm}$. The bespoke housing of the opto-mechanical unit shown in Figures 3.1a and 3.1b is composed of two customised stainless steel tubes denoted as mounting A and B, respectively. Inner sections of the components are tapped and threaded to enable precise adjustment of the distance between fibre tip and collimation lens via angular adjustments of mounting B. Both lenses are inserted to the stainless housing and are aligned with a circular spacer disk. A sapphire window is mounted with interference fit to protect the enclosed optical parts. Lastly, the fibre ferrule is locked with a set screw for component exchange.

3.2 Experimental Methodologies

This section firstly presents the experimental setup used throughout the study and a semi-automatic sequence for optimised coupling of laser source and optical fibre. Secondly, a methodology for measurement of beam characteristics of the focus unit is described. Last but not least, protocols for ablation assessment are presented.
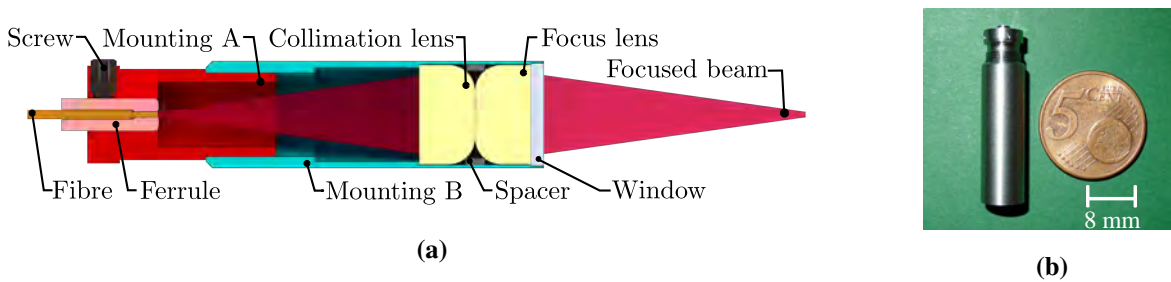
Fig. 3.1: Design and prototype of the proposed focus unit: (a) CAD model of the assembly with threaded mountings A and B, beam shaping, fibre optics, and protective window. (b) Prototype assembled and manufactured from stainless steel.

3.2.1 Hardware Setup

Studies dedicated to experimental evaluation of the focus unit use a prototypic laser scanning setup that has been customised in earlier studies for 3D hard tissue ablation [FPB$^+$15]. Those hardware components enable automation of the optical coupling sequence between Er:YAG laser source and optical fibre. The significance of accurate fibre alignment for optimal coupling efficiency is theoretically discussed in Section 2.2. The 3D beam scanning module is shown in Figure 3.2a and comprises a pulsed Er:YAG solid-state laser (DPM 15, Pantec Engineering/3m.i.k.r.o.n$^{\text{TM}}$, Ruggell, Liechtenstein) emitting the beam to shape-modulating lenses and redirecting mirrors. The beam passes through adjustable lens units and a scanner for control of axial and lateral focal positions (varioSCAN and hurrySCAN, SCANLAB AG, Purchheim, Germany). Linear lens motion of the focal scanner facilitates axial focal displacement. In contrast, Galvo mirrors are dedicated to lateral deflection of the laser beam. A f-Θ flat-field lens compensates for deflection errors and focuses the beam to focal plane with $f = 100\,\text{mm}$. This interaction constitutes a symmetric focal workspace of $(10 \times 10 \times 10)\,\text{mm}^3$. A quick exchange fibre chuck (FPH-DJ, Newport Corporation, Irvine, CA, USA) and customised mounting are employed to position the fibre tip closely to the centre of workspace volume. The scanner components are considered as accurate methodology for spatial alignment between laser focus and fibre tips.

3.2.2 Laser-To-Fibre Coupling

The experimental hardware described in Section 3.2.1 is applied to optimise the coupling efficiency based on automation of the alignment procedure between fibre tip and beam focus. It is hypothesised that this approach improves not only the optical coupling, i.e. reduction of component misalignments, but also supersedes tedious and time-consuming manual alignments by taking scanner-based 3 DoF focal displacement with focal diameter $2w_0 = 360\,\mu\text{m}$ into account.

The opto-mechanical alignment problem was addressed in related work by methodologies based on sensor readings and multi-axis positioning for decoupled translation and rotation of two facing
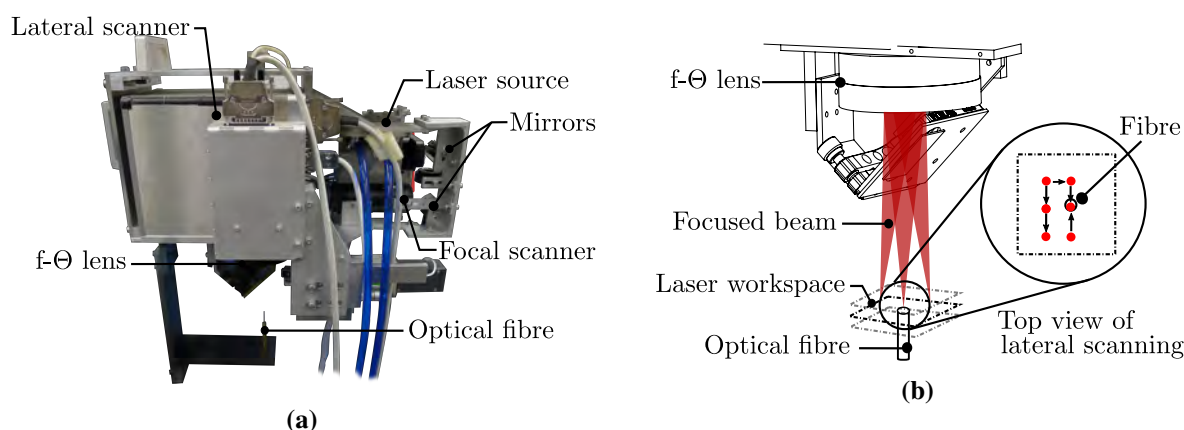
Fig. 3.2: Opto-mechanical setup for automated laser-to-fibre coupling: a) 3D beam scanner with laser source, beam shaping optics, scanning units, and fibre mounting. b) Magnified schematics of laser workspace and lateral scanning pattern for laser-to-fibre coupling.

fibres [YLLS06]. More precisely, one component is fixed and the second is manipulated in lateral and angular DoF. The procedure(unconstrained optimum design) was transferred to optimisation strategies to determine the component position with maximised intensity or vice versa minimal optical losses. The objective function generally targets the intensity and the design variables regard the component positions. This problem was solved by Hamiltonian, Simplex, and particle swarm algorithms [YLLS06].

This work considers a gradient-based (Hill-Climb) method. Input data comprises continuous sensor measurements of a pyroelectric power meter (4π power meter, Laserpoint srl, Vimodrone, Italy) and the commanded 3D focus positions of the beam scanners. In preparation, one fibre tip is prepositioned in the workspace of the scanning unit and the power meter is located at the opposite tip of the fibre. Subsequently, power meter measurements are initiated and the laser spot is commanded in spiral or rectangular patterns with lateral and axial scanner increments Δx_l and Δx_a, respectively, as shown in Figure 3.2b. This sequence is governed by the selected Hill-Climb approach. The workflow for scanner-based focus manipulation is detailed as follows:

1. Lateral coarse scan ($\Delta x_l = 100\,\mu\mathrm{m}$) until a rising power signal is detected.

2. Lateral fine scan ($\Delta x_l = 50\,\mu\mathrm{m}$) subsequent to the first phase tracking an increase of power measurements.

3. Abort lateral scan if power measurement saturates beyond threshold P_T.

4. Axial focal adjustment ($\Delta x_a = 100\,\mu\mathrm{m}$) until a local power maximum is detected.

The feasibility of the methodology was evaluated in a preliminary study with repeated reassembly, prepositioning of the fibre in the workspace, and execution of the presented automated coupling sequence ($N = 10$). The runtime until convergence was $(173 \pm 16)\,\mathrm{s}$ on average. The approach failed in one trial due to placement of the fibre in proximity of workspace boundaries. Under

consideration of an input source power of $1\,\mathrm{W}$, the average coupling efficiency yielded to $(54\pm8)\,\%$, which correlates to $(55 \pm 4)\,\%$ reported in related studies for similar conditions [PNT$^+$06].

3.2.3 Characterisation of Optical Properties

The optical characteristics of the focus module were determined with knife-edge measurements [dASdL$^+$09] according to ISO-11146 standard. In this methodology, (partial) blocking of the laser beam is realised by a sharp edge fabricated from an opaque material, e.g. a razor-blade, which is line-scanned through the propagating beam to capture its profile.

Prior to the study, the focus unit was assembled and the distance between housing components A and B was set to simulation data. Under the assumption of a Gaussian beam intensity profile, measurements were conducted with translation of a sharp-edged blade into the beam, e.g. razor blade, perpendicular to the beam propagation direction at specific distances. Hence, the blade covers the incident beam incrementally by blocking radiation. The corresponding experimental setup is shown in Figure 3.3a. The residual laser power was measured simultaneously with the power meter for each linear step $\Delta x_1 = 50\,\mu\mathrm{m}$. Pairs of power and position samples were fitted to an error function and the $1/e^2$-radius was estimated. This procedure was repeated five times within a range of $\pm4\,\mathrm{mm}$ with respect to the focal length of $20\,\mathrm{mm}$ and in steps of $0.5\,\mathrm{mm}$ along the optical axis. This assesses beam caustics in proximity of the physical focal length. Lateral and axial blade displacements with regard to the focal unit were executed by a hexapod robot (H-824, Physik Instrumente (PI), Karlsruhe, Germany). The beam waist location of the latest prototype was estimated to $z_0 = 18.65\,\mathrm{mm}$ with reference to the endoscopic tip of the module (see Figure 3.3b) based on acquired data and standard protocols. Under consideration of a window thickness of $1\,\mathrm{mm}$, the focal length offsets to $z_{0*} = 19.65\,\mathrm{mm}$ and coincides with the initial specification of $20\,\mathrm{mm}$. The Rayleigh-length was accordingly estimated to $z_{\mathrm{R}} = \pm1.75\,\mathrm{mm}$, and the beam waist diameter to $2w_0 = 506\,\mu\mathrm{m}$. The half-angle beam divergence was computed to $\Theta = 0.124\,\mathrm{rad}$. The resulting Rayleigh-length of the opto-mechanical assembly is approximately $0.25\,\mathrm{mm}$ shorter than estimated in the ZEMAX simulation environment.

3.2.4 Ablation Studies

The ablation performance of the focus module was evaluated in two studies using soft tissue substitutes, i.e. agar-agar and porcine specimens, and in a preliminary study in two human cadaver models.

Prior to the experimental series on soft tissue substitutes, agar-agar samples with concentration of $4\,\mathrm{wt.\%}$ (weight percent) were fabricated according to manufacturer guidelines (BIOVITA GmbH, Hamm, Germany). After preparation, the latter were immediately transferred to petri dishes and preserved in a refrigerator at $6\,^\circ\mathrm{C}$ ambient temperature. This ensures persistent surface hydration and minimised volume shrinkage. Likewise, fresh porcine samples were acquired and resectioned.

(a)

(b)
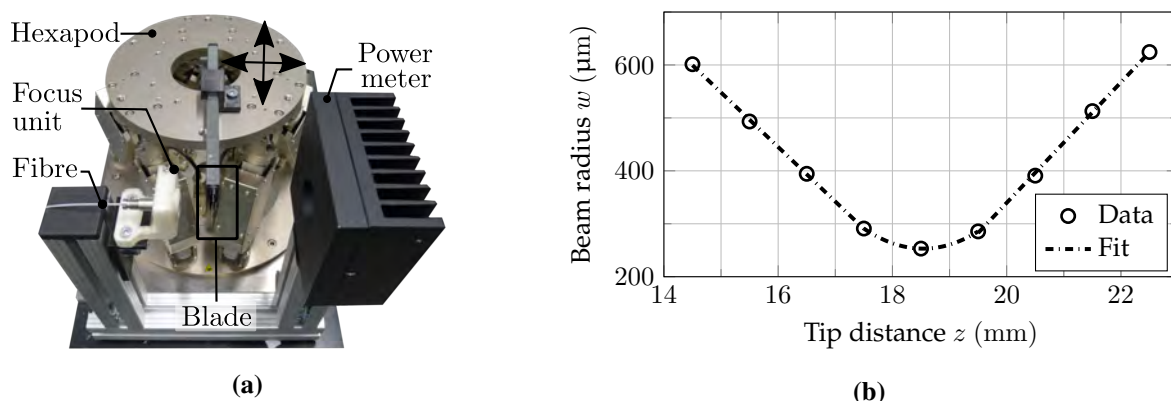
Fig. 3.3: Experimental setup for knife-edge measurements and beam caustics of the focus unit: a) Hardware layout for characterisation of optical characteristics. The hexapod enables high-resolution displacement of involved components. b) Beam caustics of the proposed module around measured focal position. Data is fitted in accordance with ISO-11146. The standard deviation (hidden) of each data point is below $25\,\mu$m.

In analogy to agar-agar samples, porcine specimens were transferred to petri dishes, stored in a refrigerator at $6\,°$C, and were humidified with saline solution.

The study employed previously described hexapod robot (see Figure 3.3a) for simulation of laser beam scanning. The focus module was mounted to the end-effector platform and the surface of each specimen was adjusted to the focal length obtained from optical characterisation in Section 3.2.3. The robotic platform executed linear motion patterns at constant Cartesian velocity $v_{\text{scan}} = 1.5\,\text{mm\,s}^{-1}$. Laser parameters were set to pulse duration $\tau_\text{P} = 200\,\mu$s and diode current $I_\text{D} = 200\,$A. Pulse frequencies f_P were timed from $30\,$Hz to $80\,$Hz for both samples. Scanning passes were varied in the range of $N_\text{S} = 2\ldots4$ with persistent surface humidification. Five linear ablation patterns were executed for each set of parameters and tissue type with a length of approximately $15\,$mm. Afterwards, each specimen was analysed with swept-source optical coherence tomography (OCT) (OCS1300SS, Thorlabs Inc., NJ, USA). A volume dataset (C-scan) of each ablation area was acquired and the incision profile was measured in width and depth at 20 randomly selected positions along the propagation directions using proprietary software. Acquisition parameters were $(256 \times 256 \times 512)\,$px with corresponding physical dimensions of $(6 \times 2 \times 3)\,\text{mm}^3$. Measurements were summarised to mean $\pm$ standard deviation (SD). Surface reflectance was assessed qualitatively to identify carbonised areas according to [ARG+18].

A feasibility study in human cadaver models was conducted in the Anatomy Laboratory of the University Hospital Besaçon, France. Two cadavers (male and female) were selected with local ethics approval. Components, laser parameters, and the optical assembly were installed similarly to Section 3.2.1. The 3D beam scanner was replaced with multi-axis positioning stages to enable adjustment of lens positions for fibre coupling. The focus module was introduced to oral cavities of both cadavers and was manually guided along the oral soft tissue. The resulting laser-tissue

interaction was monitored with a chip-on-the-tip stereoscopic camera (MO-BS0804P, MISUMI Electronics Corp., Taiwan) attached to the prototypic enclosure of the focus module.

3.3 Results

Primarily, experimental findings on the ablation performance of the prototypic unit for agar-agar and porcine samples are presented. Furthermore, preliminary study results of a prototype deployment to a human cadaver model are described.

3.3.1 Ablation Performance

Taking measurements of optical characteristics in Section 3.2.3 and laser source parameters in Section 3.2.4 into account, ablation studies on both tissue specimen were conducted with laser pulse energies $E_P = 10 \, \text{mJ}$ and corresponding focal diameter $2w_0 = 506 \, \mu\text{m}$. This resulted in average radiant exposures of $J_P = 50 \, \text{mJ} \, \text{mm}^{-2}$. This estimation includes potential coupling losses of transmission components. The commanded scan velocity generated pulse overlaps of $O_P > 85\%$ for robotic beam displacement throughout all experiments. The pulse overlap O_P is defined as ratio of pulse diameter over the translation of the point of irradiation [IH].

Measurements from OCT metrics on tissue substitute (agar-agar) and porcine specimens are summarised in Figure 3.4. Qualitative inspection of tissue surfaces with light microscopy ($10\times$ magnification) and corresponding OCT intensity responses neither indicated carbonisation nor charring. No significant degradation of tissue layers was detected. This finding was supported by global absence of highly reflective areas in OCT imaging.

However, partial sample shrinkage of porcine specimens was observed due to thermal interaction and water evaporation. Correspondence of pulse frequencies f_P and resulting ablation depths demonstrated a linear relation for both types of specimens (see Figures 3.4a and 3.4c). Those findings correlate with studies in [ZXYZ07]. Nonetheless, lower ablation depths were measured for agar-agar in comparison to porcine samples. Average depth differences within both sample types were in the range of $0.25 \, \text{mm}$ to $0.5 \, \text{mm}$. An increased number of scanning passes N_S caused increased ablation depths. Maxima of $1.75 \, \text{mm}$ and $2.7 \, \text{mm}$ were measured on agar-agar and porcine samples for parameter combination $N_S = 4$ and $f_P = 80 \, \text{Hz}$. Standard deviations of measurements were approximately increased by factor two in the porcine model for $N_S > 2$.

OCT measurements of ablation widths were consolidated for both types of tissues and depicted in Figures 3.4b and 3.4d. As opposed to depths, resulting widths were inconsistent. The correspondence of frequency, passes, and resulting width were highly non-linear. Furthermore, the number of scanning passes ($2 \leq N_S \leq 4$) did not impact widths on agar-agar for pulse frequencies in between $30 \, \text{Hz}$ to $60 \, \text{Hz}$. A maximum width of $0.83 \, \text{mm}$ was determined for parameters $N_S = 3$ and $f_P = 80 \, \text{Hz}$. Similarly to ablation depths, standard deviations related to porcine samples were

increased by factor two in comparison to agar-agar. Unlike findings on agar-agar specimens, a higher number of scanning passes enlarged the ablation widths on porcine samples.

3.3.2 Cadaver Study

The prototype of the focal unit was deployed to a cadaver model for feasibility assessment. All experiments were carried out with constant laser source power $P_{\mathrm{avg}} = 1.5\,\mathrm{W}$ and manual displacement. Primarily, the focus unit was introduced to the oral cavity. Subsequent to landmark localisation, manual scanning at approximately $v_{\mathrm{scan}} = 3\,\mathrm{mm\,s^{-1}}$ along oral tissue contours were simulated. Figure 3.5a shows the resulting laser-tissue interaction that was captured by attached stereoscopic sensors. Ablation of oral soft tissue layers was directly achieved and maintained throughout experimental series. Manual guidance resulted in gradually increasing ablation depths beyond $1\,\mathrm{mm}$ and widths of less than $0.75\,\mathrm{mm}$ with few carbonisation while motion was present (see Figure 3.5a). Lower scanning velocities at constant pulse frequencies potentially raised the probability of tissue carbonisation. Spatial overlap between laser pulses affected thermal

(a)

(b)

(c)

(d)
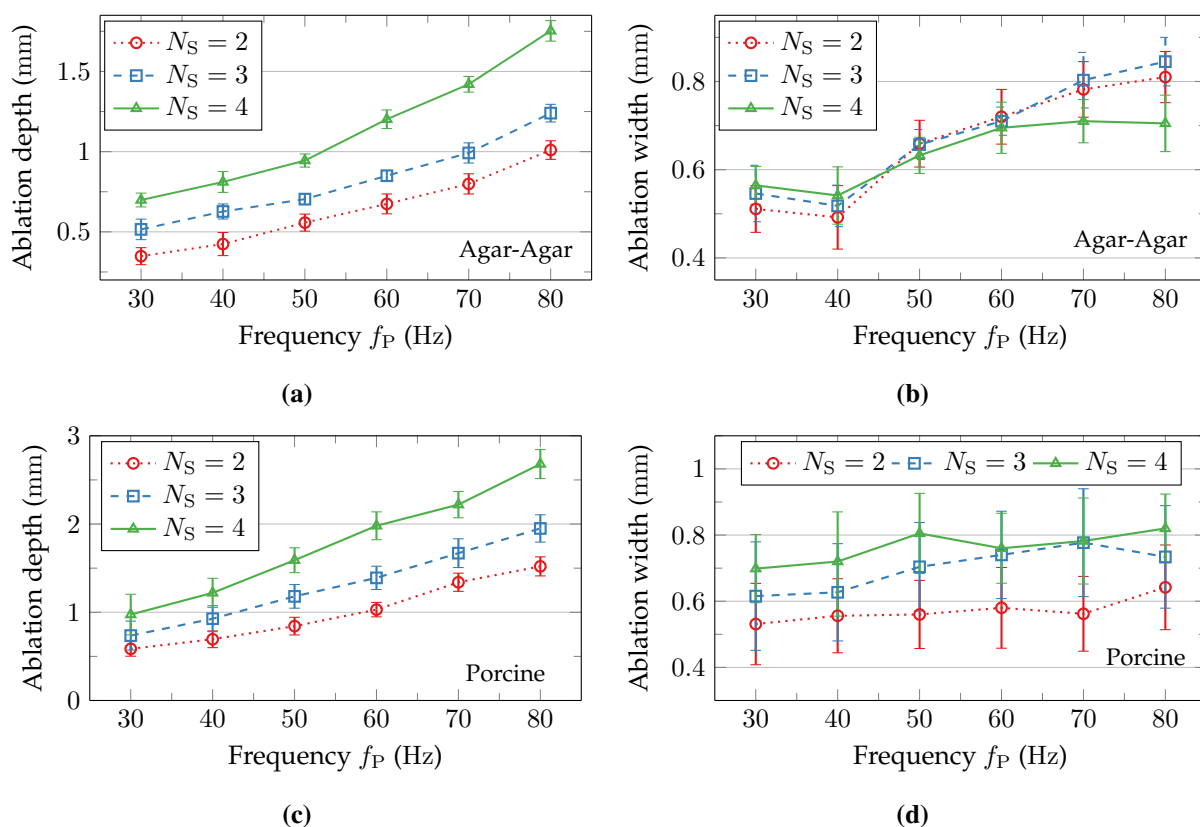
Fig. 3.4: Results of OCT ablation metrics for agar-agar and porcine tissue related to pulse frequencies f_{P} and number of scanning passes N_{S}: a) Ablation depths on agar-agar samples, b) ablation widths on agar-agar samples, c) ablation depths on porcine samples, and d) ablation widths on porcine samples.

accumulation governed by tissue-specific thresholds. Online monitoring of ablation phenomena with stereoscopic cameras enabled 3D specimen reconstruction as described in Section 2.5. Another example of laser-tissue interaction in the cadaver model is provided in Figure 3.5b. Surface indentation and shrinkage from incident laser radiation may be identified from acquired imaging data and enables online *in situ* monitoring and assessment of ablation extent and quality.

3.4 Discussion

Dexterous non-contact delivery of Er:YAG laser radiation to confined anatomy in endoscopic scenarios demands for customised laser optics. A miniaturised focus unit is proposed in this thesis and was experimentally evaluated on soft tissue models and in a preliminary cadaver study.

Experimental studies on porcine and agar-agar samples demonstrated applicability of the implemented prototype. Magnitudes of ablation depths responded linearly to selected laser settings and number of scanning passes. It was demonstrated that increased frequencies and passes caused larger ablation depths on both samples ($> 2.6\,\text{mm}$). Nonetheless, increased pulse frequencies may result in local accumulation of heat in the specific tissue volume and raise the risk of carbonisation. The achievement of larger ablation depths must be prospectively targeted with application of multiple scanning passes to enable thermal relaxation for pulsed radiation. On the other hand, the energy of single pulses must be chosen effectively to trigger ablation mechanisms and optimise absorption. On the contrary, ablation widths revealed different effects. For concerned frequency ranges, porcine samples demonstrated a trend towards constant ablation widths that scaled related to the number of scanning passes between $0.5\,\text{mm}$ to $0.7\,\text{mm}$. This observation did not apply to agar-agar samples. Widths were impacted by selected frequencies, whereas number of passes only caused minor offsets.

Standard deviations of OCT measurements were generally higher for porcine than for agar-agar samples. The difference is expected to be due to local variations of tissue properties, e.g. cellular

(a)   (b)

Fig. 3.5: Qualitative results of cadaver trials: a) Endoscopic images acquired from two cadavers showing progress of manually guided ablations on oral soft tissue. Arrows indicate ablation. b) 3D reconstruction of surface (coloured pointcloud) based on stereoscopic imaging with incision and distance measurement indicated by sphere markers.

compounds and water contents. Overall, porcine samples have shown a superior laser-tissue response due to energy deposition in cellular compounds and thermal conductivity. Thermal effects enabled larger ablation depths for identical laser source settings. The results proved that agar-agar may be considered as tissue substitute. For clinical applicability, the parameter space of laser settings and optical/thermal tissue properties must be exploited and reduced dimensionally, e.g. by learning-based modelling of interactions [PFCM15]. The identification of tissue shrinkage underlines the importance of surface humidification for optimal tissue-specific interaction mechanism. This not only prevents carbonisation, but also changes in morphology. Prospectively, the endoscopic unit may be equipped with miniaturised spray nozzles to apply a thin water layer that improves surface absorption effects and manual application of laser delivery.

The cadaver studies demonstrated feasibility of the prototype. However, precise adjustment of the focal length to the surface of the oral soft tissue was impeded due to anatomical conditions. This resulted in variations of ablation depths and widths with minor carbonisation. The latter occurred when distances exceeded the specified Rayleigh length. This shortcoming is addressed in Chapter 6 by incorporating dense 3D surface information into the ablation workflow. This enables robotic adjustment of the focal length for optimisation of local energy density to the surface.

3.5 Conclusion

Minimal-loss fibre transmission and refocusing of the transmitted beam are essential requirements for endoscopic non-contact laser delivery. This chapter presented the design and evaluation of an endoscopic focus unit for robotic non-contact laser surgery at wavelengths of $\lambda = 2.94\,\mu m$. Advantages of Er:YAG lasers for laser-tissue interactions in soft tissue surgery motivated the concept of an enclosed optical assembly of $8\,mm$ diameter for endoscopic integration. Design and component selection were supported by optical simulation and yielded a layout of two adjacent plano-convex lenses. This enables focussing of the laser beam after fibre transmission with minimal housing dimensions. Automation of the laser-to-fibre coupling based on a 3D laser scanner unit improved efficiency and procedural safety. Less experienced users were able to achieve coupling efficiencies of more than 50% for fibre diameters of $450\,\mu m$. Optical characteristics of the prototype were determined experimentally and validated against specifications. The ablation performance was assessed quantitatively on agar-agar and porcine specimens. OCT measurements revealed a linear relation of frequency and ablation depths for both specimens. However, widths were biased, i.e. a non-linear correspondence was identified. In contrast, widths on porcine specimens remained almost constant ($\pm\,0.2\,mm$) despite of parameter variations. Those findings were in accordance with reports in related work. Lastly, a feasibility study demonstrated applicability of the prototype for oral soft tissue ablation in two human cadaver models. Future work is dedicated to component miniaturisation for robotic integration and extension to a variable-focus mechanism. Experimental *ex* and *in vivo* studies may pave the way for clinical translation.

4 An Extensible Continuum Robot for Endoscopic Laser Surgery

Dexterous non-contact laser manipulation on delicate tissue in confined anatomy demands for bespoke robotic strategies. Various robotic technologies are discussed in state-of-the-art of Section 1.3 but consistently optical properties of the laser beam have been neglected, i.e. the focal length is disregarded with assumption of short working distances. Furthermore, presented endoscopic approaches only considered qualitative imaging. This impedes assistive technologies based on processing of visual information. Hence, a novel and highly integrated robotic prototype is proposed in this thesis to address systematic deficiencies of existing approaches that are outlined in Section 1.3. The remainder of this chapter discusses design concepts, methodologies, and prototypes and is structured as follows. Firstly, design objectives and the derived modular concept of the robotic platform are presented in Section 4.1. This is complemented by requirements and specifications as well as design limitations. To cover every aspect, design guidelines are revised in Section 4.2. The mechatronic design approach for subunits of the robotic platform is described (see Section 4.3). This comprises design concepts related to the continuum manipulator, endoscopic tip, actuation unit, and electronic components. Further on, the numerical optimisation of the stereoscopic sensor layout is presented in Section 4.4. The chapter closes with a description of the robotic prototype and its structural characterisation (see Section 4.5). A conclusion is provided in Section 4.6. The contributions related to the mechanism design are published in [KSKO17], early prototypes in [KSKO14b, KSKO14a, KSKO15], and the final system design with preclinical evaluation (see Chapter 7) in [KGS+20].

4.1 Design Considerations

This section presents fundamental levels of the robotic design workflow. Conclusions from related work and corresponding thesis contributions in Chapter 1.4 are transferred into an abstract robotic concept. This supports the ensuing mechatronic design approach for the endoscopic framework with the extensible continuum structure. In this regard, the overall robotic concept is presented in Section 4.1.1 and subsequently requirements and specifications for the robotic platform are derived under further consideration of related work (see Section 4.1.2). Lastly, limitations of the proposed design are outlined in Section 4.1.3.

4.1.1 Modular Robotic Concept

The state-of-the-art robotic systems for MIS and laser surgery are summarised and discussed in Chapter 2. It is outlined that proposed robotic devices consider different design approaches at the expense of versatility and usability. This manifested in systems with low technology readyness levels (TRL) that describe the maturity of technical systems according to NASA standards. Evaluation has been dedicated to preliminary experiments in laboratory environments. This shortcoming also applies to more recent devices that specifically target research challenges such as compact dimensions or enlarged workspaces, but likewise disregard advanced user studies or highly integrated prototypes to advance recent TRL. The scope of this thesis is not only limited to a robotic design that outperforms systems presented in related work. It further addresses translation to advance TRL with continuous system integration. This enables analysis and demonstration of versatility, ergonomics, and usability in preclinical environments.

In accordance with design standards for mechatronic systems (see Section 4.2), a systematic methodology is applied to realise the device features. A modular robotic concept is derived from interface abstraction outlined in Figure 4.1. The system architecture is partitioned to different units or building blocks, i.e. each item is assigned to specific features, tasks, or functions. Beyond that, technical interfaces are introduced to interconnect the robotic components. This approach is described in detail in the preceding paragraph.

The *robotic device* is composed of two different units for *extracorporeal* or *intracorporeal* deployment. The *extracorporeal* section accommodates the robot base and an actuation unit with actuators and sensors. By contrast, the *intracorporeal* unit considers the dexterous continuum manipulator, the mechanical connection to the actuation unit, and the endoscopic tip with imaging sensors, illumination, and laser delivery. The shaft between the continuum robot and the actuation unit may be implemented with rigid or flexible components and of variable length tailored to specific surgical tasks.

Both units are connected to a communication interface for data exchange (e.g. commands, status data, sensor data) between *robotic device* and *robotic controller*. The *robotic device* is controlled by the high-level building block *robotic controller* that may integrate multiple low-level controllers. For example, the latter may be dedicated to kinematics computation and transformation output, control modes (e.g. position or velocity), or computation of virtual forces for haptic rendering. Besides, status output and operating mode selection must be provided. More precisely, the *robotic controller* sends commands of nominal positions or velocities to actuator groups and receives actual data updates. A power supply interface is connected to the *robotic device* and *robotic controller*. The *intracorporeal* unit, i.e. the endoscopic manipulator, of the *robotic device* is inserted into the patient. The *tip* integrates imaging sensors and illumination to perceive the surgical environment. Similarly to the *extracorporeal* unit, this part interfaces the *robotic controller* and provides transfer of imaging data acquired by sensors located in the endoscopic tip, adjustment of illumination intensity, or activation of *laser* sources to commence tissue manipulation.
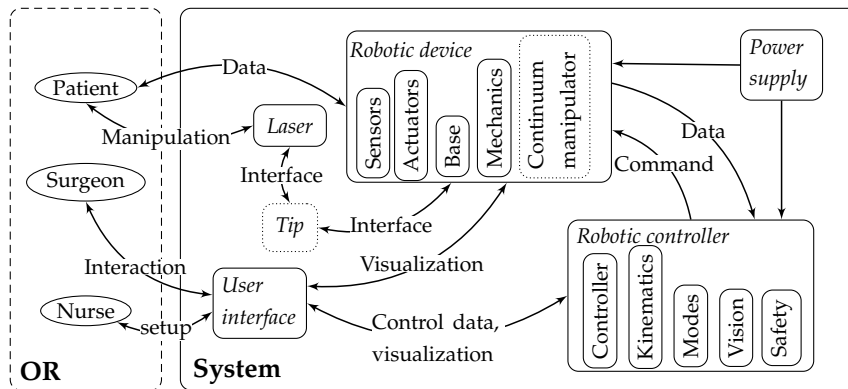
Fig. 4.1: Abstraction map of the proposed robotic system for non-contact laser surgery. Dotted items highlight components for intracorporeal use. Solid items describe extracorporeal use. Acronyms: operating room (OR).

The *user interface* is dedicated to multi-modal visualisation of intraoperative data (e.g. stereoscopic images and haptics) to the operator and represents the human-machine interface (HMI) with input devices for master-slave manipulation or interactive planning in the live scene. It further implements user notification related to status messages, maintenance, or system failures. The interchangeable base of the *robotic device* facilitates the mechanical mounting to a mobile stand or robotic assistant during setup to connect the framework to the OR infrastructure. A versatile connection is beneficial to provide a mounting in case of alternative surgical scenarios. Lastly, the *robotic controller* interfaces the entire set of subcomponents and manages the data exchange between specific building blocks. This also includes blocks for processing vision data to establish robotic perception or evaluation, maintenance, and safety.

The main findings of this section constitute the fundamentals of the subsequent design process and are summarised to the following list:

- Robotic framework with extensible endoscopic manipulator composed of intracorporeal and extracorporeal units with interface to endoscopic tip for laser-based tissue manipulation.

- High-level robotic controller handles the data exchange and implements low-level task-specific controllers.

- Power supply is connected to robotic device and controller.

- Versatile mechanical base interface for mounting to mobile stand or robotic assistants.

4.1.2 Requirements and Specifications

Technical constraints of the robotic design process are derived from related work in Section 1.3, the targeted application in TLM, and qualitative feedback from clinical experts[1]. These constraints

---

[1]Department of Otolaryngology, University Hospital Ulm, Germany

define the design manifest and its composition. The latter directs the realisation of the novel robotic endoscope based on the following list:

- *Lightweight and functional design*: The implementation of the robotic system targets a lightweight approach. The mounting of the device to a stand or passive/active assistant allocates load to the assistant's end effector. Constraints in this work are derived from two recent commercial medical robots with bedside installation. Both the robotic units of the CorPath® GRX platform (Corindus, Inc. - A Siemens Healthineers Company, Waltham, MA, USA) and the Cirq® robot (Brainlab AG, Munich, Germany) do not exceed a maximum weight of $11\,\mathrm{kg}$ [Cor, Bra]. Targeting a more lightweight design in this work, the weight of the robotic unit must not exceed $7.5\,\mathrm{kg}$ in order to comply with mounting-specific constraints and to perpetuate system dynamics, e.g. for active assistants. Furthermore, a lightweight design facilitates preoperative handling during setup, positioning, and insertion to the patient. Secondly, a functional design of the robotic system is favoured. This partitions the device to extra- and intracorporeal units as previously described in Section 4.1.1. Both units must be equipped with interchangeable interfaces for component replacement.

- *Compact dimensions*: The OR represents an environment with space restrictions. It is shared between human attendants (surgeons and nurses), bystanders, and medical equipment required for surgery, patient monitoring, imaging, and general supply. Innovation in medical technology permanently decreases the residual OR space due to introduction of novel devices. Thus, reduced dimensions of a system in combination with small footprints must be major objectives to gain clinical acceptance. This requirement is further related to intraoperative handling (e.g. repositioning) or transportation. Furthermore, effects of OR layouts and resulting distances to stations impact surgical efficiency and safety [GWP+16]. Taking the commercial robot examples of previous item *Lightweight and functional design* into account, the device footprint must not exceed an outer device diameter of more than $100\,\mathrm{mm}$ and a base length of approximately $750\,\mathrm{mm}$.

- *Quick-access housing*: The robotic prototype must enable an unobstructed access to actuators, electronics, and mechanical components. In the evaluation stage, replacements and monitoring of subsystem functionality are essential for design optimisation according to Section 4.2. Housing components must be installed with a reasonable amount of fasteners. Besides, connective elements must allow for simple detachment.

- *User-centred setup*: Surgical applications demand for integration to the OR environment. This motivates strategies towards expeditious setup procedures and fault prevention. The number of interface connections must be reduced to a minimum for manual installation. Tedious setup tasks must be prevented in order to gain device acceptance. The number of involved units (e.g. robotic device, controllers, etc.) must be as low as technically feasible to facilitate the installation procedure.

- *Maximum diameter of intracorporeal unit*: Dimensions of the unit are determined by applications in transoral, laparoscopic, or NOTES surgery. Each application has set specific limitations ranging from a diameter of $12\,\text{mm}$ in laparoscopy [RE09] to $23\,\text{mm}$ for transanal access [GCJ$^+$05]. Focussing on transoral deployment, the maximum diameter of the intracorporeal section is limited to $13\,\text{mm}$ in order to comply with the anatomy of the aerodigestive tract. Hence, laparoscopic treatments may be achieved with slightly increased trocar diameters from instrumentation in bariatric surgery.

- *Surgical imaging*: The quality of surgical scene visualisation affects human perception and particularly the performance and safety of the surgical procedure. Despite imposed size constraints, employed sensor technology must enable adequate scene visualisation to the operator and concurrently implement robotic perception without additional sensors. Following these assumptions, this work considers an endoscopic scenario with pathologies in proximity of the robotic end effector. In accordance with expert feedback on commercial endoscopy from otolaryngology departments at CHRU[2], Besançon, France and University of Genova, Genova, Italy, the imaging unit is required to cover an area of at least $(20 \times 20)\text{mm}^2$ of exposed tissue within a distance of $20\,\text{mm}$ to $25\,\text{mm}$.

- *Surgical illumination*: The endoscopic tip must integrate intrinsic scene illumination to avoid additional instrumentation. This may constrain manipulation workspaces within the body cavity or NOTES procedure. Imaging scenarios are commonly dedicated to soft tissue environments. The latter are prone to high attenuation of visible light and available endoscopic instruments suffer from weak light coupling into the delivery optics, e.g. optical fibres. Those components are paramount. Consideration of guidelines in [KSGD09, CCN$^+$12, HRHMR$^+$15] for optimal contrast generation, pioneering work on endoscopic chip-on-the-tip LED [BBB$^+$13], and optical spectra of biological tissue [Jac13], a colour temperature profile between $3{,}000\,\text{K}$ and $4{,}000\,\text{K}$ is targeted, i.e. the range between light warm to a neutral colour temperature. A luminous flux greater than $20\,\text{lm}$ is considered for improved sensor signal-to-noise ratio (SNR). The exposed area must be congruent to the *surgical imaging*. Lastly, the thermal constraints ($\leq 41\,^\circ\text{C}$) imposed by standards for design and implementation of endoscopic equipment [VDE16] must be taken into account.

- *Focal length of ablation laser*: The focal length relates to laser optics located in the endoscopic tip. It is essential for surgical workflows that the ablation is monitored within the FoV of the selected surgical imaging to ensure safe interventions. Experts from otolaryngology departments at CHRU, Besançon, France and University of Genova, Genova, Italy determined clinically relevant laser manipulation distances to a range of $20\,\text{mm}$ to $25\,\text{mm}$.

- *Manipulation workspace and dexterity*: Scenarios in transoral, laparoscopic, or transanal settings are targeted. The robotic end-effector must cover a workspace volume of at least $(30 \times 30 \times 25)\text{mm}^3$ starting from the initial manipulator configuration. This enables laser

---

[2]Centre Hospitalier Régional Universitaire

excision of large tumour volumes. Under consideration of additional kinematic constraints, for example trocar ports, a dexterous intracorporeal manipulation of the endoscopic tip must address at least 5 DoF (3 linear DoF and 2 angular DoF) in Cartesian end-effector space. Angular end effector motions must enable $\pm 10°$ for each DoF from reachable poses within the executable workspace.

- *Manipulation accuracy*: The displacement accuracy of the laser beam is derived from scanner-based laser surgery for similar surgical tasks [DOCM14]. A margin of $0.5\,\text{mm}$ (lateral deviation) is defined for lesion excisions. Due to disregard of focal adjustments in related work, this thesis proposes an axial accuracy of $0.75\,\text{mm}$ for setting the focal position. Prior work considered the depth of field of the focused beam and proved positive results [SKK$^+$15].

- *Manipulation dynamics*: The performance overview of reported devices is provided in Section 1.3. The novel endoscopic approach with eye-in-hand visualisation demands for reduced scanning velocities ($\leq 10\,\text{mm s}^{-1}$) of the ablation laser due to structural limitations of the kinematics in comparison to MEMS, piezo, or electromagnetic actuation. However, limited dynamics may be mitigated by parameter adaptation presented in Section 2.1. Beyond that, manipulation causes concurrent motion of the imaging sensor. Estimation of scene motion from integrated imaging hardware must be processed at $25\,\text{Hz}$. Hence, the maximum Cartesian velocity is restricted to $3\,\text{mm s}^{-1}$ for prototypic applications.

4.1.3 Design Limitations

Considerations on requirements for the robotic concept and assessment of feasibility result in a set of design constraints for the physical prototype presented in this thesis. These limitations affect the feasible device configuration by taking the following hard- and software limitations into account:

- *Cleaning and sterilisability* of components and materials for realisation of structural and functional parts are disregarded. This allowance excludes any additive manufacturing process in the prototyping workflow. Nonetheless, the proposed modular design approach targets prospective translation to disposable quick-exchange units exposed to the theatre environment.

- *Biocompatibility* of employed materials is disregarded to facilitate the proof of concept. However, current advances in materials development, e.g. novel polymers for additive manufacturing, may prospectively enable substitution of structural and functional components.

- *System safety* of the presented device only accommodates basic safety levels and redundant checks to prevent structural damage or operator misuse. For example, this comprises continuous evaluation of sensor data, limit checking, and disregard of user inputs that exceed predefined settings.

- *Economic aspects* are disregarded in the design workflow. This includes the economic impact on clinical routines and cost optimisation for components, materials, and manufacturing.

4.2 Design Guidelines

The design of robotic device adapts to established methodologies. In the last decade, various approaches were proposed to facilitate planning, organisation, and implementation workflows for complex mechatronic devices with multiple subsystems. This especially concerns provision of iterative instructions for concurrent device engineering within interdisciplinary teams.

A consolidated design guideline for industry and research is given by standard VDI 2221. The latter was specifically adapted to mechatronic systems based on pioneering work [Ise96] and published in VDI 2206 [VDI93, VDI04]. For example, the design process of the DLR[3] *MIRO* robot was consistently adapted to a modified version of VDI 2206 and focused on medical robotics and OR environments [Hag11]. More recent approaches target holistic processes based on incorporation of environmental, social, or scenario-related effects and modelling of interactions with mechatronic systems models (MSM) [GDP$^+$10].

This work basically follows guidelines in VDI 2206 and further takes modifications outlined in [Hag11] into account. As the proposed robotic platform is composed of sensors (e.g. imaging and joints), actuators, and kinematic assemblies to realise system features and to satisfy requested requirements, the device is regarded as a mechatronic system and the corresponding abstract model (see Figure 4.2a) is derived accordingly.

Blocks of the system model in Figure 4.2a enable segmentation and transfer of implementation phases to a V-model (see Figure 4.2b). Subsequent to specification of system requirements, corresponding subsystems are concurrently realised using a team-centred approach. Following the evaluation of each subsystem, global integration is commenced. The global system performance is evaluated after subsystem integration and the process is reverted to the initial phase if expected performance metrics are not met. This motivates an agile and iterative design process for continuous improvement of the prototype.

4.3 Mechatronic Design Approach

Major design concepts related to the realisation of the robotic platform and its implementation workflow are described and summarised in this section. The outline of subsequent paragraphs goes along with the subunit categorisation of the system model presented in Section 4.1.1 and its associated details in Section 4.1.2.

Devices discussed in related work commonly show restricted workspaces, limited Cartesian dexterity (≤ 3 DoF), and dimensional constraints due to employed actuation principles and kinematics. Addressing these deficiencies, this thesis proposes a novel kinematic concept with extensible continuum structure for laser manipulation in 5 DoF within confined anatomy. Associated re-

---

[3]German Aerospace Centre
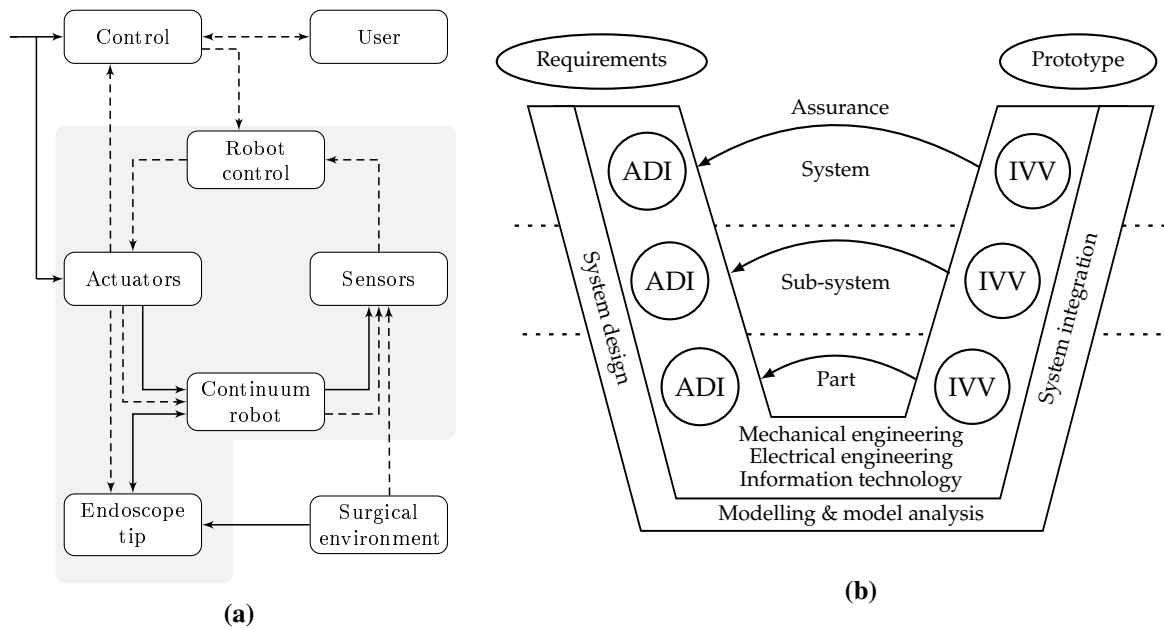
Fig. 4.2: (a) System abstraction model of the robotic platform and (b) corresponding V-model adapted from VDI 2206 of the implementation workflow. The grey area outlines robotic components. Acronyms in (b) define enumerations analysis, design, and interfaces (ADI) and integration, validation, and verification (IVV).

quirements (see Section 4.1.2) are governed by incorporating the laser propagation into kinematic considerations. As an example, adjustment of the focal distance must be considered for gentle non-contact laser delivery. This kinematic concept also demands for advanced actuation principles. Complex coordinated displacements must be generated remotely and transmitted to the flexible continuum body. This reduces component dimensions that are located within the human body. This approach is complemented by a multifunctional endoscopic tip to accommodate the laser module presented in previous Chapter 3 and state-of-the-art imaging and illumination to capture and provide assistive features from vision data.

Firstly, the novel design of the dexterous continuum manipulator at endoscopic scale is described in Section 4.3.1. Its structural composition is fundamentally inspired by a two-segmental bellow body. The latter is reinforced by embedded actuation tubes. This approach enables extensibility and increased DoF while showing low compliance and optimised stability. Numerical simulations improve the bellow design in terms of durability and flexibility. Monolithic fabrication is achieved with state-of-the-art multimaterial additive manufacturing.

Generation of coordinated joint motion for the two-segmental continuum structure with 5 DoF in task space uses an extracorporeal actuation unit. Hence, eligible mechanisms and actuator technologies are reviewed and discussed in Section 4.3.2. In contrast to industrial robotics or devices with intrinsic actuation (see Section 1.2.3), joint motion is generated remotely. Flexible actuation tubes transmit displacements/forces to specific locations along the flexible structure of the manipulator. This enhances safety as electro-mechanical components are located outside the

patient's body. Transmission components are guided within an enclosed environment to avoid any damage to the surrounding tissue, e.g. entrapment. Hence, displacement of cascaded joints for both continuum segments is implemented with novel linear motion units (LMU) (see Section 4.3.3). This enables independent motion of concentrically guided actuation tubes. This bottom-up workflow results in advanced system integration to realise an encapsulated setup in Section 4.3.5. Further details on limit sensing in Section 4.3.4, mechanical transmission interfaces in Section 4.3.6, and lastly the electronics architecture (see Section 4.3.7) complement the system presentation.

4.3.1 Extensible Continuum Manipulator

The continuum manipulator realises the kinematic manipulation of the endoscopic tip within the body cavity. Various designs with non-extensible backbone structures (primary/secondary backbones) using tendon actuation or pneumatic concepts for endoscopic deployment are summarised in Section 1.2.3. However, most of the devices show restricted inner lumen as the supporting structure and actuation principle, e.g. tendons are inherently incorporated. These principles may further cause challenging kinematic control due to backlash or structural non-linearities. Advanced functional integration, such as the endoscopic tip attached to the end effector of the manipulator, are restricted by space for sensors, wires, and fibres. Beyond that, manipulators have limited Cartesian DoF for manipulation (≤ 3) and disregard further DoF for spatial adjustment of laser optics or auxiliary sensors.

These deficiencies are addressed in this thesis by a novel concept of a continuum manipulator. Its general design is depicted in Figure 4.3 and realises an extensible continuum structure with enlarged inner lumen for signal and power wire routing. Displacements and forces generated by the actuation unit are transmitted to the proximal continuum manipulator through flexible actuation tubes. These are distributed along the circumference in radial steps of $120°$. Tubes are guided concentrically for corresponding joints of stacked continuum segments. More precisely, the continuum structure
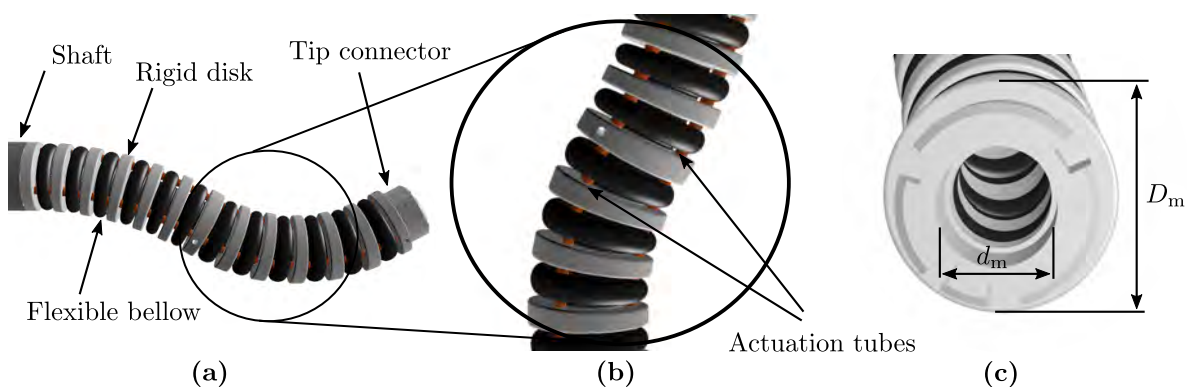
Fig. 4.3: Concept of extensible continuum manipulator: (a) lateral view, (b) detailed view, (c) exposure of the inner central lumen.

is composed of two connected flexible sections with inner lumen (see Figure 4.3) throughout the resulting body. Coordinated tube motion enables independent bending, compression, and extension of both segments.

These components constitute the structural spine of the robotic manipulator. The actuation tubing is integrated along the flexible structure and attached to specific locations. Remarkably, the structure targets manufacturing with additive technologies and shows a monolithic design (single component) that integrates both compliant and non-compliant materials. Rigid disks guide actuation tubes along the structure and implement the mechanical interface for force transmission between tubing and monolithic body. Flexible sections are consolidated to an arrangement of bellow elements that enables structural bending, compression, and elongation. Furthermore, elastic properties of the compliant material enable equidistant distribution of rigid spacer disks within the specific segment. This avoids integration of additional magnets for use of rejective forces as presented in prior work [NBK15]. Enlargement of the inner lumen is achieved by optimising the position of guidance elements located at the outer diameter of the manipulator to support the hollow-core layout. This enables wiring without obstruction or impingement. Under consideration of simulative structural optimisation presented in the subsequent paragraph, an outer diameter $D_{\mathrm{m}} = 11.5 \, \mathrm{mm}$ and inner lumen diameter $d_{\mathrm{m}} = 6 \, \mathrm{mm}$ are achieved. The monolithic structure further integrates mechanical interfaces to shaft and tip components.

Simulation-based Design Optimisation

The flexible bellow-shaped sections of the proposed manipulator must show reversible deformation characteristics to provide structural stability and fatigue strength. Particularly, this is determined by shapes and contours of the bellow elements. Besides, optimisation must consider available material properties of the additive fabrication. This work employs the Polyjet technology for monolithic multimaterial manufacturing, i.e. the joint composition of flexible and rigid materials. Resulting rubber-like hyperelastic materials were studied in related work and mechanical characteristics were derived accordingly [BVPV11]. Material parameters are transferred to hyperelastic material models (OGDEN or MOONEY-RIVLIN) that specifically assume structural reversibility after large deformation. The reader is kindly referred to the special literature for details on hyperelastic models [BVPV11].

The manipulator design presented in Figure 4.3 is decomposed to bellow elements. Iterative design optimisation of these components for enhanced structural responses is achieved by finite element analysis (FEA). Due to the hyperelastic properties (non-linear stress-strain relation) of the component's material, a non-linear FEA was conducted (Solidworks 2018, Dassault Systemes, France). CAD data preparation and simulation workflows are described in the following paragraphs.

A bellow element of the latest design iteration is shown in Figure 4.4a. Prior to the simulation, the flexible element was detached from the manipulator assembly that combines rigid and flexible
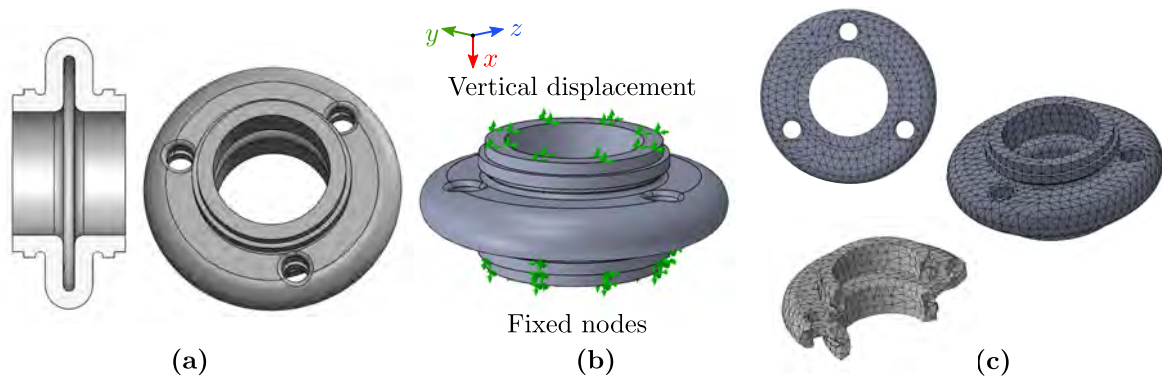
Fig. 4.4: CAD data preparation workflow: (a) Simplified CAD model, (b) definition of nodal constraints (fixation and displacement), and (c) meshed body.

components. Model edges of small shape radii ($\leq 2\,\mathrm{mm}$), such as rod cut-outs, are simplified to avoid generation of distorted mesh elements and to improve the numerical mesh quality, i.e. Jacobian and element aspect ratio. Automated model meshing with parabolic 3D tetrahedral elements was applied and locally improved with manual mesh refinement.

No distorted elements were detected by the provided mesh quality checker (see Figure 4.4c). This validates the numerical stability of the simulation results. In order to mimic the structural characteristic of the flexible bellow in a prospective use case, displacement of nodes linked to faces located at the bottom of the bellow is inhibited. Moreover, a displacement in negative x-direction is imposed to upper faces in contact with rigid spacer elements to simulate sectional extension (see Figure 4.4b).

This work considers the constitutive MOONEY-RIVLIN material law for hyperelastic photopolymers. Corresponding material parameters are extracted and supplemented from related work
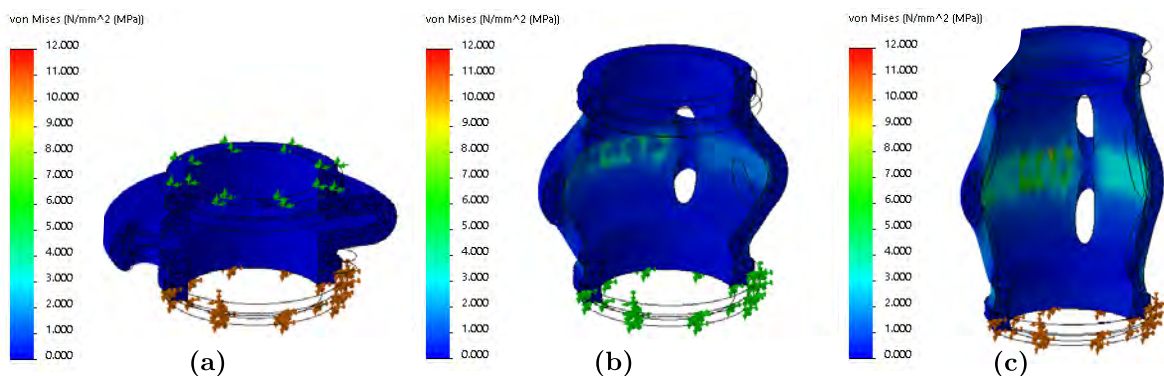
Fig. 4.5: Example of non-linear finite element analysis with $10\,\mathrm{mm}$ imposed displacement and hyperelastic Mooney-Rivlin material law. Results of initial simulation step in (a), after 8 steps in (b), and final step in (c). Increased stresses accumulate in the inner section of the bellow element under large strains.

[BVPV11, MRS$^+$20] and material data sheets (TangoBlackPlus FLX 980, Stratasys Ltd, MN, USA), respectively. The data is briefly summarised in Table 4.1. Displacement, stresses, and strains were recorded during simulation of 12 discrete time steps. Corresponding simulation results for the optimised model are presented in Figure 4.5. The degrees of freedom that were considered in the design optimisation were the radii of the bellow segment. Both design features were tuned until critical stresses in the corresponding area fell below mechanical limits. More specifically, results show the stress distribution of the bellow component under imposed displacement from $0\,\mathrm{mm}$ in Figure 4.5a to $10\,\mathrm{mm}$ in Figure 4.5c (worst-case scenario). As indicated by the coloured overlay, local component stresses did not exceed critical stress limits of approximately $12\,\mathrm{MPa}$. In this regard, the latest bellow shape was taken into account for the additive manufacturing workflow and the integration to the robotic hardware.

Additive Fabrication Workflow

The latest continuum segment prototypes are based on design concepts resulting from the optimisation workflow described in the previous paragraph. The additive fabrication of the monolithic compliant mechanism was implemented with multimaterial printing (Object 500 Connex3, Stratasys, Eden Prairie, MN, USA). A transparent PolyJet$^{\mathrm{TM}}$ photopolymer with high mechanical strength and stiffness (VeroClear$^{\mathrm{TM}}$, Stratasys, Eden Prairie, MN, USA) was assigned to the rigid spacer disks of the CAD model in the preprocessing phase. By contrast, a rubber-like blend of photopolymers VeroClear$^{\mathrm{TM}}$ and TangoBlackPlus$^{\mathrm{TM}}$ was applied to flexible bellow sections to set the desired mechanical properties, e.g. Shore Hardness and elongation at break. Preliminary experiments empirically determined digital[4] material FLX9950, a blend of aforementioned materials, to provide the required flexibility, torsional stiffness, and tensile strengths for bending up to $90°$ per segment over a large number of cycles ($N > 200$) without structural fatigue, such as material fractures in areas of high tensile stresses. For example, Figure 4.6 shows an early manipulator sample with material FLEX9910 causing a fracture in the bellow section.

The complex geometry of the continuum segments with enclosed inner lumen demands for adaptation of the recommended workflow for removal of support materials. The proposed procedure

Tab. 4.1: Simulation parameters of flexible material TangoBlackPlus$^{\mathrm{TM}}$.

Parameter	Value
Tensile strength	0.8 - 1.4 MPa
Poisson ratio	0.49 [LDL16]
C_{10}	0.1021 MPa [MRS$^+$20]
C_{01}	0.1473 MPa [MRS$^+$20]
Elongation at break	170 - 220 %

---

[4]Digital materials combine two or more PolyJet photopolymers
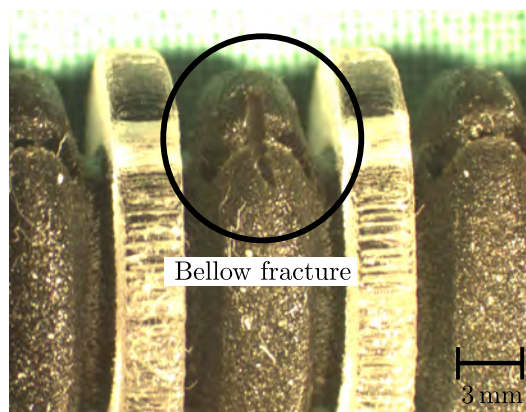
Fig. 4.6: Example of a bellow fracture after approximately 50 bending cycles applied to the continuum segment and using material FLEX9910 in fatigue studies.

alternates between manual and waterjet processing to avoid any component damage. Subsequent to fabrication, support material located in the inner compartment is gradually removed using a customised tool set. The latter includes three different rods with increasing diameters and angled tip to scrape adherent support material from the inner surface of the fabricated segments. Once an initial aperture was achieved, the waterjet was equipped with miniaturised nozzles to deflect the water spray in an angle of $45°$. This enables a gentle and gradual increase of the lumen diameter. Afterwards, the manual treatment is repeated and supported by waterjet application until remaining layers of support material adhered to the inner wall are eliminated. Residual support material or induced fractures from the cleaning process may pose risks for early structural failure, prevent extension, or reduce component fatigue strengths. An example of the manipulator structure after completion of the removal and cleaning workflow is provided in Figures 4.20a and 4.20b.

4.3.2 Actuator Selection

The actuator design and its electro-mechanical properties are core criteria for robust implementation of multi-DoF joint motions, i.e. displacement of actuation tubes embedded to the continuum manipulator. Furthermore, actuators represent the link between mechanical components and the control framework to facilitate teleoperation and automation of the robotic platform.

Conversion of electrical energy to different motion domains is considered state-of-the-art in medical robotics within the last decades. This specifically concerns transformation of electrical to angular mechanical energy. Especially in MRI-compatible robotics, design alternatives were investigated, such as pneumatic to mechanical energy conversion [SPP+07]. Intrinsic actuation principles in continuum robotics were based on joint application of fluidics and dielectric polymer actuators (DEA) to mimic muscle characteristics using contraction and extension [KGVS+18]. However, fluidic concepts demand for additional pumps, regulators, and valves which may limit integration levels [HKTK15, GWC+18]. Reliable sealing of high-pressure sections poses challenges for

bespoke components, such as additively manufactured pistons [GS18]. By contrast, muscle-like actuators and pneumatic/hydraulic pistons facilitate generation of high forces at the expense of low strokes. Direct generation of linear motion is further feasible with piezoelectric components [FKI+08] or electromagnetic direct linear drives (DLD).

Despite of available actuation strategies, this work considers rotary motors due to the following characteristics:

- Wide range of commercial motor series with selective parameters such as torques, sizes, or hollow core designs.

- Renowned and reliable low-level controllers for position, velocity, or torques.

- Superior dimension-to-torque ratio.

- Superior cost-to-size ratio.

- Scalability of mechanical conversion from angular to linear motion in combination with transmission elements.

Actuator taxonomy for rotary motors regards an assembly of a motor, a gear, and if applicable additional transmission components. The diversity of mechanisms for generation of linear motion from rotary motors is manifold and affects the motor selection. Schematics in Figure 4.7 summarise applicable mechanisms. Most widely used motion conversions make use of spindle drives, belts, or pinion-rack transmission (see Figures 4.7a to 4.7c). For example, inherently restrictive approaches are slider-crank or Scotch-Yoke mechanisms (see Figures 4.7d to 4.7e). These structures directly limit the executable motion range. Alternatively, Figure 4.7f presents a 3D printed waffle gear for concurrent linear feeding and rotation (2 DoF) [MHO17].

The next paragraph discusses characteristics of listed approaches and summarises findings in a ranking table (see Table 4.2). Mechanisms depicted in Figures 4.7d and 4.7e have increased space requirements due to the presence of the mechanical transmission with levers and passive joints. Embedded sliding joints may tend to increase wear, limit motion ranges, and show non-linear transmission characteristics.

Alternatively, mechanisms in Figures 4.7a to 4.7c comprise of less mechanical parts. Spindle drives with ball screw, metric, or trapezoidal designs support miniaturisation due to the motion principle with high integration density. This also affects a comparison of spindle and pinion-rack transmission related to the executable joint ranges. However, if high joint dynamics constitutes a major design criterion, belt-driven mechanisms may be favoured at the expense of belt tensioning units. In conclusion, the comparison of force transmission characteristics for spindle and toothed belts support the design decision towards spindle drives due to its mechanical properties:

1. Spindle-based actuators provide high stiffness, efficient force transmission with low friction losses, and a selectable range of accuracies (pretensioned designs) from commercial components. This also includes backdrivable transmission elements for safety reasons.
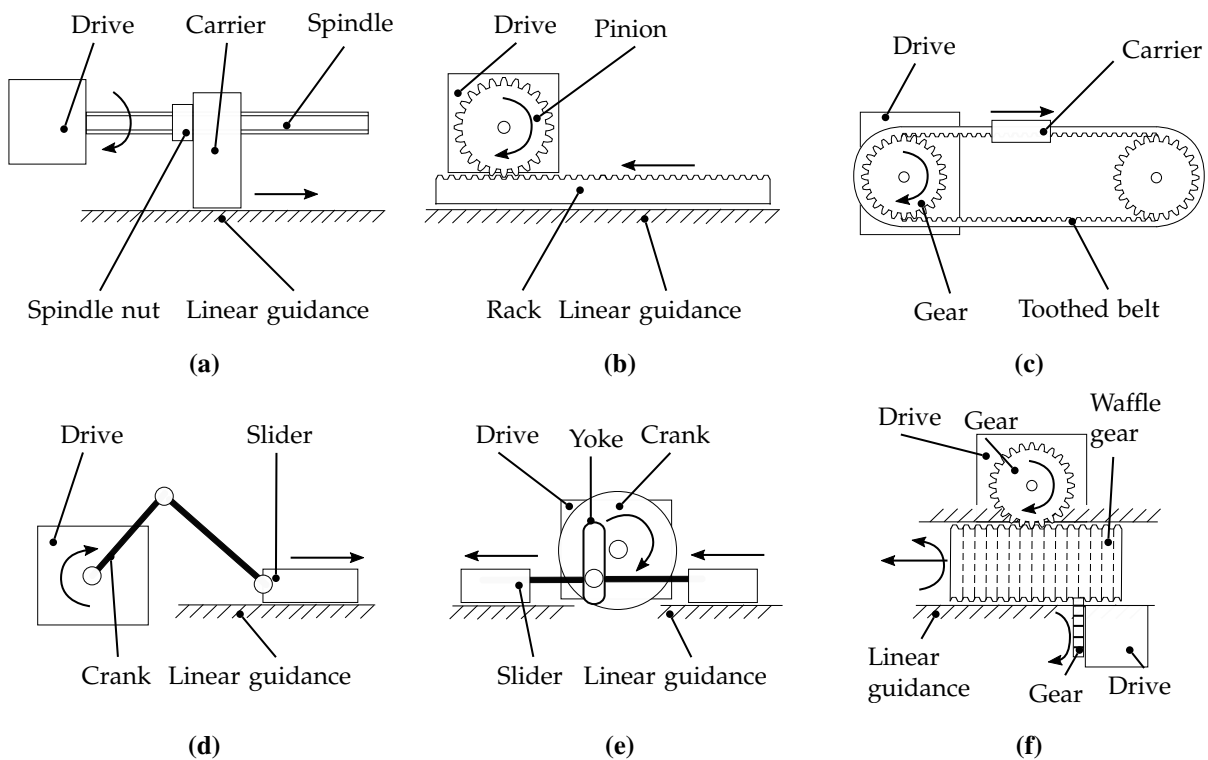
Fig. 4.7: Mechanism examples for angular to linear motion conversion: (a) spindle drive, (b) pinion and rack transmission, (c) toothed belt, (d) slider-crank mechanism, (e) Scotch-Yoke mechanism, and (f) multi-DoF waffle gear transmission.

2. Belt-driven actuation at small scale may need increased maintenance efforts to ensure tensioning of transmission elements.

Lastly, multi-DoF waffle gears are recently limited to prototypic applications and contradict a reliable long term use due to additive gear manufacturing. Previous paragraphs systematically evaluated potential compositions of actuators. This is preceded by a motor and gear selection. Corresponding technical requirements are substantiated from specifications listed in Section 4.1.2:

- Low weight ($< 150\,\mathrm{g}$) and small outer diameter ($< 30\,\mathrm{mm}$).

- High torque-to-size ratio.

- Integrated low-level control and bus interface.

- Low electric losses for reduction of heat generation.

- Commerical availability of reduction gear series.

These considerations limit the range of off-the-shelve drives to brushless servo motors (BLDC) and steppers according to guidelines in [Mor99]. In the following, only BLDC motors are regarded due to superior scalability, control, and dimensions. The final motor selection with regard to

Tab. 4.2: Assessment of mechanisms for rotary to linear motion conversion.

Criteria	Spindle	Pinion-rack	Toothed belt	Slider-crank	Scotch-Yoke	Waffle gear
Miniaturisation	+	o	o	-	-	+
Dynamics	o	+	+	+	+	-
Control	+	+	+	-	-	o
Joint range	+	o	+	-	-	-
Complexity	+	+	o	-	-	o
Scalability	+	+	o	-	-	o
Rank	1	2	3	5	5	4

(+: positive, o: neutral, -: negative)

nominal torques and sizes is governed by mechanical transmission of compatible spindle units. Characteristics of the latter are analytically described by spindle torque

$$\tau_{\mathrm{SD}} = \frac{F_{\mathrm{SD}} p_{\mathrm{SD}}}{2\pi \eta_{\mathrm{SD}}}, \tag{4.1}$$

where F_{SD} defines the nominal axial spindle force, p_{SD} the spindle lead, and η_{SD} the spindle efficiency. The latter is conservatively estimated to $\eta_{\mathrm{SD}} = 0.4$ for standard material pairings. Assuming a maximum spindle force $F_{\mathrm{SD}} = 100\,\mathrm{N}$ for standard operation of the unit, the nominal input spindle torque is determined to $\tau_{\mathrm{SD,max}} = 32.8\,\mathrm{mN\,m}$ with a metric lead $p_{\mathrm{SD}} = 1\,\mathrm{mm}$. This lead has become standard for miniaturised precision spindles from various manufactures. The nominal input torque is valid for absence of reduction gears. On the contrary, this thesis regards gears for reduction of angular velocities and to achieve nominal motor torques at small housing dimensions. The required motor torque range is conservatively derived from previous estimation between $\frac{1}{3}\tau_{\mathrm{SD,max}}$ to $\frac{2}{3}\tau_{\mathrm{SD,max}}$. A set of matching commercial motors was identified in a comprehensive review and listed in Table 4.3. Five commercial drives comply with the nominal torque range of $10\,\mathrm{mN\,m}$ to $20\,\mathrm{mN\,m}$ and likewise satisfy the design criteria for outer motor diameters of less than $30\,\mathrm{mm}$. A visual comparison of motor dimensions is provided in Figure 4.8a.

Drives listed in Table 4.3 may be equipped with bespoke reduction gears. In contrast, only motor 2232BX4CSD (Faulhaber GmbH, Schönaich, Germany) features an integrated motion controller. The remaining motors may need external configurable motion controllers, e.g. DMC-40x0 (Galil

Tab. 4.3: Overview of commercial BLDC motors with nominal torque range of $10\,\mathrm{mN\,m}$ to $20\,\mathrm{mN\,m}$.

Type	Manufacturer	Dimension (mm)	Voltage (V)	M_{N} (mN m)	$n_{\mathrm{N}}(\mathrm{min}^{-1})$	Gear	IMC
EC-max 22	maxon motor	$\varnothing 22 \times 32$	24	10.8	8250	y	n
BN12-13AF	Moog	$\varnothing 25 \times 33$	24	12.7	12736	y	n
2232BX4CSD	Faulhaber	$\varnothing 22 \times 33$	24	16	4650	y	y
cyber d17	Wittenstein	$\varnothing 17 \times 47$	48	11	9690	y	n
MBS2838-24	MCP	$\varnothing 28 \times 38$	24	18	7640	y	n

Note: Gear denotes an interface for direct gear mounting. IMC denotes availability of an integrated motion controller. Further acronyms denote yes (y) and no (n).
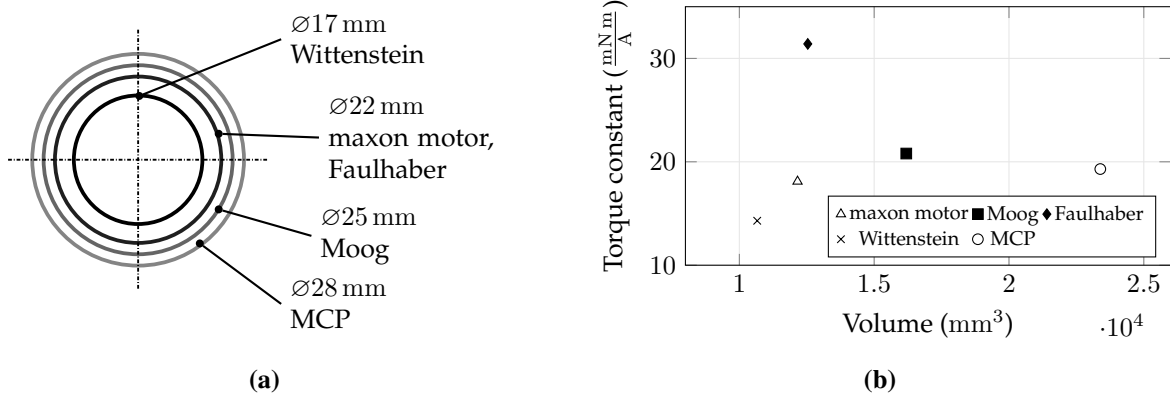
Fig. 4.8: Metrics of selected BLDC motors: (a) Housing diameters of motors at genuine scale and (b) motor specific torque constant related to housing volume. Data is extracted from manufacturer datasheets.

Motion Control, Rocklin, CA, USA). This outcome is contradictory to design paradigm integration. A comparison of motor torque constant-to-volume ratios is shown in Figure 4.8b and included in the selection process. Most drives have a torque constant of $20\,\mathrm{mN\,m\,A^{-1}}$ or below for varying motor volumes. Drive 2232BX4CSD exclusively outperforms the remaining alternatives in terms of small volume and high torque constant as provided in Figure 4.8b. Under consideration of an internal motion controller and integrated system design, drive 2232BX4CSD was selected. The corresponding gear transmission was estimated from requirements on nominal torques and spindle velocities. The resulting reduction gear ratio is defined as

$$i_{\mathrm{rg}} = \frac{n_{\mathrm{N}} p_{\mathrm{SD}}}{v_{\mathrm{max}} \cdot 60} s_{\mathrm{SD}}, \tag{4.2}$$

where n_{N} denotes shaft revolutions per minute and s_{SD} defines a safety factor (e.g. friction, unknown tissue-manipulator interaction) for torque scaling. This determines the desired ratio to $i_{\mathrm{rg}} \approx 50$ with $v_{\mathrm{max}} = 4\,\mathrm{mm\,s^{-1}}$ and $s_{\mathrm{SD}} = 2$. Thereupon, two sets of reduction ratios with $i_{\mathrm{rg}} = 51$ and $i_{\mathrm{rg}} = 66$ were selected from available two-stage planetary gear head series (Faulhaber GmbH, Schönaich, Germany).

Lastly, drive position sensors were chosen according to two criteria: 1) BLDC motors demand for low-noise commutation signals and 2) an accurate motor position signal is required for measurement of instantaneous joint states in the robotic controller. In this regard, a high resolution sensor was considered. An integrated digital Hall-sensor representing an incremental encoder with 3k ticks per revolution was selected from off-the-shelve series (Faulhaber GmbH, Schönaich, Germany).

4.3.3 Linear Motion Units

Fundamentals of the continuum manipulator and its kinematic realisation are introduced in Section 4.3.1. Each joint of the two-segmental continuum structure is actuated by individual linear

displacements of embedded six actuation tubes. Corresponding joints of the stacked structure take a concentric tube layout into consideration to realise an extensible, but compact mechanism. As an example, the outer tube actuates the joint of the first segment and the inner tube actuates the associated joint of the second segment, respectively. A mechanism that implements independent motion of both concentrically guided tubes is defined as LMU. According to a modular design, an assembly of three LMUs realises 6 DoF linear motion in joint space. More specifically, joint motion is transferred to remote sections with flexible tubing of two different diameters manufactured from polyamide (PA). Tube guidance within the shaft sections is implemented with an additional pre-curved set of protective tubing with low compliance. This approach has demonstrated applicability for remote push/pull actuation [ST04, BDN+13].

However, actuation unit concepts in related work (see Section 1.2.3) are mainly dedicated to basic deployment and evaluation in laboratory environments with low TRL and absence of user feedback. This disregards clinical requirements and may be linked to the following deficiencies:

- Bulky components (e.g. weight or large dimensions).

- Absence of enclosed housing (e.g. challenge in contaminated environments).

- Tedious handling during setup and transportation.

- Absence of intuitive interfaces (e.g. low number of connectors and cables).

- Frequent assistance and intervention of technicians mandatory (e.g. system failures).

This thesis targets particular aspects of the preceding listing to establish a highly-integrated and modular device that enables deployment to preclinical environments, e.g. *ex vivo* studies. This not only comprises an enclosed robotic unit with non-obstructed access to major components of the system, but also reduced dimensions and weight to facilitate handling and setup by an individual, e.g. trained OR staff members. Beyond that, the device must enable a reliable, safe, and plausible operation. This is supported by plug and play setup workflows providing only indispensable connectors for supply, data exchange (e.g. Ethernet interface), and laser delivery.

The proposed design for dexterous manipulation of the two-segmental continuum structure demands for independent motion of all six joints. The stacked composition of the manipulator and its corresponding actuation through concentrically guided tubes requires cascaded displacement principles to realise independent joint motion. This is implemented by described LMU and the extension to a whole robotic unit (6 Dof joint space) by composing three LMUs.

This work considered four LMU concepts in total. The corresponding designs are discussed related to criteria of scalability, extendibility to multiple DoF, and constraints presented in Section 4.1. Descriptions are further complemented by schematics at genuine scale. For the sake of brevity, LMU concepts (I) - (III) that were excluded from further design iterations are listed in Appendix A. The selected mechanical concept (IV) is described in the following. The comparison of proposed mechanisms (I) - (IV) uses a generic standard notation. This includes joint index j with $j = \{1,2\}$

for joint space q_j and drive-sided joint state $q_{\mathrm{mot},j}$ as well as its corresponding time derivatives. The range of displacement for concentrically guided tubings, i.e. tube_2 encloses tube_1, is annotated by tube_j and movable LMU carriers are labelled by $\mathrm{carrier}_j$.

Mechanical concept (IV) is depicted in Figure 4.9 and extends spindle-based concept (III) in Appendix A to a compact assembly. This eliminates mobile drive components. The linear rail is replaced with a common linear guidance for $\mathrm{carrier}_1$ and $\mathrm{carrier}_2$. $\mathrm{Carrier}_1$ implements the mechanical frame for $\mathrm{carrier}_2$. Moreover, both drives are mounted stationary. Despite motions of joint q_1 and related motion of $\mathrm{carrier}_1$, the telescopic shaft ensures continuous torque transmission to the carrier in motion. The telescopic shaft extends or shortens related to joint state q_1. The spindle linked to $\mathrm{carrier}_2$ may be actuated by drive_2 throughout the entire motion envelope of joints q_1 and q_2. In contrast to concepts (I) to (III), this strategy implements a compact mechanical setup with reduced wire routing efforts due to stationary drives. Dynamics of joint q_1 may be significantly improved due to reduced weight in motion. The coupling constraints for joint velocities and actuation forces introduced in concept (III) similarly apply to the present concept as described by Equations (A.5) and (A.6).

Concepts (I) to (IV) were compared based on specific design criteria. The results are summarised in Table 4.4. In general, all LMU concepts have feasibility in common. However, the qualitative analysis revealed that concept (IV) outperforms concept (I) due to the cascaded actuation. The intrinsic compensation mechanism of the telescopic shaft reduces drive control efforts and minimises the complexity of wire routing. Additionally, the design enables miniaturisation that may prospectively improve clinical user acceptance from small device footprints.
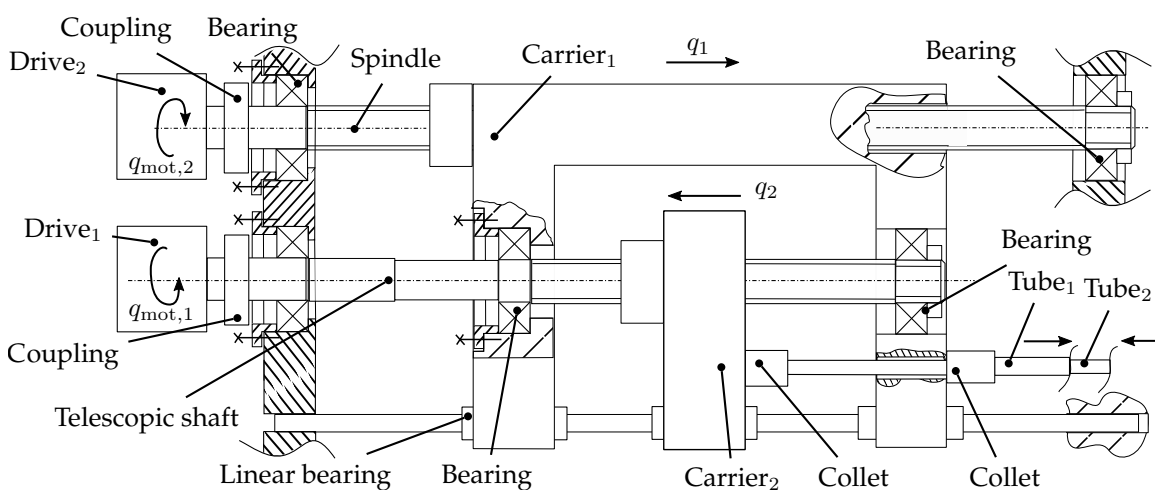
Fig. 4.9: Schematics of preferred concept (IV) for realisation of a two DoF linear motion unit with two stationary drives and a telescopic shaft.

Tab. 4.4: Assessment and ranking of LMU concepts.

Criteria	(I)	(II)	(III)	(IV)
Miniaturization	+	-	o	+
Control	-	-	+	+
Joint range	+	o	-	+
Wire routing	+	+	-	+
Dynamics	+	+	-	+
Complexity	+	-	o	o
Scalability	+	-	o	+
Rank	2	3	4	1

Note: positive (+), neutral (o), negative (-).

4.3.4 Joint Limit Sensing

The LMU design proposed in preceding Section 4.3.3 in combination with the actuator selection in Section 4.3.2 requires sensing methodologies to capture the joint state and to ensure redundant safety features for protection of structural integrity. This aims at joint limit detection as only incremental encoders are available for selected drive units (see Section 4.3.2). Actuator encoders must be referenced after initial start-up or emergency shutdown. The requirements for LMU sensor integration consolidate to:

- Highly-integrated sensor layout with minimal number of components.

- Adjustable trigger level for prototypic applications.

- Reliable and robust operation (> 10k cycles).

- Wiring and wire routing layouts with low complexity.

- Encapsulation feasible (e.g. cover or injection moulding).

Five concepts for customised LMU joint limit sensing were proposed in the design process of the robotic platform. For the sake of brevity, concepts (I) - (IV) that were disregarded in the further design process are summarised in Appendix B. These describe principles based on mechanical hard stops, mechanical and optical switches, and proximity sensors. Considered concept (V) based on HALL sensors is detailed in the subsequent section. Relevant technical background on sensor fundamentals is provided in overview literature [Fra10, RT10, WE14].

Sensing concept (V) uses Hall effect sensors for detection of a specific magnetic flux density and polarity over large working distances. For example, a moving LMU carrier is equipped with a permanent magnet and the corresponding LMU frame with a hall sensor in proximity of the mechanical joint limit. When the carrier approaches the limit, the magnetic flux density of the sensor interface increases and finally exceeds a predefined trigger threshold. The Hall voltage is proportionally generated to the magnetic flux. Commercial integrated circuits (IC) implement analogue or digital characteristics related to levels of measured flux and polarity. Hall sensors examples with sensitivities of less than $20\,\mathrm{mT}$ are provided in Table C.4 in the appendix. The latter

realise robust and contact-less detection of positions and with bespoke integration to printed circuit boards (PCB). Variations of LMU integration are feasible and comprise coaxial and perpendicular sensor-to-magnet layouts. However, both versions require preadjustment of trigger distances in reference to nominal magnetic flux thresholds.

Further disregarded sensor concepts are ultrasound sensors, linear variable displacement transducers (LVDT), and potentiometers for absolute displacement sensing [SXK$^+$09]. The latter technologies are excluded due to requirements of precise position feedback from integrated drive encoders (see Section 4.3.2) and absence of backlash in transmission components. Besides, these sensors contradict compact integration and modularity. Concepts (I) - (V) were assessed and summarised according to criteria listed in Table 4.5. Although concepts (I) and (II) realise straightforward sensing with low number of parts and industrial components with two-wire interfaces, concept (V) (hall sensors) is preferred for LMU integration. In particular, the combination of criteria for miniaturisation and adjustable working distances outperformed the characteristics of remaining concepts (I) - (IV) described in Appendix B.

4.3.5 Actuation Unit

The LMU described in Section 4.3.3 realises linear displacement in two DoF of corresponding actuation tubes. However, manipulation of the entire continuum manipulator with 5 DoF in Cartesian space is based on 6 linear DoF in joint space. Hence, three LMU with two linear DoF each are composed to an actuation unit.

A compact and integrated assembly of three LMU is achieved with a circular alignment to the corresponding tubular layout discussed for the continuum manipulator (see Section 4.3.1). Each LMU is distributed along the circumference at an angle of $120°$ to manipulate the corresponding set of concentric tubes. This approach is transferred to the proposed assembly. The selected concept presented in Section 4.3.3 is further detailed for integration purposes.

Each LMU includes a floating carrier and a carrier frame, whereas both are linked to bespoke metric spindles (MISUMI Europa GmbH, Schwalenbach, Germany) with a diameter of $d_{SD} = 5\,\text{mm}$ and lead $p_{SD} = 1\,\text{mm}$. The carrier frame mounts the spindle bearing of the floating carrier to

Tab. 4.5: Assessment and ranking of sensor concepts.

Criteria	(1)	(2)	(3)	(4)	(5)
Miniaturization	+	-	o	-	+
Robustness	-	o	-	+	+
Working distance	o	o	-	+	+
Wire routing	+	+	o	o	o
Costs	+	o	o	-	o
Rank	2	4	5	3	1

Note: positive (+), neutral (o), and negative (-).

compensate linear displacements, as both carriers are supported by a common linear bearing (drylin, igus GmbH, Cologne, Germany). Each carrier further holds a collet for tube clamping and transmission of carrier-to-tube motion. Focusing on integration, carriers have curved shapes (outer radius $42 \, \text{mm}$, inner radius $15 \, \text{mm}$) to decrease component footprints and optimise space requirements. The latest design of the actuation unit is shown in Figure 4.10.

The mechanical coupling of each LMU and associated drive units is implemented with flexible Oldham couplings (LK4-12S (jaw type), MISUMI Europa GmbH, Frankfurt, Germany) (see Figure 4.11 (c)). This accommodates angular shaft misalignments and eccentricities, while preserving torsional stiffness. Beyond that, this design enables quick disassembly and component exchange. Under consideration of a modular design, a separate drive mounting is taken into account. The latter enables ease of deinstallation for maintenance purposes. Six motors (see Section 4.3.3) are aligned circumferentially as shown in Figure 4.11 with design restrictions imposed by LMU layouts. Equiangular spacing between individual LMU is realised. Wire and fibre routings for sensors, cameras, and laser optics from distal to proximal robot compartments use cylindrical cut-outs in the centre of the motor mounting and subsequent components.

4.3.6 Tubular Force Transmission

The actuation of the distal continuum kinematics calls for remote transmission of joint displacements generated by the actuation unit. This is implemented by a mechanical interface to support and stabilise actuation tubing. Optimal transmission characteristics with minimal disturbances are achieved by full guidance along device compartments from extracorporeal to intracorporeal sections. The mechanical design targets the following objectives: 1) Spatial reduction of the tubular alignment diameter commencing from the actuation unit to the continuum sections and 2) prevention of tubular buckling for stable and precise manipulation of the continuum robot.

The design concept presented in Figure 4.12 addresses aforementioned objectives and integration paradigms. The component adapts to the LMU composition in Section 4.3.5 showing a parallel layout of actuation tubes. Gradual reduction of the layout diameters starting from the actuation unit ($b_{\text{TF},1} = 30 \, \text{mm}$, $b_{\text{TF},2} = 4.5 \, \text{mm}$) is implemented with a feeding unit and guidance elements (see Figure 4.12). These enclose the flexible actuation tubing from insertion to the rigid shaft to the base of the flexible continuum manipulator.

Reduction components applied S-shaped channels to gradually set the radial distance of the tubular guidance with minimised friction ($r_{\text{TF}} = 30 \, \text{mm}$). Friction resulting from residual material contacts within the S-shaped section must be taken into account for spindle forces and are approximated by

$$F_{\text{SD}} = e^{2\mu_0 \frac{\pi}{4}} F_{\text{T}} \, , \tag{4.3}$$
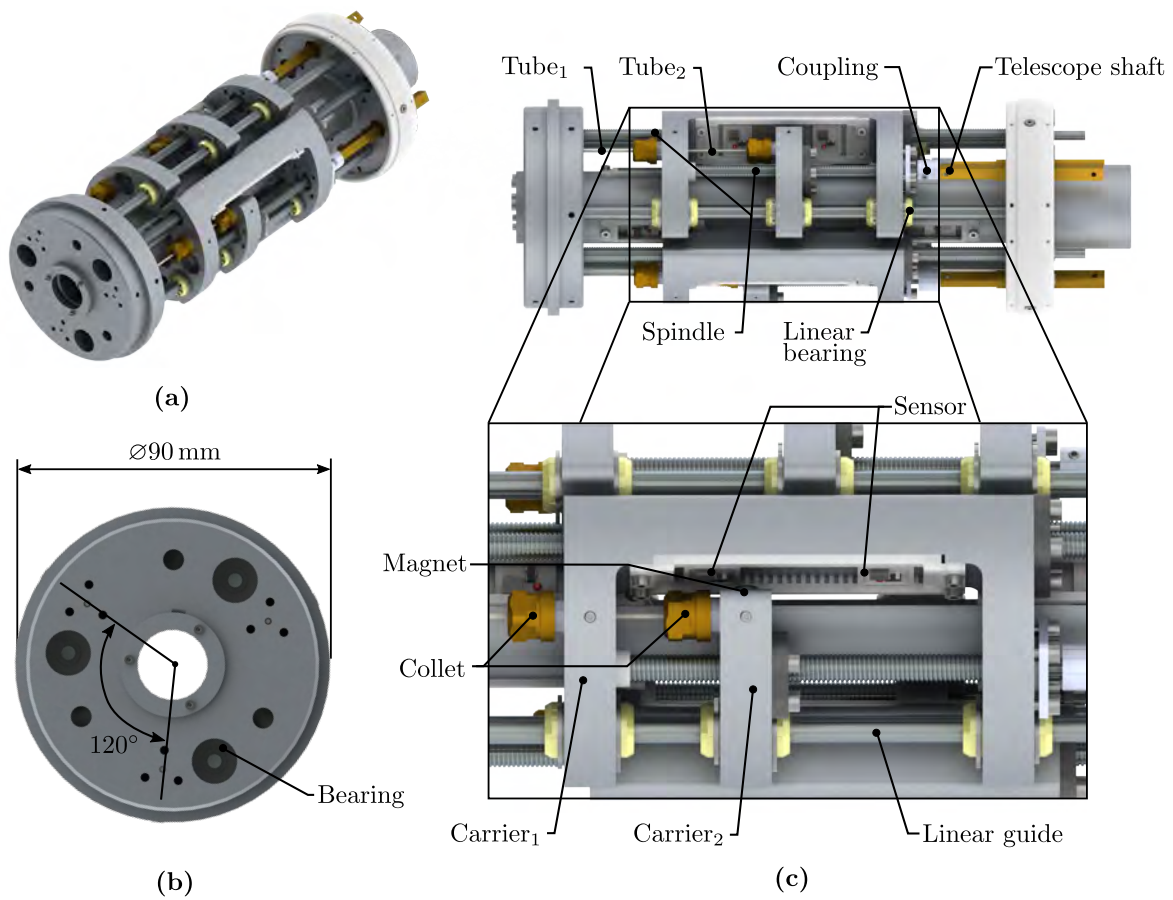
Fig. 4.10: CAD model of the proposed actuation unit: (a) Isometric view, (b) front view, and (c) side view of the unit with magnified section of a linear motion unit (LMU) and sensor locations.
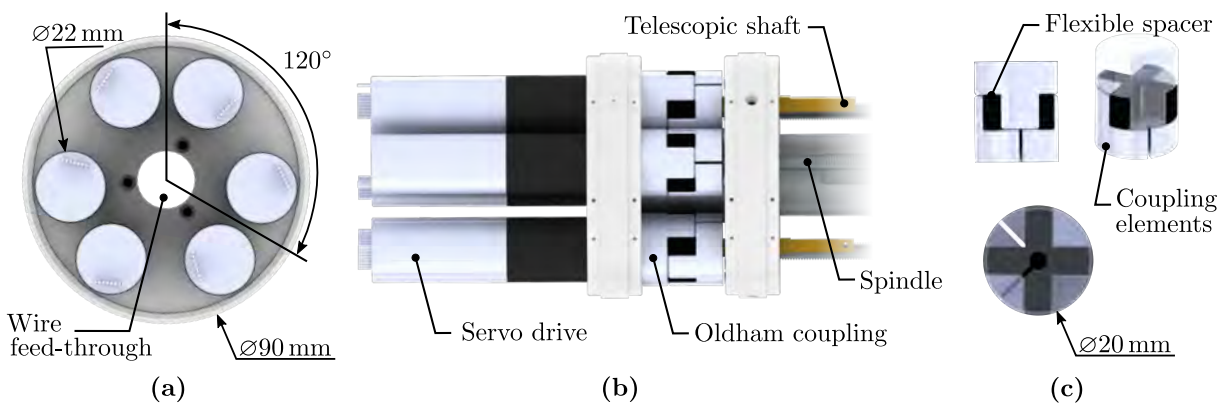
Fig. 4.11: CAD design of the drive unit: (a) Back view, (b) side view, and (c) Oldham couplings.
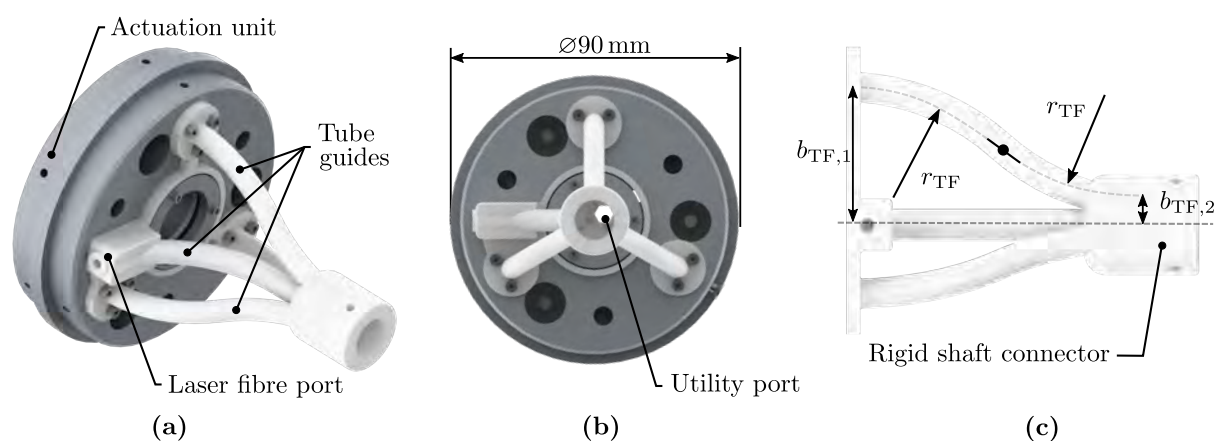
Fig. 4.12: Prototype design of the tube feeding unit: (a) Isometric view, (b) front view, and (c) side view with annotation of dimensional constraints and parameters.

where μ_0 defines the friction coefficient of the material pairing between actuation and guidance tubes and F_T is the normal force transmitted to the tube. Friction in the rigid shaft and flexible sections is neglected.

The feeding unit further shows two auxiliary ports. The laser fibre port enables safe feeding of fibres to the lumen of the shaft and feeding to the flexible manipulator. Handling is facilitated by orthogonal alignment of the port aperture with respect to the shaft axis. Secondly, a utility port is integrated to the residual space. This port enables feeding of supply and signal wiring for electronic components embedded to the endoscopic tip. Components of the unit are joined in the shaft connector. This implements the interface to the rigid shaft and prealigns actuation tubes, wires, and fibres. The feeding unit is enclosed by a tailored cone-shaped housing.

4.3.7 Electronics Architecture

The mechatronic integration of the robotic framework with sensors, actuators, and control must use a standardised communication and supply architecture. The electrical network and associated interfaces are illustrated in Figure 4.13. Modularisation of encapsulated functions and integration to the overall structure are the core criteria. In total, five modules are proposed and described in the following paragraphs including implementation details.

The external robotic controller (ERC) is based on a workstation (Intel core i7, Intel Cooperation, Santa Clara, CA, USA) with integrated video acquisition card for sequencing of camera PAL signals and parallel computing on a dedicated graphics card with general purpose graphics processing unit (GPGPU) GeForce GTX Titan (NVIDIA Corporation, Santa Clara, CA, USA). The ERC is powered by $220\,\mathrm{VAC}$ and is connected to the internal robotic controller (IRC) via Ethernet connection with $100\,\mathrm{MB\,s^{-1}}$ bandwidth. Further Ethernet connections are established to laser controllers or auxiliary computational units. The embedded controller board (BeagleBone black,
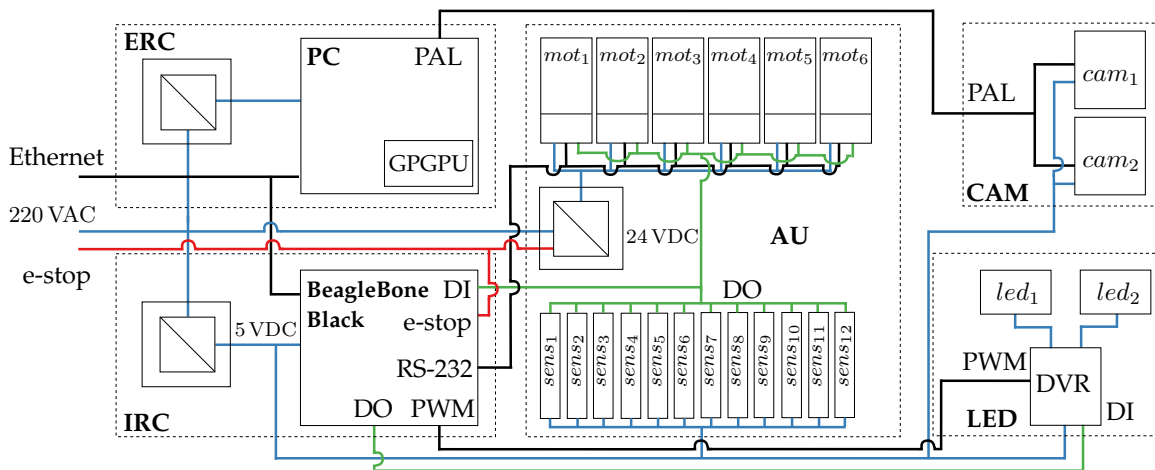
Fig. 4.13: Electrical architecture of the robotic framework with external robotic controller (ERC), an internal robotic controller (IRC), an actuation unit (AU), a camera module (CAM), and a LED module (LED).

BeagleBoard.org Foundation) of the IRC is connected to six low-level motion controllers of corresponding servo motors (see Section 4.3.2) located in the actuation unit (AU). Motors are supplied with $24\,\mathrm{VDC}$ and communication is based on asynchronous RS232 data exchange. Twelve joint limit sensor PCB are supplied with $5\,\mathrm{VDC}$. Each sensor digital output (DO) is connected to a separate digital input (DI) on the embedded board and likewise to digital interfaces on the motor controllers for redundancy features. Beyond that, an emergency stop (e-stop) interfaces the motor power supply and enables a direct power disconnection. The corresponding digital signal is routed to the embedded board for status monitoring. The two chip-on-the-tip units of the stereoscopic camera module (CAM) are supplied by $5\,\mathrm{VDC}$ and the PAL signal is routed to the video acquisition card of the ERC. High power light emitting diodes (LED) of the LED module are supplied by $5\,\mathrm{VDC}$. Both diodes are connected to a driver IC to enable current modulation, i.e. intensity adjustment. The driver is controlled by pulse width modulation (PWM) generated from a IRC real-time output.

The controller unit enables physical communication with external high-level controllers, e.g. image processing computers, and internally monitors sensors and electrical drives.

The IRC interfaces motor control, sensors, illumination and further links to the high-level ERC. This is handled by an open source single-board computer. The latter enables deployment of dedicated unix operating systems. The BeagleBone Black (BeagleBoard.org Foundation) developer platform (Rev. C) is selected for this purpose. The board integrates an AM335x 1GHz ARM® Cortex-A8 processor, 512 MB RAM, $4\,\mathrm{GB}$ on-board flash storage, and two 46 pin headers for peripheral connections on a credit card-sized PCB. The system reference manual lists general specifications with regard to design guidelines and electrical interfaces [KC17].
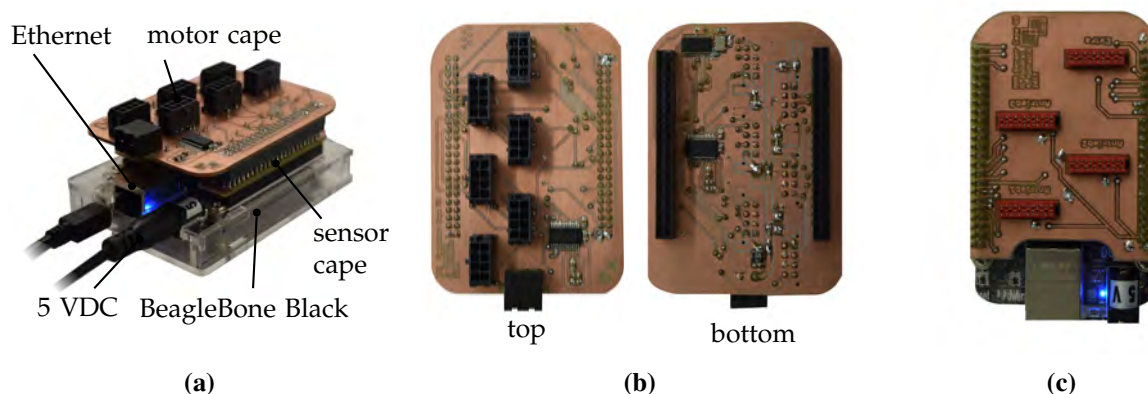
Fig. 4.14: Prototype of the internal controller unit with sensor and motor interfaces: (a) Isometric view of BeagleBone Black and cape extensions, (b) top and bottom view of motor cape, and (c) top view of sensor cape.

Two customised PCB, also denoted as capes, are shown in Figure 4.14. These are designed for electrical connection of board pin headers and peripheral components, e.g. sensors and actuators. The proprietary device is limited to four native universal asynchronous receiver/transmitter (UART) controllers, whereas six drives use RS232 communication. This limitation is mitigated by a dual serial peripheral interface (SPI) to UART converter (SC16IS752IPW, NXP Semiconductors, Eindhoven, Netherlands). The IC extends the native interface with two emulated UART controllers and communicates with the embedded controller via SPI bus. Drive units can be individually assigned to dedicated UART controllers. This prevents a RS232 device network with low data rates caused by multi-node acquisition. Level converters (MAX3241, Maxim Integrated, San Jose, CA, USA) are considered for voltage level conversion from TTL/CMOS ($3\,\mathrm{V}$) to RS232 bus levels ($\pm 5\,\mathrm{V}$).

The servo drives are further connected to the extension cape for data communication and power supply (see Figure 4.14 (b)). This cape implements a direct connection to the $24\,\mathrm{VDC}$ power supply and contains two additional safety features for each motor:

1. Overcurrent protection ($> 3\,\mathrm{A}$) with polymeric resettable positive temperature coefficient (PTC) fuses (Polyfuse 18121, Littlefuse® Inc., Chicago, IL, USA).

2. Flyback diode (SM15T, Vishay Inc., Malvern, PA, USA) for suppression of flyback currents across the motor inductor.

PCB prototypes were manufactured on a circuit board plotter (ProtoMat E34, LPKF Laser & Electronics AG, Hannover, Germany) from two-sided copper templates. The most recent cape versions and the stacked assembly of embedded boards are shown in Figure 4.14.

Joint limit sensors were equivalently customised. A digital-switch Hall sensor (DRV5023BI, Texas Instruments Inc., Dallas, Tx, USA) was selected according to sensing requirement. The IC only indicates a magnetic field if a threshold of $6\,\mathrm{mT}$ is exceeded. A corresponding digital output is

activated subsequently. The sensing workspace was chosen from expected magnetic field strengths of permanent magnets mounted to the LMU (see Section 4.3.4). Visual LED indicators were added to the PCB to facilitate commissioning, maintenance, and prototyping. The PCB footprint is $(10 \times 13 \times 2.5)\,\text{mm}^3$ and is depicted in Figure 4.15. Twelve sensors were fabricated in total and mounted to allocated locations within each LMU. Sensor PCB are connected to DI ports on the embedded board through interface capes.

Endoscopic illumination intensities of both high power LEDs are controlled with a constant current LED driver (L4242DRJR, Texas Instruments, Dallas, TX, USA). LED brightness is adjusted by PWM duty cycle modulation from timer output on the embedded board.

4.4 Numerical Optimisation of Stereoscopic Sensor Layout

The performance of a stereoscopic system is determined by sensor parameters and camera pose configurations with respect to the observed target. Firstly, a review on imaging sensors that meet requirements for endoscopic integration under consideration of clinical and technical specifications is presented. Secondly, a workflow for numerical optimisation of sensor poses with constraints on geometric and visual conditions is described. This ensures optimal scene coverage by the stereoscopic configuration embedded to the endoscopic tip. Numerical results are transferred to the prototypic hardware.

4.4.1 Sensor Review

The design of the endoscopic tip aims at miniaturisation and integration to facilitate the insertion of the robotic device through trocar ports or a deployment to confined anatomy via natural orifices. Hence, the outer diameter of the tip is restricted to a maximum of $13\,\text{mm}$. In the last decades, several optical technologies were considered for endoscopic imaging. High definition imaging, such

(a)   **(b)**
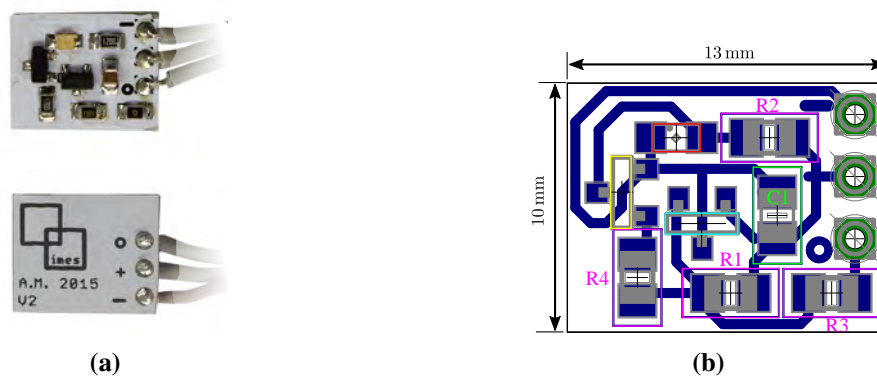
Fig. 4.15: Prototype of joint limit sensor: (a) Top and bottom PCB layers and (b) electrical schematics with board dimensions and routing to peripheral components.

as used in rigid laparoscopes, uses rod lens assemblies to transmit light from the surgical scene to an imaging sensor outside the human body. Despite this concept enables improved imaging quality, it was neglected in the considered tip design due to the presence of flexible components in the continuum structure. Alternatively, flexible images bundles were considered for light transmission from the surgical scene to an image sensor outside the human body. Recent commercially available image bundles contain up to 100k fibres with distinct configuration and outer diameter of $1.7\,\text{mm}$, e.g. bundle FIGH-100-1500N (Fujikura Ltd, Japan). However, large numbers of bundle elements constrain bending radii. For example, the radius of bundle FIGH-100-1500N is limited to $130\,\text{mm}$. This is contradictory to specified motion ranges for flexible intracorporeal manipulation and may cause bundle damage from static or dynamic fatigue. In this regard, chip-on-the-tip imaging with sensor placement in the endoscopic tip facilitates advanced image definitions and simplifies integration to flexible kinematic structures. A review of commercial sensors was conducted with boundary values on sensor parameters from design constraints of $(4.5 \times 4.5 \times 4.5)\,\text{mm}^2$, a minimum image definition of $(640 \times 480)\,\text{px}$, and depth of field (DF) between $15\,\text{mm}$ to $25\,\text{mm}$. Review findings are summarised in Table 4.6. Parameters w_s and A_px indicate sensor width and area per pixel, respectively.

Wafer-Level-Cameras (WLC) constitute a promising technology which promotes joint manufacturing of sensors and optics [BBS$^+$12]. However, depths of fields of commercial components (Nemotek, Rabat, Morocco) exceed endoscopic specifications and realisation of customised optics is restricted due to the recent production workflow.

An alternative group of devices considers highly integrated sensors with medical approval. For example, this addresses endoscopic devices from Medigus Ltd, Omer, Israel and Richard Wolf GmbH, Knittlingen, Germany. These products are sensors with task-specific optical assemblies. However, additional engineering resources for implementation of customer specific solutions are required. By contrast, the NanEye GS image sensor (AWAIBA, Nürnberg, Germany) shows high acquisition rates (maximum of $100\,\text{Hz}$) for raw image capturing but demonstrated restricted update rates of less than $10\,\text{Hz}$ after signal processing. This is mainly due to bandwidth restrictions of

Tab. 4.6: Miniaturised imaging sensors for endoscopic tip integration.

Model	Dimension (mm^3)	Resolution (px)	Sensor / Optics	FoV (°) / DF (cm)
Medigus IntroSpicio 110	$3 \times 3 \times 15$	500×582	$w_\text{s} = 1.86\,\text{mm}, A_\text{px} = 5.61\,\mu\text{m}^2$	140 / 0.5 - 10
Nemotek S42-A2	$3.4 \times 3.1 \times 2.5$	640×480	$w_\text{s} = 1/11", A_\text{px} = 4.84\,\mu\text{m}^2$	63.5 / 60 - ∞
Nemotek A12-B2	$5.6 \times 5.8 \times 3.5$	1600×1200	$w_\text{s} = 1/5", A_\text{px} = 3.1\,\mu\text{m}^2$	63.5 / 60 - ∞
Richard Wolf TVP-8	$\varnothing 8.3 \times \text{NA}$	400×400	$w_\text{s} = 1/10"$	80 / NA
Richard Wolf DAFE	$\varnothing 5.3 \times \text{NA}$	NA	NA	85 / NA
MISUMI MO-BS0804	$\varnothing 4.5 \times 4.5$	720×576	$w_\text{s} = 1/8", A_\text{px} = 7.84\,\mu\text{m}^2$	55 / 1 - 3
MISUMI MO-B1204	$\varnothing 5.3 \times 6.5$	640×480	$w_\text{s} = 1/12"$	48 / 1 - 4.5
AWAIBA NanEye GS	$\varnothing 6.5 \times 14$	640×640	NA	30 / 1.5 - ∞

Notes: Bold models indicate commercial components without OEM restrictions. Acronyms: Field of view (FoV), depth of field (DF), and original equipment manufacturer (OEM).

available USB 2.0 interface modules [AWA13]. To overcome technical limitations of reviewed technologies, a commercial imaging sensor (MO-BS0804, MISUMI, Taipeh, Taiwan) was selected for integration to the endoscopic prototype based on three criteria: 1) Compliance with design specifications, 2) off-the-shelve availability for research applications, and 3) economical aspects.

4.4.2 Geometric Model of the Endoscopic Tip

The numerical optimisation workflow for stereoscopic image sensor poses is based on analytical modelling of physical relations and constraints in the endoscopic tip design. This assumption yields a geometric model for the specific component layout located in the tip. This approach is transferred to a non-linear optimisation statement which is solved with numerical methods.

The geometric layout located in the endoscopic tip is simplified for modelling purposes as illustrated in the three viewing planes of Figure 4.16. Components in the frontal plane are described by Figure 4.16a. Fundamentally, it is assumed that the tip has a circular contour with diameter d_t. Laser optics and camera sensors are arranged in the frontal plane of the endoscopic tip with respect to laser optics. The latter are positioned at offset b from the tip centre along the y-axis. The intersection of optical axis and frontal plane determines the origin of frame $(\mathrm{CF})_\mathrm{O}$. Stereoscopic image sensors with optical centres $\boldsymbol{p}_\mathrm{SL} = (x_\mathrm{SL}, y_\mathrm{SL})^\mathrm{T} \in \mathbb{R}^2$ and $\boldsymbol{p}_\mathrm{SR} = (x_\mathrm{SR}, y_\mathrm{SR})^\mathrm{T} \in \mathbb{R}^2$ are arranged in the residual area formed by tip outline and laser optics. Image sensor diameters are d_s and the distance between sensor centres, i.e. the camera baseline, is described by b. The lateral view on the considered geometry is shown in Figure 4.16b.

Offsets z_SL and z_SR are the distances between reference origin and camera centres, whereas vertical tilt α_v is the sensor inclination in the lateral plane and ϕ_v the vertical FoV of the camera sensor. The working distance is determined by the laser focus, i.e. focal length f of laser optics. The top view in Figure 4.16c depicts auxiliary geometric parameters. Horizontal sensor inclination is described by α_h with corresponding FoV ϕ_h. The length of coverage ℓ_c inherently describes the camera
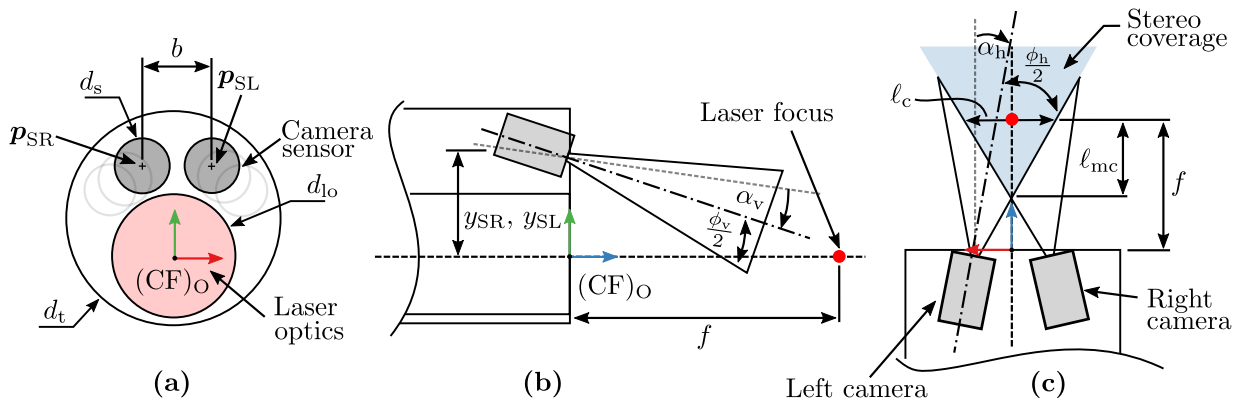
Fig. 4.16: Geometric model of the endoscopic tip for numerical optimisation of sensor poses: (a) Front, (b) lateral, and (c) top view.

overlap and ℓ_{mc} is the origin of the stereoscopic camera overlap. The independent parameters constitute the spatial sensor configuration respected in the numerical optimisation workflow:

1. Vertical camera tilt α_{v}

2. Horizontal camera tilt α_{h}

3. Camera positions $\boldsymbol{p}_{\mathrm{SL}}$ and $\boldsymbol{p}_{\mathrm{SR}}$

Table 4.7 lists auxiliary parameters and constants from sensor specifications in Section 4.4.1 and geometric constraints.

4.4.3 Optimisation Constraints

The numerical optimisation workflow considers constraints from geometric and visual boundary conditions to achieve convergence towards results with physical relevance. Based on initial specifications, the sensor FoV observes laser-tissue interaction in proximity of the tip. Hence, angular restrictions on the vertical tilt α_{v} about the y-axis of $(\mathrm{CF})_{\mathrm{O}}$ are imposed by condition

$$0 < \left(\alpha_{\mathrm{v}} - \frac{\phi_{\mathrm{v}}}{2} \right) < \frac{\pi}{2} \quad \text{with} \quad \alpha_{\mathrm{v}} > 0. \tag{4.4}$$

This range ensures that both sensors point forward in the vertical plane and have its maximal tilt perpendicular to the initial configuration. Tilt α_{h} for the left camera sensor in the horizontal plane about the z-axis of $(\mathrm{CF})_{\mathrm{O}}$ yields to

$$0 > \left(\alpha_{\mathrm{h}} + \frac{\phi_{\mathrm{h}}}{2} \right) > -\frac{\pi}{2} \quad \text{with} \quad \alpha_{\mathrm{h}} < 0, \tag{4.5}$$

where the right camera sensor tilt is given by inverse angle $|\alpha_{\mathrm{h}}|$. Optimal camera positions $\boldsymbol{p}_{\mathrm{SL}}$ and $\boldsymbol{p}_{\mathrm{SR}}$ take geometric constraints into account and assume a reduction of spatial locations to plane

Tab. 4.7: Geometric parameters and constants for numerical camera pose optimisation.

Parameter	Value
Maximum tip diameter d_{t} (mm)	13
Laser optics diameter d_{lo} (mm)	8.5
Camera head diameter d_{s} (mm)	4.5
Focal length f (mm)	20
Optics offset b (mm)	1.75
Minimum baseline b_{min}	d_{s}
Vertical FoV ϕ_{v} (°)	43
Horizontal FoV ϕ_{h} (°)	57

y-z in $(\text{CF})_\text{O}$. The camera baseline represented by Euclidean distance of left and right camera sensors must satisfy

$$b = \left\|_{(\text{O})}\boldsymbol{p}_\text{SL} - {}_{(\text{O})}\boldsymbol{p}_\text{SR}\right\|_2 > \frac{d_\text{s}}{2}, \tag{4.6}$$

where d_s is the housing diameter of the camera sensor. This implies that physical collisions of camera modules or module overlaps are excluded. Tip component positions are further constrained by geometric features and dimensional limitations:

$$d_\text{t} - d_\text{s} > \left\|_{(\text{O})}\boldsymbol{p}_\text{SL}\right\|_2 > d_\text{lo} + d_\text{s}, \tag{4.7}$$

where d_t and d_lo denote the maximal tip and laser optics diameters, respectively. This constraint maintains sensor positions within the residual area of focus optics and outer tip contour as highlighted in Figure 4.16.

Beyond that, the stereoscopic configuration enables robust depth estimation from captured surfaces in proximity of focal length f. The FoV of both cameras must overlap to facilitate stereoscopic reconstruction. A minimum coverage distance $l_\text{mc} = 0.25f$ is assumed with respect to the focal position. The geometric relation for the stereoscopic configuration is as follows:

$$\tan(\alpha_\text{h} + \phi_\text{h}) = \frac{\ell_\text{c}}{2\ell_\text{mc}}, \tag{4.8}$$

where the condition for minimal camera coverage is given by

$$\ell_\text{c} = 2\ell_\text{mc}\tan(\alpha_\text{h} + \phi_\text{h}) = 2f\tan(\alpha_\text{h} + \phi_\text{h}) - b \geq \ell_\text{c,min}. \tag{4.9}$$

Parameter ℓ_c describes the dependent coverage at focal length f and $\ell_\text{c,max}$ the minimum coverage that must be achieved for scene monitoring in clinical scenarios. This condition must be concurrently satisfied by the vertical camera tilt. Thus, the guaranteed visibility of an object in the distance of minimum coverage in both cameras is defined by

$$\frac{f - \ell_\text{mc}}{\cos(\alpha_\text{h} - \frac{\phi_\text{h}}{2})} \geq z_\text{lc}\tan(\alpha_\text{v} - \frac{\phi_\text{v}}{2}). \tag{4.10}$$

4.4.4 Cost Function

Cost functions are essential parts of the numerical solver for the given optimisation statement with constraints presented in Section 4.4.3. Limited design variations from component miniaturisation and the optimisation of camera coverage at the focal distance are regarded as core objectives. This directly impacts visualisation and robust stereoscopic depth recovery with persistent visibility of objects in both camera images. A feasible design of a cost function may comprise the area covered by both camera views. However, this may result in an ill-defined formulation as optimisation

results may converge towards infinity for larger camera distances, i.e. the covered area would increase steadily. An alternative cost function was introduced in [HK97] and is adapted to the concerned statement in the following. In contrast to the coverage area, optimisation of the coverage length (see Equation (4.9)) is targeted. Concurrently, the vertical camera tilt is optimised to ensure stereo coverage commencing from the minimal distance over the focal length and beyond. These conditions are joined into a product of corresponding parameters that constitute cost function

$$g = \ell_c \left(\alpha_v - \arctan(\frac{f}{z_{lc}}) \right) . \tag{4.11}$$

This formulation and proposed constraints are transferred to a non-linear programming environment [JOP$^+$01]. The statement is solved numerically using a generalised gradient-based methodology of the *scipy.optimize* package within the Python framework.

4.4.5 Results

The results of the parameter optimisation are summarised in Table 4.8. The algorithm was executed multiple times ($N = 5$) to validate the algorithmic convergence. In general, the latter was generally achieved within 14 to 21 iterations. Algorithmic termination was indicated if independent variables did not exceed variations greater than threshold $\varepsilon_c = 0.1$ within the last five steps. Geometric constraints discussed in Section 4.4.3 were not violated.

Based on the optimisation findings, the following parameters were incorporated to the endoscopic hardware design for optimal scene coverage:

1. Vertical tilt $\alpha_v = 16°$.

2. Horizontal tilt $\alpha_v = 7°$ (similar to [MRLW$^+$04]).

3. Left sensor position $_{(O)}\boldsymbol{p}_{SL} = (2.4\,\mathrm{mm}, 6.5\,\mathrm{mm})^T$.

4. Right sensor position $_{(O)}\boldsymbol{p}_{SR} = (-2.4\,\mathrm{mm}, 6.5\,\mathrm{mm})^T$.

5. Baseline $b = 4.8\,\mathrm{mm}$ with $b_{min} = d_s/2$.

Tab. 4.8: Results of optimised sensor configuration parameters for multiple algorithmic executions.

Variable	1	2	3	4	5
Vertical tilt α_v (°)	15.65	15.93	16.2	15.94	15.85
Horizontal tilt α_h (°)	6.45	7.1	7.33	6.72	7.03
Position $_{(O)}\boldsymbol{p}_{SL}$ (mm)	$(2.51, 6.69)^T$	$(2.38, 6.74)^T$	$(2.44, 6.64)^T$	$(2.43, 6.66)^T$	$(2.39, 6.75)^T$
Costs g	20.45	20.29	21.56	20.83	20.73

4.5 Robotic Prototype

The robotic hardware is derived, designed, and realised based on results of prior sections presented in this chapter. An overview of the most recent robotic prototype is depicted as CAD rendering in Figure 4.17 and as physical device in Figure 4.18.

Taking design the guidelines in Section 4.2 into account, the extracorporeal compartment of the device consists of five units for control and actuation. The intracorporeal section is composed of a rigid shaft, the flexible continuum manipulator, and the endoscopic tip. Each unit enables individual assembly and testing. Furthermore, electrical and mechanical interfaces to adjacent units were implemented. As detailed in Section 4.2, units implement specific subfunctions, e.g. joint motion, that contribute to high level objectives (see Section 4.1), e.g. dexterous Cartesian manipulation of the endoscopic tip.

Extracorporeal device dimensions (excluding the instrument shaft) are within $(\varnothing 90 \times 640)\,\mathrm{mm}^2$ as presented in Figure 4.17. In this regard, an OR compatible device footprint is achieved. This prospectively enables integration to active or passive positioning arms with specific payloads, e.g. LBR iiwa (KUKA AG, Augsburg, Germany). A bespoke connector (see Figure 4.18) realises the mechanical interface and paves the way for installation to auxiliary positioning devices. Beyond that, integration of the IRC to the robotic structure simplifies cable management and OR handling during setup and interventional workflows, e.g. repositioning. A bundle of three cables is used for data exchange with the ERC and electrical supply. Further design and implementation details of specific units are outlined in the following.

4.5.1 Extracorporeal Section

The extracorporeal section consolidates drive, coupling, controller, actuation, and feeding units to a decoupled 6 DoF mechatronic robotic system. The drive and coupling units were implemented according to design considerations presented in Section 4.1. This facilitates the generation of angular motion and consecutive conversion to linear joint space motion by individual LMUs. Thus, highly integrated servo drives with small footprint were selected accordingly (see Section 4.3.2).

The design of the actuation unit is inspired by electro-mechanical LMU concepts discussed in Section 4.3.3. A single LMU facilitates cascaded and decoupled displacement of two concentrically guided actuation tubes (2 DoF). Both axis of a LMU are actuated by selected servo drives. An extension to full manipulation of the two-segmental continuum body with 6 DoF in joint space was achieved with a circular arrangement of three independent LMU. The curved adaptation of structural components resulted in a compact outer housing contour ($\varnothing 90\,\mathrm{mm}$). The drive mounting flange features wire channels to connect sensors, cameras, supply, and PWM signals from the tip with the IRC presented in Section 4.3.7.
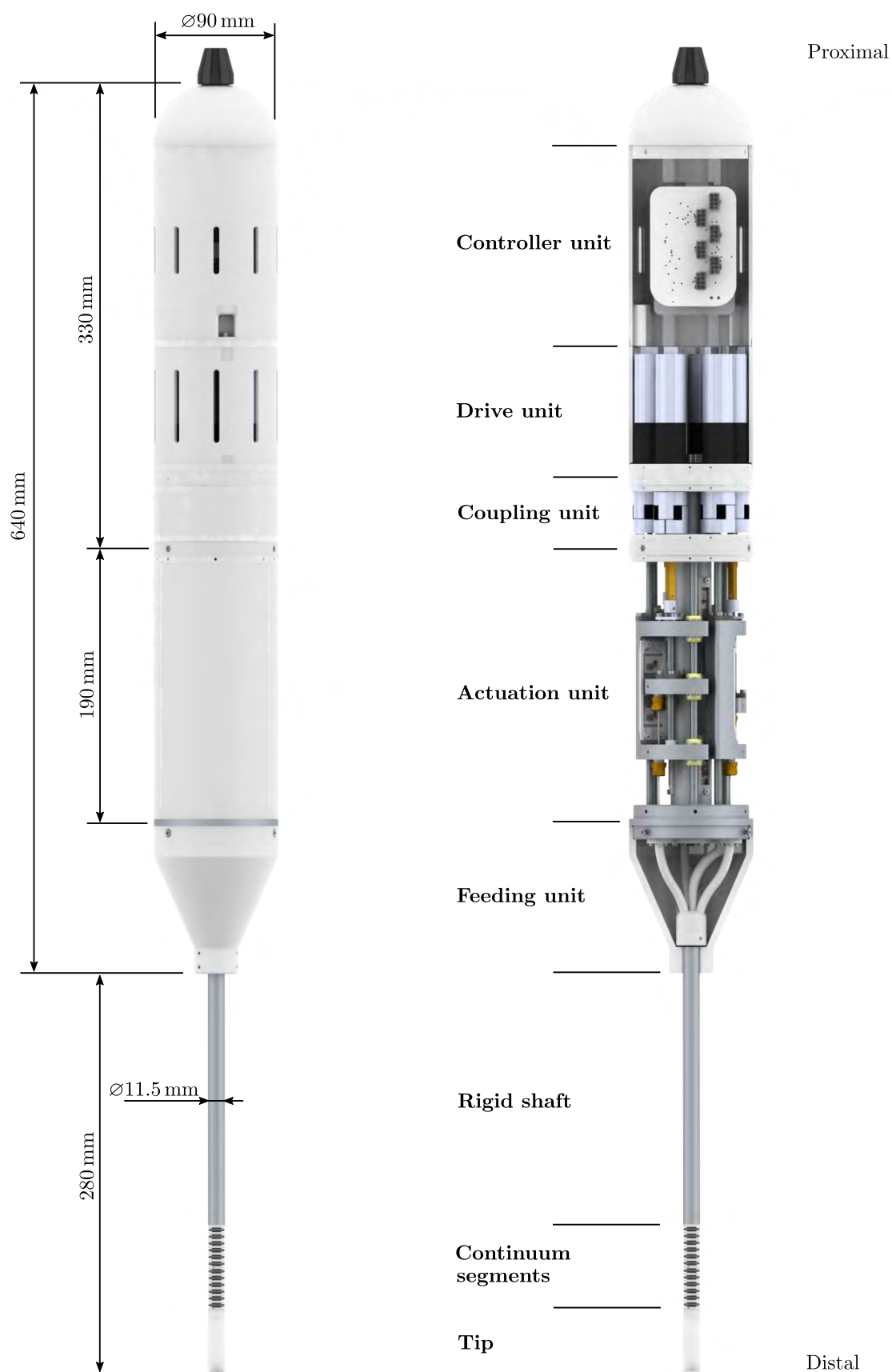
Fig. 4.17: CAD models of the proposed robotic prototype with (left) installation of housing components and (right) exposed electro-mechanical subunits. Directions are indicated with respect to the patient's body.
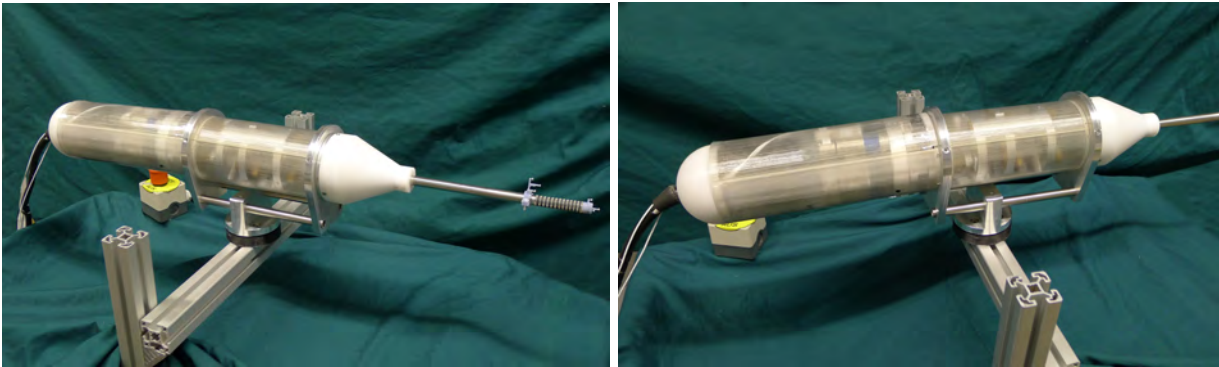
Fig. 4.18: Latest assembly of the robotic prototype mounted to a customised frame for deployment to bench experiments.

The remote actuation of the manipulator uses force transmission from the actuation unit to the continuum structure based on customised polyamide tubes (315-IV and 430-III.5, MicroLumen, Inc, Oldsmar, FL, USA). Tubes of the distal continuum segment show smaller diameters in comparison to the proximal segment. Pairs of tubes linked to individual LMU are guided concentrically to accommodate the cascaded joint space principle in each LMU. LMU carriers mount customised collets for tube clamping with circumferential force distribution to prevent the radial collapse of employed tubes. This reduces tubular friction between outer tube (outer diameter $\varnothing 1.29\,\mathrm{mm}$) and inner tube (outer diameter $\varnothing 0.99\,\mathrm{mm}$) and eliminates disturbances from displacement of the inner tube.

Position limits are indicated by customised sensors described in Section 4.3.4. Pairs of associated sensors were installed to all LMU axes to detect upper and lower position boundaries. Twelve sensors in total simultaneously monitor carrier displacements. Customised frames were applied for PCB mounting. Beyond that, pairs of NdFeB magnets (S-04-1.5-N, Webcraft GmbH, Gottmadingen, Germany) were attached to LMU carriers in proximity of PCB. Sensor positions were adjusted in the corresponding frame during initial setup to establish the full range of displacement for each carrier with prevention of physical component collision.

The LMUs are mechanically supported with a cylindrical spine connected to two facing flanges. The latter mount ball bearings (BB624, MISUMI Europe GmbH, Frankfurt am Main, Germany) to accomodate the LMU spindles. Rectangular slots were integrated to implement the wire routing between sensors and IRC. The prototype adapts design paradigm modularity as subunits can be independently assembled and tested. The most recent prototype is presented in Figure 4.19. Structural unit components, e.g. carriers, core, and flanges, were fabricated from alumina using a CAD-CAM workflow. Sensor mountings, frames, and utilities for cable management were fabricated with additive manufacturing (Object 500 Connex3, Stratasys, Eden Prairie, MN, USA).

An S-shaped feeding unit was implemented under consideration of dimensional constraints highlighted in Figure 4.12. As to suite design requirements, it was neccessary to space the three guidance channels (120° spacing) gradually away from the actuation unit to the instrument shaft.

(a)   (b)
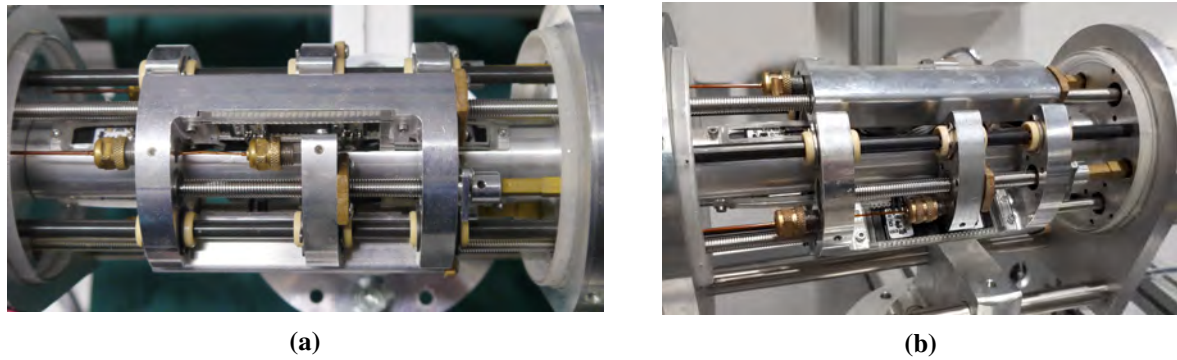
Fig. 4.19: Manufactured and assembled prototype of the robotic actuation unit.

The reduction was achieved within a length of $l_{\mathrm{TF}} < 70\,\mathrm{mm}$. The curved channels for actuation tube guidance in the feeding unit were fabricated with additive manufacturing (Object 500 Connex3, Stratasys, Eden Prairie, MN, USA). The resulting cavities were lined with braided polyamide tubes (590-IV.75, MicroLumen, Inc., Oldsmar, FL, USA) with an outer diameter of $\varnothing 1.76\,\mathrm{mm}$. This modification revealed a significant reduction of tubular friction in preliminary trials due to advantageous polyamide material pairing. The feeding unit is attached to the distal part of the actuation unit. Lastly, the instrument shaft is connected to the distal section and embedded apertures enable wiring for signal transmission to the IRC, electrical supply, and laser fibres.

4.5.2 Intracorporeal Section

The intracorporeal section gains access to the anatomy, which enables manipulation and mounts the multifunctional tip for endoscopic visualisation. A rigid instrument shaft is considered for the intended application and provides a stable base for the flexible manipulator. The installation of the fabricated continuum body was completed with attachment of six polyamide tubes to the distal part of both segments (see Figure 4.20c). The material pairing of photopolymer and polyamide requires bonding with cyanoacrylate adhesive (Loctite 406, Henkel Europe, Düsseldorf, Germany). Afterwards, signal and supply cables of the endoscopic tip were inserted into the lumen. Then,

(a)   (b)   (c)
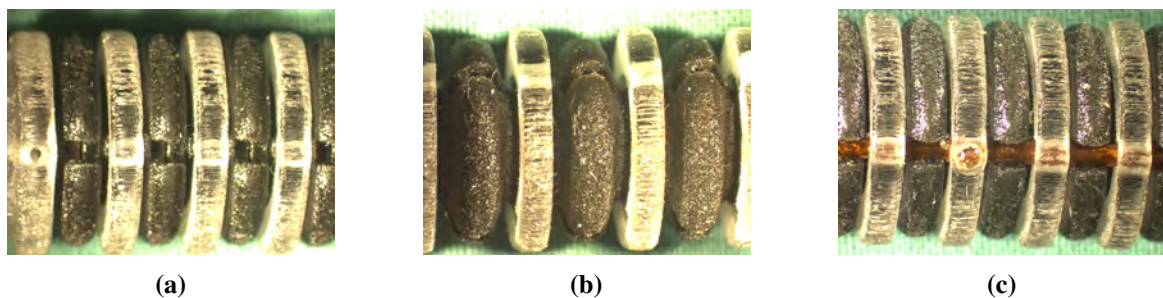
Fig. 4.20: Microscopic images of fabricated continuum manipulator ($10\times$ magnification): (a) compressed structure (b) slightly extended structure, and (c) structure with polyamide tube.

actuation tubes were fed into the corresponding guidance channels located in the rigid shaft and feeding unit. Proximal sections of actuation tubes were clamped to the matching carriers of the actuation unit. The physical assembly of the intracorporeal compartment in two different kinematic manipulator configurations is shown in Figure 4.21.

The fabrication of the endoscopic tip as discussed in Section 4.4 and shown in Figure 4.22 takes two steps. Firstly, the tip housing is fabricated with additive manufacturing analogously to previous Section 4.5.2. The housing is split into two parts to satisfy the design paradigm of modularity: 1) A distal cover shown in Figure 4.23a that mounts the camera sensors and the LED illumination, and 2) a proximal housing for accommodation of camera boards and laser optics described in Chapter 3. Two miniaturised CMOS cameras (MO-BS0804P, MISUMI Electronics Corp., Taiwan) with cylindrical housing (diameter of $4.5\,\mathrm{mm}$) were selected according to Section 4.4.1 and installed with horizontal and vertical convergences α_{h} and α_{v} computed in Section 4.4. This configuration is summarised in Figures 4.22b and 4.22c, respectively. Image sensors boast a horizontal and vertical FoV of $\phi_{\mathrm{h}} \approx 57°$ and $\phi_{\mathrm{v}} \approx 43°$. The working distance of imaging components is approximated to $20\,\mathrm{mm}$. Visual data is acquired at $25\,\mathrm{Hz}$ with image definition of $(720 \times 576)\,\mathrm{px}$. Two high power LED with outer diameters of $2.3\,\mathrm{mm}$ (Solidur® Mini LED, SCHOTT AG, Landshut, Germany) were selected for endoscopic illumination and installed adjacent to camera sensors for optimal scene coverage. Signal conditioning camera PCB and wires were installed to the proximal housing. Both components were joined and mounting of laser optics completed the assembly. The outer diameter of the tip yields $11.5\,\mathrm{mm}$. LED modules were connected to the driver board presented in Section 4.3.7 to enable PWM intensity modulation as depicted in Figure 4.23d.

4.5.3 Structural Manipulator Characterisation

The intracorporeal deployment imposes load conditions from soft tissue contact on the continuum manipulator. In this regard, the structural response of the manipulator assembly under external loads was analysed. This also concerns mechanical integrity and compliance of the monolithic

(a)   (b)
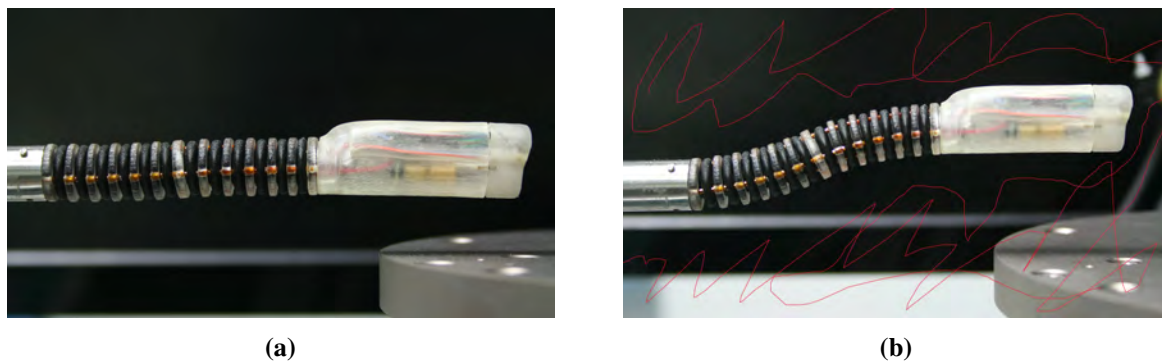
Fig. 4.21: Prototypic intracorporeal assembly composed of rigid shaft, continuum segments with $11.5\,\mathrm{mm}$ outer diameter, and endoscopic tip: (a) Straight and (b) deflected configuration.
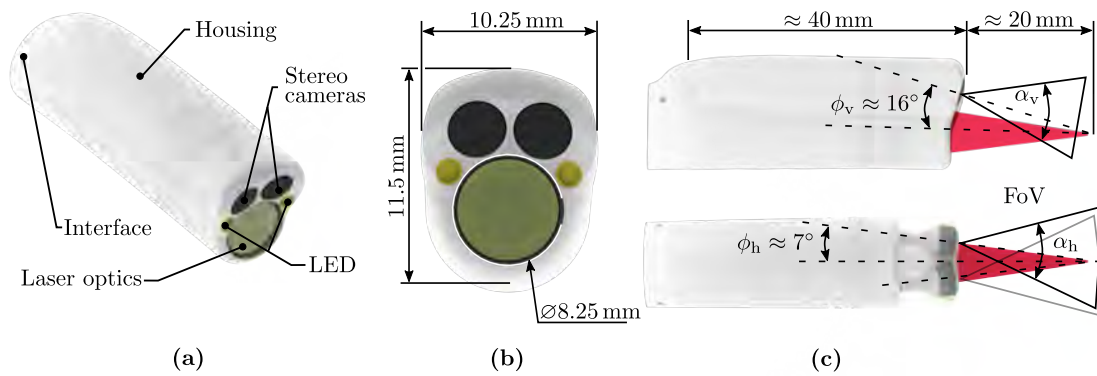
Fig. 4.22: CAD model of the endoscopic tip: (a) Isometric view (b) front view, and (c) lateral view with annotation of camera FoVs and orientation. Acronyms: Field of view (FoV) and light emitting diode (LED).
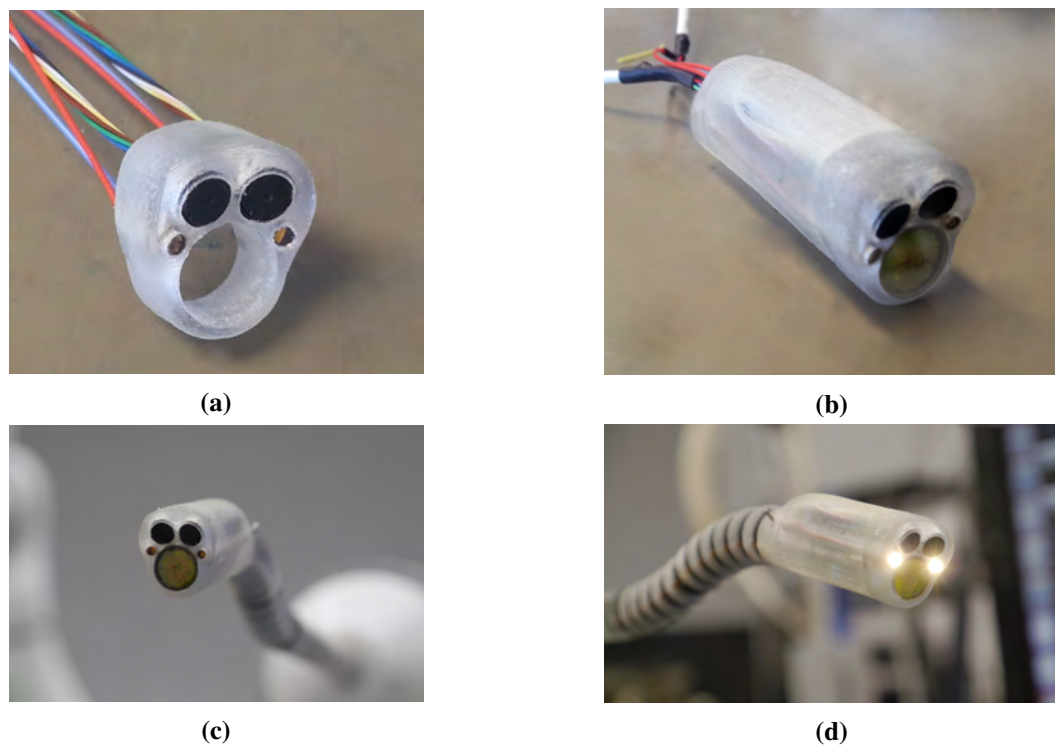
Fig. 4.23: Prototypic hardware of endoscopic tip: (a) Distal compartment with stereoscopic camera modules and high power LED and (b) assembly with focus unit and proximal compartment, (c) front view, (d) front view with activated endoscopic illumination.

body and its inherent capability of transmitting forces to enclosing soft tissue and manipulation stability.

The experimental study targeted the identification of load limits applicable to the monolithic body. These preliminary results may be taken into consideration for prospective design and material optimisation. From [BKLE11], it was hypothesised that the structure must withstand forces of at least $3\,\mathrm{N}$ to $5\,\mathrm{N}$ in axial and $1.5\,\mathrm{N}$ in lateral direction for safe application in clinical scenarios with tissue displacement. The methodology in this section adapts the characterisation workflow for soft manipulators in [RCG$^+$16].

The experimental setup considered the installation of fabricated manipulators to the actuation unit prototypes. This enabled clamping and manual displacement of embedded actuation tubes to adjust the kinematic configuration. Study trials comprised two different kinematic configurations (see Figures 4.24a and 4.24b), which are denoted *neutral* and *deflected*. Kinematic poses were set by manual displacement of the individual LMU stages. It was assumed that these configurations mimic clinical use cases. The *neutral* configuration targeted absence of structural elongation from the manufacturing length. By contrast, the manipulator was elongated by 40% in the *deflected* state and displaced by $10\,\mathrm{mm}$ in lateral direction.

Two unconstrained load scenarios were applied to continuum specimens which are labelled *axial* and *lateral*. The *axial* condition is demonstrated in Figure 4.24a and assumed a parallel alignment of z-axes between force sensor frame (CF)$_{\mathrm{FS}}$ and manipulator base frame (CF)$_{\mathrm{B}}$. Alternatively, condition *lateral* considered a perpendicular layout of force sensor and base (see Figure 4.24b). A spindle driven translation rig (one DoF) was automated using a stepper motor (1124090 NEMA17, Kysan Electronics, CA, USA) and equipped with a force sensor (Nano25, ATI Industrial Automation, Apex, NC, USA).

(a)   **(b)**
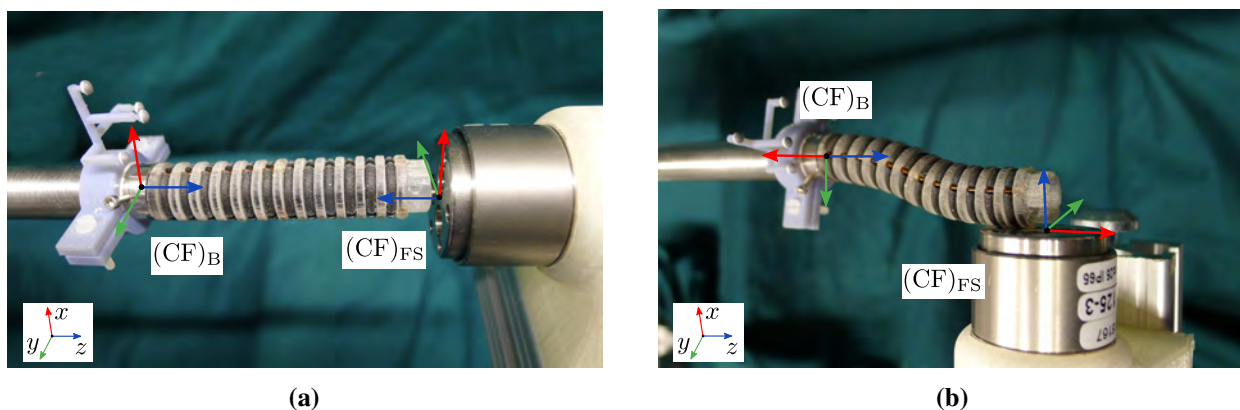
Fig. 4.24: Setup with manipulator and force sensor for experimental assessment of the continuum structure with unconstrained load conditions: (a) neutral manipulator configuration with axial load and (b) deflected manipulator configuration with lateral load.

This setup enables concurrent load of the continuum structure and measurements through stepwise sensor displacement. The sensor component was sequentially displaced in steps of $0.1\,\mathrm{mm}$ towards the continuum structure. Force measurements were synchronised to motor data. Sample acquisition was terminated after detection force discontinuities, i.e. rapidly decreasing forces. This transition indicates loss of clamping forces, mechanical fatigue, or damage of the polyamide tubing.

For each measurement, a new continuum sample was fabricated, assembled, installed to the unit, and set to *neutral* or *deflected* configuration. Subsequently, the structure was loaded in random order with *axial* or *lateral* condition. Eight measurements were conducted for each combination of configuration and load condition ($N = 32$).

Experimental results on structural performance are provided in Figure 4.25 and summarised to box plots of maximal loads in Figure 4.25b. An example of measured forces and displacements for a specific continuum specimen is demonstrated in Figure 4.25a. This data illustrates the structural response of the manipulator for *neutral* configuration and *axial* loading. Measured forces increased with successive advancement of the force sensor in physical contact with the continuum body. Once structural changes occur, e.g. due to release of friction from polyamide tubes or spacer disks, force amplitudes fluctuate. Fatigue or loss of clamping forces in the LMU was indicated by a sudden force decrease. This anomaly determined the maximum applicable structural load, i.e. experimental study metrics.

Forces (mean $\pm$ standard deviation) were consolidated from trials ($N = 32$). Forces of the *neutral* configuration yielded to $(4.3 \pm 0.24)\,\mathrm{N}$ for axial and $(1.56 \pm 0.17)\,\mathrm{N}$ for *lateral* loading directions, respectively. By analogy, forces of the extended configuration were $(4.1 \pm 0.3)\,\mathrm{N}$ for axial and $(1.26 \pm 0.2)\,\mathrm{N}$ for lateral load direction.

(a)	(b)
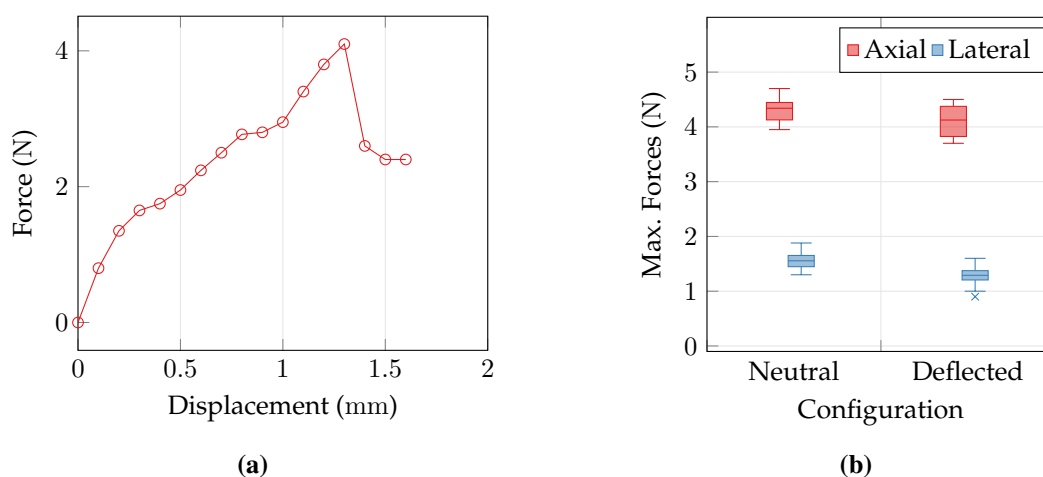
Fig. 4.25: Experimental results for static loading of continuum manipulators: (a) Example of measured forces over sensor displacement for neutral configuration with axial load and (b) box plots of maximal forces for each manipulator configuration and load direction. Boxes define 0.25 and 0.75-quantiles of input data. Upper and lower whisker span all data within 1.5 interquartile range of the nearer quartile.

Statistical analysis was applied to identify significant differences between groups associated to manipulator configurations *neutral* and *deflected*. The significance level was ($p < .05$). Distribution of residual normality was assessed for each consolidated experimental series, i.e. combination of configuration and loading condition, with Shapiro-Wilk tests ($p > .05$). There was no statistically significant difference of maximal *axial* forces between manipulator configurations ($t = 1.65, p = .059$). Contrarily, there was a statistically significant difference for *lateral* forces ($t = 3.57, p = .001$). In summary, the structural configuration impacted maximal lateral forces, i.e. the manipulator may bear lower loads in *deflected* compared to the *neutral* configuration. On the other hand, the structure may bear *axial* forces up to $4.5\,\mathrm{N}$ independently of the kinematic configuration.

The preliminary study demonstrates feasibility of the manipulator principle and its promising mechanical properties for clinical deployment. Findings are in the range of reported forces for safe tissue manipulation. In comparison to a soft robot with pneumatic actuation and a factor two scaled diameter [RCG$^+$16], measured forces for the hollow core continuum structure performed comparably. However, structural responses are dependent on the actual kinematic configuration and imposed load directions. This relation may cause significant load variations. These shortcomings must be addressed in future work with design and material modifications. Additionally, endurance and fatigue martial testing is required to determine long-term performances of additive material and adhesives. Design optimisation must address the clamping mechanism, alternative tubing materialsS, and additive manufacturing processes for multimaterial components. For example, selective laser melting demonstrated feasibility for flexible joints but is still limited with regard to miniaturisation [HZLY19].

4.6 Conclusion

This chapter presents the design and realisation workflow towards a novel extensible continuum robotic platform for endoscopic laser surgery. Platform fundamentals were derived from clinical and technical requirements for deployment in MIS. Applied methodologies considered paradigms and standards for mechatronic system design. The bottom-up workflow decomposed the system into sub-units. The latter constitute electro-mechanical features that individually contribute to high-level system objectives.

A novel extensible continuum manipulator with large inner lumen, a diameter of less than $12\,\mathrm{mm}$, and 5 DoF Cartesian dexterity is proposed to target shortcomings of recent work in non-contact laser delivery. The shape of the flexible sections was inspired by bellow elements. Structural optimisation was conducted with finite element analysis and consideration of hyperelastic material models. This improved sectional stress characteristics for enhanced flexibility and endurance from stress reduction. Optimised continuum bodies were transferred to monolithic multimaterial additive manufacturing. However, current limitations of the flexible prototypic structures concern layer separation induced by rare stress accumulation from large local strains in employed photopolymers.

Automation of remote 6 DoF joint space manipulation for the continuum structure using concentrically guided tubes was realised by a novel actuation unit. The latter is composed of three independent linear motions units. Each unit enables coordinated displacement of two cascaded DoF. Thanks to extensible shafts for torque transmission to cascaded carriers, electrical drives were located stationary. This prevents additional wire management and improves joint dynamics due to weight reduction. A tailored tube feeding unit realises a low friction transition of the tubular guidance from the actuation unit to the miniaturised extracorporeal section.

Furthermore, a highly-integrated endoscopic tip for non-contact laser surgery is presented. It integrates an optical module for beam reshaping (see Chapter 3), stereoscopic imaging sensors, and illumination. The sensor layout was determined from non-linear optimisation of camera poses. The corresponding cost function considered geometric constraints and particularly optimised independent parameters, e.g. camera sensor tilt and baseline.

Lastly, an experimental study on characterisation of manipulator loads was conducted. Assembled and installed continuum manipulators were loaded statically in two different kinematic configurations with external forces. It was demonstrated that manipulators bear loads of $4\,\mathrm{N}$ and $1.5\,\mathrm{N}$ for axial and lateral loading conditions, respectively. This enables stable manipulation under presence of robot-tissue interaction.

Future work specifically aims at miniaturisation of the actuation unit, enhanced joint state monitoring, and reduction of friction in tubular guidance channels. Deployment to different surgical interventions with tortuous access, e.g. gastric anatomy, may be approached with replacement of the rigid shaft by a passive flexible shaft. The proposed actuation unit already implements displacement compensation that must be taken into account for bending of passive shafts.

Beyond that, alternative manufacturing technologies must be exploited for continuum bodies to improve endurance and stress distributions. Multimaterial injection moulding may be considered. This can be accompanied by structural finite element analysis. More recent hyperelastic material models, e.g. customised formulations for photopolymers [BVPV11], and iterative topology optimisation can improve shape morphologies of flexible sections or enhanced material pairings [RBT14].

A dimensional reduction of a factor of two may be achieved for the actuation unit with advanced manufacturing, such as selective laser melting. Additionally, different joint state or limit sensing concepts may be investigated. As an example, sensor footprints may be reduced with optical sensors and intensity measurements of reflected light. Further performance improvement may target a shared communication bus for the IRC and drives, e.g. controlled area network (CAN). More recent technologies, e.g. dual core ESP32 boards (Espressif Systems Ltd, Shanghai, China) may replace the Beaglebone Black embedded board to provide real-time sensing and computing capabilities.

5 A Modular Toolkit for Modelling and Control of Extensible Continuum Robots

The preceding chapters have presented the concept, design, and hardware realisation of a novel extensible continuum robot. According to the mechatronic principle, the task space motion of the manipulator is realised by coordinated motion of six linear joints, which transmit the resulting displacement to the continuum bodies using a set of flexible actuation tubes. Hence, task space control demands for a kinematic framework that generates nominal joint space commands from task space input and further enables nominal tracking using control concepts. This chapter proposes a novel highly-integrated and holistic software framework for teleoperation and automation of extensible continuum robots. The framework adapts to the ROS middleware and realises dedicated software modules that are interconnected by the ROS network layers. This facilitates a system architecture with low and high level modules for kinematics, control, and visual computation. The modular architecture is deployed to three distributed host computers for safe and reliable data processing with optimal computational performance. This specifically addresses the following units: 1) kinematics and control, 2) visual acquisition and processing, as well as 3) low level actuator control and sensor monitoring. The distributed computers are physically linked by an Ethernet connection and fully embedded to the ROS architecture.

This chapter is outlined as follows. Primarily, kinematic fundamentals of the proposed robotic prototype are derived from geometric modelling of unisegmental extensible continuum bodies and their multisegmental composition. More specifically, this addresses space mappings, e.g. forward (direct), inverse, and differential kinematics, to compute nominal input for control algorithms and to estimate the spatial manipulator configurations from the current actuator states. This is complemented by strategies for joint limit avoidance to preserve the structural manipulator integrity. Furthermore, the design of the kinematic closed-loop controller is discussed.

Input to the kinematics module is captured from two sources. Firstly, teleoperation of the master device generates nominal operator input. More specifically, a haptic controller module generates nominal force input for the master device and records its kinematics data. This interface further enables online rendering of tailored 3D force feedback for operator assistance (see Chapter 6). Secondly, trajectories or via-points of nominal poses or velocities are precomputed. The framework also manages the timed transmission of commands to the low level actuator controller.

The kinematics framework is evaluated in an experimental setting using the proposed modules along with the robotic prototype presented in Chapter 4. The accuracy of the manipulator model is assessed in a comparative evaluation. The latter compares optical measurements acquired from

tracking of the physical manipulator and its corresponding simulation model. This is complemented by a discussion on user interfaces for endoscopic laser surgery. Methodologies and results of this chapter are partly published in [KSP$^+$19, KGS$^+$20]. The customised ROS software package *ExtCR* is publicly available in a *GitHub*[1] repository to promote dissemination to the scientific community.

5.1　Robot Kinematics and Control

This section is dedicated to concepts, description, and realisation of novel kinematics and control strategies for driving the proposed continuum robotic platform. At first, a unisegmental model for an extensible continuum manipulator is derived and extended to a multisegmental model by linking additional segments using multibody kinematics. Further on, kinematic constraints are described and incorporated to the kinematic model to prevent structural damage of the manipulator. Lastly, robotic and teleoperation control frameworks are presented.

5.1.1　Unisegmental Continuum Kinematics

The novel extensible continuum manipulator proposed in Chapter 4 is composed of two independent extensible continuum segments. In order to design the fundamental kinematics simulation and control framework tailored to the specific robot architecture, an unisegmental manipulator model, which takes the assumption of constant segmental curvature [RJWJ10] into account, is regarded. The approach presented in this thesis extends methodologies from constant-length designs in [SXK$^+$09, BDN$^+$13] to an extensible design. Hence, an analytical description is derived from geometric parameters assigned to the specific manipulator design. The schematics provided in Figures 5.1a and 5.1b outline relevant parameters of the refactored unisegmental model.

The full kinematic configuration of the unisegmental model is described by three different spaces. The joint space $\boldsymbol{q} = (q_1, q_2, q_3)^{\mathrm{T}} \in \mathbb{R}^3$ consists of the current set of actuation tube displacements. The corresponding configuration space $\boldsymbol{\psi} = (\theta, \delta, L)^{\mathrm{T}} \in \mathbb{R}^3$ is composed of three parameters describing the constant curvature bending with the segmental length L, the bending angle θ in the segmental bending plane π, and the corresponding angular deflection δ of plane π about the y-axis of the base frame. Additionally, bending radius R_{S} is given by the Euclidean distance between the origin of segmental base frame $(\mathrm{CF})_{\mathrm{B}}$ and the intersection between the x-axis of frame $(\mathrm{CF})_{\mathrm{E}}$ and the $x - y$ plane in frame $(\mathrm{CF})_{\mathrm{B}}$. The orthogonal projection of the origin in $(\mathrm{CF})_{\mathrm{E}}$ to the bending radius in $x - y$ plane in frame $(\mathrm{CF})_{\mathrm{B}}$ yields projected distance h_{S}. Finally, the Cartesian representation is given by end effector task space $\boldsymbol{x}_{\mathrm{E}} = (x, y, z, \alpha, \beta, \gamma)^{\mathrm{T}} \in \mathbb{R}^6$, composed of linear components x, y, and y as well as Euler angles α, β, and γ.

Primarily, the forward mapping $\boldsymbol{\psi} = f(\boldsymbol{q})$ from joint space to configuration space is derived from geometric considerations. According to proposed models for constant-length manipulators in

---

[1]https://github.com/deku-robotics/ExtCR

[SXK$^+$09, BDN$^+$13], the angle of the bending plane is computed from the joint space configuration to

$$\delta = \begin{cases} \frac{\pi}{4}, & \text{if } \varepsilon \leq 0.01 \\ \arctan\left(\sqrt{3}\frac{q_3-q_2}{q_3+q_2-2q_1}\right), & \text{otherwise} \end{cases}, \tag{5.1}$$

where $\varepsilon = \sqrt{(q_2-q_1)^2 + (q_3-q_2)^2 + (q_3-q_1)^2}$ defines the singularity threshold for a straight configuration of the manipulator ($q_1 \approx q_2 \approx q_3$). The corresponding bending angle is reported to

$$\theta = \begin{cases} 0, & \text{if } \varepsilon_\mathrm{B} \leq 0.01 \\ \frac{q_1+q_2-2q_3}{3r_\mathrm{S}\cos\left(\delta-\frac{4\pi}{3}\right)}, & \text{otherwise} \end{cases}, \tag{5.2}$$

where r_S is the radial distance between the centre of the continuum structure and the centre of embedded actuation tubes. The bending threshold ε_B indicates the transition to the singular manipulator configuration. Lastly, the segmental length of the manipulator is

$$L = L_0 + \frac{1}{3}\sum_{i=1}^{3} q_i, \tag{5.3}$$

where L_0 is the absolute length of the structure for the initial configuration. In the following, the forward mapping $\boldsymbol{x} = g(\boldsymbol{\psi})$ between configuration space and task space is presented. The bending radius of the segment is $R_\mathrm{S} = L/\theta$ and auxiliary distance $h_\mathrm{S} = R_\mathrm{S}\cos(\theta)$. Under consideration of
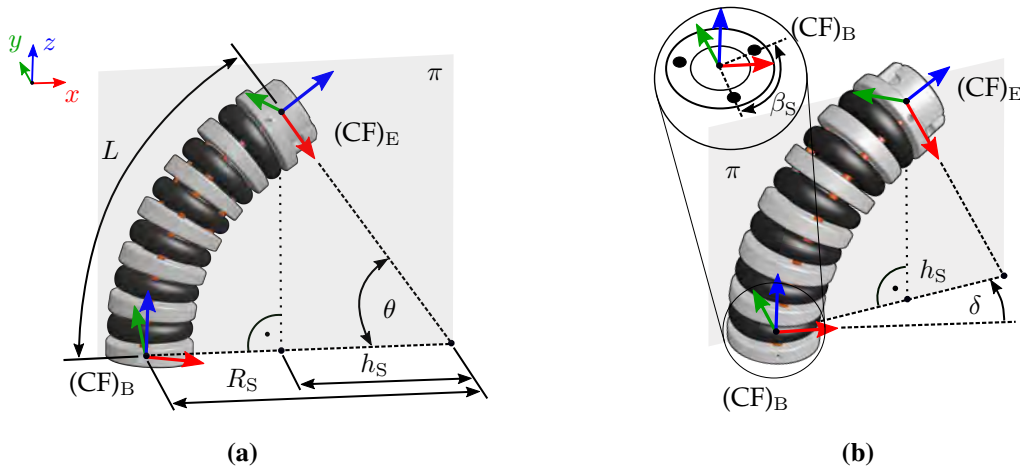
Fig. 5.1: Schematics of unisegmental continuum manipulator kinematics with assumption of constant curvature bending: (a) Right view of segment with length L and segmental bending angle θ in bending plane π. (b) Isometric view of segment and rotation of bending plane π with angle δ. The magnified section describes the configuration of the actuation tube layout. Auxiliary parameters describe the bending radius R_S and projected distance h_S.

derived trigonometry and parameters, the position of the segmental end effector $(\text{CF})_\text{E}$ in reference to frame $(\text{CF})_\text{B}$ yields

$$_{(\text{B})}\boldsymbol{P}_\text{E} = \begin{cases} \begin{bmatrix} 0 \\ 0 \\ L \end{bmatrix}, & \text{if } |\theta| \leq \varepsilon_\text{B} \leq 0.01 \\[2em] \begin{bmatrix} \cos(\delta)(1 - \cos(\theta))\frac{L}{\theta} \\ \sin(\delta)(1 - \cos(\theta))\frac{L}{\theta} \\ \sin(\theta)\frac{L}{\theta} \end{bmatrix}, & \text{otherwise} \end{cases} \in \mathbb{R}^3. \tag{5.4}$$

The orientation of the end effector frame is obtained from chaining the elemental rotations about the y and z axes of the fixed frame :

$$^\text{B}\boldsymbol{R}_\text{E} = \boldsymbol{R}_z(\delta)\boldsymbol{R}_y(\theta)\boldsymbol{R}_z(-\delta) \in \text{SO}(3). \tag{5.5}$$

The segmental pose is composed of position and orientation in homogeneous representation:

$$^\text{B}\boldsymbol{T}_\text{E} = \begin{bmatrix} ^\text{B}\boldsymbol{R}_\text{E} & _{(\text{B})}\boldsymbol{P}_\text{E} \\ \boldsymbol{0} & 1 \end{bmatrix} \in \text{SE}(3). \tag{5.6}$$

This finally features the forward kinematic mapping from joint to task space $\boldsymbol{x} = h(\boldsymbol{q}) = g(f(\boldsymbol{q}))$. The *inverse kinematic* mapping $\boldsymbol{q} = f^{-1}(\boldsymbol{\psi})$ from configuration to joint space is constituted from the manipulator geometry and extended to extensible continuum bodies:

$$q_i = -r_\text{S}\cos(\delta - (i-1)\beta_\text{S})\theta + (L - L_0), \tag{5.7}$$

where index $i = \{1,2,3\}$ and the actuation tube spacing is $\beta_\text{S} = \frac{2}{3}\pi$. The robotic control framework further demands for the *inverse differential kinematics* of the extensible continuum segment for computation of nominal actuator velocities, i.e. linear joint space velocities $\dot{\boldsymbol{q}}$, for a given task space input. The time derivative of inverse mapping $\boldsymbol{q} = g^{-1}(\boldsymbol{\psi})$ is as follows:

$$\dot{\boldsymbol{q}} = \boldsymbol{J}_{q\psi}(\boldsymbol{\psi})\dot{\boldsymbol{\psi}} \in \mathbb{R}^3, \tag{5.8}$$

where $\boldsymbol{J}_{q\psi}(\boldsymbol{\psi}) \in \mathbb{R}^{3\times3}$ denotes the corresponding Jacobian for configuration space $\boldsymbol{\psi}$. Equivalently, the time derivative of forward kinematic mapping $\boldsymbol{x} = f(\boldsymbol{\psi})$ is

$$\dot{\boldsymbol{x}} = \boldsymbol{J}_{x\psi}(\boldsymbol{\psi})\dot{\boldsymbol{\psi}} \in \mathbb{R}^6, \tag{5.9}$$

where $\boldsymbol{J}_{x\psi}(\boldsymbol{\psi}) \in \mathbb{R}^{6\times3}$ is the associated Jacobian for configuration space ψ. Reporting the inverse of Equation (5.9) into Equation (5.8) yields the desired temporal space mapping

$$\dot{\boldsymbol{q}} = \boldsymbol{J}_{q\psi}(\boldsymbol{\psi})\boldsymbol{J}_{x\psi}^{-1}(\boldsymbol{\psi})\dot{\boldsymbol{x}}. \tag{5.10}$$

More precisely, the partial derivative of inverse mapping $\boldsymbol{q} = g^{-1}(\boldsymbol{\psi})$ provides Jacobian

$$\boldsymbol{J}_{q\psi}(\boldsymbol{\psi}) = \frac{\partial \boldsymbol{q}}{\partial \boldsymbol{\psi}} = \begin{bmatrix} \frac{\partial q_1}{\partial \theta} & \frac{\partial q_1}{\partial \delta} & \frac{\partial q_1}{\partial L} \\ \frac{\partial q_2}{\partial \theta} & \frac{\partial q_2}{\partial \delta} & \frac{\partial q_2}{\partial L} \\ \frac{\partial q_3}{\partial \theta} & \frac{\partial q_3}{\partial \delta} & \frac{\partial q_3}{\partial L} \end{bmatrix} \in \mathbb{R}^{3\times3} \tag{5.11}$$

with matrix elements related to variations of the bending angle

$$\frac{\partial q_i}{\partial \theta} = -r_{\mathrm{S}} \cos\left(\delta - (i-1)\beta_{\mathrm{S}}\right), \tag{5.12}$$

related to variation of the bending plane angle

$$\frac{\partial q_i}{\partial \delta} = r_{\mathrm{S}} \sin\left(\delta - (i-1)\beta_{\mathrm{S}}\right)\theta, \tag{5.13}$$

and to variations of the segmental length

$$\frac{\partial q_i}{\partial L} = 1, \tag{5.14}$$

where index $i = \{1,2,3\}$ and the reformulation of Equation (5.7) applies the product rule. Analogously, the partial derivative of mapping $\boldsymbol{x} = f(\boldsymbol{\psi})$ yields Jacobian

$$\boldsymbol{J}_{x\psi}(\boldsymbol{\psi}) = \frac{\partial \boldsymbol{x}}{\partial \boldsymbol{\psi}} = \begin{bmatrix} \boldsymbol{J}_{x\psi,\mathrm{l}}(\boldsymbol{\psi}) \\ \boldsymbol{J}_{x\psi,\mathrm{a}}(\boldsymbol{\psi}) \end{bmatrix} \tag{5.15}$$

with linear contribution

$$\boldsymbol{J}_{x\psi,\mathrm{l}}(\boldsymbol{\psi}) = \begin{bmatrix} \frac{\partial x}{\partial \theta} & \frac{\partial x}{\partial \delta} & \frac{\partial x}{\partial L} \\ \frac{\partial y}{\partial \theta} & \frac{\partial y}{\partial \delta} & \frac{\partial y}{\partial L} \\ \frac{\partial z}{\partial \theta} & \frac{\partial z}{\partial \delta} & \frac{\partial z}{\partial L} \end{bmatrix} \in \mathbb{R}^{3\times3} \tag{5.16}$$

and angular contribution

$$\boldsymbol{J}_{x\psi,\mathrm{a}}(\boldsymbol{\psi}) = \begin{bmatrix} \frac{\partial \alpha}{\partial \theta} & \frac{\partial \alpha}{\partial \delta} & \frac{\partial \alpha}{\partial L} \\ \frac{\partial \beta}{\partial \theta} & \frac{\partial \beta}{\partial \delta} & \frac{\partial \beta}{\partial L} \\ \frac{\partial \gamma}{\partial \theta} & \frac{\partial \gamma}{\partial \delta} & \frac{\partial \gamma}{\partial L} \end{bmatrix} \in \mathbb{R}^{3\times3}. \tag{5.17}$$

The partial derivatives in Equation (5.4), which constitute the linear Jacobian $\boldsymbol{J}_{x\psi,\mathrm{l}}(\boldsymbol{\psi})$ with respect to variations of the bending angle θ, are:

$$\frac{\partial x}{\partial \theta} = \frac{L}{\theta^2} \cos(\delta) \left(\sin(\theta)\theta + \cos(\theta) - 1 \right), \tag{5.18}$$

$$\frac{\partial y}{\partial \theta} = \frac{L}{\theta^2} \sin(\delta) \left(\sin(\theta)\theta + \cos(\theta) - 1 \right), \tag{5.19}$$

and

$$\frac{\partial z}{\partial \theta} = \frac{L}{\theta^2} \left(\cos(\theta)\theta - \sin(\theta) \right). \tag{5.20}$$

Considering variations of the bending plane angle δ, the partial derivatives of Equation (5.4) yield

$$\frac{\partial x}{\partial \delta} = -\frac{L}{\theta} \sin(\delta) \left(1 - \cos(\theta) \right), \tag{5.21}$$

$$\frac{\partial y}{\partial \delta} = \frac{L}{\theta} \cos(\delta) \left(1 - \cos(\theta) \right), \tag{5.22}$$

and

$$\frac{\partial z}{\partial \delta} = 0. \tag{5.23}$$

Finally, the variations of the segmental length L applied to Equation (5.4) are:

$$\frac{\partial x}{\partial L} = -\frac{\cos(\delta)}{\theta} \left(1 - \cos(\theta) \right), \tag{5.24}$$

$$\frac{\partial y}{\partial L} = -\frac{\sin(\delta)}{\theta} \left(1 - \cos(\theta) \right), \tag{5.25}$$

and

$$\frac{\partial z}{\partial L} = \frac{\sin(\theta)}{\theta}. \tag{5.26}$$

In contrast, the angular Jacobian $\boldsymbol{J}_{x\psi,\mathrm{a}}(\boldsymbol{\psi})$ is reported from angular velocities of the specific kinematic design. By definition, $_{(\mathrm{B})}\boldsymbol{\omega}_{\mathrm{E}} \in \mathbb{R}^3$ are the angular velocities of $(\mathrm{CF})_{\mathrm{E}}$ with respect to frame $(\mathrm{CF})_{\mathrm{B}}$. Hence, $\left\| _{(\mathrm{B})}\boldsymbol{\omega}_{\mathrm{E}} \right\|_2$ defines the angular rate and $_{(\mathrm{B})}\boldsymbol{\omega}_{\mathrm{E}} / \left\| _{(\mathrm{B})}\boldsymbol{\omega}_{\mathrm{E}} \right\|_2$ describes the angular motion axis. Using the segmental orientation (see Equation (5.5)), the angular velocities of frame $(\mathrm{CF})_{\mathrm{E}}$ for an unisegmental continuum robot are given as follows:

$$_{(\mathrm{B})}\boldsymbol{\omega}_{\mathrm{E}} = \begin{bmatrix} _{(\mathrm{B})}\omega_{\mathrm{E},x} \\ _{(\mathrm{B})}\omega_{\mathrm{E},y} \\ _{(\mathrm{B})}\omega_{\mathrm{E},z} \end{bmatrix} = \begin{bmatrix} \dot{\alpha} \\ \dot{\beta} \\ \dot{\gamma} \end{bmatrix} = \begin{bmatrix} 0 \\ 0 \\ \dot{\delta} \end{bmatrix} + \boldsymbol{R}_z(\delta) \begin{bmatrix} 0 \\ \dot{\theta} \\ 0 \end{bmatrix} + \boldsymbol{R}_z(\delta)\boldsymbol{R}_y(\theta) \begin{bmatrix} 0 \\ 0 \\ -\dot{\delta} \end{bmatrix} \tag{5.27}$$

$$= \begin{bmatrix} -\cos(\delta)\sin(\theta)\dot{\delta} \\ -\sin(\delta)\sin(\theta)\dot{\delta} + \cos(\delta)\dot{\theta} \\ (1 - \cos(\theta))\dot{\delta} \end{bmatrix} = \underbrace{\begin{bmatrix} -\sin(\delta) & -\cos(\delta)\sin(\theta) & 0 \\ \cos(\delta) & -\sin(\delta)\sin(\theta) & 0 \\ 0 & (1 - \cos(\theta)) & 0 \end{bmatrix}}_{\boldsymbol{J}_{x\psi,\mathrm{a}}(\boldsymbol{\psi})} \underbrace{\begin{bmatrix} \dot{\theta} \\ \dot{\delta} \\ \dot{L} \end{bmatrix}}_{\dot{\boldsymbol{\psi}}}. \tag{5.28}$$

5.1.2 Extension to a Multisegmental Kinematic Model

The prototype of the novel continuum robot presented in Chapter 4 consists of two extensible continuum segments with similar structural composition. The analytical model of each unisegmental continuum body has been derived geometrically in the previous section to provide forward and inverse kinematic mapping for each individual segment. In order to derive the full kinematic model of the manipulator composition, the unisegmental models must be linked kinematically to meet design and structural constraints, such as stacked segmental alignment.

Formally, the forward kinematics of the end effector frame $(CF)_E$ with reference to base frame $(CF)_B$ for a continuum robot composed of N_S segments is given analogously to the DENAVIT-HARDENBERG notation of serial robots by the product of homogeneous transformations of each particular segment [JW06]:

$$^B\boldsymbol{T}_E = \prod_{k=1}^{N_S} {}^{k-1}\boldsymbol{T}_k, \tag{5.29}$$

where homogeneous transformation $^{k-1}\boldsymbol{T}_k$ is in general computed according to Section 1.2.3 and given for extensible continuum segments in Equation (5.6) with $k \in \{1, \dots, N_S\}$. The angular components are represented by dual quaternions [GW15].

The general instantaneous end effector kinematics of a manipulator with N_S segments is defined by

$$_{(B)}\dot{\boldsymbol{x}}_E = \begin{pmatrix} {}_{(B)}\dot{\boldsymbol{r}}_E \\ {}_{(B)}\boldsymbol{\omega}_E \end{pmatrix} \in \mathbb{R}^6, \tag{5.30}$$

where $_{(B)}\dot{\boldsymbol{r}}_E \in \mathbb{R}^3$ are the linear velocities and $_{(B)}\boldsymbol{\omega}_E \in \mathbb{R}^3$ constitute the corresponding angular rates of frame $(CF)_E$ in frame $(CF)_B$. Those components can be generically derived from multibody kinematics and dynamics as presented in [Cra05]. More specifically, the linear velocities yield

$$\begin{aligned} _{(B)}\dot{\boldsymbol{r}}_E = &\sum_{j=0}^{N_S-1} \left[\left(\prod_{i=0}^{j} \boldsymbol{A}_i \right) {}_{(j)}\dot{\boldsymbol{r}}_{j+1} \right] \\ &+ \sum_{j=0}^{N_S-1} \left[\left(\prod_{i=0}^{j} \boldsymbol{A}_i \right) {}_{(j)}\boldsymbol{\omega}_{j+1} \times \left(\prod_{i=0}^{j+1} \boldsymbol{A}_i \right) {}_{(j+1)}\boldsymbol{r}_{j+2} \right] \end{aligned} \tag{5.31}$$

with matrix

$$\boldsymbol{A}_i = \begin{cases} \boldsymbol{I}, & \text{if}\quad i = 0 \\ {}^{i-1}\boldsymbol{R}_i, & \text{otherwise} \end{cases} \in \mathbb{R}^{3\times3}, \tag{5.32}$$

where $(\mathrm{CF})_\mathrm{B}$ and $(\mathrm{CF})_\mathrm{E}$ are equivalent to numerical frame labelling $(\mathrm{CF})_0$ and $(\mathrm{CF})_{N_\mathrm{S}}$, respectively. This approach describes generic multibody systems composed of N_S bodies with $N_\mathrm{S}+1$ resulting reference frames.

Angular rates of the end effector frame with respect to base frame $(\mathrm{CF})_\mathrm{B}$ are analogously computed by

$$_{(\mathrm{B})}\boldsymbol{\omega}_\mathrm{E} = \sum_{j=0}^{N_\mathrm{S}-1} \left[\left(\prod_{i=0}^{j} \boldsymbol{A}_i \right)_{(j)}\boldsymbol{\omega}_{j+1} \right]. \tag{5.33}$$

For the of sake of completeness, the reader is kindly referred to related literature in the field of multibody systems.

In the following paragraphs, the derivation of a tailored analytical model is specifically discussed for the design of the robotic prototype (see Figure 5.2) which is composed of two stacked extensible continuum segments ($N_\mathrm{S} = 2$). This simplifies generic instantaneous kinematics in Equations (5.31) and (5.33) to

$$_{(\mathrm{B})}\dot{\boldsymbol{x}}_\mathrm{E} = {}_{(0)}\dot{\boldsymbol{x}}_2 = \begin{pmatrix} {}_{(0)}\dot{\boldsymbol{r}}_2 \\ {}_{(0)}\boldsymbol{\omega}_2 \end{pmatrix} = \begin{pmatrix} {}_{(0)}\dot{\boldsymbol{r}}_1 + {}^0\boldsymbol{R}_{1(1)}\dot{\boldsymbol{r}}_2 + {}_{(0)}\boldsymbol{\omega}_1 \times {}^0\boldsymbol{R}_{1(1)}\boldsymbol{r}_2 \\ {}_{(0)}\boldsymbol{\omega}_1 + {}^0\boldsymbol{R}_{1(1)}\boldsymbol{\omega}_2 \end{pmatrix}, \tag{5.34}$$

where the frame notation is equivalent to the previous definition and disregarded references are intermediate frames, such as frame $(\mathrm{CF})_1$.

For the sake of clarity, skew-symmetric matrices are introduced to transform the cross product of angular velocities and directional vector into a matrix product. Hence, the cross product of two
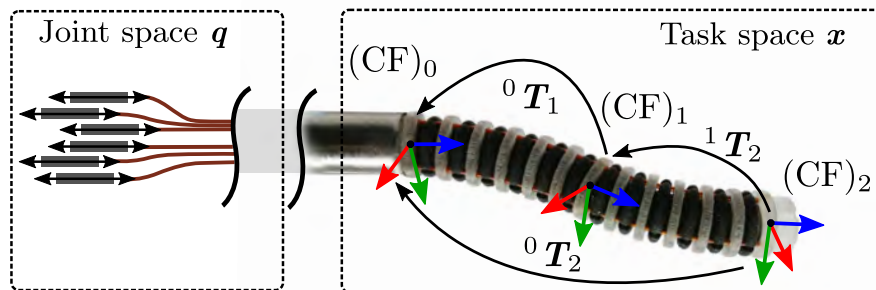
Fig. 5.2: Description of the kinematics annotation, involved spaces, and spatial transformations of the proposed multisegmental manipulator design.

arbitrary vectors $\boldsymbol{a} \in \mathbb{R}^3$ and $\boldsymbol{b} \in \mathbb{R}^3$ can be described by a skew-symmetric matrix multiplication (anticommutativity):

$$\boldsymbol{b} \times \boldsymbol{a} = [-\boldsymbol{a}]_\times \cdot \boldsymbol{b} = \begin{pmatrix} 0 & -a_3 & a_2 \\ a_3 & 0 & -a_1 \\ -a_2 & a_1 & 0 \end{pmatrix} \boldsymbol{b}, \tag{5.35}$$

where $\boldsymbol{a} \in \mathbb{R}^3$ is the skew vector and operator $[\cdot]_\times$ denotes the skew-symmetric mapping.

Considering the unisegmental model in Section 5.1.1, the instantaneous kinematics of continuum segments are defined independently in the configuration space with segment-specific Jacobian mappings:

$$_{(0)}\dot{\boldsymbol{x}}_1 = \begin{pmatrix} _{(0)}\dot{\boldsymbol{r}}_1 \\ _{(0)}\boldsymbol{\omega}_1 \end{pmatrix} = \begin{pmatrix} \boldsymbol{J}_{x\psi,\mathrm{l}}(\boldsymbol{\psi}_1)\dot{\boldsymbol{\psi}}_1 \\ \boldsymbol{J}_{x\psi,\mathrm{a}}(\boldsymbol{\psi}_1)\dot{\boldsymbol{\psi}}_1 \end{pmatrix} \tag{5.36}$$

and

$$_{(1)}\dot{\boldsymbol{x}}_2 = \begin{pmatrix} _{(1)}\dot{\boldsymbol{r}}_2 \\ _{(1)}\boldsymbol{\omega}_2 \end{pmatrix} = \begin{pmatrix} \boldsymbol{J}_{x\psi,\mathrm{l}}(\boldsymbol{\psi}_2)\dot{\boldsymbol{\psi}}_2 \\ \boldsymbol{J}_{x\psi,\mathrm{a}}(\boldsymbol{\psi}_2)\dot{\boldsymbol{\psi}}_2 \end{pmatrix}. \tag{5.37}$$

The individual segments are linked kinematically by reporting components of Equations (5.36) and (5.37) into Equation (5.34) and applying further algebraic simplification of Equation (5.34):

$$\begin{aligned}
_{(\mathrm{B})}\dot{\boldsymbol{x}}_\mathrm{E} = {}_{(0)}\dot{\boldsymbol{x}}_2 &= \begin{pmatrix} _{(0)}\dot{\boldsymbol{r}}_2 \\ _{(0)}\boldsymbol{\omega}_2 \end{pmatrix} \\
&= \begin{pmatrix} \boldsymbol{J}_{x\psi,\mathrm{l}}(\boldsymbol{\psi}_1)\dot{\boldsymbol{\psi}}_1 + \left({}^0\boldsymbol{R}_{1\,(1)}\boldsymbol{r}_2\right) \times \boldsymbol{J}_{x\psi,\mathrm{a}}(\boldsymbol{\psi}_1)\dot{\boldsymbol{\psi}}_1 + {}^0\boldsymbol{R}_1 \boldsymbol{J}_{x\psi,\mathrm{l}}(\boldsymbol{\psi}_2)\dot{\boldsymbol{\psi}}_2 \\ \boldsymbol{J}_{x\psi,\mathrm{a}}(\boldsymbol{\psi}_1)\dot{\boldsymbol{\psi}}_1 + {}^0\boldsymbol{R}_1 \boldsymbol{J}_{x\psi,\mathrm{a}}(\boldsymbol{\psi}_2)\dot{\boldsymbol{\psi}}_2 \end{pmatrix} \\
&= \left(\begin{bmatrix} \boldsymbol{I} & [-{}^0\boldsymbol{R}_{1\,(1)}\boldsymbol{r}_2]_\times \\ \boldsymbol{0} & \boldsymbol{I} \end{bmatrix} \boldsymbol{J}_{x\psi}(\boldsymbol{\psi}_1) \quad \begin{bmatrix} {}^0\boldsymbol{R}_1 & \boldsymbol{0} \\ \boldsymbol{0} & {}^0\boldsymbol{R}_1 \end{bmatrix} \boldsymbol{J}_{x\psi}(\boldsymbol{\psi}_2) \right) \begin{pmatrix} \dot{\boldsymbol{\psi}}_1 \\ \dot{\boldsymbol{\psi}}_2 \end{pmatrix} \\
&= \begin{pmatrix} \boldsymbol{B}_1 \boldsymbol{J}_{x\psi}(\boldsymbol{\psi}_1) & \boldsymbol{B}_2 \boldsymbol{J}_{x\psi}(\boldsymbol{\psi}_2) \end{pmatrix} \begin{pmatrix} \dot{\boldsymbol{\psi}}_1 \\ \dot{\boldsymbol{\psi}}_2 \end{pmatrix} \\
&= \underbrace{\begin{pmatrix} \boldsymbol{B}_1 \boldsymbol{J}_{x\psi}(\boldsymbol{\psi}_1) & \boldsymbol{B}_2 \boldsymbol{J}_{x\psi}(\boldsymbol{\psi}_2) \end{pmatrix}}_{\boldsymbol{J}^*_{x\psi}(\boldsymbol{\psi}^\star)} \dot{\boldsymbol{\psi}}^\star
\end{aligned} \tag{5.38}$$

with

$$\boldsymbol{B}_1 = \begin{pmatrix} \boldsymbol{I} & [-{}^0\boldsymbol{R}_{1\,(1)}\boldsymbol{r}_2]_\times \\ \boldsymbol{0} & \boldsymbol{I} \end{pmatrix} \qquad \boldsymbol{B}_2 = \begin{pmatrix} {}^0\boldsymbol{R}_1 & \boldsymbol{0} \\ \boldsymbol{0} & {}^0\boldsymbol{R}_1 \end{pmatrix}, \tag{5.39}$$

where matrices $\boldsymbol{I} \in \mathrm{SO}(3)$, $\boldsymbol{B}_1 \in \mathbb{R}^{6\times6}$ and $\boldsymbol{B}_2 \in \mathbb{R}^{6\times6}$ contain the geometric intersegmental kinematic coupling, and $\boldsymbol{J}^*_{x\psi}(\boldsymbol{\psi}^*)$ is the composed Jacobian of the complete robotic manipulator. The corresponding configuration space and its time derivative are given by $\boldsymbol{\psi}^\star = (\boldsymbol{\psi}_1, \boldsymbol{\psi}_2)^\mathrm{T} \in \mathbb{R}^6$ and $\dot{\boldsymbol{\psi}}^\star = \left(\dot{\boldsymbol{\psi}}_1, \dot{\boldsymbol{\psi}}_2\right)^\mathrm{T} \in \mathbb{R}^6$, respectively. Solving Equation (5.38) for the joint space velocities and applying the segmental Jacobian mappings (see Equation (5.11)), the resulting expression

constitutes the primary kinematic task objective with full instantaneous mapping from task to joint space:

$$\dot{\boldsymbol{q}}_{\mathrm{P}} = \underbrace{\boldsymbol{J}_{q\psi}^{\star}(\boldsymbol{\psi}^{\star})\boldsymbol{J}_{x\psi}^{\star-1}(\boldsymbol{\psi}^{\star})}_{\boldsymbol{J}_{qx}^{\star}(\boldsymbol{\psi}^{\star})}\,\dot{\boldsymbol{x}}_{\mathrm{E}} \in \mathbb{R}^6 \qquad (5.40)$$

with

$$\boldsymbol{J}_{q\psi}^{\star}(\boldsymbol{\psi}^{\star}) = \begin{pmatrix} \boldsymbol{J}_{q\psi}(\boldsymbol{\psi}_1) & \boldsymbol{0} \\ \boldsymbol{0} & \boldsymbol{J}_{q\psi}(\boldsymbol{\psi}_2) \end{pmatrix} \in \mathbb{R}^{6\times 6}, \qquad (5.41)$$

where $\boldsymbol{0} \in \mathbb{R}^{3\times 3}$ is the null matrix and $\boldsymbol{J}_{q\psi}$ is the segmental Jacobian for mapping the configuration space to the joint space.

5.1.3 Additional Kinematic Constraints

Reaching the nominal end effector pose is considered to be the primary task objective in robotic manipulation. However, additional task constraints have been proposed in related work for safe execution of complex motion envelopes involving the full kinematic assembly. This not only regards the device deployment to challenging environments and conditions but also obstacle recognition in path planning, joint velocity limits, dexterity measures, or avoidance of specific robotic configurations, e.g. in [TD95, AC03, DAHH06]. Those kinematic constraints are incorporated to the primary kinematic task by secondary task formulations. This assumption generally reports the composed joint velocities of the robotic prototype to

$$\dot{\boldsymbol{q}} = \dot{\boldsymbol{q}}_{\mathrm{P}} + \dot{\boldsymbol{q}}_{\mathrm{S}} \in \mathbb{R}^6, \qquad (5.42)$$

where $\dot{\boldsymbol{q}}_{\mathrm{P}}$ and $\dot{\boldsymbol{q}}_{\mathrm{S}}$ are the joint space velocities related to the primary and secondary tasks. This assumption can be similarly expressed in the manipulator configuration space

$$\dot{\boldsymbol{\psi}} = \dot{\boldsymbol{\psi}}_{\mathrm{P}} + \dot{\boldsymbol{\psi}}_{\mathrm{S}} \in \mathbb{R}^6, \qquad (5.43)$$

where $\dot{\boldsymbol{\psi}}_{\mathrm{P}}$ and $\dot{\boldsymbol{\psi}}_{\mathrm{S}}$ are the configuration space velocities with respect to primary or secondary task contributions.

In this thesis, the secondary task targets assertion of structural manipulator integrity. This addresses mapping of design limits, e.g. the minimum and maximum length of each continuum segment and its corresponding bending angle limitation, to the kernel of the primary task. The consideration of further constraints at the joint level of the actuation unit is disregarded due to continuous hardware monitoring using sensor data (see Section 4.3.4). This prevents physical contacts. The secondary task addresses a novel approach for structural manipulator safety on segmental level, i.e. limits of the individual segmental configuration space are monitored and avoided.

The proposed methodology applies approaches from related work on joint limit avoidance for revolute joints in industrial robotics [MC10] to the configuration space of continuum manipu-

lators. This enables a model-based protection of the segmental structure. Taking the minimal set of configuration space parameters $\boldsymbol{\psi} = (\theta,\delta,L)^{\mathrm{T}}$ of a single extensible continuum segment into account (see Section 5.1.1), the safe parameter domains are introduced analogously to rotational or prismatic joints of serial robot kinematics. The segmental bending angle θ and length L show lower and upper domain limits which correlate to structural boundary conditions for safe deformation of the continuum bodies. The angle of the bending plane θ is disregarded as limits are absent. The trigger limits of each segment for activation of the secondary task are $\boldsymbol{\theta}_{\mathrm{lim}} = (\theta_{\mathrm{min}},\theta_{\mathrm{max}})^{\mathrm{T}} \in \mathbb{R}^{1\times2}$ and $\boldsymbol{L}_{\mathrm{lim}} = (L_{\mathrm{min}},L_{\mathrm{max}})^{\mathrm{T}} \in \mathbb{R}^{1\times2}$. The resulting limit matrix composition yields $\boldsymbol{\psi}_{\mathrm{lim}} = (\boldsymbol{\theta}_{\mathrm{lim}},\boldsymbol{0},\boldsymbol{L}_{\mathrm{lim}})^{\mathrm{T}} \in \mathbb{R}^{2\times3}$ with null matrix $\boldsymbol{0} \in \mathbb{R}^{2\times1}$. Taking the limits of both segmental configuration spaces into account and applying a decomposition to column-wise representation, the parameter domain for safe operation reports to

$$(\boldsymbol{\psi}_{\mathrm{lim},1},\boldsymbol{\psi}_{\mathrm{lim},2}) = (\boldsymbol{\psi}_{\mathrm{min}},\boldsymbol{\psi}_{\mathrm{max}}) \in \mathbb{R}^{6\times2}. \tag{5.44}$$

In general, the secondary task for constraint-based avoidance of segmental limits reports to

$$\dot{\boldsymbol{\psi}}_{\mathrm{S}} = \boldsymbol{\lambda}_{\mathrm{AG}}\boldsymbol{\lambda}_{\mathrm{TF}}\boldsymbol{P}_{\mathrm{K}}\boldsymbol{h}_{\mathrm{AF}} \in \mathbb{R}^{6}, \tag{5.45}$$

where matrix $\boldsymbol{\lambda}_{\mathrm{AG}} \in \mathbb{R}^{6\times6}$ adjusts the level of the limit avoidance task, matrix $\boldsymbol{\lambda}_{\mathrm{TF}} \in \mathbb{R}^{6\times6}$ holds the tuning function for the injection magnitudes to the primary task, $\boldsymbol{P}_{\mathrm{K}} \in \mathbb{R}^{6\times6}$ is the kernel projection matrix, and $\boldsymbol{h}_{\mathrm{AF}} \in \mathbb{R}^{6}$ contains the results of the limit activation functions. More specifically, the parameter activation function evaluates each actual parameter condition ψ_i with respect to its predefined limits and further determines the direction of activation:

$$h_{\mathrm{AF},i} = \begin{cases} -1, & \text{if } \psi_i \leq \psi_{\mathrm{min},i} \text{ for } i \neq 2 \vee 5 \\ 1, & \text{if } \psi_i \geq \psi_{\mathrm{max},i} \text{ for } i \neq 2 \vee 5 \\ 0, & \text{otherwise} \end{cases} \tag{5.46}$$

with joint index $i = \{1,\dots,6\}$. Bending plane angle δ of both continuum segments is excluded from constraint computation as the corresponding parameter space has no physical limits, i.e. the second and fifth element are skipped in the activation function.

The corresponding elemental composition yields vector

$$\boldsymbol{h}_{\mathrm{AF}} = (h_{\mathrm{AF},1},h_{\mathrm{AF},i},\dots,h_{\mathrm{AF},6})^{\mathrm{T}} \in \mathbb{R}^{6}. \tag{5.47}$$

The injection magnitudes are controlled by the tuning function evaluated at the actual configuration state:

$$
\lambda_{\mathrm{TF},i}(\psi_i) = \begin{cases} 1, & \text{if } \psi_i \le \psi_{\min,i} \vee \psi_i \ge \psi_{\max,i} \text{ for } i \ne 2 \vee 5 \\ w_{\max}(\psi_i), & \text{if } 0.8\psi_{\max,i} \le \psi_i \le \psi_{\max,i} \text{ for } i \ne 2 \vee 5 \\ w_{\min}(\psi_i), & \text{if } \psi_{\min,i} \ge \psi_i \ge 0.8\psi_{\min,i} \text{ for } i \ne 2 \vee 5 \\ 0, & \text{if } \psi_{\min,i} \le \psi_i \le \psi_{\max,i} \end{cases}
\tag{5.48}
$$

with index $i = \{1,\dots,6\}$ and start of the domain transition defined by 80% of the limit range. The composition of the matrix elements yields

$$
\boldsymbol{\lambda}_{\mathrm{TF}}(\boldsymbol{\psi}) = \begin{pmatrix} \lambda_{\mathrm{TF},1}(\psi_1) & \dots & 0 \\ \vdots & \ddots & \vdots \\ 0 & \dots & \lambda_{\mathrm{TF},6}(\psi_6) \end{pmatrix}.
\tag{5.49}
$$

A smooth transition between inactive and fully active states of the tuning function is generated with customised sigmoid functions. The characteristics of the function are derived from [MC10] and a related example is shown in Figure 5.3. This refers to the following expressions:

$$
w_{\max}(\psi_i) = \frac{1}{1 + \exp\left(-12\frac{\psi_i - \psi_{\max,i}}{0.8\psi_{\max,i} - \psi_{\max,i}} + 6\right)}
\tag{5.50}
$$

and

$$
w_{\min}(\psi_i) = \frac{1}{1 + \exp\left(-12\frac{\psi_i - \psi_{\min,i}}{0.8\psi_{\min,i} - \psi_{\min,i}} + 6\right)}.
\tag{5.51}
$$
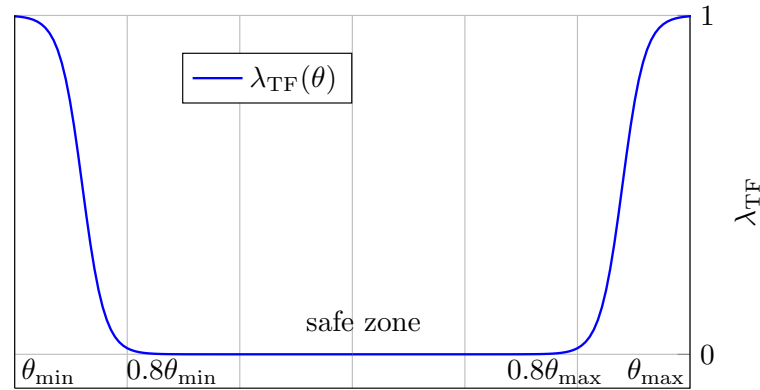
Fig. 5.3: Example of the secondary task tuning function λ_{TF} evaluated for segmental bending angles.

The kernel projection, which maps the results of the limit activation functions to the null space of the primary task, is computed by

$$\boldsymbol{P}_{\mathrm{K}} = \boldsymbol{I} - \boldsymbol{J}_{x\psi}^{\star\mathrm{T}}(\boldsymbol{\psi}^{\star})\boldsymbol{J}_{x\psi}^{\star}(\boldsymbol{\psi}^{\star}), \tag{5.52}$$

where $\boldsymbol{I} \in \mathbb{R}^{6\times6}$ is the identity matrix and $\boldsymbol{J}_{x\psi}^{\star}(\boldsymbol{\psi}^{\star})$ are composed Jacobian matrices (see Section 5.1.2). Lastly, the adjustable task gains report to

$$\lambda_{\mathrm{AG,i}} = \begin{cases} (\lambda_i + 1)\frac{\dot{q}_{\mathrm{P},i}}{\|\boldsymbol{P}_{\mathrm{K}}\boldsymbol{h}_{\mathrm{AF}}\|_2}, & \text{if } h_{\mathrm{AF},i} \neq 0 \\ 0, & \text{otherwise}, \end{cases} \tag{5.53}$$

where index $i = \{1,\dots,6\}$, $\lambda_i \in \mathbb{R}$ is a constant gain scalar, $\dot{q}_{\mathrm{P},i}$ is the corresponding primary joint velocity, and $\|\boldsymbol{P}_{\mathrm{K}}\boldsymbol{h}_{\mathrm{AF}}\|_2$ controls the gain magnitude based on the evaluation of the activation function. The composition of task gains to the global gain matrix is defined by

$$\boldsymbol{\lambda}_{\mathrm{AG}}(\boldsymbol{\psi}) = \begin{pmatrix} \lambda_{\mathrm{AG},1}(\psi_1) & \dots & 0 \\ \vdots & \ddots & \vdots \\ 0 & \dots & \lambda_{\mathrm{AG},6}(\psi_6) \end{pmatrix}. \tag{5.54}$$

Only constant gain scalars λ_i demanded for manual tuning with $0 \leq \lambda_i \leq 1$ for each parameter of the composed multisegmental configuration space.

5.1.4 Teleoperation Architecture

Teleoperation, i.e. robotic control at low autonomy levels, is still regarded state-of-the-art in robotic surgery. Hence, various HMIs have been considered for teleoperated control of novel platforms in robotic laser surgery, such as graphic tablets, to generate nominal path or trajectory data (see Section 1.2.4). The use of an extensible manipulator for laser-based MIS facilitates inclusion of the focal dimension but demands for enhanced robotic dexterity. This also requires advanced HMI to master the device safely. The surgeon is enabled to remain in complete control of the robotic platform and to take decisions on each step of the surgical workflow. This work considers a stylus-based HMI. In comparison to a graphics tablet, the free floating stylus supports the user with 3D drawing of the desired laser path and concurrent rendering of haptic feedback for surgical assistance.

The *Geomagic Touch* device (3D Systems Inc., Rock Hill, SC, USA), also formerly known as *Phantom Omni*, is depicted in Figure 5.4 and comprises of a pen-like stylus which is connected to a hinge and linked to a stationary base module through a serial chain of robotic components. Each joint of the assembly is equipped with angular joint encoders, which measure the corresponding angular displacement of the kinematic chain resulting from stylus manipulation. In total, the kinematic design realises three linear and three angular DoF of the stylus. Beyond that, the device

accommodates three rotary actuators. These are each connected to a corresponding link of the serial manipulator with Bowden wires. In combination with the kinematic and dynamic model of the master device, this facilitates rendering of haptic feedback to the linear manipulator space. The spatial resolution is approximately $0.1\,\mathrm{mm}$. The haptic force maximum is $3.3\,\mathrm{N}$. The maximal end effector stiffness settings are anisotropic with reference to frame (CF)$_\mathrm{M}$: $k_x = 1.26\,\mathrm{N}\,\mathrm{mm}^{-1}$, $k_y = 2.31\,\mathrm{N}\,\mathrm{mm}^{-1}$, and $k_z = 1.02\,\mathrm{N}\,\mathrm{mm}^{-1}$. The dimensions of the workspace are $(160 \times 120 \times 70)\,\mathrm{mm}^3$. Torque rendering to the stylus has not been featured in this hardware and demands for advanced haptic devices, such as Omega series with 6 DoF feedback (Force Dimension, Nyon, Switzerland). The reader is kindly referred to related work for further details on design and low level control of the *Geomagic Touch* [SRVO09].

The architecture of the master-slave teleoperation network is presented in Figure 5.4. The master device is connected to a dedicated workstation via Ethernet. As position or velocity-based control schemes are targeted, the operator displacement of the master stylus generates nominal data $\boldsymbol{x}_\mathrm{S}$ or $\dot{\boldsymbol{x}}_\mathrm{S}$ depending on the selected control mode which is forwarded to the controller framework. The data is fed to the kinematics module (see Section 5.1.6) to compute nominal joint data $\boldsymbol{q}^*$ or $\dot{\boldsymbol{q}}^*$ using the multisegmental kinematics model. Likewise, the actual linear joint states $\boldsymbol{q}$ or $\dot{\boldsymbol{q}}$ are returned from the joint encoders of the slave device. The kinematic framework is updated accordingly to reflect the latest hardware configuration. This workflow may be affected by external disturbances from the surgical environment. Regarding the latest robot and nominal master configuration, the haptic controller updates the nominal forces $\boldsymbol{f}$ on the master hardware.

The realisation of full, transparent, and intuitive teleoperation of the slave robot requires referencing of the master and slave workspaces to a common frame, as orientation, scaling, and volumes of both workspaces differ inherently. The master origin is interactively redefined using a sequence linked to the upper stylus button. Once the operator activates the button for at least two seconds, the origin of frame (CF)$_\mathrm{S}$, i.e. position of the master stylus, is offset by Cartesian $_{(\mathrm{M})}\boldsymbol{x}_\mathrm{SO} \in \mathbb{R}^3$ to the present stylus pose. This further resets the orientation of the stylus. The second button of the stylus activates a linear motion scaling which only maps a subvolume of the master workspace to the slave kinematics. In this thesis, only one-sixth of the entire workspace is regarded using a isotropic scaling matrix $\boldsymbol{S}_\mathrm{M} \in \mathbb{R}^{3\times3}$. Hence, the nominal position of the robotic end effector is as follows:

$$\boldsymbol{x}_\mathrm{S}^* = \boldsymbol{S}_{\mathrm{M(M)}}\boldsymbol{x}_\mathrm{S} + {}_{(\mathrm{M})}\boldsymbol{x}_\mathrm{SO}. \tag{5.55}$$

By contrast, the actual orientation of the stylus ${}^\mathrm{M}\boldsymbol{R}_\mathrm{S} \in \mathrm{SO}(3)$ sets the orientation of the robotic end effector ${}^\mathrm{B}\boldsymbol{R}_\mathrm{E}$, such as ${}^\mathrm{M}\boldsymbol{R}_\mathrm{S} = {}^\mathrm{B}\boldsymbol{R}_\mathrm{E}$.

Once the reference frames of master and slave devices are matched, the generated feedback can be directly mapped to the HMI. This, in particular, addresses the generation of haptic feedback to moderate the user inputs under consideration of velocity constraints of the slave kinematics, i.e. to avoid structural damage, and to realise a protection from sudden operator inputs. The applied haptic rendering is inspired by friction models. Generally, rendered forces are modulated by the
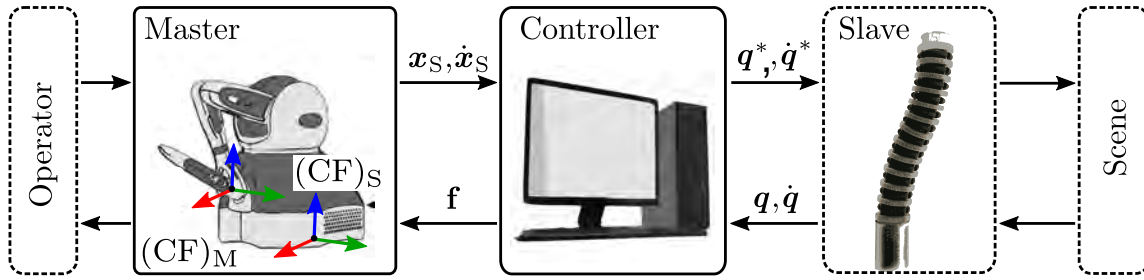
Fig. 5.4: Teleoperation architecture with master and slave device .

position offsets between slave and master kinematics. As an example, rendered forces are low for small displacements. On the contrary, increasing position offsets generate larger forces to slow down and moderate HMI input. The position residuals result from actual and desired end effector positions:

$$\Delta \boldsymbol{x}_\mathrm{S} = \boldsymbol{x}_\mathrm{E,l} - \boldsymbol{x}_\mathrm{S}^* \in \mathbb{R}^3, \tag{5.56}$$

where $\boldsymbol{x}_\mathrm{E,l}$ is the actual Cartesian manipulator position computed from the joint state and forward kinematics (see Section 5.1.2) and $\boldsymbol{x}_\mathrm{S}^*$ are the nominal master positions (see Equation (5.55)). Translating the residuals into a virtual force model, the force amplitudes are modulated equivalently. In order to mitigate oscillations caused by small displacements and network latencies from data propagation through the master-slave architecture, the force amplitudes are modelled by smoothstep-functions. This features the following nominal Cartesian forces:

$$f_i(\Delta x_{\mathrm{S},i}) = \begin{cases} 0 & \Delta x_{\mathrm{S},i} < \varepsilon_\mathrm{H} \\ \left(3\Delta x_{\mathrm{S},i}^2 - 2\Delta x_{\mathrm{S},i}^3\right) \hat{f}_i \, \mathrm{sgn}\left(\Delta x_{\mathrm{S},i}\right) & 0 \le \Delta x_{\mathrm{S},i} \le r_\mathrm{ST} \\ \hat{f}_i \, \mathrm{sgn}\left(\Delta x_{\mathrm{S},i}\right) & \Delta x_{\mathrm{S},i} \ge r_\mathrm{ST} \end{cases} \tag{5.57}$$

with index $i = \{1, \ldots, 3\}$ and composition to

$$\boldsymbol{f}(\Delta \boldsymbol{x}_\mathrm{S}) = \left(f_1(\Delta x_{\mathrm{S},1}), \ldots, f_3(\Delta x_{\mathrm{S},3})\right)^\mathrm{T}, \tag{5.58}$$

where ε_H is the feedback activation threshold, r_ST is the smooth-step radius, and $\hat{f}_i$ is the direction-specific maximum haptic force.

This strategy enables independent rendering of haptic feedback to the three linear DoF of the master hardware. Furthermore, data fusion is realised from two different sampling rates provided by the joint state mapping and actual master data, i.e. $100\,\mathrm{Hz}$ and $1\,\mathrm{kHz}$. Models, algorithms, and processing sequences are integrated into the haptic controller framework which is described in detail in Section 5.1.6. The performance of the realised teleoperation using the proposed master-slave network architecture is evaluated in experimental preclinical user studies as described in Chapter 7.

5.1.5 Closed-Loop Kinematics Controller

The analytical kinematic model of the proposed extensible continuum manipulator has been derived in the previous section. The model enables computation of the spatial manipulator representation for arbitrary robotic configurations with proposed space mappings and supports setup of a simulation environment for motion prototyping. However, complex robotic task space motion with accurate, reliable, and safe performance demands for advanced control strategies. The most common approach is closed-loop inverse differential kinematics (CLIK). The latter does not require any prior learning process or system knowledge with the robot, other than its Jacobian [CT15]. As discussed in preceding sections, those methodologies can solve the inverse kinematic mapping problem, e.g. mapping of task space velocities to the joint space under consideration of kinematic singularities or secondary constraints [CT15]. Regarding the proposed extensible continuum robot, the solution of the inverse kinematics of the continuum kinematics (5 DoF) focuses on optimal results with presence of actuation redundancy (6 DoF). Furthermore, various criteria for non-redundant and redundant kinematics, such as Jacobian weighting, task priority, or task augmentation as summarised in [CT15]. This work targets multiple tasks, i.e. task space error regulation and joint limit avoidance, and applies an optimisation approach by projecting a secondary task to the kernel of the primary task using gradient projection. The concept of the general control workflow is shown in Figure 5.5. The cascaded feedback design represents the CLIK methodology. The inner loop comprises of the actuators with low-level PI velocity control and the outer loop is dedicated to task space tracking using a task space PID controller.

At the start of each control cycle, joint state q is updated with the latest sensor data. Subsequently, configuration state ψ and end effector pose x_E are computed from q using the direct kinematics described in Section 5.1.3. The resulting task space error is given by the pose difference between nominal and actual pose of the end effector:

$$\Delta x_E = {}_{(B)}x_E^* - {}_{(B)}x_E \in \mathbb{R}^5, \tag{5.59}$$
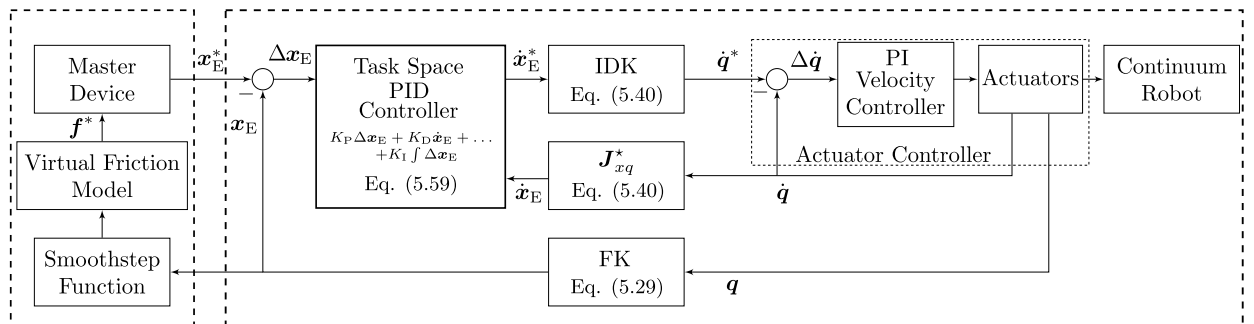
Fig. 5.5: Block diagram of the fundamental control principles used in the proposed robotic framework. The input from the master device can be replaced by input from trajectory planning or visual servoing. Controller gains K_P, K_D, and K_I are tuned empirically. Acronyms: Inverse differential kinematics (IDK) and forward kinematics (FK).

where angular elements are represented using quaternion notation. The nominal task space end effector pose $\boldsymbol{x}_\mathrm{E}^*$ can be provided by path planning modules, visual servoing controllers, or from direct HMI input. Angular contributions about the z-axis of the manipulator are disregarded due to the mechanical design that prevents any motion in this dimension. Thus, the dimension of the nominal pose vector is reduced by one DoF. The nominal end effector velocities result from

$$\dot{\boldsymbol{x}}_\mathrm{E}^* = \frac{\Delta \boldsymbol{x}_\mathrm{E}}{t_\mathrm{C}} \in \mathbb{R}^5, \tag{5.60}$$

where t_C denotes the actual cycle time of the kinematics control-loop.

Once the robotic state is updated, the nominal joint state, i.e. actuator commands, for the recent cycle is computed using CLIK. The latter enables additional consideration of the proposed segmental limit avoidance (see Section 5.1.3). In this work, the CLIK is constituted in the configuration space and divided into two task objectives. As discussed in previous Section 5.1.2, the primary task objective regards minimisation of the pose errors:

$$\dot{\boldsymbol{\psi}}_\mathrm{P}^* = \hat{\boldsymbol{J}}_{x\psi}^{-1}(\boldsymbol{\psi})\dot{\boldsymbol{x}}_\mathrm{E}^* \in \mathbb{R}^6, \tag{5.61}$$

where $\hat{\boldsymbol{J}}_{x\psi}^{-1}(\boldsymbol{\psi}) \in \mathbb{R}^{6 \times 5}$ is the composed, reduced, and inverted Jacobian of the manipulator which refers to end effector frame $\mathrm{(CF)_E}$. The Jacobian end effector transformation is given by:

$$\hat{\boldsymbol{J}}_{x\psi}(\boldsymbol{\psi}) = \boldsymbol{S}_\mathrm{E} \begin{pmatrix} {}^\mathrm{E}\boldsymbol{R}_\mathrm{B} & \boldsymbol{0} \\ \boldsymbol{0} & {}_\mathrm{E}\boldsymbol{R}_\mathrm{B} \end{pmatrix} \boldsymbol{J}_{x\psi}^\star(\boldsymbol{\psi}) \in \mathbb{R}^{5 \times 6}, \tag{5.62}$$

where $\boldsymbol{J}_{x\psi}^\star(\boldsymbol{\psi}) \in \mathbb{R}^{6 \times 6}$ is the full manipulator Jacobian in base frame $\mathrm{(CF)_B}$, ${}^\mathrm{E}\boldsymbol{R}_\mathrm{B} \in \mathrm{SO}(3)$ is the corresponding rotation matrix from forward kinematics, and $\boldsymbol{S}_\mathrm{E} \in \mathbb{R}^{5 \times 6}$ is a selection matrix for the dimensional adjustment of the Jacobian. To solve Equation (5.61) for velocities $\dot{\boldsymbol{\psi}}_\mathrm{P}^*$, a numerically stable inverse of the robot Jacobian $\hat{\boldsymbol{J}}_{x\psi}(\boldsymbol{\psi})$ is required to prevent large values of matrix elements close to singular configurations.

Although the Moore-Penrose pseudoinverse of any $\boldsymbol{J}^{-1} = \boldsymbol{J}^\mathrm{T}(\boldsymbol{J}\boldsymbol{J}^\mathrm{T})^{-1}$ is frequently used in robotic applications [SK16], an advanced methodology with singular value decomposition (SVD) of the Jacobian is used to accommodate numerical conditions. This generally yields $\boldsymbol{J} = \boldsymbol{U}\boldsymbol{\Sigma}\boldsymbol{V}^\mathrm{T}$, where $\boldsymbol{U}$, $\boldsymbol{\Sigma}$, and $\boldsymbol{V}$ are orthonormal matrices. Thus, the corresponding inverse is given by $\boldsymbol{J}^{-1} = \boldsymbol{V}\boldsymbol{\Sigma}^{-1}\boldsymbol{U}^\mathrm{T}$. This methodology is equivalently applied to Jacobian $\hat{\boldsymbol{J}}_{x\psi}(\boldsymbol{\psi})$ of the manipulator.

The secondary task velocities comprise of the direct kernel projection related to structural limit avoidance as described in Section 5.1.3:

$$\dot{\boldsymbol{\psi}}_\mathrm{S}^* = \boldsymbol{\lambda}_\mathrm{AG}\boldsymbol{\lambda}_\mathrm{TF}\boldsymbol{P}_\mathrm{K}\boldsymbol{h}_\mathrm{AF}, \tag{5.63}$$

The sum of both tasks yields the complete closed-loop inverse differential kinematics for the extensible continuum manipulator:

$$\dot{\boldsymbol{\psi}}^* = \dot{\boldsymbol{\psi}}_{\mathrm{P}}^* + \dot{\boldsymbol{\psi}}_{\mathrm{S}}^* = \hat{\boldsymbol{J}}_{x\psi}^{-1}(\boldsymbol{\psi})\dot{\boldsymbol{x}}_{\mathrm{E}}^* + \boldsymbol{\lambda}_{\mathrm{AG}}\boldsymbol{\lambda}_{\mathrm{TF}}\boldsymbol{P}_{\mathrm{K}}\boldsymbol{h}_{\mathrm{AF}} \in \mathbb{R}^6. \tag{5.64}$$

The mapping to the joint space of the actuation joint is as follows

$$\dot{\boldsymbol{q}}^* = \boldsymbol{J}_{q\psi}(\boldsymbol{\psi})\left(\hat{\boldsymbol{J}}_{x\psi}^{-1}(\boldsymbol{\psi})\dot{\boldsymbol{x}}_{\mathrm{E}}^* + \boldsymbol{\lambda}_{\mathrm{AG}}\boldsymbol{\lambda}_{\mathrm{TF}}\boldsymbol{P}_{\mathrm{K}}\boldsymbol{h}_{\mathrm{AF}}\right) \in \mathbb{R}^6. \tag{5.65}$$

The reader is kindly referred to related work on comprehensive fundamentals and CLIK methodology comparisons [CT15]. The control iteration cycle is completed by commanding the nominal joint states $\dot{\boldsymbol{q}}^*$ to the *actuator controller* node and updated sensor data is requested from the actuator hardware prior to the transition to the next control cycle.

5.1.6 ROS Modules

The kinematics and control architecture of the extensible continuum robot is the central element of device automation and additionally integrates with the ROS network. The modular structure of the framework depicted in Figure 5.6 has been inherited from state-of-the-art design patterns and best practices[2] which separates the algorithmic workflow to independent nodes. The nodes are dedicated to processing, functions, tasks, or computational methodologies. The kinematics and control framework, also denoted as *ExtCR*, is made publicly available in an online repository[3] for dissemination and refactoring.

The overall architecture of the *kinematics_controller* node adapts an object-oriented bottom-up design and uses the *Eigen* library for computationally efficient matrix operations. The kinematic model of a continuum segment (see Section 5.1.1) and its associated space states are summarised and encapsulated to class *SegKinematics*. This class consists of forward and inverse space mappings, the computation of segmental Jacobians, and handling of actual parameter settings as well as the storage of manipulator configurations. The extension of the model to a multisegmental manipulator regards an instance of class *MultiSegKinematics*. The latter links multiple instances of *SegKinematics* (see Section 5.1.2). Apart from the spatial model, this composition facilitates whole-body motion generation using *inverse differential kinematics*. This also includes methodologies for joint limit avoidance, e.g. structural protection with gradient projection (see Section 5.1.3). The node exchanges data bilaterally with the high level ROS network and subscribes to the actual joint state output of intermediate node *joint_controller* to acquire the latest joint configuration $\boldsymbol{q}$ from the robotic hardware. More specifically, the *joint_controller* uses a subscription to the actual actuator states provided by low level node *actuator_controller* and converts the raw data of rotary

---

[2] http://wiki.ros.org/ROS/Patterns
[3] https://github.com/deku-robotics/ExtCR
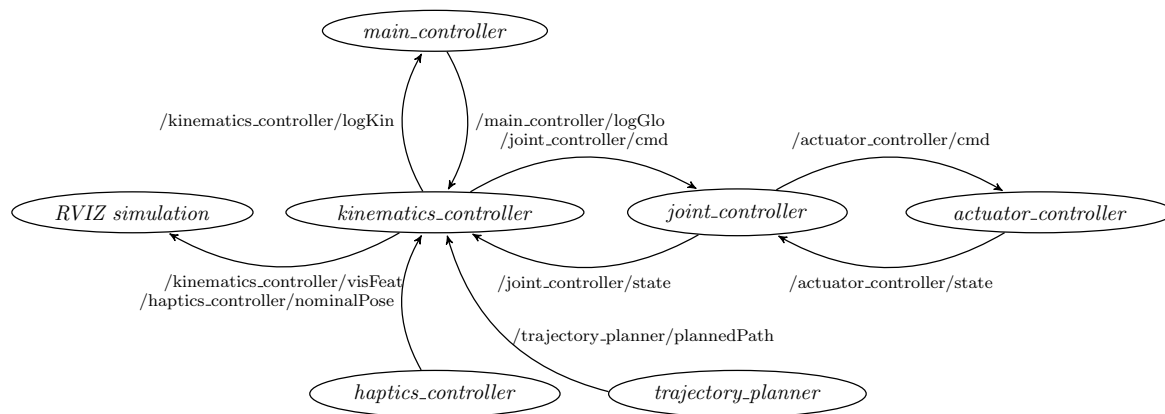
Fig. 5.6: The simplified ROS graph output of the core architecture of the realised ROS network. The schematics illustrates only a subset of nodes/connection used in the online data exchange based on ROS messages. For the sake of visual clarity, nodes for processing of visual information (e.g. 3D reconstruction and tracking), ROS services, and ROS actionlib message have been omitted. The complete graph comprises of approximately 30 ROS messages, 35 ROS services, and 4 ROS actionlib messages.

actuators using spindle parameters, encoder resolution, and transmission ratios to joint space. The *joint_controller* further enables adjustment of offsets related to joint state q in order to complement the referencing sequences of each actuator. The joint state is published to the ROS network at a rate of $100 \, \text{Hz}$. Publishing of nominal joint positions and/or velocities, e.g. computed by the closed-loop inverse differential kinematics from master input, transmits the corresponding commands to the *actuator_controller*. The latter realises the low level communication with all six Faulhaber actuators via the BeagleBoneBlack board and manages data delegation on the bidirectional RS232 bus across the network members. This includes diagnostic data and the subsequent analysis for condition monitoring. The *actuator_controller* also manages the referencing sequences of each linear joint. This includes monitoring of limit sensors and actuator position control to safely determine the range of motion of each DoF. The actuator driver classes adopt versatile design patterns which simplify a prospective transition to advanced actuator technologies. Lastly, the node publishes fundamental visual simulation features of the continuum structure which consist of spatially transformed markers and primitives. These features mimic backbones and spacer disks in the RVIZ[4] simulation environment to support prototyping of novel motion sequences prior to execution on the robotic hardware.

The *haptic_controller* of the Geomagic Touch master device inherits the implementation of the proprietary Phantom Omni package[5] and its integration to a later version[6] of the ROS environment. The packages use the *Open Haptics* library[7] to configure, parameterise, and access low level functionality of the Geomagic Touch. The fusion of reported packages is further complemented

---

[4]http://wiki.ros.org/rviz
[5]http://wiki.ros.org/phantom_omni
[6]https://github.com/danepowell/phantom_omni
[7]https://www.3dsystems.com/haptics-devices/openhaptics

by previously discussed workflows (see Section 5.1.4), which are required for haptic control of the extensible manipulator and rendering of assistive feedback. Basically, the *haptic_controller* handles the initialisation of the device pairing via Ethernet with the host computer and manages the bilateral data exchange. Furthermore, the *OpenHaptics* library provides kinematic and dynamic models of the master hardware. The average control and update rate is $1\,\mathrm{kHz}$. More specifically, the manipulator model is updated from embedded sensor information and the internal force controller regulates the output to the nominal forces. The package additionally realises a cyclic data exchange with the ROS network. The corresponding node publishes a multidimensional array of stylus pose, button status, and active force settings to the network. On the other hand, the node subscribes to nominal task space stiffness settings and further device customisation, such as button assignments for left or right-handed operators.

5.2 Experimental Evaluation of Kinematics Modelling

A novel kinematics framework for extensible continuum robots has been derived in the previous section. One of the major challenges associated with modelling of robotic devices and, in particular, flexible continuum structures is the quality of fit between model and physical prototype. This level of fit can be affected by uncertainties which are not represented by the analytical model, e.g. inaccuracies from prototype assembly. In this regard, the dedicated kinematic analysis presented in this section may reveal significant effects. The results can be regarded in future work referring to the design of advanced modelling and control strategies.

5.2.1 Hardware Setup

The experimental assessment of the kinematic model uses an external optical tracking system for acquisition of reference measurements. The robotic manipulator has been equipped with customised and unique marker configurations (rigid bodies) located at the base and the end effector of the multisegmental continuum structure. The corresponding rigid bodies and applied marker geometries are shown in Figure 5.7a. The markers are composed of support structures with unique dimensions and link geometries. Each of the structures is further equipped with four reflective hemispheres of $2.5\,\mathrm{mm}$ diameter (Loligo Systems, Viborg, Denmark) which are attached to the tip of each link. The spatial alignment of the spheres was selected according to guidelines on optimal 6 DoF rigid body pose estimation for optical tracking [GGvdS12]. The spatial configuration of the coordinate frames $(CF)_{TB}$ and $(CF)_{TE}$ is depicted in Figure 5.7a. The centre spheres determine the origin of the frames, whereas the two remaining spheres define the direction of the x- and y-axes. The direction of the z-axis is defined implicitly. The support structure of the rigid bodies show customised features to facilitate mounting to the base and end effector of the continuum manipulator (see Figures 5.7a and 5.7b).

Rigid body poses have been tracked using an optical near-field tracking system (Axios 3D CamBar B1, Axios 3D GmbH, Oldenburg, Germany). The device (see Figure 5.7c) has a specified tracking distance of $150\,\text{mm}$ to $300\,\text{mm}$. Furthermore, the workspace dimensions at $150\,\text{mm}$ and $300\,\text{mm}$ distance are $(50 \times 80)\text{mm}^2$ and $(210 \times 200)\text{mm}^2$, respectively. This volume compares to a truncated pyramid. Prior to experimental use of the bespoke tracking bodies, the specific sphere configurations must be configured in the proprietary tracking software and optimised using the online learning algorithm. The spatial (reflective marker) localization accuracy and precision is below $50\,\mu\text{m}$ [AXI14].

The corresponding kinematic transformations of the tracking markers and the manipulator are shown in Figure 5.7b and for the global setup in Figure 5.7c. The poses of both rigid bodies, i.e. base and end effector, are described by $^{\text{TC}}\boldsymbol{T}_{\text{TB}}$ and $^{\text{TC}}\boldsymbol{T}_{\text{TE}}$ with respect to frame $(\text{CF})_{\text{TC}}$ of the tracking camera. The kinematic assessment considers both the optical measurements and analytical models of the robotic manipulator (see Section 5.1.2). This approach uses a comparison of end effector poses with respect to the robotic base. However, as shown in Figure 5.7b, reference frames of tracking measurements $(\text{CF})_{\text{TB}}$ and $(\text{CF})_{\text{TE}})$ are offset from model frames $(\text{CF})_{\text{B}}$ and $(\text{CF})_{\text{E}}$. The pose offsets are described by unknown homogeneous transformations $^{\text{B}}\boldsymbol{T}_{\text{TB}}$ and $^{\text{E}}\boldsymbol{T}_{\text{TE}}$. The latter were determined applying an intermodal registration between tracking and model spaces. This procedure includes tactile measurements using a coordinate measurement machine (CMM) (FARO® Gage, FARO Technologies, FL, USA) and is described in detail in the following section.

5.2.2 Intermodal Manipulator Registration

Pose variations of the robotic manipulator are continuously acquired using optical tracking of the attached rigid bodies, i.e. the motion of tip frame $(\text{CF})_{\text{TE}}$ with respect to static base frame $(\text{CF})_{\text{TB}}$.
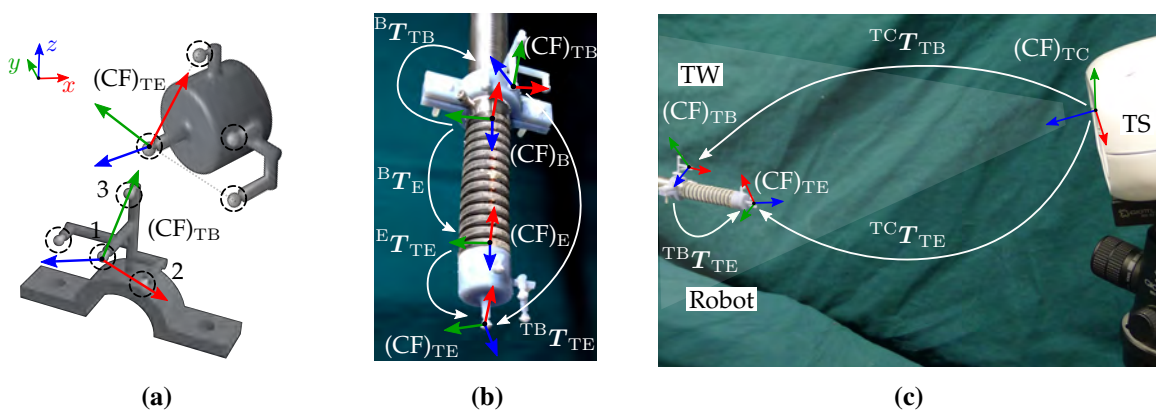
Fig. 5.7: Experimental setup for kinematic assessment: (a) Customised rigid bodies for optical tracking. Black circles indicate retro-reflective hemispheres. (b) Spatial configuration and kinematic transformations between tracking markers and continuum manipulator. (c) Setup and kinematic transformation of the robotic manipulator and optical tracking system. Acronyms: Tracking workspace (TW) and tracking system (TS).

However, those optical measurements are not directly linked to the robot frames, such as base (CF)_B and end effector (CF)_E. This prevents the direct comparison of kinematic model and physical prototype. Hence, additional spatial transformations for linking the frames of the robotic model and optical tracking must be determined.

This thesis applies a hybrid approach which joins the tactile and optical measurements to estimate the transformations of base and tip. Tactile measurements were conducted using a hand-guided coordinate measurement machine (FARO Gage, FARO Inc., Lake Mary, FL, USA) equipped with a probe of $2\,\text{mm}$ diameter. The entity of tactile measurements is related to machine frame (CF)_CM and denoted by the hat symbol.

Primarily, pose $^\text{CM}\boldsymbol{T}_\text{B}$ of the manipulator base frame (CF)_B, i.e. equivalent to analytical and CAD model frames, was determined using tactile CMM measurements. The origin was given by the centre of circumferential measurements at the cylindrical surface of the base element and projection to the adjacent frontal plane. The directions of corresponding coordinate axes were determined using a set of notches at the component surface.

Subsequently, the pose of the tracking base frame $^\text{CM}\boldsymbol{T}_\text{TB}$ was obtained from repeated tactile measurements at the hemisphere surfaces and subsequent data fitting. This determines the position $_{(\text{CM})}\boldsymbol{P}_{\text{TB},i}$ of each spherical centre with $i \in \{1,\dots,4\}$ (see Figure 5.7a for index allocation). Hence, this provides transformation

$$^\text{CM}\boldsymbol{T}_\text{TB} = \begin{pmatrix} ^\text{CM}\boldsymbol{R}_\text{TB} & _{(\text{CM})}\boldsymbol{P}_{\text{TB},1} \\ \boldsymbol{0} & 1 \end{pmatrix}, \tag{5.66}$$

where the origin $_{(\text{CM})}\boldsymbol{P}_{\text{TB},1} \in \mathbb{R}^3$ is given by the first spherical marker. The angular component

$$^\text{CM}\boldsymbol{R}_\text{TB} = \begin{pmatrix} _{(\text{CM})}\boldsymbol{e}_x^{(\text{TB})} & _{(\text{CM})}\boldsymbol{e}_y^{(\text{TB})} & _{(\text{CM})}\boldsymbol{e}_z^{(\text{TB})} \end{pmatrix} \tag{5.67}$$

is composed of independent unit vectors

$$_{(\text{CM})}\boldsymbol{e}_x^{(\text{TB})} = \frac{_{(\text{CM})}\boldsymbol{P}_{\text{TB},2} - _{(\text{CM})}\boldsymbol{P}_{\text{TB},1}}{\left\|_{(\text{CM})}\boldsymbol{P}_{\text{TB},2} - _{(\text{CM})}\boldsymbol{P}_{\text{TB},1}\right\|_2} \quad _{(\text{CM})}\boldsymbol{e}_y^{(\text{TB})} = \frac{_{(\text{CM})}\boldsymbol{P}_{\text{TB},3} - _{(\text{CM})}\boldsymbol{P}_{\text{TB},1}}{\left\|_{(\text{CM})}\boldsymbol{P}_{\text{TB},3} - _{(\text{CM})}\boldsymbol{P}_{\text{TB},1}\right\|_2} \tag{5.68}$$

and resultant unit vector

$$_{(\text{CM})}\boldsymbol{e}_z^{(\text{TB})} = _{(\text{CM})}\boldsymbol{e}_x^{(\text{TB})} \times _{(\text{CM})}\boldsymbol{e}_y^{(\text{TB})} \tag{5.69}$$

under assumption of orthogonality. Finally, the transformation between the base tracking marker and the model frame is given by

$$^\text{B}\boldsymbol{T}_\text{TB} = \left(^\text{CM}\boldsymbol{T}_\text{B}\right)^{-1} {}^\text{CM}\boldsymbol{T}_\text{TB}. \tag{5.70}$$

This workflow was similarly applied to the end effector tracking and model frames in order to compute transformation $^\text{E}\boldsymbol{T}_\text{TE}$.

However, the evaluation of the kinematics data with input from optical tracking and analytical model demands for an additional registration step to fuse optical measurements and model data. The spherical landmarks attached to the tracking bodies enable an intermodal rigid point-based registration of optical and CMM data. The homologous fiducials are measured with different methods and/or reference frames and enable the estimation of a transformation between associated frames. In this thesis, two sets of spherical centres (fiducials), were acquired from two different reference spaces, i.e. optical and CMM measurements:

$$_{\text{(TC)}}\boldsymbol{P}_{\text{TB}} = \{_{\text{(TC)}}\boldsymbol{P}_{\text{TB},1}, \ldots, _{\text{(TC)}}\boldsymbol{P}_{\text{TB},4}\} \tag{5.71}$$

and

$$_{\text{(CM)}}\boldsymbol{P}_{\text{TB}} = \{_{\text{(CM)}}\boldsymbol{P}_{\text{TB},1}, \ldots, _{\text{(CM)}}\boldsymbol{P}_{\text{TB},4}\}. \tag{5.72}$$

The estimation of the intermodal registration is transferred to an optimisation problem. As an example, the latter minimises the objective function of the fiducial registration error

$$\text{FRE}^2 = \frac{1}{N_{\text{F}}} \sum_{i=1}^{N_{\text{F}}} |\boldsymbol{R}_{\text{TB}} {}_{\text{(TC)}}\boldsymbol{P}_{\text{TB},i} + \boldsymbol{t}_{\text{TB}} - {}_{\text{(CM)}}\boldsymbol{P}_{\text{TB},i}|^2 \tag{5.73}$$

applying iterative transformation of the regarded base fiducials [FWM98], where $\boldsymbol{R}_{\text{TB}} \in \text{SO}(3)$ and $\boldsymbol{t}_{\text{TB}} \in \mathbb{R}^3$ describe the estimated intermodal rotation and translation, respectively. This work applies a rigid point-based registration with SVD algorithm to determine the optimal intermodal space transformation [ONK16]. Hence, spherical markers ($N_{\text{F}} = 4$) of the tracking base and end effector frames were captured with the optical system and CMM. Each fiducial was measured five times in both modalities. Subsequently, homogeneous transformations

$$\boldsymbol{W}_{\text{TB}} = \begin{pmatrix} \boldsymbol{R}_{\text{TB}} & \boldsymbol{t}_{\text{TB}} \\ \boldsymbol{0} & 1 \end{pmatrix} \in \text{SE}(3) \tag{5.74}$$

and

$$\boldsymbol{W}_{\text{TE}} = \begin{pmatrix} \boldsymbol{R}_{\text{TE}} & \boldsymbol{t}_{\text{TE}} \\ \boldsymbol{0} & 1 \end{pmatrix} \in \text{SE}(3) \tag{5.75}$$

were estimated from the provided fiducial sets. Assuming an isotropic fiducial localisation error (FLE) distribution, the corresponding registration errors were $\text{FRE}_{\text{TB}} = 0.22\,\text{mm}$ and $\text{FRE}_{\text{TE}} = 0.18\,\text{mm}$.

In order to complete the mapping from optical tracking space to the model frames, the transformation between the base tracking frame and model base (see Equation (5.70)) is complemented by intermodal transformation:

$$^{\text{B}}\widehat{\boldsymbol{T}}_{\text{TB}} = {}^{\text{B}}\boldsymbol{T}_{\text{TB}} \left(\boldsymbol{W}_{\text{TB}}\right)^{-1}. \tag{5.76}$$

Likewise, this applies to end effector transformation $^{\mathrm{E}}\boldsymbol{T}_{\mathrm{TE}}$ adjusted by registration matrices:

$$^{\mathrm{E}}\widehat{\boldsymbol{T}}_{\mathrm{TE}} = {}^{\mathrm{E}}\boldsymbol{T}_{\mathrm{TE}} \left(\boldsymbol{W}_{\mathrm{TE}}\right)^{-1} . \tag{5.77}$$

Taking Equations (5.76) and (5.77) into account, the end effector transformations mapped to the corresponding model frames are composed of captured optical pose data, static offset transformations, and intermodal registration matrices:

$$^{\mathrm{B}}\boldsymbol{T}_{\mathrm{E}} = {}^{\mathrm{B}}\widehat{\boldsymbol{T}}_{\mathrm{TB}} \left(^{\mathrm{TC}}\boldsymbol{T}_{\mathrm{TB}}\right)^{-1} {}^{\mathrm{TC}}\boldsymbol{T}_{\mathrm{TE}} \left(^{\mathrm{E}}\widehat{\boldsymbol{T}}_{\mathrm{TE}}\right)^{-1} . \tag{5.78}$$

This data finally reflects the actual continuum robot poses from optical tracking with respect to the base and end effector frame of the model representation.

5.2.3 Study Design

The registration and fusion workflow of manipulator tracking data to the corresponding model spaces (see Section 5.2.2) enables the direct comparison of kinematics captured from the robotic prototype and analytical model. This evaluation has targeted analysis of the kinematic accuracy within the workspace limits of the extensible continuum manipulator. Various nominal manipulator poses were commanded in jointspace $\boldsymbol{q}$ and executed as a point-to-point motion. This is realised by sending commands through the *ExtCR* framework to the low level controller of the actuators. An overview of commanded nominal joint space configurations is provided in Table 5.1. This sequence commences with neutral deflection and minimal extension of both continuum segments (approximately $11\,\mathrm{mm}$) to prevent interference with limit avoidance constraints. This analysis further assumes that the steady-state control error of tracking the nominal commands in joint space is below $0.5\,\mathrm{mm}$ (see Section 4.3).

The execution of the joint space commands has induced the following task space motion sequence. Firstly, both continuum segments were extended from the initial configuration by $11\,\mathrm{mm}$ to circumvent the activation of limit avoidance. Subsequently, the list of commands was executed in the given order. The end effector tracked a point-to-point motion covering each workspace quadrant perpendicular to the central manipulator axis in two different planes. The continuum structure was extended again and four additional poses were executed. In total, $N = 9$ different poses were taken into consideration for the evaluation workflow. Hence, each joint space configuration results in a corresponding manipulator task space pose which covers extensive parts of the executable end effector workspace.

The evaluation of the kinematic performance metrics adapts the guidelines of international standard ISO 9283 on performance criteria and test methods of robots for determination of positioning accuracy $\mathrm{AP_P}$ and precision RP [ISO98]. The orientation accuracy and precision were disregarded

in this work due challenging tracking conditions resulting from the limited tracking volume and overlap of markers.

The proposed task space poses ${}^{\mathrm{B}}\boldsymbol{T}_{\mathrm{E}}$ of the prototype ($N = 9$) were captured with the optical tracking system and mapped to the model space. The pose sequence was executed multiple times ($N_{\mathrm{PR}} = 5$) following the random execution sequence introduced earlier in this section. The recorded task space poses were decomposed to linear component ${}_{(\mathrm{B})}\boldsymbol{p}^*_{\mathrm{E},ij} \in \mathbb{R}^3$ of pose $i \in \{1, \ldots, N_{\mathrm{P}}\}$ and repetition $j \in \{1, \ldots, N_{\mathrm{PR}}\}$. The components were consecutively stored to measurement matrix $\widetilde{\boldsymbol{P}}^*_{\mathrm{E}}$. After execution of robotic pose sequences, the mean tracked Cartesian end effector position is computed for each pose i:

$$
{}_{(\mathrm{B})}\overline{\boldsymbol{p}}^*_{\mathrm{E},i} = \frac{1}{N_{\mathrm{PR}}} \sum_{j=1}^{N_{\mathrm{PR}}} {}_{(\mathrm{B})}\boldsymbol{p}^*_{\mathrm{E},j}.
\tag{5.79}
$$

The corresponding pose data of the analytical robot model were concurrently obtained from the forward kinematics presented in the preceding sections. Hence, the end effector positions of the kinematics model yielded ${}_{(\mathrm{B})}\boldsymbol{p}^*_{\mathrm{E},i}$ with poses $i \in \{1, \ldots, N_{\mathrm{P}}\}$.

The positioning accuracy according to ISO 9283 of the extensible continuum manipulator for each executed end effector pose i is given by

$$
\mathrm{AP}_{\mathrm{P},i} = \left\| {}_{(\mathrm{B})}\overline{\boldsymbol{p}}^*_{\mathrm{E},i} - {}_{(\mathrm{B})}\boldsymbol{p}_{\mathrm{E},i} \right\|_2.
\tag{5.80}
$$

The positioning precision is the second performance metric proposed in standard ISO 9283. This metric takes the repeated execution into account and describes the end effector task space error after repeated execution of similar joint space configurations. The mean Cartesian end effector repeatability of a particular joint pose $\boldsymbol{q}_{\mathrm{AE},i}$

$$
\overline{l}_i = \frac{1}{M} \sum_{j=1}^{M} l_j
\tag{5.81}
$$

with individual measurement error

$$
l_j = \left\| {}_{(\mathrm{B})}\boldsymbol{p}^*_{\mathrm{E},j} - {}_{(\mathrm{B})}\overline{\boldsymbol{p}}^*_{\mathrm{E},i} \right\|_2,
\tag{5.82}
$$

enables the error analysis from repeated execution of commanded joint poses. Finally, the Cartesian precision related to joint space pose $\boldsymbol{q}_{\mathrm{AE},i}$ yields to

$$
\mathrm{RP}_{1,i} = \overline{l}_{\mathrm{AE},i} + 3S_{1,i} \quad \text{with} \quad S_{1,i} = \sqrt{\frac{\sum_{j=1}^{M}(\overline{l}_i - l_j)^2}{M - 1}}.
\tag{5.83}
$$

Tab. 5.1: Commanded joint space poses q for kinematic accuracy and precision assessment.

Poses	Joint space q (mm)					
	q_1	q_2	q_3	q_4	q_5	q_6
$q_{\mathrm{P},1}$	11.0	11.0	11.0	11.0	11.0	11.0
$q_{\mathrm{P},2}$	10.0	12.0	10.0	12.0	10.0	12.0
$q_{\mathrm{P},3}$	10.0	10.0	12.0	12.0	10.0	10.0
$q_{\mathrm{P},4}$	12.0	10.0	10.0	10.0	12.0	12.0
$q_{\mathrm{P},5}$	10.0	12.0	12.0	12.0	10.0	10.0
$q_{\mathrm{P},6}$	17.0	20.0	17.0	20.0	17.0	20.0
$q_{\mathrm{P},7}$	17.0	17.0	20.0	20.0	20.0	17.0
$q_{\mathrm{P},8}$	20.0	17.0	17.0	17.0	20.0	20.0
$q_{\mathrm{P},9}$	17.0	20.0	20.0	20.0	17.0	17.0

5.2.4 Results

The results of the experimental evaluation on kinematic and control performance assessed on the proposed extensible continuum robot are summarised in Table 5.2. The table shows mean accuracies and precisions for each executed task space pose. After the initial extension of the segmental lengths, the accuracy of the first pose was below $0.25\,\mathrm{mm}$. However, recorded accuracies increased to a range of $2\,\mathrm{mm}$ to $2.5\,\mathrm{mm}$ related to poses executed in the first motion plane. This effect was even more significant for poses executed in the second plane, i.e. with larger segmental extension. On the contrary, the results of end effector pose precisions were unambiguous. These metrics were determined in the range of $0.1\,\mathrm{mm}$ to $0.6\,\mathrm{mm}$ within the range of task space poses. Further, details of the comparison are presented in Figure 5.8. The executed poses are specifically depicted in Figure 5.8a. Qualitative examples of recorded and mapped optical tracking and associated model data are shown in Figure 5.8b with reference to the common task space representation.

Statistical analysis was applied to the results in order to determine significant effects. The characteristics of the optical tracking workflow resulted in nine groups of task space pose measurements. Each group consisted of ten pose samples. The metric *accuracy* was the dependent study variable at continuous scale. These conditions resulted in statistical assessment of mean differences between multiple measurement groups using the R framework. The level of significance was set to $\alpha = 0.05$. The assumption of residual normality within measurement groups was assessed for each group using Shapiro-Wilk testing and outliers were examined with normal QQ-plots. No outliers were identified and normality was confirmed ($p < 0.01$). Subsequently, group mean differences were compared by ANOVA testing. There were statistically significant differences between measured poses ($p < 0.001$, $F(8,18) = 292$). Additionally, pairwise t-tests with Bonferroni adjustment were conducted to identify pairs of statistically significant pose differences. All pose pairs showed statistically significant mean differences ($p < 0.01$) except for the following: 2/3, 4/6, 4/7, 6/7, 2/9, and 3/9 ($p > 0.05$).

Accordingly, a similar statistical assessment was applied to metric *precision* which was recorded and computed at continuous scale. In comparison to metric *accuracy*, ANOVA testing revealed that there was no statistical significance within the recorded pose precisions ($p = 0.08$, $F(8,18) = 172$).

5.2.5 Discussion

The experimental study evaluated the performance of the proposed kinematics framework in combination with deployment to the prototypic robotic platform. The results have demonstrated that the presented analytical modelling approach is suitable to represent the geometric characteristics of the realised extensible continuum manipulator with low residual kinematic tracking errors between model and tracked prototype.

The performance evaluation considered the two metrics positioning *accuracy* and *precision*. The positioning accuracy enabled a comparison of model and prototype performances as well as uncertainties resulting from the kinematics design. Taking the experimental results into account, the positioning accuracy was significantly lowered for increased segmental lengths. This may be related to presence of larger model inaccuracies for extended continuum segments. This effect was further levered for poses which required larger deflection/bending of both continuum segments. However, the achieved range of accuracies ($\leq 2\,\mathrm{mm}$) within the commanded cylindrical workspace boundaries (diameter $30\,\mathrm{mm}$, height $20\,\mathrm{mm}$) enables deployment to the robotic prototype as resulting errors at the measured scale are inherently compensated by the human operator. The study also demonstrated that repeated execution of pose patterns in a random order has shown promising precision of the end effector positioning of approximately $0.5\,\mathrm{mm}$. This proofs that the manipulator design concept and its implementation enable reliable and reproducible motion envelopes. This particularly addresses absence of motion disturbances caused by component friction resulting from assembly or installation of embedded actuation tubes. One approach for compensation of residual pose error in future is linear/non-linear kinematic calibration from external sensor input. The latter can be provided by similar optical tracking approaches such as presented in this contribution. The recorded data can be additionally integrated to optimisation or learning-based calibration strategies. The resulting output may enable specific kinematic model updates. Beyond that, incorporation of intrinsic sensing concepts, e.g. embedded fibre-based sensors for shape detection, facilitates online compensation of kinematic errors.

Tab. 5.2: Study metrics *accuracy* and *precision* of kinematic experiments in mm.

Metric	Poses								
	$x_{P,1}$	$x_{P,2}$	$x_{P,3}$	$x_{P,4}$	$x_{P,5}$	$x_{P,6}$	$x_{P,7}$	$x_{P,8}$	$x_{P,9}$
AP_P	0.23	2.29	2.20	2.48	1.75	2.47	2.67	2.79	2.16
RP_1	0.11	0.21	0.34	0.32	0.41	0.37	0.45	0.29	0.63

(a)

(b)
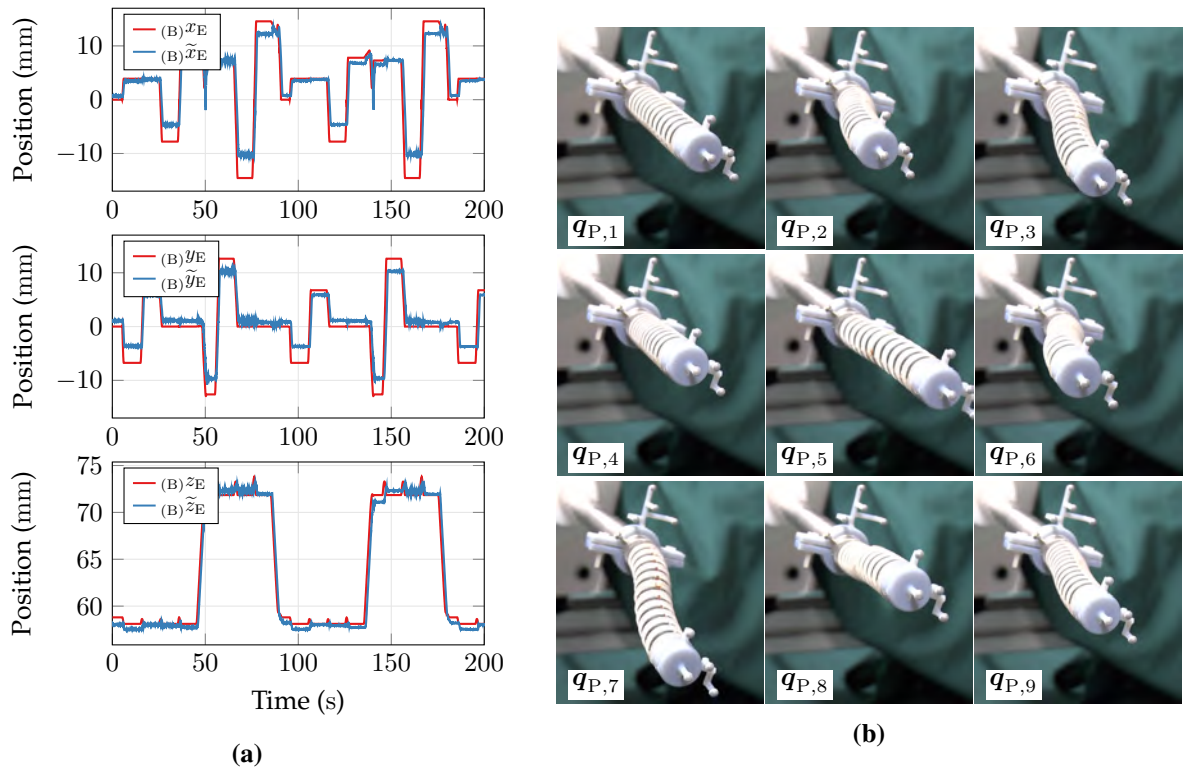
Fig. 5.8: Experimental evaluation of kinematic performance: (a) Comparison of model (red) and recorded optical tracking (blue) data in reference frame $(CF)_B$. (b) Qualitative overview of end effector poses $\boldsymbol{x}_P$ after execution of commands in joint space $\boldsymbol{q}_P$.

Model-free kinematic concepts based on machine learning may represent a promising approach that has already been applied to concentric tube robots [GMBK18]. This involves data-driven methodologies which use tracking data acquired from execution of various poses within the entire robotic workspace using the physical robotic prototype to obviate the need for specific model representations. Following this strategy, uncertainties and non-linearities are inherently considered in the learning workflow, which may cause significant reductions of the resulting pose errors. On the other hand, machine learning inference for online computation of the desired kinematic parameters, e.g. the inverse kinematic mapping from task to joint space, must enable timed results to be used in the cascaded control loops at low computational efforts.

Taking the results of the evaluation study into account, the distributed processing on different host computers within the ROS architecture realises a stable kinematic control cycle. However, the likelihood of disturbances related to communication timing sequences is increased due to the presence of non-real time data management within the present ROS ecosystem. This may result in instabilities of the control cycle which are forwarded to the kinematics module, commanded to the actuators, and cause excitation of structural end effector oscillations. Low amplitude oscillations may be suppressed and damped by the physical interaction of the operator and haptic master [HASH14]. This deficiency may be eliminated with a transition to real-time operating

environments and hardware. As an example, critical device infrastructures may run FreeRTOS compatible hardware[8]. On the contrary, this approach may increase prototyping efforts and needs further investigation.

5.3 Hand-Eye Calibration for Advanced Control

The design of the endoscopic continuum robot in this thesis considers a rigid attachment of both imaging sensors to the endoscopic tip. This constitutes an eye-in-hand imaging configuration, i.e. the sensors are manipulated by the continuum robot. Hence, advanced control concepts, which use visual information from endoscopic imaging, require calibration of the spatial transformation between imaging sensors and robotic end effector.

The metric perception of the surgical setting, e.g. from scene reconstruction or tracking data described in Sections 2.5 or 2.6, is generally expressed in camera frame $(CF)_L$. However, the spatial information expressed by transformation ${}^E\boldsymbol{T}_L$ to end effector frame $(CF)_E$, as depicted in Figure 5.9, is unknown and prevents the direct consolidation of sensor information to robotic control. This shortcoming generally addresses visual servoing and demands for application of hand-eye calibration to estimate the unknown transformation ${}^E\boldsymbol{T}_L$.

Various methods have been reported in robotics to solve the systems of equations for the unknown spatial transformation. This has incorporated calibration targets [HD95], structure-from-motion [AHE01], or hybrid approaches [MH03]. However, the restricted workspace of the endoscopic robot and the clinical deployment demand for reliable results and fast convergence. This favours methodologies using calibration targets. The corresponding fundamentals are briefly described in the following paragraphs.
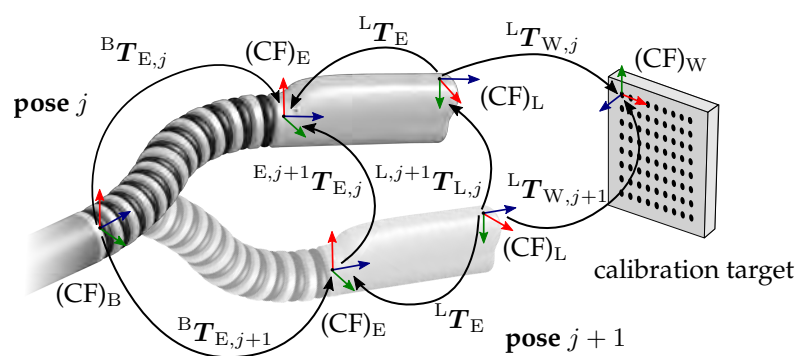
Fig. 5.9: Workflow of hand-eye calibration applied to an extensible continuum robot. As an example, the execution of two consecutive poses j and $j+1$ and the corresponding kinematic transformations are annotated.

The transformations ${}^{\mathrm{B}}\boldsymbol{T}_{\mathrm{E},j}$ and ${}^{\mathrm{L}}\boldsymbol{T}_{\mathrm{W},j}$ are related to pose j for N measurements in total (see Figure 5.9), where $j = \{1, \ldots, N\}$. Thus, transformation ${}^{\mathrm{B}}\boldsymbol{T}_{\mathrm{E},j}$ is computed using the kinematic model in Section 5.1.2, whereas ${}^{\mathrm{L}}\boldsymbol{T}_{\mathrm{W},j}$ is estimated from image-based pose estimation of frame (CF)$_{\mathrm{W}}$ in reference to the planar calibration target. This assumes a full calibration of stereoscopic imaging sensors according to Section 2.5. Thus, the differential transformation of two consecutively acquired poses in reference to base and end effector frame is given by

$$
{}^{\mathrm{E},j+1}\boldsymbol{T}_{\mathrm{E},j} = \left({}^{\mathrm{B}}\boldsymbol{T}_{\mathrm{E},j+1}\right)^{-1} {}^{\mathrm{B}}\boldsymbol{T}_{\mathrm{E},j} \tag{5.84}
$$

and linked to world and camera frame by

$$
{}^{\mathrm{L},j+1}\boldsymbol{T}_{\mathrm{L},j} = {}^{\mathrm{L}}\boldsymbol{T}_{\mathrm{W},j+1} \left({}^{\mathrm{L}}\boldsymbol{T}_{\mathrm{W},j}\right)^{-1} . \tag{5.85}
$$

The set of measurements in combination with the unknown transformation must satisfy the homogeneous set of equations

$$
\underbrace{\begin{pmatrix} {}^{\mathrm{L},1}\boldsymbol{T}_{\mathrm{L},0}\,{}^{\mathrm{L}}\boldsymbol{T}_{\mathrm{E}} \\ {}^{\mathrm{L},j+1}\boldsymbol{T}_{\mathrm{L},j}\,{}^{\mathrm{L}}\boldsymbol{T}_{\mathrm{E}} \\ \vdots \\ {}^{\mathrm{L},N}\boldsymbol{T}_{\mathrm{L},N-1}\,{}^{\mathrm{L}}\boldsymbol{T}_{\mathrm{E}} \end{pmatrix}}_{\boldsymbol{AX}} = \underbrace{\begin{pmatrix} {}^{\mathrm{L}}\boldsymbol{T}_{\mathrm{E}}\,{}^{\mathrm{E},1}\boldsymbol{T}_{\mathrm{E},0} \\ {}^{\mathrm{L}}\boldsymbol{T}_{\mathrm{E}}\,{}^{\mathrm{E},j+1}\boldsymbol{T}_{\mathrm{E},j} \\ \vdots \\ {}^{\mathrm{L}}\boldsymbol{T}_{\mathrm{E}}\,{}^{\mathrm{E},N}\boldsymbol{T}_{\mathrm{E},N-1} \end{pmatrix}}_{\boldsymbol{XB}} . \tag{5.86}
$$

The system in Equation (5.86) can be reduced to $\boldsymbol{AX} = \boldsymbol{XB}$, where $\boldsymbol{A}$ and $\boldsymbol{B}$ are composed of the stacked measurements and $\boldsymbol{X}$ is a stacked matrix which holds the unknown transformations. To solve the system for unknown matrix $\boldsymbol{X}$, related work used explicit camera models or intermediate transformations to solve Equation (5.86) [HD95, RDLD97], or addressed advanced strategies with global polynomial optimisation [HHP14].

Once a minimal set of at least three measurements was acquired, the linear system can be decomposed to linear and angular components as proposed in related work. Taking the characteristics of rotation matrices into account, the unknown angular component of ${}^{\mathrm{L}}\boldsymbol{T}_{\mathrm{E}}$ can be solved algebraically in the first step followed by the linear components. Related work has complemented this approach applying a dual quaternion representation for singularity-free representations [Dan98].

This workflow is summarised in Figure 5.10. The procedure uses a calibration target with circle pattern (9×8 grid size) and $1\,\mathrm{mm}$ pattern size. The target is located in front of the imaging unit and the endoscopic robot is commanded to nominal task space poses. The poses are generated randomly under the constraint of continuous target visibility to enable adequate excitation of linear and angular components. The commanded linear and angular ranges are within $\pm 5\,\mathrm{mm}$ and $\pm 10°$, respectively.

After each pose j was executed, the transformations ${}^{\mathrm{B}}\boldsymbol{T}_{\mathrm{E},j}$ and ${}^{\mathrm{L}}\boldsymbol{T}_{\mathrm{W},j}$ are recorded. Hereafter, the linear system in Equation (5.86) is composed and solved for the unknown transformation ${}^{\mathrm{E}}\boldsymbol{T}_{\mathrm{L}}$ applying the aforementioned described methodology. If the resulting RMS error $\varepsilon_{\mathrm{HC}}$ exceeds the predefined threshold $\tilde{\varepsilon}_{\mathrm{HC}}$, additional poses are requested to optimise the parameter excitation and achieve algorithmic convergence. This workflow was integrated into the ROS node *eyehandcalib* which uses customised code of the VISP library [MSC05] for target pose estimation.

An example of convergence characteristics and resulting linear and angular errors of an eye-in-hand calibration workflow are depicted in Figure 5.11. The demonstrates the convergence related to the increasing number of iterations of the optimisation algorithm. More specifically, the differences decrease with increasing number of acquired poses. The unknown transformation between the left camera sensor and end effector is estimated after 12 pose iterations to

$$
{}^{\mathrm{E}}\boldsymbol{T}_{\mathrm{L}} = {}^{\mathrm{L}}\boldsymbol{T}_{\mathrm{E}}^{-1} = \begin{pmatrix} 0.92 & -0.38 & -0.02 & -3.46 \\ -0.05 & -0.06 & -0.99 & 3.75 \\ 0.38 & 0.92 & -0.07 & 51.9 \\ 0 & 0 & 0 & 1 \end{pmatrix}. \tag{5.87}
$$

The workflow and transformation estimation has been executed repeatedly ($N = 8$). The results have been validated against ground-truth data obtained from CAD information of the endoscopic tip. The linear component has shown a relative RMSE of $8.9\,\%$ and the angular component of $10.2\,\%$. This demonstrates the applicability of the calibration procedure in combination with the extensible continuum robot. However, it is worth noting that the forward kinematic model has not been calibrated in the presented work. As outlined in [SH06], erroneous estimation of involved transformations due to disturbances of the encoder readings, modelling errors, or structural mismatch of the manipulator may impact the quality of the hand-calibration significantly. This can be addressed by involving external sensors for a comparative study on transformation estimation.

To the best of the authors knowledge, this is the first complete eye-in-hand workflow applied to dexterous multisegmental continuum robots. As discussed above, the calibration results may generally be affected by the quality of the intrinsic camera parameter estimation and the accuracy of the kinematic model. However, future work aims at improvements from ground-truth data based on tomographic assessment of the real sensor location in the prototypic tip or external tracking for
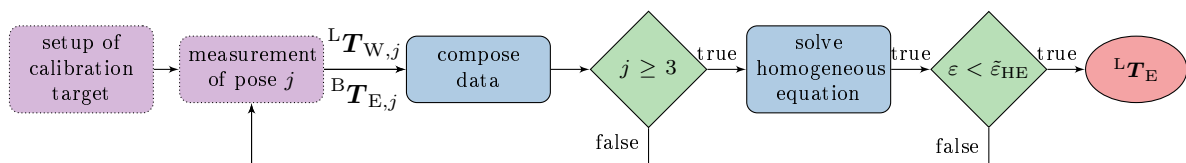
Fig. 5.10: Workflow for the hand-eye calibration of the endoscopic continuum robot. This enables estimation of the unknown transformation between end effector and left camera frame.
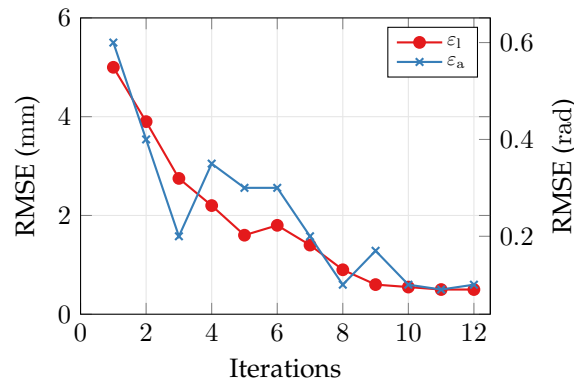
Fig. 5.11: Example of a hand-eye calibration convergence obtained from an eye-in-hand setup of an extensible continuum robot and a planar calibration target. The RMSE refers to the translational and angular residuals ε_l and ε_a between two consecutive pose measurements.

validation purposes. Furthermore, advanced deployment strategies to autonomous robotic tasks based on visual information are intended.

5.4 User Interface

The UI constitutes one of the core interface between the human operator and the robotic device. With respect to clinical deployment, UI designs must match clinical requirements and in particular enable application in potential use cases with low cognitive burden. The first challenge of the UI design targets its visualisation in an OR setting. Inspired by the review in [DF15] and the importance of 3D visualisation for MIS, two different stereoscopic visualisation strategies are proposed for ease integration of the presented system into clinical workflows.

The first concept uses a stereoscopic monitor with active shutter glasses. The concept of using a monitor integrates well into established OR environments and wireless, lightweight shutter glasses do not disturb clinical routines. The second approach considers a stereoscopic head mounted display (HMD), i.e. virtual-reality glasses. According to [DF15], this technology optimises immersion and can simulate a microscope-like setting comparable to well-recognised devices in laser surgery. Nonetheless, the operator must wear an additional device, which is not common in conventional clinical settings. The additional gear prevents an immediate transition in critical phases of surgical interventions.

Visualisation interfaces in this work use customised OpenGL shader pipelines provided by the *Oculus Rift DK 2* development kit to compensate the distortion of lenses of the HMD. Beyond that, further OpenGL libraries are considered for generation, rendering, and operator interaction with UI elements. To accommodate intuitive and comfortable interaction, a customised ROS node initialises a connection to the *Oculus Rift DK 2* hardware and reconfigures the general display settings automatically to generate the stereoscopic image composition from the grabbed endoscopic

chip-on-the-tip camera images. Afterwards, a side-by-side image stream is composed and redirected to the HMD. Once the initialisation of considered hardware components has been acknowledged, the endoscopic image raw data can be either displayed in the HMD or stereoscopic monitor. The image stream can be augmented with UI elements or assitive visual features.

This thesis has applied a tailored UI concept which only renders robotic core features at a glance to the operator and minimises the operator distraction. In this regard, UI elements were assigned to a central bar menu located at the top of the image stream. This location facilitates the user interaction while using different input devices. The menu is only visible if a user intention is detected, e.g. a button sequence is executed on the HMI. Otherwise, the set of elements fades out and restores the endoscopic image stream at full resolution. This concept only renders system information in case of user interaction or error messages. The composition and layout of the bar menu further follow a user-centred design, i.e. essential elements are grouped together and sub-menus are obviated. The menu consists of several buttons which enable activation of the laser beam, kinematic velocity settings, or abortion of the current task. Further on, visual servoing can be activated. The interface concept applies different colour schemes to indicate the progress of the surgical workflow and to inform the operator according to the notification level. As an example, visual elements dedicated to specific sequences of the clinical workflow change the colour from red over yellow to green, reflecting the sequence from initialisation of corresponding algorithm over requests for user interaction to the final execution of the selected task. To fulfil the requirements of stereoscopic visualisation for optimal user experience, UI elements are projected to the right endoscopic image using an average scene disparity. This eliminates visual disturbances from floating UI perception, which in particular distracts the operator from the surgical intervention due to continuous refocusing efforts of his eyes while switching elements in the augmented menu.

5.5 Conclusion

This chapter presented a novel robotic software framework for extensible continuum robots and its experimental evaluation. Firstly, a novel analytical approach for modelling the deflection and extension mechanisms of an unisegmental extensible continuum body was derived and extended from related work on manipulators with constant segmental lengths. These findings were included in spatial manipulator representations expressed in different kinematic spaces and complemented by inverse, forward, and inverse differential kinematics. Further on, the unisegmental model was transferred to an advanced manipulator description based on multibody kinematics in order to realise the full analytical model for the proposed two-segmental robotic design. Beyond that, the model was integrated into a kinematic control architecture to realise a closed-loop approach for task space tracking. Teleoperation of the slave robot using a commercial haptic master device was additionally addressed with respect to the presented framework. The workspace of the master manipulator was matched to the slave robot applying a registration workflow. The generation of

haptic feedback for common manipulation tasks was described. Taking those results into account, the model and control framework were evaluated in an experimental scenario and validated against measurements acquired from optical tracking of the continuum structure. The results demonstrated promising accuracies and precisions after assessment of the robotic prototype. In order to match the results of the simulation model and physical prototype measurements, a novel intermodal registration methodology was proposed. Lastly, key concepts of advanced visual control were demonstrated with a preliminary study on hand-eye calibration. This is further complemented by user interface concepts for optimisation of the human-machine interaction. The concepts focused on minimisation of cognitive burdens and distraction during clinical deployment. Future work addresses optimisation of the control latencies and model-free kinematic representations, such as learning-based strategies.

6 Assistive Technologies for Focal Adjustment in Teleoperated Laser Surgery

Laser ablation has been successfully introduced to various clinical scenarios. To the present day, lasers in soft tissue surgery mainly provide an alternative instrumentation to scalpels or electro-surgery due to challenging optical requirements, e.g. adjustment of the focal distance. Besides microscopic setups [Ste93], laser radiation is predominantly delivered through optical fibres in clinical applications, but particle deposits at the fibre tip may gradually decrease efficiency [MTK09]. Non-contact delivery of a focused beam (see Chapter 3) can result in constant intensities and prevent obstruction of the surgical view from instrument handling. This regards two modes of application: 1) A focused beam for local energy densities beyond ablation thresholds, and 2) a defocused beam for coagulation. However, manual non-contact delivery requires bulky spacers attached to the tip of the fibre or a direct line-of-sight. Extensive user training can further contribute to avoid laser-induced trauma.

As reported in Section 1.3, different robotic mechanisms were proposed to overcome limitations of manual laser manipulation in delicate anatomy. Major drawbacks of these devices are associated with disregard of spatial beam characteristics, i.e. the focal length of laser optics was neglected for ablation planning and execution nor dynamic focal adaptation were foreseen. Commonly, distances were set empirically with pilot ablations on the target area prior to the procedure while risks of tissue damage due to focal maladjustment constantly remain. This workflow is detrimental to results that were demonstrated with closed-loop laser processing units. Dynamic focusing systems with stereoscopic imaging [SKKO15] or optical coherence tomography [ZPW$^+$14] enable online adaptation of the laser focus to the specimen surface. Non-contact soft tissue ablation must consider accurate focal adjustment to the sample surface. In this thesis, robotic manipulation within Rayleigh length $z_\mathrm{R} \leq 1.75\,\mathrm{mm}$ is targeted for optimal energy delivery based on proposed laser optics (see Chapter 3). Recent closed-loop approaches fail to meet requirements of miniaturisation for intracorporeal deployment nor take use of manual intervention. Restricted intraoperative imaging of anatomical cavities and mandatory safety measures hamper straightforward concepts. Hence, teleoperation is still considered the gold standard for robot-assisted procedures [YCC$^+$17].

To overcome these limitations, spatial manipulation of the focussed laser at endoscopic scale is realised with the extensible continuum robot presented in previous Chapter 4. Teleoperation of robot kinematics enables online focal adaptation of fix-focus laser optics (see Chapter 3) with respect to the tissue surface. Beyond that, stereo imaging integrated to the endoscopic tip is used twofold: 1) scene visualisation to the operator and 2) generation of metrics for visual and/or
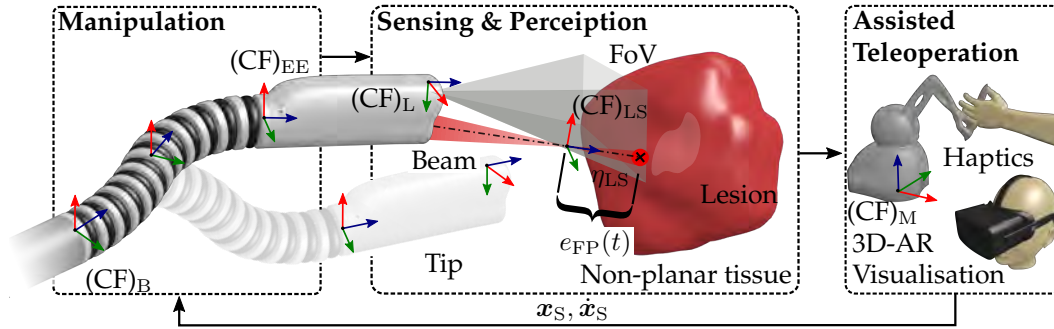
Fig. 6.1: Concept of assisted robotic focal positioning for non-contact laser ablation. The intersection of laser axis and tissue surface (red dot with cross marker) is monitored within the field of view (FoV) of the stereoscopic camera. Haptic and visual assistive features aim to minimise focal error e_{FP} between focal point $(CF)_{LS}$ and laser axis-surface intersection $\boldsymbol{\eta}_{IS}$.

haptic feedback for focal adjustment assistance. The latter has not been implemented in prior state-of-the-art laser surgery.

The performance of the proposed assistive concept was assessed in an experimental study with novice and expert users (15 subjects in total). This is the first study on combination of assistive feedback and an extensible continuum robot framework that specifically addresses requirements of non-contact laser surgery. The study comprised teleoperated adjustment tasks of registered focal position and a phantom surface with different feedback cues. The study aims to target and identify the effects from focal adjustment assistance deployed to the teleoperated continuum robotic framework and subject groups on study metrics, i.e. focal position error and task completion time. It is hypothesised that proposed feedback cues may enable intuitive and accurate adjustment of the registered focus position to the sample surface with errors of less than $0.75\,\mathrm{mm}$. Another assumption regards superior metrics of combined visuo-haptic[1] over haptic or visual assistance only. Methodologies and results are published to a great extend in [KSP+19].

In the following chapter, the robotic framework and study conditions are discussed in Section 6.1. Subsequently, the laser-camera-registration workflow is introduced in Section 6.2 and followed by implementation details related to the assistance framework (see Section 6.3). After the latter section, methodologies of the experimental study and assessment are presented in Section 6.4. Results are provided in Section 6.5. Lastly, the chapter closes with discussion and conclusion in Sections 6.6 and 6.7.

---

[1]also known as visual haptic in related work

6.1 Robotic Hardware

Considerations were made with the robotic platform described in Chapter 4 for teleoperation of the endoscopic tip. Operator input was captured by the haptic master stylus and transmitted to the slave robot. Relevant coordinate frames for kinematics and vision are indicated in Figure 6.1. The kinematics and control frameworks described in Chapter 5 were used. Motions of the endoscopic end effector were constrained explicitly for this study to one DoF, i.e. segmental extension and compression in z-direction of robotic base frame $(CF)_B$ with $_{(B)}x_S \approx 0$ and $_{(B)}y_S \approx 0$, respectively. Along with the release of the master stylus, the current position of the stylus was offset to $\boldsymbol{x}_{S,t} = (0,0,0)^T$ and stylus motion was locked to the x-direction of frame $(CF)_M$, whereas deviations in y and z directions were penalised with maximum device stiffness, i.e. $_{(M)}y_S \approx 0$ and $_{(M)}z_S \approx 0$. This facilitated one dimensional guidance of the master stylus along the x-axis of its reference frame. Additionally, users perceived a resistive force while executing motions in x-direction to moderate dynamic user inputs and to limit velocities to $v_{S,max} = 2\,\mathrm{mm\,s^{-1}}$ (see Section 5.1.4). Hence, forces rendered to the master with restricted y and z directions yield to

$$_{(M)}\boldsymbol{f}_{VL} = \begin{bmatrix} f_{VL,x} \\ k_y y_S \\ k_z z_S \end{bmatrix}, \tag{6.1}$$

where forces along the x-axis of the master device are defined by

$$f_{VL,x} = \begin{cases} -\frac{\kappa_x}{4}\dot{x}_S, & \text{if} \quad \frac{|\dot{x}_S|}{v_{S,max}} \leq 1 \\ -\kappa_x \dot{x}_S, & \text{otherwise} \end{cases}. \tag{6.2}$$

Parameters $\kappa_x = 5\,\mathrm{N\,s\,mm^{-1}}$, $k_y = 2.5\,\mathrm{N\,mm^{-1}}$, and $k_z = 1.5\,\mathrm{N\,mm^{-1}}$ defined anisotropic direction and temporal stiffness maxima of the hardware. The operator additionally perceived vibrotactile feedback whilst approaching manipulator workspace limits. The joint limit observer was activated and rendered vibrational bursts to the master device. This enabled indication of system warnings to the operator without disturbance of the main task. Rendered forces in Equation (6.2) were increased to hardware maximum if predefined limits were exceeded. The vibrational burst was computed for a duration of $t_B = 250\,\mathrm{ms}$ according to

$$_{(M)}\boldsymbol{f}_V = \beta \begin{bmatrix} \sin(\frac{2\pi}{t_B} f_B t) \\ 0 \\ 0 \end{bmatrix}, \tag{6.3}$$

where remaining parameters describe the vibration frequency $f_B = 150\,\mathrm{Hz}$, corresponding force amplitude $\beta = 1\,\mathrm{N}$, and time t starting from initialisation of the burst. As discussed in [FPO$^+$16], the selected frequency specifically stimulates human receptors and is well distinguishable. The
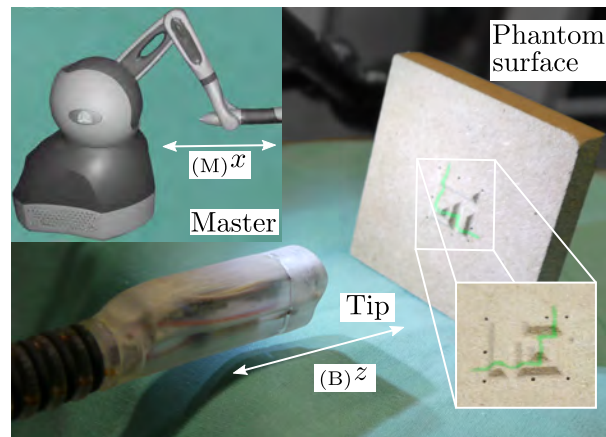
Fig. 6.2: Close-up view of endoscopic tip and phantom with haptic master in the top left corner. The arrow denotes the adjustment direction under consideration. The magnified view shows an example of the phantom design.

burst amplitude and duration were adapted to hardware limitations of the master device. This further enables rendering of system warnings to the operator without disturbance of the main task.

The laser optics presented in Section 3 were substituted with a laser diode (FLEXPOINT MINI, Laser Components GmbH, Olching, Germany) that emits radiation at a wavelength of $\lambda = 650\,\text{nm}$ to evade attenuation of visible radiation with fibre optics optimised for infrared transmission. The experimental scene in Figure 6.2 was additionally illuminated by an external cold light source to lower the heat flux within the endoscopic prototype. Stereoscopic camera images and augmented information were rendered to the user using a head-mounted display (Oculus Rift DK2, Oculus VR, Irvine, CA, USA) or stereoscopic monitor with 3D shutter glasses (VG278H, ASUSTeK Computer Inc., Taipeh, Taiwan). Kinematics and main controller ran at $100\,\text{Hz}$, vision at $25\,\text{Hz}$, and the haptic controller at $1\,\text{kHz}$. Stereoscopic camera images were processed using the optimised real-time surface reconstruction described in Section 2.5 on a workstation (Intel core i7, Intel Cooperation, Santa Clara, CA, USA) supported by GPGPU computation on a GeForce GTX Titan (NVIDIA Corporation, Santa Clara, CA, USA). Sensor and control data were processed on a dedicated workstation (Intel core i7, Intel Cooperation, Santa Clara, CA, USA).

6.2 Laser-To-Camera Registration

The incorporation of spatial properties of a focused laser beam to the robotic control and teleoperation framework requires registration of propagation axis and beam waist (focal position) with respect to an imaging modality. The rigid tip layout with imaging sensors and opto-mechanical components (see Chapter 4) motivated a spatial beam registration workflow prior to clinical deployment. This enables an initial localisation of the beam axis and focal spot in a customised setup without the need for re-registration prior to each clinical use. Likewise, challenging online

detection of the laser spot on nascent surfaces is eliminated. The latter was frequently applied to laser beam steering but disregarded spatial beam properties and posed risk of detection failure, e.g. specular highlights on glossy tissue surfaces [DMC15a, RTR$^+$17].

The proposed concept targets registration of laser characteristics with respect to the integrated stereoscopic camera and consideration of spatial information for robot kinematics. The corresponding experimental sequence of laser-to-camera registration is conceptually illustrated in Figure 6.3.

The stereoscopic camera observes the scene within the FoV and the visible red laser is activated. Laser spot $_{(LI)}\boldsymbol{p}_{LS,i} = (_{(LI)}u_i, _{(LI)}v_i)^T \in \mathbb{N}^2$ is detected in the left image plane. Robust detection applies colour segmentation in HSV^2 space followed by analysis of the binary image with connected-component labelling. The spot is subsequently mapped according to

$$_{(L)}\boldsymbol{P}_{LS,i} = h(\boldsymbol{D}, _{(LI)}\boldsymbol{p}_{LS,i}) = (_{(L)}x_i, _{(L)}y_i, _{(L)}z_i)^T \in \mathbb{R}^3, \qquad (6.4)$$

where $i = \{1, \ldots, N_{LS}\}$ describes the number of measurements, N_{LS} the total number of measured laser spots, and h the direct transformation $\mathbb{R}^2 \rightarrow \mathbb{R}^3$ between image plane and Cartesian space of (CF)$_L$ provided by depth map $\boldsymbol{D}$ (depth information linked to left image pixels) of real-time scene reconstruction. Position $_{(L)}\boldsymbol{P}_{LS,i}$ contains the three-dimensional intersection of laser spot and target. The latter is consecutively displaced and aforementioned procedure is repeated N_{LS}-times. Acquired laser positions are concatenated to measurement matrix

$$\boldsymbol{M}_{LS} = (_{(L)}\boldsymbol{P}_{LS,1}^T, _{(L)}\boldsymbol{P}_{LS,i}^T, \ldots, _{(L)}\boldsymbol{P}_{LS,N_{LS}}^T) \in \mathbb{R}^{N_{LS} \times 3}. \qquad (6.5)$$

An orthogonal distance regression is applied to $\boldsymbol{M}_{LS}$ to determine the laser propagation in camera frame (CF)$_L$. Firstly, mean-centred measurement data are obtained from linear transformation

$$\widehat{\boldsymbol{M}}_{LS} = \boldsymbol{H}_T \boldsymbol{M}_{LS} \in \mathbb{R}^{N_{LS} \times 3}. \qquad (6.6)$$
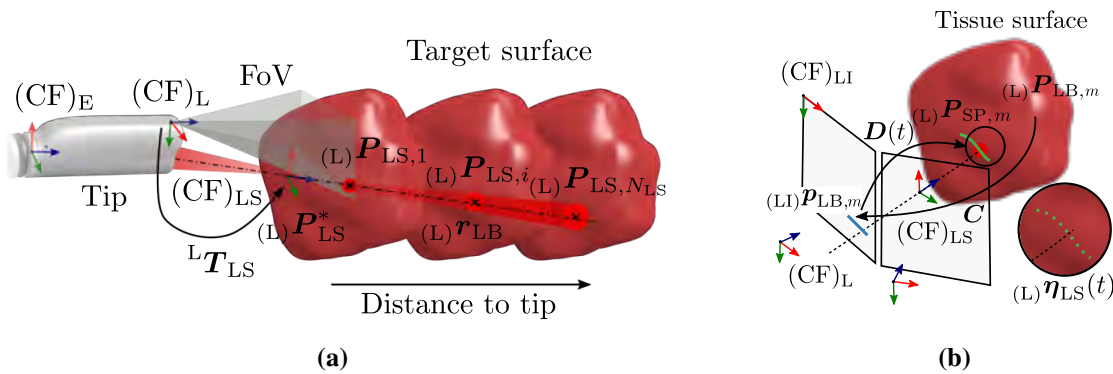
Fig. 6.3: (a) Laser-to-camera registration with increasing distance of the sample. (b) Estimation of laser-surface intersection with projection to image space (blue line) and tissue surface (green line).

---

^{2}Acronym for hue, saturation, and value. HSV separates intensity from colour information space.

The linear mapping is given by transformation matrix

$$\boldsymbol{H}_{\mathrm{T}} = \left(\boldsymbol{I} - \boldsymbol{b} \left(\boldsymbol{b}^{\mathrm{T}} \boldsymbol{b} \right)^{-1} \boldsymbol{b}^{\mathrm{T}} \right) \in \mathbb{R}^{N_{\mathrm{LS}} \times N_{\mathrm{LS}}}, \tag{6.7}$$

where $\boldsymbol{I} \in \mathbb{R}^{N_{\mathrm{LS}} \times N_{\mathrm{LS}}}$ is the identity matrix and $\boldsymbol{b} = (1,1,\ldots,1)^{\mathrm{T}} \in \mathbb{R}^{N_{\mathrm{LS}} \times 1}$ an all-ones vector. Singular value decomposition of the measurement matrix yields

$$\boldsymbol{U}\boldsymbol{\Sigma}\boldsymbol{V}^{\mathrm{T}} = \widehat{\boldsymbol{M}}_{\mathrm{LS}}^{\mathrm{T}}, \tag{6.8}$$

where unitary matrix $\boldsymbol{U} = (\boldsymbol{u}_1, \boldsymbol{u}_j, \ldots, \boldsymbol{u}_N) \in \mathbb{R}^{3 \times N_{\mathrm{LS}}}$ holds left-singular column vectors $\boldsymbol{u}_j \in \mathbb{R}^3$ of $\widehat{\boldsymbol{M}}_{\mathrm{LS}}^{\mathrm{T}}$ with $j = \{1, \ldots, N_{\mathrm{LS}}\}$. Hence, the directional vector of the laser axis is described by the first column of $\boldsymbol{U}$:

$$_{(\mathrm{L})}\boldsymbol{r}_{\mathrm{LB}} = \boldsymbol{u}_1. \tag{6.9}$$

The parametric linear laser beam propagation with respect to $(\mathrm{CF})_{\mathrm{L}}$ yields to

$$_{(\mathrm{L})}\boldsymbol{t}_{\mathrm{LB}} = \boldsymbol{P}_{\mathrm{LS}}^* + g_{(\mathrm{L})}\boldsymbol{r}_{\mathrm{LB}}, \tag{6.10}$$

where $\boldsymbol{P}_{\mathrm{LS}}^*$ is the experimentally determined focal position [KFS$^+$16] and $g \in \mathbb{R}$ is an arbitrary scaling factor along the beam axis. The position of the beam waist satisfies $_{(\mathrm{L})}\boldsymbol{t}_{\mathrm{LB}}(g = 0)$.

6.3 Assistance Concepts

Three novel assistive features for robot-assisted laser focus positioning are proposed in the following paragraphs. Feedback generation is generally based on focal position error

$$e_{\mathrm{FP}} = \left\| _{(\mathrm{L})}\boldsymbol{P}_{\mathrm{LS}}^* - {}_{(\mathrm{L})}\boldsymbol{\eta}_{\mathrm{IS}} \right\|_2 \tag{6.11}$$

which is computed at each control cycle from Euclidean distances between registered focal position $_{(\mathrm{L})}\boldsymbol{P}_{\mathrm{LS}}^*$ and intersection $_{(\mathrm{L})}\boldsymbol{\eta}_{\mathrm{IS}}$ of laser axis and recent surface reconstruction. The corresponding online estimation sequence is presented in Algorithm 6.1. The latter estimates intersection $_{(\mathrm{L})}\boldsymbol{\eta}_{\mathrm{IS}}$ without computationally expensive point cloud processing, such as Delaunay triangulation and ray casting. Initially, parametric beam $_{(\mathrm{L})}\boldsymbol{t}_{\mathrm{LB}}$ in Equation (6.10) is discretised with resolution $\gamma = 0.01\,\mathrm{mm}$ to positions $_{(\mathrm{L})}\boldsymbol{P}_{\mathrm{LB},m} = (_{(\mathrm{L})}\boldsymbol{P}_{\mathrm{LB},m}, 1)^{\mathrm{T}} \in \mathbb{R}^4$ in homogeneous representation and is added to set $B = \{_{(\mathrm{L})}\boldsymbol{P}_{\mathrm{LB},1}, {}_{(\mathrm{L})}\boldsymbol{P}_{\mathrm{LB},m}, \ldots, {}_{(\mathrm{L})}\boldsymbol{P}_{\mathrm{LB},N_{\mathrm{LB}}}\}$ with N_{LB} points in total and $m = \{1, \ldots, N_{\mathrm{LB}}\}$. Subsequently, elements of B are projected to image plane:

$$_{(\mathrm{LI})}\boldsymbol{p}_{\mathrm{LB},m} = \boldsymbol{C}_{\mathrm{L}(\mathrm{L})}\boldsymbol{P}_{\mathrm{LB},m}, \tag{6.12}$$

where $C_{\mathrm{L}} \in \mathbb{R}^{3\times 4}$ is the left camera matrix (see Section 2.5). As given in Equation (6.4), points $_{(\mathrm{LI})}p_{\mathrm{LB},m}$ are finally mapped to the reconstructed surface:

$$_{(\mathrm{L})}P_{\mathrm{SP},m} = h\left(D_{,(\mathrm{LI})}p_{\mathrm{LB},m}\right) \in \mathbb{R}^3. \tag{6.13}$$

Mapped surface positions are summarised to set

$$S = \{s_1, s_m, \ldots, s_{N_{\mathrm{LB}}}\} = \{_{(\mathrm{L})}P_{\mathrm{SP},1,(\mathrm{L})}P_{\mathrm{SP},m}, \ldots,_{,(\mathrm{L})}P_{\mathrm{SP},N_{\mathrm{LB}}}\}. \tag{6.14}$$

Distances of points $_{(\mathrm{L})}P_{\mathrm{SP},m}$ and parametric beam $_{(\mathrm{L})}t_{\mathrm{LB}}$ are computed as follows:

$$d_m = \left\| w_m - \left(w_m^{\mathrm{T}} u_r\right) u_r \right\|_2, \tag{6.15}$$

where unit vector $u_r = \frac{_{(\mathrm{L})}r_{\mathrm{LB}}}{\left\|_{(\mathrm{L})}r_{\mathrm{LB}}\right\|_2}$ of the laser beam direction (see Figure 6.3) is precomputed during algorithmic initialisation and $w_m = {}_{(\mathrm{L})}P_{\mathrm{LS}}^* - {}_{(\mathrm{L})}P_{\mathrm{SP},m}$ is computed for each element of set S. Lastly, estimated intersection is given by $_{(\mathrm{L})}\eta_{\mathrm{IS}} = {}_{(\mathrm{L})}P_{\mathrm{SP,min}} = \min\limits_{\forall s \in S} d(s)$. More specifically, the surface point with minimal distance to the parametric beam determines the estimated intersection of laser beam and surface. This approach shows robust algorithmic performance even in presence of protruding tissue or cavities due to direct line-of-sight assumptions.

The following list summarises implementation details, parameters, and settings for proposed assistive features:

Condition V: The distance between focal registration and actual target surface is exclusively visually encoded. This contribution extends visual augmentation that demonstrated feasibility in non-robotic adjustment tasks [SKL$^+$16]. In contrast to numerical representation of distances as implemented in commercial navigation suites, distances are processed, encoded into a colour-map, and are augmented with transparency to the endoscopic live view (see Figure 6.4a). The estimated laser spot position is highlighted with an augmented cross marker on the tissue surface. A symmetric colour model transforms temporal focal position error e_{FP} to a map obtained from real-time stereo reconstruction and focal registration within a range of $\pm 5\,\mathrm{mm}$. More precisely, the distance between focal position $_{(\mathrm{L})}P_{\mathrm{LS}}^*$ and surface intersection $_{(\mathrm{L})}\eta_{\mathrm{IS}}$ is computed along the laser axis for each pixel of D and transferred to a map composed of continuous colour gradients starting from red ($e_{\mathrm{max,u}} = 5\,\mathrm{mm}$) over green ($e_{\mathrm{min}} = 0\,\mathrm{mm}$) to red ($e_{\mathrm{max,l}} = -5\,\mathrm{mm}$). Optimal focal adjustment is achieved with green colour in close vicinity of the augmented cross marker. Distances out of the specified range were excluded. The resulting map is finally augmented to stereoscopic images using an opacity level of 50%, full image resolution of $(720 \times 576)\,\mathrm{px}$, and update rate of $23\,\mathrm{Hz}$.

Condition H: Haptic (kinaesthetic) feedback implements an active constraint rendered to the user through the master device. This thesis refers to an attractive constraint, i.e. the user is actively guided along the master x-axis. Force amplitudes are modulated by distance e_{FP} (see Equation (6.11)).

Algorithm 6.1:   Online estimation of intersection between laser axis and surface.

Input: Depth map D and parametric laser beam $_{(L)}t_{LB}$

1 (0) Initialise point sets B, S
2 (1) Discretisation of $_{(L)}t_{LB}$ to point set B
3 (2) Precompute unit vector u_r
4 (3) Project elements of B with camera matrix C_L to $(CF)_{(LI)}$
5 (4) Map projected elements with D to surface and add to set S
6 **foreach** s_m *in set S* **do**
7 $\quad$ (5) Compute vector w_m
8 $\quad$ (6) Compute distance d_m
9 $\quad$ **if** $d_m < d_{m-1}$ **then**
10 $\quad\quad$ (7) $d_{\min} = d_m$
11 $\quad$ **end**
12 **end**
13 **return** $_{(L)}\boldsymbol{\eta}_{IS}(t) = s(d_{\min})$
$\quad$ **Output:** Estimated laser-surface intersection $_{(L)}\boldsymbol{\eta}_{IS}(t)$

The corresponding active constraints

$$f_{AC} = \begin{cases} \frac{1}{f_{\max}} e_{FP}^2, & \text{if} \quad e_{\min} \leq e_{FP} \leq e_{\max,u} \\ -\frac{1}{f_{\max}} e_{FP}^2, & \text{if} \quad e_{\max,l} \leq e_{FP} \leq e_{\min} \quad \in \mathbb{R}, \\ \pm f_{\max} & \text{otherwise} \end{cases} \tag{6.16}$$

are equivalently mapped to a range of $\pm 5\,\text{mm}$ and amplitudes are moderated by a quadratic polynomial as shown in Figure 6.4b, where $f_{\max} = 3.3\,\text{N}$ is the force limit of the haptic device. Finally, forces rendered to the master device are given by

$$_{(M)}\boldsymbol{f}_H = \begin{bmatrix} f_{AC} \\ 0 \\ 0 \end{bmatrix} + {}_{(M)}\boldsymbol{f}_{VL} + {}_{(M)}\boldsymbol{f}_V \in \mathbb{R}^3. \tag{6.17}$$

Force f_{AC} only contributes to the x-direction of frame $(CF)_M$, i.e. in the direction of focal adjustment along the optical axis. Beyond that, force $\boldsymbol{f}_H$ is activated after the user initiates the measurement. No additional visual information or assistance was provided apart from the virtual laser intersection.

Condition VH: Assistive features V and H are combined to a novel visuo-haptic guidance for laser surgery. The user is concurrently provided with visual information related to condition V and haptic feedback from condition H. Hence, a decreasing force towards approaching a green colour adjacent to the augmented laser marker is perceived. Feature settings are equivalent to previous conditions.

Condition N: This condition regards deactivation of all assistance features. No visual augmentation or haptic rendering related to the actual error e_{FP} is provided. Forces $_{(\text{M})}\boldsymbol{f}_{\text{VL}}$ and $_{(\text{M})}\boldsymbol{f}_{\text{V}}$ vibration are exclusively rendered . The augmented laser marker is additionally provided. Users are encouraged to estimate and adjust the distance only from endoscopic stereo imaging. This condition is the reference for benchmarking proposed assistive features.

6.4 Study Methodologies

In the following, methodologies of experimental subject trials, postexperimental evaluation, and assessment are summarised and detailed.

6.4.1 Experimental Protocol

The user study evaluated the performance of assistive conditions for interactive focal adjustment using the teleoperated robotic framework. The scenario targeted a one DoF motion for exclusion of task interferences expected from movements in multiple DoF. Subjects received written information, and gave informed consent for participation and data processing. Data were recorded and stored anonymously.

The experimental supervisor introduced each subject to the scientific background and robotic framework. A five minutes introductory phase was given to get accustomed to the experimental hardware. Prior to each experimental series, sequences related to the four conditions were randomised with four repeated measurements per condition ($N = 16$). Before activation of each condition, the supervisor moved the slave robot to an arbitrary position with respect to the target surface to establish a random initial configuration.

Phantom targets with levels of planar surfaces and unknown visual characteristics to all subjects were fabricated from medium-density fibreboards (MDF) with stamped patterns for exclusion of side effects. The patterns (see Figure 6.2) acted as visual references, i.e. landmarks for distance estimation. The overall dimensions were $(50 \times 50 \times 10)\,\text{mm}^3$ with pattern sizes of approximately $(10 \times 10)\,\text{mm}^2$ to enable imaging within the endoscopic FoV.

Subjects initiated each measurement with the stylus front button and started completion of the given task. The latter considered teleoperation of the slave robot in one DoF with endoscopic visualisation until error e_{FP} at the location of the augmented laser marker was minimised under assigned condition. Completion of the task was triggered by pressing the front button again. The procedure was repeated until the sequence of the assigned user task was completed.

Scaling matrix $\boldsymbol{S}_{\text{M}} = \text{diag}\{0.8, 0, 0\}$ was applied to user inputs. Thus, motions in x-direction of the master frame were scaled, whereas y and z directions were locked. This scaling factor was heuristically determined for optimal coverage of the master workspace. Joint limit avoidance was
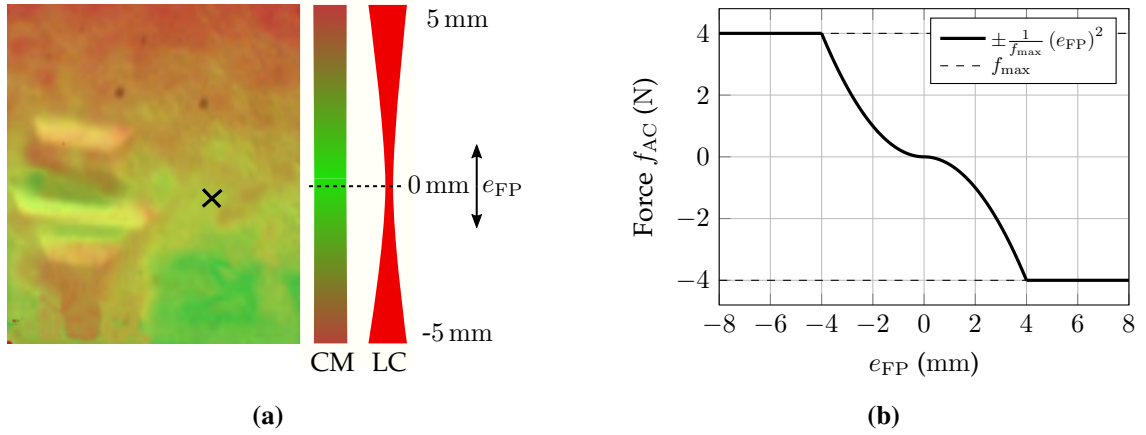
Fig. 6.4: Assistive features: (a) Condition V: Example of augmented colour overlay showing a planar surface with stepped pyramids in lower left corner. Colour map (CM) and associated laser caustics (LC) of distance e_{FP} within range $\pm 5\,\mathrm{mm}$. The augmented cross marker indicates the intersection of laser axis and surface. (b) Condition H: Forces f_{AC} related to error e_{FP} are rendered to the user using a quadratic polynomial. Distances exceeding the specified range are mapped to maximum output forces of the master.

activated for protection of the robotic hardware. This prevents excessive extension and contraction of the continuum manipulator. Workspace limits were indicated to the operator with vibrational bursts.

Data for task performance assessment was continuously acquired, synchronised after user activation, and labelled with timestamps. In particular, error time series

$$\boldsymbol{e}_{\mathrm{FP}} = (e_{\mathrm{FP}}(t_0), e_{\mathrm{FP}}(t_k), \ldots, e_{\mathrm{FP}}(t_{N_{\mathrm{K}}}))^{\mathrm{T}}, \tag{6.18}$$

was recorded for each time instance in Equation (6.11), where t_0 indicates the start of the experiment, t_k the k-th sample with $k = \{0, \ldots, N_{\mathrm{K}}\}$, and $t_{N_{\mathrm{K}}}$ the end of the experiment with N_{K} samples in total. The temporal resolution of the captured data was approximately $40\,\mathrm{ms}$ governed by imaging acquisition rates. Additional data comprised master/slave kinematics, image data, and haptic controller output. Following the trials, participants were asked to complete a subjective assessment. The questionnaire in Table 6.1 was composed of a bespoke NASA task load index protocol [HS88] and an after scenario questionnaire [Lew91]. A set of 16 statements was associated to a five point Likert scale that is ranked from rejection to agreement with ordinal numbers from 0 to 4.

6.4.2 Evaluation Workflow

Task completion time (TCT) and *focal position error* (FPE) are the task performance metrics. The TCT determines the duration from the first robotic motion after user activation of the master until device deactivation. The FPE describes the residual Euclidean error between registered focal

position $_{\text{(L)}}\boldsymbol{P}^*_{\text{LS}}$ and intersection $_{\text{(L)}}\boldsymbol{\eta}_{\text{IS}}(t)$ of laser axis and target surface at the end of each task after period TCT. This relation yields to

$$\text{FPE} = e_{\text{FP}}(t = \text{TCT}).\tag{6.19}$$

Corresponding time series e_{FP} were postprocessed for determination of metrics FPE and TCT related to each experiment. Typically, temporal data of e_{FP} comprised three sections (see Figure 6.5): 1) Start phase without robot motion, 2) random motion phases (teleoperation), and 3) end phase without device motion. Thanks to the recurrent patterns in recorded data, semi-automatic computation of TCT and FPE was feasible.

Main contributions of the evaluation workflow are highlighted in Figure 6.5. At first, user interaction is required for coarse selection of regions of interest RoI_{j} with $j = \{1,2\}$ for start (RoI_1) and end (RoI_2) phases. Selected data points of e_{FP} for each RoI_j are assigned to set

$$\zeta_{\text{R,j}} = \{e_{\text{FP}}(t_1), e_{\text{FP}}(t_k), \ldots, e_{\text{FP}}(t_{N_k})\}\tag{6.20}$$

with $k = \{1, \ldots, N_k\}$ time steps. Afterwards, phases are automatically detected in each RoI_j with upper and lower thresholds

$$\kappa_{\text{u},j} = \mu_{\text{FPE},j} + 2\sigma_{\text{FPE},j}\tag{6.21}$$

$$\kappa_{\text{l},j} = \mu_{\text{FPE},j} - 2\sigma_{\text{FPE},j},\tag{6.22}$$

where $\mu_{\text{FPE},j}$ and $\sigma_{\text{FPE},j}$ are the mean and standard deviation of elements in set $\zeta_{\text{R},j}$. Subset $\zeta_{\text{P},j} \subset \zeta_{\text{R},j}$ aggregates elements that comply with start and end phase condition

$$\{e_{\text{FP}}(t_k) \in \zeta_{\text{R},j} | \kappa_{\text{l},j} < e_{\text{FP}}(t_k) < \kappa_{\text{u},j}\}.\tag{6.23}$$

The TCT is indicated as duration between first e_{FP} exceeding thresholds of start phase ($e_{\text{FP}}(t_k) < \kappa_{\text{l},1} \vee e_{\text{FP}}(t_k) > \kappa_{\text{u},1}$) and the first e_{FP} that fell within these boundaries related to the final phase. Finally, the mean of elements in set $\zeta_{\text{P},2}$ expresses the error metric, i.e. $\text{FPE} = |e_{\text{FP}}(t = \text{TCT})| = \mu_{\text{FPE},2}$.

6.4.3 Statistical Analysis

The statistical analysis determines effects of conditions or experimental parameters on performance metrics FPE and TCT. The latter represent dependent variables. This work further introduces three independent variables: assistive *condition*, repeated *measurement*, and subject *experience*. Within-subject factors are represented by four-level factors *condition* and *measurement*. Condition *measurement* regards the number of trials per condition and subject (four). *Condition* decodes investigated feedback scenarios, i.e. V, VH, N, and H. Between-subject factor *experience* adapts a two-level description based on subject experience, i.e. novice or expert. Concisely, dependent
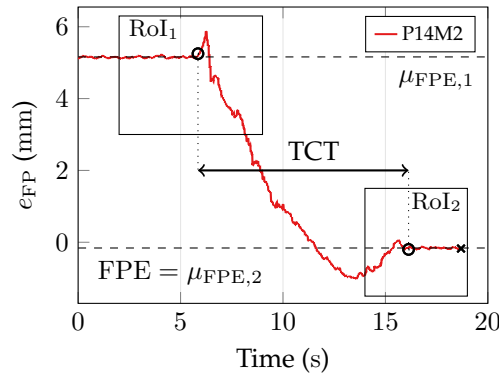
Fig. 6.5: Overview of performance evaluation for measured focal position error e_{FP}. Regions of interest (RoI) are selected interactively for data processing. Task completion time (TCT) and static focal position error (FPE) were determined accordingly. The data was extracted from trial M2 of subject P14.

Tab. 6.1: Questionnaire for subjective task evaluation.

No.	Statement	Score
1	The focus position can be adjusted more satisfactory with activated assistance.	R (0) - A (4)
2	I prefer a visual feedback over a haptic feedback.	R (0) - A (4)
3	I prefer a combined feedback over a single feedback.	R (0) - A (4)
4	The system is easy to operate.	R (0) - A (4)
5	The application of the system is precise.	R (0) - A (4)
6	I need more time for familiarisation with device and application.	R (0) - A (4)
7	I think I need the support of a technician for device operation.	R (0) - A (4)
8	I find the system unnecessarily complex.	R (0) - A (4)
9	I think I would use the system frequently.	R (0) - A (4)
10	I think the system functions are well integrated.	R (0) - A (4)
11	I am satisfied with my performance in the given task.	R (0) - A (4)
12	The application of the system is safe.	R (0) - A (4)
13	I would recommend the system to peers.	R (0) - A (4)
14	I felt stressed or languid with this task.	R (0) - A (4)
15	The use has made me physically tired.	R (0) - A (4)
16	The technical characteristics of the system were sufficient to complete the task.	R (0) - A (4)

Note: Rejection (R) and acceptance (A).

variables were acquired during experimental series for every combination of within-subject and one level of between-subject factors.

The analysis targets to identify significant differences between populations of data grouped by factors. Initially, participants were regarded as joint group with within-subject factors only. Secondly, a mixed design of within- and accommodated between-subject factor *experience* was introduced. These assumptions motivated the consideration of parametric multi-way analysis of variances (ANOVA).

Data was analysed with statistical framework R [R C15]. The general workflow of data analysis comprised the following steps as discussed in [Mac11]: 1) Data preparation to group metrics and selected factors, 2) outlier inspection, 3) verification of residual normality, 4) two- or three way ANOVA dependent on factors (within/between), and 5) post-hoc tests if main effects were statistically significant. If required, further tests, e.g. sphericity for between-subject factors, were applied.

Package *lme4* was used for model fitting [BMBW15], *lmerTest*[KBC17] for ANOVA, and *lsmeans* for post-hoc analysis [Len16]. The data model addressed an interaction of factors *condition* and *measurement* related to fixed effects (each subject performed all conditions) and incorporated a random effect model for selected *subject*.

6.5 Results

The study comprised 15 subjects and multiple experimental series per subject and condition ($N = 240$). In detail, three participants (assistant physicians, senior physician) from the Department of Otorhinolaryngology, University Hospital Ulm, Germany completed trials ($N = 47$) in the group of experts with two males, one female, and an age of 30.1 years on average. In the group of novices, 12 subjects (graduate students, research assistants) from the Institute of Mechatronic Systems, Leibniz Universität Hannover, Germany participated in experiments ($N = 180$) with ten males, two females, and an age of 25.8 years on average. Experts had prior training in endoscopic procedures and vision. In contrast, novices had no prior experience in endoscopy. A limited set of measurements ($N = 13$) was excluded from postexperimental evaluation due to interrupted data recordings. All subjects selected the 3D monitor for visualisation of the endoscopic image stream.

6.5.1 User Study Metrics

An example of user performances for different assistance conditions is presented in Figure 6.6. It is noticeable in Figure 6.6a that condition N resulted in FPE of above $1.75\,\mathrm{mm}$. After an initial adjustment, no further corrective motion was introduced by the operator due to absence of feedback. Thus, the FPE exclusively depends on visual estimation and experience of the operator. By contrast, conditions V (see Figure 6.6b) and H (see Figure 6.6c) show comparable results. Subjects that were
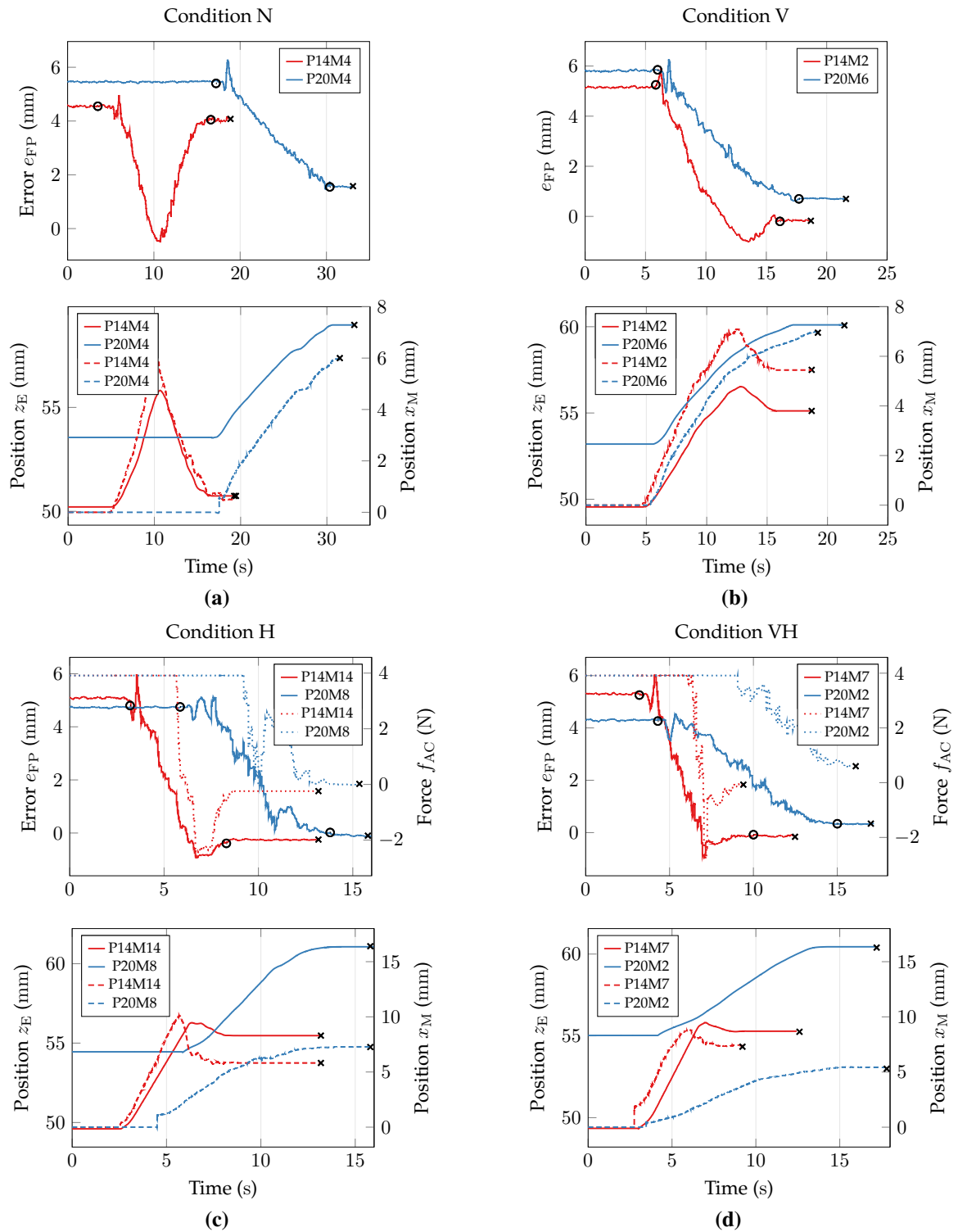
Fig. 6.6: Examples of study results for subjects P14 and P20 with (a) no (N), (b) visual (V), (c) haptic (H), and (d) visuo-haptic feedback (VH). If applicable, line styles define: e_{FP} (solid), slave position z_E (solid), master position x_M (dashed), and active constraint f_{AC} (dotted). Markers × and ○ indicate end of measurement and detected phase of interaction.

already familiar with the symmetric representation of the colour augmentation or active constraints immediately converged to FPE below $0.5\,\text{mm}$. On the contrary, lack of familiarisation resulted in overshooting followed by convergence in the first trial. Nonetheless, force feedback lowered TCT in comparison to visual feedback. Notably, combined visuo-haptic feedback in condition VH (see Figure 6.6d) further reduced FPE below $0.3\,\text{mm}$ at the expense of increased TCT.

Study metrics are consolidated to box plots in Figure 6.7 and listed in detail in Tables 6.2 and 6.3. The merits of proposed assistance on FPE reduction are demonstrated in Figures 6.7a and 6.7c. Haptic, visual, and visuo-haptic feedback reduced FPE and corresponding outliers to below $1\,\text{mm}$ already after the first trial of each subject. The results further match optical requirements for laser-tissue interaction given by the Rayleigh length [KFS$^+$16] and prove a quick and intuitive subject familiarisation. Remarkably, Figure 6.7e reveals lower FPE for experts compared to novices with respect to condition N.

Inferential statistics were applied to determine significant effects and interactions of the study. The significance level was $\alpha = .05$ and confidence intervals (CI) are reported. A two-way repeated measures ANOVA with two-within (*condition*, *measurement*) and no between-subject factor were selected. A tree-way mixed ANOVA was chosen for split subject groups (*condition*, *measurement*, *experience*). As detailed in Section 6.4.3, factor *measurement* refers to the number of experimental trials.

Data residuals satisfied assumption of normality after logarithmic transformation as assessed by normal Q-Q plots and Shapiro-Wilk tests ($p > .05$). There were no statistically significant results for two-way interaction of *condition* and *measurement*, ($F_{9,113} = 1.501, p = .109$), and main effect of *measurement* ($F_{3,39} = 2.158, p = .156$). On the contrary, a main effect of *condition* revealed a statistically significant difference of FPE, ($F_{3,40} = 24.893, p < .001$). Thus, a post-hoc test of pairwise comparisons without Bonferroni adjustment was considered. Contrasts of levels V - VH, V - H, and VH - H did not show statistically significant differences ($p > .05$). However, FPE were significantly different for comparison of levels V to N, a mean difference of $0.81\,\text{mm}$, 95% CI [0.40, 1.22], levels VH and N, a mean difference of $0.92\,\text{mm}$, 95% CI [0.50, 1.34], and levels H and N, a mean difference of $0.8\,\text{mm}$, 95% CI [0.38, 1.22]. In brief, proposed conditions significantly reduced the FPE in comparison to absence of assistance.

By analogy, TCT data was inspected for outliers using the box plot representation. Normality of residuals was assessed with normal Q-Q plots and a Shapiro-Wilk test ($p > .05$). There was no statistically significant interaction of *condition* $\times$ *measurement* ($F = 1.06, p = .39$). However, there were statistically significant main effects of *condition* ($F = 7.11, p < .05$) and *measurement* ($F = 6.39, p < .05$). A post-hoc test was conducted and TCT differences were not statistically significant for contrasts V - N, VH - H, VH - N, and H - N ($p > .05$). On the other hand, TCT were significantly different for comparison of levels V and VH, a mean difference of $4.6\,\text{s}$, 95% CI [3.3, 5.9], and levels V and H, a mean difference of $5.7\,\text{s}$, 95% CI [4.4, 7.1]. In short, haptic and visuo-haptic feedback significantly reduced TCT compared to visual feedback only.
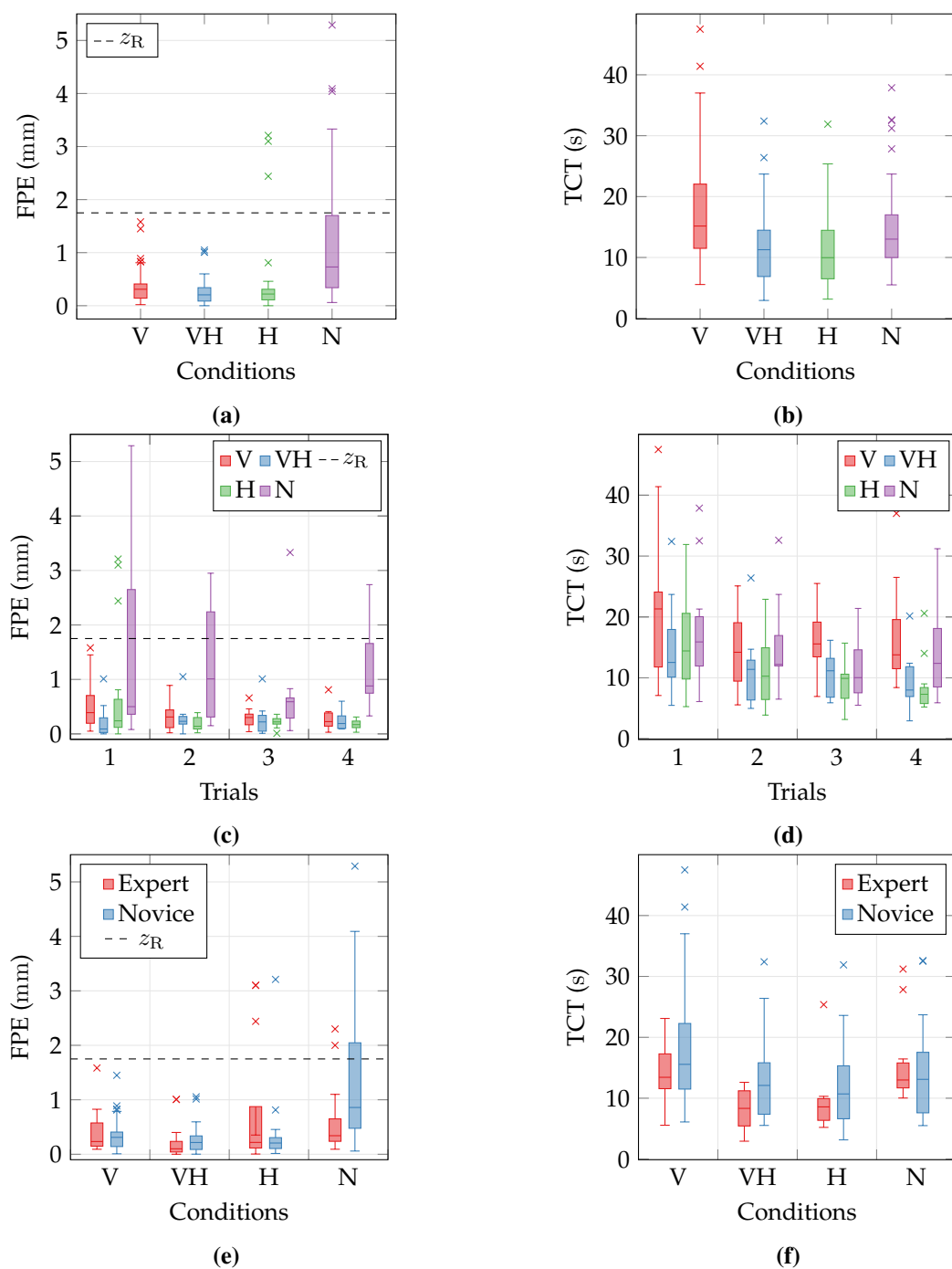
Fig. 6.7: Box plots of focal position error (FPE) and task completion time (TCT) metrics for visual (V), visuo-haptic (VH), haptic (H), and no feedback (N): (a), (d) Condition-resolved results. (b), (e) Trial-resolved results. (c), (f) Condition-resolved split to subject groups. Rayleigh length z_R is provided for comparison. Horizontal dashes in the box depict the median and cross symbols indicate outliers. Boxes define 0.25 and 0.75-quantiles of input data. Upper and lower whisker span all data within 1.5 interquartile range of the nearer quartile.

Split subject groups were assessed with a three-way mixed ANOVA. Residual normality of each subset was tested after logarithmic transformation and validated according to previous analysis. Mauchly's test indicated violation of sphericity for *measurement* ($W = 0.39, p = .001, \varepsilon = 0.57$) and *condition* ($W = 0.18, p = .0001, \varepsilon = 0.55$). Greenhouse-Geisser estimates of sphericity correction was applied. There was interaction of *experience* $\times$ *condition* ($F_{3,39} = 5.95, p = .01$) and a statistically significant main effect of *condition* ($F_{3,39} = 9.52, p = .002$). This indicates that *condition* impacted FPE linked to *experience*. A post-hoc test without Bonferroni adjustment was applied and indicated significant differences within the subject group of novices for pairs V - N, VH - N, and H - N ($p < .05$) and in between subject groups for corresponding pairs of H and N ($p < .05$). In summary, results related to novices reflect statistical study findings. In contrast, experts did not cause statistically significant differences due to lower FPE of condition N.

TCT data of split subject groups was inspected with normal Q-Q plots. Normality of subsets was validated with Shapiro-Wilk tests ($p > .05$). Mauchly's test indicated that sphericity was violated for interaction *measurement* $\times$ *condition* ($W = 0.01, p = .001, \varepsilon = 0.40$). After Greenhouse-Geisser correction, there was statistical significant interaction of *experience* $\times$ *condition* ($F_{9,117} = 4.61, p = .007$) and a main effect of *measurement* ($F_{3,39} = 4.29, p = .01$). There were no statistically significant effects related to *condition* ($p > .05$).

6.5.2 User Experience

Results of the postexperimental survey are presented in Figure 6.8. Statements are consolidated to groups of interest and assigned to categories *learning curve* (S6, S7, S9), *stress* (S4, S8, S14, S15), *performance* (S5, S11, S16), and *design* (S10, S12, S13). Results are detailed in Figure 6.8a and for categories in Figure 6.8b. The reported user experience generally corroborates the experimental findings. Results (mean $\pm$ SD) of categories *learning curve* (3.43 ± 0.87), *performance* (3.44 ± 0.59), and *design* (3.37 ± 0.63) were consistently rated within the upper quarter of the five-point Likert scale. This indicated a positive user consent for the robotic hard- and software in use. The *stress* rating (1.07 ± 0.38) indicated a low overall stressor. Moreover, statements S1-S3 describe task specific user experiences. Most of the subjects favoured assisted

Tab. 6.2: Focal position error (FPE) in mm of assisted focal positioning study per subject group and condition.

	V			VH			H			N		
	Mean $\pm$ SD	Mdn	Max	Mean $\pm$ SD	Mdn	Max	Mean $\pm$ SD	Mdn	Max	Mean $\pm$ SD	Mdn	Max
	0.36 ± 0.32	0.31	1.58	**0.25 ± 0.25**	0.21	1.05	0.37 ± 0.67	0.22	3.21	*1.20 ± 1.21*	0.73	5.29
Expert	0.43 ± 0.44	0.23	1.58	**0.26 ± 0.37**	0.10	1.01	*0.85 ± 1.24*	0.22	3.10	0.66 ± 0.74	0.34	2.30
Novice	0.35 ± 0.28	0.31	1.45	**0.25 ± 0.22**	0.22	1.05	0.27 ± 0.46	0.21	3.20	*1.34 ± 1.21*	0.86	5.29

Note: Visual (V), visuo-haptic (VH), haptic (H), and no feedback (N). Numbers marked in bold indicate the best performance; numbers marked in italics indicate the worst performance.

Tab. 6.3: Task completion time (TCT) in s of assisted focal positioning study per subject group and condition.

	V			VH			H			N		
	Mean ± SD	Mdn	Max	Mean ± SD	Mdn	Max	Mean ± SD	Mdn	Max	Mean ± SD	Mdn	Max
	17.2 ± 8.3	15.2	47.5	12.5 ± 9.2	11.3	62.7	**11.5 ± 6.5**	9.9	31.9	14.7 ± 7.4	13.0	37.9
Expert	**11.2 ± 5.4**	9.4	22.5	15.2 ± 5.2	13.2	23.7	*17.1 ± 6.5*	18.9	23.6	15.3 ± 9.7	14.5	32.6
Novice	*18.2 ± 8.3*	16.8	47.5	12.2 ± 9.5	10.2	62.7	**10.7 ± 6.2**	9.8	31.9	14.6 ± 7.1	13.0	37.9

Note: Visual (V), visuo-haptic (VH), haptic (H), and no feedback (N). Numbers marked in bold indicate the best performance per group; numbers marked in italics indicate the worst performance per group.

(3.87 ± 0.35) over non-assisted scenarios. Subjects mainly disagreed with statement S2 and tend to haptic over visual assistance (1.33 ± 1.05). Likewise, visuo-haptic feedback was preferred over single feedbacks (3.72 ± 0.67).

Similar results were observed within subject groups (see Figures 6.8c and 6.8d). However, expert scores were consistently lower for the majority of statements in comparison to novices. Statistical analysis was applied to category related data. A non-parametric Mann-Whitney-U test was considered for assessment of statistical significance of mean differences between categories due to nonconformity of residual normality $(p < .05)$. No significant differences of categories *learning curve* $(W = 196, p = .3)$ and *stress* $(W = 321, p = .48)$ were revealed. However, *performance* $(W = 70, p < .05)$ and *design* $(W = 45, p < .05)$ were statistically significant with differences towards higher mean scores of novice users.

6.6 Discussion

The optimal setting of the focus-to-tissue distance is one of the key factors for successful non-contact laser surgery. Applications for osteotomy addressed these challenges with closed-loop scanning and dynamic focus units based on additional sensor information, e.g. OCT [FPB⁺15]. However, deployment in MIS requires miniaturised and safe concepts that empower clinicians to adjust the focal position online as part of the interventional workflow. Currently, this cannot be realised by full procedural automation as regulatory guidelines prevent high levels of robotic autonomy. Hence, assistance for teleoperation enables clinicians to benefit from symbiosis of passive or active feedback augmented to the main task and dexterous robotic manipulation.

Commenting on the study findings, the proposed assistance framework demonstrated effective application of haptic and visual feedback mechanisms for operator guidance during focal adjustment. Based on visual distance estimation from endoscopic images only, large FPE beyond $5.5\,\mathrm{mm}$ with means of $1.25\,\mathrm{mm}$ were measured. These results impede atraumatic non-contact delivery due to insufficient local energy densities and motivated assistive concepts. By contrast, effects of visual and/or active haptic assistance were extensively studied in this contribution. The FPE was

reduced by a factor of four to below of $0.4\,\mathrm{mm}$ for the entire set of assistive features in combination with robotic distance adjustments using the extensible continuum manipulator. The comparison of results with activated assistance shows a superior effect of visuo-haptic condition VH over conditions V and H. Haptic guidance occasionally lead to FPE outliers of $3\,\mathrm{mm}$, almost factor two compared to condition V. This was expected to individual perception of force transitions described in Figure 6.4b or operators with low acceptance for active guidance, i.e. enforcement of various counter movements. On the other hand, visual assistance drastically minimised outliers at the expense of prolonged TCT. The latter was associated with familiarisation and perception of the gradually changing symmetric colour map and the diversion of subjects' attention to avoid overshooting of target positions, whereas completion times were comparable to condition N. Conditions VH and H have resulted in lower

These findings were correlated to survey results, e.g. combined features VH were favoured by individuals over individual feature V or H. Results grouped to categories described a positive
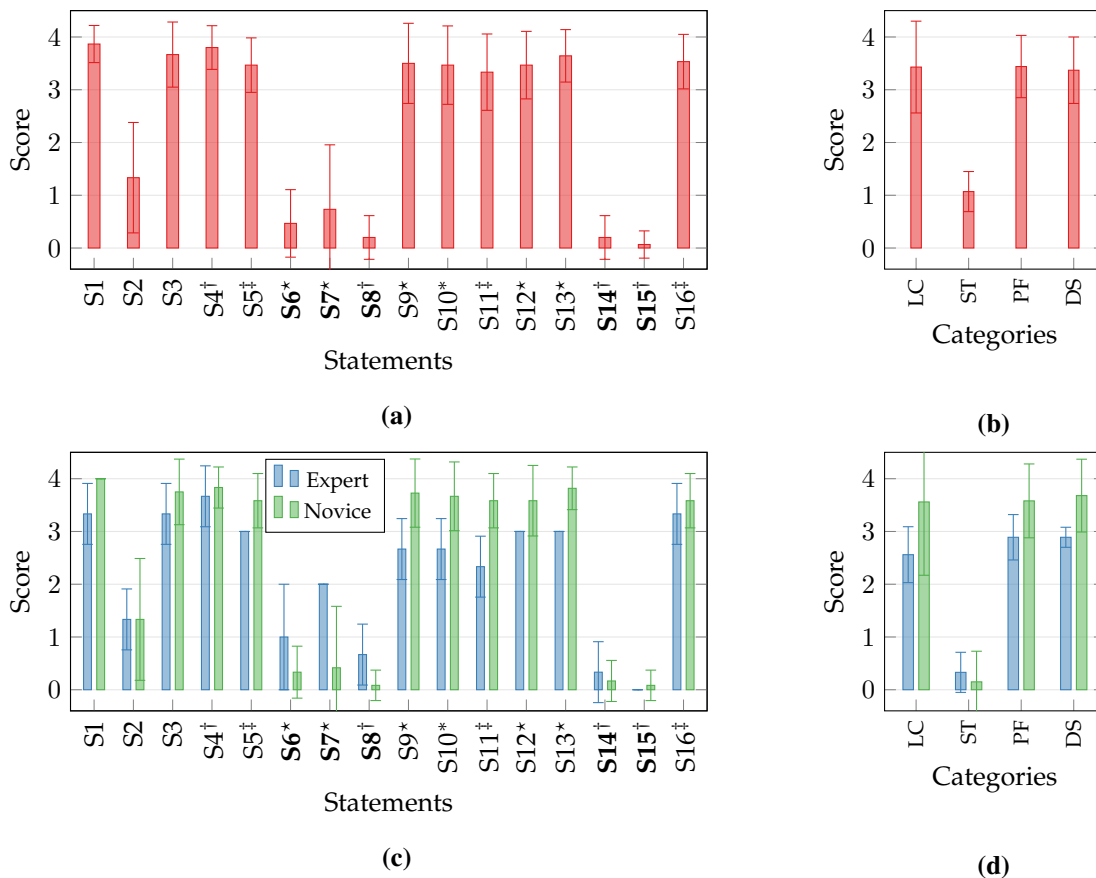
Fig. 6.8: Results of the qualitative user feedback: (a) Scores related to individual statements and (b) grouped to categories. (c) Scores of between-subject factor split to subject groups related to individual statements and (d) grouped to categories. Category labels indicate learning curve (LC), stress (ST), system performance (PF), and system design (DS). **Bold** labels indicate negative statements. Statements are assigned to categories by markers: † to ST, ‡ to PF, ∗ to LC, and ⋆ to DS.

user satisfaction in the upper quarter of the scoring range for learning curve, performance, and system design with low task-associated stress. This underlines the user-centred design approach and motivates future improvements driven by end user feedback.

The results underline that the proposed assistance is applicable to adjust and maintain the FPE within the nominal Rayleigh range [KFS+16]. However, current limitations of the system are: 1) Measurements are subject to RMSE of approximately $0.1\,\mathrm{mm}$ from employed reconstruction algorithm and camera hardware [SKL+16]. 2) Tube displacement accuracies are in the range of $0.1\,\mathrm{mm}$ and are limited by available drive encoders. 3) Occasional stick-slip oscillation with amplitudes below $0.1\,\mathrm{mm}$ in lateral direction resulted from material pairing of concentric tubes and may be optimised with specific tubular surface coatings.

6.7 Conclusion

The adjustment of the focus-to-tissue distance must be considered for gentle and atraumatic tissue ablation in teleoperated robotic non-contact laser surgery. To this aim, novel feedback concepts for user guidance were proposed and evaluated on a robotic platform for minimally invasive laser surgery. Subject trials with novices and clinical experts demonstrated positive effects. Users were able to adjust the focal position accurately within a short time. Future performance evaluation will be conducted in cadaver studies and with multi-DoF laser manipulations. Proposed assistance may become an add-on for robotic laser surgery using commercial platforms, e.g. the SPORT system (Titan Medical Inc., Toronto, ON, Canada) or the Flex®-System (Medrobotics Inc., Raynham, MA, USA).

Future work may address aforementioned limitations and more importantly the integration of the high power laser source to the endoscope. The platform will be further assessed with advanced user studies on *ex vivo* tissue and cadaver models with multi-DoF beam manipulation. Based on survey results, future directions may comprise alternative modalities for haptic guidance in proximity of the nominal position with user specific attractive or repulsive characteristics, hybrid schemes with coarse and fine mode, or vibration features. Last but not least, shared autonomy with partial task automation may be considered to lower cognitive operator loads.

7 Preclinical Performance Evaluation of the Robotic Framework

Atraumatic non-contact laser surgery is based on optimal adjustment of the laser focus (see Chapter 6) and the accurate delineation of pathologies with manipulation of the laser spot on the tissue surface to preserve delicate structures. These two criteria endow an optimal surgical outcome with reduced collateral trauma of adjacent healthy tissue and consideration of tumour margins. However, accurate control of laser displacement in confined luminal spaces is challenging. An alternative robotic platform for endoscopic laser delivery is presented in Chapter 4 aiming at dexterous beam manipulation in MIS. The robotic kinematics in combination with a highly integrated endoscopic tip target shortcomings of related work and facilitate clinical deployment. The kinematics merits of extensible continuum segments are demonstrated for user assistance of intraprocedural one DoF focal adjustment (see Chapter 6). By contrast, this chapter targets evaluation of the overall robotic multi-DoF manipulation and control performance. Proposed methodologies and results are published to a great extend in [KGS$^+$20].

The chapter is outlined as follows. Firstly, a preclinical user study focuses on the robotic teleoperation performance in simulated preclinical tasks, i.e. planar pathology delineation. Secondly, the previous study is extended to three-dimensional laser manipulation supported by assistance introduced in Chapter 6. Feasibility studies complement the preceding work with a stability analysis of the visuo-haptic controller and spatial laser manipulation on porcine samples. The chapter closes with a report on preliminary device deployment to an *ex vivo* animal model and conclusion.

7.1 Teleoperated Laser Manipulation on Planar Surfaces

This section is dedicated to the evaluation of manipulator performances of the integrated robotic platform. An experimental user study with twenty subjects from clinical and engineering background was conducted. Associated tasks mimicked laser tracing and delineation of tissue pathologies. Side effects during robot manipulation resulting from the design of the master device were mitigated by imposed constraints on the executable task space and assumption of planar target surfaces, i.e. lateral laser spot motion in two DoF only, as shown in Figure 7.1. This concentrates subjects' perception on task completion. However, the integration of the stereoscopic camera to the endoscopic tip causes scene motion corresponding to teleoperation input. This may cause operator confusion and discomfort while directing attention to the laser beam and surgical site. The augmentation of motion stabilisation to the endoscopic live view may support the intraoperative perception as

reported for vessel outlining in surgical videos [SLKO16]. Two different visualisation concepts are proposed to analyse effects of dynamic scenes. Motion stabilised and non-stabilised stereoscopic images are rendered to the operator. Path tracing error and task completion times constitute the study metrics.

7.1.1 Experimental Setup

This study considered a teleoperated robotic setup composed of master and slave devices introduced in Chapters 6 and depicted in Figure 7.2b. Cartesian motion of the robotic end effector is computed by the kinematic controller and differential kinematics described in Chapter 5 with specific workspace mapping between master and slave robot. However, end effector motion was restricted to three DoF translation for initial experiments and to two DoF during task execution as detailed in the introduction of this chapter. Master input was captured initially as $_{(M)}\boldsymbol{x}_{S,t}(t) = \left(_{(M)}x_S(t), _{(M)}y_S(t), _{(M)}z_S(t)\right)^T$ and for task completion as $_{(M)}\boldsymbol{x}_{S,t}(t) = \left(0, _{(M)}y_S(t), _{(M)}z_S(t)\right)^T$. This constraint ensures execution of lateral motion only. Master input was scaled isotropically with matrix $\boldsymbol{S}_M = \mathrm{diag}\{0.5, 0.5, 0.5\}$. Angular input to the master device is neglected due to absence of torque feedback and degenerated usability. The maximum Cartesian velocity of the master was limited by haptic cues to $v_{S,max} = 5\,\mathrm{mm\,s^{-1}}$ and the gains of the kinematic pose controller were heuristically tuned to $\boldsymbol{K}_C = \mathrm{diag}\{0.5, 0.9, 0.9\}$. Joint limit avoidance was immediately activated after release of the stylus to preserve structural integrity.

Bespoke specimens with nominal ablation patterns were designed and manufactured from planar MDF samples. Derived from clinical ablation patterns, five different shapes (S-shape, half circle, line, inclined line, and square) were applied to the surface (1 mm line width) using customised stamps and green coating (NEON Pigment Ink, Rico Design GmbH, Brakel, Germany) (see Figure 7.2a). The selection of a distinctive colour facilitated the image processing workflows.
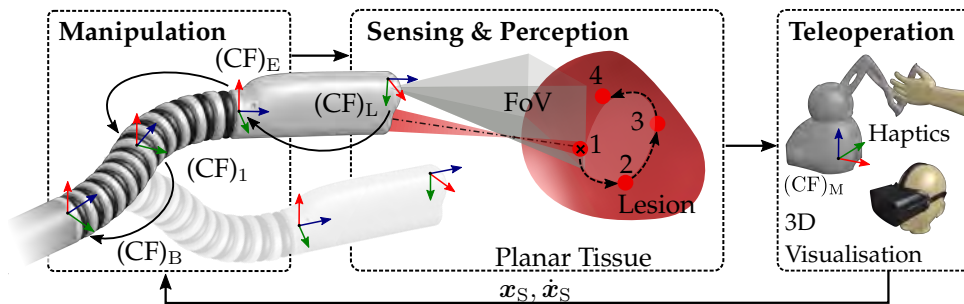
Fig. 7.1: General setup for robot-assisted laser delineation of a lesion on a planar tissue sample. The intersection of the laser and surface (red dot with cross marker) is continuously monitored and displaced in two DoF by the operator using a haptic master device. The laser spot is guided along via locations (1 - 4) along the outline of the lesion. Endoscopic images are visualised by a head-mounted display or stereoscopic monitor.

Average pattern lengths were between $12\,\mathrm{mm}$ and $44\,\mathrm{mm}$. During task execution, specimens were located arbitrarily within the FoV of the endoscopic stereo camera as shown in Figure 7.2b.

Subjects were provided with two different visualisation conditions. Condition NS concerns absence of motion compensation and renders the endoscopic raw image stream to the operator. Contrarily, condition AS augments scene motion compensation to the user interface. More precisely, the motion of the observed scene resulting from the robotic eye-in-hand camera setup and executed tracing motion is compensated to provide the user with a virtually created static scene. This focusses the user attention on the pattern tracing tasks using the pilot laser. Further on, it is hypothesised that distraction from scene motion is minimised. This approach is based on tracking methodologies presented in Section 2.6 and the algorithmic parametrisation according to [SKKO17]. The image warping technique to generate motion-compensated scene images in this work extends the fundamental work in [SLKO16] to a virtual stereoscopic visualisation setting using obtained disparity information.

Images are overlaid to the user interface and displayed on a stereoscopic monitor (VG278H, ASUSTeK Computer Inc., Taipeh, Taiwan) or head-mounted display (Oculus Rift DK2, Oculus VR, Irvine, CA, USA).

Data acquisition for computation of task metrics comprised: 1) detection of the nominal path at the beginning of each task, (2) online detection and processing of the laser centroid, and (3) recording of master/slave kinematics data as well as image streams. The latter were acquired at rates of $100\,\mathrm{Hz}$ and $25\,\mathrm{Hz}$, respectively.

7.1.2 User Study Design

The user study considered a quantitative device performance assessment in a preclinical deployment scenario. A custom task was designed to recreate intraoperative laser ablation workflows for resection soft tissue pathologies. Hence, a predefined nominal path must be traced with a visible laser beam using robotic teleoperation in multiple DoF. As described in Section 7.1.1, two different visualisation conditions were considered to assess effects of the eye-in-hand camera layout. Subjects manipulate the slave robot in two in-plane DoF to facilitate tracing motion and an initial out-of-plane DoF for adjustment of the distance to the specimen. Participants received written information on the study and gave consent for study participation and postexperimental data analysis. All experiments were conducted according to ethical standards of Leibniz Universität Hannover. No user experiments were performed with high power laser radiation due to local safety regulations. The laser radiation source was replaced by a visible red laser (FLEXPOINT MINI, Laser Components GmbH, Olching, Germany).

Prior to each experimental series, the supervisor introduced individuals to the procedure, hardware, and scientific background. Twenty subjects were asked to select a preferred visualisation modality,
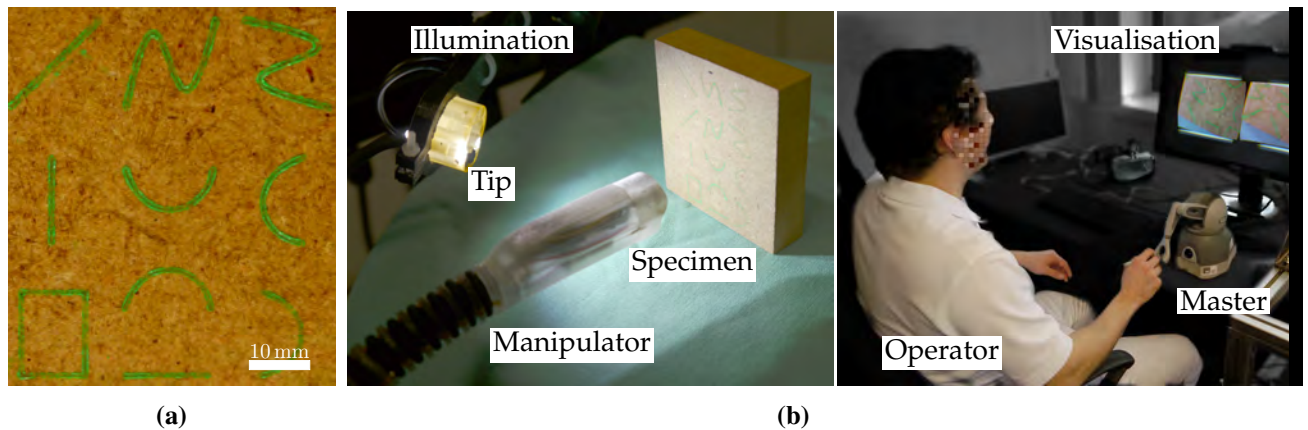
Fig. 7.2: Experimental setup for evaluation of robotic performance on a planar phantom: (a) Set of coated patterns with various shapes on MDF specimen. (b) Operator with haptic master and scene visualisation through 3D monitor. Side-by-side images are provided for demonstration purposes.

i.e. 3D monitor or head-mounted display, and were given a familiarisation period of five minutes. Subjects were not allowed to change the modality throughout the entire experimental series.

Nominal delineation paths ($N = 10$) and visualisation conditions (no image stabilisation, active image stabilisation) were randomised prior to each subject series with five repeated measurements per visualisation condition. Selections from the five different path patterns in Figure 7.2a must comply with an equal drawing distribution.

At the beginning of each experiment, the supervisor moved the endoscopic tip, i.e. the laser spot, in proximity to the nominal path. Subsequently, a RoI enclosing the selected pattern was defined in the user interface of endoscopic live images to initialise the image-based measurements. The subject started the task by activating the visible red laser with a foot pedal. The master device was released with a stylus button and the operator was asked to complete the tracing task with objectives of minimal path error and as fast as possible. Termination of measurements were triggered by executing previous steps in reverse order. The operator commanded the robot during tasks execution in two in-plane DoF, whereas the initial phase considered adaptation of the distance to the tissue in the additional out-of-plane DoF with visuo-haptic assistance. During this experiment the focal position error threshold of $\pm 1\,\mathrm{mm}$ was set, axial displacement of the master stylus was locked, the visuo-haptic assistance was deactivated, and measurements for postexperimental evaluation were initiated. Lateral motion of the laser spot in two DoF was feasible to trace the nominal pattern. The previous experimental workflow was repeated until randomised series were completed.

Subsequent to trial completion, participants contributed to a survey for subjective assessment of experimental conditions and user experience. The customised questionnaire listed in Table 7.1 combines the NASA task load index protocol (TLX) [HS88] and the after scenario questionnaire (ASQ) [Lew91]. Statements were rated on a five point Likert scale with scoring 0 - 4 ranging from rejection to agreement. In total, 14 statements were composed and linked to the scoring range.

Tab. 7.1: Questionnaire for subjective task evaluation.

No.	Statement	Score
1	The system is easier to operate with image stabilization activated than without.	R (0) - A (4)
2	The system is easy to operate.	R (0) - A (4)
3	The application of the system is precise.	R (0) - A (4)
4	I need more time for familiarisation with with device and application .	R (0) - A (4)
5	I think I need the support of a technician for device operation.	R (0) - A (4)
6	I find the system unnecessarily complex.	R (0) - A (4)
7	I think I would use the system frequently.	R (0) - A (4)
8	I think the system functions are well integrated.	R (0) - A (4)
9	I am satisfied with my performance in the given task.	R (0) - A (4)
10	The application of the system is safe.	R (0) - A (4)
11	I would recommend the system to peers.	R (0) - A (4)
12	I felt stressed or languid with this task.	R (0) - A (4)
13	The use has made me physically tired.	R (0) - A (4)
14	The technical characteristics of the system were sufficient to complete the task.	R (0) - A (4)

Note: Rejection (R) and acceptance (A).

7.1.3 Image-based Measurements

Quantitative evaluation of user tasks demands for measurements of the laser spot position and nominal path to determine deviations. This approach considers two steps: 1) Detection of the nominal path at the beginning of each trial within the selected RoI and 2) online detection of the laser spot with respect to the nominal centreline. The camera configuration constitutes an eye-in-hand setup, i.e. the camera displacement corresponds to the motion of the robotic end effector, which correlates with the use of integrated stereoscopic sensors in combination with online scene recovery and tracking algorithms for deviation assessment. Details of the computational pipeline are presented in the following paragraphs.

Detection of Nominal Laser Path

The detection workflow of the nominal path assumes that the scene is captured by the embedded camera system and a coated green path was selected for the tracing task in accordance with the experimental protocol in Section 7.1.2. A RoI enclosing the nominal path, is defined in the user

interface and visual processing depicted in Figure 7.3 is triggered at time step t_0 at the beginning of each experiment.

Stereoscopic image acquisition and depth map processing were executed as explained in Section 2.5. The left image $\boldsymbol{I}_\mathrm{L}$ is converted to HSV colour space and colour segmentation with heuristic parametrisation of thresholds is applied to match the properties of the green coating. The resulting binary image $\boldsymbol{I}_\mathrm{BP}$ is further analysed with morphological operators for connected areas. A thinning algorithm is applied to the remaining binary area [ZS84] to obtain a nominal path $_{\mathrm{(LI)}}\boldsymbol{t}_\mathrm{NP} = \left(\boldsymbol{p}_{\mathrm{NP},1}, \boldsymbol{p}_{\mathrm{NP},i}, \ldots, \boldsymbol{p}_{\mathrm{NP},N}\right)$ composed of points $_{\mathrm{(LI)}}\boldsymbol{p}_{\mathrm{NP},i} = (u_{\mathrm{NP},i}, v_{\mathrm{NP},i})^\mathrm{T} \in \mathbb{N}^2$ given in left pixel space $(\mathrm{CF})_\mathrm{LI}$ with $i = \{1, \ldots, N\}$, where N defines the total number of segmented points. Subsequently, elements of $_{\mathrm{(LI)}}\boldsymbol{t}_\mathrm{NP}$ are mapped to camera frame $(\mathrm{CF})_\mathrm{L}$:

$$_{\mathrm{(L)}}\boldsymbol{P}_{\mathrm{NP},i} = h\left(\boldsymbol{D}(t_0), {}_{\mathrm{(LI)}}\boldsymbol{p}_{\mathrm{NP},i}\right) = \left({}_{\mathrm{(L)}}x_{\mathrm{NP},i}, {}_{\mathrm{(L)}}y_{\mathrm{NP},i}, {}_{\mathrm{(L)}}z_{\mathrm{NP},i}\right)^\mathrm{T} \in \mathbb{R}^3, \tag{7.1}$$

where h is the direct transformation $\mathbb{R}^2 \to \mathbb{R}^3$ with corresponding depth map $\boldsymbol{D}$ provided by scene reconstruction. Finally, concatenation of elements yields nominal path

$$_{\mathrm{(L)}}\boldsymbol{t}_\mathrm{NP} = \left({}_{\mathrm{(L)}}\boldsymbol{P}_{\mathrm{NP},1}, {}_{\mathrm{(L)}}\boldsymbol{P}_{\mathrm{NP},i}, \ldots, {}_{\mathrm{(L)}}\boldsymbol{P}_{\mathrm{NP},N}\right) \in \mathbb{R}^{3 \times N}. \tag{7.2}$$

Completion of the processing pipeline is indicated to the operator to commence the task. Data is stored persistently for analysis. In case of detection errors, the workflow is automatically reinitialised, image frames are acquired, and data is revalidated.

Detection of Laser Spot Positions

After nominal laser path detection, subjects activated teleoperation and started task completion. The experimental assessment of the resulting tracing error necessitates for detection and computation of the actual laser spot position on the specimen surface with processing workflows presented in the following paragraphs.

Visual measurements in general comprise data sets composed of motion-compensated images of the left camera $\boldsymbol{I}_\mathrm{LS}(t_k)$ and corresponding depth map $\boldsymbol{D}(t_k)$. Data is consolidated from both sources and is then synchronised at discrete time step t_k with approximate-time policies provided by the ROS framework[1].

The experimental protocol in Section 7.1.2 ensures that the operator must activate the visible laser, which causes the incident beam to reflected from the target surface. Consequently, the centroid of the visible laser spot $\boldsymbol{p}_\mathrm{LC}(t_k) = (u_\mathrm{LC}(t_k), v_\mathrm{LC}(t_k))^\mathrm{T} \in \mathbb{N}^2$ must be detected in image $\boldsymbol{I}_\mathrm{LS}(t_k)$ to provide correlated measurements for the experiment.

---

[1]`http://wiki.ros.org/message_filters`
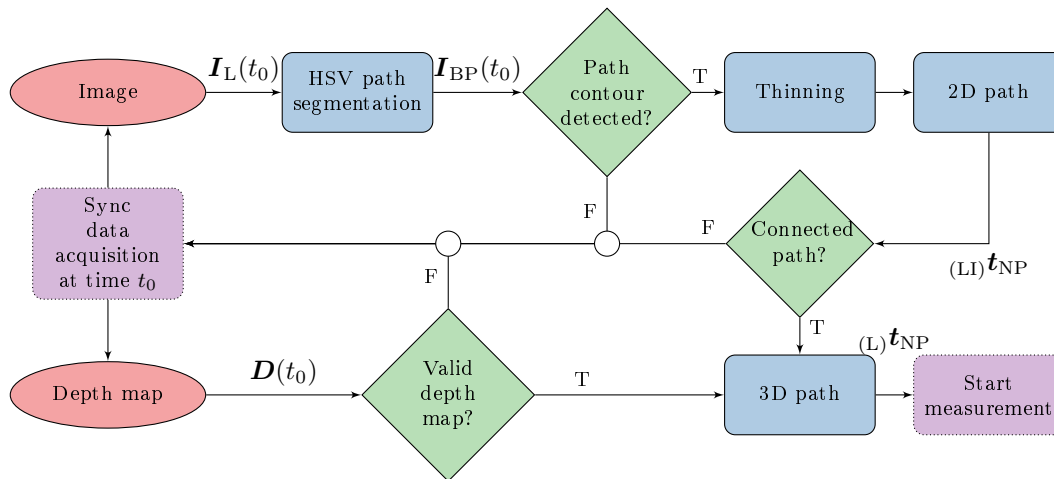
Fig. 7.3: Flowchart of image processing phases for nominal path detection, segmentation, extraction, and mapping from image to 3D camera space. Once the operator commences the given task, a single set of stereoscopic images is acquired and processed accordingly. Acronyms: False (F) and true (T).

Robust and fault-tolerant detection of laser spots incident to technical or tissue surfaces was addressed in prior work. The latter assumes a salient optical response of laser-tissue-interaction, i.e. appearance of unique bright spots or saturation of the image sensor. However, disturbances, such as specular highlights or absorption, caused by irregular structures or challenging illumination may impact detection rates. Preceding approaches used for laser spot detection in the image space include template matching, modified circular Hough detectors, frame-to-frame analysis, colour-based segmentation (visible radiation), mesh-based approaches, Fourier and Zernike transforms, diffusion models, or convolutional neuronal networks (CNN) [JWJBLWJ05, Ban11, KSM14, GMKL14, VOKSA$^+$16].

Since algorithms for robust spot detection are useful to potential applications and the surgical environment, sequences of incident laser radiation were recorded with embedded imaging of the robotic platform using external illumination to simulate realistic conditions, i.e. specimen inclination and/or surface moisture with saline solution. As an example, scene images that concern nascent challenges of the user study are shown in Figure 7.4. Optical responses of tissue substitutes and porcine samples differ in terms of sensor saturation, spot size, and speckle intensity. The speckle intensity corresponded to the level of moisture, surface roughness, and sample inclination; however, Gaussian-shaped intensity distributions were present in the spot areas.

An analysis of reported algorithms was conducted to assure optimal performance throughout the user study. Two methods were investigated in detail on acquired image sequences: 1) template matching (TM) with normalized cross correlation measure [CFA$^+$12] and 2) colour-based thresholding (CBT) for frame-wise spot detection of the laser spot in stabilised left image $I_{\mathrm{LS}}(t_k)$. CBT uses the HSV colour space and is complemented by morphological operators for artefact removal and a minimal area filter yielding binary map $I_{\mathrm{BC}}(t_k)$. Image moments applied to the binary image enables estimation of the laser centroid $_{(\mathrm{LI})}p_{\mathrm{LC}}(t_k)$. Selected algorithms were integrated to the

vision framework and executed on acquired imaging sequences ($N = 5$) corresponding to each type of specimen/tissue with approximately 50 frames each. The TM sequence was initialized using a template of the pilot spot subsequent to laser activation. CBT was parametrized with a heuristically-tuned threshold of saturated pixels in HSV colour space. Ground truth was obtained from frame-wise manual expert annotation of the spot centre location. The evaluation metric was denoted as detection rate. Positive outcomes were indicated if the determined spot positions in the actual frame matched a margin box of (5×5) px in the approximate area of the annotated ground truth. If the determined spot positions were out of the margin box where the annotated ground truth was located, the results were referred to as a false detection.

TM and CT performed with high detection rates on sequences of tissue substitutes with scores of 97% and 95%, respectively. On the contrary, TM exhibited multiple false detections on porcine tissue and rates decreased to below of 64%. Reflections and major changes in local appearance caused erroneous results. On the contrary, CBT still realised detection scores of 95% for porcine tissue. These results motivated the use of CBT for online laser spot detection as part of the measurement workflow in Figure 7.5.

Subsequent to processing of stabilised input image $\boldsymbol{I}_{\mathrm{LS}}(t_k)$ with preceding spot detection algorithm, the resulting binary output $\boldsymbol{I}_{\mathrm{LC}}(t_k)$ is analysed with connected-component labelling to eliminate satellite areas caused by challenging illumination conditions. The remaining binary image is filtered with following rules: Area size ($> 10\,\mathrm{px}$) and circular shape conformity ($> 75\%$). Lastly, temporal spot consistency is ensured by discarding frame-to-frame centre shifts of more than $5\,\mathrm{px}$.

As depicted in Figure 7.5, segmentation and centroid estimation was executed in two individual phases to reject intermediate results if previous validation rules are violated. Detected spot position $_{(\mathrm{LI})}\boldsymbol{p}_{\mathrm{LC}}(t_k)$ given image space is mapped to camera frame $(\mathrm{CF})_{\mathrm{L}}$ according to

$$_{(\mathrm{L})}\boldsymbol{P}_{\mathrm{LC}}(t_k) = h\left(\boldsymbol{D}(t_k), {}_{(\mathrm{LI})}\boldsymbol{p}_{\mathrm{LC}}(t_k)\right) = \left({}_{(\mathrm{L})}x_{\mathrm{LC}}(t_k), {}_{(\mathrm{L})}y_{\mathrm{LC}}(t_k), {}_{(\mathrm{L})}z_{\mathrm{LC}}(t_k)\right)^{\mathrm{T}} \in \mathbb{R}^3, \qquad (7.3)$$

(a)   (b)
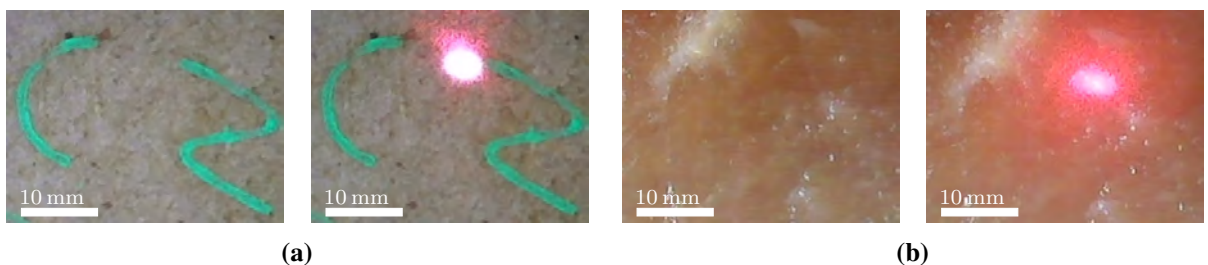
Fig. 7.4: Examples for endoscopic imaging with incident laser radiation on different surfaces: (a) Optical response of tissue substitute (MDF) without (left) and with laser (right) causing local sensor saturation. (b) Optical response of porcine tissue without (left) and with active laser (right) causing lowered saturation but increased speckles compared to (a).

where h defines the direct transformation $\mathbb{R}^2 \to \mathbb{R}^3$ with depth map $\boldsymbol{D}(t_k)$ provided by scene reconstruction. Lastly, laser centroids $\boldsymbol{P}_{\mathrm{LC}}(t_k)$ are processed for each discrete time step t_k and are sequentially concatenated to tracing trajectory

$$_{(\mathrm{L})}\boldsymbol{t}_{\mathrm{LC}} = \begin{pmatrix} \boldsymbol{P}_{\mathrm{LC}}(t_1), \boldsymbol{P}_{\mathrm{LC}}(t_k), \dots, \boldsymbol{P}_{\mathrm{LC}}(t_N) \\ t_1, t_k, \dots, t_N \end{pmatrix} \in \mathbb{R}^{4 \times N} \tag{7.4}$$

until the user completed the task and triggered the completion event after N recorded samples. Hence, trajectory $\boldsymbol{t}_{\mathrm{LC}}$ aggregates the temporal motion of the teleoperated laser spot. Figure 7.5 illustrates assessment of data consistency with decision guidelines, if algorithmic constraints were violated, by such criteria as erroneous spot detection or inconsistent depth maps.

7.1.4 Postexperimental Evaluation and Statistics

The quantitative assessment of laser spot deviations from the nominal path builds upon visual measurements described in Section 7.1.3. Computation of spatial and temporal metrics in combination with inferential statistics may determine significant effects of experimental conditions on study results.

Path Deviation Assessment

The evaluation of the path tracing study considers two metrics denoted as task completion time TCT and path tracing error PTE. Metric TCT determines the time duration from laser activation and release of the master device to deactivation of both features following task completion. The
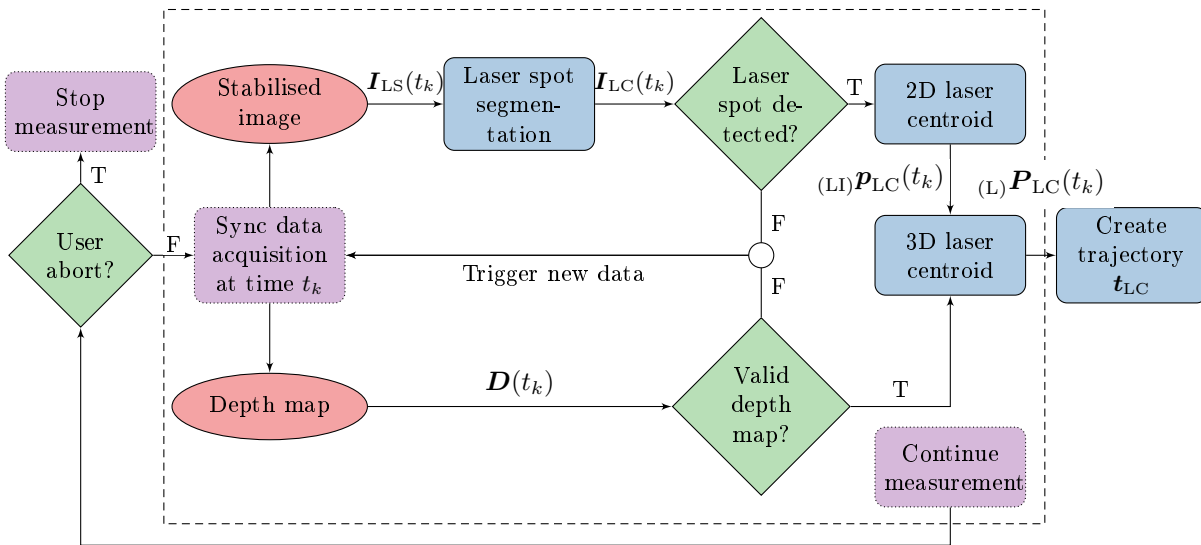
Fig. 7.5: Flowchart of the image processing pipeline for laser spot segmentation and spatial mapping for online measurement of the spot location during user tasks. Acronyms: False (F) and true (T).

metric is defined as $\text{TCT} = t_N - t_1$, where t_N and t_1 describe the final and initial timestamp of the laser centroid detected in each task.

By contrast, determination of the path tracing error demands for sequential computation. Acquired measurements for nominal path $\boldsymbol{t}_{\text{NP}}$ and laser spot trajectory $\boldsymbol{t}_{\text{LC}}$ are depicted schematically in Figure 7.6. The metric PTE assesses geometric deviations between recorded nominal and traced paths. Common metrics for path or trajectory similarity analysis are discrete Hausdorff or Frechet distances [SM04]. However, orthogonal distances between measured laser spots and nominal path are a well-accepted metric in the domain of robotic laser surgery [DOCM14]. The following paragraph generalises the methodology in [DOCM14] from planar to 3D space to consider the quantitative evaluation of tracing patterns on both planar and non-planar surfaces (see Section 7.2).

Since both measurements are given in common reference frame $(\text{CF})_{\text{L}}$, orthogonal projections of laser spot measurements $\boldsymbol{P}_{\text{LC},k} = {}_{(\text{L})}\boldsymbol{P}_{\text{LC}}(t_k)$ on segments constituting nominal path $\boldsymbol{t}_{\text{NP}}$ are computed as illustrated in Figure 7.6:

$$\boldsymbol{P}_{\text{LC},k}^{*} = \boldsymbol{P}_{\text{NP},i} + (\boldsymbol{P}_{\text{NP},i+1} - \boldsymbol{P}_{\text{NP},i}) \underbrace{\frac{(\boldsymbol{P}_{\text{LC},k} - \boldsymbol{P}_{\text{NP},i})(\boldsymbol{P}_{\text{NP},i+1} - \boldsymbol{P}_{\text{NP},i})}{\|\boldsymbol{P}_{\text{NP},i+1} - \boldsymbol{P}_{\text{NP},i}\|_2}}_{r_{\text{LC},k}}, \qquad (7.5)$$

where $k = \{1, \dots, N\}$ and $i = \{1, \dots, M\}$, respectively. If scaling factor $r_{\text{LC},k}$ of the projected position on the path segment satisfies boundary condition $0 \leq r_{\text{LC},k} \leq 1$, the spot measurement is projected orthogonally to the corresponding path segment and is taken into consideration for further processing. On the contrary, distances $r_{\text{LC},k}$ and corresponding path segments that violate the conditions are rejected. This yields orthogonal path tracing error of the k-th spot measurement to the corresponding segmental projection on the nominal path:

$$e_{\text{PT},k} = \left\| \boldsymbol{P}_{\text{LC},k} - \boldsymbol{P}_{\text{LC},k}^{*} \right\|_2. \qquad (7.6)$$

Path errors of each pattern are composed to error vector $\boldsymbol{e}_{\text{PT}} = (e_{\text{PT},1}, e_{\text{PT},k}, \dots, e_{\text{PT},N})^{\text{T}}$ with $k = \{1, \dots, N\}$. The RMSE of the error vector defines study metric

$$\text{PTE} = \sqrt{\frac{1}{N} \sum_{k=1}^{N} (e_{\text{PT},k})^2}. \qquad (7.7)$$

Mean, standard deviation, and median of metrics PTE were consolidated for subjects and study trials.

Statistical Analysis

Statistics are applied to study data in order to identify effects of visualisation condition or subject-related parameters on task metrics PTE and TCT. Both metrics are dependent variables that

are complemented by three independent variables. The latter are described by factors subject *experience*, visualisation *condition*, and repeated *measurement*. The between-subject factor of *experience* accommodates a two-level description of the educational background of each subject, e.g. novice or expert. Stabilised and non-stabilised visualisation *condition* yields a two-level within-subject factor decoded by acronyms NS and AS. Repeated recordings of subject samples are considered by the within-subject factor *measurement* with five levels pursuant to the number of trials per factor *condition*. These metrics are captured for all factorial combinations of within-subject and one between-subject factor.

Statistical tests target to reveal significant differences between sets of metrics grouped by factors. Primarily, all participants are considered as a joint group for within-subject analysis only. In the second part, a mixed design is introduced to consolidate within-subject factors with between-subject factors *experience*. These assumptions lead to application of parametric multi-way analysis of variances (ANOVA) or non-parametric equivalents [Fey16]. In a preparatory step, data was assessed under four assumptions [FFW13]: 1) presence of outliers, 2) normal distribution of data residuals, 3) equal variances of dependent variables related to between-subject factors, and 4) equal variance of differences between factor-related groups. Normality of data residuals was inspected with normal Q-Q plots and Shapiro-Wilk tests [MRY11]. On the contrary, homoscedasticity was examined using Levene's test, whereas Mauchly's test was applied to identify equality of differences for within-subject factors.
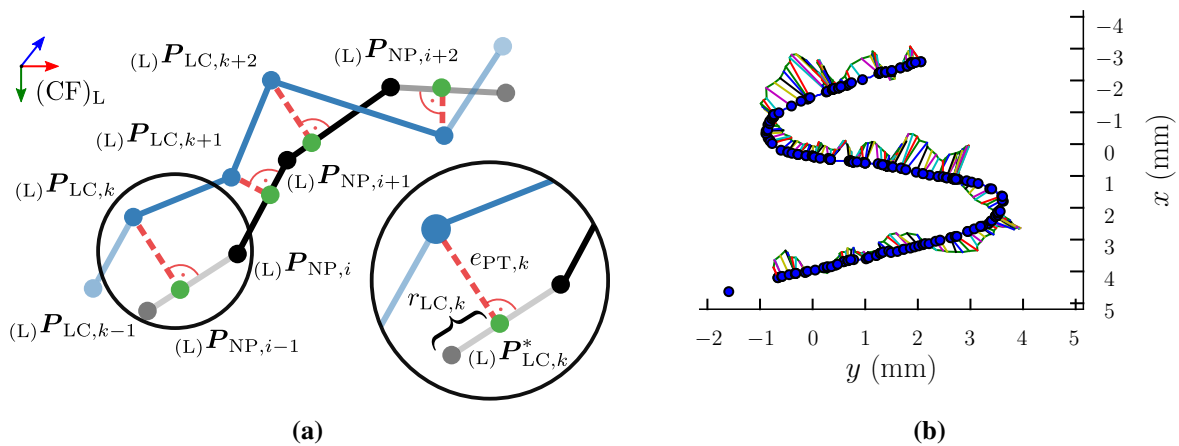
Fig. 7.6: Evaluation workflow of path tracing study: (a) Discrete representation and geometric annotation for task metrics and (b) example of processed trajectory in x-y plane of $(CF)_L$. Coloured features in (a) indicate the nominal path (black), measured laser spot positions (blue), orthogonal path errors (red), and projected positions (green). Circle markers denote a sparse set. Only one-fifths of full data is depicted for visualisation purposes.

7.1.5 Results

The user study comprised 20 subjects from two experience levels and multiple trials per subject and visualisation condition ($N = 171$). More precisely, 7 subjects (3 females, 4 males) from the Department of Otorhinolaryngology, University Hospital of Ulm, Germany completed trials ($N = 42$) with an intermediate to expert background in endoscopy as assistant or senior physician. Subjects had an age of 30.1 ± 4.9 years on average. On the other hand, 13 subjects (2 females, 11 males) from the Institute of Mechatronic Systems, Leibniz Universität Hannover, Germany equivalently completed trials ($N = 129$) and had no prior experience in endoscopy (novices) as graduate engineering student or research assistant with an age of 28.1 ± 3.1 years on average. A minor set of measurements from both groups ($N = 29$) was excluded from postexperimental analysis due to incomplete data acquisition. Visualisation of the endoscopic image stream with the head-mounted display was preferred by 3 subjects, whereas 17 subjects selected the 3D monitor.

User Study Metrics

A study example of results obtained from postprocessing according to the described evaluation workflow in Section 7.1.4 is shown in Figure 7.7. Images were analysed to segment nominal path and laser spot locations (see Figures 7.7a and 7.7b). Afterwards, nominal path and laser spot positions identified in image data were mapped to 3D space and Euclidean distances, as such path tracing errors e_{PT}, were computed for the entire path length as illustrated in Figures 7.7c and 7.7d. Performances of this example (S-shaped pattern) are generalizable to other primitives. In the initial phase, the subject displaced the laser spot from the start position to the centre line of the pattern and introduced a linear tracing motion with deviations of $e_{\mathrm{PT}} < 0.4\,\mathrm{mm}$. While approaching a turn, errors increased beyond $0.6\,\mathrm{mm}$ until the operator inputs corrective motions to terminate the pattern. Errors e_{PT} and task completions times per subject and trial were taken into consideration for metrics PTE and TCT (see Section 7.1.4). Both metrics were consolidated to box plots in Figure 7.8 and summarised to Tables 7.2 and 7.3. In summary, both task metrics only show minor differences related to visualisation conditions. In contrast, an effect of repeated trials on completion time reduction was observed. Lastly, tracing errors and completion times were slightly increased for experts in comparison to novices.

Statistical analysis following methodologies in Section 7.1.4 was applied to identify significant effects on task metrics, which resulted in a significance level of $\alpha = .05$. Primarily, a two-way repeated ANOVA with two-within and no between-subject factor (*condition*, *measurement*) was conducted. PTE data was split into ten subsets according to factorial combinations. Three outliers were identified by visual inspection of corresponding box plots. Skewness and kurtosis tests indicated a slightly right-skewed distribution. In consequence, logarithmic transformation was applied and Shapiro-Wilk tests validated normality for all subsets ($p > .05$). Application of Mauchly's test of sphericity investigated homogeneity of variances for each combination of subsets

Tab. 7.2: Path tracing error (PTE) metrics in mm per subject group and condition.

	NS			AS		
	Mean $\pm$ SD	Mdn	Max	Mean $\pm$ SD	Mdn	Max
	0.55 $\pm$ 0.12	0.50	0.90	0.56 $\pm$ 0.13	0.52	1.12
Expert	**0.62 $\pm$ 0.15**	0.56	0.90	0.66 $\pm$ 0.10	0.67	0.87
Novice	0.53 $\pm$ 0.08	0.53	0.75	**0.51 $\pm$ 0.14**	0.58	1.12

Note: No image stabilisation (NS) and active image stabilisation (AS). Numbers marked in bold indicate the best performance per group.

Tab. 7.3: Task completion time (TCT) in s per subject group and condition.

	NS			AS		
	Mean $\pm$ SD	Mdn	Max	Mean $\pm$ SD	Mdn	Max
	30.6 $\pm$ 14.2	27.2	72.9	32.3 $\pm$ 16.7	28.4	82.6
Expert	**40.5 $\pm$ 17.6**	33.2	72.9	42.0 $\pm$ 21.7	41.0	82.6
Novice	**25.2 $\pm$ 7.7**	23.7	37.5	27.1 $\pm$ 10.0	22.5	50.8

Note: No image stabilisation (NS) and active image stabilisation (AS). Numbers marked in bold indicate the best performance per group.

for factors *condition* and *measurement*. There was homogeneity within subsets for all factors: *measurement* ($W = 0.17, p = 0.94$), the interaction of *condition* $\times$ *measurement* ($W = 0.27, p = .28$), and directly for *condition* with only two levels. There was no statistically significant two-way interaction of *condition* and *measurement* ($F_{4,40} = 0.32, p = .86$) nor main effects of *measurement* ($F_{4,40} = 2.47, p = .06$) and *condition* ($F_{4,40} = 2.06, p = .18$). Otherwise, there was no statistical evidence for differences of PTE metrics related to factors *measurement* and *condition*.

A two-way repeated measures ANOVA was equivalently applied to TCT metrics. Visual inspection of subset box plots detected six outliers and skewness analysis indicated right-skewed distributions. A logarithmic transformation was applied and normality of subset residuals was tested with normal Q-Q plots and Shapiro-Wilk tests ($p > .05$). As verified by Mauchly's test, there was sphericity for interaction of *condition* $\times$ *measurement* ($W = 0.15, p = .08$) and *measurement* ($W = 0.23, p = .21$). There was no statistically significant two-way interaction between *condition* and *measurement* ($F_{4,40} = .21, p = .93$) nor a main effect of *condition* ($F_{1,10} = 2.84, p = .12$). On the other hand, a main effect of *measurement* indicated a statistically significant difference of TCT related to trial numbers per subject for non-stabilised visualisation from the first trial to the last trial of $18.7\,\mathrm{s}$ and for motion-compensated visualisation of $20.0\,\mathrm{s}$, ($F_{4,40} = 3.86, p = .009$). The results of the statistical analysis confirmed previous observations. There is no main effect of *condition* on TCT but the latter decreases significantly with increasing number of trials (factor *measurement*).

(a)

(b)

(c)

(d)
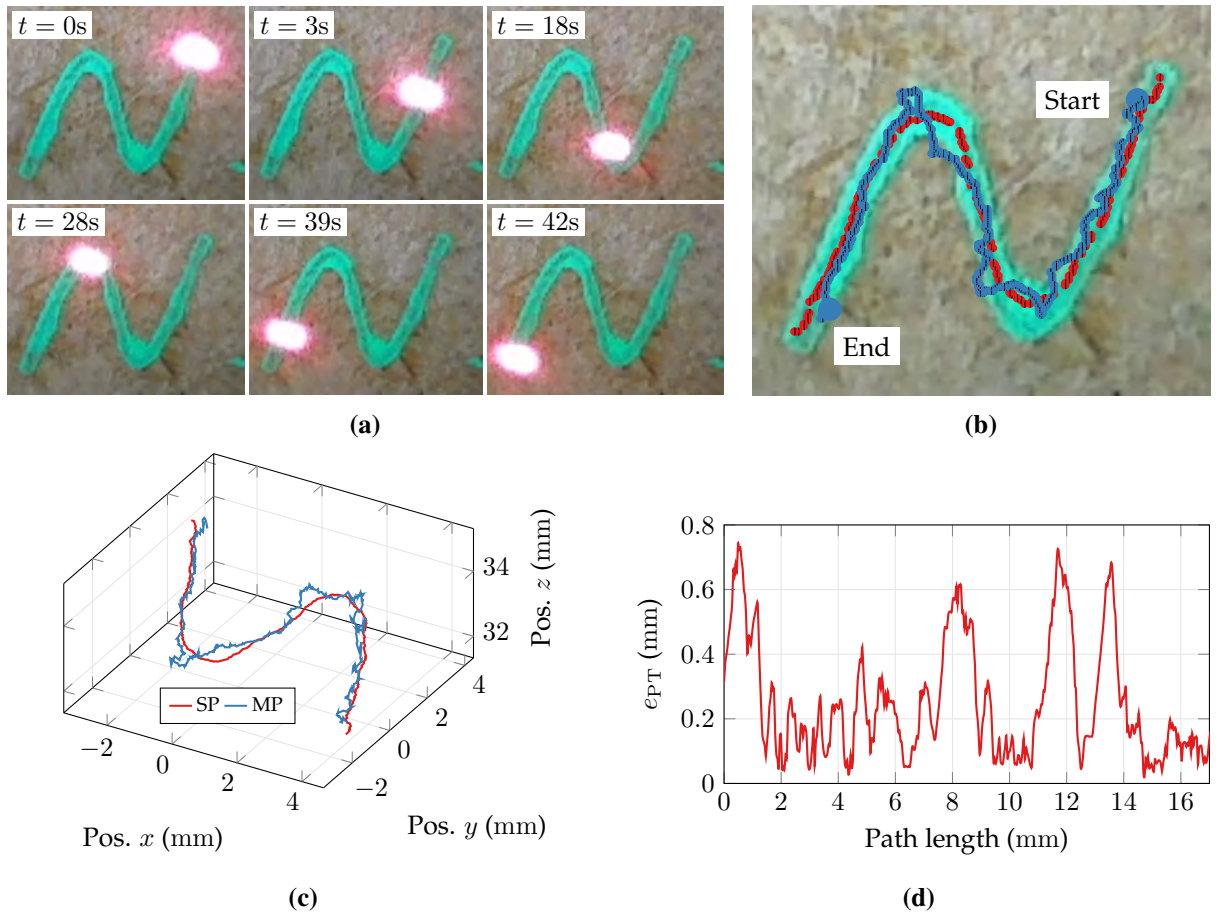
Fig. 7.7: Evaluation workflow and results for subject P18 and trial M10 on a planar sample. (a) Temporal sequence of teleoperated tracing motion on S-shaped pattern. (b) Postexperimental representation of automatically segmented nominal centreline (red) and measured laser spot positions (blue). (c) Mapping of measurements in (b) to Euclidean space in $(CF)_L$. (d) Path tracing errors over length of nominal path. Acronyms: Segmented path (SP) and measured path (MP).

Between-subject factor *experience* was added to previous within-subject designs yielding a three-way mixed ANOVA. Metric PTE of split subject groups was assessed and split to ten subsets corresponding to factorial combinations. The number of outliers equalled previous findings. Residuals of data subsets satisfied normality after logarithmic transformation as assessed by normal Q-Q plots and Shapiro-Wilk tests ($p > .05$). Due to a mixed design, testing equality of variances between subsets associated to between-subject factors is substantial. There was homogeneity of variances as assessed by Levene's test ($F = 0.06, p = .82$). Subsequently, Mauchly's test indicated that sphericity was satisfied for all levels of within-subject factors: *measurement* ($W = 0.24, p = .15$), the interaction of *condition* $\times$ *measurement* ($W = 0.34, p = .34$), and directly for *condition* with only two levels, i.e. the three-way mixed ANOVA is not biased. There was no statistically significant three-way interaction between within-subject factors *condition*, *measurement*, and between-subject factor *experience* ($F_{4,44} = 0.71, p = .59$). Further on, two-way interactions of *experience* $\times$ *condition* ($F_{1,11} = 1.55, p = .24$), *experience* $\times$ *measurement* ($F_{4,44} = 0.99, p =$

.42), and *condition* × *measurement* ($F_{4,44} = 0.08, p = .99$) were not statistically significant. Beyond that, factors *measurement* ($F_{1,11} = 2.27, p = .08$) and *condition* ($F_{1,11} = 1.13, p = .31$) did not show significant main effects. On the contrary, factor *experience* yielded a statistically significant main effect ($F_{1,11} = 11.95, p = .005$). This finding supported the observation of increased PTE of experts in comparison to novices.

Lastly, metric TCT was analysed related to split subject groups after logarithmic data transformation. Residuals satisfied normality as proven by visual inspection of Q-Q plots and Shapiro-Wilk tests ($p > .05$). There was homogeneity of variances as assessed by Levene's test ($F = 1.03, p = .32$) and Mauchly's test has proven sphericity for all levels of within-subject factors: *measurement* ($W = 0.43, p = .52$), the interaction of *condition* × *measurement* ($W = 0.21, p = .12$), and directly for *condition* with two levels. There was no statistically significant three-way interaction ($F_{4,44} = 1.34, p = .18$), no two-way interaction of *experience* × *condition* ($F_{4,44} = 0.34, p = .37$), nor main effects of *condition* ($F_{1,11} = 2.34, p = .77$) or *measurement* ($F_{1,11} = 1.21, p = .53$). However, there was a two-way interaction of *experience* × *measurement* ($F_{4,44} = 6.21, p = .02$). These findings are consistent with observations of decreasing TCT over number of trials.

User Experience

Scores of the postexperimental survey are summarised in Figure 7.9. Statements are consolidated to categories *learning curve* (S4, S5, S7), *stress* (S2, S6, S12, S13), *performance* (S3, S9, S14), and *design* (S8, S10, S11). Figures 7.9a and 7.9b describe user scores on the five-point Likert scale related to statements and grouped to categories. The subjective assessment basically corroborates conclusions from PTE and TCT metrics. User scores (mean ± SD) in category *learning curve* (3.08 ± 0.91) have proven ease and intuitive familiarisation with the robotic hardware, i.e. users were able to complete the tracing task already after the first trial. Subjects were above average satisfied with their *performance* in terms of accuracy and duration (3.16 ± 0.84) and appreciated the integrated *design* of the robotic hardware (3.17 ± 0.65). Users highlighted that the repeated use of the hardware exerted low *stress* (0.47 ± 0.59). Remarkably, scores of statement S1 related to specific visualisation did not indicate a preferential mode (2.42 ± 1.02). Both modes, i.e. no and active motion compensation, were equally preferred.

Results of split subject groups are shown in Figures 7.9c and 7.9d. A direction towards lower overall Likert scores for experts versus novices was observable. Inferential statistics were applied to data sets grouped by categories. Violation of data normality was detected with Shapiro-Wilk tests ($p < 0.05$). A non-parametric Mann-Whitney-U test was considered. There were no significant differences between mean populations of expert and novice users for categories *performance* ($W = 279, p = .07$) and *stress* ($W = 527, p = .08$) nor related to statement S1 (motion compensation condition) ($W = 24, p = .1$). However, statistically significant differences were identified for *design* ($W = 198, p = .002$) and *learning curve* ($W = 133, p < .001$). This corroborates previous observations on lower subjective scores for device familiarisation related to expert operators.
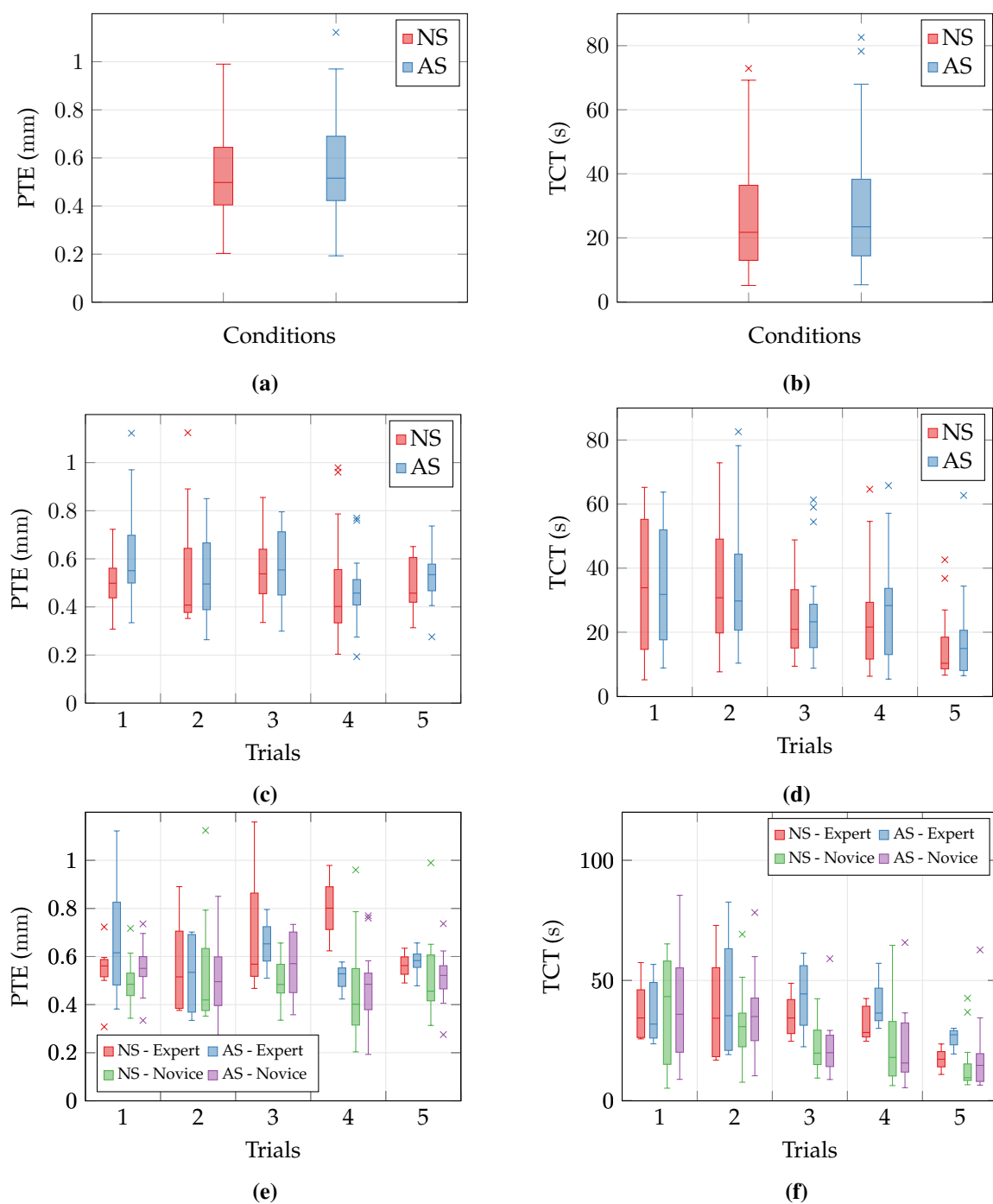
Fig. 7.8: Box plots of path tracing error (PTE) and task completion time (TCT) metrics for non-stabilised (NS) and active scene stabilisation (AS): (a) & (b) Condition-related results. (c) & (d) Trial-resolved results. (e) & (f) Condition-resolved split to subject groups. Horizontal dashes in the box depict the median and cross symbols indicate outliers. Boxes define 0.25 and 0.75-quantiles of input data. Upper and lower whisker span all data within 1.5 interquartile range of the nearer quartile.
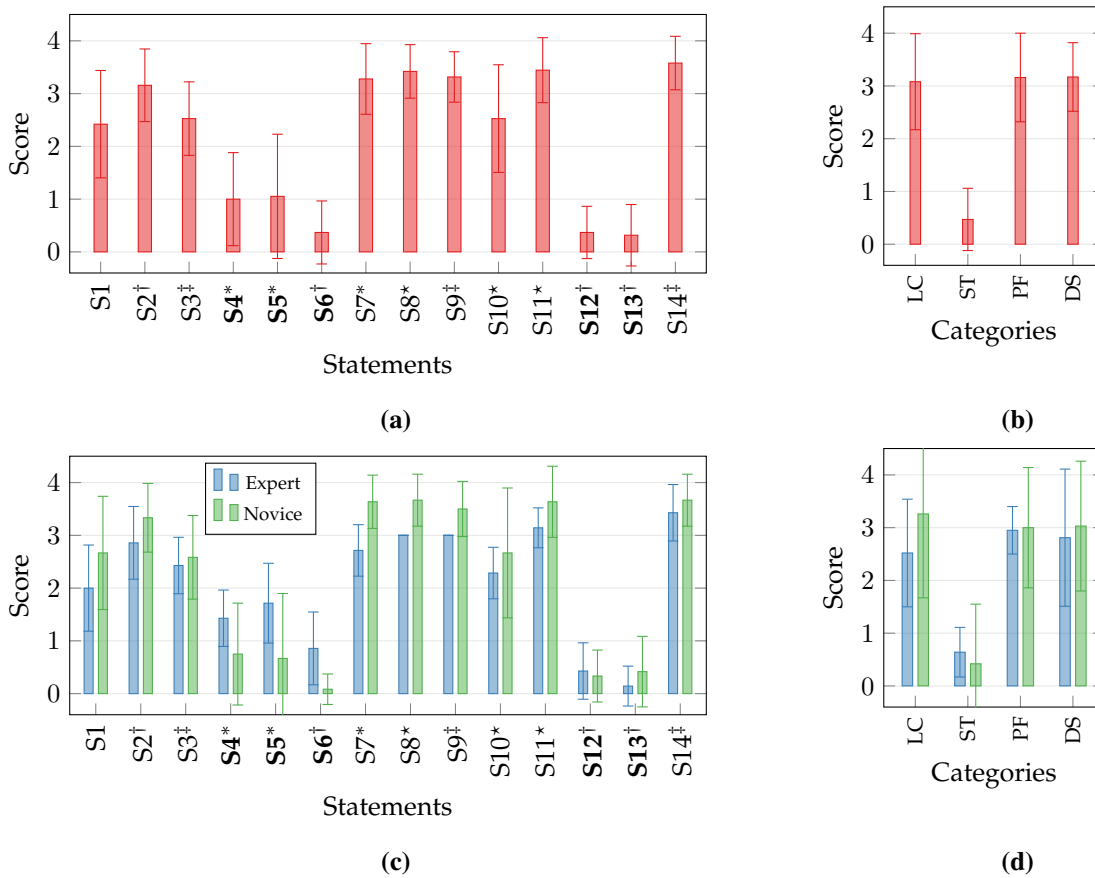
Fig. 7.9: Scores of the postexperimental user survey for the path tracing study: (a) Results of individual statements and (b) grouped to categories. (c) Results of between-subject factor split to subject groups for individual statements and (d) grouped to categories. Category labels define learning curve (LC), stress (ST), performance (PF), and system design (DS). **Bold** labels indicate negative statements. Statements are linked to categories with markers: † to ST, ‡ to PF, ∗ to LC, and ⋆ to DS.

7.1.6 Discussion

The user study revealed promising results from acquired performance metrics and supported the initial hypothesis that teleoperation of an extensible continuum robot may achieve tracing RMSE below $1\,\text{mm}$ in surgical tasks. All subjects completed the given tasks with median PTE of $0.4\,\text{mm}$ to $0.6\,\text{mm}$ while manipulating the robot within the entire kinematic workspace and using non-stabilised or motion-compensated endoscopic visualisation. Likewise, presence of error outliers were limited. These results are similar to extracorporeal scanner-based ablation [DOCM14] but were reached with the proposed dexterous continuum robot. The results further demonstrated that PTE was not significantly biased by increasing number of measurements but likewise TCT diminished gradually. This supports the initial assumption of an efficient device familiarisation with steep learning curves. Subjects already performed with low PTE after a few minutes of induction which was also substantiated by scores of the subject survey on the robotic design. This also applies to reduction of completion times over the number of trials by approximately one-third.

However, PTE were on average slightly higher for stabilised compared to non-compensated endoscopic visualisation. This effect was expected to be caused by accumulation of temporal delays of $10\,\mathrm{ms}$ to $30\,\mathrm{ms}$ from computational efforts related to tracking and image warping pipelines. This occasionally generated minor overshooting of targeted positions, i.e. the centre line of the nominal pattern, from delayed visual feedback of the current laser location and corresponding counteracted input. Nevertheless, scores of the survey confirmed promising directions for applicability of motion-compensated endoscopic vision. Noticeably, novices facilitated slightly lower PTE, while using stabilised endoscopic visualisation. It is expected that prior use and familiarisation to endoscopic equipment in clinical routines necessitate adaptation to novel input strategies. Early stage surgical trainees and novices are probably more adapted to the use of electronic devices and may have less difficulty in integrating robotics into a clinical workflow, as they may have had prior familiarisation to such devices through other electronic media e.g. videogames [MPF$^+$17].

Although study results demonstrated a superior performance of the robotic platform, shortcomings of this study are dedicated to: 1) Cartesian velocity limitation ($5\,\mathrm{mm\,s^{-1}}$) of the manipulator to ensure structural integrity, robust visual processing, and control stability. This condition impacts achievable TCT and may restrict frequencies of pulsed lasers for optimal pulse overlap. 2) Online processing of vision data and sensor acquisition ($25\,\mathrm{Hz}$) caused latencies that must be optimised for enhanced system dynamics, i.e. end effector velocities beyond $5\,\mathrm{mm\,s^{-1}}$. Apart from that, PTE metrics were affected by occasional stick-slip originating from concentrically-guided actuation tubes with different relative velocities. This effect impacted subjects' perception and resulted in minor path deviations or snapping motion of the tip. Mitigation may be accomplished by advanced tubular coatings, e.g. PTFE. 3) Visual measurements used in the evaluation workflow were subject to systematic RMSE of $\pm 0.1\,\mathrm{mm}$ related to the performance of employed stereoscopic reconstruction and tracking algorithms.

7.2 Assisted Laser Manipulation on Non-Planar Surfaces

Clinical device deployment to scenarios with MIS access deals with non-planar soft tissue surfaces. In contrast to the ideal planar scenario addressed in previous Section 7.1, dynamic online adaptation of the focal length constituted by integrated laser optics gains importance for delineation of pathologies on non-planar samples to support atraumatic laser delivery.

This section focuses on integration of assistance presented in Chapter 6 for dynamic laser focus adaptation to delineation tasks. Reduction of cognitive loads on the operator is expected during task execution. The operator may exclusively concentrate on the delineation task to preserve delicate anatomy and healthy tissue. Furthermore, optimal laser-tissue interaction may be realised as assessed in related studies [SKK$^+$15].

The assistive concept enables partial automation of dynamic focus adaptation. Following the outcome of the study survey in Section 7.1.5, clinicians actually preferred low autonomy levels for

task execution. Thus, visuo-haptic features discussed in Chapter 6 were integrated to the robotic framework and can be deactivated or bypassed by the operator at any time if necessary. Subjects are encouraged to use both conditions (NS and AS) related to scene motion compensation (see Section 7.1.5). Previously described path tracing and focal position errors substantiate task metrics of this preliminary study setting.
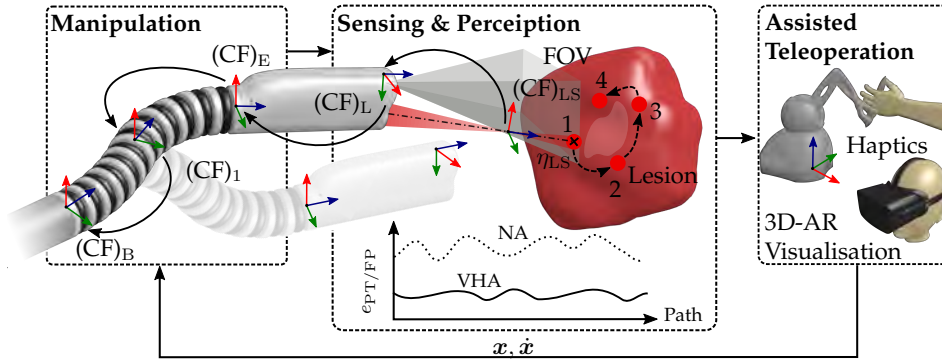
Fig. 7.10: Conceptual setup of three-dimensional robot-assisted contactless laser delineation on non-planar surfaces. The laser spot (red dot with cross marker) is displaced laterally. Simultaneously, distances of beam intersection η_{LS} on the surface and focal position are minimised. It is hypothesised that no assistance (NA) results in larger focal position and tracing errors ($e_{\mathrm{PT/FPE}}$) than with visuo-haptic assistance (VHA).

7.2.1 Experimental Setup and Study Design

The experimental trials extend prior work on planar path delineation (see Section 7.1) to a non-planar setting. This transition demands for additional manipulation DoF of the robotic slave in order to accommodate adaptation of the focal position. Executable DoF of the slave robot are increased to three translational DoF, so that restrictions on robotic extension and compression are lifted. Unrestricted master input was captured by $_{(\mathrm{M})}\boldsymbol{x}_{\mathrm{S,t}}(t) = \left(_{(\mathrm{M})}x_{\mathrm{S}}(t), \, _{(\mathrm{M})}y_{\mathrm{S}}(t), \, _{(\mathrm{M})}z_{\mathrm{S}}(t) \right)^{\mathrm{T}}$ and mapped to the differential slave kinematics under consideration of anisotropic scaling matrix $\boldsymbol{S}_{\mathrm{M}} = \mathrm{diag}\{0.3, 0.5, 0.5\} \in \mathbb{R}^{3 \times 3}$. This moderates inputs for distance adjustment and supports stable tracing motions. By analogy to Section 7.1.1, angular master input is disregarded and set to $_{(\mathrm{M})}\boldsymbol{x}_{\mathrm{S,o}} = (0,0,0)^{\mathrm{T}}$. The Cartesian master velocity was limited by rendered friction (see Section 6.3) to $v_{\mathrm{S,max}} = 3\,\mathrm{mm\,s^{-1}}$ and the kinematics controller gain was set to $\boldsymbol{K}_{\mathrm{C}} = \mathrm{diag}\{0.5, 1, 1\} \in \mathbb{R}^{3 \times 3}$. The joint limits were activated after release of the stylus to enforce system integration and the executable robotic workspace.

The experimental setup was similar to the previous planar studies. However, target specimens were replaced by non-planar surfaces. A phantom sample with distinct surface relief was designed and manufactured from MDF on a CNC milling machine (FP3NC Dialog11, Deckel AG, Munich, Germany). This resulted in significant changes in local surface morphology within the observing

endoscopic FoV. The relief depicted in Figure 7.11a consists of a layout with truncated and stepped pyramids showing dimensional variations (see Figure 7.11b). The manufacturing accuracy was assessed in prior work in a comparative study on stereoscopic reconstruction of the physical model and a CAD model obtained from coordinate measurement machine data yielding ground truth data with a root-mean-square error of $11.2\,\mu m$ [SKKO15]. A nominal path on the surface was created using a distinct green coating (NEON Pigment Ink, Rico Design GmbH, Brakel, Germany). The linear path was applied sequentially with a stamp (line width $1\,mm$) to connect line sections crossing different geometric features of surface elevations.

At the beginning of each user trial, the specimen was randomly located within the FoV of the endoscopic stereo camera. Visuo-haptic assistance was activated and rendered to the user with parametric configuration as described in Chapter 6. The experimental supervisor moved the robot to an initial pose that enabled instant tracing of the nominal path after activation of the visible laser. Subsequently, subjects were demanded to complete the given task following the procedural workflow described in Section 7.1.2. Vision and kinematics data were captured at similar rates as described in Section 7.1.1.

7.2.2 Postexperimental Evaluation

The evaluation of 3D path delineation essentially adapts methodologies presented in preceding Sections 6.4 and 7.1.4. Specific amendments for trial assessment are highlighted in the following paragraphs.

Streams of visual and kinematics data were synchronized at discrete time steps t_k of approximately $40\,ms$ using the approximate-time policies of the ROS framework with $k = \{0, \ldots, N\}$ for N samples in total. Similarly to Section 7.1.3, measurement vectors of nominal 3D path $_{(L)}\boldsymbol{t}_{NP} \in$

(a)   **(b)**
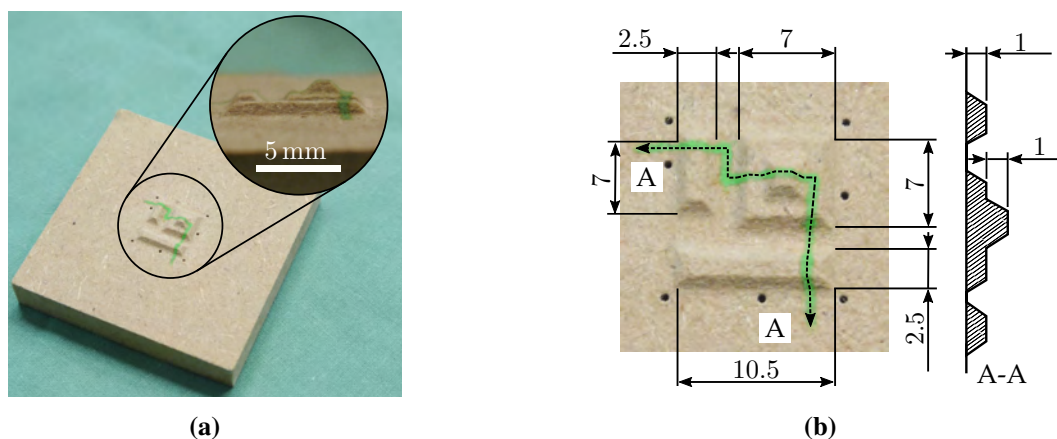
Fig. 7.11: Phantom for experimental performance evaluation on 3D path delineation: (a) Isometric and magnified view of the specimen. (b) Base dimensions of the surface relief and elevations in mm in top view and the corresponding cross-section along the coated path.

$\mathbb{R}^{3 \times N}$, laser spot positions $_{\mathrm{(L)}}\boldsymbol{t}_{\mathrm{LC}} \in \mathbb{R}^{4 \times N}$, and focal position errors $\boldsymbol{e}_{\mathrm{FP}} \in \mathbb{R}^{N}$ were recorded. Accordingly, image-based measurements and estimation of surface intersection serve computation of path and focal positions errors $e_{\mathrm{PT}}(t_k)$ and $e_{\mathrm{FP}}(t_k)$, respectively. Path tracing errors PTE were determined with the workflow in Section 7.1.4. By contrast, prior definition of focal position error FPE is modified and now regards the focal position errors $e_{\mathrm{FP}}(t_k)$ for the entire duration of the task:

$$\mathrm{FPE} = \sqrt{\frac{1}{N} \sum_{k=1}^{N} (e_{\mathrm{FP}}(t_k))^2}. \tag{7.8}$$

For comparative reasons, path and focal errors are consolidated to total path errors

$$e_{\mathrm{TP}}(t_k) = \sqrt{(e_{\mathrm{PT}}(t_k))^2 + (e_{\mathrm{FP}}(t_k))^2}. \tag{7.9}$$

This distance metric equally weights both error contributions. Temporal concatenation gives vector $\boldsymbol{e}_{\mathrm{TP}} = (e_{\mathrm{TP}}(t_1), e_{\mathrm{TP}}(t_k), \ldots, e_{\mathrm{TP}}(t_N))^{\mathrm{T}} \in \mathbb{R}^{N}$. RMSE of elements in $\boldsymbol{e}_{\mathrm{TP}}$ finally yields total path error

$$\mathrm{TPE} = \sqrt{\frac{1}{N} \sum_{k=1}^{N} (e_{\mathrm{TP}}(t_k))^2}. \tag{7.10}$$

Statistical mean, standard deviation, and median were determined for metrics FPE, PTE, and TPE of recorded subject data.

7.2.3 Results

The preliminary experimental trials consisted of repeated completion of tasks ($N = 12$) by three male subjects with an age of 29.3 ± 1.2 years on average and all with an engineering background (research assistants). This study exclusively addressed subjects with senior experience in operating the robotic framework from participation in predecessor studies and prototyping. Each subject completed four teleoperated delineation tasks according to the study protocol with randomly assigned assistance conditions NA and VHA. Motion compensation of the observed scene, such as considered in the previous study, was excluded from the study protocol due to eliminate disturbances related to computational efforts of the tracking and warping algorithms (see Section 7.1.6).

An exemplary temporal sequence of 3D path tracing with condition NA is shown in Figure 7.12a. The corresponding surface representation is obtained from dense scene reconstruction (see Section 2.5) and presented in Figure 7.12b. Data was processed using the methodologies described in Section 7.2.2 for computation of error metrics. The spatial path information related to frame $(\mathrm{CF})_{\mathrm{L}}$ is depicted in Figure 7.12c and the corresponding two-dimensional projection is shown in Figure 7.12d. Steps of the pyramidal geometry are observable along the path segmentation in Figure 7.12c. Absence of assistance due to applied condition NA caused deviation of focal spot positions within $1\,\mathrm{mm}$ to $3\,\mathrm{mm}$ in z-direction of reference frame $(\mathrm{CF})_{\mathrm{L}}$. Likewise, master input for

compensation of directional disturbances caused oscillations along the centre line of the nominal path as exposed in Figure 7.12d. Furthermore, sensor acquisition and corresponding algorithmic processing of the dynamic environment induces white noise of high frequency and low amplitudes to reconstructed surface data. This may propagate to control layers.

Study metrics PTE, FPE, and TPE are grouped by assistive conditions VHA and NA in Table 7.4 and summarized to box plots in Figure 7.13b. Data is reported as mean $\pm$ SD, unless described otherwise. The average length of segmented paths was $(22.4 \pm 3.56)\,\mathrm{mm}$. Comparison of box plots in Figure 7.13b substantiates an increased presence of outliers for condition VHA. Remarkably, mean PTE of condition VHA $(1.04 \pm 0.61)\,\mathrm{mm}$ is increased by 80% in comparison to condition NA $(0.66 \pm 0.29)\,\mathrm{mm}$. On the contrary, mean FPE of condition NA $(2.39 \pm 0.51)\,\mathrm{mm}$ was increased by a factor of four in comparison to VHA $(0.59 \pm 0.51)\,\mathrm{mm}$. Metric TPE indicated an improved overall performance of condition VHA, as such there was an absolute error reduction of approximately $1\,\mathrm{mm}$. An example of error distributions along the delineated pattern is depicted in Figure 7.13a. Peaks of path errors e_{FP} are closely linked to gradual changes of the pyramidal geometry. Focal position errors e_{FP} of condition VHA were mostly within specified boundaries constituted by Rayleigh length $z_{\mathrm{R}} = \pm 1.75\,\mathrm{mm}$. In summary, condition VHA achieved an improved performance for joint consideration of tracing and focal position errors given by metric TPE. However, activated assistance impacted the presence of error outliers and resulted in lower delineation accuracies, i.e. an increase of metric PTE.

Lastly, observed results were substantiated by inferential statistics. A paired-samples t-test was taken into account to determine statistically significant mean differences of TPE related to assistive conditions. Outliers were assessed by visual inspection of box plots. The assumption of residual normality was satisfied as validated by inspection of normal Q-Q plots and Shapiro-Wilk tests $(p = .11)$. As indicated by quantitative data analysis, there was a statistically significant mean difference of $-1.11\,\mathrm{mm}$ in between conditions NA and VHA, 95% CI $[-1.02, -1.38]$, $(t(5) = 17.09, p < .001, d = 5.18)$. Additionally, analysis of Cohen's $d > 0.8$ surmised a large effect of VHA on metric TPE [SM10].

Tab. 7.4: Error metrics in mm for 3D path tracing study per subject and condition.

	VHA					NA				
	PTE		FPE		TPE	PTE		FPE		TPE
	Mean±SD Mdn Max		Mean±SD Mdn Max			Mean±SD Mdn Max		Mean±SD Mdn Max		
S1	0.97±0.65 0.82 3.66		0.39±0.25 0.35 1.33		1.25	0.63±0.33 0.61 3.24		1.96±0.48 2.29 3.24		2.31
S2	1.18±0.55 1.12 2.71		0.78±0.56 0.76 2.23		1.67	0.62±0.28 0.64 2.34		2.43±0.61 2.63 2.91		2.75
S3	1.10±0.47 1.34 2.15		0.58±0.39 0.57 1.58		1.50	0.69±0.32 0.64 2.14		2.51±0.38 2.56 3.20		2.89
	1.04±0.61 0.92 3.66		**0.59±0.51** 0.47 2.23		**1.50**	**0.66±0.29** 0.64 3.24		2.39±0.51 2.48 3.24		2.59

Note: Visuo-haptic assistance (VHA) and no assistance (NA). Path tracing error (PTE), focal position error (FPE), and total path error (TPE). Bold numbers indicate the best performance of each error category.

(a)

(b)

(c)

(d)
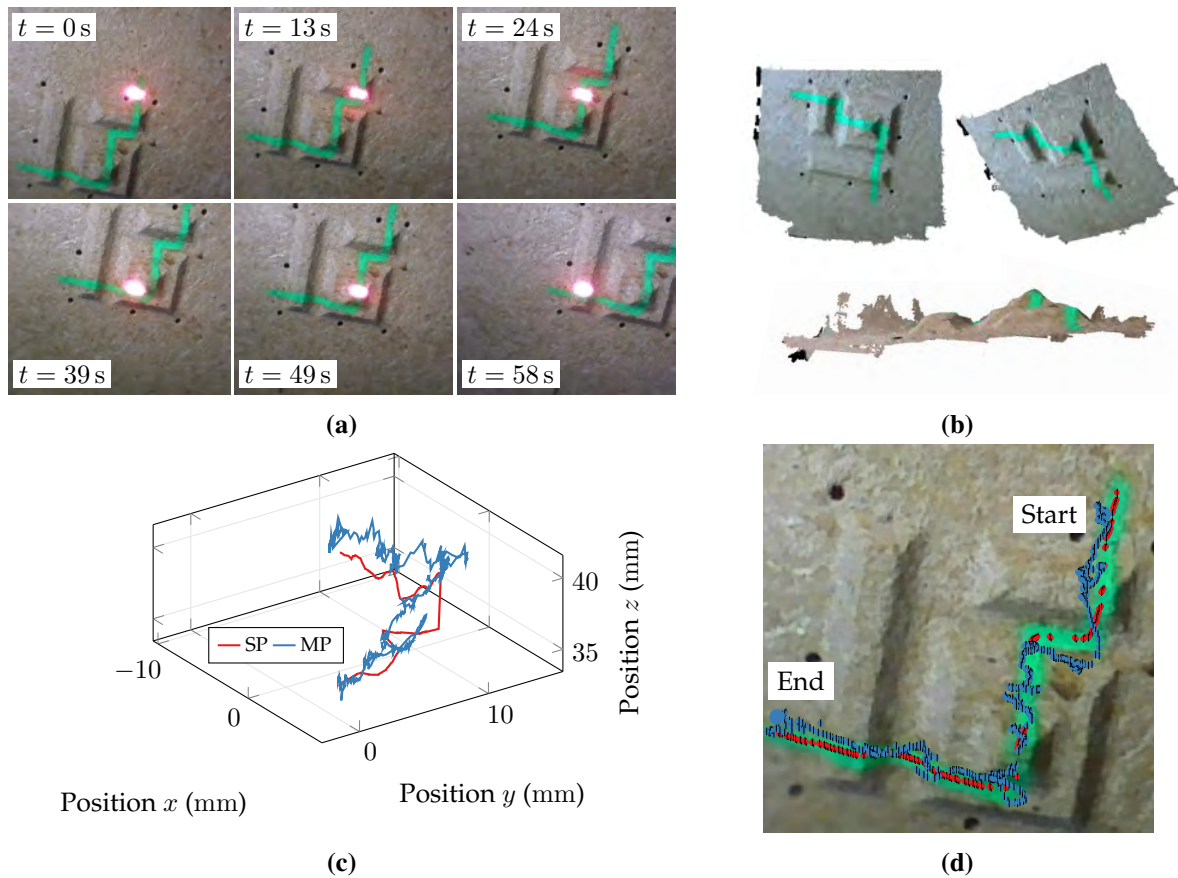
Fig. 7.12: Evaluation of 3D path tracing tasks: (a) Spatial reconstruction of specimen with non-planar surface relief and coated path. (b) Temporal series of motion-compensated left camera view (trial T2). (c) Postexperimental segmented nominal path (red) and projected spot positions (blue). (d) Postexperimental segmented nominal path (SP) and measured laser spot trajectory (MT).

(a)

(b)
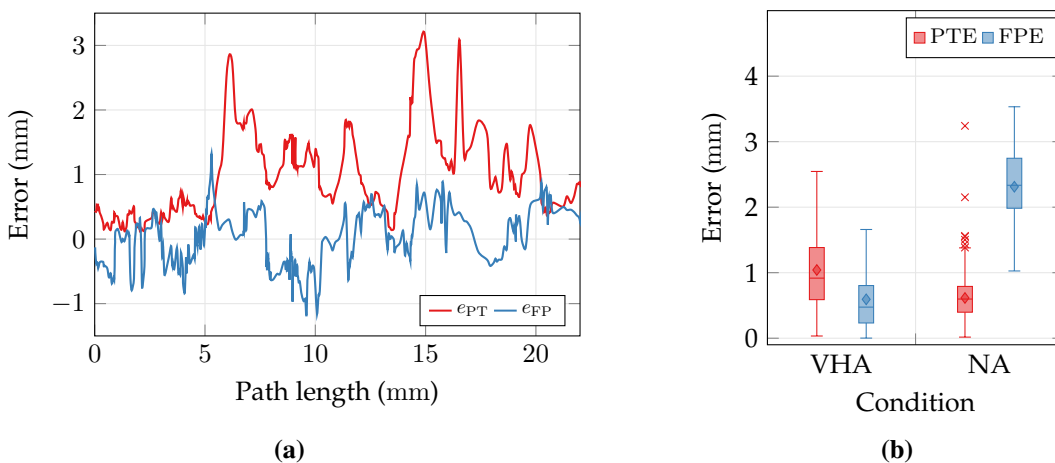
Fig. 7.13: Results of teleoperated 3D path tracing trials: (a) Distribution of errors e_{PT}, e_{FP}, and e_{TP} along the nominal path for condition VHA (trial T3). (b) Box plot of metrics PTE, FPE, and TPE. Horizontal dashes in the box define the median, diamonds mark the mean, and cross symbols indicate outliers. Boxes define 0.25 and 0.75-quantiles of input data. Upper and lower whisker span all data within 1.5 interquartile range of the nearer quartile.

7.2.4 Discussion

Study results demonstrated feasibility of concurrent application of dynamic focal positioning assistance and spatial manipulation of the laser spot. This motivates further optimisation of methodologies and system hardware in future work.

Despite challenging imaging conditions (e.g. specular highlights and motion artefacts), activation of assistive condition VHA enables the reduction of focal errors FPE below $1.8\,\mathrm{mm}$ during lateral motion with a maximum velocity $v_{\mathrm{s,max}} = 3\,\mathrm{mm\,s^{-1}}$. During the initial phase of the trial, before assistive condition VHA was enabled, there were outliers of up to $3.9\,\mathrm{mm}$. However, scene conditions caused non-deterministic computational efforts due to optimisation-based strategies in the visual processing pipeline. This caused latencies that are injected to the main control loops resulting in moderate oscillations or path deviations due to phase shift that 1) limit the control bandwidth and 2) affect the closed-loop stability of the kinematics controller. This resulted in increased path tracing errors for activated assistance (see Figure 7.13b).

By contrast, PTE and outliers were reduced for absence of assistance, but however, caused the contrary effects, such as increased FPE. Thereupon, the actual limitations of the sensing and processing hardware show a trade-off between minimisation of path and focal errors. In particular, Cartesian velocities beyond $3\,\mathrm{mm\,s^{-1}}$ contributed significantly to the presence of error outliers. Additionally, limited dynamics of the robotic actuators impact Cartesian position control, i.e. limited bandwidths of the internal actuator controller and more importantly delays originating from the communication layer between kinematics and actuator controllers. Prospectively, end effector velocities of more than $6\,\mathrm{mm\,s^{-1}}$ are feasible if the sensor acquisition and image processing are optimised for latency reduction. This also comprises consideration of approaches for mitigating time delays in the control framework, e.g. predictive control-based or passivity-based methods or more recent strategies using statistical models for time series prediction in teleoperation frameworks [FYP].

Further improvements are expected from adaptive gains of the haptic controller to moderate amplitudes of attractive forces. Most importantly, damping of jerks transmitted to the master during delineation tasks is expected. Furthermore, the addition of a sequential workflow, which would include consecutive steps with adaptive switching scheme, could decouple procedural phases. This strategy may comprise of the following phases: (1) Initial reduction of the focal position error with haptic constraint on lateral motion, (2) activation of user assistance with presented concepts in Chapter 6 until focal position errors have reached a specified threshold, and finally (3) release of lateral motion and active focal assistance.

This approach separates lateral and axial motion in the initial phase which is generally prone to larger errors. Therefore, a significant improvement of system's usability is expected. Beyond that, extended studies may focus on disturbances from illumination, incorporation of surfaces with weak appearance, or complex 3D surfaces, e.g. *ex vivo* tissue.

7.3 Feasibility Studies

In continuation of Section 7.2, a preliminary study on assisted spatial laser manipulation using porcine soft tissue is presented to demonstrate applicability and transfer of proposed methodologies to *ex vivo* models. Beyond that, disturbances on vision-based focal distance estimation and the related impact on the dynamic response of the haptic controller were simulated with a stepped surface. In contrast to the stepped pyramid with moderate slopes in Section 7.2, the steeper slopes generate an injection of depth discontinuities to the control layer. This section concludes with a pilot study that simulates a preclinical setting using a porcine model.

7.3.1 Assisted Laser Manipulation on Porcine Tissue

Imaging and algorithmic processing of soft tissues in medical applications is challenging. The studies presented in Sections 7.1 and 7.2 considered tissue substitutes to assess the performance of the robotic hardware with exclusion of environmental disturbances. In consequence, this section presents a preliminary study on assisted robotic laser manipulation on *ex vivo* tissue samples to explore the system performance in a more clinically relevant scenario.

Fresh porcine tissue was acquired from a local slaughterhouse. Tissue samples were further resected and isolated to establish a distinct and varying surface morphology. The samples were moistened with 0.9 w-% saline solution (AlleMan Pharma GmbH, Pfullingen, Germany), covered with surgical wipes, and stored in a fridge at $8\,°\mathrm{C}$ until experimental use. Prior to the experiment, the sample surfaces were moistened with saline solution to simulate *in vivo* conditions.

The specimen was located arbitrarily in the FoV of the stereoscopic camera of the endoscopic tip within a distance of $30\,\mathrm{mm}$. Its surface was slightly tilted with respect to the image sensor (see Figure 7.14). An external cold light source was employed for additional illumination at 75% of full intensity. The internal illumination was deactivated in order to reduce thermal disturbances on the integrated stereoscopic imaging sensors. Controller, assistance, and haptics were parametrised equivalently to prior experiments (see Sections 7.1 and 7.2). Maximum Cartesian velocities of the master device were lowered by 50% to $v_{\mathrm{s,max}} = 1.5\,\mathrm{mm\,s^{-1}}$ to mitigate the findings on limited control bandwidths and phase shifts of the framework in Section 7.2.4. Lastly, visuo-haptic assistance, tracking, and visible laser were activated by the operator. The visible laser spot was subsequently manipulated in lateral direction (negative y-direction of frame $(\mathrm{CF})_{\mathrm{B}}$) to trace the surface contour as shown in image sequence A-E in Figure 7.14.

Study findings are summarised in Figure 7.15. Focal position errors e_{FP} and corresponding haptic forces f_{AC} rendered to the master device are shown in Figure 7.15a. End effector kinematics $_{(\mathrm{B})}\boldsymbol{x}_{\mathrm{E}}$ are presented in Figure 7.15b with decomposition to axial component z_{E} and lateral components x_{E} and y_{E}, respectively.
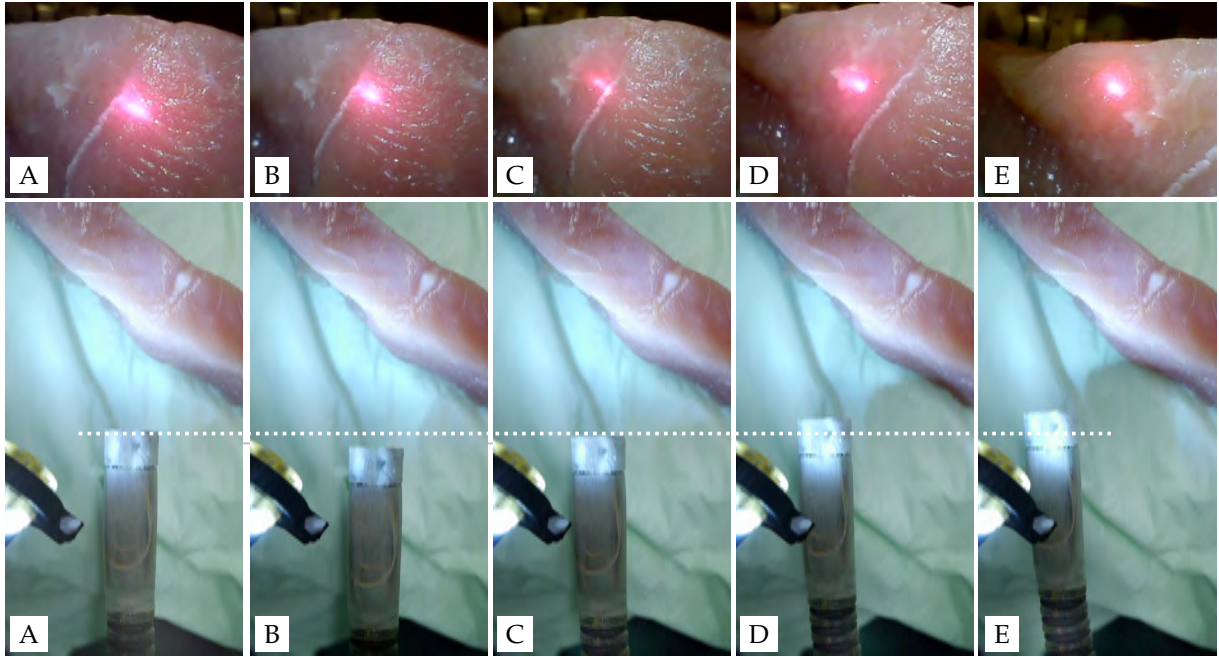
Fig. 7.14: Evaluation of teleoperated focal position adaptation on porcine tissue and with haptic assistance: Image sequence A-E (bottom row) shows the time series of top views containing target specimen and robotic endoscope. Sequence B shows the initial retraction step to adjust the distance. The dotted line enables comparison to initial pose in A and final pose in E after assisted teleoperation. Image sequence A-E (top row) shows the left camera view of the endoscopic camera and illustrates the temporal lateral motion of the visible laser spot.

The initial variation of e_{FP} in Figure 7.15a confirmed that the robotic starting pose in sequence A was approximately $7\,\mathrm{mm}$ offset to the optimal focal position. Thus, the specimen was located too close to the endoscopic tip. Consequently, the haptic controller output maximal force f_{max} to the master device to guide the operator towards decreasing e_{FP}. This uniaxial motion in negative z-direction of approximately $7\,\mathrm{mm}$ until $t = 15\,\mathrm{s}$ (see sequence B) was caused by segmental compression and is observable in Figure 7.15b and accompanied by gradually decreasing errors (see Figure 7.15a) . Force f_{AC} is successively lowered by the corresponding error-to-force mapping discussed in Section 6.3. Hence, the operator initiated a lateral motion to follow the contour of the tissue surface. Variations in kinematics data in Figure 7.15b indicate that the length, i.e. end effector z-position, of the robot is continuously adjusted with increasing lateral displacement to concurrently minimise deviations of e_{FP}.

In the final phase of the experiment (sequence D-E), focal error e_{FP} fell below Rayleigh length z_{R}. During lateral acceleration of the tip, error e_{FP} oscillated with an amplitude of $\pm 1\,\mathrm{mm}$ around a local mean of $2.75\,\mathrm{mm}$ and steadied to $1\,\mathrm{mm}$ towards end of sequence C. Forces f_{AC} exhibited minor oscillations around a local mean of $\pm 0.75\,\mathrm{N}$ within sequence C-E due to challenging conditions in depth estimation and correlated noise. Due to the low Cartesian velocities, actuator

dynamics acted as low-pass filter and did not contribute to any disturbance of the kinematics or the continuum structure.

### 7.3.2 Controller Stability under External Disturbances

Depth discontinuities in surface reconstruction caused by varying surface morphologies may result in large error amplitudes and excitation of associated controller frameworks. This section investigates controller dynamics and responses based on an artificial scenario with stepped discontinuities to generate maximum excitation. A customised specimen with step geometry shown in Figure 7.16a was manufactured from MDF material using an end mill (FP3NC Dialog11, Deckel AG, Munich, Germany) and consists of three sections with steps of different heights. This study considers the centre area with two adjacent steps of $2\,\text{mm}$ height and $4\,\text{mm}$ width each.

The experimental setup was equivalent to Section 7.3.1, so that the bespoke specimen was located in proximity of the endoscopic tip (see Figure 7.16b). Dense depth information is acquired by scene reconstruction shown in Figure 7.16c. Further suppression of camera noise is achieved from auxiliary illumination with an external cold light source. Cycle rates of the visuo-haptic and master controller are set to $100\,\text{Hz}$ and $1\,\text{kHz}$, respectively. Depth information is additionally processed using a moving average filter with window size $N_{\text{AVG}} = 5$. Cartesian velocities of the master device are restricted to $v_{\text{s,max}} = 2\,\text{mm}\,\text{s}^{-1}$. Scene tracking and visuo-haptic assistance were enabled and the manipulator was commanded laterally targeting the laser spot towards steps of increasing height as illustrated by image sequences A, B, and C in Figure 7.16b.

Analysis of control dynamics and stability in presence of large amplitude disturbances and the effects of user interaction with employed haptic feedback were taken into account. These findings are presented in Figure 7.17. More precisely, focal position errors e_{FP} and z-component of laser-surface intersection $_{(\text{L})}\boldsymbol{\eta}_{\text{LS}}$ are depicted in Figure 7.17a. Master and slave kinematics data is provided in Figure 7.17b with active constraint f_{AC} applied to the master device and z-component of end-effector pose $_{(\text{B})}\boldsymbol{x}_{\text{E}}$.

The estimation of laser-surface intersections given by component $_{(\text{L})}z_{\text{LS}}$ captures the distinct stepped geometry of the specimen discernibly within highlighted sequences A-C of Figure 7.17a. Two steps of $2\,\text{mm}$ each are observable and transitions between steps manifest as plateau with depth deviations of less than $0.5\,\text{mm}$. The latter exclusively resulted from initial random placement of the specimen with respect to the endoscopic tip, i.e. non-perpendicular alignment of sensor frames. The temporal variations over $2.5\,\text{s}$ of estimated intersection with Cartesian end effector velocity of $1.5\,\text{mm}\,\text{s}^{-1}$ corresponds to a physical step width of $4\,\text{mm}$. Dynamics of errors e_{FP} were affected by human factors due to teleoperation, the visuo-haptic control layer, and computational latencies from visual processing.

The first disturbance highlighted in sequence A-B of Figure 7.17a was detected and injected to the control layer after a delay of $175\,\text{ms}$ and induced an erratic error increase of $1.5\,\text{mm}$. The

(a)

(b)
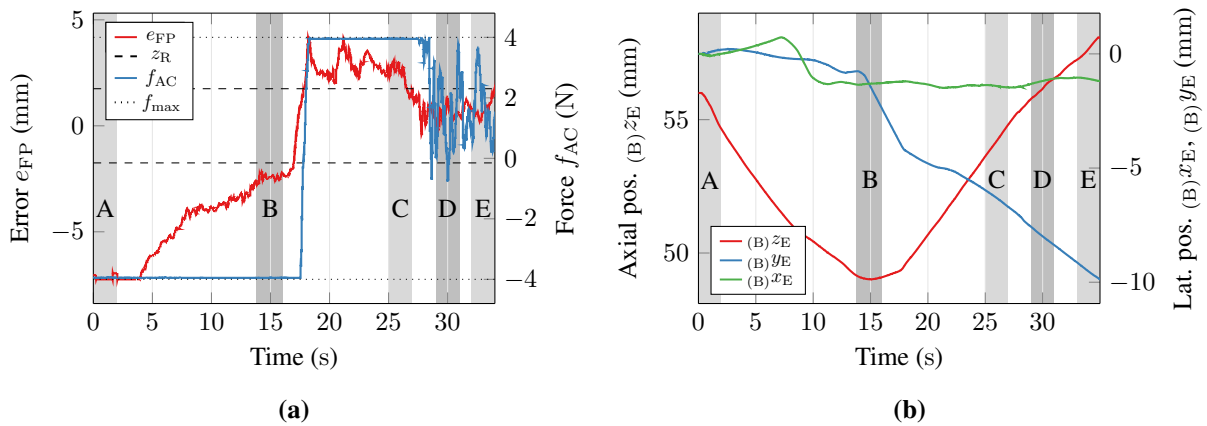
Fig. 7.15: Performance data of the contour tracing study on porcine tissue: (a) Focal position error e_{FP} and haptic force f_{AC}. The dashed line marks Rayleigh length $z_R = \pm 1.75\,\mathrm{mm}$, and the dotted line indicates maximum haptic forces f_{max} of the master. (b) Axial and lateral robotic end-effector positions of pose $_{(B)}x_E$.

(a)

(b)

(c)
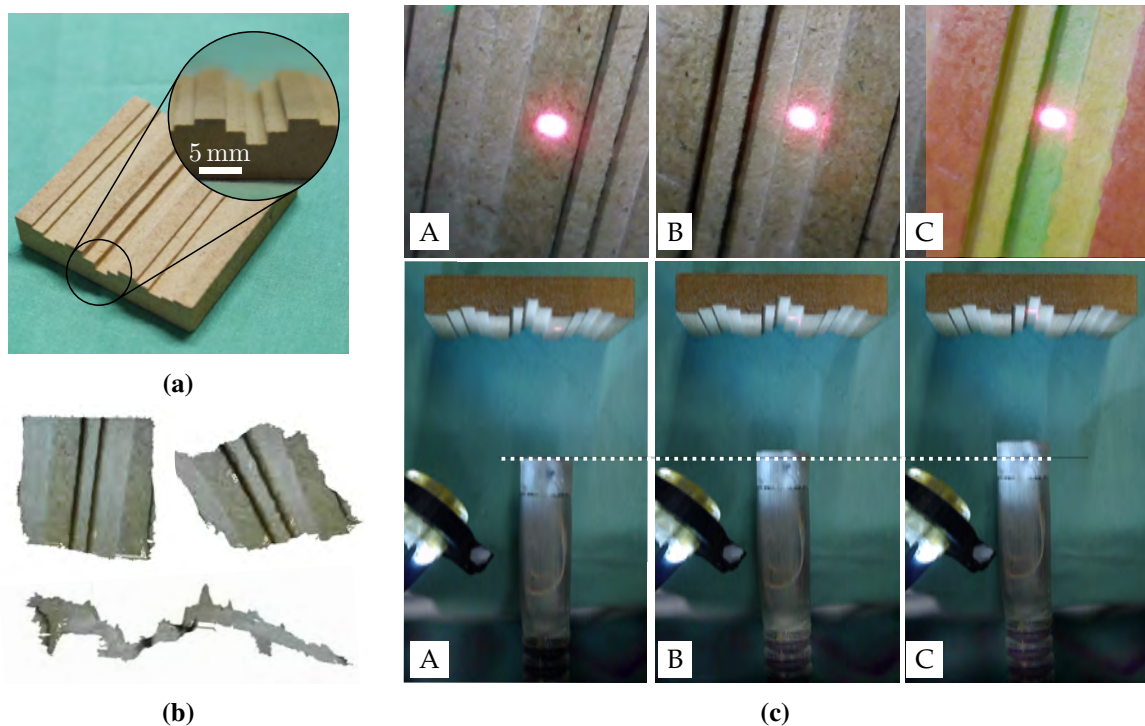
Fig. 7.16: Stability assessment of the visuo-haptic and kinematic controller for depth disturbances: (a) Bespoke sample with stepped surface morphology. (b) Surface reconstruction of employed specimen. (c) Example of teleoperated lateral motion with stepped discontinuity on the target surface. For visualisation purposes, the AR overlay is only presented in top row sequence C and faded out in sequences A and B. The bottom row depicts the corresponding lateral and distance adaptation of the robot.
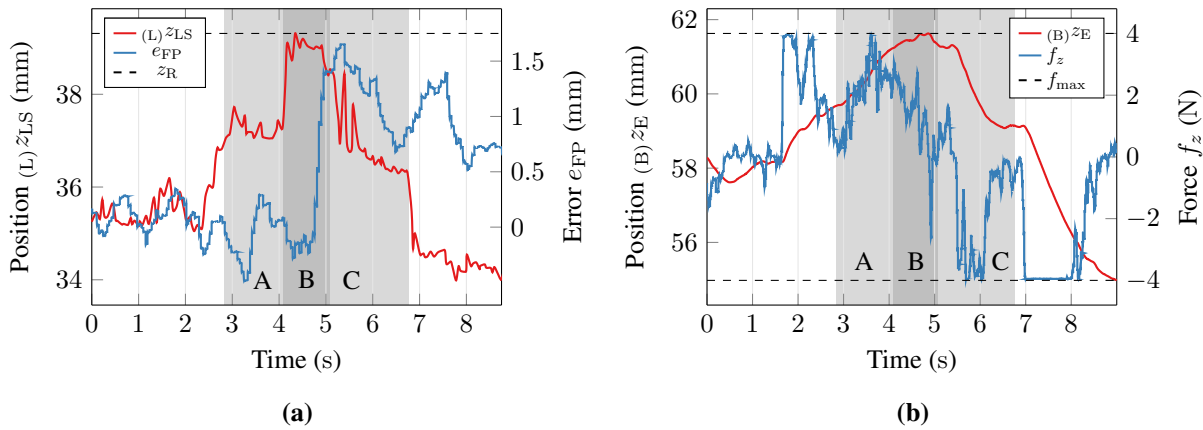
Fig. 7.17: Performance data of experimental controller stability analysis: (a) z-component of laser-surface intersection $_{(L)}\boldsymbol{\eta}_{LS}$ and focal error e_{FP}. Motion sequences are highlighted in grey and annotated by A, B, and C. Rayleigh length $z_R = \pm 1.75\,\mathrm{mm}$ is provided for comparison. (b) Component $_{(B)}z_E$ of end-effector position $_{(B)}\boldsymbol{x}_E$ and active constraints f_{AC} rendered to the master. Dashed lines denote master force limits f_{max}.

second disturbance in sequence B-C is analogously observed. Following the disturbances, focal errors were gradually minimised towards $e_{FP} \to 0\,\mathrm{mm}$. Rayleigh length $z_R = \pm 1.75\,\mathrm{mm}$ was not exceeded at any time during the experiment.

For the sake of completeness, the z-component of the end effector kinematics $\boldsymbol{x}_E$ presented in Figure 7.17a confirmed continuous adaptation of the manipulator length as result of visuo-haptic operator assistance. The adjustment along the manipulator axis followed the surface profile as demonstrated by intersection $_{(L)}z_{LS}$.

On the one hand, measurements appeared to be smoothed due to low bandwidth of current actuator dynamics. On the other hand, estimates of the surface intersection tend to generate an increased number of outliers if discontinuities of the camera motion are present. This particularly results in oscillation phenomena as shown sequence C of Figure 7.17a. Beyond that, a segmental elongation of $4\,\mathrm{mm}$, which in total composed of two sequential $2\,\mathrm{mm}$ extensions is illustrated in Figure 7.16c. Forces f_{AC} given as output of the haptic controller and applied to the master device did not exhibit any vibrations. After the disturbances, forces immediately stepped up to hardware limits of $\pm 4\,\mathrm{N}$ and guided the operator towards minimised errors with finally $f_{AC} \to 0\,\mathrm{N}$. Concisely, force oscillations in the study did not exceed $\pm 1.25\,\mathrm{N}$.

7.3.3 Deployment to Ex Vivo Animal Model

A porcine larynx model represents a validated anatomy for preclinical pilot studies due to the similarities to human anatomy and functionality [SMH⁺12]. The porcine anatomy of the larynx only shows minor morphological differences in comparison to the human counterpart [AFJ13]. The porcine epiglottis is defined by a wider shape and emanates in the front face of the cricoid

cartilage. Major differences regard the twin-paired arytenoid cartilages, which not only penetrate deeper into the inner larynx but also show a second pair of interarytenoid cartilages. Additionally, the porcine laryngeal lumen is narrowed by an intralaryngeal fat pad.

A simulated clinical scenario was generated using an ex vivo porcine larynx model for assessment of device applicability. To implement a resemblance to actual surgery with a patient lying on its back, the specimens with tongue, epiglottis, outer/inner larynx and trachea were positioned in a bespoke frame (see Figure 7.18a). The robotic system remained on its surgical cart as used in the previous studies (see Section 7.1.1). This enabled access to the porcine specimen from the top. The operator controlled the system after insertion to the specimen with the master device. The pilot study aimed at feasibility of deployment and manipulation of the endoscopic tip within the inner larynx in Figure 7.18b to visualise the relevant anatomical structures and to highlight them using the integrated aiming laser as demonstrated by image sequences in Figure 7.19.

The porcine larynx was explored with repeated access to the anatomy ($N = 5$) and marking of anatomical landmarks was executed with robotic teleoperation. In each trial, deployment of the system to the laryngeal anatomy was feasible. All relevant structures such as the epiglottic surface, lateral, dorsal and ventral faces of the supraglottic inlet and especially the glottic region itself, could be visualized by the endoscopic imaging. Moreover, the red pilot laser was visible to the operator and easily manoeuvrable along the vestibular and vocal cords imitating a surgical motion as applied in endolaryngeal laser microsurgery. In comparison to previous studies on specimens with nominal path information, the presented studies were limited to qualitative assessment of the robotic platform due to the absence of nominal tracing markers on the surfaces of the porcine specimen and the feasibility of prior ground truth data acquisition. The latter are mandatory requirements for quantitative ex vivo performance measurements and must be addressed in future work including CT/MRI scanning of the specimens and online registration to the actual scene using stereoscopic scene reconstruction.

7.4 Conclusion

In this chapter, performance evaluation of the robotic framework was presented. The experimental analysis comprised two user studies under consideration of different tasks and conditions as well as complementing feasibility trials.

Manipulation performance of the robotic teleoperation framework was firstly assessed in a user study. The latter comprised robotic tracing tasks of nominal ablation paths with accuracy and temporal metrics. Novices and experts commanded the visible laser beam integrated to the robotic platform on planar tissue substitutes. During the trials, two different visualisation modes were provided for motion-compensated and raw endoscopic views. Even though subjects had a familiarisation of less than $10\,\mathrm{min}$, delineation was completed with errors below $0.5\,\mathrm{mm}$ compared to the nominal paths. The results validated that the proposed kinematic design facilitates delineation of

(a) (b)
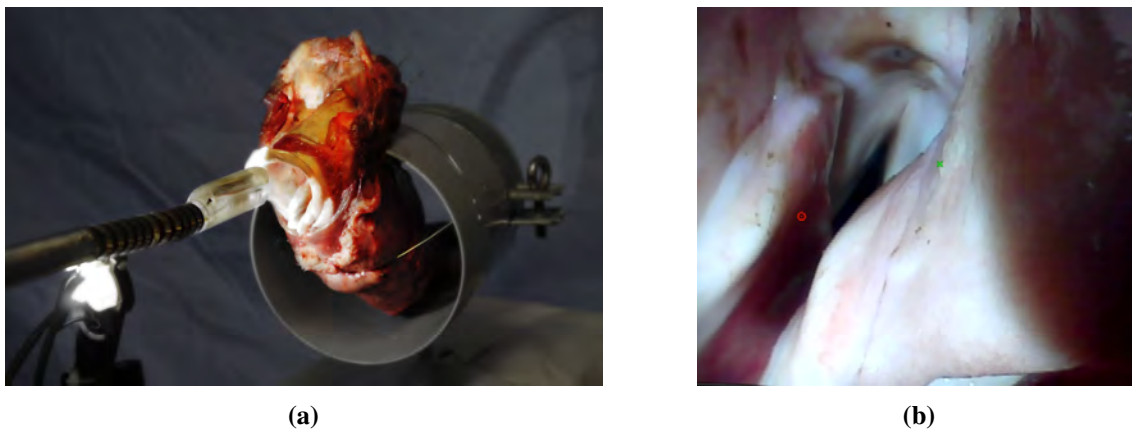
Fig. 7.18: Experimental setup with porcine larynx mounted to customised frame: (a) Insertion of the manipulator to the specimen. (b) Endoscopic view of the surgical site with anatomical landmarks (false and true vocal cords).
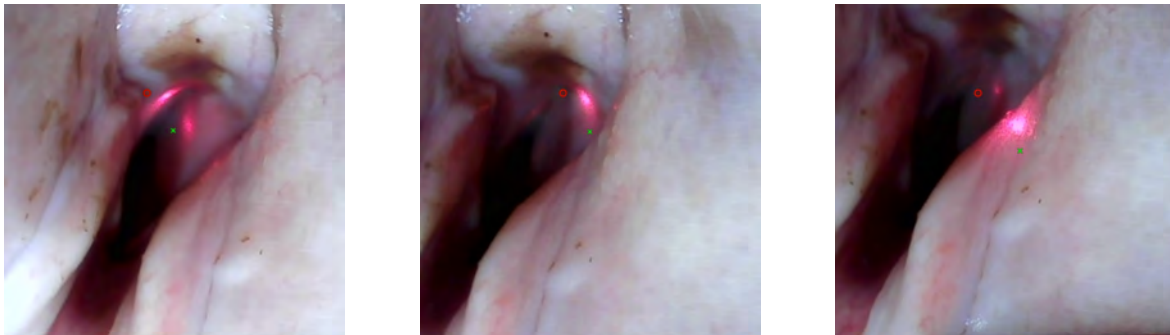
Fig. 7.19: Image sequence of teleoperated robotic landmark tracing using a visible pilot laser.

delicate pathologies. Beyond that, results of postexperimental surveys corroborate the experimental findings.

Following up on promising outcomes of the first user study, preliminary user trials on 3D path tracing on tissue substitutes were conducted. Experimental findings demonstrated that the robotic hardware accommodated even small elevations in the surface topology by extension and compression of continuum segments while concurrently following the nominal path with lateral spot motion. However, limitations on sensing and actuation currently restricts dynamics of the robotic end effector.

A variety of feasibility studies complemented the subject trials, which included a preliminary study on simultaneous tracing and adjustment of the focal position along surfaces on porcine tissue samples. It was demonstrated that the framework enabled successful completion of the tracing task on porcine tissue. Algorithms robustly computed laser-tissue distances and generated corresponding user assistance. Although challenging conditions were present due to illumination angles, surface moisture, and sensor noise, the framework enabled the user to adjust the focal position accurately to the surface during lateral motion.

The injection of external disturbances to control layers caused by depth discontinuities was investigated. Although, specimens with stepped surfaces generated large focal position errors, which were forwarded to kinematic and visuo-haptic controllers, only minor oscillations of the closed-loop framework were observable. The physical interaction of operator and haptic device immediately suppressed formation of any nascent oscillation.

A pilot deployment to an *ex vivo* porcine larynx displayed the ease of handling the device while inserting the manipulator into the specimen. Teleoperation of the endoscopic tip within the inner larynx enabled localisation and tracing of anatomical landmarks.

Future work may consider hardware optimisation to reduce system latencies affecting the control and particularly end effector velocities. This motivates studies in clinically relevant environments, such as cadavers or animal models. Lastly, studies may be repeated with integration of high power laser optics presented in Chapter 3.

8 Vision-based Task Automation for Robotic Laser Surgery

In the last decades, teleoperation has been considered the gold standard in medical robotics. Additionally, assistive concepts were introduced to provide clinical operators with haptic feedback, augmentation of imaging data, or partial automation of surgical tasks. An analogy of this evolution has been applied to the work in the preceding chapters of this thesis. Teleoperation of the remote manipulator was considered for manipulation of the laser beam with respect to the tissue surface. However, the intrinsic sensing capabilities of the endoscopic platform, such as the stereoscopic imaging and online processing of image data, motivate partial or full task automation of the surgical workflow. The integration of novel automation concepts into the presented robotic framework may reduce the cognitive load, improve clinical usability, and enhance the delineation accuracy.

Concepts based on imaging sensors generally target visual servoing control that has been deployed to tasks in endoscopy, laparoscopy, and ultrasound imaging. Vision-driven control schemes are derived from image features as in image-based visual servoing (IBVS) or direct estimation of 3D poses as applied in position-based visual servoing (PBVS) [SK16]. Scheme objectives include reconfiguration of the robot kinematics to optimise camera or instrument poses [AWL+14]. A review on visual control in medical robotics summarises several application examples [AKNP13] and discusses an extension to tomographic imaging [ANKP14]. Alternatively, knowledge-based guidance with incorporation of clinical data was proposed for robotic camera adjustment in laparoscopy [Bih16]. Lastly, a robotic platform for tele-echography enabled online localisation and tracking of targets in tomographic images. Features were automatically maintained in the FoV of the imaging probe during teleoperation [KFN+16]. In the field of laser surgery, visual control is limited to beam steering (see Section 1.3) and basic feature extraction for scanner-based feed-forward ablation [KRW+08].

In this chapter, two automation concepts with visual servoing schemes (see Figure 8.1) are proposed. The schemes extend the robotic control framework to a nested controller design with different loop frequencies, i.e fast inner robotic loop and slow outer imaging loop. Firstly, the vision-based user assistance for optimal visibility of specific surgical targets is described in Section 8.1. Secondly, interactive definition of 3D ablation trajectories in the endoscopic live image and subsequent automated laser delineation are presented in Section 8.2.
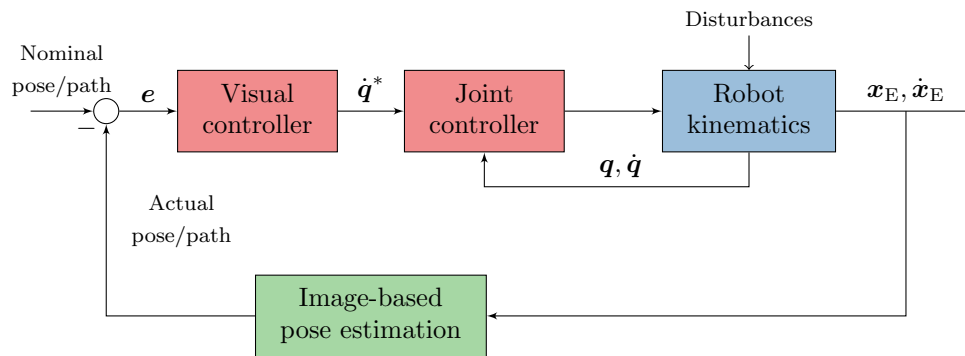
Fig. 8.1: Control chart of the position-based visual servoing scheme deployed to the extensible continuum robot framework.

8.1 Assistance for Endoscopic View Optimisation

Automated vision-based user assistance complements the visuo-haptic assistance presented in Chapter 6. The system would automate the adjustment of the endoscopic view during teleoperation or after scene motion to maintain target visibility. This may facilitate intraoperative usability and task performance as surgical targets are prone to perturbation or external reconfiguration of the robotic unit located in the operating theatre. Beyond that, operators would be able to focus on primary tasks, rather than having to continously adjust the vision of the robot. The overall concept is outlined in Figure 8.2. An integration to a prospective surgical workflow may result in the following sequence:

1. Insertion of the robotic endoscope to the anatomy (e.g. larynx, abdomen, etc.) and attachment of the base to a positioning unit.

2. Teleoperation of the endoscope in basic mode (3 DoF translation) or advanced mode (combined 5 DoF translation/orientation) for exposure and assessment of pathologies.

3. User input of the desired surgical view and activation of the PBVS controller.

4. PBVS maintains continuous visibility or view recovery of the surgical target.

5. Operators may deactivate the feature at any time for transition to manual input.

The robotic endoscope proposed in Chapter 4 presents an eye-in-hand configuration. Thus, automation of camera pose adjustments, i.e. reduction of the Cartesian pose errors, motivates a controller design with PBVS applied to the kinematics framework of the extensible continuum structure. The following sections describe the algorithmic details and the control design. Finally, the experimental protocol and setup for feasibility evaluation are presented and complemented with study results.
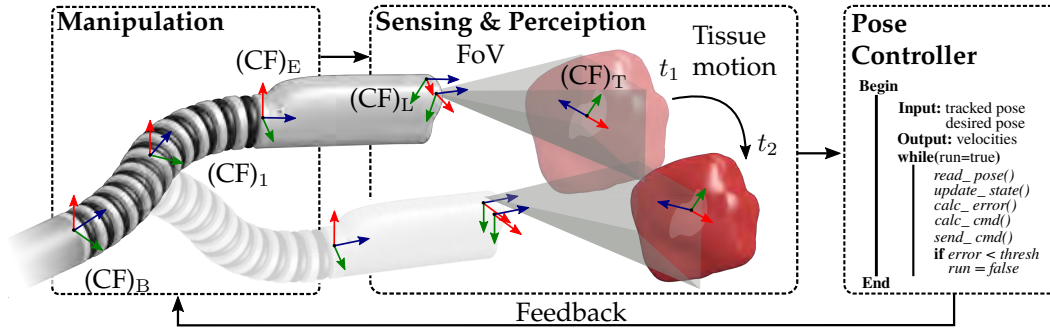
Fig. 8.2: Pose controller concept for vision-based view adjustment to maintain permanent visibility of the surgical target in motion between time instances t_1 and t_2 or to initiate a readjustment after scene motion.

8.1.1 Target Pose Estimation

Consideration of PBVS involves online estimation of the actual target poses to control deviations from nominal state. State-of-the-art methods estimate poses of scene features or objects from integrated vision sensors or external measurements, e.g. optical tracking of fiducials [SK16]. However, use of the robotic hardware in confined anatomy prevents external sensing concepts. Thus, pose estimation must rely on integrated stereoscopic imaging of the robotic eye-in-hand configuration.

The initialisation workflow of the estimation algorithm includes the following phases: 1) The operator adjusts the robotic endoscope to a desired view for exposure and assessment of the surgical scene. 2) Tablet-based UI input enables RoI drawing for specification of surgical targets in the endoscopic live image. 3) The operator finally confirms the selected RoI to activate the pose controller framework.

The subsequent workflow uses acquisition and processing of arbitrary captured surfaces enclosed by the RoI from stereoscopic reconstruction (see Section 2.5). A sparse grid of points $_{(LI)}\boldsymbol{p}_{T,i} = \left(_{(LI)}u_{T,i}, _{(LI)}v_{T,i}\right)^{T} \in \mathbb{N}^2$ is populated at initial time step t_0 within the RoI in image space $(CF)_{LI}$ with $i = \{1, \ldots, N_G\}$. N_G denotes the total number of points populated in a $(n \times m)$ grid. Here, equidistant grid population $(n = m = 10)$ and dynamic resampling to variable RoI sizes are taken into account. Allocated points are consolidated to set

$$\Omega_G = \{_{(LI)}\boldsymbol{p}_{T,1}, _{(LI)}\boldsymbol{p}_{T,i}, \ldots, _{(LI)}\boldsymbol{p}_{T,N_G}\}. \tag{8.1}$$

Scene tracking (see Section 2.6) is activated and initialised with point set Ω_G. This enables measurement of temporal displacement $\Omega_G(t_k)$. Set elements are further mapped to the left camera space according to

$$_{(L)}\boldsymbol{P}_{T,i}(t_k) = h\left(\boldsymbol{D}(t_k), _{(LI)}\boldsymbol{p}_{T,i}(t_k)\right) \in \mathbb{R}^3, \tag{8.2}$$

where h is the direct transformation $\mathbb{R}^2 \to \mathbb{R}^3$ between image plane and Euclidean space given by depth map $\boldsymbol{D}$. This enables mapping of the tracked grid points to the target surface which yields set

$$\widetilde{\Omega}_{\mathrm{G}}(t_k) = \{{}_{(\mathrm{L})}\boldsymbol{P}_{\mathrm{T},1}(t_k), {}_{(\mathrm{L})}\boldsymbol{P}_{\mathrm{T},i}(t_k), \ldots, {}_{(\mathrm{L})}\boldsymbol{P}_{\mathrm{T},N}(t_k)\}. \tag{8.3}$$

The centroid of this set is determined to

$$_{(\mathrm{L})}\boldsymbol{P}_{\widetilde{\Omega}_{\mathrm{G}}}(t_k) = \frac{1}{N_{\mathrm{G}}} \sum_{i=1}^{N_{\mathrm{G}}} {}_{(\mathrm{L})}\boldsymbol{P}_{\mathrm{T},i}(t_k) \in \mathbb{R}^3. \tag{8.4}$$

Centroid $_{(\mathrm{L})}\boldsymbol{P}_{\widetilde{\Omega}_{\mathrm{G}}}(t_0) = {}_{(\mathrm{L})}\boldsymbol{P}_{\widetilde{\Omega}_{\mathrm{G}}}^0$ from user initialisation is stored and constitutes the linear component of the nominal pose. This work has disregarded online point-based registration for framewise pose estimation using the tracked grid as this may cause further latencies in the processing workflow and does not consider larger surface deformations.

The angular component of the nominal pose is derived from a local surface approximation and corresponding surface normal estimation. The sparse local surface approximation is represented by set $\widetilde{\Omega}_{\mathrm{G}}(t_k)$. Under consideration of related work, SVD plane estimation is selected due to lower computational efforts [KAWB09, HBZS14]. In consequence, set $\widetilde{\Omega}_{\mathrm{G}}(t_k)$ is organised to mean-centred measurement matrix

$$\boldsymbol{H}(t_k) = \begin{pmatrix} {}_{(\mathrm{L})}\boldsymbol{P}_{\mathrm{T},1}^{\mathrm{T}}(t_k) - {}_{(\mathrm{L})}\boldsymbol{P}_{\widetilde{\Omega}_{\mathrm{G}}}^{\mathrm{T}}(t_k) \\ \vdots \\ {}_{(\mathrm{L})}\boldsymbol{P}_{\mathrm{T},N}^{\mathrm{T}}(t_k) - {}_{(\mathrm{L})}\boldsymbol{P}_{\widetilde{\Omega}_{\mathrm{G}}}^{\mathrm{T}}(t_k) \end{pmatrix} \in \mathbb{R}^{N_{\mathrm{G}} \times 3}. \tag{8.5}$$

The SVD of Equation (8.5) yields

$$\boldsymbol{U}\boldsymbol{\Sigma}\boldsymbol{V}^{\mathrm{T}} = \boldsymbol{H}(t_k), \tag{8.6}$$

where $\boldsymbol{U} \in \mathbb{R}^{N_{\mathrm{G}} \times N_{\mathrm{G}}}$ and $\boldsymbol{V} \in \mathbb{R}^{3 \times 3}$ are unitary matrices and $\boldsymbol{\Sigma} \in \mathbb{R}^{N_{\mathrm{G}} \times 3}$ is diagonal. The first two eigenvectors of $\boldsymbol{V}^{\mathrm{T}} = (\boldsymbol{v}_1, \boldsymbol{v}_2, \boldsymbol{v}_3)$ are associated with the largest eigenvalues and determine the optimal plane parameters of the local surface approximation to

$$\langle {}_{(\mathrm{L})}\boldsymbol{n}_{\widetilde{\Omega}_{\mathrm{G}}}(t_k), {}_{(\mathrm{L})}\boldsymbol{t}_{\widetilde{\Omega}_{\mathrm{G}}}(t_k) \rangle = 0, \tag{8.7}$$

where $\langle .,. \rangle$ denotes the dot product, $_{(\mathrm{L})}\boldsymbol{n}_{\widetilde{\Omega}_{\mathrm{G}}}(t_k)$ a normal, and $_{(\mathrm{L})}\boldsymbol{t}_{\widetilde{\Omega}_{\mathrm{G}}}(t_k)$ a tangent of the estimated plane. The latter are computed by

$$_{(\mathrm{L})}\boldsymbol{n}_{\widetilde{\Omega}_{\mathrm{G}}}(t_k) = \boldsymbol{v}_1 \times \boldsymbol{v}_2, \quad {}_{(\mathrm{L})}\boldsymbol{t}_{\widetilde{\Omega}_{\mathrm{G}}}(t_k) = {}_{(\mathrm{L})}\boldsymbol{r}^*(t_k) - {}_{(\mathrm{L})}\boldsymbol{r}_0(t_k), \tag{8.8}$$

where $_{(\mathrm{L})}\boldsymbol{r}_0(t_k) = {}_{(\mathrm{L})}\boldsymbol{P}_{\widetilde{\Omega}_{\mathrm{G}}}(t_k)$. Arbitrary point $_{(\mathrm{L})}\boldsymbol{r}^*(t_k) \in \mathbb{R}^3$ in the estimated plane is given by

$$_{(\mathrm{L})}\boldsymbol{r}^*(t_k) = {}_{(\mathrm{L})}\boldsymbol{r}_0(t_k) + \alpha\boldsymbol{v}_1 + \beta\boldsymbol{v}_2, \tag{8.9}$$

where $\alpha, \beta \in \mathbb{R}$ are arbitrary scalars. Orthogonality of vectors enables the pose definition of target frame $(CF)_T$ with origin ${}_{(L)}\boldsymbol{P}_{\widetilde{\Omega}_G}(t_k)$ and orientation

$$
{}^L\boldsymbol{R}_T(t_k) = \begin{pmatrix} \left({}_{(L)}\boldsymbol{n}_{\widetilde{\Omega}_G}(t_k) \times {}_{(L)}\boldsymbol{t}_{\widetilde{\Omega}_G}(t_k) \right)^T \\ {}_{(L)}\boldsymbol{t}_{\widetilde{\Omega}_G}^T(t_k) \\ {}_{(L)}\boldsymbol{n}_{\widetilde{\Omega}_G}^T(t_k) \end{pmatrix} \in \mathrm{SO}(3). \tag{8.10}
$$

The angular contribution of the nominal pose constitutes to ${}^L\boldsymbol{R}_T(t_0) = {}^L\boldsymbol{R}_T^0$ and is defined by initial orientation of the operator camera view selection. Both components are merged to PBVS task features expressed in camera frame $(CF)_L$ with actual feature $\boldsymbol{s}(t_k) = \{ {}_{(L)}\boldsymbol{P}_{\widetilde{\Omega}_G}(t_k), {}^L\boldsymbol{R}_T(t_k) \}$ and nominal features $\boldsymbol{s}^* = \{ {}_{(L)}\boldsymbol{P}_{\widetilde{\Omega}_G}^0, {}^L\boldsymbol{R}_{\widetilde{\Omega}_G}^0 \}$. Angular components of $\boldsymbol{s}$ and $\boldsymbol{s}^*$ are converted to quaternions to overcome control deficiencies. The reader is kindly referred to standard literature for further information [SK16]. The conversion is generally given by inverse solution of equation

$$
\boldsymbol{R}(\boldsymbol{h}) = \boldsymbol{I} - 2h_0[\boldsymbol{h}_v]_\times + 2\left([\boldsymbol{h}_v]_\times\right)^2 = (h_0^2 - \boldsymbol{h}_v^T\boldsymbol{h}_v)\boldsymbol{I} + 2\boldsymbol{h}_v\boldsymbol{h}_v^T + 2h_0[\boldsymbol{h}_v]_\times, \tag{8.11}
$$

where $\boldsymbol{I} \in \mathrm{SO}(3)$ is the identity matrix, $[\cdot]_\times$ defines the skew-symmetric operator, and $\boldsymbol{h} = (h_0, \boldsymbol{h}_v)^T$ describes a unit quaternion with $\boldsymbol{h}^T\boldsymbol{h} = 1$. The mapping in [HGD10] is considered for angular representations:

$$
h_0 = \frac{\sqrt{1 + tr(\boldsymbol{R})}}{2} \qquad \boldsymbol{h}_v = \pm\frac{\boldsymbol{u}\sqrt{3 - tr(\boldsymbol{R})}}{2}, \tag{8.12}
$$

where $tr(\cdot)$ defines the trace operator and $\boldsymbol{u} \in \mathbb{R}^3$ the rotation axis given by unit eigenvectors corresponding to the eigenvalue of any given rotation matrix $\boldsymbol{R} \in \mathrm{SO}(3)$.

8.1.2 Pose Controller Design

Since actual and nominal target poses are estimated according to Section 8.1.1, a controller framework based on PBVS is designed for error regulation of actual and nominal poses. A scenario dedicated to temporal variation of robot poses and/or tissue motion is illustrated in Figure 8.3. The latter further shows kinematic annotations for derivation of the robotic state space controller.

The proposed PBVS controller adapts the decoupled formulation of linear and angular error state spaces in [TMCG02] and is extended with an angular quaternion representation [HGD10]. The general error state space $\boldsymbol{\xi}$ is composed of linear and angular components. For a discrete time step t_k, it yields to

$$
\boldsymbol{\xi} = {}_{(N)}\boldsymbol{e}(t_k) = \begin{pmatrix} {}_{(N)}\boldsymbol{e}_l(t_k) \\ {}_{(N)}\boldsymbol{e}_a(t_k) \end{pmatrix} \in \mathbb{R}^6, \tag{8.13}
$$

where ${}_{(N)}\boldsymbol{e}_l \in \mathbb{R}^3$ and ${}_{(N)}\boldsymbol{e}_a \in \mathbb{R}^3$ are linear and angular pose errors between actual camera frame $(CF)_L$ and nominal camera frame $(CF)_N$. In the following, the linear error state space is derived
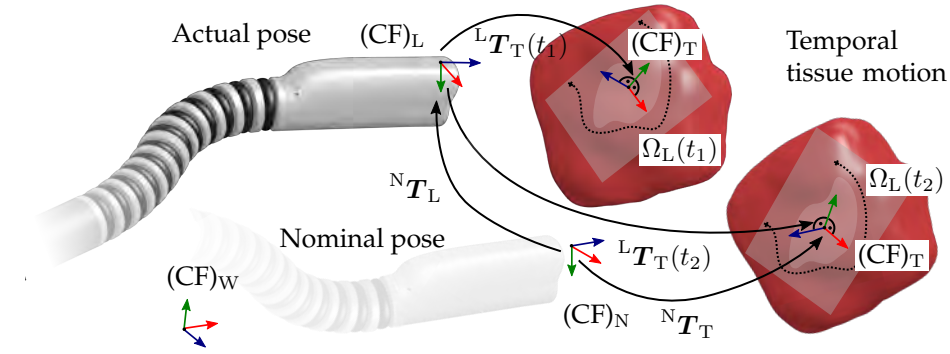
Fig. 8.3: PBVS concept for optimal target visibility. Relevant coordinate frames and homogeneous transformations for the pose controller design are indicated. Consecutive time steps t_1 and t_2 describe the exemplary tissue motion.

under consideration of a temporary world frame $(\text{CF})_\text{W}$. This intermediate frame simplifies the derivation of relevant transformations between initial, nominal, and target frames. By definition, linear errors are reported to

$$_{(\text{N})}\boldsymbol{e}_\text{l}(t_k) = {}_{(\text{N})}\boldsymbol{P}_\text{L}(t_k) = {}^{\text{N}}\boldsymbol{R}_\text{W}(t_k)\underbrace{\left({}_{(\text{W})}\boldsymbol{P}_\text{L}(t_k) - {}_{(\text{W})}\boldsymbol{P}_\text{N}(t_k)\right)}_{_{(\text{W})}\boldsymbol{e}_\text{l}(t_k)}. \tag{8.14}$$

The time derivative of Equation (8.14) is determined by applying the product rule:

$$_{(\text{N})}\dot{\boldsymbol{e}}_\text{l}(t_k) = {}^{\text{N}}\boldsymbol{R}_\text{W}(t_k)\left({}_{(\text{W})}\dot{\boldsymbol{p}}_\text{L}(t_k) - {}_{(\text{W})}\dot{\boldsymbol{p}}_\text{N}(t_k)\right) + {}^{\text{N}}\dot{\boldsymbol{R}}_\text{W}(t_k){}_{(\text{W})}\boldsymbol{e}_\text{l}(t_k). \tag{8.15}$$

Substitution of actual camera frame velocities $_{(\text{W})}\dot{\boldsymbol{p}}_\text{L} = {}_{(\text{W})}\boldsymbol{v}_\text{L}$, nominal camera frame velocities $_{(\text{W})}\dot{\boldsymbol{p}}_\text{N} = {}_{(\text{W})}\boldsymbol{v}_\text{N}$, and time derivative ${}^{\text{N}}\dot{\boldsymbol{R}}_\text{W} = -[\boldsymbol{\omega}_\text{N}]_\times {}^{\text{N}}\boldsymbol{R}_\text{W}$, where $[.]_\times$ denotes the skew-matrix operator and $\boldsymbol{\omega}_\text{N} \in \mathbb{R}^3$ are angular velocities of frame $(\text{CF})_\text{N}$, concludes to:

$$_{(\text{N})}\dot{\boldsymbol{e}}_\text{l}(t_k) = {}^{\text{N}}\boldsymbol{R}_\text{W}(t_k)\left({}_{(\text{W})}\boldsymbol{v}_\text{L}(t_k) - {}_{(\text{W})}\boldsymbol{v}_\text{N}(t_k)\right) - \left[{}_{(\text{N})}\boldsymbol{\omega}_\text{N}(t_k)\right]_\times \underbrace{{}^{\text{N}}\boldsymbol{R}_\text{W}(t_k){}_{(\text{W})}\boldsymbol{e}_\text{l}(t_k)}_{_{(\text{N})}\boldsymbol{e}_\text{l}(t_k)}. \tag{8.16}$$

Reporting $_{(\text{W})}\boldsymbol{v}_\text{L} = {}^{\text{W}}\boldsymbol{R}_{\text{L}(\text{L})}\boldsymbol{v}_\text{L}$ into Equation (8.16) provides:

$$_{(\text{N})}\dot{\boldsymbol{e}}_\text{l}(t_k) = \underbrace{{}^{\text{N}}\boldsymbol{R}_\text{W}(t_k){}^{\text{W}}\boldsymbol{R}_\text{L}(t_k)}_{^{\text{N}}\boldsymbol{R}_\text{L}(t_k)}{}_{(\text{L})}\boldsymbol{v}_\text{L}(t_k) - \underbrace{{}^{\text{N}}\boldsymbol{R}_\text{W}(t_k){}_{(\text{W})}\boldsymbol{v}_\text{N}(t_k)}_{_{(\text{N})}\boldsymbol{v}_\text{N}(t_k)} - \left[{}_{(\text{N})}\boldsymbol{\omega}_\text{N}(t_k)\right]_\times {}_{(\text{N})}\boldsymbol{e}_\text{l}(t_k). \tag{8.17}$$

Unknown rotation ${}^{\text{N}}\boldsymbol{R}_\text{L}(t_k)$ between actual and nominal camera frames is obtained from online pose estimation of surgical target frame $(\text{CF})_\text{T}$ (see Equation (8.10)) and constant nominal orientation: ${}^{\text{N}}\boldsymbol{R}_\text{L}(t_k) = {}^{\text{N}}\boldsymbol{R}_\text{T}^0{}^{\text{L}}\boldsymbol{R}_\text{T}^\text{T}(t_k)$. Analogously, the linear error is given by

$$_{(\text{N})}\boldsymbol{e}_\text{l}(t_k) = {}_{(\text{N})}\boldsymbol{P}_\text{L}(t_k) = {}_{(\text{N})}\boldsymbol{P}_\text{T}^0 - {}^{\text{N}}\boldsymbol{R}_\text{T}^0{}^{\text{L}}\boldsymbol{R}_\text{T}^\text{T}(t_k){}_{(\text{L})}\boldsymbol{P}_\text{T}(t_k) \tag{8.18}$$

and rigid coupling of target and nominal frame determines the corresponding angular velocities to

$$_{(N)}\boldsymbol{\omega}_N(t_k) = {}^N\boldsymbol{R}_L(t_k)_{(L)}\boldsymbol{\omega}_T(t_k). \tag{8.19}$$

This constitutes the open-loop linear error state space:

$$_{(N)}\dot{\boldsymbol{e}}_l(t_k) = {}^N\boldsymbol{R}_L(t_k)_{(L)}\boldsymbol{v}_L(t_k) - {}_{(N)}\boldsymbol{v}_N(t_k) - \left[_{(N)}\boldsymbol{\omega}_N(t_k)\right]_\times {}_{(N)}\boldsymbol{e}_l(t_k). \tag{8.20}$$

Following related work in [HGD10], the angular control objective of the servoing task addresses ${}^N\boldsymbol{R}_L(t \to \infty) = \boldsymbol{I} \in \mathrm{SO}(3)$. This objective can be converted to equivalent quaternion condition $\|\boldsymbol{h}_{v,a}(t \to \infty)\|_2 \to 0$ using the space mapping introduced in Equation (8.11).

Taking these assumptions into consideration, the angular error state reports to

$$_{(N)}\boldsymbol{e}_a(t_k) = \boldsymbol{h}_{v,a} \in \mathbb{R}^3. \tag{8.21}$$

The time derivative of Equation (8.21) according to [Dix03] yields open-loop state space

$$_{(N)}\dot{\boldsymbol{e}}_a(t_k) = \dot{\boldsymbol{h}}_{v,a}(t_k) = \frac{1}{2}\left(h_{0,a}(t_k)\boldsymbol{I} + [\boldsymbol{h}_{v,a}(t_k)]_\times\right)_{(N)}\boldsymbol{\omega}_L(t_k), \tag{8.22}$$

where $\boldsymbol{I} \in \mathrm{SO}(3)$ denotes the identity matrix, $_{(L)}\boldsymbol{\omega}_L \in \mathbb{R}^3$ are angular velocities of the camera frame, and components of quaternion $\boldsymbol{h}_a$ are computed as in Equation (8.12). Finally, linear and angular state spaces are expressed by time derivatives of the state space

$$\dot{\boldsymbol{\xi}} = \begin{pmatrix} _{(N)}\dot{\boldsymbol{e}}_l(t_k) \\ _{(N)}\dot{\boldsymbol{e}}_a(t_k) \end{pmatrix} = \begin{pmatrix} {}^N\boldsymbol{R}_L(t_k)_{(L)}\boldsymbol{v}_L(t_k) - {}_{(N)}\boldsymbol{v}_N(t_k) - \left[_{(N)}\boldsymbol{\omega}_N(t_k)\right]_\times {}_{(N)}\boldsymbol{e}_l(t_k) \\ \frac{1}{2}\left(h_{0,a}(t_k)\boldsymbol{I} + [\boldsymbol{h}_{v,a}(t_k)]_\times\right)_{(N)}\boldsymbol{\omega}_L(t_k) \end{pmatrix}$$

$$= \underbrace{\begin{pmatrix} -\left[_{(N)}\boldsymbol{\omega}_N(t_k)\right]_\times & \boldsymbol{0} \\ \boldsymbol{0} & \boldsymbol{0} \end{pmatrix}}_{\boldsymbol{L}_0} \begin{pmatrix} _{(N)}\boldsymbol{e}_l(t_k) \\ _{(N)}\boldsymbol{e}_a(t_k) \end{pmatrix} +$$

$$\underbrace{\begin{pmatrix} \boldsymbol{I} & \boldsymbol{0} \\ \boldsymbol{0} & \boldsymbol{C} \end{pmatrix} \begin{pmatrix} {}^N\boldsymbol{R}_L(t_k) & \boldsymbol{0} \\ \boldsymbol{0} & {}^N\boldsymbol{R}_L(t_k) \end{pmatrix}}_{\boldsymbol{L}(\boldsymbol{\xi})} \begin{pmatrix} _{(L)}\boldsymbol{v}_L(t_k) - {}^N\boldsymbol{R}_L^T(t_k)_{(N)}\boldsymbol{v}_N(t_k) \\ _{(L)}\boldsymbol{\omega}_L(t_k) - {}^N\boldsymbol{R}_L^T(t_k)_{(N)}\boldsymbol{\omega}_N(t_k) \end{pmatrix} \tag{8.23}$$

with coefficient

$$\boldsymbol{C} = \frac{1}{2}\left(h_{0,a}(t_k)\boldsymbol{I} + [\boldsymbol{e}_a(t_k)]_\times\right) \tag{8.24}$$

and

$$_{(N)}\boldsymbol{\omega}_L(t_k) = {}^N\boldsymbol{R}_L(t_k)_{(L)}\boldsymbol{\omega}_L(t_k) - {}_{(N)}\boldsymbol{\omega}_N(t_k). \tag{8.25}$$

This simplifies the open-loop error state space to

$$\dot{\boldsymbol{\xi}} = \boldsymbol{L}_0\boldsymbol{\xi} + \boldsymbol{L}(\boldsymbol{\xi})\begin{pmatrix} {}_{(\mathrm{L})}\boldsymbol{v}_{\mathrm{L}}(t_k) - {}^{\mathrm{N}}\boldsymbol{R}_{\mathrm{L}}^{\mathrm{T}}(t_k){}_{(\mathrm{N})}\boldsymbol{v}_{\mathrm{N}}(t_k) \\ {}_{(\mathrm{L})}\boldsymbol{\omega}_{\mathrm{L}}(t_k) - {}^{\mathrm{N}}\boldsymbol{R}_{\mathrm{L}}^{\mathrm{T}}(t_k){}_{(\mathrm{N})}\boldsymbol{\omega}_{\mathrm{N}}(t_k) \end{pmatrix}. \tag{8.26}$$

The closed-loop controller state space assumes an exponential error decay according to:

$$\dot{\boldsymbol{\xi}} = -\underbrace{\begin{pmatrix} \lambda_{\mathrm{l}}\boldsymbol{I} & \boldsymbol{0} \\ \boldsymbol{0} & \lambda_{\mathrm{a}}\boldsymbol{I} \end{pmatrix}}_{\boldsymbol{\lambda}_{\mathrm{G}}}\boldsymbol{\xi}, \tag{8.27}$$

where $\boldsymbol{I} \in \mathrm{SO}(3)$ is the identity matrix, $\boldsymbol{\lambda}_{\mathrm{G}} \in \mathbb{R}^{6\times6}$ a gain matrix, and $\lambda_{\mathrm{l}}, \lambda_{\mathrm{a}} \in \mathbb{R}^+$ are proportional linear and angular controller gains. Substitution of Equation (8.27) into Equation (8.26) and solving for camera velocities yields the decoupled control law:

$$\begin{pmatrix} {}_{(\mathrm{L})}\boldsymbol{v}_{\mathrm{L}}(t_k) \\ {}_{(\mathrm{L})}\boldsymbol{\omega}_{\mathrm{L}}(t_k) \end{pmatrix} = -\boldsymbol{L}^{-1}(\boldsymbol{\xi})\left((\boldsymbol{\lambda}_{\mathrm{G}} + \boldsymbol{L}_0)\boldsymbol{\xi}\right) + \begin{pmatrix} {}^{\mathrm{N}}\boldsymbol{R}_{\mathrm{L}}^{\mathrm{T}}(t_k){}_{(\mathrm{N})}\boldsymbol{v}_{\mathrm{N}}(t_k) \\ {}^{\mathrm{N}}\boldsymbol{R}_{\mathrm{L}}^{\mathrm{T}}(t_k){}_{(\mathrm{N})}\boldsymbol{\omega}_{\mathrm{N}}(t_k) \end{pmatrix}. \tag{8.28}$$

Finally, camera velocities are transformed to the robotic end effector frame with correspondences obtained from hand-eye calibration. This enables computation of linear and angular nominal end effector velocities

$$\underbrace{\begin{pmatrix} {}_{(\mathrm{E})}\boldsymbol{v}_{\mathrm{E}}(t_k) \\ {}_{(\mathrm{E})}\boldsymbol{\omega}_{\mathrm{E}}(t_k) \end{pmatrix}}_{{}_{(\mathrm{E})}\dot{\boldsymbol{x}}_{\mathrm{E}}(t_k)} = \underbrace{\begin{pmatrix} {}^{\mathrm{L}}\boldsymbol{R}_{\mathrm{E}}^{\mathrm{T}} & -{}^{\mathrm{L}}\boldsymbol{R}_{\mathrm{E}}^{\mathrm{T}}\boldsymbol{t}_{\mathrm{L}} \\ \boldsymbol{0} & {}^{\mathrm{L}}\boldsymbol{R}_{\mathrm{E}}^{\mathrm{T}} \end{pmatrix}}_{\boldsymbol{L}_{\mathrm{HE}}}\underbrace{\begin{pmatrix} {}_{(\mathrm{L})}\boldsymbol{v}_{\mathrm{L}}(t_k) \\ {}_{(\mathrm{L})}\boldsymbol{\omega}_{\mathrm{L}}(t_k) \end{pmatrix}}_{{}_{(\mathrm{L})}\dot{\boldsymbol{x}}_{\mathrm{L}}(t_k)}. \tag{8.29}$$

Constant components ${}^{\mathrm{L}}\boldsymbol{R}_{\mathrm{E}} \in \mathrm{SO}(3)$ and $\boldsymbol{t}_{\mathrm{L}} \in \mathbb{R}^3$ are determined from prior hand-eye calibration and describe the rigid spatial relation between image sensors and end effector frame. The resulting controller output $\dot{\boldsymbol{x}}_{\mathrm{L}}(t_k)$ is finally mapped to nominal joint space velocities

$$\dot{\boldsymbol{q}}_{\mathrm{d}}(t_k) = \boldsymbol{J}^{-1}(\boldsymbol{q}_{\mathrm{d}}(t_k))\boldsymbol{L}_{\mathrm{HE}(\mathrm{L})}\dot{\boldsymbol{x}}_{\mathrm{L}}(t_k) \in \mathbb{R}^6, \tag{8.30}$$

where $\boldsymbol{J}(\boldsymbol{q}_{\mathrm{d}}(t_k)) \in \mathbb{R}^{6\times6}$ is the geometric Jacobian of the extensible continuum kinematics presented in Chapter 5.

8.1.3 Experimental Setup

The evaluation of the proposed controller considered two different scenarios based on the experimental setup shown in Figure 8.4a. These scenarios addressed: 1) static environments and 2) dynamic environments. In this work, the latter consisted of rigid body motions. Both experiments used a bespoke laryngeal phantom with prominent pathology close to the edge of the vocal folds (see Figure 8.4b) to simulate a clinical case. More precisely, the phantom was composed of additively fabricated structural parts derived from open source full scale anatomical models

(BodyParts3D, The Database Center for Life Science, Japan). The parts were enclosed by flexible layers of coloured foam to mimic laryngeal texture and appearance. A pathology, e.g. cyst, was mimicked by a dyed foam sample located at the vibratory edge.

The static experiment addresses an automated and markerless reconstitution of an initially selected target view within the FoV after arbitrary displacement of the robotic endoscope. In the initial phases, the workflow incorporates estimation of the nominal view pose related to the observed surgical target as described in Section 8.1.1. Afterwards, the endoscopic tip was teleoperated in 5 DoF with linear and angular input. Lastly, the servoing task was activated and the view controller regulated the residual pose errors. The resulting view adjustment was monitored by the operator and could be aborted at any time. Control of the pose errors was the primary task objective, whereas joint limit avoidance was the secondary objective.

The dynamic performance of the controller was evaluated in a dynamic environment. The corresponding workflow consisted of an initial selection of a nominal target view in the UI and subsequent temporal phantom (rigid body) motion executed by a robotic hexapod (H-824 6-Axis, Physik Instrumente, Karlsruhe, Germany). The linear displacement consisted of semi-circular (5 mm radius) motion patterns with augmented angular pan-tilt motions of $\pm 3°$. Cartesian robot velocities were limited to $v_{E,max} = 2\,\text{mm}\,\text{s}^{-1}$ to provide reliable surface tracking. Linear and angular controller gains were heuristically tuned for optimal convergence to $\lambda_l = 1.4$ and $\lambda_a = 0.7$.

8.1.4 Results

Four experimental trials were performed to assess the vision-based control performance in the static scenario. Exemplary data of controller output with respect to Cartesian pose errors and commanded velocities are summarised in Figures 8.5a and 8.5b. The assumption of an exponential decrease in the design of the state space controller is reflected by results in Figure 8.5a. Linear errors converged from initial offsets beyond $3\,\text{mm}$ towards zero with progressing time. Equivalently, angular components of the tip (pan-tilt) have been reduced (see Figure 8.5b). However, a minor residual angular error about the y-axis was identified. The commanded nominal velocities and angular rates of the robot controller are shown in Figure 8.5c. Velocities corresponded to pose errors characteristics, i.e. decreasing errors have caused decreasing velocities towards completion of the task objective. Beyond that, the associated Cartesian motion of the end effector frame is presented in Figure 8.5d and constitutes a linear path. This motion is further illustrated in Figure 8.6. The findings confirm the design objectives of the decoupled visual controller. Pose errors of the remaining trials on static targets are listed in Table 8.1. Residual linear errors after activation of the visual controller generally yielded less than $0.5\,\text{mm}$ in reference to initial displacements in all linear axes in the range of $2\,\text{mm}$ to $5\,\text{mm}$. Execution times were approximately $12\,\text{s}$ to $15\,\text{s}$ until steady residual errors were detected. Remarkably, linear errors along the z-axis were consistently below $0.2\,\text{mm}$. Angular errors analogously decreased from initial $30\,\text{mrad}$ to $50\,\text{mrad}$ for both axes to below $20\,\text{mrad}$. In particular, the controller performance of the y-axis outperformed the
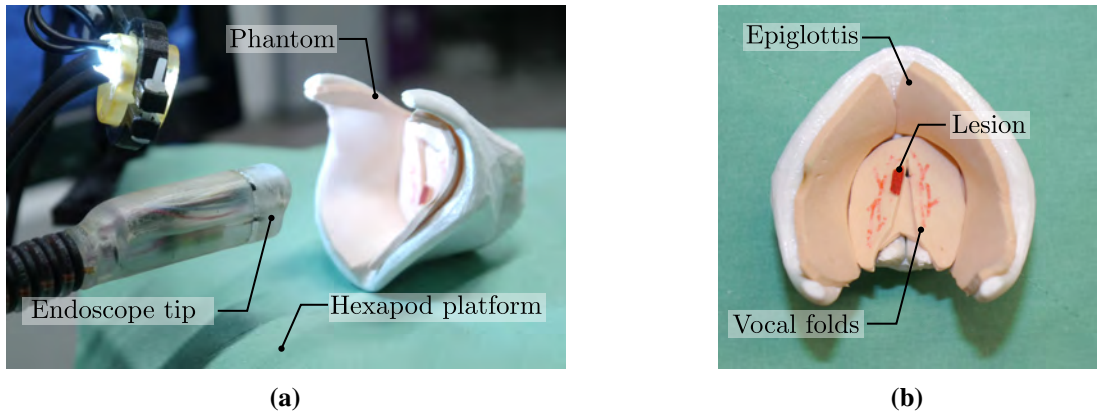
Fig. 8.4: Experimental setup for automation of endoscopic view optimisation: (a) Setup with endoscopic manipulator, phantom, and hexapod platform. (b) Craniocaudal view of the employed laryngeal phantom.

x-axis due to activation of the joint limit avoidance from actuator displacements as indicated in Table 8.1. For the sake of completeness, overall trial performance is given by RMSE control from initial linear offset $e_{l,RMS}(t = 0) = 5.17\,\mathrm{mm}$ to $e_{l,RMS}(t \to \infty) = 0.36\,\mathrm{mm}$ and by adjustment of initial angular offset $e_{a,RMS}(t = 0) = 68\,\mathrm{mrad}$ to $e_{a,RMS}(t \to \infty) = 25\,\mathrm{mrad}$.

On the contrary, exemplary data of the dynamic controller performance is provided in Figure 8.7. The linear error characteristics are shown in Figure 8.7a and present increasing errors after commencement of target motions. Consecutively, the controller immediately compensated the pose errors and stabilised linear residuals to less than $\pm 3.75\,\mathrm{mm}$. Angular errors were regulated analogously (see Figure 8.7b). However, a residual offset of $40\,\mathrm{mrad}$ about the y-axis was identified at the end of the target motion similarly to the static scenario. Temporal error dynamics further constituted in the commanded linear and angular velocities shown in Figure 8.7c. The corresponding Cartesian motion of the endoscopic end effector is summarised in Figure 8.7d. The acquired robotic trajectory replicated the semicircular motion of the target that was displaced by the hexapod platform. The results of four experimental trials under dynamic conditions are summarised in

Tab. 8.1: Results (mean $\pm$ SD) of initial and residual control errors in mm and mrad for static targets.

	$\boldsymbol{e_l}(t=0)$			$\boldsymbol{e_l}(t=\infty)$			$\boldsymbol{e_a}(t=0)$		$\boldsymbol{e_a}(t=\infty)$	
	$e_{l,x}$	$e_{l,y}$	$e_{l,z}$	$e_{l,x}$	$e_{l,y}$	$e_{l,z}$	$e_{a,x}$	$e_{a,y}$	$e_{a,x}$	$e_{a,y}$
T1	2.9 ± 0.2	2.4 ± 0.2	1.8 ± 0.3	0.2 ± 0.1	0.1 ± 0.1	0.1 ± 0.1	45 ± 3	52 ± 3	21 ± 1	17 ± 3
T2	4.3 ± 0.1	2.1 ± 0.1	2.0 ± 0.1	0.4 ± 0.1	0.1 ± 0.1	0.1 ± 0.1	38 ± 2	67 ± 4	27 ± 1	10 ± 2
T3	4.8 ± 0.2	1.4 ± 0.2	4.7 ± 0.1	0.4 ± 0.3	0.1 ± 0.1	0.1 ± 0.1	12 ± 2	56 ± 3	16 ± 2	10 ± 4
T4	4.0 ± 0.2	2.4 ± 0.2	3.0 ± 0.2	0.3 ± 0.2	0.2 ± 0.1	0.1 ± 0.1	41 ± 2	62 ± 3	22 ± 1	14 ± 3
	3.8 ± 0.2	2.1 ± 0.2	2.9 ± 0.2	0.3 ± 0.2	0.1 ± 0.1	0.1 ± 0.1	34 ± 2	59 ± 3	21 ± 2	13 ± 3

Note: Nominal poses were selected randomly. Cartesian velocity limit of $v_{E,max} = 3\,\mathrm{mm\,s^{-1}}$. The last row summarises the results.
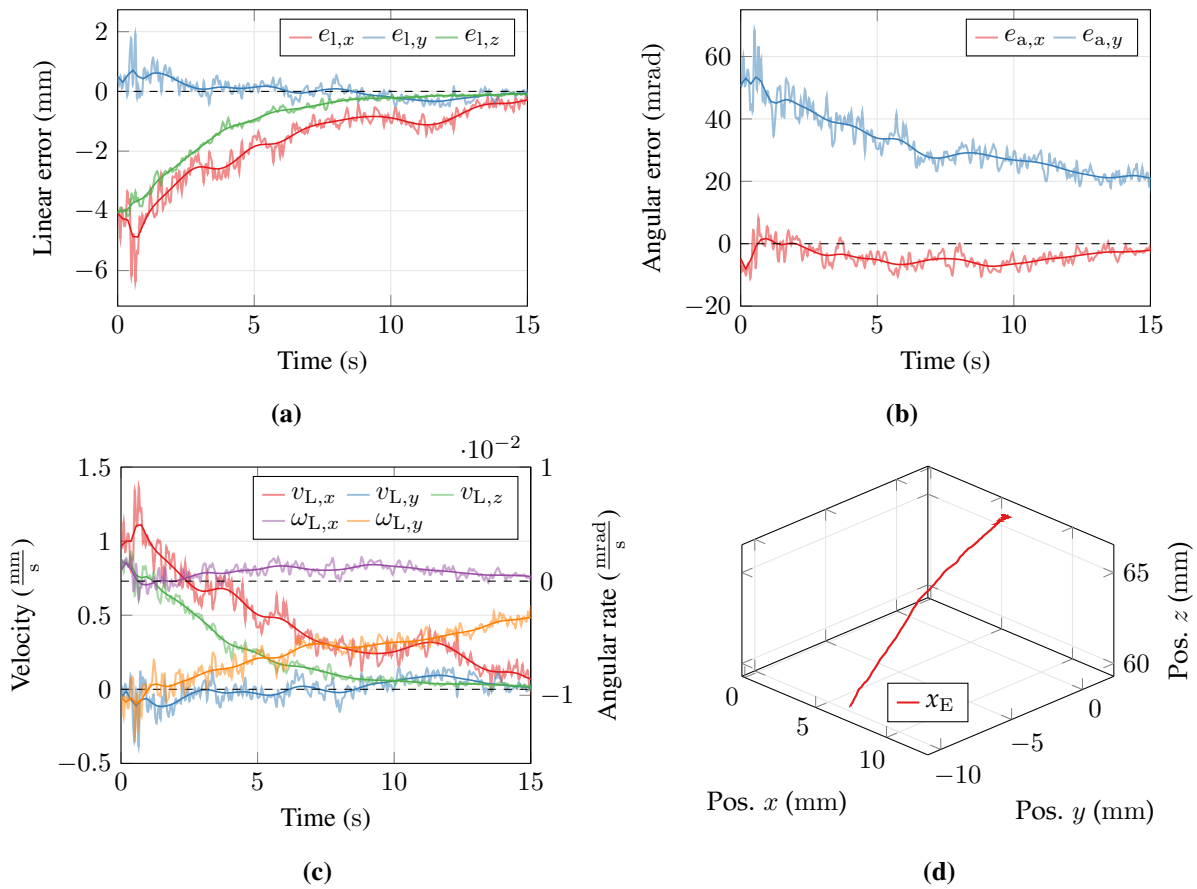
Fig. 8.5: Example of performance data for vision-based pose regulation in a static environment: (a) Linear and (b) angular errors for actual and nominal poses. (c) Camera velocities computed by the controller framework. (d) Resulting Cartesian motion trajectory of the endoscopic end effector position $\boldsymbol{x}_\mathrm{E}$ in base frame $(\mathrm{CF})_\mathrm{B}$.
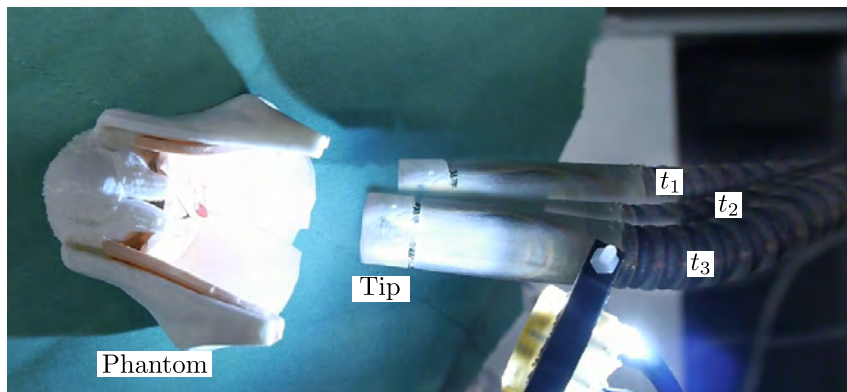
Fig. 8.6: Blending of three images at time instances t_1 to t_3 of the visual servoing task to recover a desired scene view.

Table 8.2. The overall performance for dynamic environments is consolidated by RMSE to linear $e_{l,\mathrm{RMS}} = 2.62\,\mathrm{mm}$ and angular $e_{a,\mathrm{RMS}} = 35\,\mathrm{mrad}$ contributions.
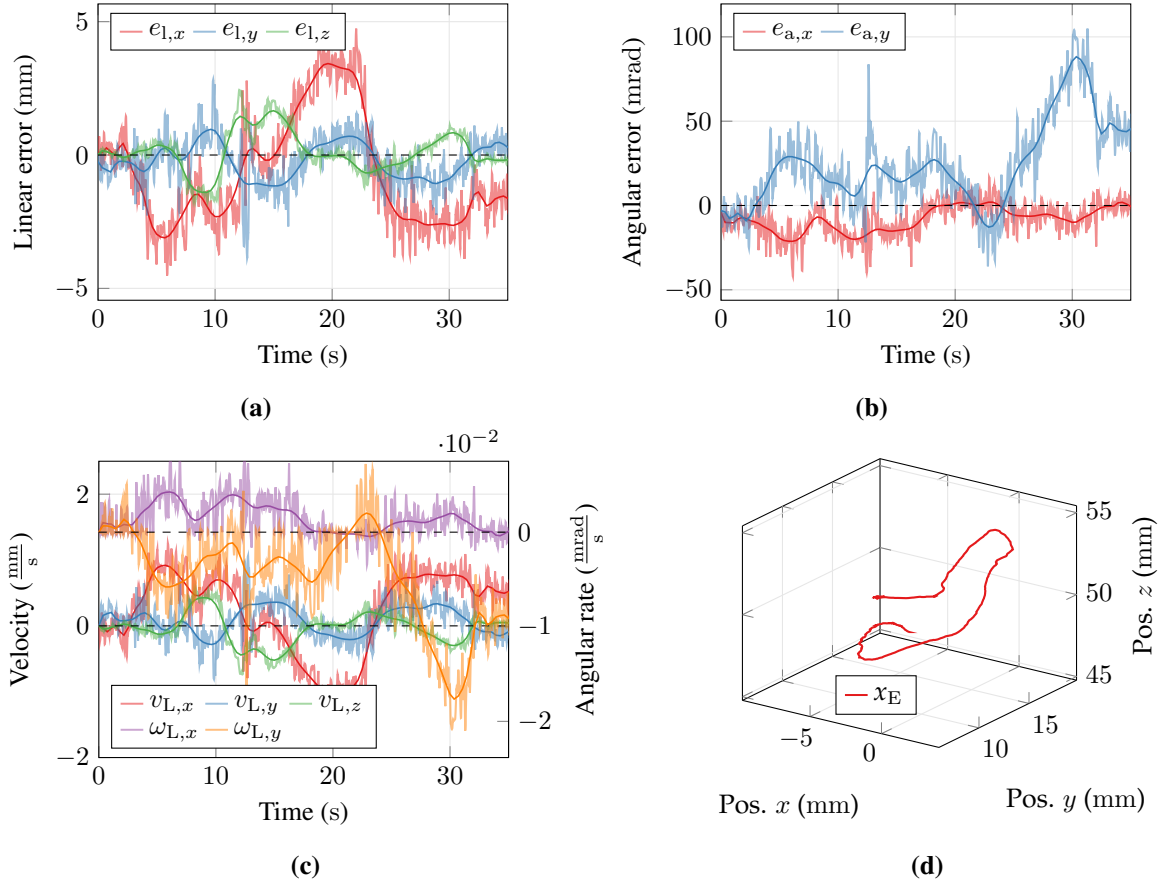
Fig. 8.7: Example of performance data for vision-based pose regulation in dynamic environments with semicircular target motion: (a) Linear and (b) angular errors. (c) Camera velocities computed by the controller framework. (d) Resulting Cartesian motion trajectory of the endoscopic end effector position x_{E} in robot base frame $(\mathrm{CF})_{\mathrm{B}}$.

8.1.5 Discussion

In this section, a vision-based assistance for robotic view adjustment in endoscopic laser surgery was proposed. A decoupled controller framework was derived to maintain or restore a nominal view on a specific surgical area. The framework was deployed to the previously proposed robotic device and evaluated on static and dynamic environments. Experimental results on static scenes demonstrated feasibility. Linear pose disturbances were regulated from a few millimetres to less than $0.5\,\mathrm{mm}$ within approximately $15\,\mathrm{s}$. Angular disturbances were adjusted equivalently, however presence of joint limit avoidance restricted compensation of residual errors about the y-axis of the camera frame. Further actuator displacements, which were required for regulation of the residual angular error, were prevented due to approximation of the predefined joint limits the resulting

Tab. 8.2: Results of residual errors in mm and mrad for dynamic pose control.

	$e_{l,x}$		$e_{l,y}$		$e_{l,z}$		$e_{a,x}$		$e_{a,y}$	
	Mean $\pm$ SD	Mdn	Mean $\pm$ SD	Mdn	Mean $\pm$ SD	Mdn	Mean $\pm$ SD	Mdn	Mean $\pm$ SD	Mdn
T1	1.9 ± 1.1	2.0	0.7 ± 0.6	0.6	0.6 ± 0.6	0.4	10 ± 8	8	28 ± 23	22
T2	2.0 ± 1.6	1.5	1.0 ± 1.3	0.8	0.8 ± 1.5	0.5	27 ± 65	13	48 ± 74	27
T3	3.1 ± 1.7	3.1	1.1 ± 1.1	0.8	0.8 ± 1.2	0.6	13 ± 27	10	27 ± 30	21
T4	2.0 ± 1.2	2.5	2.0 ± 1.3	1.0	0.7 ± 1.7	0.6	36 ± 57	20	42 ± 64	31
	2.2 ± 1.4	2.3	1.2 ± 1.1	0.8	0.7 ± 1.2	0.5	22 ± 39	13	26 ± 48	26

Note: Velocity limit of $v_{\mathrm{E,max}} = 2\,\mathrm{mm\,s^{-1}}$. The last row summarises the overall results.

kinematic constraints were mapped to the actual robot Jacobian to protect the mechanical structure from collisions. The maximal joint limit velocities have not been violated in the presented set of trials.

In dynamic environments, linear errors of less than $2.5\,\mathrm{mm}$ were maintained throughout specimen motion. Both experiments were affected by non-deterministic processing latencies (25 - $80\,\mathrm{ms}$) of acquisition and algorithmic pipelines as well as activation of the joint limit avoidance. The latter restricts full compensation of angular residuals as this requires larger displacements in joint space. Prospectively, enlargement of linear joint strokes may avoid mechanical restrictions. On the other hand, improved sensor acquisition with low computational efforts for image processing may enable optimised convergence due to adaptation of control gains and evade limitations on Cartesian velocities.

Despite weak visual appearance of the phantom surface, poses of the target specimen were estimated and tracked reliably throughout the experimental series with end effector velocity constraints to $2\,\mathrm{mm\,s^{-1}}$. Improved tracking dynamics beyond $2\,\mathrm{mm\,s^{-1}}$ may be achieved prospectively with novel sensor technologies and parallelisation of processing to eliminate latency injection to the control loop. Overall, a detailed assessment of control loop characteristics, e.g. analysis in the frequency domain, is mandatory to optimise stability and convergence performance of the vision-based control framework.

The preliminary study demonstrated feasibility of the derived state space controller in a phantom scenario with decoupled control and exponential convergence of linear and angular pose errors. This approach presents the first eye-in-hand visual servoing deployed to an extensible 5 DoF continuum robot and markerless target pose estimation for automated view assistance in robotic laser surgery.

8.2 Autonomous Execution of 3D Ablation Paths

Several approaches for HMI within the robotic framework were discussed in this thesis and preferably comprised teleoperation. On the one hand, this provides the clinical operator with

the direct spatial manipulation of the laser beam. On the other hand, closed-loop control of the procedure is absent and frequent surgical training is mandatory to master the robotic dexterity in up to 5 DoF. This also brings the concern of safe delivery of high power radiation. To address these shortcomings, an alternative concept of a surgical workflow with two phases is proposed: 1) Intuitive ablation planning and 2) subsequent automated vision-based laser delineation of the defined trajectory. The procedures are conceptually depicted in Figure 8.8. Methodologies are detailed in the following paragraphs.

The concept basically targets advanced system usability by introducing integrated UI ablation planning on endoscopic live images as presented for microscopic scanner devices [MCP$^+$16]. This includes visual identification of the pathology and assessment of required excision margins. These are directly drawn onto the UI using tablet-based input strategies, e.g. a graphics stylus. Prospectively, this phase may be enhanced with preoperative imaging. This enables validation of safety margins and definition of safe areas as discussed in [DMC15a]. The deployment to an endoscopic robot with embedded image sensors further motivates consideration of motion-compensated scene rendering (see Chapter 7).

The interactive definition of ablation paths is converted from image space to a geodesic path, i.e. the ablation path is mapped to the reconstructed 3D tissue surface. This is followed by instantiation of scene tracking and activation of the path controller that ensures laser spot guidance along the nominal path. Beyond that, updates of tracked path and actual focus position are fed into a control law. Delineation errors of less than $0.6\,\mathrm{mm}$ (see clinical requirements in Section)are expected from vision-based closed-loop control, as such the results would outperform teleoperated studies presented in Chapter 7 due to absence of human disturbances. The execution can be separated into two phases denoted as *path approximation* (PA) and *path following* (PF). The PA phase is dedicated to approximation of the laser focus to the first element of the path starting from a random robotic configuration. Subsequently, transition to the PF phase is foreseen until the laser spot has sequentially passed all elements of the user-defined path (see Figure 8.8). Additional safety measures in combination with human supervision enable task abortion and resumption at any time. The following sections describe the design of the vision-based controller framework and its preliminary experimental evaluation.

8.2.1 Path Controller Design

The main task of the path controller is dedicated to vision-based robotic guidance of the preregistered laser focus along a non-parametric path in Cartesian space. Pioneering research in related work was inspired by path following tasks in mobile robotics and was transferred to vision-based laser steering on scanning platforms [AT15, STA15, TRS$^+$18]. This work further distinguishes between path and trajectory following to accommodate temporal aspects, i.e. velocity at any temporal instance along the path. However, prior work exclusively assumed laser delivery with visible spots and neglected beam shapes, i.e. the focal point and its distance to the target surface.
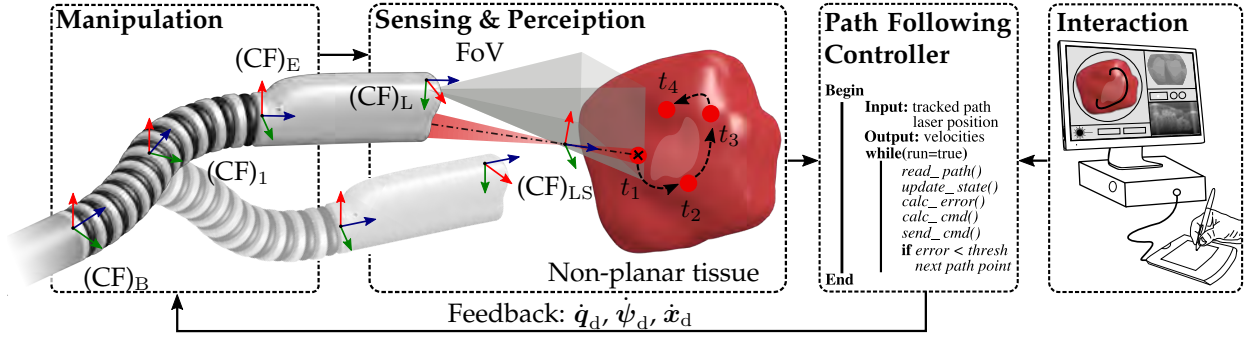
Fig. 8.8: Concept for online planning and automated execution of laser ablation using an extensible contin-
uum robot and proprioceptive sensing. The operator interactively defines the desired ablation path
in the endoscopic live image. The path following controller fuses path tracking and the registered
laser focus position to compute velocity commands for driving the robot from time instances t_1 to
instance t_4.

Hence, the concept in this thesis adapts a controller strategy for robotic path following with surgical
tools under remote centre of motion constraints [DTA18]. Previous work is extended with intuitive
path planning, online scene tracking, and consideration of an eye-in-hand sensor configuration.
This yields a novel vision-based closed-loop path controller for non-contact robotic laser surgery.

At first, the operator directly draws the desired ablation path in the UI onto the live endoscopic image
stream. As shown in Figure 8.9 for the corresponding mapping of subsequent data to 3D space
at time instance t_k, the path is composed of elements $_{(LI)}\boldsymbol{p}_{P,i} = (_{(LI)}u_{P,i},_{(LI)}v_{P,i})^T \in \mathbb{N}^2$ sampled
at interval δ_P and stacked to path set $\Omega_P = \{_{(LI)}\boldsymbol{p}_{P,1},_{(LI)}\boldsymbol{p}_{P,i} \cdots,_{(LI)}\boldsymbol{p}_{P,N_P}\}$ with $i = \{1,\dots,N_P\}$.
N_P describes the total number of path elements. Analogously to Section 8.1.1, scene tracking is
initialised with path set Ω_P to track the temporal surface displacement $\Omega_P(t_k)$ at time step t_k. Set
elements are mapped to Cartesian space as follows:

$$_{(L)}\boldsymbol{P}_{P,i}(t_k) = h\left(\boldsymbol{D}(t_k),_{(LI)}\boldsymbol{p}_{P,i}(t_k)\right) \in \mathbb{R}^3, \tag{8.31}$$

and are concatenated to geodesic path set

$$\Omega_P(t_k) = \{_{(L)}\boldsymbol{P}_{P,1}(t_k),_{(L)}\boldsymbol{P}_{P,i}(t_k),\dots,_{(L)}\boldsymbol{P}_{P,N_P}(t_k)\}, \tag{8.32}$$

where h is the direct transformation $\mathbb{R}^2 \to \mathbb{R}^3$ between image plane and Cartesian space given
by depth map $\boldsymbol{D}$. Line segments constitute $\boldsymbol{s}_j = (_{(L)}\boldsymbol{P}_{P,i},\,_{(L)}\boldsymbol{P}_{P,i+1})^T$ with $j = \{1,\dots,N_P - 1\}$.
The laser focus $_{(L)}\boldsymbol{P}_{LS} \in \mathbb{R}^3$ was registered as described in Section 6.2.

The main path controller consists of two subcontrollers PA and PF. The PA controller implements
the approximation sequence of the robotic endoscope and the corresponding motion of the laser
focus to the first path element $_{(L)}\boldsymbol{P}_{PS}(t_k) = {}_{(L)}\boldsymbol{P}_{P,1}(t_k)$. This phase commences from a random

robot configuration and target within the stereoscopic FoV. Accordingly, the control task considers linear error

$$_{(L)}\boldsymbol{e}_{PA}(t_k) = {}_{(L)}\boldsymbol{P}_{PS}(t_k) - {}_{(L)}\boldsymbol{P}_{LS} \in \mathbb{R}^3 \tag{8.33}$$

with task objective

$$e_{PA}(t \to \infty) = \left\| {}_{(L)}\boldsymbol{e}_{PA}(t \to \infty) \right\|_2 = 0. \tag{8.34}$$

The control design fundamentally uses PBVS as discussed in Section 8.1.2. By contrast, the proposed control law in this section is reduced to linear DoF only. Hence, the time derivative of Equation (8.33) yields error state space

$$_{(L)}\dot{\boldsymbol{e}}_{PA}(t_k) = {}_{(L)}\dot{\boldsymbol{P}}_{PS}(t_k) - {}_{(L)}\dot{\boldsymbol{P}}_{LS}. \tag{8.35}$$

Reporting constant focal registration $_{(L)}\dot{\boldsymbol{P}}_{LS} = \boldsymbol{0}$ and the residual error caused by robot motion into Equation (8.35), the state space reduces to

$$_{(L)}\dot{\boldsymbol{e}}_{PA}(t_k) = {}_{(L)}\dot{\boldsymbol{P}}_{PS}(t_k) = {}_{(L)}\boldsymbol{v}_{L}(t_k), \tag{8.36}$$

where $_{(L)}\boldsymbol{v}_{L}(t_k) \in \mathbb{R}^3$ is the velocity of the camera frame from robotic end effector displacement. Perturbations from target motions are neglected in the remainder of this section as a static environment is assumed. Substitution of exponential error gradient $_{(L)}\dot{\boldsymbol{e}}_{PA} = -\boldsymbol{\lambda}_{PA\,(L)}\boldsymbol{e}_{PA}$ into Equation (8.36) determines nominal camera velocities

$$_{(L)}\boldsymbol{v}_{L}(t_k) = -\boldsymbol{\lambda}_{PA}(t_k)_{(L)}\boldsymbol{e}_{PA}(t_k), \tag{8.37}$$

where $\boldsymbol{\lambda}_{PA}(t_k) = \lambda_{PA}(t_k)\boldsymbol{I} \in \mathbb{R}^{3\times3}$ is a diagonal gain matrix. Lastly, an adaptive gain for jerk-free transition to subsequent PF control is computed as follows according to [OSK10]:

$$\lambda_{PA}(t_k) = \lambda_0 + \lambda_\infty e^{-\frac{\tilde{\lambda}}{\lambda_\infty}\|e_{PA}(t_k)\|_2} \in \mathbb{R}^+, \tag{8.38}$$

where λ_∞ defines the adaptive gain component, λ_0 the static gain, and $\tilde{\lambda}$ the desired temporal gradient. The PA controller is considered active until condition $\|e_{PA}\|_2 < \delta_{PA}$ is satisfied. Parameter δ_{PA} describes the controller transition threshold.

After transition, the PF controller is activated to guide the focal position $_{(L)}\boldsymbol{P}_{LS}$ along the predefined path $_{(L)}\boldsymbol{P}_{P}(t_k)$ at speed $v_P(t_k) \in \mathbb{R}$. Accordingly, the control task error is given by

$$_{(L)}\boldsymbol{e}_{PF}(t_k) = {}_{(L)}\widetilde{\boldsymbol{P}}(t_k) - {}_{(L)}\boldsymbol{P}_{LS} \tag{8.39}$$

with task objective

$$e_{PF}(t \to \infty) = \left\| {}_{(L)}\boldsymbol{e}_{PF}(t_k) \right\|_2, \tag{8.40}$$
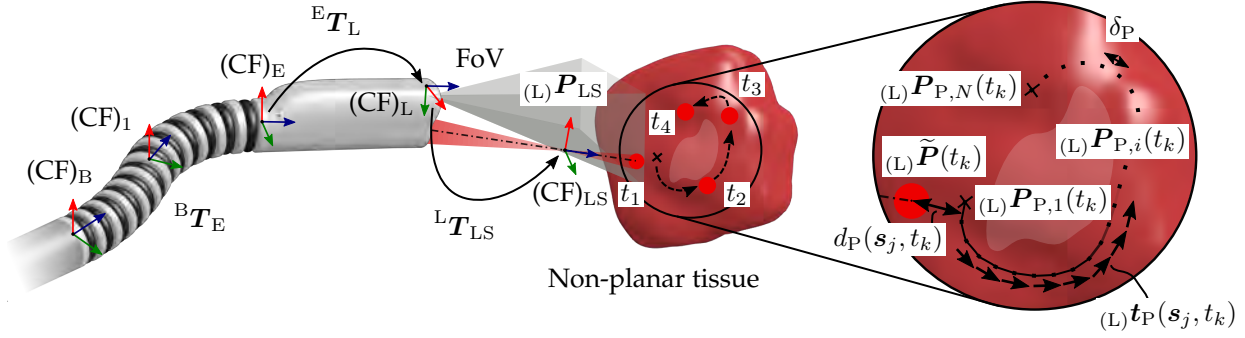
Fig. 8.9: Schematics of automated laser ablation using an extensible continuum robot and interactive path definition. The magnified area highlights and annotates visual, kinematic, and geometric parameters of the ablation path. The surface projection of the laser spot $_{(L)}\widetilde{\boldsymbol{P}}(t_k)$ is required for the design of the path following controller.

where $_{(L)}\widetilde{\boldsymbol{P}}(t_k)$ describes the geometric orthogonal projection of $_{(L)}\boldsymbol{P}_{LS}$ on path set $\Omega_P(t_k)$. For this reason, the orthogonal distance of the actual focus position related to the line segments is computed as:

$$d_P(\boldsymbol{s}_j(t_k)) = \frac{\left\| \left(_{(L)}\boldsymbol{P}_{LS} - {}_{(L)}\boldsymbol{P}_{P,i}(t_k) \right) \times \left(_{(L)}\boldsymbol{P}_{LS} - {}_{(L)}\boldsymbol{P}_{P,i+1}(t_k) \right) \right\|_2}{\left\| {}_{(L)}\boldsymbol{P}_{P,i+1}(t_k) - {}_{(L)}\boldsymbol{P}_{P,i}(t_k) \right\|_2}. \tag{8.41}$$

Subsequently, the orthogonal projection of the focal position to line segments $\boldsymbol{s}_j(t_k)$ is given by:

$$_{(L)}\widetilde{\boldsymbol{P}}(\boldsymbol{s}_j(t_k)) = {}_{(L)}\boldsymbol{P}_{P,i}(t_k) + \ldots$$

$$+ \underbrace{\frac{\left\langle \left(_{(L)}\boldsymbol{P}_{LS} - {}_{(L)}\boldsymbol{P}_{P,i}(t_k) \right), \left(_{(L)}\boldsymbol{P}_{P,i+1}(t_k) - {}_{(L)}\boldsymbol{P}_{P,i}(t_k) \right) \right\rangle}{\left\| {}_{(L)}\boldsymbol{P}_{LS} - {}_{(L)}\boldsymbol{P}_{P,i}(t_k) \right\|_2 \left\| {}_{(L)}\boldsymbol{P}_{P,i+1}(t_k) - {}_{(L)}\boldsymbol{P}_{P,i}(t_k) \right\|_2}}_{g(\boldsymbol{s}_j(t_k))} \left(_{(L)}\boldsymbol{P}_{P,i+1}(t_k) - {}_{(L)}\boldsymbol{P}_{P,i}(t_k) \right),$$

$$\tag{8.42}$$

where $g(\boldsymbol{s}_j(t_k))$ describes the on-segment constraint given by the normalised ratio of current projection and segmental length. Expression $\langle \cdot, \cdot \rangle$ describes the inner vector product. Data of corresponding segments $\boldsymbol{s}_j$ is stacked to distances

$$\boldsymbol{d}_P(t_k) = (d_p(\boldsymbol{s}_1(t_k)), d_p(\boldsymbol{s}_j(t_k)), \ldots, d_p(\boldsymbol{s}_{N_P-1}(t_k)))^T \in \mathbb{R}^{(N_P-1)}, \tag{8.43}$$

projections

$$\widetilde{\boldsymbol{P}}(t_k) = \left(_{(L)}\widetilde{\boldsymbol{P}}(\boldsymbol{s}_1(t_k)), {}_{(L)}\widetilde{\boldsymbol{P}}(\boldsymbol{s}_j(t_k)), \ldots, {}_{(L)}\widetilde{\boldsymbol{P}}(\boldsymbol{s}_{N_P-1}(t_k)) \right) \in \mathbb{R}^{3 \times (N_P-1)}, \tag{8.44}$$

and scaling coefficients

$$\boldsymbol{g}(t_k) = (g(\boldsymbol{s}_1(t_k)), g(\boldsymbol{s}_j(t_k)), \ldots, g(\boldsymbol{s}_{N_P-1}(t_k)))^T \in \mathbb{R}^{(N_P-1)}. \tag{8.45}$$

The corresponding path segment $s_P(t_k)$ of the current focal projection is determined from minimal orthogonal distance and on-segment constraints:

$$\{s_P(t_k) \in S(t_k) \,|\, (0 \leq g(s_P(t_k)) \leq 1) \wedge d_P(s_P) = \min(d_P)\}. \tag{8.46}$$

This finally constitutes the projected focal position

$$_{(L)}\widetilde{P}_P(t_k) = {}_{(L)}\widetilde{P}(s_P(t_k)). \tag{8.47}$$

The subsequent paragraph outlines the error state space of the PF control law. Thereby, error dynamics are described by the time derivative of Equation (8.36) as

$$\begin{aligned}
_{(L)}\dot{e}_{PF}(t_k) &= {}_{(L)}\dot{\widetilde{P}}_P(t_k) - {}_{(L)}\dot{P}_{LS} \\
&= {}_{(L)}v_{\widetilde{P}}(t_k),
\end{aligned} \tag{8.48}$$

where rigid focal registration causes $_{(L)}\dot{P}_{LS} = 0$ and $v_{\widetilde{P}} \in \mathbb{R}^3$ are the actual velocities of the projected spot. The latter can be expressed as

$$_{(L)}\dot{e}_{PF}(t_k) = v_P(t_k)t_P(s_j(t_k)), \tag{8.49}$$

where $v_P(t_k) \in \mathbb{R}$ is the speed along the line segment and $t_P(t_k) \in \mathbb{R}^3$ indicates the tangent to the corresponding line segment. The latter is determined by

$$_{(L)}t_P(s_j, t_k) = \frac{_{(L)}P_{P,i+1}(t_k) - {}_{(L)}P_{P,i}(t_k)}{\left\|_{(L)}P_{P,i+1}(t_k) - {}_{(L)}P_{P,i}(t_k)\right\|_2}. \tag{8.50}$$

Reporting exponential error gradient $_{(L)}\dot{e}_{PF}(t_k) = -\lambda_{PF\,(L)}e_{PF}(t_k)$ into Equation (8.49) and expression $t_P t_P^T = 1$, the speed of the projected laser spot along the line segment yields to

$$v_P(t_k) = -t_P^T(s_j(t_k))\lambda_{PF\,(L)}e_{PF}(t_k), \tag{8.51}$$

where $\lambda_{PF} = \text{diag}\{\lambda_{PF}\} \in \mathbb{R}^{3 \times 3}$ denotes a diagonal gain matrix and λ_{PF} a proportional gain. The eye-in-hand robot configuration inherently defines the nominal velocities of the imaging sensor frame to:

$$_{(L)}v_L(t_k) = v_P(t_k)_{(L)}t_P(s_j, t_k). \tag{8.52}$$

In equivalence to Equation (8.30), camera velocities are mapped to the end effector frame:

$$_{(E)}v_E(t_k) = {}^{L}R_{E\,(L)}^T v_L(t_k), \tag{8.53}$$

where $\boldsymbol{v}_\mathrm{E} \in \mathbb{R}^3$ is the nominal end effector velocity. Rotation $^\mathrm{L}\boldsymbol{R}_\mathrm{E} \in \mathrm{SO}(3)$ is determined from hand-eye calibration. Under disregard of angular velocities, the linear controller output is given by $_{(\mathrm{E})}\dot{\boldsymbol{x}}_\mathrm{E}(t_k) = \big(_{(\mathrm{E})}\boldsymbol{v}_\mathrm{L}(t_k),\boldsymbol{0}\big)^\mathrm{T}$ and mapped to the robot joint space as follows:

$$\dot{\boldsymbol{q}}^*(t_k) = \hat{\boldsymbol{J}}^{*-1}_{xq}(\boldsymbol{q}(t_k))_{(\mathrm{E})}\dot{\boldsymbol{x}}_\mathrm{E}(t_k), \tag{8.54}$$

where $\hat{\boldsymbol{J}}^*_{xq}(\boldsymbol{q}(t_k)) \in \mathbb{R}^{6 \times 5}$ is the composed and reduced geometric Jacobian of the robot kinematics (see Section 5.1.2) and $\dot{\boldsymbol{q}}^*(t_k) \in \mathbb{R}^6$ are the nominal joint space velocities for low-level actuator control.

8.2.2 Experimental Setup

Vision-based automation of endoscopic non-contact laser delivery was evaluated in a pilot study. Experimental settings were chosen equivalently to the user study presented in Chapter 7. For this reason, the performance of the path controller was validated on a planar surface with coated nominal patterns. In total, eight patterns were randomly selected and each shape (semicircle, line, S-shape, rectangle) was taken into account twice. Specimens were randomly located within the camera FoV in front of the robotic endoscope and the operator commenced as per description of the task protocol.

An example of the interaction workflow is depicted in Figure 8.10. The operator primarily teleoperates the endoscope and locates the desired target area, e.g. coated pattern. Motion compensation of the endoscopic view must be enabled to accommodate scene disturbances. A RoI is defined in the live image to enclose the target region. After valid initialisation of motion compensation, interactive user input on the RoI canvas using a graphics stylus (Intuos, Wacom, Kazo, Japan) is enabled for drawing of the nominal ablation path. The operator is advised to delineate the coated pattern as accurate as possible using the stylus interface. Successful completion of path input and scene tracking is rendered to the operator with yellow visual elements. Subsequent to laser beam activation in the UI header, path execution is initiated to instantiate the path controller framework. If needed, motion compensation of endoscopic images may be deactivated in the UI footer. Valid instantiation of the framework is indicated with blue visual elements. Abortion of the process can be triggered at any time in the UI header. This workflow was repeated until randomised experimental series were completed.

Kinematics and control parameters were specifically adapted for this study. The Cartesian velocity of the robotic end effector was $v_\mathrm{E,max} = 1\,\mathrm{mm\,s}^{-1}$ to ensure reliable visual computation in presence of acquisition and processing latencies. Controller gains for approximation and path following were heuristically tuned to $\lambda_\mathrm{PA} = 0.85$ and $\lambda_\mathrm{PF} = 0.6$. This considered smooth transitions in between trajectory elements and temporal stability. The transition threshold was set to $\delta_\mathrm{PA} = 0.3\,\mathrm{mm}$. Tracking data was acquired and processed at $25\,\mathrm{Hz}$. The latter was transferred to a KALMAN filter with linear velocity model for prediction and upsampling to $100\,\mathrm{Hz}$, processed in the proposed

control framework and lastly forwarded to the kinematics controller at $100\,\mathrm{Hz}$. Parameters of the visual processing stack were set similarly to previous Chapter 7. The evaluation of the path delineation performance, i.e. path tracing error (PTE) and task completion time (TCT), is adapted from methodologies described in Section 7.1.4.

8.2.3 Results

Eight automated delineation experiments were conducted on different planar patterns. An example of experimental results is presented in Figure 8.11 for trial T6. Subsequent to interactive path input and initialisation of the tracking and controller framework, the laser beam approaches the first element of the path. The approach to threshold δ_P triggers transition to the PF controller and the visible spot was guided along the predefined path following target positions at a Cartesian velocity of below $1\,\mathrm{mm\,s^{-1}}$ (see Figure 8.11a). The task was completed after approximately $46\,\mathrm{s}$. The nominal pattern was fully delineated by the pilot laser. Figure 8.11b summarises the postexperimental evaluation of the nominal path and the segmented laser spot centroids. A corresponding path representation in Cartesian space is shown in Figure 8.11c. Noticeably, the PF controller caused a minor deviation of less than $1\,\mathrm{mm}$ from the nominal path in the controller transition but stabilised after further iterations and continued path delineation with absence of oscillation. These findings correlate with error distribution in Figure 8.11d that reveals deviations of less than $0.4\,\mathrm{mm}$ for major sections of the regarded path segment.

Overall study metrics of PTE and TCT are summarised to box plots of Figures 8.12a and 8.12b. Both diagrams provide a comparison to results obtained from teleoperated delineation presented in Chapter 7. The PTE is reduced by approximately $0.15\,\mathrm{mm}$ on average compared to teleoperation and PTE distribution is evidently narrowed due to absence of human input. An independent-samples t-test was conducted to determine if there was a statistical significant difference of PTE between teleoperated and autonomous execution. Data samples of both visualisation conditions from Chapter 7 were unified to a common set. PTE outliers were determined by visual inspection and kept in the analysis. Both sets demonstrated normality as assessed by Shapiro-Wilk tests ($p > .05$). Levene's test demonstrated homogeneity of variances ($p = .264$). PTE (mean $\pm$ SD) were lower for autonomous $(0.41 \pm 0.11)\,\mathrm{mm}$ than for teleoperated execution $(0.55 \pm 0.22)\,\mathrm{mm}$, a statistically significant difference of $0.14\,\mathrm{mm}$ (95% CI, 0.03 to 0.24 mm, $t(18) = 2.97$, $p = .016$).

By contrast, TCT increased for autonomous execution. A Welch independent-sample t-test was applied to determine corresponding effects on TCT. An unpaired test was preferred due to violation of homogeneity of variances as assessed by Levene's test ($p = .004$). In analogy to PTE data, completion times of teleoperated trials were aggregated to a common set. Visual inspection revealed a low number of outliers ($n < 5$) that were kept in the analysis. Data residuals satisfied normality assessed by Shapiro-Wilk tests ($p > .05$). TCT were generally lower for teleoperated $(28.5 \pm 19.4)\,\mathrm{s}$ than for autonomous execution $(40.2 \pm 5.7)\,\mathrm{s}$, a statistically significant difference of $11.74\,\mathrm{s}$ (95% CI, 6.83 to 16.64 s, $t(26) = 4.92$, $p = .001$).
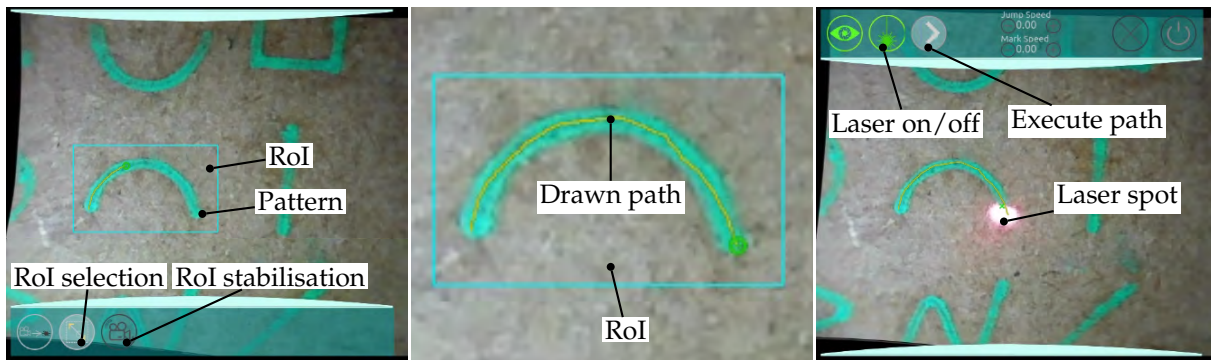
Fig. 8.10: Workflow example of UI interaction for tablet-based ablation path input and execution: (left) selection of target RoI and activation of motion-compensated (stabilised) visualisation. (centre) user-centred drawing of nominal path on compensated RoI. (right) Activation of laser beam and path execution.
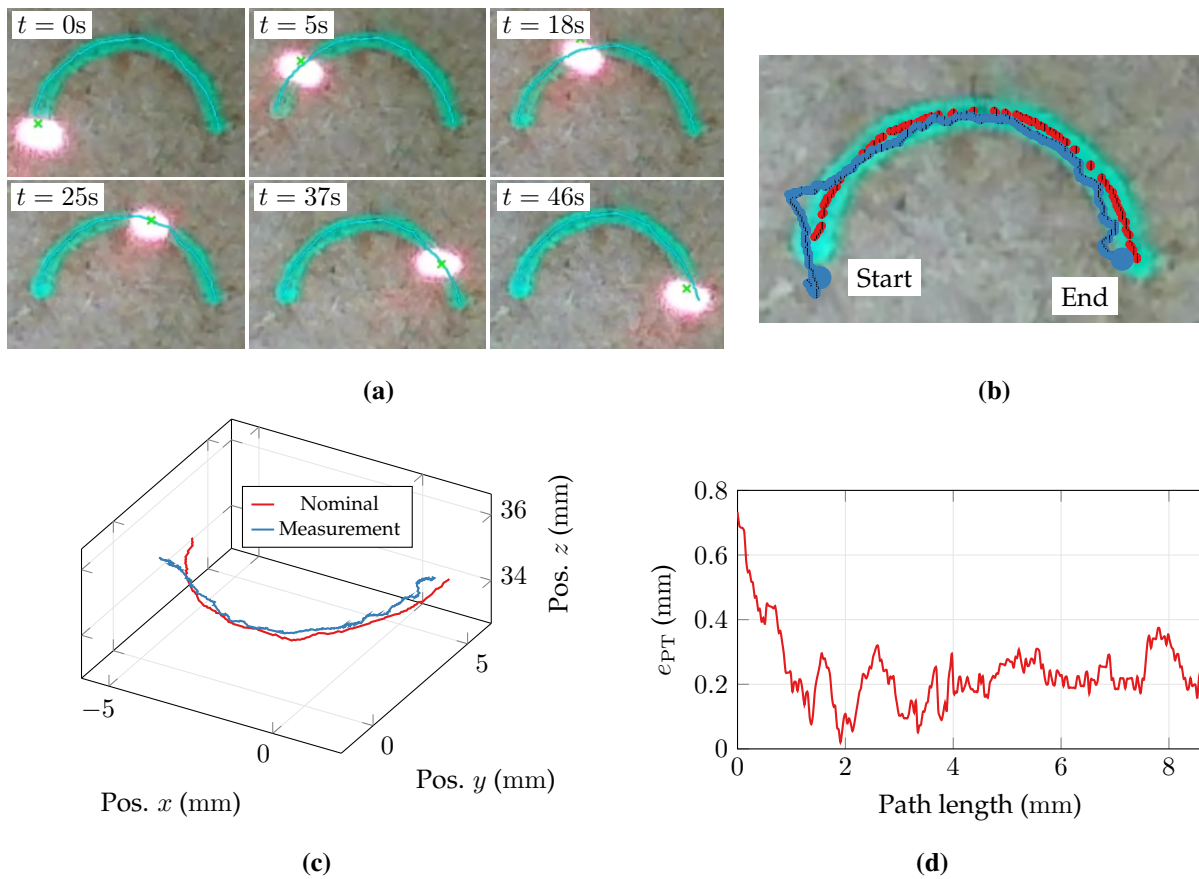
Fig. 8.11: Results example of automated ablation trial T6. (a) Temporal image sequence of autonomous path delineation on semicircular pattern. (b) Postexperimental evaluation of segmented nominal path extracted from coated pattern (red) and measured laser positions (blue). (c) Depth map mapping of data in (b) to Cartesian space in $(CF)_L$. (d) Path tracing errors e_{PT} over a selected section of the pattern centreline (approach/start).
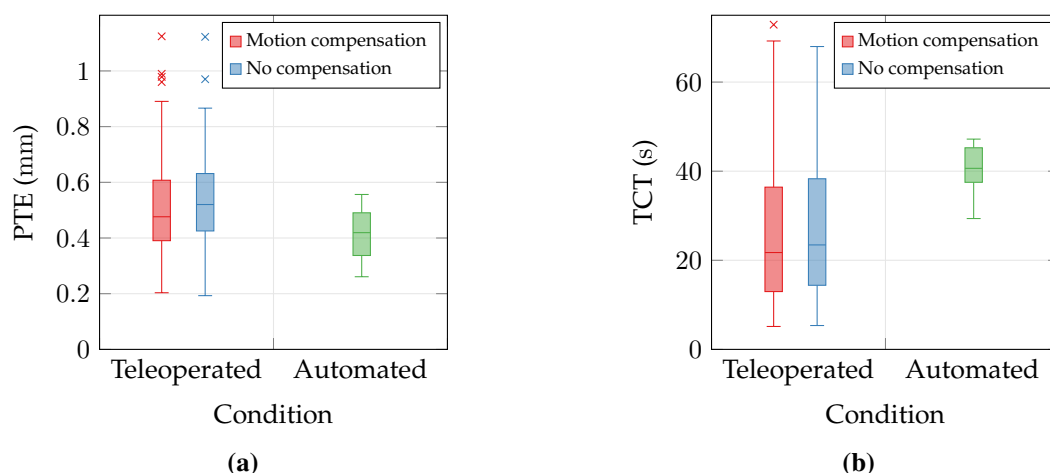
Fig. 8.12: Performance metrics of experimental study on automated laser delineation: a) Path tracing errors (PTE) and b) task completion times (TCT) for teleoperated and autonomous task execution.

8.2.4 Discussion

To the present day, deployment of non-contact lasers to confined anatomy poses challenges. Dexterous endoscopic robots such as discussed in previous chapters bear great potential but demand for surgical training to master the robotic dexterity in clinical settings. First steps towards intraoperative assistance were elaborated in Chapter 6. However, tasks were fully teleoperated at low autonomy levels. This section demonstrated the feasibility of automated ablation for non-contact laser delivery with extensible continuum kinematics and intrinsic sensing of the environment. A PBVS control scheme with two phases for approaching and following the interactively defined path was successfully realised to automate execution of laser delineation on arbitrary surfaces. Hence, this obviates teleoperation and optimises the HMI. Experimental evaluation confirmed the control-cycle performance with 100% task completion rates on phantom specimens and 3 DoF task space manipulation. The preliminary study further supports the initial assumption of reduced PTE for automation in comparison to teleoperation, i.e. PTE of approximately $0.4\,\mathrm{mm}$ were achieved. Related work on mirror-based scanning reported similar performance with RMSE of $0.3\,\mathrm{mm}$ to $1.0\,\mathrm{mm}$ at slightly increased scanning velocities ($> 1\,\mathrm{mm\,s^{-1}}$) [TRS+18]. On the contrary, optical beam properties were neglected, i.e. the focal position was disregarded in the planning or control, and manipulation workspaces were restricted. These shortcomings were incorporated by the proposed concept to achieve optimal laser-tissue interaction. However, limitations on acquisition hardware and computational efforts impact system dynamics and constrain the closed-loop controller to low bandwidths. For example, this results in minor path deviations (see Figure 8.11c) related to the controller initialisation with tracking data input. Hence, improved control bandwidths require sensors with high update rates ($> 30\,\mathrm{Hz}$) and low-latency processing ($< 20\,\mathrm{ms}$). This will also expand executable Cartesian robot velocities. Rendering of confidence measures to the UI related to tracking and control parameters may support procedural safety. Future

work addresses experimental studies with integration of the high-power laser module introduced in Chapter 3.

8.3 Conclusion

This chapter elaborated feasibility of vision-based task autonomy in combination with extensible continuum robots for non-contact laser surgery. Therefore, two automation concepts for enhancement of clinical tasks were integrated to the robotic framework and evaluated experimentally.

Firstly, intraoperative assistance for view optimisation was presented to restore or maintain a desired operator view onto the anatomy of interest. The proposed view controller enabled successful execution of 5 DoF markerless visual servoing control on static and dynamic scenes with residual position errors of below $0.5\,\mathrm{mm}$. However, system dynamics were constrained to Cartesian velocities of $1\,\mathrm{mm\,s^{-1}}$ due to latencies of image acquisition and processing. Otherwise, disturbances may be injected to the controller framework.

The second concept targeted automation of laser path delineation. Hence, the endoscopic kinematics automatically manipulates the focal position of the laser beam on the target surface in 3 linear DoF. Interactive path definition on the endoscopic live stream and design of a path controller framework were described. Results of the experimental study demonstrated superior metrics of the automation concept over teleoperated performance with path tracing errors of less than $0.4\,\mathrm{mm}$. This confirms feasibility of automated kinematics-based laser delivery in endoscopic settings. In future, this strategy may enable operators to focus on primary tasks, i.e. monitoring of laser-tissue interaction. Nonetheless, system dynamics are likewise restricted by sensing and processing hardware which has caused longer task completion times in comparison to teleoperated execution. These findings motivate advanced robotic designs and high-performance hardware for minimally invasive laser surgery.

Conclusively, vision-based task automation in combination with extensible continuum kinematics was presented. This comprised fusion of markerless pose estimation from stereoscopic scene tracking and control frameworks for use with extensible continuum kinematics. Experimental results of both concepts pave the way for intuitive clinical application with lowered cognitive burden.

9 Conclusion and Outlook

The application of lasers in endoscopic MIS enables accurate and gentle treatment of soft tissue pathologies, such as tumours or lesions, with improved postoperative patient outcome. However, manual laser delivery to confined spaces is associated with limited dexterity due to instrument handling and friction phenomena, degradation of optical fibres, and absence of technologies for intraoperative assistance.

This dissertation addresses these challenges and proposes a novel robotic platform and framework for endoscopic non-contact soft tissue laser surgery. The remainder of this chapter summarises major technical contributions and results. The chapter concludes with future perspectives.

Primarily, implementation and evaluation of a miniaturised opto-mechanical unit for focusing an Er:YAG laser beam after fibre transmission within confined anatomy is presented. Emphasis has been given to dimensional reduction to endoscopic scale while preserving a modular assembly. The optical coupling efficiency of fibre and laser source is optimised with automated component alignment. Practical demonstration and ablation performance of the optical setup composed with the laser source, transmission fibre, and focus unit are assessed on agar-agar samples and in preliminary cadaver experiments. Quantitative results reveal that desired ablation characteristics of the optical components, i.e. incision width and depth, are achieved with minimal thermal damage. Nonetheless, focused laser beams demand for accurate positioning of the focal length with respect to the tissue surface and manipulation dexterity within confined spaces to facilitate ablation on delicate pathologies.

This contribution presents the design and realisation of a novel robotic platform that includes a dexterous variable-length manipulator with two continuum segments, a multifunctional endoscopic tip with stereo imaging, illumination, and integration of aforementioned focus unit for laser beam shaping. Contrary to related work, the segmental design of the continuum manipulator enables compression and extension. Task space motion of the end effector in five DoF is realised with a novel actuation unit that facilitates remote push/pull displacement of flexible tubes embedded to the manipulator. A modular controller framework based on the ROS environment for high-level integration of continuum kinematics, haptics, user interfaces, and vision modules complements the mechatronic hardware. Forward and inverse kinematics are derived from the geometry of the extensible continuum structure. Instantaneous kinematics are proposed for velocity-based teleoperation control and trajectory planning. Practical demonstration is given by an experimental accuracy evaluation of the described kinematic model. Mean errors of less than $2\,\mathrm{mm}$ are measured and compared against ground truth data from optical tracking within the considered robotic

workspace. A telemanipulation controller of the robotic master-slave configuration is realised for kinematics and haptics. Force augmentation to the master device is achieved along with motion scaling. For example, a friction model dynamically generates velocity constraints to damp operator inputs which could potentially result in misdirection of the laser beam.

Atraumatic and gentle tissue ablation is only feasible if the focal length of the laser optics is adjusted to the tissue surface. This is addressed by a novel user guidance framework which incorporates online scene reconstruction and estimation of the laser-tissue intersection. The framework maps information related to distances between focal spot and tissue surface to visual, haptic, and visuo-haptic cues. An experimental user study with clinical and non-clinical subjects evaluates the proposed assistance in combination with one DoF teleoperation of the robotic platform. Augmentation of visuo-haptic cues outperforms alternative concepts and achieves residual focal errors below $0.5\,\mathrm{mm}$ and a reduction of task completion times.

The delineation performance and usability of the robotic platform is assessed in a user study. The study considers teleoperation of the robotic master-slave setup and involves three DoF tracing and delineation tasks of random target patterns using a pilot beam and endoscopic vision. Operators are additionally provided with two different visualization modes. The study reveals path tracing errors below $0.5\,\mathrm{mm}$ and the postexperimental user survey confirms subjects confidence. This matches interventional requirements and metrics are comparable to studies on mirror-based scanners. Findings are further translated to a feasibility study with joint teleoperated multi-DoF path tracing and visuo-haptic feedback.

Lastly, vision-based control is presented to establish full automation of the ablation procedure with interactive path definition. Experiments demonstrate the practicability of visual control in combination with endoscopic kinematics for tracking and following surgical targets to maintain an optimal scene view. Beyond that, the UI is extended to interactive tablet-based input of nominal laser paths. A path following controller realises the laser spot control on the target surface. A preliminary study verifies that path tracing errors can be further reduced with proposed methodologies. This paves the way for integration to robotic devices in laser surgery as the concept was successfully applied to scanner-based applications with utmost clinical acceptance [MCP+16].

Contributions of this dissertation demonstrate feasibility and potentials of the novel robotic platform in combination with vision-based assistance and control. Even though pilot studies with novices and experts assessed the device performance and assistance, future work aims at more comprehensive studies. The subsequent paragraph discusses future work for improvement of surgical performance, procedural safety, and user compliance. Device miniaturisation and integration are main objectives. A dimensional reduction of the robotic manipulator and endoscopic tip below $8\,\mathrm{mm}$ with latest imaging and illumination technologies. For example, recent LED technologies may enable effective heat dissipation to the enclosing structure at small scale. Alternative lens materials, tailored optics (e.g. laser processing), or different lens configurations must be analysed for miniaturization of beam shaping optics. This goes along with selection of surface coatings to minimise optical losses

at selected wavelengths and to improve the transmission of the visible pilot beam. A redesign of the focus module must include the evaluation of laser-tissue interactions and histological sample analysis to identify cellular responses.

Contributions of this dissertation demonstrate feasibility and potentials of the novel robotic platform in combination with vision-based assistance and control. Even though pilot studies with novices and experts assessed the device performance and assistance, future work aims at more comprehensive user cohorts. The subsequent paragraph discusses future work for improvement of surgical performance, procedural safety, and user compliance.

Device miniaturisation and integration are main objectives of future perspectives. A dimensional reduction of the robotic manipulator and endoscopic tip below $8\,\mathrm{mm}$ with latest imaging and illumination technologies. For example, recent LED technologies may enable effective heat dissipation to the enclosing structure at small scale. Likewise, alternative lens materials, bespoke optics (e.g. laser processing), or different lens configurations must be analysed for miniaturisation of beam shaping optics. This goes along with selection of surface coatings to minimise optical losses at selected wavelengths and to improve the transmission of the visible pilot beam. A redesign of the focus module must include the evaluation of laser-tissue interactions and histological sample analysis to identify cellular responses.

The latest design of the robotic actuation unit motivates electro-mechanical miniaturisation using bespoke spindle units and carriers, as such rotary drives may be adapted and downsized. Based on early prototypes, it is assumed that the latest device footprint may be reduced by a factor of two. Durability and high fatigue strengths of articulated continuum segments are expected from alternative fabrication technologies. This specifically addresses limitations of additive manufacturing, e.g. temporal degradation of adjacent layer bonding or layer delamination due to shear loads. Alternative manufacturing candidates are injection moulding or selective laser sintering (SLS). The structural response of flexible components is significantly optimised with non-linear finite element analysis. Despite this contribution, it takes isolated bellow units into account for the design optimisation, as structural failure was significantly reduced throughout design iterations and prototypes. Advanced simulation settings must target manipulator assemblies, emerging non-linear material models for flexible sections, and detailed loading conditions exerted by embedded tubes, and mutual component friction as investigated analytically in [RBT14].

Further design optimisation must comply with clinical standards, e.g. sterilisation or disposable components. A major manipulation and control improvement is expected from elimination of friction between concentrically guided tubes or additively fabricated components. Tubular stick-slip oscillations are generated by different relative velocities, circumferential forces, and friction coefficients of specific material pairings. A promising approach concerns customised surface coatings applied to employed polyamide tubing to mitigate parasitic effects of dynamic friction.

Furthermore, a conversion from a rigid to a flexible instrument shaft is feasible as demonstrated in [BDN$^+$13] for transnasal access. This eases instrument deployment to tortuous luminal anatomy

and paves the way for novel device applications. However, this approach requires displacement compensation of actuation tubes. The commanded end effector poses are affected by the deflection of the passive shaft. This effect must be corrected with intrinsic sensing of pose deviations, e.g. fibre Bragg gratings. The proposed mechanical design of the actuation unit inherently enables augmentation of corrective tube displacements to nominal joint motions.

Since robotic beam manipulation allows for lower scanning velocities compared to mirror-based designs, joint consideration of robot kinematics and laser parameters (e.g. pulse frequency and duration) may advance state-of-the-art technologies and enables dynamic updates of system parameters based on actual robot velocities and tissue properties analysed by endoscopic imaging. As an example, a decision support model is learned from multidimensional input, such as visual conditions of tissue condition, laser settings, scan velocities, or focal distance. Related work demonstrates the feasibility of a similar approach for ablation depth control [FPO$^+$16]. The presented assistance framework may be extended with generation of optimal pulse overlaps and adaptation of laser settings, e.g. pulse duration. Finally, the integration of an advanced master device is recommended to render haptics (forces/torques) in six DoF.

The robotic performance has been evaluated experimentally with restrictions on commanded task space velocities due to low acquisition frequencies of embedded imaging sensors and suppression of stick-slip oscillations. The limitation on operator velocity inputs particularly affects task completion times. Besides, image-based methodologies, such as assistance for focal adjustment and automation of the scanning process, it is also linked to robustness and accuracy of stereoscopic scene reconstruction and tracking. Temporal motion sensing or spatial variations in dynamic environments may be enhanced with high image acquisition rates as suggested for mirror-based designs [RTR$^+$17]. This is accompanied by alternative reconstruction and tracking algorithms (see [Sch18]). The latter concerns reliable outlier detection, confidence metrics, and parallelisation of data processing to distribute computational efforts to GPGPU. This is essential to gain online processing of high-speed imaging data ($> 50\,\mathrm{Hz}$). Additionally, online evaluation of algorithmic confidence is required for clinical scenarios. As an example, tracking of challenging scenes may cause results with low confidence. A decision process must immediately trigger abortion of the automated procedure and transfer robotic control to the operator for task completion with minimal procedural interruption.

Lastly, a cadaver model must be considered for further device clearance including performance assessment for distinct scenarios with high power tissue ablation. This goes along with validation of redundancy and safety of the system hardware, scene reconstruction, and tracking algorithms in real environments. The clinical workflow may be further optimised with additional positioning kinematics, e.g. active or passive serial robots.

Bibliography

[AB16]   AZADGOLI, BEINA and REGINA Y. BAKER: *Laser applications in surgery*. Ann Transl Med, 4(23):452–452, Dec 2016.

[ABRP07]   ABBOTT, D. J., C. BECKE, R. I. ROTHSTEIN and W. J. PEINE: *Design of an endoluminal NOTES robotic system*. In *2007 IEEE/RSJ International Conference on Intelligent Robots and Systems*, pages 410–416, Oct 2007.

[AC03]   ADHAMI, L. and E. COSTE-MANIERE: *Optimal planning for minimally invasive surgical robots*. IEEE Transactions on Robotics and Automation, 19(5):854–863, 2003.

[AFJ13]   ALIPOUR, FARIBORZ, EILEEN M. FINNEGAN and SANYUKTA JAISWAL: *Phonatory Characteristics of the Excised Human Larynx in Comparison to Other Species*. Journal of Voice, 27(4):441 – 447, 2013.

[AGB17a]   AMANOV, E., J. GRANNA and J. BURGNER-KAHRS: *Toward improving path following motion: Hybrid continuum robot design*. In *2017 IEEE International Conference on Robotics and Automation (ICRA)*, pages 4666–4672, May 2017.

[AGB17b]   AMANOV, E., J. GRANNA and J. BURGNER-KAHRS: *Toward improving path following motion: Hybrid continuum robot design*. In *2017 IEEE International Conference on Robotics and Automation (ICRA)*, pages 4666–4672, May 2017.

[AHE01]   ANDREFF, NICOLAS, RADU HORAUD and BERNARD ESPIAU: *Robot Hand-Eye Calibration Using Structure-from-Motion*. The International Journal of Robotics Research, 20(3):228–248, 2001.

[AKF$^+$16] ATAOLLAHI, A., R. KARIM, A. S. FALLAH, K. RHODE, R. RAZAVI, L. D. SENEVIRATNE, T. SCHAEFFTER and K. ALTHOEFER: *Three-Degree-of-Freedom MR-Compatible Multisegment Cardiac Catheter Steering Mechanism*. IEEE Transactions on Biomedical Engineering, 63(11):2425–2435, Nov 2016.

[AKNP13]   AZIZIAN, MAHDI, MAHTA KHOSHNAM, NIMA NAJMAEI and RAJNI V. PATEL: *Visual servoing in medical robotics: a survey. Part I: endoscopic and direct vision imaging - techniques and applications*. The International Journal of Medical Robotics and Computer Assisted Surgery, 10(3):263–274, 2013.

[AM17]   ACEMOGLU, A. and L. S. MATTOS: *Magnetic laser scanner for endoscopic microsurgery*. In *2017 IEEE International Conference on Robotics and Automation*

(ICRA), pages 4215–4220, May 2017.

[AML+11]   ANANTHARAMAN, DEVASENA, MANUELA MARRON, PAGONA LAGIOU, EVAN-
           GELIA SAMOLI, WOLFGANG AHRENS, HERMANN POHLABELN, ALENA SLAM-
           OVA, MIRIAM SCHEJBALOVA, FRANCO MERLETTI, LORENZO RICHIARDI,
           KRISTINA KJAERHEIM, XAVIER CASTELLSAGUE, ANTONIO AGUDO, RE-
           NATO TALAMINI, LUIGI BARZAN, TATIANA V. MACFARLANE, MARTIN
           TICKLE, LORENZO SIMONATO, CRISTINA CANOVA, DAVID I. CONWAY, PATRI-
           CIA A. MCKINNEY, PETER THOMSON, ARIANA ZNAOR, CLAIRE M. HEALY,
           BERNARD E. MCCARTAN, MIA HASHIBE, PAUL BRENNAN and GARY J. MAC-
           FARLANE: *Population attributable risk of tobacco and alcohol for upper aerodi-
           gestive tract cancer*. Oral Oncology, 47(8):725 – 731, 2011.

[ANB+95]   ANSON, KEN, JAN NAWROCKI, JOHN BUCKLEY, CHRIS FOWLER, ROGER
           KIRBY, WILLIAM LAWRENCE, PETER PATERSON and GRAHAM WATSON: *A
           multicenter, randomized, prospective study of endoscopic laser ablation versus
           transurethral resection of the prostate*. Urology, 46(3):305 – 310, 1995.

[ANKP14]   AZIZIAN, MAHDI, NIMA NAJMAEI, MAHTA KHOSHNAM and RAJNI PATEL:
           *Visual servoing in medical robotics: a survey. Part II: tomographic imaging
           modalities - techniques and applications*. The International Journal of Medical
           Robotics and Computer Assisted Surgery, 11(1):67–79, 2014.

[AOS18]   ABAH, C., A. L. OREKHOV and N. SIMAAN: *Design Considerations and Re-
           dundancy Resolution for Variable Geometry Continuum Robots*. In *2018 IEEE
           International Conference on Robotics and Automation (ICRA)*, pages 767–774,
           May 2018.

[APM19]   ACEMOGLU, A., D. PUCCI and L. S. MATTOS: *Design and Control of a Magnetic
           Laser Scanner for Endoscopic Microsurgeries*. IEEE/ASME Transactions on
           Mechatronics, 24(2):527–537, April 2019.

[ARG+18]   ABBASI, HAMED, GEORG RAUTER, RAPHAEL GUZMAN, PHILIPPE C. CATTIN
           and AZHAR ZAM: *Laser-induced breakdown spectroscopy as a potential tool
           for autocarbonization detection in laserosteotomy*. Journal of Biomedical Optics,
           23(7):1 – 7, 2018.

[AT15]   ANDREFF, NICOLAS and BRAHIM TAMADAZTE: *Laser steering using virtual
           trifocal visual servoing*. International Journal of Robotics Research, 1:1–24, 2015.

[Aup20]   AUPÉRIN, ANNE: *Epidemiology of head and neck cancers: an update*. Current
           Opinion in Oncology, 32(3), 2020.

[AWA13]   AWAIBA: *NanEye GS USB Evaluation Unit*, 7 2013. Version 1.0.0.

[AWL+14]   AGUSTINOS, A., R. WOLF, J. A. LONG, P. CINQUIN and S. VOROS: *Visual*

servoing of a robotic endoscope holder based on surgical instrument tracking. In *5th IEEE RAS/EMBS International Conference on Biomedical Robotics and Biomechatronics*, pages 13–18, Aug 2014.

[AXI14] AXIOS 3D SERVICES GMBH: *Datasheet Optical Tracking System CamBar B1*, June 2014. V2 EN.

[BA05] BAILLY, Y. and Y. AMIRAT: *Modeling and Control of a Hybrid Continuum Active Catheter for Aortic Aneurysm Treatment.* In *Proceedings of the 2005 IEEE International Conference on Robotics and Automation*, pages 924–929, April 2005.

[Ban11] *Laser spot tracking with sub-pixel precision based on subdivision mesh*, volume 8004, 2011.

[BBB⁺13] BRÜGGEMANN, D., B. BLASE, F. BÜHS, R. DREYER, M. KELP, H. LEHR, S. OGINSKI and S. SCHLEGEL: *Endoscope with distal LED for illumination.* In LONG, MIAN (editor): *World Congress on Medical Physics and Biomedical Engineering May 26-31, 2012, Beijing, China*, pages 2107–2110, Berlin, Heidelberg, 2013. Springer Berlin Heidelberg.

[BBS⁺12] BOUVIER, C., S. BOLIS, D. SAINT-PATRICE, A. POUYDEBASQUE, F. JACQUET, C. BRIDOUX, S. MOREAU, G. SIMON, N. SILLON and E. VIGIER-BLANC: *Enabling technologies for advanced wafer level camera integration.* In *2012 IEEE 62nd Electronic Components and Technology Conference*, pages 1345–1350, May 2012.

[BDM⁺13] BARRESI, G., N. DESHPANDE, L. S. MATTOS, A. BROGNI, L. GUASTINI, G. PERETTI and D. G. CALDWELL: *Comparative usability and performance evaluation of surgeon interfaces in laser phonomicrosurgery.* In *2013 IEEE/RSJ International Conference on Intelligent Robots and Systems*, pages 3610–3615, Nov 2013.

[BDN⁺13] BAJO, A., L. M. DHARAMSI, J. L. NETTERVILLE, C. G. GARRETT and N. SIMAAN: *Robotic-assisted micro-surgery of the throat: The trans-nasal approach.* In *2013 IEEE International Conference on Robotics and Automation*, pages 232–238, May 2013.

[BDWN07] BRAGANZA, D., D. M. DAWSON, I. D. WALKER and N. NATH: *A Neural Network Controller for Continuum Robots.* IEEE Transactions on Robotics, 23(6):1270–1277, Dec 2007.

[BDyB14] BOWYER, S. A., B. L. DAVIES and F. RODRIGUEZ Y BAENA: *Active Constraints/Virtual Fixtures: A Survey.* IEEE Transactions on Robotics, 30(1):138–157, Feb 2014.

[BFFD⁺16] BALDINI, ARNAUD, HAKIM FASSI-FEHRI, RICARDO C. DUARTE, SEBASTIEN

CROUZET, RENÉ ECOCHARD, NADIA ABID, XAVIER MARTIN, LIONEL BADET and MARC COLOMBEL: *Holmium Laser Enucleation of the Prostate versus Laparoscopic Transcapsular Prostatectomy: Perioperative Results and Three-Month Follow-Up*. Current Urology, 10(2):81–86, 2016.

[BFS⁺18]   BRAY, FREDDIE, JACQUES FERLAY, ISABELLE SOERJOMATARAM, REBECCA L. SIEGEL, LINDSEY A. TORRE and AHMEDIN JEMAL: *Global cancer statistics 2018: GLOBOCAN estimates of incidence and mortality worldwide for 36 cancers in 185 countries*. CA: A Cancer Journal for Clinicians, 68(6):394–424, 2018.

[BGV⁺15]   BERGELES, C., A. H. GOSLINE, N. V. VASILYEV, P. J. CODD, P. J. DEL NIDO and P. E. DUPONT: *Concentric Tube Robot Design and Optimization Based on Task and Anatomical Constraints*. IEEE Transactions on Robotics, 31(1):67–84, Feb 2015.

[BHCS11]   BLANCO, RAY GERVACIO F., PATRICK K. HA, JOSEPH A. CALIFANO and JOHN M. SAUNDERS: *Transoral Robotic Surgery of the Vocal Cord*. Journal of Laparoendoscopic & Advanced Surgical Techniques, 21(2):157–159, 2011.

[BHP⁺99]   BOPPART, STEPHEN A., JUERGEN HERRMANN, COSTAS PITRIS, DEBRA L. STAMPER, MARK E. BREZINSKI and JAMES G. FUJIMOTO: *High-Resolution Optical Coherence Tomography-Guided Laser Ablation of Surgical Tissue*. Journal of Surgical Research, 82(2):275 – 284, 1999.

[Bih16]   BIHLMAIER, ANDREAS: *Learning Dynamic Spatial Relations: The Case of a Knowledge-based Endoscopic Camera Guidance Robot*. 08 2016.

[BJK⁺14]   BÖTTCHER, A., N. JOWETT, S. KUCHER, R. REIMER, U. SCHUMACHER, R. KNECHT, W. WÖLLMER, A. MÄNSCHER and C.V. DALCHOW: *Use of a microsecond Er:YAG laser in laryngeal surgery reduces collateral thermal injury in comparison to superpulsed CO2 laser*. European Archives of Oto-Rhino-Laryngology, 271:1121–1128, 2014.

[BKK⁺15]   BOETTCHER, A., S. KUCHER, R. KNECHT, N. JOWETT, P. KROTZ, R. REIMER, U. SCHUMACHER, S. ANDERS, A. MUNSCHER, C. V. DALCHOW and R. J. D. MILLER: *Reduction of thermocoagulative injury via use of a picosecond infrared laser (PIRL) in laryngeal tissues*. Eur Arch Otorhinolaryngol, 272(4):941–948, Apr 2015.

[BKLE11]   BERG, DEVIN R., TIMOTHY P. KINNEY, PERRY Y. LI and ARTHUR G. ERDMAN: *Determination of Surgical Robot Tool Force Requirements Through Tissue Manipulation and Suture Force Measurement*. Journal of Medical Devices, 5(2):027517–027517–1, Jun 2011.

[BM11]   BURDETT, ED and VIKI MITCHELL: *Anatomy of the larynx, trachea and bronchi*. Anaesthesia & Intensive Care Medicine, 12(8):335 – 339, 2011.

[BMBW15]   BATES, DOUGLAS, MARTIN MÄCHLER, BEN BOLKER and STEVE WALKER:
             Fitting Linear Mixed-Effects Models Using lme4. Journal of Statistical Software,
             67(1):1–48, 2015.

[BOK+04]   BETHEA, BRIAN T., ALLISON M. OKAMURA, MASAYA KITAGAWA, TORIN P.
             FITTON, STEPHEN M. CATTANEO, VINCENT L. GOTT, WILLIAN A. BAUM-
             GARTNER and DAVID D. YUH: *Application of Haptic Feedback to Robotic Surgery*.
             J Laparoendosc Adv Surg Tech A, 14(3):191–195, Jun 2004.

[BPZ+13]   BETKA, J., J. PLZAK, M. ZÁBRODSKY, J. KASTNER and J. BOUCEK: *18 -
             Lasers in otorhinolaryngology (ORL) and head and neck surgery*. In JELÍNKOVÁ,
             HELENA (editor): *Lasers for Medical Applications*, Woodhead Publishing Series
             in Electronic and Optical Materials, pages 556 – 572. Woodhead Publishing, 2013.

[Bra]   BRAINLAB AG: *Brainlab Robotics for every surgery patient*.

[BRC15]   BURGNER-KAHRS, J., D. C. RUCKER and H. CHOSET: *Continuum Robots for
             Medical Applications: A Survey*. IEEE Transactions on Robotics, 31(6):1261–1280,
             Dec 2015.

[BRGL+18]   BERTHET-RAYNE, PIERRE, GAUTHIER GRAS, KONRAD LEIBRANDT, PIYA-
             MATE WISANUVEJ, ANDREAS SCHMITZ, CARLO A. SENECI and GUANG-
             ZHONG YANG: *The i2Snake Robotic Platform for Endoscopic Surgery*. Annals of
             Biomedical Engineering, 46(10):1663–1675, Oct 2018.

[BS12]   BAJO, A. and N. SIMAAN: *Kinematics-Based Detection and Localization of
             Contacts Along Multisegment Continuum Robots*. IEEE Transactions on Robotics,
             28(2):291–302, April 2012.

[BS16]   BAJO, ANDREA and NABIL SIMAAN: *Hybrid motion/force control of multi-
             backbone continuum robots*. The International Journal of Robotics Research,
             35(4):422–434, 2016.

[BSMJ99]   BREEDVELD, PAUL, HENK G. STASSEN, DIRK W. MEIJER and J. JAKIMOW-
             ICZ: *Manipulation in Laparoscopic Surgery: Overview of Impeding Effects and
             Supporting Aids*. Journal of Laparoendoscopic & Advanced Surgical Techniques,
             9(6):469–480, 1999.

[Bur10]   BURGNER, JESSICA: *Robot Assisted Laser Osteotomy*. KIT Scientific Publishing,
             Karlsruhe, 2010.

[BVB+09]   BECKER, B. C., C. R. VALDIVIESO, J. BISWAS, L. A. LOBES and C. N. RIV-
             IERE: *Active guidance for laser retinal surgery with a handheld instrument*. In
             *2009 Annual International Conference of the IEEE Engineering in Medicine and
             Biology Society*, pages 5587–5590, Sept 2009.

[BVPV11]   BERSELLI, GIOVANNI, ROCCO VERTECHY, MARCELLO PELLICCIARI and

GABRIELE VASSURA: *Hyperelastic Modeling of Rubber-Like Photopolymers for Additive Manufacturing Processes*. In HOQUE, MUHAMMAD ENAMUL (editor): *Rapid Prototyping Technology*, chapter 6. IntechOpen, Rijeka, 2011.

[BW04]   BLESSING, MARSHAL and IAN D. WALKER: *Novel Continuum Robots with Variable-Length Sections*. IFAC Proceedings Volumes, 37(14):55 – 60, 2004. 3rd IFAC Symposium on Mechatronic Systems 2004, Sydney, Australia, 6-8 September, 2004.

[BWD15]   BUCKMIRE, ROBERT, YU-TUNG WONG and ALLISON M. DEAL: *The application of robotics to microlaryngeal laser surgery*. The Laryngoscope, 125(6):1393–1400, 2015.

[ByB13]   BOWYER, S. A. and F. RODRIGUEZ Y BAENA: *Dynamic frictional constraints for robot assisted surgery*. In *2013 World Haptics Conference (WHC)*, pages 319–324, April 2013.

[CBR+18]   CHIKHAOUI, MOHAMED TAHA, AMINE BENOUHIBA, PATRICK ROUGEOT, KANTY RABENOROSOA, MORVAN OUISSE and NICOLAS ANDREFF: *Developments and Control of Biocompatible Conducting Polymer for Intracorporeal Continuum Robots*. Annals of Biomedical Engineering, 46(10):1511–1521, Oct 2018.

[CCN+12]   CLANCY, N. T., J. CLARK, D. P. NOONAN, G. Z. YANG and D. S. ELSON: *Light sources for single-access surgery*. Surg Innov, 19(2):134–144, Jun 2012.

[CFA+12]   CHÁVEZ, F., F. FERNÁNDEZ, R. ALCALÁ, J. ALCALÁ-FDEZ, G. OLAGUE and F. HERRERA: *Hybrid laser pointer detection algorithm based on template matching and fuzzy rule-based systems for domotic control in real home environments*. Applied Intelligence, 36(2):407–423, Mar 2012.

[CGSB18]   CHIKHAOUI, M. T., J. GRANNA, J. STARKE and J. BURGNER-KAHRS: *Toward Motion Coordination Control and Design Optimization for Dual-Arm Concentric Tube Continuum Robots*. IEEE Robotics and Automation Letters, 3(3):1793–1800, July 2018.

[CHC15]   CHNG, C. B., Y. HO and C. K. CHUI: *Automation of retinal surgery: A shared control robotic system for laser ablation*. In *2015 IEEE International Conference on Information and Automation*, pages 1957–1962, Aug 2015.

[CLKB19]   CHIKHAOUI, M. T., S. LILGE, S. KLEINSCHMIDT and J. BURGNER-KAHRS: *Comparison of Modeling Approaches for a Tendon Actuated Continuum Robot With Three Extensible Segments*. IEEE Robotics and Automation Letters, 4(2):989–996, April 2019.

[CMC+08]   CAMARILLO, D. B., C. F. MILNE, C. R. CARLSON, M. R. ZINN and J. K.

SALISBURY: *Mechanics Modeling of Tendon-Driven Continuum Manipulators.* IEEE Transactions on Robotics, 24(6):1262–1273, Dec 2008.

[CO16]   COLONNESE, NICK and ALLISON OKAMURA: *Stability and quantization-error analysis of haptic rendering of virtual stiffness and damping.* The International Journal of Robotics Research, 35(9):1103–1120, 2016.

[Cor]   CORINDUS, INC.: *CorPath GRX System Operator's Manual.*

[Cra05]   CRAIG, JOHN J.: *Introduction to Robotics: Mechanics and Control.* Addison-Wesley Longman Publishing Co., Inc., Boston, MA, USA, 3rd edition, 2005.

[CRA16]   CHIKHAOUI, MOHAMED TAHA, KANTY RABENOROSOA and NICOLAS AN-DREFF: *Kinematics and performance analysis of a novel concentric tube robotic structure with embedded soft micro-actuation.* Mechanism and Machine Theory, 104:234 – 254, 2016.

[CRG+13]   CIANCHETTI, M., T. RANZANI, G. GERBONI, I. DE FALCO, C. LASCHI and A. MENCIASSI: *STIFF-FLOP surgical manipulator: Mechanical design and experimental characterization of the single module.* In *2013 IEEE/RSJ International Conference on Intelligent Robots and Systems*, pages 3576–3581, Nov 2013.

[CRG+14]   CIANCHETTI, MATTEO, TOMMASO RANZANI, GIADA GERBONI, THRISHAN-THA NANAYAKKARA, KASPAR ALTHOEFER, PROKAR DASGUPTA and ARIANNA MENCIASSI: *Soft Robotics Technologies to Address Shortcomings in Today's Minimally Invasive Surgery: The STIFF-FLOP Approach.* Soft Robotics, 1(2):122–131, 2014.

[CT15]   COLOMÉ, A. and C. TORRAS: *Closed-Loop Inverse Kinematics for Redundant Robots: Comparative Assessment and Two Enhancements.* IEEE/ASME Transactions on Mechatronics, 20(2):944–955, 2015.

[CWT+09]   CHOPRA, SASCHA SANTOSH, GEORG WILTBERGER, ULF TEICHGRAEBER, IOANNIS PAPANIKOLAOU, MICHAEL SCHWABE, SVEN SCHMIDT, PANAGIOTIS FIKATAS, FLORIAN STREITPARTH, CARSTEN PHILIPP, FLORIAN WICHLAS, CHRISTIAN SEEBAUER and GUIDO SCHUMACHER: *Evaluation of Laparoscopic Liver Resection with Two Different Nd:YAG Lasers for Future Use in a High-Field Open MRI.* Photomedicine and Laser Surgery, 27(2):281–286, 2009.

[CYF04]   CHANEY, CHARLES A., YUBING YANG and NATHANIEL M. FRIED: *Hybrid germanium/silica optical fibers for endoscopic delivery of erbium:YAG laser radiation.* Lasers in Surgery and Medicine, 34(1):5–11, 2004.

[CZ17]   CONRAD, B. L. and M. R. ZINN: *Interleaved Continuum-Rigid Manipulation: An Approach to Increase the Capability of Minimally Invasive Surgical Systems.* IEEE/ASME Transactions on Mechatronics, 22(1):29–40, Feb 2017.

[DAHH06]   DE LUCA, A., A. ALBU-SCHAFFER, S. HADDADIN and G. HIRZINGER: *Collision Detection and Safe Reaction with the DLR-III Lightweight Manipulator Arm.* In *2006 IEEE/RSJ International Conference on Intelligent Robots and Systems*, pages 1623–1630, 2006.

[Dal16]   DALLAROSA, J.L.: *Articulated arm for delivering a laser beam*, June 21 2016. US Patent 9,371,957.

[Dan98]   DANIILIDIS, KONSTANTINOS: *Hand-Eye Calibration Using Dual Quaternions.* International Journal of Robotics Research, 18:286–298, 1998.

[dASdL⁺09] ARAÚJO, MARCOS A. DE, RUBENS SILVA, EMERSON DE LIMA, DANIEL P. PEREIRA and PAULO C. DE OLIVEIRA: *Measurement of Gaussian laser beam radius using the knife-edge technique: improvement on data analysis.* Appl. Opt., 48(2):393–396, Jan 2009.

[DCK⁺91]   DICKINSON, M.R., A. CHARLTON, T.A. KING, A.J. FREEMONT and R. BRAMLEY: *Studies of Er-YAG laser interactions with soft tissue.* Lasers in Medical Science, 6(2):125–131, 1991.

[DCWZ06]   DEGANI, A., H. CHOSET, A. WOLF and M. A. ZENATI: *Highly articulated robotic probe for minimally invasive surgery.* In *Proceedings 2006 IEEE International Conference on Robotics and Automation, 2006. ICRA 2006.*, pages 4167–4172, May 2006.

[DDVD14]   DANG, Q. V., A. DEQUIDT, L. VERMEIREN and M. DAMBRINE: *Experimental study on stability of a haptic system with variable time delays.* In *2014 IEEE/ASME International Conference on Advanced Intelligent Mechatronics*, pages 554–559, July 2014.

[DF15]   DUNKIN, BRIAN J. and CAROLINE FLOWERS: *3D in the Minimally Invasive Surgery (MIS) Operating Room: Cameras and Displays in the Evolution of MIS*, pages 145–155. Springer New York, New York, NY, 2015.

[DFW⁺19]   DING, MINGJIE, DESHENG FAN, WENYU WANG, YANHUA LUO and GANGDING PENG: *Basics of Optical Fiber Measurements*, pages 1099–1137. Springer Singapore, Singapore, 2019.

[DH07]   DEPPE, HERBERT and HANS-HENNING HORCH: *Laser applications in oral surgery and implant dentistry.* Lasers in Medical Science, 22(4):217–221, Nov 2007.

[Dic17]   DICK, ANDREJ: *Inbetriebnahme eines mehrsegmentalen Kontinuumsroboters für die endoluminale Laserchirurgie.* Project thesis, Institute of Mechatronic Systems, Leibniz Universität Hannover, Hannover, Germany, 2017.

[Dix03]   DIXON, WARREN E.: *Nonlinear Control of Engineering Systems: A Lyapunov-*

Based Approach. Birkhauser Boston, Inc., USA, 2003.

[DLIB10]   DUPONT, P. E., J. LOCK, B. ITKOWITZ and E. BUTLER: *Design and Control of Concentric-Tube Robots*. IEEE Transactions on Robotics, 26(2):209–225, April 2010.

[DMC15a]   DAGNINO, GIULIO, LEONARDO S. MATTOS and DARWIN G. CALDWELL: *A vision-based system for fast and accurate laser scanning in robot-assisted phonomicrosurgery*. International Journal of Computer Assisted Radiology and Surgery, 10(2):217–229, Feb 2015.

[DMC15b]   DESHPANDE, N., L. S. MATTOS and D. G. CALDWELL: *New motorized micromanipulator for robot-assisted laser phonomicrosurgery*. In *2015 IEEE International Conference on Robotics and Automation (ICRA)*, pages 4755–4760, May 2015.

[DMH⁺18]   DRERUP, MARTIN, AHMED MAGDY, MARTINA HAGER, DANIELA COLLESELLI, THOMAS KUNIT, LUKAS LUSUARDI, GÜNTER JANETSCHEK and MICHAEL MITTERBERGER: *Non-ischemic laparoscopic partial nephrectomy using 1318-nm diode laser for small exophytic renal tumors*. BMC Urology, 18(1), November 2018.

[DNBS06]   DIOLAITI, N., G. NIEMEYER, F. BARBAGLI and J. K. SALISBURY: *Stability of Haptic Rendering: Discretization, Quantization, Time Delay, and Coulomb Effects*. IEEE Transactions on Robotics, 22(2):256–268, April 2006.

[DOCM14]   DESHPANDE, NIKHIL, JESÚS ORTIZ, DARWIN G. CALDWELL and LEONARDO S. MATTOS: *Enhanced computer-assisted laser microsurgeries with a "virtual microscope" based surgical system*. In *2014 IEEE International Conference on Robotics and Automation, ICRA 2014, Hong Kong, China, May 31 - June 7, 2014*, pages 4194–4199, 2014.

[DSA⁺15]   DEIBEL, WALDEMAR, ADRIAN SCHNEIDER, MARCELLO AUGELLO, ALFREDO E. BRUNO, PHILIPP JUERGENS and PHILIPPE CATTIN: *A compact, efficient, and lightweight laser head for CARLO: integration, performance, and benefits*, 2015.

[DTA18]   DAHROUG, BASSEM, BRAHIM TAMADAZTE and NICOLAS ANDREFF: *Task Controller for Performing Remote Centre of Motion*, pages 117–132. Springer International Publishing, Cham, 2018.

[EA15]   ERNAR AMANOV, THIEN-DANG NGUYEN, JESSICA BURGNER-KAHRS: *Additive manufacturing of patient-specific tubular continuum manipulators*, 2015.

[EMF16]   ENAYATI, N., E. DE MOMI and G. FERRIGNO: *Haptics in Robot-Assisted Surgery: Challenges and Benefits*. IEEE Reviews in Biomedical Engineering, 9:49–65, 2016.

[FCM⁺15]   FRAS, J., J. CZARNOWSKI, M. MACIAS, J. GLOWKA, M. CIANCHETTI and

A. MENCIASSI: *New STIFF-FLOP module construction idea for improved actuation and sensing.* In *2015 IEEE International Conference on Robotics and Automation (ICRA)*, pages 2901–2906, May 2015.

[FDM+18]   FRIEDRICH, DANIEL T., L. DÜRSELEN, B. MAYER, S. HACKER, F. SCHALL, J. HAHN, T. K. HOFFMANN, P. J. SCHULER and J. GREVE: *Features of haptic and tactile feedback in TORS-a comparison of available surgical systems.* Journal of Robotic Surgery, 12(1):103–108, Mar 2018.

[Fey16]   FEYS, JOS: *Nonparametric Tests for the Interaction in Two-way Factorial Designs Using R.* The R Journal, 8(1):367 – 378, 2016.

[FFW13]   FOX, JOHN, MICHAEL FRIENDLY and SANFORD WEISBERG: *Hypothesis tests for Multivariate Linear Models Using the car package.* The R Journal, 5(1), 2013. In press.

[FKI+08]   FISCHER, G. S., A. KRIEGER, I. IORDACHITA, C. CSOMA, L. L. WHITCOMB and F. GABOR: *MRI compatibility of robot actuation techniques–a comparative study.* Med Image Comput Comput Assist Interv, 11(Pt 2):509–517, 2008.

[FKS18]   FIZ, IVANA, JAN CONSTANTIN KOELMEL and CHRISTIAN SITTEL: *Nature and role of surgical margins in transoral laser microsurgery for early and intermediate glottic cancer.* Current Opinion in Otolaryngology & Head and Neck Surgery, 26(2), 2018.

[FKW18]   FRAZELLE, C. G., A. D. KAPADIA and I. D. WALKER: *A Nonlinear Control Strategy for Extensible Continuum Robots.* In *2018 IEEE International Conference on Robotics and Automation (ICRA)*, pages 7727–7734, May 2018.

[FPB+15]   FUCHS, A., S. PENGEL, J. BERGMEIER, L. KAHRS and T. ORTMAIER: *Fast and automatic depth control of iterative bone ablation based on optical coherence tomography data.* In *Proc. SPIE 9542, Medical Laser Applications and Laser-Tissue Interactions VII*, 2015.

[FPO+16]   FICHERA, L., C. PACCHIEROTTI, E. OLIVIERI, D. PRATTICHIZZO and L. S. MATTOS: *Kinesthetic and vibrotactile haptic feedback improves the performance of laser microsurgery.* In *Proc. IEEE Haptics Symposium (HAPTICS)*, pages 59–64, Philadelphia, PA, USA, 2016.

[Fra10]   FRADEN, JACOB: *Handbook of Modern Sensors: Physics, Designs, and Applications (Handbook of Modern Sensors).* SpringerVerlag, 2010.

[FSG+16]   FRIEDRICH, DANIEL T., MARC O. SCHEITHAUER, JENS GREVE, THOMAS K. HOFFMANN and PATRICK J. SCHULER: *Recent advances in robot-assisted head and neck surgery.* The International Journal of Medical Robotics and Computer Assisted Surgery, 13(2):e1744, 2016.

[FTV00]   FUSIELLO, ANDREA, EMANUELE TRUCCO and ALESSANDRO VERRI: *A compact algorithm for rectification of stereo pairs.* Machine Vision and Applications, 12(1):16–22, Jul 2000.

[FWM98]   FITZPATRICK, J. M., J. B. WEST and C. R. MAURER: *Predicting error in rigid-body point-based registration.* IEEE Transactions on Medical Imaging, 17(5):694–702, 1998.

[FYCF04]   FRIED, NATHANIEL M., YUBING YANG, CHARLES A. CHANEY and DANIEL FRIED: *Transmission of Q-switched erbium:YSGG (λ=2.79 μm) and erbium:YAG (λ=2.94 μm) laser radiation through germanium oxide and sapphire optical fibres at high pulse energies.* Lasers in Medical Science, 19(3):155–160, Dec 2004.

[FYP]   FARAJIPARVAR, PARINAZ, HAO YING and ABHILASH PANDYA: *A Brief Survey of Telerobotic Time Delay Mitigation.* 7:198.

[FYSBY14]   FERHANOGLU, ONUR, MURAT YILDIRIM, KAUSHIK SUBRAMANIAN and ADELA BEN-YAKAR: *A 5-mm piezo-scanning fiber device for high speed ultrafast laser microsurgery.* Biomed. Opt. Express, 5(7):2023–2036, Jul 2014.

[FZC+18]   FAN, YINGWEI, BOYU ZHANG, WEI CHANG, XINRAN ZHANG and HONGEN LIAO: *A novel integration of spectral-domain optical-coherence-tomography and laser-ablation system for precision treatment.* International Journal of Computer Assisted Radiology and Surgery, 13(3):411–423, Mar 2018.

[GA09]   GROTE, K. and E. ANTONSSON: *Handbook of Mechanical Engineering.* Springer, 2009.

[GBLF10]   G., DOGANGIL, DAVIES B. L. and RODRIGUEZ Y BAENA F.: *A review of medical robotics for minimally invasive soft tissue surgery.* Proceedings of the Institution of Mechanical Engineers, Part H: Journal of Engineering in Medicine, 224(5):653–679, 2010.

[GBM+13]   GOLDMAN, R. E., A. BAJO, L. S. MACLACHLAN, R. PICKENS, S. D. HERRELL and N. SIMAAN: *Design and Performance Evaluation of a Minimally Invasive Telerobotic Platform for Transurethral Surveillance and Intervention.* IEEE Transactions on Biomedical Engineering, 60(4):918–925, April 2013.

[GBS14]   GOLDMAN, R. E., A. BAJO and N. SIMAAN: *Compliant Motion Control for Multisegment Continuum Robots With Actuation Force Sensing.* IEEE Transactions on Robotics, 30(4):890–902, Aug 2014.

[GCJ+05]   GUILLEM, JOSE G., DAVID B. CHESSIN, SEUNG-YONG JEONG, WON KIM and JEANNE-MARIE FOGARTY: *Contemporary Applications of Transanal Endoscopic Microsurgery: Technical Innovations and Limitations.* Clinical Colorectal Cancer, 5(4):268 – 273, 2005.

[GDP+10]   GAUSEMEIER, JÜRGEN, RAFAL DOROCIAK, SEBASTIAN POOK, ALEXANDER
            NYSSEN and AXEL TERFLOTH: *Computer-Aided Cross-Domain Modeling of
            Mechatronic Systems*. In *Proceedings of the International Design Conference -
            DESIGN 2010*, May 2010.

[GG19]   GILBERT, H. B. and I. S. GODAGE: *Validation of an Extensible Rod Model for
            Soft continuum Manipulators*. In *2019 2nd IEEE International Conference on Soft
            Robotics (RoboSoft)*, pages 711–716, April 2019.

[GGvdS12]   GIERLACH, D., A. GUSTUS and P. VAN DER SMAGT: *Generating marker stars
            for 6D optical tracking*. In *2012 4th IEEE RAS EMBS International Conference on
            Biomedical Robotics and Biomechatronics (BioRob)*, pages 147–152, June 2012.

[GMBK18]   GRASSMANN, REINHARD, VINCENT MODES and JESSICA BURGNER-KAHRS:
            *Learning the Forward and Inverse Kinematics of a 6-DOF Concentric Tube Con-
            tinuum Robot in SE(3)*. In *2018 IEEE/RSJ International Conference on Intelligent
            Robots and Systems (IROS)*, pages 5125–5132, 2018.

[GMKL14]   GOERLACH, F. S., A. MENZ, V. KARAS and T. C. LUETH: *Precision of near-
            infrared laser spot detection on different skin tissues featuring an NDI stereo
            camera*. In *2014 IEEE International Conference on Robotics and Biomimetics
            (ROBIO 2014)*, pages 303–308, Dec 2014.

[GMP+15]   GRAS, GAUTHIER, HANI J. MARCUS, CHRISTOPHER J. PAYNE, PHILIP PRATT
            and GUANG-ZHONG YANG: *Visual Force Feedback for Hand-Held Microsurgical
            Instruments*. In NAVAB, NASSIR, JOACHIM HORNEGGER, WILLIAM M. WELLS
            and ALEJANDRO FRANGI (editors): *Medical Image Computing and Computer-
            Assisted Intervention – MICCAI 2015*, pages 480–487, Cham, 2015. Springer
            International Publishing.

[GNBK19]   GRANNA, JOSEPHINE, ARYA NABAVI and JESSICA BURGNER-KAHRS:
            Computer-assisted planning for a concentric tube robotic system in neurosurgery.
            International Journal of Computer Assisted Radiology and Surgery, 14(2):335–344,
            Feb 2019.

[GNSA19]   GIFARI, M. WILDAN, HAMID NAGHIBI, STEFANO STRAMIGIOLI and MOMEN
            ABAYAZID: *A review on recent advances in soft surgical robots for endoscopic
            applications*. The International Journal of Medical Robotics and Computer Assisted
            Surgery, 0(0):e2010, 2019. e2010 RCS-18-0160.R2.

[Gru08]   GRUNWALD, MARTIN: *Human Haptic Perception: Basics and Applications*. 11
            2008.

[GS13]   GAL, THOMAS J. and NATALIE SILVER: *Transoral Laser Resection of Larynx*,
            pages 2867–2871. Springer Berlin Heidelberg, Berlin, Heidelberg, 2013.

[GS18]   GROENHUIS, V. and S. STRAMIGIOLI: *Rapid Prototyping High-Performance MR Safe Pneumatic Stepper Motors*. IEEE/ASME Transactions on Mechatronics, 23(4):1843–1853, Aug 2018.

[GW15]   GODAGE, I. S. and I. D. WALKER: *Dual Quaternion based modal kinematics for multisection continuum arms*. In *2015 IEEE International Conference on Robotics and Automation (ICRA)*, pages 1416–1422, May 2015.

[GW16]   GILBERT, HUNTER B. and ROBERT J. 3RD WEBSTER: *Rapid, Reliable Shape Setting of Superelastic Nitinol for Prototyping Robots*. IEEE robotics and automation letters, 1(1):98–105, 2016.

[GWC⁺18]   GARBIN, N., L. WANG, J. H. CHANDLER, K. L. OBSTEIN, N. SIMAAN and P. VALDASTRI: *A disposable continuum endoscope using piston-driven parallel bellow actuator*. In *2018 International Symposium on Medical Robotics (ISMR)*, pages 1–6, March 2018.

[GWC⁺19]   GARBIN, N., L. WANG, J. H. CHANDLER, K. L. OBSTEIN, N. SIMAAN and P. VALDASTRI: *Dual-Continuum Design Approach for Intuitive and Low-Cost Upper Gastrointestinal Endoscopy*. IEEE Transactions on Biomedical Engineering, 66(7):1963–1974, July 2019.

[GWP⁺16]   GOFRIT, OFER, CHARLES WEISSMAN, ERAN PELEG, NAHUM LIFSHITS, RAMI PINCHOVER and YUVAL WEISS: *Designing a modern surgical facility*. Perioperative Care and Operating Room Management, Jun 2016.

[Hag11]   HAGN, ULRICH: *The Aspect of Versatility in the Design of a Lighweight Robot for Surgical Applications*. Dr. Hut, 2011.

[HASH14]   HULIN, T., A. ALBU-SCHÄFFER and G. HIRZINGER: *Passivity and Stability Boundaries for Haptic Systems With Time Delay*. IEEE Transactions on Control Systems Technology, 22(4):1297–1309, July 2014.

[HBE⁺07]   HARADA, K., Z. BO, S. ENOSAWA, T. CHIBA and M. G. FUJIE: *Bending Laser Manipulator for Intrauterine Surgery and Viscoelastic Model of Fetal Rat Tissue*. In *Proceedings 2007 IEEE International Conference on Robotics and Automation*, pages 611–616, April 2007.

[HBZS14]   HARMS, H., J. BECK, J. ZIEGLER and C. STILLER: *Accuracy analysis of surface normal reconstruction in stereo vision*. In *2014 IEEE Intelligent Vehicles Symposium Proceedings*, pages 730–736, June 2014.

[HD95]   HORAUD, RADU and FADI DORNAIKA: *Hand-Eye Calibration*. The International Journal of Robotics Research, 14(3):195–210, 1995.

[HFS⁺11]   HARTL, DANA M., ALFIO FERLITO, CARL E. SILVER, ROBERT P. TAKES, SANDRO J. STOECKLI, CARLOS SUÁREZ, JUAN P. RODRIGO, ANDREAS M.

SESTERHENN, CARL H. SNYDERMAN, DAVID J. TERRIS, ERIC M. GENDEN and ALESSANDRA RINALDO: *Minimally invasive techniques for head and neck malignancies: current indications, outcomes and future directions.* European Archives of Oto-Rhino-Laryngology, 268(9):1249–1257, Sep 2011.

[HGD10]   HU, GUOQIANG, NICHOLAS GANS and WARREN DIXON: *Quaternion-based visual servo control in the presence of camera calibration error.* International Journal of Robust and Nonlinear Control, 20(5):489–503, 2010.

[HHP14]   HELLER, JAN, DIDIER HENRION and TOMAS PAJDLA: *Hand-Eye and Robot-World Calibration by Global Polynomial Optimization.* In *IEEE International Conference on Robotics and Automation (ICRA 2014)*, page 18p., Hong Kong, China, May 2014.

[HHW14]   HENDRICK, R. J., S. D. HERRELL and R. J. WEBSTER: *A multi-arm hand-held robotic system for transurethral laser Prostate surgery.* In *2014 IEEE International Conference on Robotics and Automation (ICRA)*, pages 2850–2855, May 2014.

[HIMH96]   H., WATANABE, I. ISHIKAWA, S. MOTOYUKI and K. HASEGAWA: *Clinical Assessments of the Erbium:YAG Laser for Soft Tissue Surgery and Scaling.* Journal of Clinical Laser Medicine and Surgery, 14:67–75, 1996.

[His14]   HISLEITER, JANNEK: *Inbetriebnahme eines Embedded-Linux-Systems zur Entwicklung von Hardware Schnittstellen für das Robot Operating System zum Einsatz in der Medizintechnik.* Bachelor thesis, Institute of Mechatronic Systems, Leibniz Universität Hannover, Hannover, Germany, 2014.

[HK97]   HUANG, W. H. and E. P. KROTKOV: *Optimal stereo mast configuration for mobile robots.* In *Proceedings of International Conference on Robotics and Automation*, volume 3, pages 1946–1951 vol.3, April 1997.

[HKCY18]   HAOUCHINE, N., W. KUANG, S. COTIN and M. YIP: *Vision-Based Force Feedback Estimation for Robot-Assisted Surgery Using Instrument-Constrained Biomechanical Three-Dimensional Maps.* IEEE Robotics and Automation Letters, 3(3):2160–2165, July 2018.

[HKTK15]   HARAGUCHI, D., T. KANNO, K. TADANO and K. KAWASHIMA: *A Pneumatically Driven Surgical Manipulator With a Flexible Distal Joint Capable of Force Sensing.* IEEE/ASME Transactions on Mechatronics, 20(6):2950–2961, Dec 2015.

[HPD17]   HA, J., F. C. PARK and P. E. DUPONT: *Optimizing Tube Precurvature to Enhance the Elastic Stability of Concentric Tube Robots.* IEEE Transactions on Robotics, 33(1):22–37, Feb 2017.

[HPT08]   HARP, W. R., A. G. PALEOCRASSAS and J. F. TU: *A Practical method for determining the beam profile near the focal spot.* The International Journal of

Advanced Manufacturing Technology, 37(11):1113–1119, Jul 2008.

[HRHMR⁺15] HUIHUI, WANG, CUIJPERS RAYMOND H., LUO MING R, HEYNDERICKX IN-GRID and ZHENG ZHENRONG: *Optimal illumination for local contrast enhancement based on the human visual system*. Journal of Biomedical Optics, 20:20 – 20 – 8, 2015.

[HRvdD⁺12] HOREMAN, TIM, SHARON P. RODRIGUES, JOHN J. VAN DEN DOBBELSTEEN, FRANK-WILLEM JANSEN and JENNY DANKELMAN: *Visual force feedback in laparoscopic training*. Surg Endosc, 26(1):242–248, Jan 2012.

[HS88] HART, SANDRA G and LOWELL E STAVELAND: *Development of NASA-TLX (Task Load Index): Results of empirical and theoretical research*. In *Advances in psychology*, volume 52, pages 139–183. Elsevier, 1988.

[HSJ17] HWANG, KYUNGMIN, YEONG-HYEON SEO and KI-HUN JEONG: *Microscanners for optical endomicroscopic applications*. Micro and Nano Systems Letters, 5(1):1, Jan 2017.

[HZLY19] HU, Y., L. ZHANG, W. LI and G. YANG: *Design and Fabrication of a 3-D Printed Metallic Flexible Joint for Snake-Like Surgical Robot*. IEEE Robotics and Automation Letters, 4(2):1557–1563, April 2019.

[IH] IVANENKO, MIKHAIL M. and PETER HERING: *Hard-tissue ablation with a mechanically Q-switched CO_2 laser*. In BOWN, STEPHEN G., GUY P. DELACRETAZ, GUILHEM GODLEWSKI M.D., GERHARD J. MUELLER, ROBERTO PINI, HANS-DIETER REIDENBACH, RUDOLF W. STEINER, LARS OTHAR SVAASAND and KARL-GORAN TRANBERG (editors): *Thermal Therapy, Laser Welding, and Tissue Interaction*, volume 3565, pages 110 – 115. International Society for Optics and Photonics, SPIE.

[Ise96] ISERMANN, R.: *Modeling and design methodology for mechatronic systems*. IEEE/ASME Transactions on Mechatronics, 1(1):16–28, March 1996.

[ISO94] *Accuracy (trueness and precision) of measurement methods and results - Part 1: General principles and definitions*. Standard, International Organization for Standardization, Geneva, CH, 1994.

[ISO98] *Manipulating industrial robots - Performance criteria and related test methods*. Standard, International Organization for Standardization, Geneva, CH, 1998.

[ITAP11] IANNACCI, FRANCIS, ERIK TURNQUIST, DANIEL AVRAHAMI and SHWETAK N. PATEL: *The Haptic Laser: Multi-sensation Tactile Feedback for At-a-distance Physical Space Perception and Interaction*. In *Proceedings of the SIGCHI Conference on Human Factors in Computing Systems*, CHI '11, pages 2047–2050, New York, NY, USA, 2011. ACM.

[Jac13]   JACQUES, STEVEN L: *Optical properties of biological tissues: a review*. Physics in Medicine & Biology, 58(11):R37, 2013.

[JAH+15]   JELÍNEK, FILIP, EWOUT A. ARKENBOUT, PAUL W. J. HENSELMANS, ROB PESSERS and PAUL BREEDVELD: *Classification of Joints Used in Steerable Instruments for Minimally Invasive Surgery–A Review of the State of the Art*. Journal of Medical Devices, 9(1):010801–010801–11, Mar 2015.

[Joh16]   JOHNSON, JEANNE: *Opto-Mechanical Optimization of Fiber Coupling for a Surgical Laser System*. Bachelor thesis, Institute of Mechatronic Systems, Leibniz Universität Hannover, Hannover, Germany, 2016.

[JOP+01]   JONES, ERIC, TRAVIS OLIPHANT, PEARU PETERSON et al.: *SciPy: Open source scientific tools for Python*, 2001.

[JW06]   JONES, B. A. and I. D. WALKER: *Kinematics for multisection continuum robots*. IEEE Transactions on Robotics, 22(1):43–55, Feb 2006.

[JWJBLWJ05]   J. W., CUI, TAN J. B., AO L. and KANG W. J.: *Optimized algorithm of laser spot center location in strong noise*. Journal of Physics: Conference Series, 13(1):312, 2005.

[KAK15]   KAJIMOTO, HIROYUKI, HIDEYUKI ANDO and KI-UK KYUNG: *Haptic Interaction: Perception, Devices and Applications*. Springer Publishing Company, Incorporated, 2015.

[KAWB09]   KLASING, K., D. ALTHOFF, D. WOLLHERR and M. BUSS: *Comparison of surface normal estimation methods for range sensing applications*. In *2009 IEEE International Conference on Robotics and Automation*, pages 3206–3211, May 2009.

[KBC17]   KUZNETSOVA, ALEXANDRA, PER B. BROCKHOFF and RUNE H. B. CHRISTENSEN: *lmerTest Package: Tests in Linear Mixed Effects Models*. Journal of Statistical Software, 82(13):1–26, 2017.

[KC17]   KRIDNER, J. and G. COLEY: *BeagleBone Black System Reference Manual*. BeagleBoneFoundation.com, Revision C edition, October 2017.

[KCD18]   KIM, Y., S. S. CHENG and J. P. DESAI: *Active Stiffness Tuning of a Spring-Based Continuum Robot for MRI-Guided Neurosurgery*. IEEE Transactions on Robotics, 34(1):18–28, Feb 2018.

[KCKI14]   KIM, Y., S. CHENG, S. KIM and K. IAGNEMMA: *A Stiffness-Adjustable Hyperredundant Manipulator Using a Variable Neutral-Line Mechanism for Minimally Invasive Surgery*. IEEE Transactions on Robotics, 30(2):382–395, April 2014.

[Ker14]   KERN, THORSTEN A.: *Engineering Haptic Devices: A Beginner's Guide for Engineers*. Springer Publishing Company, Incorporated, 2nd edition, 2014.

[KFN+16]   KRUPA, A., D. FOLIO, C. NOVALES, P. VIEYRES and T. LI: *Robotized Tele-Echography: An Assisting Visibility Tool to Support Expert Diagnostic*. IEEE Systems Journal, 10(3):974–983, Sept 2016.

[KFS+16]   KUNDRAT, D., A. FUCHS, A. SCHOOB, LA. KAHRS and T. ORTMAIER: *Endoluminal non-contact soft tissue ablation using fiber-based Er:YAG laser delivery*. In *Proceedings of the Society of Photo-Optical Instrumentation Engineers, Photonics West BiOS*, 2016.

[KFW14]   KAPADIA, A. D., K. E. FRY and I. D. WALKER: *Empirical investigation of closed-loop control of extensible continuum manipulators*. In *2014 IEEE/RSJ International Conference on Intelligent Robots and Systems*, pages 329–335, Sep. 2014.

[KGS+20]   KUNDRAT, D., R. GRAESSLIN, A. SCHOOB, D. T. FRIEDRICH, M. O. SCHEITHAUER, T. K. HOFFMANN, T. ORTMAIER, L. A. KAHRS and P. J. SCHULER: *Preclinical Performance Evaluation of a Robotic Endoscope for Non-Contact Laser Surgery*. Annals of Biomedical Engineering, Aug 2020.

[KGVS+18]   KELLARIS, NICHOLAS, VIDYACHARAN GOPALUNI VENKATA, GARRETT M. SMITH, SHANE K. MITCHELL and CHRISTOPH KEPLINGER: *Peano-HASEL actuators: Muscle-mimetic, electrohydraulic transducers that linearly contract on activation*. Science Robotics, 3(14), 2018.

[KKM+14]   KNEZEVIC, NIKOLA, TOMISLAV KULIS, MARJAN MARIC, MARIJA TOPALOVIC GRKOVIC, IVAN KRHEN and ZELJKO KASTELAN: *Laparoscopic Partial Nephrectomy with Diode Laser: A Promising Technique*. Photomedicine and Laser Surgery, 32(2):101–105, February 2014.

[KMS+09]   KWOK, KA-WAI, GEORGE P. MYLONAS, LOI WAH SUN, MIRNA LEROTIC, JAMES CLARK, THANOS ATHANASIOU, ARA DARZI and GUANG-ZHONG YANG: *Dynamic Active Constraints for Hyper-Redundant Flexible Robots*. In YANG, GUANG-ZHONG, DAVID HAWKES, DANIEL RUECKERT, ALISON NOBLE and CHRIS TAYLOR (editors): *Medical Image Computing and Computer-Assisted Intervention – MICCAI 2009*, pages 410–417, Berlin, Heidelberg, 2009. Springer Berlin Heidelberg.

[KOK+16]   KATO, TAKAHISA, ICHIRO OKUMURA, HIDEKAZU KOSE, KIYOSHI TAKAGI and NOBUHIKO HATA: *Tendon-driven continuum robot for neuroendoscopy: validation of extended kinematic mapping for hysteresis operation*. International Journal of Computer Assisted Radiology and Surgery, 11(4):589–602, Apr 2016.

[KRSH11]   KARNI, RON J., JASON T. RICH, PARUL SINHA and BRUCE H. HAUGHEY: *Transoral laser microsurgery: A new approach for unknown primaries of the head and neck*. The Laryngoscope, 121(6):1194–1201, 2011.

[KRW⁺08]   Kahrs, Lueder A., Joerg Raczkowsky, Martin Werner, Felix B.
            Knapp, Markus Mehrwald, Peter Hering, Joerg Schipper, Thomas
            Klenzner and Heinz Woern: *Visual servoing of a laser ablation based
            cochleostomy*, 2008.

[KSGD09]   Knulst, Arjan, Laurents Stassen, Cornelis Grimbergen and Jenny
            Dankelman: *Choosing Surgical Lighting in the LED Era*. 16:317–23, 12 2009.

[KSKO14a]   Kundrat, D., A. Schoob, LA. Kahrs and T. Ortmaier: *An Actuated,
            Flexible Endoscope for Laser Surgery inside the Larynx*. In *Proceedings of the
            4th Joint Workshop on New Technologies for Computer/Robot Assisted Surgery
            (CRAS)*, 2014.

[KSKO14b]   Kundrat, D., A. Schoob, LA. Kahrs and T. Ortmaier: *Rapid Prototyping
            of Rod-driven Continuum Robots*. In *Proceedings of the 4th Joint Workshop on
            New Technologies for Computer/Robot Assisted Surgery (CRAS)*, 2014.

[KSKO15]   Kundrat, D., A. Schoob, L. Kahrs and T. Ortmaier: *Soft Robotics*, chapter
            Flexible Robot for Laser Phonomicrosurgery, pages 265–271. Springer-Verlag
            Berlin Heidelberg, 2015.

[KSKO17]   Kundrat, Dennis, Andreas Schoob, Lüder Alexander Kahrs and
            Tobias Ortmaier: *Linearstellmechanismus*, 2017. DE102017101875 (B4).

[KSM14]   Krstini, D., A. K. Skelin and I. Milati: *Laser spot tracking based on mod-
            ified circular Hough transform and motion pattern analysis*. Sensors (Basel),
            14(11):20112–20133, Oct 2014.

[KSP⁺19]   Kundrat, D., A. Schoob, T. Piskon, R. Grässlin, P. J. Schuler, T. K.
            Hoffmann, L. A. Kahrs and T. Ortmaier: *Toward Assistive Technologies
            for Focus Adjustment in Teleoperated Robotic Non-Contact Laser Surgery*. IEEE
            Transactions on Medical Robotics and Bionics, 1(3):145–157, Aug 2019.

[KTD03]   Kehrl, W, J Tolkemitt and Pia Duesterhus: *[Comparison between transo-
            ral microsurgery by CO2 laser and conventional surgical therapy for T2 glottic
            carcinoma]*. Laryngo- rhino- otologie, 82:189–94, 04 2003.

[KW11]   Kapadia, A. and I. D. Walker: *Task-space control of extensible continuum
            manipulators*. In *2011 IEEE/RSJ International Conference on Intelligent Robots
            and Systems*, pages 1087–1092, Sep. 2011.

[KW13]   Kapadia, A. D. and I. D. Walker: *Self-motion analysis of extensible continuum
            manipulators*. In *2013 IEEE International Conference on Robotics and Automation*,
            pages 1988–1994, May 2013.

[LDL16]   Li, Dong, Liang Dong and Roderic S. Lakes: *A unit cell structure with
            tunable Poisson's ratio from positive to negative*. Materials Letters, 164:456 – 459,

2016.

[Len16]   LENTH, RUSSELL V.: *Least-Squares Means: The R Package lsmeans*. Journal of Statistical Software, 69(1):1–33, 2016.

[Lew91]   LEWIS, JAMES R.: *AN AFTER-SCENARIO QUESTIONNAIRE FOR USABILITY STUDIES: PSYCHOMETRIC EVALUATION OVER THREE TRIALS*. SIGCHI Bull., 23(4):79–, October 1991.

[LHJ18]   LOTFAVAR, A., S. HASANZADEH and F. JANABI-SHARIFI: *Cooperative Continuum Robots: Concept, Modeling, and Workspace Analysis*. IEEE Robotics and Automation Letters, 3(1):426–433, Jan 2018.

[LIR17]   LEE, GI SOO, ALEXANDRA IRACE and REZA RAHBAR: *The efficacy and safety of the flexible fiber CO2 laser delivery system in the endoscopic management of pediatric airway problems: Our long term experience*. International Journal of Pediatric Otorhinolaryngology, 97:218 – 222, 2017.

[LKL+14]   LEE, J., J. KIM, K. LEE, S. HYUNG, Y. KIM, W. KWON, K. ROH and J. CHOI: *Modeling and control of robotic surgical platform for single-port access surgery*. In *2014 IEEE/RSJ International Conference on Intelligent Robots and Systems*, pages 3489–3495, Sep. 2014.

[LKLF05]   LUBART, R., G. KESLER, R. LAVIE and H. FRIEDMANN: *Er:YAG Laser promotes Gingival Wound Repair by Photo-Dissociating Water Molecules*. Photomedicine and Laser Surgery, 23:369–372, 2005.

[LKP+13]   LOPEZ, E., K. W. KWOK, C. J. PAYNE, P. GIATAGANAS and G. Z. YANG: *Implicit Active Constraints for Robot-Assisted Arthroscopy*. IEEE Int Conf Robot Autom, 2013:5390–5395, May 2013.

[LKR+13]   LEE, J., Y. KIM, S. ROH, J. KIM, Y. LEE, J. KIM, B. CHOI and K. ROH: *Tension propagation analysis of novel robotized surgical platform for transumbilical single-port access surgery*. In *2013 IEEE/RSJ International Conference on Intelligent Robots and Systems*, pages 3083–3089, Nov 2013.

[LNM+10]   LIAO, H., M. NOGUCHI, T. MARUYAMA, Y. MURAGAKI, H. ISEKI, E. KOBAYASHI and I. SAKUMA: *Automatic Focusing and Robotic Scanning Mechanism for Precision Laser Ablation in Neurosurgery*. In *2010 IEEE/RSJ International Conference on Intelligent Robots and Systems*, pages 325–330, Oct 2010.

[LWG+17]   LEIBRANDT, K., P. WISANUVEJ, G. GRAS, J. SHANG, C. A. SENECI, P. GIATAGANAS, V. VITIELLO, A. DARZI and G. YANG: *Effective Manipulation in Confined Spaces of Highly Articulated Robotic Instruments for Single Access Surgery*. IEEE Robotics and Automation Letters, 2(3):1704–1711, July 2017.

[LWRY17]   LI, ZHENG, LIAO WU, HONGLIANG REN and HAOYONG YU: *Kinematic comparison of surgical tendon-driven manipulators and concentric tube manipulators*. Mechanism and Machine Theory, 107:148 – 165, 2017.

[LYR+15]   LI, Z., H. YU, H. REN, P. W. Y. CHIU and R. DU: *A novel constrained tendon-driven serpentine manipulator*. In *2015 IEEE/RSJ International Conference on Intelligent Robots and Systems (IROS)*, pages 5966–5971, Sep. 2015.

[Mac11]   MACFARLAND, T.W.: *Two-Way Analysis of Variance: Statistical Tests and Graphics Using R*. SpringerBriefs in Statistics. Springer New York, 2011.

[MC10]   MAREY, M. and F. CHAUMETTE: *New strategies for avoiding robot joint limits: Application to visual servoing using a large projection operator*. In *2010 IEEE/RSJ International Conference on Intelligent Robots and Systems*, pages 6222–6227, 2010.

[MCC+06]   MCMAHAN, W., V. CHITRAKARAN, M. CSENCSITS, D. DAWSON, I. D. WALKER, B. A. JONES, M. PRITTS, D. DIENNO, M. GRISSOM and C. D. RAHN: *Field trials and testing of the OctArm continuum manipulator*. In *Proceedings 2006 IEEE International Conference on Robotics and Automation, 2006. ICRA 2006.*, pages 2336–2341, May 2006.

[MCDG10]   MATTOS, L. S., D. G. CALDWELL, M. DELLEPIANE and E. GRANT: *Design and control of a robotic system for assistive laser phonomicrosurgery*. In *2010 Annual International Conference of the IEEE Engineering in Medicine and Biology*, pages 5411–5415, Aug 2010.

[MCF+13]   MERIGO, E., F. CLINI, C. FORNAINI, A. OPPICI, C. PATIES, A. ZANGRANADI, M. FONTANA, J.-P. ROCCA, M. MELETI, M. MANFREDI, L. CELLA and P. VESCOVI: *Laser-assisted surgery with different wavelengths: a preliminary ex vivo study on thermal increase and histological evaluation*. Laser Med Sci, 28:497–504, 2013.

[MCP+16]   MATTOS, L. S., D. G. CALDWELL, G. PERETTI, F. MORA, L. GUASTINI and R. CINGOLANI: *Microsurgery robots: addressing the needs of high-precision surgical interventions*. Swiss Med Wkly, 146:w14375, 2016.

[MCS+16]   MASTRONARDI, LUCIANO, GUGLIELMO CACCIOTTI, ETTORE DI SCIPIO, GIUSEPPE PARZIALE, RAFFAELINO ROPERTO, MARIA PIA TONELLI and ETTORE CARPINETA: *Safety and usefulness of flexible hand-held laser fibers in microsurgical removal of acoustic neuromas (vestibular schwannomas)*. Clinical Neurology and Neurosurgery, 145:35 – 40, 2016.

[MFA+16]   MECCARIELLO, GIUSEPPE, FEDERICO FAEDI, SALEH ALGHAMDI, FILIPPO MONTEVECCHI, ELISABETTA FIRINU, CLAUDIA ZANOTTI, DAVIDE CAVALIERE, ROBERTA GUNELLI, MARCO TAURCHINI, ANDREA AMADORI and

CLAUDIO VICINI: *An experimental study about haptic feedback in robotic surgery: may visual feedback substitute tactile feedback?* Journal of Robotic Surgery, 10(1):57–61, Mar 2016.

[MGI18]   MAHONEY, ARTHUR W., HUNTER B. GILBERT and ROBERT J. WEBSTER III: *A review of concentric tube robots: Modeling, control, design, planning, and sensing*, chapter Chapter 7, pages 181–202. 2018.

[MH03]   MALM, H. and A. HEYDEN: *Simplified intrinsic camera calibration and hand-eye calibration for robot vision.* In *Proceedings 2003 IEEE/RSJ International Conference on Intelligent Robots and Systems (IROS 2003) (Cat. No.03CH37453)*, volume 1, pages 1037–1043 vol.1, Oct 2003.

[MHH$^+$17]   MATTHEIS, STEFAN, PIA HASSKAMP, LAURA HOLTMANN, CHRISTINA SCHÄFER, URBAN GEISTHOFF, NINA DOMINAS and STEPHAN LANG: *Flex Robotic System in transoral robotic surgery: The first 40 patients.* Head & Neck, 39(3):471–475, 2017.

[MHO17]   MORIMOTO, T. K., E. W. HAWKES and A. M. OKAMURA: *Design of a Compact Actuation and Control System for Flexible Medical Robots.* IEEE Robot Autom Lett, 2(3):1579–1585, Jul 2017.

[Mic16]   MICHAILIK, ALEXANDER: *Entwicklung eines mehrsegmentigen Kontinuumsroboters für die endoluminale Laserchirurgie.* Diploma thesis, Institute of Mechatronic Systems, Leibniz Universität Hannover, Hannover, Germany, 2016.

[MIT$^+$18]   MODES, VINCENT, SONTJE IHLER, TOBIAS TOBIAS, ARYA NABAVI, LÜDER ALEXANDER KAHRS and JESSICA BURGNER-KAHRS: *Towards Concentric Tube Robots for Microsurgery: First Results in Eye-to-hand Visual Servoing.* pages 77–78, 06 2018.

[MJW05]   MCMAHAN, W., B. A. JONES and I. D. WALKER: *Design and implementation of a multi-section continuum robot: Air-Octor.* In *2005 IEEE/RSJ International Conference on Intelligent Robots and Systems*, pages 2578–2585, Aug 2005.

[MKHA13]   MOSES, M. S., M. D. M. KUTZER, HANS MA and M. ARMAND: *A continuum manipulator made of interlocking fibers.* In *2013 IEEE International Conference on Robotics and Automation*, pages 4008–4015, May 2013.

[MLY$^+$17]   MO, HAI-LAN, JIE LI, XIANG YANG, FENG ZHANG, JUN-WEI XIONG, ZHI-LING YANG, JIAN TAN and BING LI: *Transoral laser microsurgery versus radiotherapy for T1 glottic carcinoma: a systematic review and meta-analysis.* Lasers in Medical Science, 32(2):461–467, Feb 2017.

[MO16]   MORIMOTO, T. K. and A. M. OKAMURA: *Design of 3-D Printed Concentric Tube Robots.* IEEE Transactions on Robotics, 32(6):1419–1430, Dec 2016.

[Mor99]   MORETON, P.: *Industrial Brushless Servomotors*. Newnes Power Engineering Series. Elsevier Science, 1999.

[MP12]   MIHELJ, MATJAZ and JANEZ PODOBNIK: *Haptics for Virtual Reality and Teleoperation*, volume 64. 01 2012.

[MPF⁺17]   MOGLIA, ANDREA, VITTORIO PERRONE, VINCENZO FERRARI, LUCA MORELLI, UGO BOGGI, MAURO FERRARI, FRANCO MOSCA and ALFRED CUSCHIERI: *Influence of videogames and musical instruments on performances at a simulator for robotic surgery*. Minimally Invasive Therapy & Allied Technologies, 26(3):129–134, 2017.

[MPP17]   MELI, L., C. PACCHIEROTTI and D. PRATTICHIZZO: *Experimental evaluation of magnified haptic feedback for robot-assisted needle insertion and palpation*. Int J Med Robot, 13(4), Dec 2017.

[MRLW⁺04]   MUELLER-RICHTER, U. D. A., A. LIMBERGER, P. WEBER, K. W. RUPRECHT, W. SPITZER and M. SCHILLING: *Possibilities and limitations of current stereo-endoscopy*. Surgical Endoscopy And Other Interventional Techniques, 18(6):942–947, Jun 2004.

[MRM⁺06]   MCGEE, MICHAEL F., MICHAEL J. ROSEN, JEFFREY MARKS, RAYMOND P. ONDERS, AMITABH CHAK, ASHLEY FAULX, VICTOR K. CHEN and JEFFREY PONSKY: *A Primer on Natural Orifice Transluminal Endoscopic Surgery: Building a New Paradigm*. Surgical Innovation, 13(2):86–93, 2006.

[MRS⁺20]   MORRIS, KARCHER, ANDREAS ROSENKRANZ, HENNING SEIBERT, LARS RINGEL, STEFAN DIEBELS and FRANK E. TALKE: *Uniaxial and biaxial testing of 3D printed hyperelastic photopolymers*. Journal of Applied Polymer Science, 137(8):48400, 2020.

[MRY11]   MOHD RAZALI, NORNADIAH and BEE YAP: *Power Comparisons of Shapiro-Wilk, Kolmogorov-Smirnov, Lilliefors and Anderson-Darling Tests*. J. Stat. Model. Analytics, 2, 01 2011.

[MSC05]   MARCHAND, E., F. SPINDLER and F. CHAUMETTE: *ViSP for visual servoing: a generic software platform with a wide class of robot control skills*. IEEE Robotics and Automation Magazine, 12(4):40–52, December 2005.

[MTK09]   MUES, ADAM C., JOEL M.H. TEICHMAN and BODO E. KNUDSEN: *Quantification of Holmium:Yttrium Aluminum Garnet Optical Tip Degradation*. Journal of Endourology, 23(9):1425–1428, 2009.

[MY08]   MOUNTNEY, PETER and GUANG-ZHONG YANG: *Soft Tissue Tracking for Minimally Invasive Surgery: Learning Local Deformation Online*. In METAXAS, DIMITRIS, LEON AXEL, GABOR FICHTINGER and GÁBOR SZÉKELY (editors):

Medical Image Computing and Computer-Assisted Intervention – MICCAI 2008, pages 364–372, Berlin, Heidelberg, 2008. Springer Berlin Heidelberg.

[NBK15] NGUYEN, T. D. and J. BURGNER-KAHRS: *A tendon-driven continuum robot with extensible sections.* In *2015 IEEE/RSJ International Conference on Intelligent Robots and Systems (IROS)*, pages 2130–2135, Sept 2015.

[NBK16] NEUMANN, M. and J. BURGNER-KAHRS: *Considerations for follow-the-leader motion of extensible tendon-driven continuum robots.* In *2016 IEEE International Conference on Robotics and Automation (ICRA)*, pages 917–923, May 2016.

[Nie07] NIEMZ, M.H.: *Laser-Tissue Interactions: Fundamentals and Applications.* Biological and Medical Physics, Biomedical Engineering. Springer Berlin Heidelberg, 2007.

[NJ07] NEPPALLI, S. and B. A. JONES: *Design, construction, and analysis of a continuum robot.* In *2007 IEEE/RSJ International Conference on Intelligent Robots and Systems*, pages 1503–1507, Oct 2007.

[NSB+14] NOH, Y., S. SAREH, J. BACK, H. A. WÜRDEMANN, T. RANZANI, E. L. SECCO, A. FARAGASSO, H. LIU and K. ALTHOEFER: *A three-axial body force sensor for flexible manipulators.* In *2014 IEEE International Conference on Robotics and Automation (ICRA)*, pages 6388–6393, May 2014.

[OBCM17] OLIVIERI, E., G. BARRESI, D. G. CALDWELL and L. S. MATTOS: *Haptic Feedback for Control and Active Constraints in Contactless Laser Surgery: Concept, Implementation and Evaluation.* IEEE Transactions on Haptics, page 1, 2017.

[ODK+07] ORTMAIER, TOBIAS, BARBARA DEML, BERNHARD KÜBLER, GEORG PASSIG, DETLEF REINTSEMA and ULRICH SEIBOLD: *Robot Assisted Force Feedback Surgery*, pages 361–379. Springer Berlin Heidelberg, Berlin, Heidelberg, 2007.

[Oka09] OKAMURA, A. M.: *Haptic feedback in robot-assisted minimally invasive surgery.* Curr Opin Urol, 19(1):102–107, Jan 2009.

[OMK+13] OBATA, DAISUKE, YOSHINORI MORITA, RINNA KAWAGUCHI, KATSUNORI ISHII, HISANAO HAZAMA, KUNIO AWAZU, HIROMU KUTSUMI and TAKESHI AZUMA: *Endoscopic submucosal dissection using a carbon dioxide laser with submucosally injected laser absorber solution (porcine model).* Surgical Endoscopy, 27(11):4241–4249, Nov 2013.

[ONK16] OOMORI, SHINJI, TAKESHI NISHIDA and SHUICHI KUROGI: *Point cloud matching using singular value decomposition.* Artificial Life and Robotics, 21(2):149–154, Jun 2016.

[OOS+10] ONDA, K., T. OSA, N. SUGITA, M. HASHIZUME and M. MITSUISHI: *Asynchronous force and visual feedback in teleoperative laparoscopic surgical system.*

In *2010 IEEE/RSJ International Conference on Intelligent Robots and Systems*, pages 844–849, Oct 2010.

[OPCK13]   ONISOR, IOANA M., RALUCA PECIE, IVONNE CHASKELIS and IVO KREJCI: *Cutting and coagulation during intraoral soft tissue surgery using Er:Yag laser*. European Journal of Paediatric Dentistry, 14(2):140–145, 2013.

[OSK10]   OSA, TAKAYUKI, CHRISTOPH STAUB and ALOIS KNOLL: *Framework of automatic robot surgery system using Visual servoing*. In *2010 IEEE/RSJ International Conference on Intelligent Robots and Systems*, pages 1837–1842, 2010.

[OVRM11]   OKAMURA, A. M., L. N. VERNER, C. E. REILEY and M. MAHVASH: *Haptics for Robot-Assisted Minimally Invasive Surgery*. In KANEKO, MAKOTO and YOSHIHIKO NAKAMURA (editors): *Robotics Research*, pages 361–372, Berlin, Heidelberg, 2011. Springer Berlin Heidelberg.

[PAK$^+$18]   PETERS, BRIAN S., PRISCILA R. ARMIJO, CRYSTAL KRAUSE, SONGITA A. CHOUDHURY and DMITRY OLEYNIKOV: *Review of emerging surgical robotic technology*. Surgical Endoscopy, 32(4):1636–1655, Apr 2018.

[PBSH15]   PICKENS, RYAN B., ANDREA BAJO, NABIL SIMAAN and DUKE HERRELL: *A Pilot Ex Vivo Evaluation of a Telerobotic System for Transurethral Intervention and Surveillance*. Journal of Endourology, 29(2):231–234, 2015. PMID: 25091196.

[PCD87]   PIETRAFITTA, JOSEPH J., MICHAEL H. CARSTENS and RICHARD M. DWYER: *Endoscopic laser therapy for the treatment of malignant esophageal obstruction*. Lasers in Surgery and Medicine, 7(6):487–490, 1987.

[PDBPN12]   PIAZZA, CESARE, FRANCESCA DEL BON, GIORGIO PERETTI and PIERO NICOLAI: *Narrow band imaging in endoscopic evaluation of the larynx*. Current Opinion in Otolaryngology & Head and Neck Surgery, 20(6), 2012.

[PFCM15]   PARDO, DIEGO, LORIS FICHERA, DARWIN CALDWELL and LEONARDO S. MATTOS: *Learning Temperature Dynamics on Agar-Based Phantom Tissue Surface During Single Point CO2 Laser Exposure*. Neural Process. Lett., 42(1):55–70, August 2015.

[Pis17]   PISKON, THOMAS: *Bildbasierte Pfadplanung und haptische Assistenz in der endoskopischen Laserchirurgie*. Master thesis, Institute of Mechatronic Systems, Leibniz Universität Hannover, Hannover, Germany, 2017.

[PKW$^+$16]   PELLER, MAXIMILIAN, ALEXANDER KATALINIC, BARBARA WOLLENBERG, INGO U. TEUDT and JENS-E. MEYER: *Epidemiology of laryngeal carcinoma in Germany, 1998–2011*. European Archives of Oto-Rhino-Laryngology, 273(6):1481–1487, Jun 2016.

[PNT$^+$06]   POLETTO, T.J., A. K. NGO, A. TCHAPYJNIKOV, K. LEVON, D. TRAN and N. M.

FRIED: *Comparison of germanium oxide fibers with silica and sapphire fiber tips for transmission of Erbium: YAG laser radiation.* Lasers in Surgery and Medicine, 38:787–791, 2006.

[PPO18] PAULL, J. O., N. PUDALOV and V. OBIAS: *Medrobotics Flex transanal excision of a rectal gastrointestinal stromal tumour: first video of the transanal Flex robot used in a human - a video vignette.* Colorectal Disease, 20(11):1048–1049, 2018.

[PPVP18] PIAZZA, CESARE, GIORGIO PERETTI and VINCENT VANDER POORTEN: *Editorial: Advances in Transoral Approaches for Laryngeal Cancer.* Frontiers in Oncology, 8:455, 2018.

[PRAR19] PEYRON, Q., K. RABENOROSOA, N. ANDREFF and P. RENAUD: *A numerical framework for the stability and cardinality analysis of concentric tube robots: Introduction and application to the follow-the-leader deployment.* Mechanism and Machine Theory, 132:176 – 192, 2019.

[PRK+12] PATEL, SNEHAL, MILIND RAJADHYAKSHA, STEFAN KIROV, YONGBIAO LI and RICARDO TOLEDO-CROW: *Endoscopic laser scalpel for head and neck cancer surgery*, 2012.

[PRRA14] PENGWANG, E., K. RABENOROSOA, M. RAKOTONDRABE and N. ANDREFF: *Characterization and micro-assembly of electrostatic actuators for 3-DOF micro-manipulators in laser phonomicrosurgery.* In *2014 IEEE/ASME 10th International Conference on Mechatronic and Embedded Systems and Applications (MESA)*, pages 1–6, Sep. 2014.

[PW74] PALMER, KENT F. and DUDLEY WILLIAMS: *Optical properties of water in the near infrared∗.* J. Opt. Soc. Am., 64(8):1107–1110, Aug 1974.

[QQL+14] QI, P., C. QIU, H. LIU, J. S. DAI, L. SENEVIRATNE and K. ALTHOEFER: *A novel continuum-style robot with multilayer compliant modules.* In *2014 IEEE/RSJ International Conference on Intelligent Robots and Systems*, pages 3175–3180, Sep. 2014.

[R C15] R CORE TEAM: *R: A Language and Environment for Statistical Computing.* R Foundation for Statistical Computing, Vienna, Austria, 2015.

[RA11] RUBINSTEIN, MARC and WILLIAM B. ARMSTRONG: *Transoral laser microsurgery for laryngeal cancer: A primer and review of laser dosimetry.* Lasers in Medical Science, 26(1):113–124, Jan 2011.

[RAB+08] REILEY, C. E., T. AKINBIYI, D. BURSCHKA, D. C. CHANG, A. M. OKAMURA and D. D. YUH: *Effects of visual force feedback on robot-assisted surgical task performance.* J. Thorac. Cardiovasc. Surg., 135(1):196–202, Jan 2008.

[RBT14] RONE, WILLIAM S. and PINHAS BEN-TZVI: *Mechanics Modeling of Multi-*

segment Rod-Driven Continuum Robots. Journal of Mechanisms and Robotics, 6(4):041006–041006–12, Jun 2014.

[RCG+16] RANZANI, T., M. CIANCHETTI, G. GERBONI, I. D. FALCO and A. MENCIASSI: *A Soft Modular Manipulator for Minimally Invasive Surgery: Design and Characterization of a Single Module*. IEEE Transactions on Robotics, 32(1):187–200, Feb 2016.

[RD99] ROBINSON, G. and J. B. C. DAVIES: *Continuum robots - a state of the art*. In *Proceedings 1999 IEEE International Conference on Robotics and Automation (Cat. No.99CH36288C)*, volume 4, pages 2849–2854 vol.4, May 1999.

[RDLD97] REMY, S., M. DHOME, J. M. LAVEST and N. DAUCHER: *Hand-eye calibration*. In *Intelligent Robots and Systems, 1997. IROS '97., Proceedings of the 1997 IEEE/RSJ International Conference on*, volume 2, pages 1057–1065 vol.2, Sep 1997.

[RdLvdB+14] RINKEL, R.N.P.M., I.M. VERDONCK DE LEEUW, N. VAN DEN BRAKEL, R. DE BREE, S.E.J. EERENSTEIN, N. AARONSON and C.R. LEEMANS: *Patient-reported symptom questionnaires in laryngeal cancer: Voice, speech and swallowing*. Oral Oncology, 50(8):759 – 764, 2014.

[RDM15] RUSSO, S., P. DARIO and A. MENCIASSI: *A Novel Robotic Platform for Laser-Assisted Transurethral Surgery of the Prostate*. IEEE Transactions on Biomedical Engineering, 62(2):489–500, Feb 2015.

[RDM18] RUNCIMAN, MARK, ARA DARZI and GEORGE P. MYLONAS: *Soft Robotics in Minimally Invasive Surgery*. Soft Robotics, 0(0):null, 2018.

[RE09] ROMANELLI, J. R. and D. B. EARLE: *Single-port laparoscopic surgery: an overview*. Surg Endosc, 23(7):1419–1427, Jul 2009.

[RJWJ10] ROBERT J. WEBSTER, III and BRYAN A. JONES: *Design and Kinematic Modeling of Constant Curvature Continuum Robots: A Review*. The International Journal of Robotics Research, 29(13):1661–1683, 2010.

[RK11] RAULIN, C. and S. KARSAI: *Laser and IPL Technology in Dermatology and Aesthetic Medicine*. Springer Berlin Heidelberg, 2011.

[RLND08] REMACLE, MARC, GEORGES LAWSON, MARIE-CÉCILE NOLLEVAUX and MONIQUE DELOS: *Current State of Scanning Micromanipulator Applications with the Carbon Dioxide Laser*. Annals of Otology, Rhinology & Laryngology, 117(4):239–244, 2008.

[RLP+12] ROMEO, U., F. LIBOTTE, G. PALAIA, A. DEL VECCHIO, G. TENORE, P. VISCA, S. NAMMOUR and A. POLIMENI: *Histological in vitro evaluation of the effects of Er:YAG laser on oral soft tissues*. Laser Med Sci, 27:749–753, 2012.

[RMNPL+15]   REMACLE, M., V. M. N. PRASAD, G. LAWSON, L. PLISSON, V. BACHY and S. VAN DER VORST: *Transoral robotic surgery (TORS) with the Medrobotics Flex™ System: first surgical application on humans.* European Archives of Oto-Rhino-Laryngology, 272(6):1451–1455, Jun 2015.

[RS05]   RIZUN, P. R. and G. R. SUTHERLAND: *Surgical Laser Augmented with Haptic Feedback and Visible Trajectory.* In *IEEE Proceedings. VR 2005. Virtual Reality, 2005.*, pages 241–244, March 2005.

[RSG+17]   ROSEN, J., L. N. SEKHAR, D. GLOZMAN, M. MIYASAKA, J. DOSHER, B. DELLON, K. S. MOE, A. KIM, L. J. KIM, T. LENDVAY, Y. LI and B. HANNAFORD: *Roboscope: A flexible and bendable surgical robot for single portal Minimally Invasive Surgery.* In *2017 IEEE International Conference on Robotics and Automation (ICRA)*, pages 2364–2370, May 2017.

[RT10]   RIPKA, P. and A. TIPEK: *Modern Sensors Handbook.* Wiley-Blackwell, 2010.

[RTR+17]   RENEVIER, R., B. TAMADAZTE, K. RABENOROSOA, L. TAVERNIER and N. ANDREFF: *Endoscopic Laser Surgery: Design, Modeling, and Control.* IEEE/ASME Transactions on Mechatronics, 22(1):99–106, Feb 2017.

[RVNG06]   RAIF, JOSHUA, MICHAEL VARDI, ODED NAHLIELI and ISRAEL GANNOT: *An Er:YAG laser endoscopic fiber delivery system for lithotripsy of salivary stones.* Lasers in Surgery and Medicine, 38(6):580–587, 2006.

[SACB17]   STARKE, J., E. AMANOV, M. T. CHIKHAOUI and J. BURGNER-KAHRS: *On the merits of helical tendon routing in continuum robots.* In *2017 IEEE/RSJ International Conference on Intelligent Robots and Systems (IROS)*, pages 6470–6476, Sep. 2017.

[SAK+15]   SAWABE, M., A. AOKI, M. KOMAKI, K. IWASAKI, M. OGITA and Y. IZUMI: *Gingival tissue healing following Er:YAG laser ablation compared to electrosurgery in rats.* Lasers Med Sci, 30(2):875–883, Feb 2015.

[SBD+16]   SMOLJKIC, GABRIJEL, GIANNI BORGHESAN, ALAIN DEVREKER, EMMANUEL VANDER POORTEN, BENOIT ROSA, HERBERT DE PRAETERE, JORIS DE SCHUTTER, DOMINIEK REYNAERTS and JOS VANDER SLOTEN: *Control of a hybrid robotic system for computer-assisted interventions in dynamic environments.* International Journal of Computer Assisted Radiology and Surgery, 11(7):1371–1383, Jul 2016.

[Sch18]   SCHOOB, ANDREAS: *Stereo vision-guided laser microsurgery.* PhD thesis, 2018.

[SD06]   SEARS, P. and P. DUPONT: *A Steerable Needle Technology Using Curved Concentric Tubes.* In *2006 IEEE/RSJ International Conference on Intelligent Robots and Systems*, pages 2850–2856, Oct 2006.

[SDGD+18]   SARLI, NIMA, GIUSEPPE DEL GIUDICE, SMITA DE, MARY S. DIETRICH,
            STANLEY DUKE HERRELL and NABIL SIMAAN: *Preliminary Porcine In Vivo
            Evaluation of a Telerobotic System for Transurethral Bladder Tumor Resection
            and Surveillance*. Journal of Endourology, 32(6):516–522, 2018.

[SDY05]   STOYANOV, DANAIL, ARA DARZI and GUANG ZHONG YANG: *A practical
            approach towards accurate dense 3D depth recovery for robotic laparoscopic
            surgery*. Computer Aided Surgery, 10(4):199–208, 2005.

[SGS+09]   STÜBINGER, S., S. GHANAATI, B. SALDAMLI, C. J. KIRKPATRICK and
            R. SADER: *Er:YAG Laser Osteotomy: Preliminary Clinical and Histological
            Results of a New Technique for Contact-Free Bone Surgery*. European Surgical
            Research, 42(3):150–156, 2009.

[SH06]   STROBL, KLAUS H. and GERD HIRZINGER: *Optimal Hand-Eye Calibration*. In
            2006 IEEE/RSJ International Conference on Intelligent Robots and Systems, pages
            4647–4653, 2006.

[SK16]   SICILIANO, BRUNO and OUSSAMA KHATIB: *Springer Handbook of Robotics*.
            Springer Publishing Company, Incorporated, 2nd edition, 2016.

[SKD+11]   SCHELINSKI, U., J. KNOBBE, H.-G. DALLMANN, H. GRÖGER, M. FÖRSTER,
            M. SCHOLLES, M. SCHWARZENBERG and R. RIESKE: *MEMS-based laser
            scanning microscope for endoscopic use*, 2011.

[SKG+19]   SCHULER, P., D. KUNDRAT, R. GRÄSSLIN, D. FRIEDRICH, M. O. SCHEI-
            THAUER, T. ORTMAIER, T. K. HOFFMANN and L. KAHRS: *Assistive functions for
            a novel laser surgery system - a pilot study*. Laryngo-Rhino-Otol, 98(S 02):10964,
            2019. 10964.

[SKH94]   SAKURAMACHI, S., T. KIMURA and Y. HARADA: *Experimental study of la-
            paroscopic selective proximal vagotomy using a carbon dioxide laser*. Surgical
            Endoscopy, 8(8):857–861, Aug 1994.

[SKK+15]   SCHOOB, A., D. KUNDRAT, L. KLEINGROTHE, L. A. KAHRS, N. ANDREFF and
            T. ORTMAIER: *Tissue surface information for intraoperative incision planning and
            focus adjustment in laser surgery*. Int J Comput Assist Radiol Surg, 10(2):171–181,
            Feb 2015.

[SKKO15]   SCHOOB, A., D. KUNDRAT, L. A. KAHRS and T. ORTMAIER: *Comparative study
            on surface reconstruction accuracy of stereo imaging devices for microsurgery*.
            International Journal of Computer Assisted Radiology and Surgery (JCARS), 2015.

[SKKO17]   SCHOOB, A., D. KUNDRAT, L. A. KAHRS and T. ORTMAIER: *Stereo vision-
            based tracking of soft tissue motion with application to online ablation control in
            laser microsurgery*. Med Image Anal, 40:80–95, Aug 2017.

[SKL+16]   SCHOOB, ANDREAS, DENNIS KUNDRAT, STEFAN LEKON, LÜDER A. KAHRS
             and TOBIAS ORTMAIER: *Color-encoded distance for interactive focus positioning
             in laser microsurgery.* Optics and Lasers in Engineering, 83(Complete):71–79,
             2016.

[SLKO16]   SCHOOB, ANDREAS, MAX-HEINRICH LAVES, LÜDER ALEXANDER KAHRS and
             TOBIAS ORTMAIER: *Soft tissue motion tracking with application to tablet-based
             incision planning in laser surgery.* International Journal of Computer Assisted
             Radiology and Surgery, 11(12):2325–2337, Dec 2016.

[SLL+18]   SACCOMANDI, PAOLA, ALFONSO LAPERGOLA, FABIO LONGO, EMILIANO
             SCHENA and GIUSEPPE QUERO: *Thermal ablation of pancreatic cancer: A sys-
             tematic literature review of clinical practice and pre-clinical studies.* International
             Journal of Hyperthermia, 35(1):398–418, 2018.

[SLQ+17]   SHI, C., X. LUO, P. QI, T. LI, S. SONG, Z. NAJDOVSKI, T. FUKUDA and H. REN:
             *Shape Sensing Techniques for Continuum Robots in Minimally Invasive Surgery: A
             Survey.* IEEE Transactions on Biomedical Engineering, 64(8):1665–1678, Aug
             2017.

[SM04]   SHON, YOUNGUNG and S. MCMAINS: *Evaluation of drawing on 3D surfaces
             with haptics.* IEEE Computer Graphics and Applications, 24(6):40–50, Nov 2004.

[SM10]   SINK, CHRISTOPHER A. and NYARADZO H. MVUDUDU: *Statistical Power,
             Sampling, and Effect Sizes: Three Keys to Research Relevancy.* Counseling
             Outcome Research and Evaluation, 1(2):1–18, 2010.

[SMH+12]   SWINDLE, M. M., A. MAKIN, A. J. HERRON, JR F. J. CLUBB and K. S. FRA-
             ZIER: *Swine as Models in Biomedical Research and Toxicology Testing.* Veterinary
             Pathology, 49(2):344–356, 2012.

[SMH+19]   STOCK, KARL, DANIEL MEITINGER, FLORIAN HAUSLADEN, THOMAS
             STEGMAYER and HOLGER WURM: *Primary investigations on defined thermal
             effects on soft tissue using a diode pumped Er:YAG laser system.* In BEIER,
             HOPE THOMAS and BENNETT L. IBEY (editors): *Optical Interactions with Tissue
             and Cells XXX*, volume 10876, pages 156 – 163. International Society for Optics
             and Photonics, SPIE, 2019.

[SNP+11]   SHANG, J., D. P. NOONAN, C. PAYNE, J. CLARK, M. H. SODERGREN, A. DARZI
             and G. . YANG: *An articulated universal joint based flexible access robot for
             minimally invasive surgery.* In *2011 IEEE International Conference on Robotics
             and Automation*, pages 1147–1152, May 2011.

[SPB+15]   SCHNEIDER, ADRIAN, SIMON PEZOLD, KYUNG-WON BAEK, DILYAN MARI-
             NOV and PHILIPPE C. CATTIN: *Direct Calibration of a Laser Ablation System
             in the Projective Voltage Space.* In NAVAB, NASSIR, JOACHIM HORNEGGER,

WILLIAM M. WELLS and ALEJANDRO FRANGI (editors): *Medical Image Computing and Computer-Assisted Intervention – MICCAI 2015*, pages 274–281, Cham, 2015. Springer International Publishing.

[SPK+13]   SCHOOB, ANDREAS, FLORIAN PODSZUS, DENNIS KUNDRAT, LÜDER A. KAHRS and TOBIAS ORTMAIER: *Stereoscopic Surface Reconstruction in Minimally Invasive Surgery using Efficient Non-Parametric Image Transforms*. In *Proceedings of the 3rd Joint Workshop on New Technologies for Computer/Robot Assisted Surgery (CRAS) 2013*, 2013.

[SPP+07]   STOIANOVICI, D., A. PATRICIU, D. PETRISOR, D. MAZILU and L. KAVOUSSI: *A New Type of Motor: Pneumatic Step Motor*. IEEE/ASME Transactions on Mechatronics, 12(1):98–106, Feb 2007.

[SRVO09]   SILVA, A. J., O. A. D. RAMIREZ, V. P. VEGA and J. P. O. OLIVER: *PHANToM OMNI Haptic Device: Kinematic and Manipulability*. In *2009 Electronics, Robotics and Automotive Mechanics Conference (CERMA)*, pages 193–198, 2009.

[SSDL07]   STOPP, S., D. SVEJDAR, H. DEPPE and T. C. LUETH: *A new method for optimized laser treatment by laser focus navigation and distance visualization*. Conf Proc IEEE Eng Med Biol Soc, 2007:1738–1741, 2007.

[SSL+14a] SENECI, C. A., J. SHANG, K. LEIBRANDT, V. VITIELLO, N. PATEL, A. DARZI, J. TEARE and G. YANG: *Design and evaluation of a novel flexible robot for transluminal and endoluminal surgery*. In *2014 IEEE/RSJ International Conference on Intelligent Robots and Systems*, pages 1314–1321, Sep. 2014.

[SSL14b]   SU, B., Z. SHI and H. LIAO: *Micro laser ablation system integrated with image sensor for minimally invasive surgery*. In *2014 IEEE/RSJ International Conference on Intelligent Robots and Systems*, pages 2043–2048, Sept 2014.

[SSN+16]   SHIVA, A., A. STILLI, Y. NOH, A. FARAGASSO, I. D. FALCO, G. GERBONI, M. CIANCHETTI, A. MENCIASSI, K. ALTHOEFER and H. A. WURDEMANN: *Tendon-Based Stiffening for a Pneumatically Actuated Soft Manipulator*. IEEE Robotics and Automation Letters, 1(2):632–637, July 2016.

[SSN+19]   SHIVA, ALI, S.M. HADI SADATI, YOHAN NOH, JAN FRAS, AHMAD ATAKA, HELGE WUERDEMANN, HELMUT HAUSER, IAN D. WALKER, THRISHANTHA NANAYAKKARA and KASPAR ALTHOEFER: *Elasticity Versus Hyperelasticity Considerations in Quasistatic Modeling of a Soft Finger-Like Robotic Appendage for Real-Time Position and Force Estimation*. Soft Robotics, 6(2):228–249, 2019.

[ST04]   SIMAAN, NABIL and RUSSELL TAYLOR: *A dexterous system for laryngeal surgery - multi-backbone bending snake-like slaves for teleoperated dexterous surgical tool manipulation*. In *in IEEE International Conference on Robotics and Automation*, pages 351–357, 2004.

[STA15]   SEON, JEAN-ANTOINE, BRAHIM TAMADAZTE and NICOLAS ANDREFF: *Decoupling Path Following and Velocity Profile in Vision-Guided Laser Steering.* IEEE Transactions on Robotics, 31(2):280–289, March 2015.

[Ste93]   STEINER, WOLFGANG: *Results of curative laser microsurgery of laryngeal carcinomas.* American Journal of Otolaryngology, 14(2):116 – 121, 1993.

[STL15]   SU, B., J. TANG and H. LIAO: *Automatic laser ablation control algorithm for an novel endoscopic laser ablation end effector for precision neurosurgery.* In *2015 IEEE/RSJ International Conference on Intelligent Robots and Systems (IROS)*, pages 4362–4367, Sept 2015.

[Sve16]   SVELTO, O.: *Principles of Lasers.* Springer US, 2016.

[SWA14]   STILLI, A., H. A. WURDEMANN and K. ALTHOEFER: *Shrinkable, stiffness-controllable soft manipulator based on a bio-inspired antagonistic actuation principle.* In *2014 IEEE/RSJ International Conference on Intelligent Robots and Systems*, pages 2476–2481, Sep. 2014.

[SXK+09]   SIMAAN, NABIL, KAI XU, ANKUR KAPOOR, WEI WEI, PETER KAZANZIDES, PAUL FLINT and RUSSELL TAYLOR: *Design and Integration of a Telerobotic System for Minimally Invasive Surgery of the Throat.* 28:1134–1153, 09 2009.

[SZ11]   SANDELL, JULIA L. and TIMOTHY C. ZHU: *A review of in-vivo optical properties of human tissues and its impact on PDT.* Journal of Biophotonics, 4(11-12):773–787, 2011.

[TBR+03]   TANG, HSIAO-WEI, H. VAN BRUSSEL, D. REYNAERTS, J. VANDER SLOTEN and P. R. KONINCKX: *A laparoscopic robot with intuitive interface for gynecological laser laparoscopy.* In *2003 IEEE International Conference on Robotics and Automation*, volume 2, pages 2646–2650 vol.2, Sept 2003.

[TBS+05]   TANG, H-W, H VAN BRUSSEL, J VANDER SLOTEN, D REYNAERTS and P R KONINCKX: *Implementation of an Intuitive Writing Interface and a Laparoscopic Robot for Gynaecological Laser Assisted Surgery.* Proceedings of the Institution of Mechanical Engineers, Part H: Journal of Engineering in Medicine, 219(4):293–302, 2005.

[TBS+06]   TANG, HSIAO-WEI, HENDRIK VAN BRUSSEL, JOS VANDER SLOTEN, DOMINIEK REYNAERTS, GUNTER DE WIN, BEN VAN CLEYNENBREUGEL and PHILIPPE R. KONINCKX: *Evaluation of an intuitive writing interface in robot-aided laser laparoscopic surgery.* Computer Aided Surgery, 11(1):21–30, 2006.

[TD95]   TAN FUNG CHAN and R. V. DUBEY: *A weighted least-norm solution based scheme for avoiding joint limits for redundant joint manipulators.* IEEE Transactions on Robotics and Automation, 11(2):286–292, 1995.

[TGW14]   TONAPI, M. M., I. S. GODAGE and I. D. WALKER: *Design, modeling and performance evaluation of a long and slim continuum robotic cable*. In *2014 IEEE/RSJ International Conference on Intelligent Robots and Systems*, pages 2852–2859, Sep. 2014.

[THE+14]   TAUDORF, E. H., C. S. HAAK, A. M. ERLENDSSON, P. A. PHILIPSEN, R. R. ANDERSON, U. PAASCH and M. HAEDERSDAL: *Fractional ablative erbium YAG laser: histological characterization of relationships between laser settings and micropore dimensions*. Lasers Surg Med, 46(4):281–289, Apr 2014.

[TMCG02]   THUILOT, B., P. MARTINET, L. CORDESSES and J. GALLICE: *Position based visual servoing: keeping the object in the field of vision*. In *Proceedings 2002 IEEE International Conference on Robotics and Automation (Cat. No.02CH37292)*, volume 2, pages 1624–1629 vol.2, May 2002.

[TNR+17]   TONTINI, GIAN EUGENIO, HELMUT NEUMANN, ALESSANDRO RIMONDI, SARA VAVASSORI, BARBARA BRUNI, GREGORIO CATTIGNOLI, PING-HONG ZHOU, LUCA PASTORELLI and MAURIZIO VECCHI: *Ex vivo experimental study on the Thulium laser system: new horizons for interventional endoscopy (with videos)*. Endoscopy international open, 5(6):E410–E415, Jun 2017.

[Trä12]   TRÄGER, F.: *Springer Handbook of Lasers and Optics*. Springer Handbooks. Springer Berlin Heidelberg, 2012.

[TRS+18]   TAMADAZTE, B., R. RUPERT, J. A. SEON, A. KUDRYAVTSEV and N. ANDREFF: *Laser Beam Steering Along 3D Paths*. IEEE/ASME Transactions on Mechatronics, pages 1–1, 2018.

[TSWJ16]   TORRE, LINDSEY A., REBECCA L. SIEGEL, ELIZABETH M. WARD and AHMEDIN JEMAL: *Global Cancer Incidence and Mortality Rates and Trends—An Update*. Cancer Epidemiology and Prevention Biomarkers, 25(1):16–27, 2016.

[TWD07a]   TATLICIOGLU, E., I. D. WALKER and D. M. DAWSON: *Dynamic Modelling for Planar Extensible Continuum Robot Manipulators*. In *Proceedings 2007 IEEE International Conference on Robotics and Automation*, pages 1357–1362, April 2007.

[TWD07b]   TATLICIOGLU, E., I. D. WALKER and D. M. DAWSON: *New dynamic models for planar extensible continuum robot manipulators*. In *2007 IEEE/RSJ International Conference on Intelligent Robots and Systems*, pages 1485–1490, Oct 2007.

[UMF+13]   URICH, A., R.R.J. MAIER, Y. FEI, J.C. KNIGHT, D.P. HAND and J.D. SHEPHARD: *Flexible delivery of Er:YAG radiation at 2.94 µm with negative curvature silica glass fibers: A new solution for minimally invasive surgical procedures*. Biomedical Optics Express, 4(2), 2013.

[VCM+10] VESCOVI, PAOLO, LUIGI CORCIONE, MARCO MELETI, ELISABETTA MERIGO, CARLO FORNAINI, MADDALENA MANFREDI, MAURO BONANINI, PAOLO GOVONI, JEAN-PAUL ROCCA and SAMIR NAMMOUR: *Nd:YAG laser versus traditional scalpel. A preliminary histological analysis of specimens from the human oral mucosa*. Lasers in Medical Science, 25(5):685–691, Sep 2010.

[VDE16] VDE - ASSOCIATION FOR ELECTRICAL, ELECTRONIC & INFORMATION TECHNOLOGIES: *DIN EN 60601-2-18:2016-10 - Medical electrical equipment - Part 2-18: Particular requirements for the basic safety and essential performance of endoscopic equipment*. Technical Report, VDE - Association for Electrical, Electronic & Information Technologies, 2016.

[VDI93] VDI - ASSOCIATION OF GERMAN ENGINEERS: *VDI 2221 - Systematic approach to the development and design of technical systems and products*. Technical Report, May 1993.

[VDI04] VDI - ASSOCIATION OF GERMAN ENGINEERS: *VDI 2206 - Design methodology for mechatronic systems*. Technical Report, 2004.

[vdMS09] MEIJDEN, O. A. J. VAN DER and M. P. SCHIJVEN: *The value of haptic feedback in conventional and robot-assisted minimal invasive surgery and virtual reality training: a current review*. Surgical Endoscopy, 23(6):1180–1190, Jun 2009.

[vdPGJD08] PUTTEN, E. P. WESTEBRING VAN DER, R. H. M. GOOSSENS, J. J. JAKIMOWICZ and J. DANKELMAN: *Haptics in minimally invasive surgery - a review*. Minimally Invasive Therapy & Allied Technologies, 17(1):3–16, 2008.

[VLCY13] VITIELLO, V., S. LEE, T. P. CUNDY and G. YANG: *Emerging Robotic Platforms for Minimally Invasive Surgery*. IEEE Reviews in Biomedical Engineering, 6:111–126, 2013.

[VOKSA+16] VAZQUEZ-OTERO, A., D. KHIKHLUKHA, J. M. SOLANO-ALTAMIRANO, R. DORMIDO and N. DURO: *Laser Spot Detection Based on Reaction Diffusion*. Sensors (Basel), 16(3):315, Mar 2016.

[WCMG06] WALKER, IAN D., CARLOS CARRERAS, ROBIN MCDONNELL and GEORGE GRIMES: *Extension versus Bending for Continuum Robots*. International Journal of Advanced Robotic Systems, 3(2):26, 2006.

[WD89] WALSH, J. T. and T. F. DEUTSCH: *Er:YAG laser ablation of tissue: measurement of ablation rates*. Lasers Surg Med, 9(4):327–337, 1989.

[WE14] WEBSTER, J.G. and H. EREN: *Measurement, Instrumentation, and Sensors Handbook, Second Edition: Electromagnetic, Optical, Radiation, Chemical, and Biomedical Measurement*. CRC Press, 2014.

[WE15] WEBER, BERNHARD and CLARA EICHBERGER: *The Benefits of Haptic Feedback*

in Telesurgery and Other Teleoperation Systems: A Meta-Analysis. In ANTONA, MARGHERITA and CONSTANTINE STEPHANIDIS (editors): *Universal Access in Human-Computer Interaction. Access to Learning, Health and Well-Being*, pages 394–405, Cham, 2015. Springer International Publishing.

[WNV+16] WALKER, I. D., D. NAHAR, S. VERMA, M. B. WOOTEN and A. D. KAPADIA: *Challenges in creating long continuum robots.* In *2016 21st International Conference on Methods and Models in Automation and Robotics (MMAR)*, pages 339–344, Aug 2016.

[WOC06] WEBSTER, R. J., A. M. OKAMURA and N. J. COWAN: *Toward Active Cannulas: Miniature Snake-Like Surgical Robots.* In *2006 IEEE/RSJ International Conference on Intelligent Robots and Systems*, pages 2857–2863, Oct 2006.

[WSJH07] WAGNER, C. R., N. STYLOPOULOS, P. G. JACKSON and R. D. HOWE: *The Benefit of Force Feedback in Surgery: Examination of Blunt Dissection.* Presence, 16(3):252–262, June 2007.

[WT82] WAGNER, R. E. and W. J. TOMLINSON: *Coupling efficiency of optics in single-mode fiber components.* Appl. Opt., 21(15):2671–2688, Aug 1982.

[WvG11] WELCH, A.J. and M.J.C. VAN GEMERT: *Optical-Thermal Response of Laser-Irradiated Tissue.* Springer Netherlands, 2011.

[YCC+17] YANG, GUANG-ZHONG, JAMES CAMBIAS, KEVIN CLEARY, ERIC DAIMLER, JAMES DRAKE, PIERRE E. DUPONT, NOBUHIKO HATA, PETER KAZANZIDES, SYLVAIN MARTEL, RAJNI V. PATEL, VERONICA J. SANTOS and RUSSELL H. TAYLOR: *Medical robotics—Regulatory, ethical, and legal considerations for increasing levels of autonomy.* Science Robotics, 2(4), 2017.

[YG12] YEUNG, BALDWIN PO MAN and TERENCE GOURLAY: *A technical review of flexible endoscopic multitasking platforms.* International Journal of Surgery, 10(7):345 – 354, 2012.

[YLLS06] YU, M.-T., T.-Y. LIN, Y.-Y. LI and P.-F. SHU: *Study on the Optimization Methods for Optomechanical Alignment.* In *Proc. of SPIE Vol. 6289*, 2006.

[YMI09] YANO, H., Y. MIYAMOTO and H. IWATA: *Haptic interface for perceiving remote object using a laser range finder.* In *World Haptics 2009 - Third Joint EuroHaptics conference and Symposium on Haptic Interfaces for Virtual Environment and Teleoperator Systems*, pages 196–201, March 2009.

[YMM+16] YANG, S., R. A. MACLACHLAN, J. N. MARTEL, L. A. LOBES and C. N. RIVIERE: *Comparative Evaluation of Handheld Robot-Aided Intraocular Laser Surgery.* IEEE Transactions on Robotics, 32(1):246–251, Feb 2016.

[YSLL19] YU, XIA, BIAO SUN, JIAQI LUO and ELIZABETH LEE: *Optical Fibers for*

High-Power Lasers, pages 877–894. Springer Singapore, Singapore, 2019.

[YYM⁺10]   YAMANAKA, N., H. YAMASHITA, K. MASAMUNE, T. CHIBA and T. DOHI: *An Endoscope With 2 DOFs Steering of Coaxial Nd:YAG Laser Beam for Fetal Surgery*. IEEE/ASME Transactions on Mechatronics, 15(6):898–905, Dec 2010.

[Zha00]   ZHANG, Z.: *A flexible new technique for camera calibration*. IEEE Transactions on Pattern Analysis and Machine Intelligence, 22(11):1330–1334, Nov 2000.

[ZPW⁺14]   ZHANG, YAOKUN, TOM PFEIFFER, MARCEL WELLER, WOLFGANG WIESER, ROBERT HUBER, JÖRG RACZKOWSKY, JÖRG H. SCHIPPER, HEINZ WÖRN and THOMAS KLENZNER: *Optical Coherence Tomography Guided Laser Cochleostomy: Towards the Accuracy on Tens of Micrometer Scale*. In *BioMed research international*, 2014.

[ZQD16]   ZHANG, KETAO, CHEN QIU and JIAN S. DAI: *An Extensible Continuum Robot With Integrated Origami Parallel Modules*. Journal of Mechanisms and Robotics, 8(3):031010–031010–9, Mar 2016.

[ZS84]   ZHANG, T. Y. and C. Y. SUEN: *A Fast Parallel Algorithm for Thinning Digital Patterns*. Commun. ACM, 27(3):236–239, March 1984.

[ZSJ⁺18]   ZHANG, Y., H. SUN, Y. JIA, D. HUANG, R. LI, Z. MAO, Y. HU, J. CHEN, S. KUANG, J. TANG, X. XIAO and B. SU: *A Continuum Robot with Contractible and Extensible Length for Neurosurgery*. In *2018 IEEE 14th International Conference on Control and Automation (ICCA)*, pages 1150–1155, June 2018.

[ZVM⁺04]   ZAFFE, D., M. C. VITALE, A. MARTIGNONE, F. SCARPELLI and A. R. BOTTICELLI: *Morphological, Histochemical, and Immunocytochemical Study of CO2 and Er:YAG Laser Effect on Oral Soft Tissues*. Photomedicine and Laser Surgery, 22(3):185–189, 2004.

[ZXYZ07]   ZHANG, X., S. XIE, Q. YE and Z. ZHAN: *An Observation of Ablation Effect of Soft Biotissue by pulsed Er:YAG Laser*. In *Proc. of SPIE*, volume 6435, 2007.

A Linear Motion Unit Concepts

Note: In the following, joint index j with $j = \{1,2\}$ indicates joint space q_j and drive-sided joint state $q_{\mathrm{mot},j}$ as well as its corresponding time derivatives. The range of displacement for concentrically guided tubings, i.e. tube_2 encloses tube_1, is annotated by tube_j and movable LMU carriers are labelled by $\mathrm{carrier}_j$.

Concept (I)**:** The first concept describes a spindle-based LMU design with stationary drive components. The proposed design targets a parallel layout of drive units, shafts, and spindles as depicted in Figure A.1. Linear motion is generated from direct rotary-to-linear conversion in combination with force constraints from guidance with additional linear bearings. Linear motion of each axis is transmitted to $\mathrm{carrier}_1$ and $\mathrm{carrier}_2$ that constitute joint spaces q_1 and q_2, respectively. Carriers mount detachable collets for clamping of actuation tubes or sensors. By analogy with design considerations presented in Section 4.3.1, the spatial alignment of collets in the LMU structure must be coaxial, i.e. tubes show relative motion with minimal friction (absence of tube bending is assumed). In accordance with [GA09], this mechanism yields joint velocities

$$\begin{pmatrix} \dot{q}_1 \\ \dot{q}_2 \end{pmatrix} = \begin{pmatrix} i_{\mathrm{rg},1} p_{\mathrm{SD},1} & 0 \\ 0 & i_{\mathrm{rg},2} p_{\mathrm{SD},2} \end{pmatrix} \begin{pmatrix} \dot{q}_{\mathrm{mot},1} \\ \dot{q}_{\mathrm{mot},2} \end{pmatrix}, \tag{A.1}$$

where $i_{\mathrm{rg},j}$ is the reduction ratio of the associated gearheads and $p_{\mathrm{SD},j}$ are the spindle leads. Forces acting on each carrier are

$$\begin{pmatrix} F_{\mathrm{SD},1} \\ F_{\mathrm{SD},2} \end{pmatrix} = \begin{pmatrix} i_{\mathrm{rg},1}^{-1} \frac{2\pi \eta_{\mathrm{SD},1}}{p_{\mathrm{SD},1}} & 0 \\ 0 & i_{\mathrm{rg},2}^{-1} \frac{2\pi \eta_{\mathrm{SD},2}}{p_{\mathrm{SD},2}} \end{pmatrix} \begin{pmatrix} \tau_{\mathrm{mot},1} \\ \tau_{\mathrm{mot},2} \end{pmatrix}, \tag{A.2}$$

where $\eta_{\mathrm{SD},j}$ defines the spindle transmission efficiency and $\tau_{\mathrm{mot},j}$ are drive-sided torques. A spindle-driven design enables a compact implementation. Specifically, complex wire routing is prevented with stationary drives. Minor challenges arise from parallel shaft alignment for guidance of linear bearings and spindles. Major drawbacks are dedicated to disregard of mechanical coupling in joint space. For example, as shown in Figure A.1, when $\mathrm{carrier}_1$ is displaced in the indicated motion direction, the displacement range of tube_1 increases by Δq_1. The length of tube_2 decreases equivalently. Hence, the configuration of the second segment is affected. Mitigation can be achieved at control level by generation of compensation displacements related to position differences Δq_1 added to current joint state q_2. This ensures perpetuation of the free length of tube_2 while motion of tube_1 is present.

Sensors for joint limit detection may be integrated adjacent to moving carriers and attached to housing components.
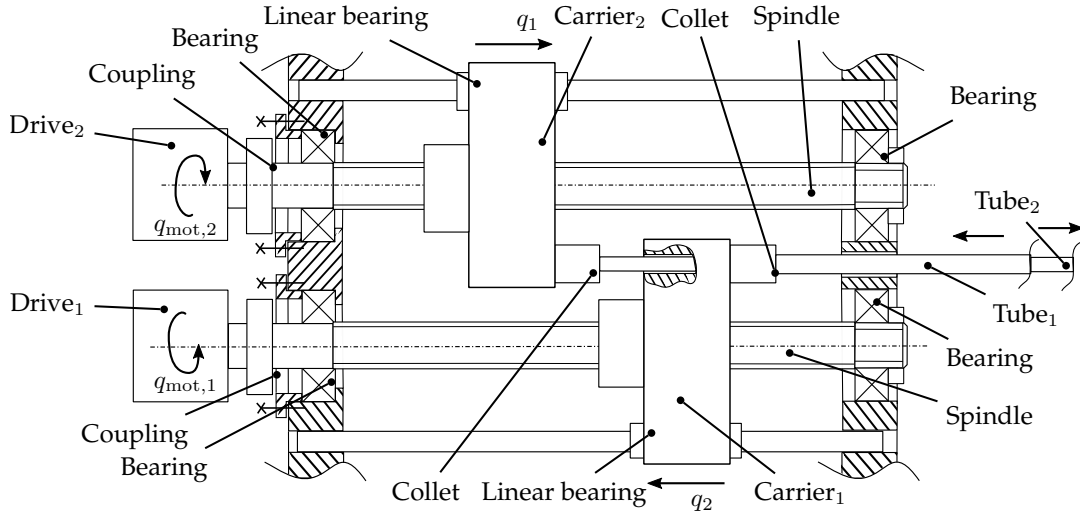
Fig. A.1: Schematics of concept (I) for realisation of a two DoF linear motion unit with stationary spindle drives.

Concept (II)**:** The concept in Figure A.2 is inspired by concept (I) but uses belt-driven motion generation for carrier$_1$ and carrier$_2$. Toothed belts are employed for angular to linear motion conversion. Bevel gears with intersecting orthogonal axis in combination with connectors are considered for compact implementation of drive pulley axes. Both belts are supported by a secondary adjustable axis for belt pretensioning. Motion of both carriers results in linear tube displacement described by joint state q_1 and q_2. This enables tube displacement with collet clamping of corresponding concentric tubes. With assumption of simplified mechanical effects (e.g. disregard of friction), LMU joint velocities are:

$$\begin{pmatrix} \dot{q}_1 \\ \dot{q}_2 \end{pmatrix} = \begin{pmatrix} i_{\mathrm{rg},1} i_{\mathrm{bg},1} \frac{d_{\mathrm{p},1}}{2} & 0 \\ 0 & i_{\mathrm{rg},2} i_{\mathrm{bg},2} \frac{d_{\mathrm{p},2}}{2} \end{pmatrix} \begin{pmatrix} \dot{q}_{\mathrm{mot},1} \\ \dot{q}_{\mathrm{mot},2} \end{pmatrix}, \tag{A.3}$$

where $i_{\mathrm{rg},j}$ is the reduction ratio of the gearhead (e.g. planetary gear), $i_{\mathrm{bg},j}$ the bevel gear ratio, and $d_{\mathrm{p},j}$ is the diameter of belt pulleys. Circumferential forces transmitted to carriers yield under disregard of carrier friction to

$$\begin{pmatrix} F_{\mathrm{SD},1} \\ F_{\mathrm{SD},2} \end{pmatrix} = \begin{pmatrix} i_{\mathrm{rg},1}^{-1} i_{\mathrm{bg},1}^{-1} \frac{2}{d_{\mathrm{p},1}} & 0 \\ 0 & i_{\mathrm{rg},2}^{-1} i_{\mathrm{bg},2}^{-1} \frac{2}{d_{\mathrm{p},2}} \end{pmatrix} \begin{pmatrix} \tau_{\mathrm{mot},1} \\ \tau_{\mathrm{mot},2} \end{pmatrix}. \tag{A.4}$$

Beyond advantages of concept (I), this design demonstrates improved joint dynamics compared to spindle transmission, but the belt tension must be maintained in order to avoid backlash. Magnitudes of transmitted forces are lower. Bespoke mechanisms for belt ten-

sioning must be integrated to the assembly and may contradict a compact implementation. On the contrary, the total weight of a LMU may be reduced from substitution of spindle components.
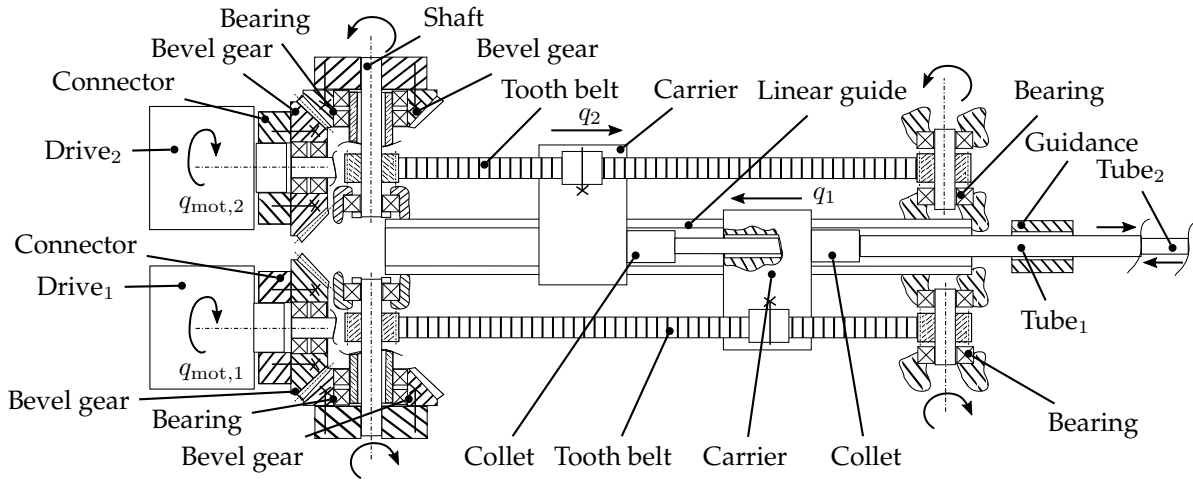
Fig. A.2: Schematics of concept (II) for realisation of a belt driven two DoF linear motion unit.

Concept (III)**:** The approach depicted in Figure A.3 extends concept (I) but augments a cascaded and coupled mechanism for mechanical compensation of tubular free length differences as proposed in [SXK$^+$09]. The cascaded structure is implemented with stationary drive$_1$ and mobile drive$_2$. Drive$_1$ displaces carrier$_1$ supported by a linear rail which represents the mechanical frame for carrier$_2$ and drive$_2$. Invoked motion of carrier$_1$ is implicitly transmitted to carrier$_2$ such that free lengths differences are intrinsically compensated and segmental configurations are maintained.

The impact of mechanical coupling on joint velocities is expressed in a fixed reference frame as follows:

$$\begin{pmatrix} \dot{q}_1 \\ \dot{q}_2 \end{pmatrix} = \begin{pmatrix} i_{\mathrm{rg},1} p_{\mathrm{SD},1} & 0 \\ i_{\mathrm{rg},1} p_{\mathrm{SD},1} & i_{\mathrm{rg},2} p_{\mathrm{SD},2} \end{pmatrix} \begin{pmatrix} \dot{q}_{\mathrm{mot},1} \\ \dot{q}_{\mathrm{mot},2} \end{pmatrix}. \tag{A.5}$$

Actuation forces are equivalently given by

$$\begin{pmatrix} f_{\mathrm{SD},1} \\ f_{\mathrm{SD},2} \end{pmatrix} = \begin{pmatrix} i_{\mathrm{rg},1}^{-1} \frac{2\pi \eta_{\mathrm{SD},1}}{p_{\mathrm{SD},1}} & 0 \\ i_{\mathrm{rg},1}^{-1} \frac{2\pi \eta_{\mathrm{SD},1}}{p_{\mathrm{SD},1}} & i_{\mathrm{rg},2}^{-1} \frac{2\pi \eta_{\mathrm{SD},2}}{p_{\mathrm{SD},2}} \end{pmatrix} \begin{pmatrix} \tau_{\mathrm{mot},1} \\ \tau_{\mathrm{mot},2} \end{pmatrix}. \tag{A.6}$$

This approach obviates compensation of joint space displacement q_2 at control level due to the intrinsic displacement of the entire corresponding spindle unit. However, drive$_2$ experiences motion and the additional weight may reduce dynamics of joint q_1. An adapted wire routing is mandatory to avoid motion-induced damage or disturbances of signal transmission, i.e. compliance with electromagnetic compatibility (EMC). As discussed for concept (I), a

parallel component layout facilitates integration of sensors for joint limit detection or position measurement.
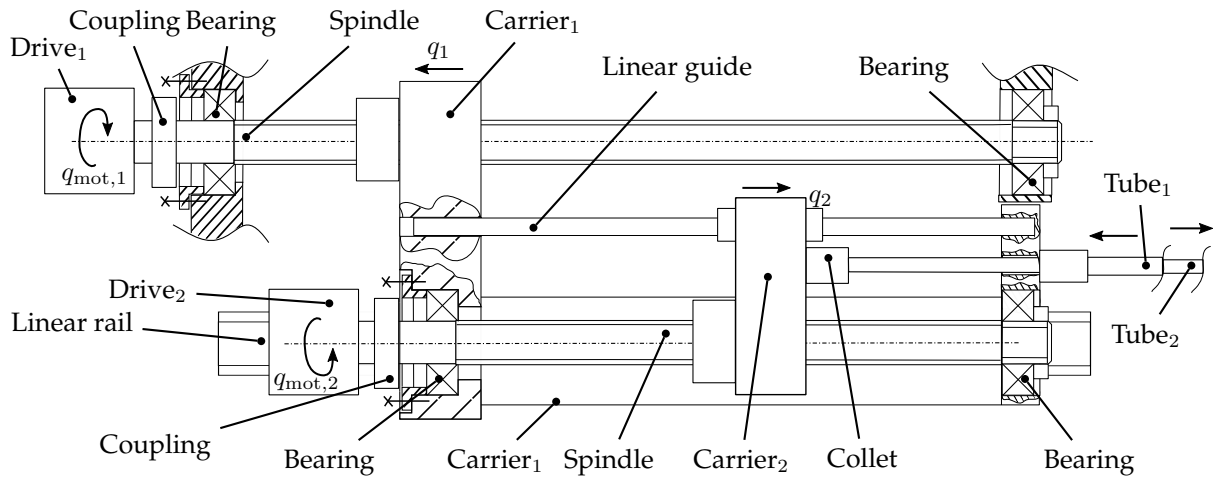
Fig. A.3: Schematics of concept (III) for realisation of a two DoF linear motion unit with stationary and mobile drive units.

B Joint Limit Sensing Concepts

Concept (I): The range of motion of each stage in a LMU may be limited by mechanical hard stops and monitored with current sensing at drive side. This approach avoids additional sensors if motor currents can be measured and processed. Motion of LMU stages approaching position limits is inhibited by mechanical end stops. This causes a motor stall and a corresponding current peak to maintain the nominal motion. If the monitored current exceeds a predefined threshold, the end stop is detected and the drive control is set to idle. However, disadvantages are linked to calibration and sensitivity of the stall detection, noisy motor readings, and impact of non-linear friction on mechanical components. Stall detection may be indicated at incorrect positions causing disturbance of reference motions. Nonetheless, precision engineered spindle drives are highly prone to structural damage from torque exposure and non-axial forces.

Concept (II): Mechanical limit switches are an electromechanical approach for proximity detection of stationary and moving components. Commercial limit switches use spring-loaded lever mechanisms in different design variants triggered by contact forces for interruption of the ground-level connection and switching to a specific trigger level. A set of reviewed sensors is provided in Table C.1 in Appendix C. This enables economical limit detection based on physical contacts. However, reviewed housing footprints violate dimensional requirements and design paradigms. Additionally, a high number of switching cycles may cause degradation of the lever mechanism and inhibit trigger detection. Industrial limit switches further restrict integration. Firstly, orthogonally aligned levers may be triggered by normal forces generated from moving carriers in contact. Secondly, sensor levers may be aligned in parallel to carrier motions. This layout requires precise adjustment of the activation threshold and prevents compact integration due to protruding parts.

Concept (III): Optical limit switches are composed of light emitting diodes and phototransistors. The sensing principle uses interruption of the emitted and collected light. Two design variations, i.e. slotted and reflective layouts, are commercially available. Slotted designs consider an opposite arrangement of emitter and collector that is interrupted by slot coverage. By contrast, the reflective design uses an adjacent layout and intensity modulation is triggered by distances to reflective objects. A selection of miniature optical sensors is listed in Table C.2. The availability of sensors at small scale and contactless triggers enables integration to LMU designs. However, the sensor principle requires direct line-of-sight and optimal environmental conditions, i.e. absence of illumination disturbances. Lastly, working distances are physically limited and determined by the sensor layout. Less hysteresis compared to lever mechanisms

is expected from wire installation and covers. This prevents inadvertent activation from optical path interruption.

Concept (IV): This concept considers capacitive or inductive proximity sensors. The latter may be mounted to stationary or moving LMU components to sense the proximity of adjacent elements within the specific sensing range. Both sensors use high-frequency electromagnetic fields generated by coil-based oscillators. Sensors in short distance to moving target surfaces form a capacitor. It changes the capacity related to the surface distance. This effect attenuates the amplitude of the oscillator and may be detected by signal postprocessing. Inductive sensors use metallic targets for generation of eddy currents from electromagnetic induction. The inducted current increases with decreasing distance of the surface and likewise attenuates the oscillation. Processing of the oscillation signal enables mapping to a distance measure. Common sensor designs enable adjustment of activation distances in specific ranges. Despite of small housing diameters ($<$ 4 mm) of commercial capacitive and inductive sensors listed in appendix Table C.3, sensor lengths may exceed 20 mm due to the integration of oscillators and embedded circuits. Sensing ranges are restricted to less than 2 mm. One variant comprises a sensor interface alignment parallel to carrier motion directions. A second approach concerns perpendicular integration. The latter significantly increases housing diameters due to protruding sensor elements. This is contradictory to a compact integration.

C Sensor Specifications

Tab. C.1: Selection of commercially available mechanical limit switches.

Type	Manufacturer	Dimension (mm)	Length (mm)
SHL	OMRON	48×17.5	45
SS-5GL	OMRON	17×6	20
V15W	Honeywell	10.3×15.9	33
V7-1C17D8	Honeywell	10.2×18.2	28.8
54-417-BP	NTE Electronics	7×18	22

Tab. C.2: Selection of commercially available optical limit switches with slotted (S) and reflective designs (R).

Type	Manufacturer	Range (mm)	Dimension (mm)	Length (mm)	Type
EE-SX1321	OMRON	2	5×4	3	S
VCNT2020	Vishay	0.2 - 2.5	0.8×2	2.5	R
OPB9000	TT Electronics	12	2.2×1.5	4	R
TCPT1600X01	Vishay	3	5.7×3.4	5.5	S
OPB890P55Z	TT Electronics	3.18	15.75×4.5	18.47	S

Tab. C.3: Selection of commercially available capacitive (C) and inductive (I) miniature proximity sensors.

Type	Manufacturer	Working distance (mm)	Dimension (mm)	Length (mm)	Principle
S3870	Fargo Control, Inc.	1	$\varnothing 3$	25	I
CQ4	Sick AG	8	12×16	39	C
E2E-C03N	OMRON	2	$\varnothing 3$	22	C
TL-W5MC1	OMRON	1.5	8×5	25	I
03N1505	Baumer	0.8	$\varnothing 3$	12	I
871C3	Rockwell	1	$\varnothing 3$	22	I
D-E21	Physik Instrumente (PI)	1	$\varnothing 5$	22	C

Tab. C.4: Selection of commercially available unipolar Hall effect switches.

Type	Manufacturer	Sensitivity (mT)	Dimension (mm)	Length (mm)
DRV5023BI	Texas Instruments	14.5	1.3×1.2	2.92
AH1389	Diodes Incorporated	4	1.7×1.2	1.8
HAL3725DJ-A	Micronas	20	6×1.2	5
Si7201-B-05-IVR	Silicon Labs	4	3×1.6	4
US5683ESE	Melexis	5.5	3×1.1	3

D Reprint Permissions

Table D.1 summarises third-party references where figures/images were reused with kind permission of the publishers. If available, this includes the license numbers provided by the Copyright Clearance Center.

Tab. D.1: Credits to third-party references for reprinting of figures.

	Reference	Publisher	License
Figure 1.6a	[SNP$^+$11]	IEEE	No license required for reuse in thesis
Figure 1.6b	[BRGL$^+$18]	Springer Nature	CCBY license
Figure 1.6c	[SSL$^+$14a]	IEEE	No license required for reuse in thesis
Figure 1.6d	[DCWZ06]	IEEE	No license required for reuse in thesis
Figure 1.6e	[LYR$^+$15]	IEEE	No license required for reuse in thesis
Figure 1.6f	[LKL$^+$14]	IEEE	No license required for reuse in thesis
Figure 1.7a	[LWG$^+$17]	IEEE	No license required for reuse in thesis
Figure 1.7b	[ABRP07]	IEEE	No license required for reuse in thesis
Figure 1.7c	[LKR$^+$13]	IEEE	No license required for reuse in thesis
Figure 1.8a	[SXK$^+$09]	IEEE	No license required for reuse in thesis
Figure 1.8b	[GWC$^+$19]	IEEE	No license required for reuse in thesis
Figure 1.8c	[KOK$^+$16]	IEEE	No license required for reuse in thesis
Figure 1.8d	[AKF$^+$16]	IEEE	No license required for reuse in thesis
Figure 1.8e	[KCD18]	IEEE	No license required for reuse in thesis
Figure 1.8f	[SBD$^+$16]	Springer Nature	5046911477656
Figure 1.8g	[MKHA13]	IEEE	No license required for reuse in thesis
Figure 1.8h	[AOS18]	IEEE	No license required for reuse in thesis
Figure 1.8i	[WOC06]	IEEE	No license required for reuse in thesis

Table D.2 summarises the publications related to research contributions of this thesis. The figures, tables, and content of chapters have partially been reproduced from listed references with kind permission of the publishers. If available, the list includes the license numbers provided by the Copyright Clearance Center.

Tab. D.2: Credits to references associated with the research of this thesis.

	Reference	Publisher	License
Figures 1.2a / 1.2b	[KSKO14a]	Springer Nature	5020901349349
Figures 2.8a / 2.8b	[SKKO15]	Springer Nature	5047120533337
Figures 2.9b / 2.9a / 2.9c / 2.9d	[SKKO17]	Elsevier	CCBY license
Figures, tables, and content of Chapter 3	[KFS$^+$16]	SPIE	Granted by email (K. Sinclair, Ed. Office)
Figures, tables, and content of Chapter 4	[KGS$^+$20]	Springer Nature	CCBY license
Figures, tables, and content of Chapter 6	[KSP$^+$19]	IEEE	No license required for reuse in thesis
Figures, tables, and content of Chapter 7	[KGS$^+$20]	Springer Nature	CCBY license

E Curriculum Vitae

Personal Details

Name	Dennis Kundrat
Nationality	German

Work Experience

since Jan/22	Senior Researcher
	RAM Group, University of Twente
Nov/20 - Dec/21	Innovation and Technology Transfer Manager
	Hannover Medical School
Jul/18 - Nov/20	Research Associate
	Hamlyn Centre for Robotic Surgery, Imperial College London
Jul/12 - Oct/17	Research Assistant
	Institute of Mechatronic Systems, Leibniz Universität Hannover

Academic education

Apr/12	Mechanical Engineering (Diplom-Ingenieur)
	Leibniz Universität Hannover
Mar/08	Aerospace Engineering (Prediploma)
	Technische Universität Berlin

Student Experiences and Internships

Sep/10 - Feb/11	Internship
	Product Innovation, Weinmann Geräte für Medizin GmbH, Hamburg
Mar/09 - Aug/10	Student Assistant
	Laboratory for Biomechanics, Hannover Medical School
Sep/09 - Oct/09	Internship
	R & D and Manufacturing, Otto Bock Healthcare GmbH, Duderstadt
Aug/07 - Oct/07	Internship
	Technology Services, Continental AG, Hannover

School education

Aug/97 - Jul/04	Otto Hahn Gymnasium, Springe
Aug/95 - Jul/97	Orientierungsstufe Süd, Springe
Aug/91 - Jul/95	Grundschule Hinter der Burg, Springe